THE MECHANICAL BEHAVIOR OF MARAGING STEEL UNDER EXTREME ELECTROMECHANICAL AND THERMAL CONDITIONS

by

Peter J. Raboin

B.S. Georgia Institute of Technology
(1982)

S.M. Massachusetts Institute of Technology
(1985)

Submitted to the
Department of Mechanical Engineering
in Partial Fulfillment of the Requirements for
the Degree of

DOCTOR OF SCIENCE

at the

MASSACHUSETTS INSTITUTE OF TECHNOLOGY

May 26, 1989

Signature of Author_____
Department of Mechanical Engineering
May 26, 1989

Certified by_____
F.A. McClintock
Chairman, Doctoral Committee

Accepted by_____
Ain A. Sonin
Chairman, Graduate Committee

THE MECHANICAL BEHAVIOR OF MARAGING STEEL UNDER EXTREME ELECTROMECHANICAL AND THERMAL CONDITIONS

by

PETER J. RABOIN

Submitted to the department of Mechanical Engineering
on May 10, 1989 in partial fulfillment of the
requirements for the Degree of Doctor of Science in
Mechanical Engineering

ABSTRACT

The mechanical behavior of maraging steel is studied for the design and analysis of short pulse, high magnetic field magnets. First, the mechanical behavior of maraging steel is tested between 770 and 1080 K for plastic strain rates between 10^{-6} and 10^{-2} s^{-1}. Then models are proposed to predict flow strength and dilatational strain. Second, these models are incorporated into a time-dependent plastic finite element analysis program which models the extreme loading conditions. Shape changes and double necking were successfully predicted in uniaxial tapered, constrained pulse-cycled specimens. A program was written to predict the pulsed Lorentz body forces (350 N/mm^3) and temperature changes (298-1450 K) within a short pulse (50 T in 45 μs) magnet. The final part of this thesis details the design, construction, testing, and failure analysis of a test coil. This experiment confirmed design predictions, and the coil failed because melting at crack tips caused an electrical explosion. From a crack-tip model, and pulse-cycled experiments, an "adiabatic" crack size is calculated and used as a critical size for fatigue life predictions. Recommendations are made for predicting and improving the life of short pulse magnets.

Thesis Advisor : Dr. Emanuel S. Bobrov
Title : Project Leader, Francis Bitter National Magnet Laboratory
Chairman, Doctoral Committee : Dr. Frank A. McClintock
Title : Professor of Mechanical Engineering

ACKNOWLEDGEMENTS

The author wishes to thank his wife Ellen for her love, patience and sacrifices during these six years of graduate work. The author also wishes to thank his parents for their encouragement and support. The author is indebted to Dr. Emanuel Bobrov, his thesis advisor, for his enduring support, advise and experience. The author is grateful to Prof. McClintock for his valuable guidance, insight and contributions to this research and thesis. The unique perspectives and expertise of both Dr. Bobrov and Prof. McClintock have been a valuable source of knowledge to this thesis. The author thanks John Williams for the opportunity, confidence, advice and time he has given to this work. The author also wishes to thank thank Prof. Anand for his thesis committee participation and especially his advice on matters concerning the implementation of time-dependent plasticity into the finite element method. The author thanks Glen Romanoski for his work on the cyclic fatigue tests. Special recognition goes to Guy Pollard who machined the destructible test coil, most of the tensile specimens and the thermal cycling apparatus. He has also contributed several fine photographs to this thesis. His excellent work is appreciated. Finally, the author wants to acknowledge Ken Holmes for his assistance this last year and Ray Cravey for drawing Fig. 6.4.

Funding for this project has been provided by the National Science Foundation through the Francis Bitter National Magnet Laboratory.

TABLE OF CONTENTS

LIST OF TABLES AND FIGURES

Tables

Figures

INTRODUCTION

The purpose of our research into the mechanical behavior of maraging steel under extreme electromechanical and thermal conditions is to predict the behavior, for improving the design, of short pulse, very high magnetic field magnets. The work is divided into three parts, a study of the microstructure and strength of maraging steel, an electromagnetic, thermal and mechanical analysis of a short pulse magnet, and a failure and fatigue analysis of a short pulse magnet made of maraging steel. The design and operation of short pulse, high magnetic field magnets is limited by the electrical, thermal and mechanical properties of maraging steel. This thesis examines and proposes some limits to the electromechanical and thermal conditions imposed on maraging steel, and it examines the suitability of maraging steel as an electrical conductor for short pulse magnets. This introduction begins with a description of the extreme electromechanical and thermal conditions which are mentioned throughout this work.

The magnet geometry is a solid helix, where the cross section of the magnet turn is rectangular. Short pulse magnets generate magnetic fields of 50 T (Tesla) and higher, and they achieve these fields with pulses that have half periods between 120 and 150 μs and longer. A 250 kJ capacitor bank is the energy source for the magnetic pulses. These short pulse magnets operate at voltages of 20 kV, with peak electrical currents of 400 kA. The large electrical currents which flow through short pulse magnets are unevenly distributed within the magnet turn. The current densities are largest at the inner radius of a magnet and decrease sharply as the radius increases. This distribution changes as a function of time during the pulse. Under the combined conditions of high magnetic field and large electrical current, the magnets experience peak Lorentz body forces of 350 N / mm^3 (which would give the TS = 2000 N/mm^2 in 6 mm). Extreme mechanical conditions occur during a typical 120 μs pulse.

The temperature rise during a short pulse can exceed 1150 K, and non-uniform current densities cause temperature gradients of 200 K / mm. During the first half period of a pulse, the heating rate can exceed 20×10^6 K / s at the inside radius. The temperature gradients within the magnet are reduced to less than 1 K / mm after 1 min, and at that time, the magnet temperature is 690 K. It takes approximately 15 min to cool the magnet down to room temperature.

The electromagnetic body forces are large enough to cause plastic deformation, and then as these forces diminish, the thermal gradients cause reverse plastic deformation in the magnet. The cyclic plastic strain increments are less than 1 % per pulse. The small plastic strains predicted and observed in the short pulse magnet application are due to the geometry of the magnet and the short time available for plastic deformation.

The first section of this thesis examines maraging steel and identifies the significant material processes which change its microstructure and strength. Chapter 1 focuses on information gained from an extensive literature search on maraging steel. The phase transformation behavior, aging and annealing processes are discussed in detail, because they can significantly affect the strength of maraging steel. The strengthening mechanisms which contribute to the flow strength of maraging steel are described and an evolutionary flow strength equation is proposed. Finally, the fatigue life of maraging steel is modeled with Paris and Tomkin's equations for crack growth given an initial crack size.

In the second Chapter, the focus shifts to determining of the strength of maraging steel in the high temperature ($\theta > 750$ K,) high plastic strain rate (10^{-6} to 10^{-2} s^{-1}) and small plastic strain range ($\Delta\varepsilon^p < 2\%$.) These conditions are close to the expected operating conditions for the short pulse magnet. The tensile test and cyclic fatigue test results performed under these conditions show that the strength of maraging steel decreases to less than a third of its room temperature strength. In addition, the strain rate effects encountered here can more than double the flow strength at high temperatures.

Two plastic strain rate (kinetic) equations are used in Chapter 2 to model the mechanical behavior of maraging steel over the range of temperatures and plastic strain rates discussed above. The constants in the first (phenomenological) kinetic equation and the second Arrhenius power law kinetic equation are found from tensile tests. Cyclic fatigue tests show a lack of cyclic strain hardening or softening through half the fatigue life, and a Bauschinger effect. They are used to model monotonic and cyclic strain hardening. The flow strength of maraging steel is approximated on the basis of material tests conducted under conditions which came as close to the expected service conditions as our testing equipment allowed. The expected strain rates are 10^{-6} to 10^{2} s^{-1}, and the testing strain rates went up to 10^{-2}. The expected temperature range is 298 to 1460 K, and the testing temperature range went up to 1080 K.

For the last part of Chapter 2, data from the literature are used to model the thermal and phase transformation strains as functions of temperature and material phase. With this model, the thermal and phase transformation strain distributions are calculated for extreme thermal loading conditions.

The material strength equations and the plastic strain model for maraging steel are incorporated into a mechanical analysis to study structural behavior under extreme electromechanical and thermal conditions. The finite element method is best suited for this problem. The extreme loading conditions create special demands on the finite element analysis, so a finite element program was written to specifically implement the axisymmetric mechanical behavior of maraging steel. With this program, the viscoplastic and temperature-dependent material behavior of maraging steel are modeled using a time-dependent implicit analysis, where the temperature and Lorentz body force distributions change as a function of time and position.

The second part of this thesis examines thermal cycling tests which were performed on specimens of maraging steel to investigate the effects of extreme thermal loading conditions in the absence of electromagnetic body forces. By discharging a capacitor bank through a restrained tensile specimen, it is possible to investigate the effects parameters (such as peak current density, peak temperature and thermo mechanical loads) have on the number of cycles to failure. Several different specimen geometries are examined and discussed. The hardness is measured for some of these specimens, and the data are compared to the predicted martensite-to-austenite transition position at the moment of peak temperature. Experimental results confirm finite element analyses of the tapered and hourglass specimens. The double necking phenomenon and the deformed barrel shape observed in some specimens are predicted. The cyclic stress strain predictions for the thermal cycling specimens indicate continued plastic deformation with each thermal cycle. Increases in temperature cause local deformations which further increase the temperature, leading to instability. Thus, the short number of cycles to failure observed in the laboratory (less than 50) is predicted by the finite element analyses.

In Chapter 5, the focus is on short pulse magnets. The selection of maraging steel for short pulse magnets is discussed, along with the important parameters which affect short pulse magnet design. A method for calculating current densities, magnetic fields, Lorentz body forces and temperature distributions

within the magnet is described. A short pulse destructible test coil has been designed, constructed and pulsed to failure. The purpose of this coil is to predict its mechanical behavior and life and to observe its failure. Finite element analyses show that the extreme thermal conditions cause more plastic deformation than the electromechanical loads. The mechanical behavior predicted in this chapter is used in the fatigue analysis of the destructible test coil.

Chapter 6 begins with a description and discussion of the short pulse magnet failure (after 16 pulses). This is compared to the fatigue analyses and failures from the low cycle fatigue tests of Chapter 2, the thermal cycling experiments from Chapter 4 and the short pulse magnet in Chapter 5. Crack growth in the short pulse magnet is affected by large electrical currents which flow around cracks on the inner radius of the magnet. A thermal crack-tip model suggests that current density concentrations at the crack-tip cause crack-tip melting, and this results in a geometric crack growth rate. With the model, an "adiabatic" (critical) crack size is defined as the minimum crack length necessary for crack tip melting. For cracks smaller than the "adiabatic" crack size, thermal conduction prevents crack tip melting. The model predicts an "adiabatic" crack size of 11 μm for the destructible test coil. The analysis shows that when parameters such as pulse length and peak coil temperature increase, the "adiabatic" crack size decreases. When thermal diffusivity and melting temperature increase, the "adiabatic" crack size increases. Chapter 6 concludes with recommendations for the use of maraging steel in short pulse magnets along with their operation.

Chapter 1

Maraging Steel

Maraging steel is a high strength iron nickel alloy. The name is derived from the process of martensite aging. It is available in four grades, 200,250,300 and 350, referring to the respective tensile strengths in ksi. A description of maraging steel must center on the three processes which most affect its material behavior. First, there are phase transformations which occur between the high temperature FCC austenite phase and the lower temperature BCC martensite phase. Second, there is precipitation growth which occurs at high temperatures in the martensite phase, and finally, there is solutionizing which occurs in the austenite phase.

In this chapter, the material composition, physical properties, phase transformations, aging process, solution annealing, evolutionary flow strength and fatigue behavior of maraging steel are discussed. The information comes from the published results of numerous researchers. A more comprehensive review of maraging steel literature can be found in the book "Source Book on Maraging Steel" by R.F. Decker [1].

Composition and Physical Properties

The 300 grade of maraging steel was chosen for short pulse, high field magnets because of its high tensile strength, 2070 MPa. The composition is 18.5% Ni, 4.8% Mo, 9.0% Co, 0.6% Ti, 0.1% Al, 0.03% C and the remainder Fe. There are also trace elements of Si, Mn, S, P, Zr and B in the steel. All of the material used in this study was purchased from Teledyne Vasco Inc.

Before various material processes are mentioned and discussed, it is helpful to first give brief descriptions of the important phenomena observed in maraging steel, along with the temperature ranges over which they occur (Table 1.1). On cooling, there is a phase transformation from FCC austenite to BCC martensite which begins at 473 K and ends at 373 K. On heating, from 700 to 970 K aging occurs in the martensite phase, with the growth of Ni_3Mo and FeTi precipitates and an accompanying increase in hardness. When precipitates grow too large, and the hardness decreases, the alloy is said to be overaged. Austenite reversion

is the phase transition which converts martensite into a low-nickel BCC phase and a high-nickel FCC phase. It is associated with overaging, since it occurs in the aging temperature regime, and decreases the hardness.

Next, there is the phase transformation from martensite to austenite which begins at 968 K and is complete at 1008 K. Grain boundary segregation of TiC occurs in the austenite regime, and it reduces the fracture toughness of the steel. Finally, there is solution annealing. The meaning of this commonly used term is imprecise. The intention of the phrase is to describe the process by which precipitates, and locally high concentrations of elements dissolve and disperse into an austenite solution. A more descriptive term is solutionizing. Solutionizing occurs over a wide range of temperatures, and the time necessary for solutionizing is short (<15 min at temperatures above 1030 K).

The nickel content in maraging steel affects the martensite structure, the martensite transformation temperatures and the extent of austenite reversion during aging. Martensite is a metastable crystal structure which has the same composition as the austenite phase from which it forms. The alloy elements, which are in solution in the austenite phase, are supersaturated in the martensite phase. Consider the binary iron nickel phase diagram of Fig. 1.1. At 25% Ni, the austenite is 90% transformed to martensite at 333 K, while at 5% Ni, that temperature rises to 922 K. For the 18% Ni content, the 90% martensite temperature is 505 K .

Transformed austenite has the same composition as the martensite, while reverted austenite has a nigh nickel content. After 10 hr at 755 K, the volume percent of reverted austenite is 65% for a 30% Ni, 18% for 24% Ni and just 2% for an 18% Ni alloy [2]. 18% Ni steel has a tough martensitic structure with a reasonably high transformation temperature, where the formation of reverted austenite at high temperatures is small. The higher Ni content of reverted austenite lowers the austenite-to-martensite phase transformation temperature, so the presence of reverted austenite can affect the phase transformation behavior during thermal cycling. In addition, reverted austenite is ferromagnetic, while transformed austenite is paramagnetic.

The elements Mo and Co play several important roles in the precipitation hardening of maraging steel. Aging at 755 K precipitates particles of Ni_3Mo from the martensite solution. Co accelerates the precipitate formation and growth by

increasing the supersaturation of Mo. It also retards the formation of reverted austenite [3]. Mo inhibits the precipitation of carbide phases during cooling by broadening the temperature range over which the other elements remain in solution [4]. Mo lowers and Co raises the martensite start temperature [5][6]. The interaction between Mo and Co results in a fine dispersion of precipitates with superior fracture toughness [7].

A Ti compound also contributes to precipitation hardening in maraging steel. The identity of this intermetallic compound has not been determined conclusively. Diffraction patterns suggest that it is a tetragonal compound of FeTi, CoTi or NiTi, and not Ni_3Ti, Fe_2Ti or cubic FeTi [8]. The increase in hardness due to the Ti precipitates is 690 MPa per % Ti content [9]. The difference in strength between the 250 and 300 grade maraging steel is due primarily to the higher Ti content [10]. Overaging can cause thermal embrittlement which is characterized by the formation of large coarse TiC precipitates on grain boundaries [11]-[13]. Finally, the electrical resistivity of maraging steel is sensitive to and increases with the Ti content.

The properties of maraging steel are temperature-dependent, and in some cases they depend on magnetic field. In this paper, only the density d and the Poisson's ratio ν (see below) are assumed constant. The heat capacity c_p, thermal conductivity κ, and electrical resistivity ρ are all approximated with polynomials which are functions of temperature θ. Figs. 1.2 - 1.4 illustrate the temperature-dependence of these variables, along with the approximations used with the finite element analysis. Fig. 1.2 compares the specific heat calculated from a classical formula of $c_p = 3R/M$ (0.45 J/kg/K); R and M are the universal gas constant and molecular weight; higher values are due to the impending phase transformation. Table 1.2 gives the functions describing them for aged 300 grade maraging steel. The data shown for the heat capacity and thermal conductivity come from two reference works [14][15]. The electrical resistivity data was measured by the Francis Bitter National Magnet Laboratory. For temperatures above 970 K, the behavior of maraging steel is more complicated because of phase transformations and microstructural changes. The properties mentioned above have not been investigated in the high temperature austenite regime. Heat capacity, thermal conduction and electrical resistivity generally increase with temperature, but the phase transformation to austenite likely causes

a decrease in these properties. Without data, it is not known if the high temperature (> 800 K) approximations are too large or too small. The error in these approximations could be as high as 50 %.

Changes in temperature and material phase affect the Young's modulus. Fig. 1.5 shows data obtained from two reference works [14][15], along with high temperature data which comes from static measurements made for this work. An empirical curve approximates the Young's modulus E (GPa) versus temperature θ (K) data:

$$E = 153.7 + 44.1\ exp\left(-\left(\frac{\theta}{734}\right)^{3.81}\right). \tag{1.1}$$

It is interesting to note that the decrease in Young's modulus occurs over a temperature range which is at least 200 K less than the martensite-to-austenite phase transformation temperature. Physical theories for the temperature dependence of elastic constants relate the bulk modulus K to the Debye temperature and the Grüneisen parameter ($\alpha\ K\ /\ c_p\ d$) [16]-[18]. These theories, with no phase transformations, show a linear decrease in bulk modulus from 2/3 the Debye temperature to 0.8 K_0 (K_0 is the bulk modulus at absolute zero) at θ_m. Data on many metals show a similar behavior for the shear modulus, dropping to 0.6 G_0 at θ_m.

Phase Transformations

It is important to understand the nature of martensitic transformations, and how they are affected by thermal cycling. Fig. 1.6 shows the dilatation versus temperature for an annealed maraging steel [19]. The heating rate was 4.4 K/s, and the 2 mm diameter wire was held at 1088 K for 2 hr and then air cooled. The martensite-to-austenite transformation start and finish temperatures are 968 and 1008 K respectively. Likewise, the austenite-to-martensite transformation start and finish temperatures are 473 and 373 K respectively. The martensite-to-austenite dilatation strain change is -0.18% and the reverse is 0.52%.

The phase transformation is a shearing process in a monocrystalline structure, but in a polycrystalline solid with a random orientation of crystal microstructure, the individual shearing displacements cancel, leaving a total transformation strain which is predominantly dilatational. When maraging steel has

been cold worked, the phase transformation strains are anisotropic. Martensitic transformations are temperature-dependent, and they occur by a diffusionless shearing process [20]. The martensitic transformation has been classified as a lattice distortive displacement [21]. Phase transformations occur because thermodynamic free energy differences between the two crystal structures become large enough to drive a crystallographic change which lowers the energetic state of the material [22][23]. "The kinetics and morphology during the transformation are dominated by strain energy" and lattice energies [21]. Applied stress and magnetic fields can induce phase transformations by increasing the Gibb's free energy difference [24]-[26]. For example, in Fe-22.5Ni-4Mn, stress and magnetic fields can raise the martensitic start temperature by approximately 1.0 K/Ksi of applied stress and 0.03 K/T of applied magnetic field.

When austenite transforms into martensite, the resulting martensitic microstructure is influenced by the austenite grain size and orientation and the applied temperatures and stresses. The structure of martensite in maraging steel has been described as follows; "an austenite grain contains several packets which consist of parallel laths, and each packet is made up of parallel blocks" [27][28] The formation process of martensite has been studied using the Greninger-Troiano heat treatment, and the following process is given. First, parallel laths form in clusters, and they partition the austenite grain. As the transformation progresses, new parallel laths form in the untransformed austenite regions until each of the martensitic packets is completely transformed. The formation of martensite laths occurs by independent nucleation within each packet. This process is sketched in Figs. 1.7a-1.7c. The martensite laths are approximately 1 μm thick [29][30].

The transformation behavior of maraging steel depends on its microstructure which can change with each thermal cycle. Four thermal cycling variables affect the microstructure and hence, the transformation behavior. They are heating rate, peak temperature, time spent at the peak temperature and the number of cycles. Two separate processes precede and influence the transformation from martensite to austenite. The first is aging and the second is austenite reversion which peaks at 933 K [31]. These processes are time-dependent, so a slow rate of heating will increase the precipitate sizes and the quantity of reverted austenite. The peak temperature and time spent at that temperature are important, because at temperatures above 1008 K the higher concentrations of nickel in the reverted austenite diffuse into the lower nickel concentrations

of transformed austenite. As the amount of reverted austenite increases, the austenite start and finish temperatures increase and the martensite start temperature decreases. Fig. 1.8 illustrates how these temperatures change according to the number of thermal cycles [19]. The heating rate in these curves is 300 to 500 K / s, and the solutionized specimens are immediately air cooled. When the heating rate is increased, the number of thermal cycles necessary to change the start and finish temperatures is also increased. Thus, under short pulse conditions (heating rates greater than 10^6 K / s,) the phase transformation curves are unlikely to change [32].

Anisotropic phase transformation strains are associated with prior cold work in this material [30][33]. Two mechanisms are responsible for this behavior. First, during a transformation when both phases are present, the martensite is stronger, so plastic yielding in the softer austenite results in plastic strains which affect the dilatometric behavior. Secondly, when maraging steel is cold worked, there is an observable banding in the martensite structure. This banding creates a preferred orientation for subsequent shearing transformation displacements. In other words, an isotropic microstructure will give isotropic dilatational transformation strains, but an anisotropic microstructure will yield anisotropic transformation strains. Solutionizing does restore maraging steel to an isotropic microstructure, eliminating any further anisotropic phase transformation strains.

Thermal cycling also affects the grain size, and this has a small effect on the flow strength (discussed later in this Chapter.) It has been determined from thermal gradient heat treatments that the grain size of maraging steel can be refined by thermal cycling between the martensite and austenite phases [20][34][35]. Phase transformations are crucial to this process since without both transformations, the grain size refinement does not occur. It has been observed that the martensite lath packets which form within old austenite grains become the new austenite grains upon reheating. In a short pulse magnet, the grain size will shrink because of phase transformations, and then grow at high temperatures.

Aging and Solution Annealing

The recommended aging heat treatment for maraging steel is annealing at 1255 K for 1 hr, air cooling to room temperature followed by aging for 4 hr

at 755 K [36]. A nitrogen atmosphere is used in the heat treatment to prevent carburization, sulphurization, and oxidation [15]. Nitriding normally requires a 48 hr exposure at the aging temperature, so these phenomena are not significant during aging. This heat treatment is used for the short pulse magnets and for all of the experiment specimens. Fig. 1.9 shows the HV hardness versus aging time for an 18% Ni maraging steel that was annealed at 1255 K. Aging increases the tensile strength from 1170 to 2074 MPa. Increases in the aging temperature cause the hardness to reach its peak value sooner. This is because aging is a time-dependent diffusion process, where the diffusion coefficient increases with temperature. At higher temperatures, the formation of nickel rich austenite (austenite reversion) is significant, and this decreases the hardness.

The purpose of aging is to precipitate and grow fine Mo and Ti particles. The aging reactions proceed as follows. The Co in the Fe-Ni matrix causes the Mo to be finely dispersed in atom clusters [7][10]. Short-ordered Fe-Co regions reject Ni, leading to Ni_3Mo precipitates. This precipitate forms along dislocation lines [8], and the precipitate has been observed in annealed material [37]. This is in agreement with the short incubation times observed, since Co acts as a catalyst nucleating the precipitates [3]. The short-ordered Fe-Co (nickel lean) regions are also favorable towards the formation of tetragonal FeTi precipitates. The aging of these precipitates causes them to grow in size and to increase their interparticle spacings.

In overaging, the strength decreases from its maximum value. Three different processes are involved. First, there is the coarsening of Ni_3Mo and tetragonal $FeTi$ precipitates. Next, is the formation of large stable Fe_2Mo precipitates, and finally, there is austenite reversion. The Ni_3Mo and tetragonal $FeTi$ precipitates are metastable [38], so they ultimately coarsen and dissolve back into solution [10]. From Fig. 1.9, overaging happens after 100 hr at 755 K (900 F).

For most applications, the service temperature of maraging steel is less than the aging and phase transformation temperatures, so these phenomena are not important to any changes in the material. In the short pulse magnet application, there are two different thermal cycling zones. The first zone (Zone 1) is at the inner radius and extends about 3 mm into the magnet. This zone heats to a peak temperature of 1460 K in 250 μs, cools to an intermediate temperature of 690 K in 5 s, and then cools to 298 K in 15 min. The second zone (Zone 2) extends from the middle of the magnet turn to the outer radius,

and its thermal cycle consists of heating to 690 K in 5 s followed by cooling to room temperature in 15 min. Overaging is not significant during the 40 μs Zone 1 spends at high temperatures in the martensite phase. In Zone 2 however, approximately 1 min per pulse is spent at 690 K, so time-dependent aging processes have a detrimental effect on the material microstructure after approximately 6000 pulses. Since the desired coil life is 1000 cycles, overaging is not expected to play an important role in Zone 2. Between the two zones, there is a small region where about 3 sec is spent at 900 K followed by 1 min at 690 K. Overaging in this region is significant after the first pulse.

For homogenizing, Teledyne Vasco recommends 30 min at 1090 K to ensure a homogeneous microstructure in the steel. When Zone 1 transforms to the austenite phase, the change in microstructure is rapid. For example, solutionizing for 5 min at 1033 K can reduce the room temperature strength of aged steel from an HV hardness of 520 to 355 kg/mm^2. In Zone 1, the time spent at temperatures greater than 1033 K is over 3 s per pulse. Thus, for this portion of the magnet, the aged strength is solutionized after a minimum of 100 pulses; even sooner than homogenizing. Micro-hardness measurements made on cross sections of thermal cycling specimens and the short pulse magnet indicate that significant solutionizing occurs in just 52 s (16 pulses). The peak cycling temperature is greater than 1400 K, so without a doubt, thermal cycling to these very high temperatures solutionizes the aged steel and reduces its strength.

Finally, there are the high temperature effects on grain boundary segregation. Intermediate holding temperatures between 1088 K and 1144 K for 1 to 2 hr cause a serious loss in fracture toughness as measured with Charpy V-notch impact energies; from 91 to 9 N-m for annealed material, and from 26 to 4 N-m for aged material [11]. The cause of this embrittlement is grain boundary segregation of TiC precipitates. Maximum embrittlement occurs after 1 hr at 1144 K [13]. Normally, the annealing process occurs at temperatures greater than 1144 K, and the Ti remains in solution. Upon cooling, if the rate is slow (-0.3 K/s), the material becomes embrittled, and this is a concern to manufacturers when dealing with large sections of maraging steel. The cooling rate of the short pulse magnet in this temperature regime is -100 K/s, so grain boundary segregation is not a significant phenomenon.

The Evolutionary Flow Strength of Maraging Steel

The flow strength of maraging steel depends on its chemical composition, material phase, temperature, and dislocation structure. For strain reversals less than 1 %, polarization of the dislocation structure is important. The mechanisms which contribute to the strength of monocrystalline maraging steel are the lattice and solution shear resistance $\tau_{\ell \cdot s}$, the precipitate shear resistance τ_p and the dislocation shear resistance τ_d. The flow strength s equals the Taylor factor m_T (3.1) times the total shear resistance τ_t plus a contribution from the grain boundary resistance s_b.

$$\tau_t = \tau_{\ell \cdot s} + \tau_p + \tau_d \tag{1.2}$$

$$s = m_T \tau_t + s_b \tag{1.3}$$

For room temperature, the tensile strength is apportioned in Table 1.3 among the mechanisms given in Eqs. 1.2 and 1.3 [39]. Each component of shear resistance is given in terms of a flow strength variable s and is divided by the tensile strength to show its relative magnitude.

The lattice and solution shear resistance $\tau_{\ell \cdot s}$ is the stress required to drive a dislocation through a faultless crystal [40]. Maraging steel has a solute concentration of 33%, containing both interstitial and substitutional elements. The solute atoms increase the dislocation resistance by creating differences in local stress fields and in elastic moduli. The lattice and solution strength comprises 38% of the tensile strength.

The development of maraging steel was a direct result of an attempt by R.F. Decker et al [9] to enhance the strength of iron nickel alloys through precipitation hardening. The magnitude of the precipitation hardening depends on the precipitate width w, the volume fraction of precipitate f_p, the precipitate strength per unit width dK/dw, the shear modulus G, and the Burgers vector b. The precipitation shear resistance for widely spaced precipitates of a single species in the underaged condition, when dislocations cut through precipitates is

$$\tau_p = G\left(\frac{\frac{dK}{dw}}{Gb}\right)^{\frac{3}{2}}\left(\frac{b}{w}\right)^{\frac{1}{2}}(f_p)^{\frac{1}{2}} \tag{1.4}$$

[41][42]. In the overaged condition, when dislocations bypass precipitates

$$\tau_p = G\left(\frac{b}{w}\right)(f_p)^{\frac{1}{2}}. \tag{1.5}$$

Eq. 1.4 predicts an increasing shear resistance as particle width grows and precipitate volume fraction increases. Eq. 1.5 predicts a decrease in shear resistance as the width grows, because the interparticle distance increases, allowing dislocations to bow between the particles. The optimum particle width can be found by equating Eq. 1.4 to 1.5, and solving for w. For maraging steel, the precipitates of Mo and Ti contribute 51% of the total flow strength (Table 1.3.)

As plastic deformation by dislocation motion occurs in a material, the density and distribution of dislocations change. Dislocations are generated under an applied stress, and they are annihilated by dynamic and static recovery. In general, during plastic deformation, the dislocation density increases, and the stress required for further deformation increases. The dislocation shear resistance τ_d is proportional to the square root of the dislocation density Λ:

$$\tau_d \propto Gb\sqrt{\Lambda} \tag{1.6}$$

In Table 1.2 the flow strength contribution due to dislocation shear resistance is assumed to be the difference between the tensile and yield strength, so the strain hardening contribution to the tensile strength is only 4%. This estimate is low, because of the initial dislocation density. The transformed martensite contains fine elongated laths with high dislocation densities. The dislocation density of aged maraging steel strained to 0.1 % is about 10^{11}-10^{12} cm^{-2} [43]. A high density dislocation structure is one characteristic of martensite. Transformed martensite begins with a high dislocation density and further strain hardening does not increase the flow strength by as large a fraction as a material that initially had a small dislocation density.

The grain boundary resistance contribution to the tensile strength is just 7%. For the martensite phase, the Hall-Petch equation shown below predicts the change in yield strength with grain size [39]. This equation predicts a decrease in yield strength σ_y, when the grain size ℓ_{gs} increases. The constants σ_0 and k_y are respectively equal to 789 MPa and 4.74 MPa mm$^{\frac{1}{2}}$ for unaged material and 1850 MPa and 10.1 MPa mm$^{\frac{1}{2}}$ for aged material.

$$\sigma_y = \sigma_0 + k_y \ell_{gs}^{-\frac{1}{2}} \tag{1.7}$$

In the austenite phase at high temperatures, reductions in grain size cause a decrease in yield strength. This indicates that grain boundary sliding may be significant [20]. Thus, the effect of grain size on the flow strength varies with the material phase and deformation mechanism.

The flow strength of maraging steel changes significantly with different thermal and loading histories. Several processes and mechanisms cause these changes, and they have been identified and studied to determine their effects on the flow strength. The important parameters defining an evolution of flow strength are current stress σ, flow strength s, temperature θ, martensite phase volume fraction f_M, precipitate width w, precipitate volume fraction f_p and dislocation density Λ. Eq. 1.9 shows the parameters which affect the evolution of the four mechanisms mentioned in Eq. 1.2.

$$\dot{s} = \dot{s}\left(s, \sigma, \theta, f_M, w, f_p, \Lambda\right) \tag{1.8}$$

$$\dot{s} = \dot{s}_{l\text{-}s}\left(\theta, f_M\right) + \dot{s}_p\left(\theta, f_M, w, f_p,\right) + \dot{s}_d\left(s, \sigma, \theta, f_M, w, f_p, \Lambda\right) + \dot{s}_b\left(\theta, f_M, w, f_p\right) \tag{1.9}$$

Additional evolutionary equations are needed for $\dot{w}$, $\dot{f}$ and $\dot{\Lambda}$, since these parameters also change with different thermal and mechanical loading histories.

To understand what parameters affect the evolution of flow strength, return to Eq. 1.2 and consider how this equation might be modified to satisfy the entire solid temperature range. To simplify this discussion, it is assumed from this point forward that the formation of low-nickel martensite and nickel-rich austenite (austenite reversion), and grain boundary segregation are not significant. Another assumption made here is to neglect the grain boundary sliding. The dislocation shear resistance is not neglected because stress strain data in the austenite regime shows that strain hardening represents a larger percentage of the total flow strength than it does in the martensite regime.

The phase composition of maraging steel can be described in terms of the volume fractions of martensite f_M and austenite f_A. Each of the flow strength contributions of Eq. 1.2 depend on the material phase. For two phases, each large compared to the mean free path of dislocations, homogeneous plasticity holds and a rule of mixtures can be used to determine the composite flow strength [44]. Under a non-hardening uniform strain condition, this strength represents an upper bound approximation to the limit load. Using this approach, Eq. 1.2 is

rewritten below to include the martensite and austenite phases. The superscript M and A on $\tau_{i.s}$, τ_p and τ_d refer to martensite and austenite respectively.

$$1 = f_M + f_A \tag{1.10}$$

$$\tau_t = f_M \left(\tau_{i.s}^M + \tau_p^M + \tau_d^M\right) + (1 - f_M)\left(\tau_{i.s}^A + \tau_p^A + \tau_d^A\right) \tag{1.11}$$

The challenge then is to determine each term in Eq. 1.11 and calculate the flow strength of maraging steel. The difficulty with this formulation is describing the evolution of each component as a function of the parameters given in Eq. 1.9. This study does not solve this problem, but it does use the general form of these equations to approximate the flow strength.

For maraging steel, four processes are primarily responsible for changes in flow strength: phase transformations, precipitation, diffusion and dislocation structural changes. Temperature changes cause the martensite and austenite phase transformations. The growth and dissolution of precipitates in the martensite and austenite phases respectively is controlled by chemical reactions and the diffusion of precipitate elements in the solid solution. Both processes are time and temperature dependent. Applied stresses can cause plastic straining which changes the dislocation structure and hence the flow strength through τ_d. Temperature plays an additional role in the flow strength because it affects the shear modulus G.

Material phase transformations affect the flow strength by changing the material phase volume fraction, the dislocation density and the crystal structure and hence the lattice friction, the shear modulus. Changes in precipitate size, spacing, and volume fraction affect the precipitation shear resistance. These changes occur by the second and third processes of precipitation and diffusion of alloy elements. Depending on the temperature and the material phase which surrounds the precipitate, the precipitate will either grow or shrink. The solutionizing process is a complex process by which precipitates return into solution. Studies of this behavior in maraging steel have not been found by this author and may not exist. Predicting the evolution of precipitate shear resistance requires a focused research effort into the chemical reactions and diffusion equations for both the Mo and Ti precipitates. The heat treatment used in this study produces precipitates which give the maximum flow strength. Thus, any changes in precipitate size decrease the flow strength. In the high temperature zone (Zone 1) of a short pulse magnet, the precipitates solutionize, and in the outer low

temperature zone (Zone 2) the precipitates overage. In both cases this leads to a decrease in flow strength.

The fourth process which changes the flow strength is strain hardening. The change in the dislocation shear resistance $\dot{s}_d$ is commonly described by a strain hardening product $h\dot{\epsilon}^p$. The strain hardening coefficient h depends on temperature, material phase, precipitate width, precipitate volume fraction f_p, dislocation density Λ and the polarization of dislocations Λ_p. Although Λ_p is a tensor, with proportional loading the tensorial nature can be neglected. The plastic strain rate $\dot{\epsilon}^p$ is determined with a kinetic or flow equation which depends on the total flow strength. The kinetic equation models metal deformation with parameters similar to those given in Eq. 1.8. A kinetic equation for maraging steel is proposed later in Chapter 2.

$$h \equiv \frac{\partial s}{\partial \epsilon^p} \tag{1.11}$$

$$h = h(\theta, f_M, w, f_p, \Lambda, \Lambda_p) \tag{1.12}$$

The mechanisms of strain hardening involve several competing phenomena. Dislocation pileup, forest dislocations, and the pinning of dislocations on precipitates lead to a positive strain hardening effect, while dynamic recovery, dislocation climb, and other diffusion processes have a strain softening effect on the flow strength.

Fracture and Fatigue Behavior

The fracture toughness of maraging steel is dependent on several factors. First, the higher the grade of maraging steel, the lower its fracture toughness. The K_{1c} values are 100, 67 and 33 $MNm^{-\frac{3}{2}}$ for the 250,300 and 350 grade (aged) maraging steels respectively. The corresponding critical crack lengths for room temperature at a working stress of half the yield strength are 3.8, 1.3 and 0.2 mm. Secondly, the steel in the annealed condition is more ductile than material in the aged condition (the annealed and aged 300 grade fracture strains are 1.43 and 0.69 respectively). Third, the impact transition temperature range for maraging steel is broad. The rise in Charpy V-notch work is gradual, going from 8 J at 73 K up to 36 J at 473 K. The broad transition makes maraging steel a useful material for low temperature applications. Fourth, the fracture toughness is dependent on the production procedures used in manufacturing. Improved fatigue lives are observed when the material is machined first and then aged versus aging followed by machining. Lastly, still higher aging temperatures improve the fracture toughness, but then the quantity of reverted austenite decreases the tensile strength to a level comparable to that of a lower grade maraging steel [45].

Observations of fracture surfaces reveal fatigue striations, tire tracks, fractured or cleaved particles, and ductile rupture dimples [37][46]. The fatigue striations are parallel to the crack front, and they have been used to measure crack growth rates. Tire tracks are caused by a particle trapped between the two fracture surfaces. As the surfaces move relative to one another, a particle indents the surface creating a short row of parallel markings similar to tire tracks. The intermetallic compounds are harder and tend to fracture or separate from the surrounding matrix material. This explains the presence of tire tracks, caused by a trapped loose particle. The matrix material is more ductile and cavities form around the particles. These cavities appear as dimples when the fracture surface separates them in half. Dimples have been observed for both the TiC and Ni_3Mo precipitates.

For the 300 grade maraging steel, the endurance limits are 510 and 676 MPa (0.44 and 0.33 TS) for the annealed and aged conditions respectively. The low ratio of endurance limit to tensile strength for the aged condition is attributed to the extensive cyclic softening which is observed. Analysis of fatigue crack tips reveals softening at the crack front for both the annealed and aged

conditions [47]. One theory for this phenomenon is that the dislocation structure cyclically rearranges itself around the intermetallic precipitates, and this lowers the material strength [48].

In 1973, a fatigue study of 300 grade maraging steel by Van Swam [43] showed that the fatigue life can be predicted with the Coffin-Manson law or Tomkin's theory, which uses the Paris law. The Coffin Manson law is in terms of the fatigue life N_f, the total strain range $\Delta\varepsilon$, and the constants ε'_f, σ'_f, c and b of Table 1.4.

$$\frac{\Delta\varepsilon}{2} = \varepsilon'_f (2N_f)^c + \frac{\sigma'_f}{E} (2N_f)^b \tag{1.13}$$

The data for this equation are shown in Figs. 1.10 and 1.11 for the annealed and aged conditions respectively.

The Paris law shown below in Eq. 1.14 predicts crack growth as a function of the stress intensity factor range ΔK. Various researchers have reported exponents γ which vary from 2 to 4 for aged 300 grade maraging steel [46][47]. Fig. 1.12 shows crack growth data from the work of Van Swam, and Table 1.4 contains the constants for Eq. 1.14:

$$\frac{dl}{dN} = A (\Delta K)^\gamma \tag{1.14}$$

Tomkin's theory uses cyclic stress strain data, a hypothetical initial crack length, $\gamma = 2$ in Eq. 1.14, and an endurance limit at $\Delta\varepsilon^p = 10^{-5}$ to predict fatigue life. The theory ignores the time spent initiating cracks. It uses a simple crack tip model and assumes the crack growth per cycle is related to the crack tip opening displacement and the length of flow bands extending at 45° from the crack front. Without detailing the derivation of Tomkin's theory [49][50], the equations which predict the fatigue life N_f for either a plastic strain range $\Delta\varepsilon^p$ or a stress range $\Delta\sigma$ are given with Eqs. 1.15 and 1.16. C and β are the cyclic strength and exponent for Eq. 1.17, and Table 1.4 gives appropriate values for the material constants in the annealed and aged condition. l_0 is the initial crack

length, and a value of 10 μm gives the best fit to experimental data (typical grain sizes are about 50 μm in diameter.) l_f is the final crack length.

$$\Delta\varepsilon^p N_f^{\frac{1}{2\beta+1}} = \left[(2\beta+1)\frac{8}{\pi^2\sqrt{2}}\cdot(2\beta)^{2\beta}\, ln\frac{l_f}{l_0}\right]^{\frac{1}{2\beta+1}} \tag{1.15}$$

$$\Delta\sigma N_f^{\frac{\beta}{2\beta+1}} = C\left[(2\beta+1)\frac{8}{\pi^2\sqrt{2}}\cdot(2\beta)^{2\beta}\, ln\frac{l_f}{l_0}\right]^{\frac{\beta}{2\beta+1}} \tag{1.16}$$

where

$$\Delta\sigma = C\,(\Delta\varepsilon^p)^\beta \tag{1.17}$$

This theory predicts endurance limits of 483 and 621 MPa for a plastic strain amplitude of $\Delta\varepsilon^p = 10^{-5}$ for annealed and aged maraging steel respectively. These endurance limits are smaller than the observed values by 27 and 55 MPa respectively.

In the high temperature austenite regime, the fracture toughness and the fatigue behavior of maraging steel are unknown. The material microstructure can change rapidly, and factors such as environment and thermal history have a significant effect on fracture and fatigue. The high temperature fatigue results of this thesis are reported in Chapter 6.

For the benefit of researchers looking for more information on maraging steel, references [51]-[84] are additional papers which concern maraging steel. These papers have contributed to the author's understanding of maraging steel; those specifically relevant to this study have been mentioned above.

Conclusions

300 grade maraging steel is a complex very low carbon alloy steel with a high tensile strength, 2070 MPa. Four alloy elements, Ni, Mo, Co and Ti most affect its strength. The Ni causes the formation of martensite from the austenite phase, and varying the Ni content changes the martensite and austenite transformation temperatures. Annealed maraging steel is tough, and it has a tensile strength of 1170 MPa. When the material is aged at 755 K, Mo combines with Ni, and Ti probably combines with Fe to form precipitates in the martensite

phase. The precipitation and growth of these particles increases the tensile strength.

In this study, the Poisson's ratio is assumed constant. Thermal expansion, heat capacity, thermal conductivity, electrical resistivity and Young's modulus are all approximated with functions of temperature.

The three processes which most affect the material behavior of maraging steel under short pulse conditions are phase transformations, aging and solutionizing. The magnet can be divided into two zones, where Zone 1 thermally cycles to 1460 K and Zone 2 thermally cycles to 690 K. Phase transformations and solutionizing occurs in Zone 1, and aging is the dominant process in Zone 2. Grain boundary segregation of TiC compounds and the formation of nickel rich austenite (austenite reversion) are judged not to be significant in this application.

Martensitic phase transformations are temperature dependent and diffusionless. Strain energy dominates the kinetics and morphology of martensitic phase transformations. Maraging steel transforms from austenite to martensite beginning at 470 K and ending at 370 K. The transformation from martensite to austenite starts at 970 K and is finished at 1010 K. Under rapid thermal cycling conditions ($\dot{\theta} > 300$ K/s), these temperatures are unlikely to change, and the processes of aging and austenite reversion do not affect the phase transformation characteristics. In a single crystal, martensite phase transformations are a shearing process, but in a polycrystalline material, the result of all the individual shearing displacements is a predominately dilatational transformation strain of approximately 0.25 %. If the microstructure becomes anisotropic through cold working for example, then phase transformations strains are also anisotropic.

Maraging steel derives its name from the process of martensite aging. The recommended heat treatment for maraging steel is annealing at 1255 K for 1 hr, air cooling to room temperature followed by aging at 755 K for 4 hr. We used the 300 Grade maraging steel throughout this work. The material was purchased from Teledyne Vasco in the annealed condition, and aged for 4 hr at 755 K in a nitrogen atmosphere. In the aging temperature regime (700 to 970 K), three material processes are responsible for overaging and a decrease in material strength. They are growth and coarsening of Mo and Ti precipitates, the

formation of stable Fe_2Mo precipitates and the formation of nickel rich austenite and nickel lean martensite (austenite reversion.) In the high temperature austenite regime, solutionizing causes the precipitates formed during the aging process to diffuse back into solution. A 5 min exposure at 1033 K can reduce the HV hardness from 520 to 355 kg/mm^2.

The large difference between the annealed and aged tensile strength shows how significantly the flow strength can change. The flow strength depends on chemical composition, material phase, temperature, and dislocation structure. Four mechanisms contribute to the high tensile strength of maraging steel: lattice and solution resistance 38 %, the precipitate resistance 51%, dislocation resistance 4%, and the grain boundary resistance 7%. Four material processes cause the flow strength to evolve: phase transformations, precipitation reactions, diffusion, and plastic deformation. Using a rule of mixtures, an evolutionary flow strength equation is proposed which could be used to model the flow strength of maraging steel. To do so, evolutionary equations for the four strengthening mechanisms are still needed.

Finally, the following results have been reported on the fracture and fatigue properties of maraging steel at room temperature. The 300 grade steel has a K_{1c} value of 67 MNm$^{-\frac{3}{2}}$ and a critical crack length of 0.69 mm. There is a broad transition in the Charpy V-notch energy, going from 8 J at 73 K up to 36 J at 473 K. Fracture surfaces show tire tracks, cracked and cleaved precipitates and ductile rupture dimples. The endurance limits in the annealed and aged condition are 510 and 676 MPa respectively. At room temperature, cyclic softening occurs in both the annealed and aged steels. Tomkin's equations and the Paris law are used to predict the fatigue life of maraging steel. The fracture and fatigue properties of maraging steel in the austenite regime are unknown.

Table 1.1 Significant maraging steel processes for various temperature regimes.

Temperature	Process
470 - 370 K	Austenite to martensite transformation
700 - 970 K	Aging
750 - 980 K	Austenite reversion from martensite
970 - 1010 K	Martensite to austenite transformation
1090 - 1140 K	Grain boundary segregation
1030 - 1500 K	Solutionizing

Table 1.2 Material properties and functions for aged 300 grade maraging steel.

Density	$d = 8000$	kg m^{-3}	[14]
Poisson Ratio	$\nu = 0.3$		[14]
Melting Temp.	θ_m = 1727-1755	K	[14]
Debye Temp.	$\theta_d = 421$	K	[14]
Heat Capacity		J kg^{-1} K^{-1}	[14], Fig. 1.2

$$c_p = 14.2 + 1.16\theta \quad for \ \theta \leq 731K$$
$$c_p = 862 \quad for \ \theta > 731K$$

Thermal Conductivity — W m^{-1} K^{-1} — [15], Fig. 1.3

$$\kappa = 9.38 + 4.94 \times 10^{-2}\theta - 3.28 \times 10^{-5}\theta^2 \quad for \ \theta \leq 753K$$
$$\kappa = 28.0 \quad for \ \theta > 753K$$

Electrical Resistivity — Ω m — Fig. 1.4

$$\rho = 3.76 \times 10^{-7} + 5.96 \times 10^{-10}\theta + 5.81 \times 10^{-14}\theta^2$$

Table 1.3 Tensile strength contributions for aged maraging steel at room temperature [36], with s_d = TS-YS.

	Strength (MPa)	Percentage of Total
$s_{l\text{-}s}$	789.0	38.0
s_p	1061.0	51.0
s_d	78.0	4.0
s_b	146.0	7.0
Total	2074.0	100.0

Table 1.4 Fatigue behavior constants for annealed and aged maraging steel.

	Annealed	Aged
b	-0.045	-0.090
c	-0.85	-0.75
ε'_f	2.4	1.3
σ'_f/E	0.78	1.15
β	0.09	0.11
C'	380 MPa	610 MPa
l_f	2500 μm	2500 μm
l_0	10 μm	10 μm
γ	2.03	-
A	1.79×10^{-10} m/c (MPa $m^{\frac{1}{2}}$)$^{\frac{1}{\gamma}}$	-

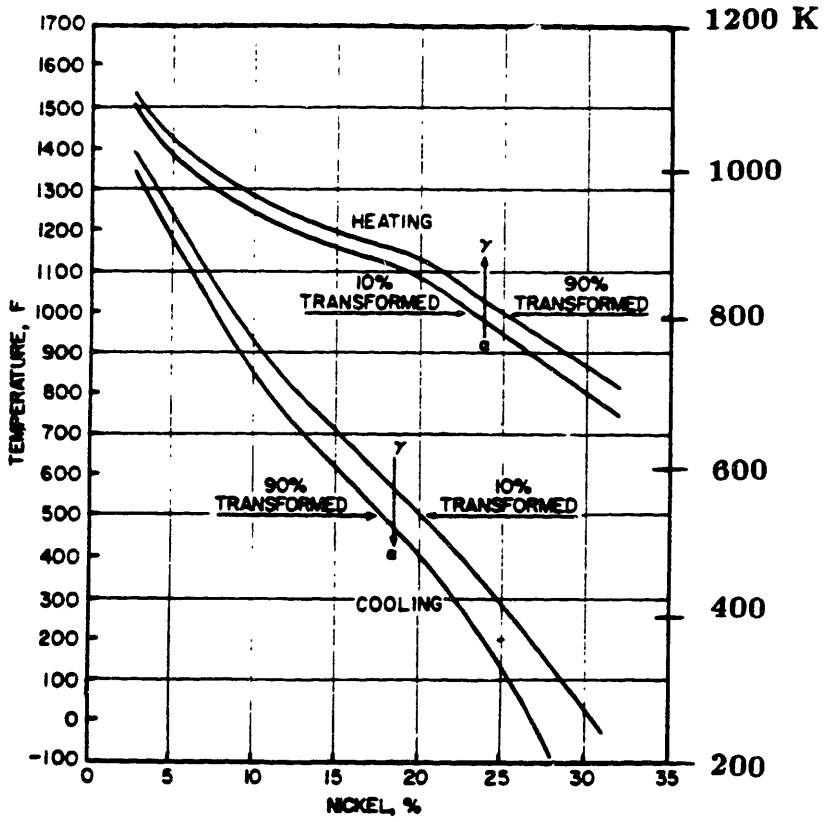

Fig. 1.1 Fe-Ni transformation diagram [9].

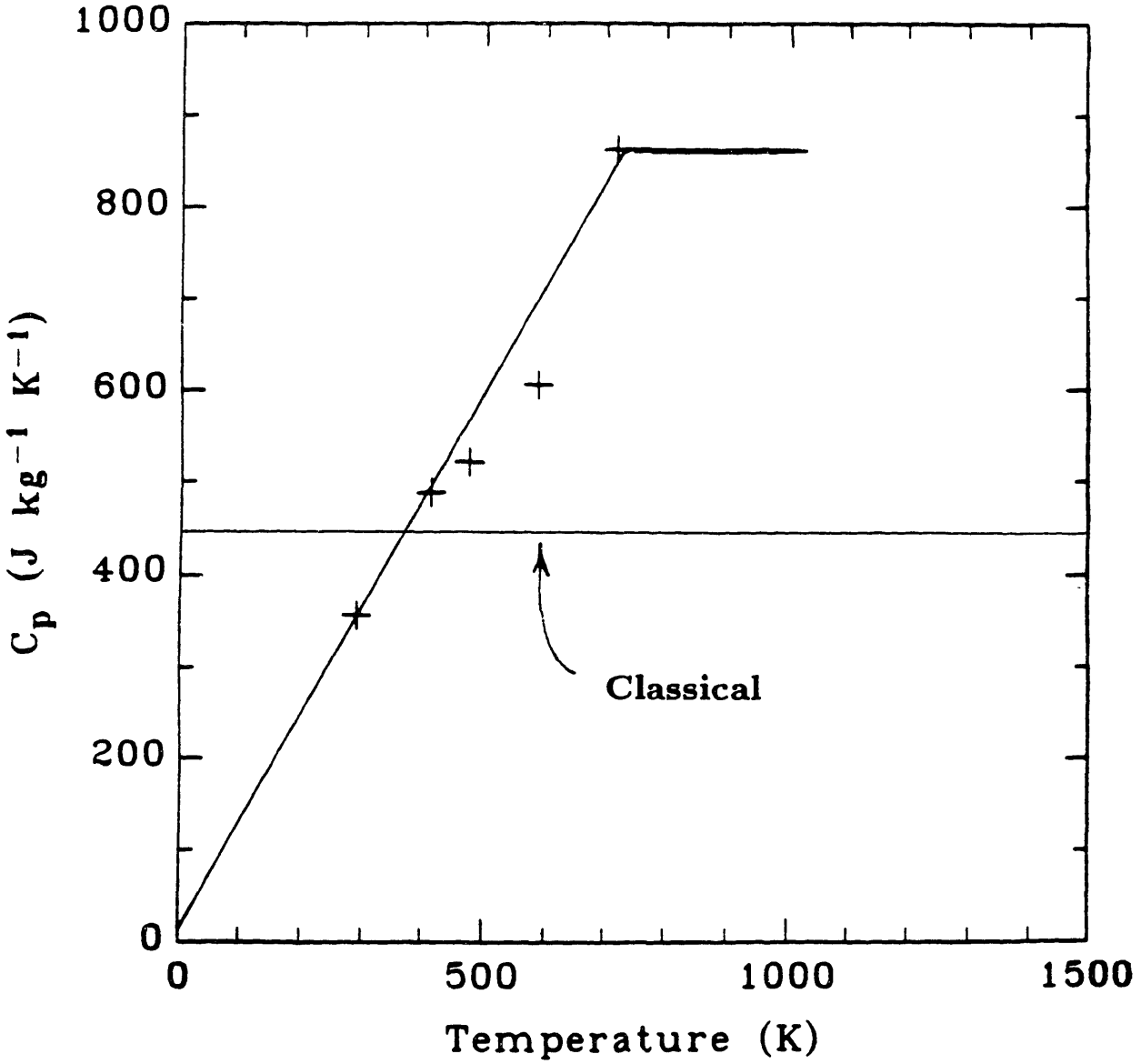

Fig. 1.2 Heat capacity versus temperature [14].

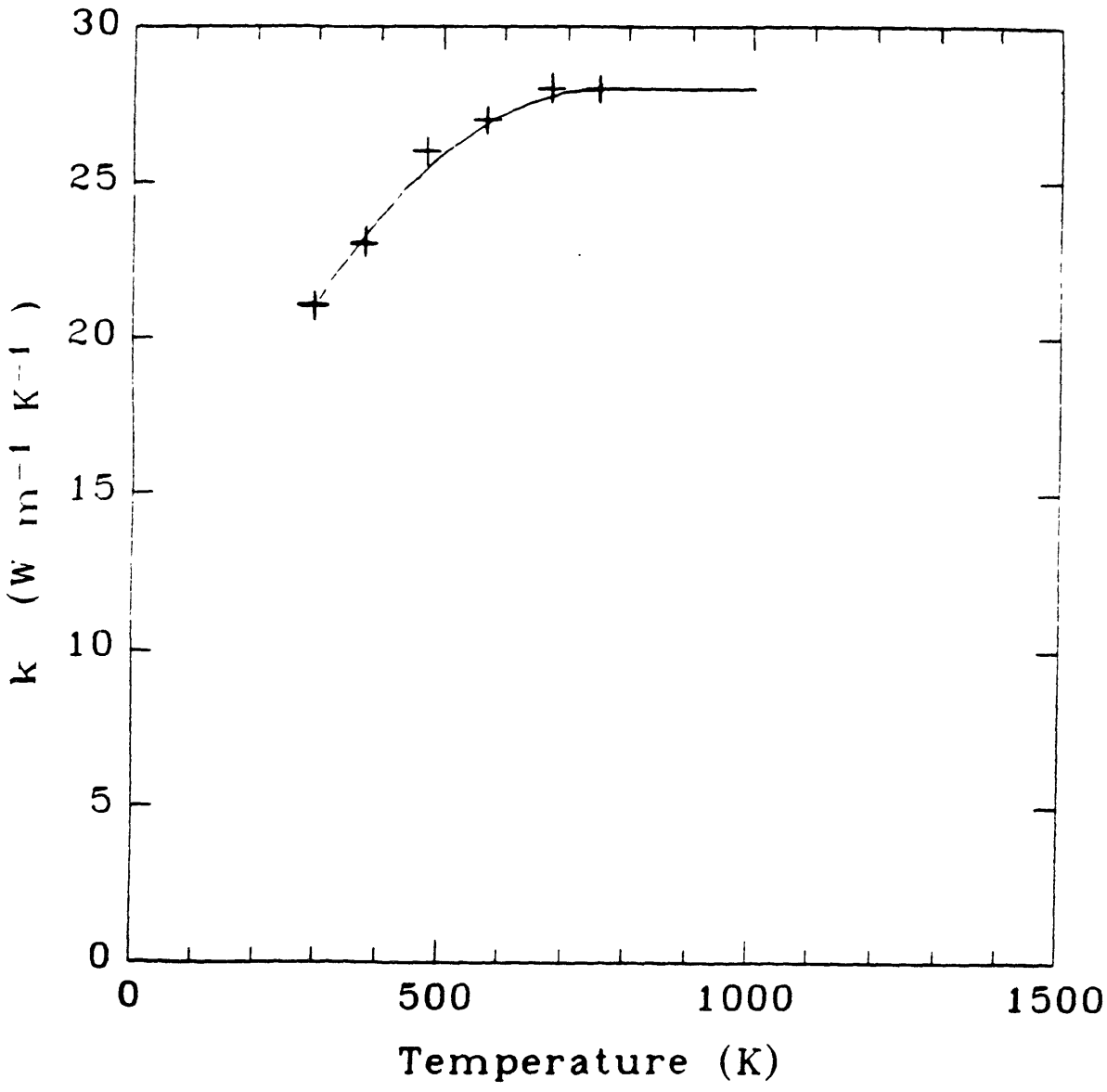

Fig. 1.3 Thermal conductivity versus temperature [15].

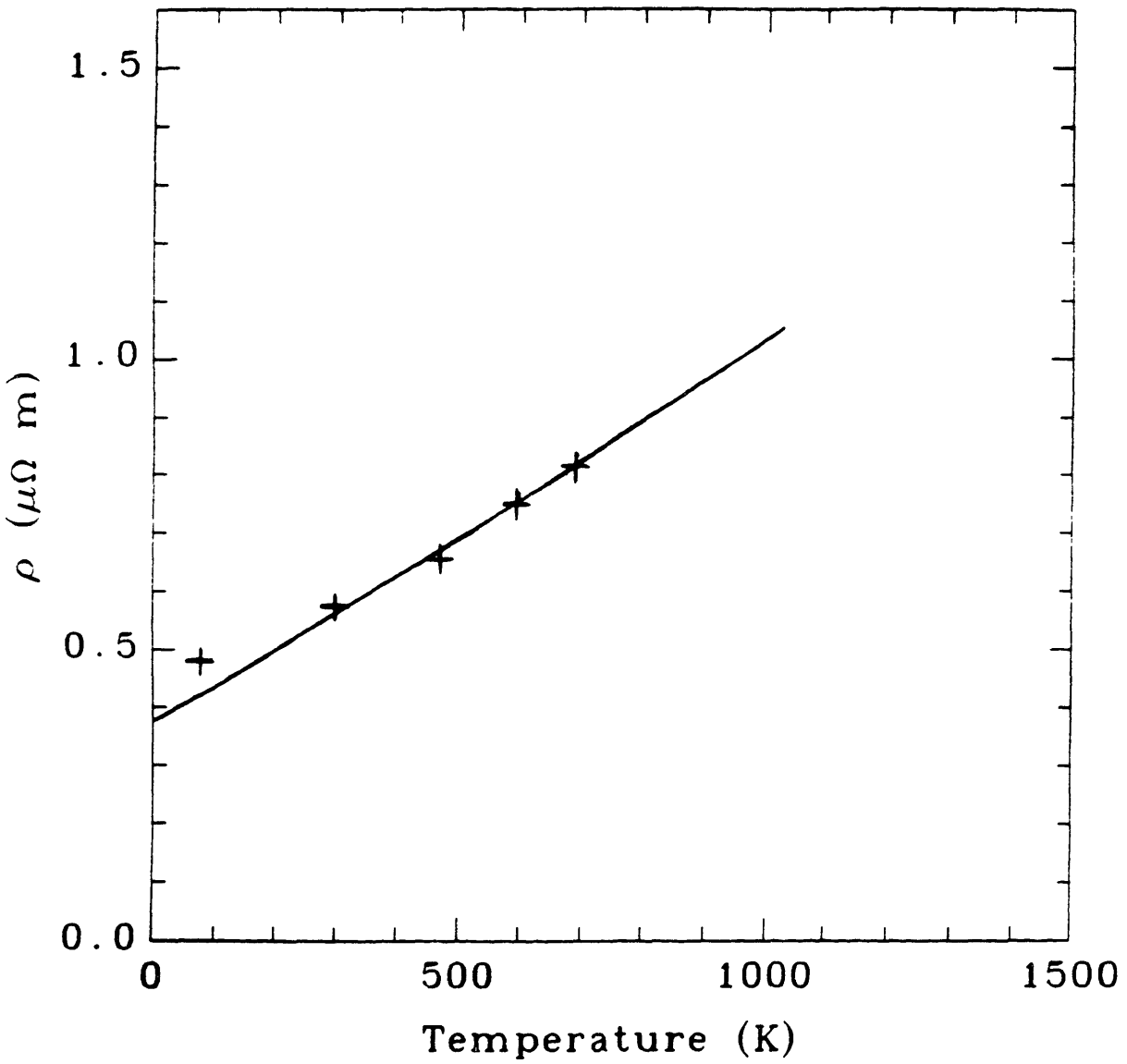

Fig. 1.4 Electrical resistivity versus temperature.

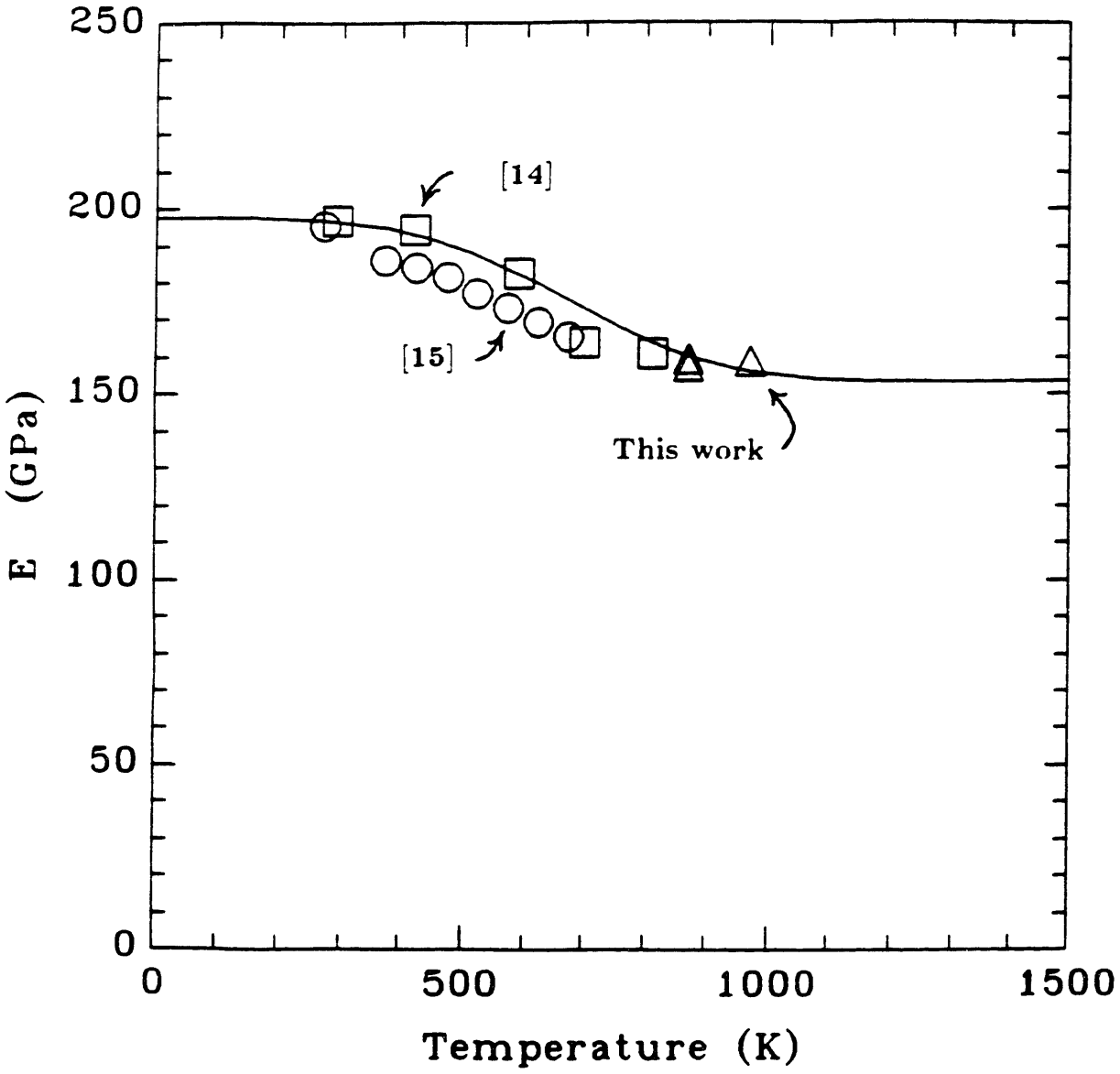

Fig. 1.5 Young's modulus versus temperature.

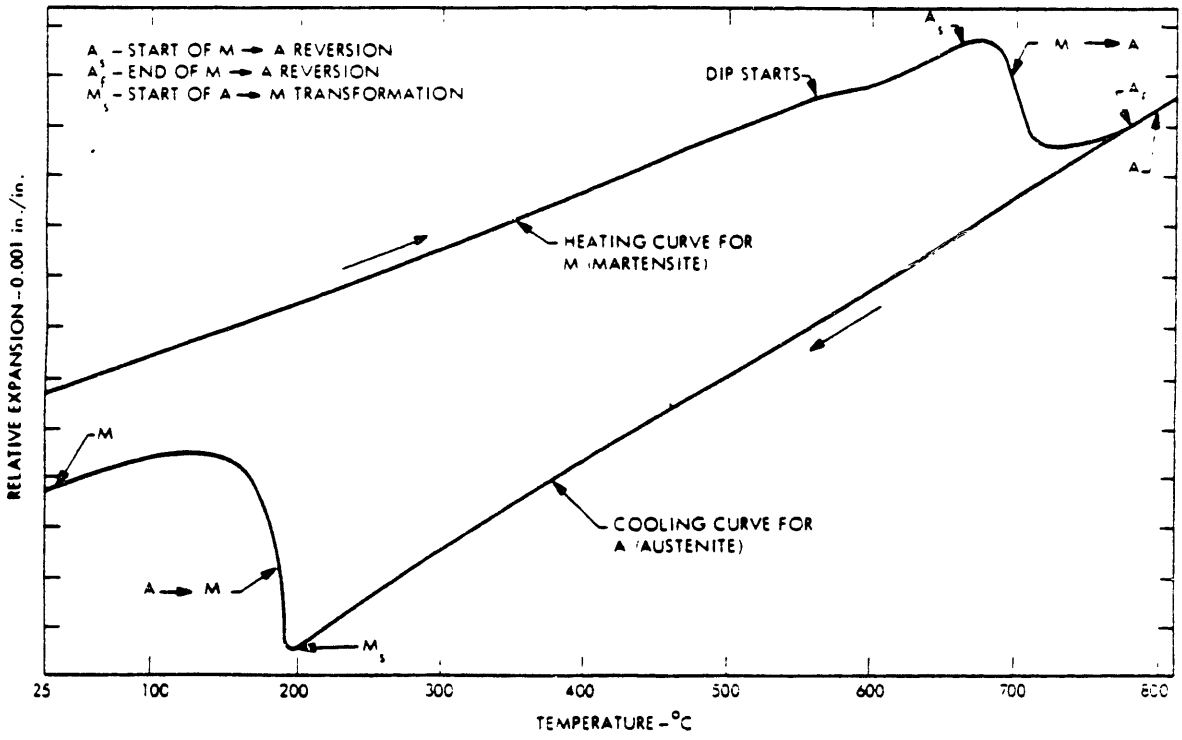

Fig. 1.6 Dilatometric heating and cooling curve for 300 grade maraging steel initially in the annealed martensitic conditions. Specimen was heated at 4.4 C/s from 25 to 815 C, and then air cooled [19].

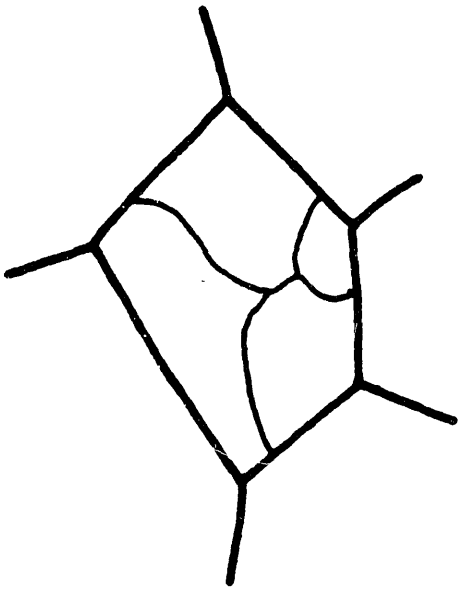

Fig. 1.7a Packets form inside austenite grain.

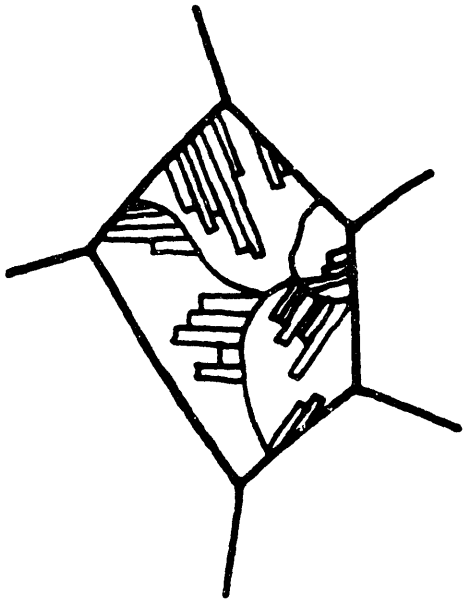

Fig. 1.7b Blocks of martensite laths form within austenite packets.

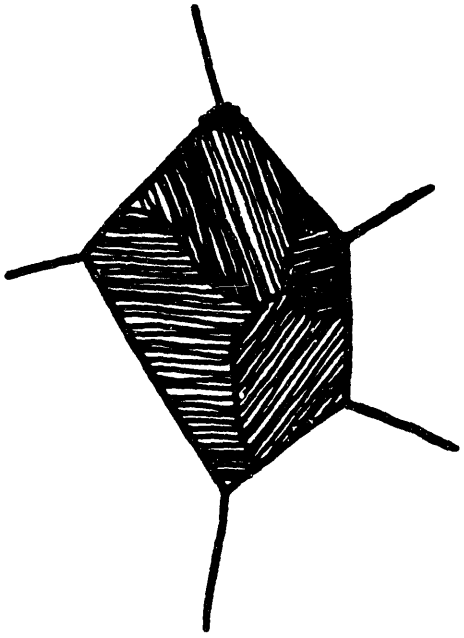

Fig. 1.7c Complete transformation to martensite from austenite.

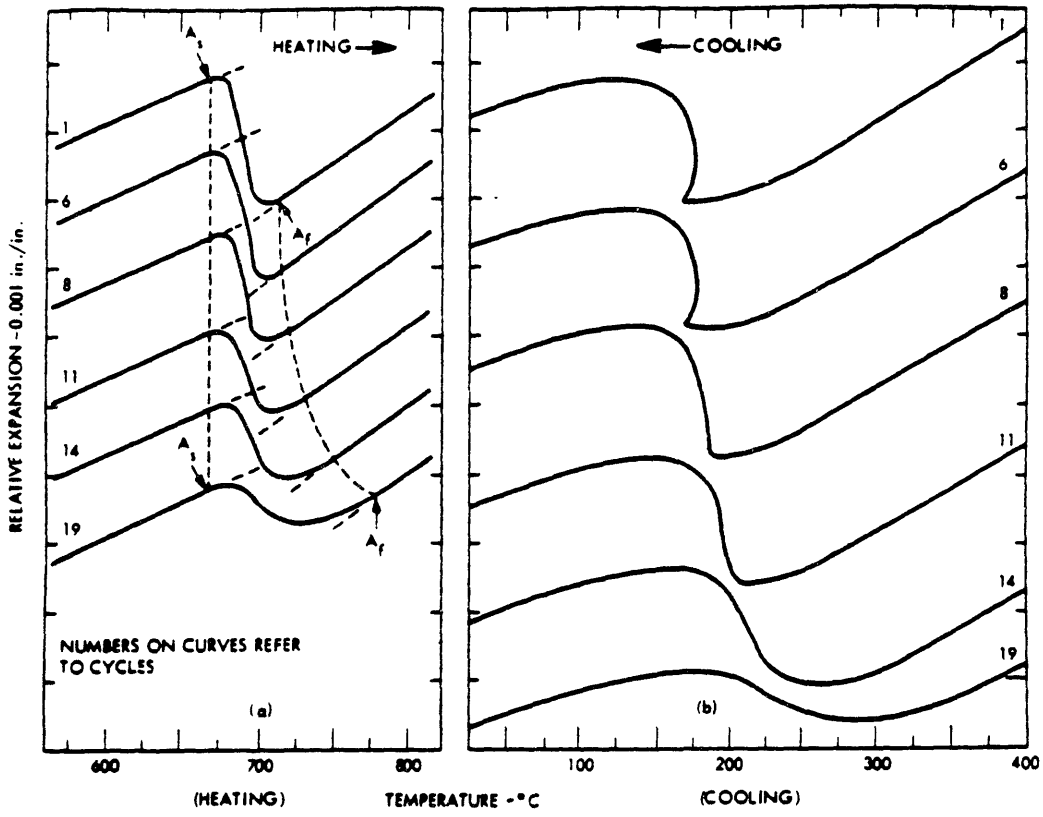

Fig. 1.8 Effect of the number of thermal cycles between ambient temperature and 815 C on the dilatometric heating and cooling curves. The resistance-heated wire specimen, initially in the annealed martensitic maraging steel initially in the annealed martensitic conditions, was heated at 300 to 500 C/s and air cooled for each cycle [16].

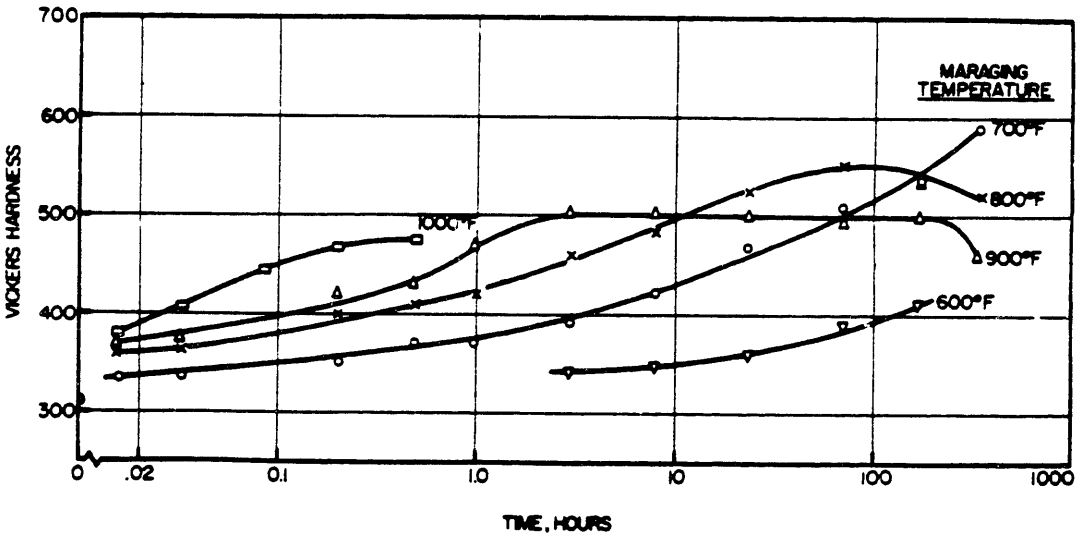

Fig. 1.9 Effect of maraging on Vicker's hardness of 18% Ni steel. Initially annealed at 1800 F [33].

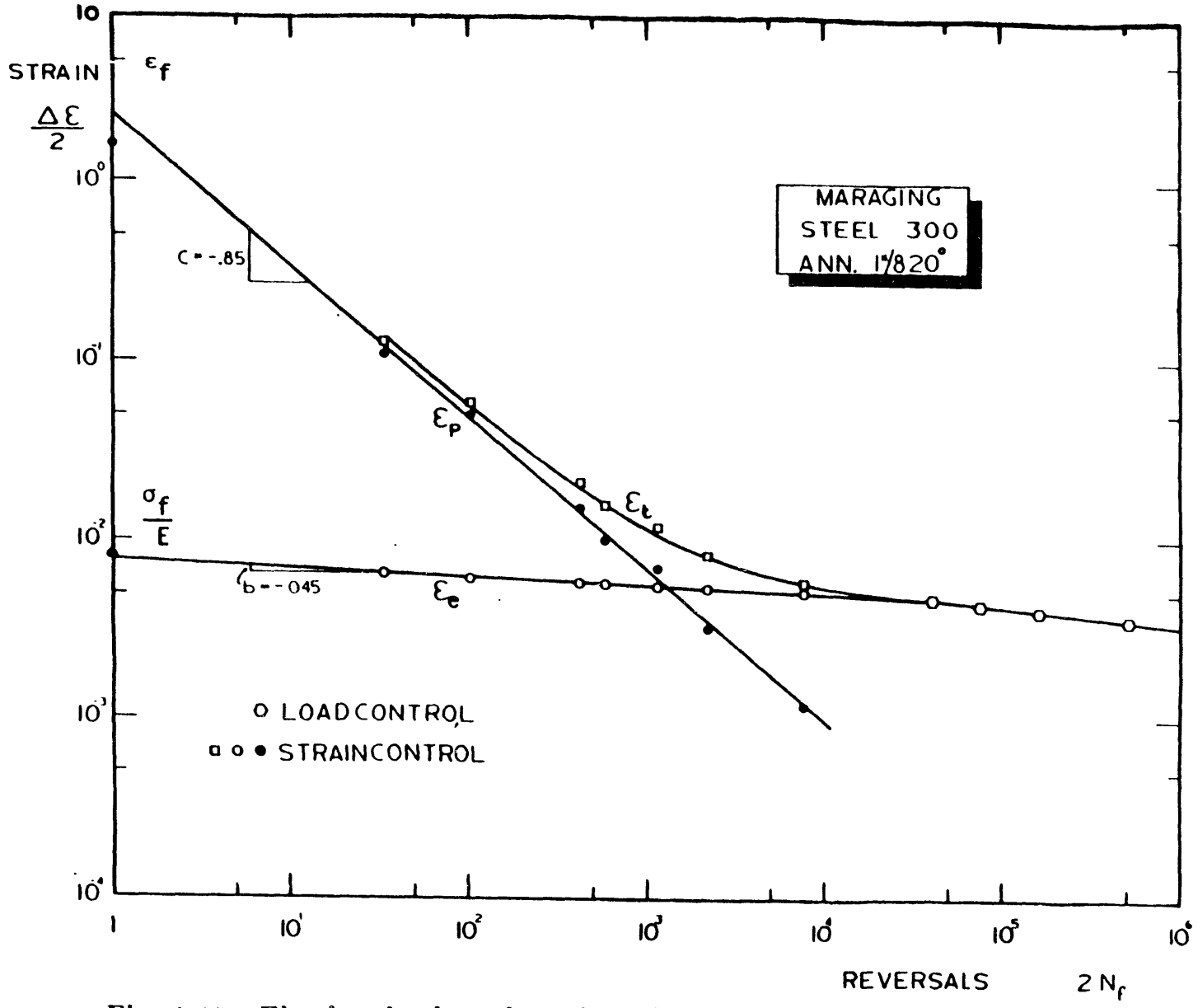

Fig. 1.10 **Elastic, plastic and total strain versus the number of reversals to failure for annealed maraging steel (1 hr at 820 C) [40].**

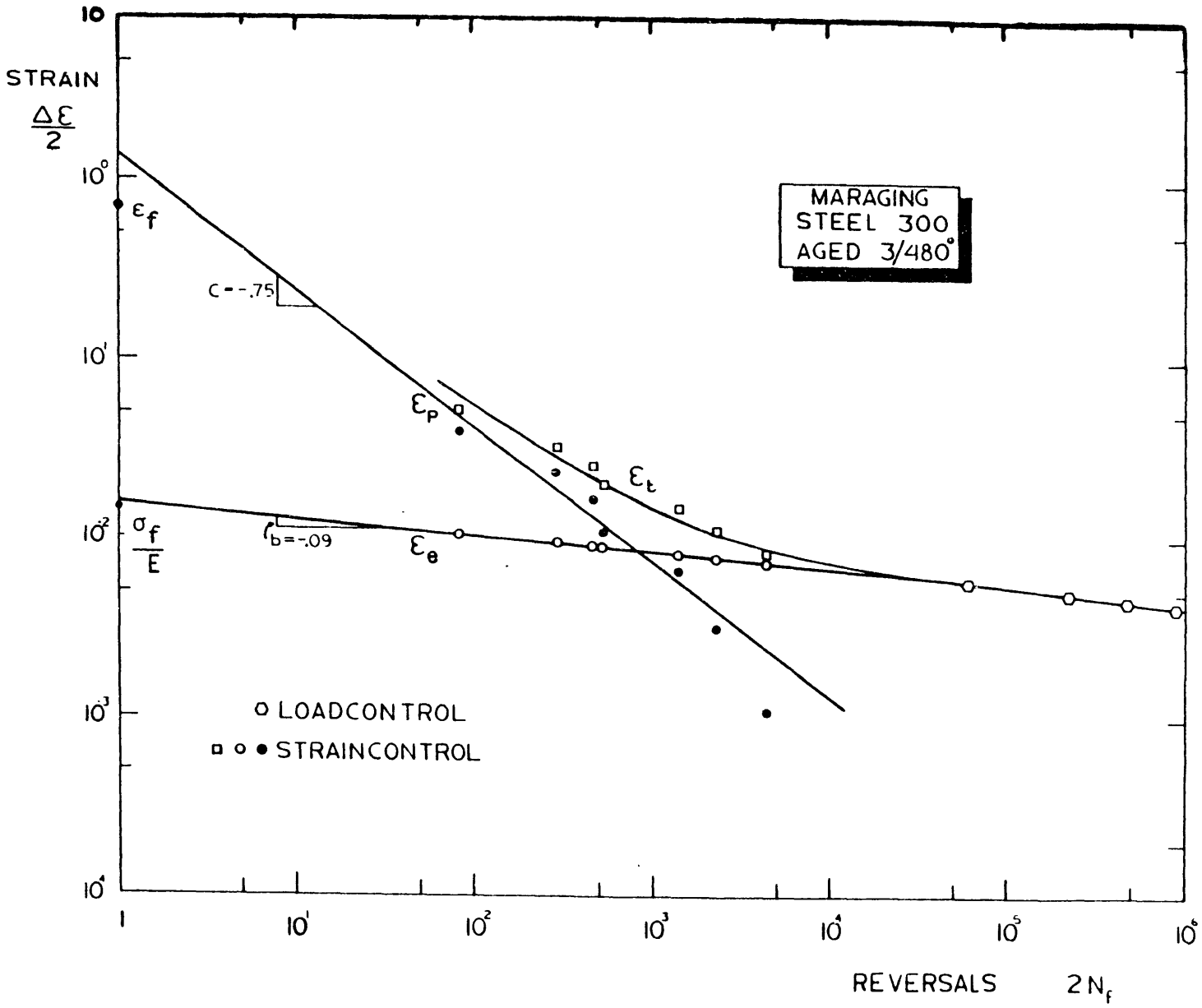

Fig. 1.11 Elastic, plastic and total strain versus the number of reversals to failure for aged maraging steel (3 hr at 480 C) [40].

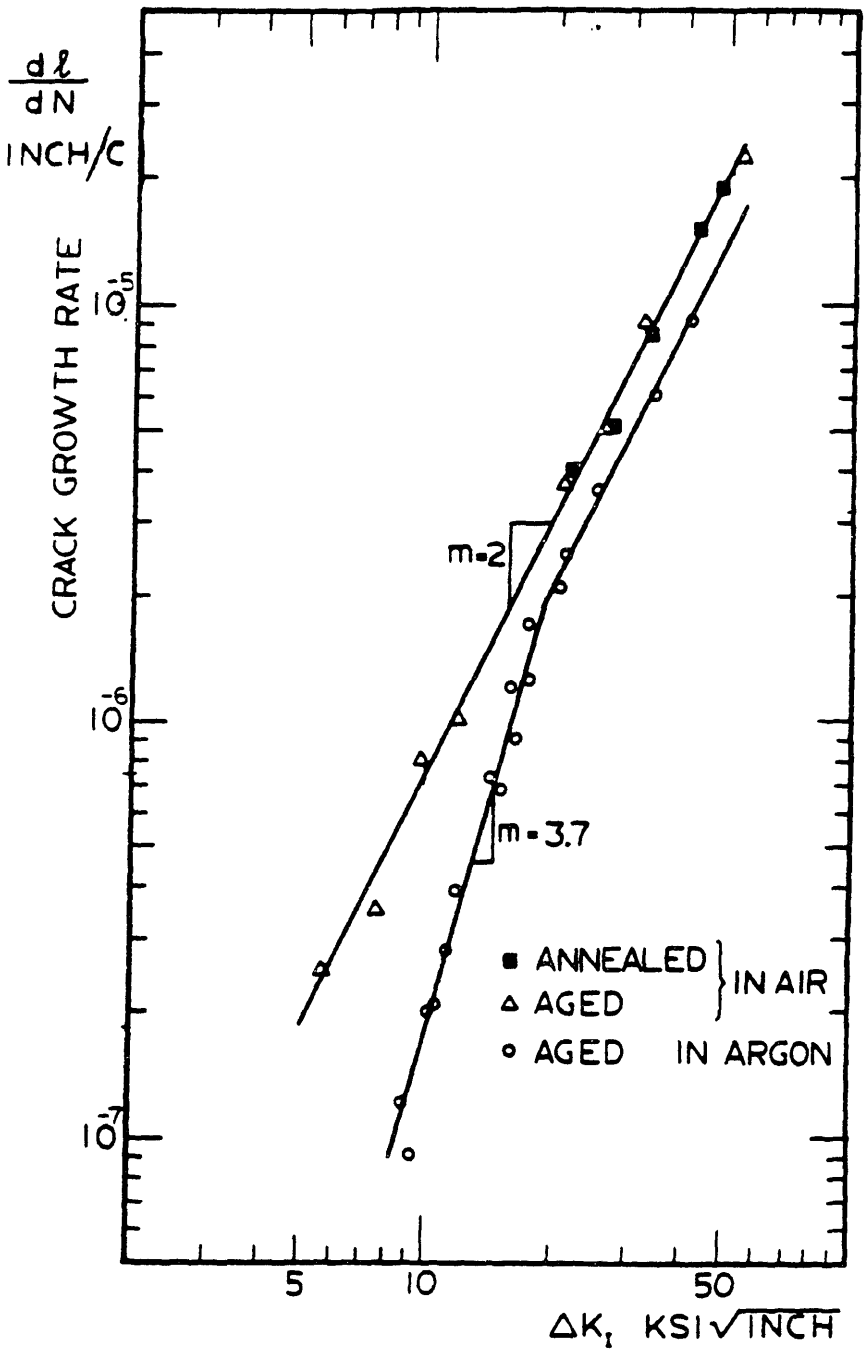

Fig. 1.12 Fatigue crack growth rate as a function of ΔK for annealed and aged maraging steel tested in air and dry argon (dewpoint -50 C) [40].

References

[1] R.F. Decker, *Source Book on Maraging Steels*. 1979, American Society for Metals, Metal Park, Ohio.

[2] D.T. Peters, "A Study of Austenite Reversion During Aging of Maraging Steels," Transactions of the ASM, Vol. 61, 1968.

[3] Peters D.T. and Cupp C.R. "The Kinetics of Aging Reactions in 18 Pct Ni Maraging Steels," Transactions of the Metallurgical Society of AIME, October 1966, Vol. 236, pp. 317-325.

[4] Petrova E.F. and Shvartsman L.A., "Effect of Molybdenum on Precipitation of Carbide Phase in Maraging Steel N18K9M5T," Metallovedenie i Termicheskaya Obrabotka Metallov, September 1978, No. 9, pp. 19-21.

[5] Tolstykh L.G., Usynin V.F. and Arnautov B.V., "Effect of Cr, Ni, and Mo on the Hardeness and Change Points of Maraging Steel of the 0Kh6N8M7S Type," Metallovedenie I Termicheskaya Obrabotka Metallov, December 1978, No. 12, pp. 20-23.

[6] G.P. Miller and W.I. Mitchell, "Structure and Hardening Mechanisms of 18Steels," Journal of The Iron and Steel Institute, Sept. 1965, pp. 899-904.

[7] S. Floreen and G.R. Speich, "Some Observations on the Strength and Toughness of Maraging Steels," Transactions of ASM, Vol. 57, 1964.

[8] W.A. Spitzig, J.M. Chilton and C.J. Barton, "Structure and Strengthening Mechanisms in 300-Grade 18Ni-Co-Mo-Ti Maraging Steel," Transactions of ASM, Vol. 61, 1968.

[9] R.F. Decker, J.T. Eash and A.J. Goldman, "18Maraging Steel," Transactions of the ASM, Vol. 55, 1962.

[10] H.J. Rack and D. Kalish, "The Strength and Fracture Toughness of 18 Ni (350) Maraging Steel," Metallurgical Transactions, Vol. 2, Nov 1971, pp. 3011-3020.

[11] Kalish D. and Rack H.J., "Thermal Embrittlement of 18 Ni (350) Maraging Steel," Metallurgical Transactions, September 1971, Vol. 2, pp. 2665-2672.

[12] Rack H.J. and Holloway P.H., "Grain Boundary Precipitation in 18 Ni Maraging Steels," Metallurgical Transactions A, August 1977, Vol. 8A, pp. 1313-1315.

[13] Johnson W.C. and Stein D.F. "A Study of Grain Boundary Segregants in Thermally Embrittled Maraging Steel," Metallurgical Transactions, March 1974, Vol. 5, pp. 549-554.

[14] Wei R.P., *Aerospace Structural Metals Handbook*, 1972, Belfout Stulen Inc.

[15] "The 18 Per Cent Nickel Maraging Steels" (INCO Databook), Source Book on Maraging Steels, American Society for Metals, R.F. Decker Editor, 1979, pp 351-377.

[16] Valderrama J., "The Temperature Dependence of Bulk and Shear Moduli of Elasticity", B.S. Thesis, Mass. Inst. of Tech., 1988.

[17] Anderson O.L., "Derivation of Wachtman's Equation for the Temperature Dependence of Elastic Moduli of Oxide Compounds", Physical Review, 144, pp. 553-558.

[18] Grimvall, G., *Thermophysical Properties of Materials*, 1986, Elsevier Science Publishers, Amsterdam.

[19] Goldberg A., "Effects of Repeated Thermal Cycling on the Microstructure of 300-Grade Maraging Steel", Transactions of ASM, Vol. 61, 1968, pp. 41-51.

[20] G. Saul, J.A. Roberson and A.M. Adair, "The effects of Thermal Treatment on Austenitic Grain Size and Mechanical Properties of 18 Pct Ni Maraging Steels," Metallurgical Transactions, Vol. 1, Feb 1970.

[21] M. Cohen, G.B. Olson, P.C. Clapp, "On the Classification of Displacive Phase Transformations", Proceedings of the International Conference on Martensitic Transformations ICOMAT 1979, Cambridge Mass USA, June 24-29 1979, pp. 1-11.

[22] P.G. Shewmon, "Transformations in Metals", Copyright 1969 McGraw-Hill, Inc.

[23] Christian J.W., "Thermodynamics and Kinetics of Martensite", Proceedings of the International Conference on Martensitic Transformations, ICOMAT 1979, pp. 220-234.

[24] Korenko M.K. and Cohen M., "Martensitic Transformation in High Magnetic Fields," Proceedings of the International Conference on Martensitic Transformations, ICOMAT 1979, Cambridge, MA USA, pp. 388-393.

[25] Shimizu K., "Effect of Stresses and Magnetic Fields on Martensitic Transformations," Transactions of the Japan Institute of Metals, Vol. 27, No. 12, Dec. 1986, pp. 907-922.

[26] Kakeshita T. and Shimizu K., "Magnetic Effects on the Shift of Ms Temperature of Martensitic Transformation and their Quantitative Evaluation," Proceedings of the International Conference on Martensitic Transformations, (1986) pp. 230-235, The Japan Institute of Metals.

[27] J.M. Marder and A.R. Marder, "The Morphology of Iron-Nickel Massive Martensite," Transactions of the ASM, Vol. 62, 1969, pp. 1-10.

[28] Maki T., Tsuzaki K., and Tamura I., "Formation Process and Construction of Lath Martensite Structure in Fe-C and Fe-Ni Alloys", Proceedings of the International Conference on Martensitic Transformations, ICOMAT 1979, Cambridge, Mass USA, 24-29 June 1979, pp. 22-27.

[29] G.P. Miller, and W.I. Mitchell, "Structure of Nickel-Cobalt -Molybdenum Maraging Steels in the Air-Cooled Condition," Journal of The Iron and Steel Institute," Sept. 1965, pp. 895-898.

[30] A. Goldberg, "Morphology of Martensite Formation in a 300 Grade Maraging Steel", Transactions of the ASM, Vol. 62, 1969, pp. 219-229.

[31] Vialatte B. and Dubois B., "Investigation of the Dilatometric Behavior of Maraging Steel 18Ni-8Co-4Mo," Journal of the Iron and Steel Institute, Feb. 1971, pp. 147-148.

[32] Goldberg A. and O'Connor D.G., "Influence of Heating Rate on Transformations in an 18 per cent Nickel Maraging Steel,", Nature, January 14, 1967, pp. 170-171.

[33] Goldberg A., "Anisotropic Transformations Strains in a 300-Grade Maraging Steel," Journal of the Iron and Steel Institute, March 1970, pp. 289-297.

[34] Fokina A.E., Smirnov L.V. and Sadovskii V.D., "Refining of the Structure of Maraging Steels 03Kh11N10M2T and 03Kh11N10M2TK6," Metallovedenie I Termicheskaya Obrabotka Metallov, October 1974, No. 10, pp. 32-35.

[35] Maslakova T.M., "Effect of Thermal Cycling on the (Gamma- Alpha) Properties of Maraging Steel," Metallovedenie I Termicheskaya Obrabotka Metallov, December 1978, No. 12, pp. 23-27.

[36] S. Floreen and R.F. Decker, "Heat Treatment of 18Maraging Steel," Transactions of ASM, Vol. 55, 1962.

[37] Argon A.S. and Im J. "Separation of Second Phase Particles in Spheroidized 1045 Steel, Cu-0.6Pct Cr Alloy, and Maraging Steel in Plastic Straining," Metallurgical Transactions A, April 1975, Vol. 6A, pp. 839-851.

[38] K. Detert, "Investigation of Transformation and Precipitation in 15the ASM, Vol. 59, 1966, pp. 262-276.

[39] Rack H.J., "Age Hardening-Grain Size Relationships in 18Ni Maraging Steels," Materials Science and Engineering, 34, 1978, pp. 263-270.

[40] F.A. McClintock and A.S. Argon, *Mechanical Behavior of Materials*, 1966, Addison-Wesley Co. Inc., pp. 114-118.

[41] A.S. Argon, "Plastic Deformation:Time Independent Dislocation Mechanisms," Encyclopedia of Materials Science and Engineering, 1986, Pergamon Press Ltd., pp. 3543-3554.

[42] M.A. Meyers and K.K. Chawla, *Mechanical Metallurgy*, 1984, Prentice Hall Inc., pp. 409-413.

[43] L.F.P. Van Swam, "Fatigue Behavior of Maraging Steel 300," ScD Thesis at Mass. Inst. of Tech., Materials Science Dept., 1973.

[44] W.-B. Li, K.E. Easterling and M.F. Ashby, "Laser Transformation Hardening of Steel - II. Hypereutectoid Steels," Acta Metall, Vol. 34, No. 8, 1986, pp. 1533-1543.

[45] C.S. Carter, "Fracture Toughness and Stress Corrosion Characteristics of a High Strength Maraging Steel," Metallurgical Transactions, Vol. 2, June 1971.

[46] Carman C.M. and Schuler M.F., "Some Fractographic Observations of Fatigue-Crack Growth in Maraging Steel," Journal of the Iron and Steel Institute, May 1970, pp. 463-468.

[47] C. Bathias and R.M. Pelloux, "Fatigue Crack Propagation in Martensitic and Austenitic Steels," Metallurgical Transactions, Vol. 4, May 1973, pp. 1265-1273.

[48] Swam L.F.V., Pelloux R.M., and Grant N.J., "Fatigue Behavior of Maraging Steel 300," Metallurgical Transactions A, January 1975, Vol. 6A, pp. 45-54.

[49] Tomkins B., "Fatigue Crack Propagation - An Analysis," Phil. Mag., 18, No. 155, 1968, pp. 1041-1066.

[50] Tomkins B., "Fatigue Failure in High Strength Materials," Phil. Mag., 23, No. 183, 1971, pp. 687-703

[51] D. Kalish and H.J. Rack, "The Strength Differential in a Maraging Steel," Metallurgical Transactions, Vol. 3, August 1972, pp. 2289-2290.

[52] D.C. Drucker, "Plasticity Theory, Strength-Differential (SD) Phenomenon, and Volume Expansion in Metals and Plastics," Metallurgical Transactions, Vol. 4, March 1973, pp. 667-673.

[53] Ledbetter H.M. and Read D.T., "Low Temperature Elastic Properties of a 300-Grade Maraging Steel," Metallurgical Transactions A, November 1977, Vol. 8A, pp. 1805-1808.

[54] R.L. Cairns, "Ultra High-Strength Maraging Steel Wire", Transactions of the ASM, Vol. 62, 1969 pp. 244-256.

[55] Goldberg A., "Influence of Repeated Thermal Cycling under Various Conditions on the Hardness of a Maraging Steel", Welding Journal, Vol. 47, 1968, pp. 199s-202s.

[56] Baker A.J. and Swann P.R. "The Hardening Mechanism in Maraging Steels," Transactions of the ASM, 1964, Vol. 57, pp. 1008-1011.

[57] Joubert F.L. and Valentin G.H., "Notch Strength of Maraging Steel," Engineering Fracture Mechanics, 1976, Vol. 8, pp. 669-676.

[58] Fisher D.M. and Repko A.J., "Plane Strain Fracture Toughness Tests on 2.4 and 3.9-inch-Thick Maraging Steel Specimens at Various Yield Strength Levels," Journal of Materials, JMLSA, Vol. 7, No. 2, June 1972, pp. 167-174.

[59] Edneral A.F., Zhukov O.P. and Perkas M.D., "Effect of Cobalt on Aging of Martensite and Ferrite in Fe-Co-W and Fe-Co-Mo Alloys," Metallovedenie I Termicheskaya Obrabotka Metallov, Oct. 1974, No. 10, pp. 24-28.

[60] Chernyavskaya S.G., Rusinovich Yu. I. and Fridman V.S., "Phases Precipitated in Grain Boundaries During Slow Cooling of Maraging Steels," Metallovedenie I Termicheskaya Obrabotka Metallov, October 1974, No. 10, pp. 45-47.

[61] Lashko N.F., Zaslavskaya L.V., Nikol'skaya V.L. and Solov'eva G.G., "Phase Composition, Structure, and Properties of Maraging Steel Kh14K9N6M5," Metallovedenie I Termicheskaya Obrabotka Metallov, October 1974, No. 10, pp. 39-42.

[62] Leibova N.M., Zot'eva A.S., Kagan E.S. and Felikson A.E., "Use of Maraging Steels for Parts of Metal Working Machines," Translated from Metallovedenie I Termicheskaya Obrabotka Metallov, October 1974, No. 10, pp. 35-39.

[63] Spiridonov V.B., Fridman V.S., Rodionov Yu. L. and Gruzin P.L., "Structural Changes During Aging of Maraging Steel 03Kh11N10M2T," Metallovedenie I Termicheskaya Obrabotka Metallov, October 1974, No. 10, pp. 28-32.

[64] Masyutin V.A. and Shakhnazarov Yu. V., "Effect of Deformation on the Properties of Maraging Steel 04Kh14K13N4M3T," Metallovedenie I Termicheskaya Obrabotka Metallov, December 1978, No. 12, pp. 32-35.

[65] Malinochka Ya.N., Krasnikova S.I., Chernyavskaya S.G. and Pavlenko N.E., "Transformations in Maraging Steel 03Kh11N10M2T Heated to High Temperatures," Metallovedenie I Termicheskaya Obrabotka Metallov, December 1978, No. 12, pp. 28-32.

[66] Alekseeva L.E., Perkas M.D. and Sarrak V.I., "Improvement in the Mechanical Properties of Steel N18K9M5T under the Influence of Applied Stress During Aging," December 1978, No. 12, pp. 15-19.

[67] Tsyrlin E.S., Lakhtin Yu.M. and Blinov V.M., "Effect of Nitriding on the Resistance to Fracture of High-Strength Maraging Steel N18K9M5T," Metallovedenie I Termicheskaya Obrabotka Metallov, December 1978, No. 12, pp. 11-14.

[68] Maloletnev A.Ya., L'vov Yu.B., Pestov I.V. and Perkas M.D., "Resistance of Maraging Steel N18K9M5T to Cyclic Impact Loads," Metallovedenie I Termicheskaya Obrabotka Metallov, July 1975, No. 7, pp. 37-41.

[69] Spiridonov V.B. and Fridman V.S., "High Temperature Brittleness and Selection of Quenching Temperature for Stainless Maraging Steels," July 1975, No. 7, pp. 42-47.

[70] Pigenko A.A., Chernyshova T.A., Shorshorov M.Kh. and Dontsova A.Ya., "Structure Formation in Cast and Deposited Maraging Steel N18K8M3TYu," Metallovedenie i Termicheskaya Obrabotka Metallov, September 1975, No. 9, pp. 24-26.

[71] Dolotova T.S., Kucheryavyi V.I. and Ul'yanova N.V., "Effect of Alloying Elements on Structural Recrystallization of Stainless Maraging Steels," Metallovedenie I Termicheskaya Obrabotka Metallov, September 1975, No. 9, pp. 21-24.

[72] Kazenina A.D., Filimonov G.N. and Soldakov N.K., "Effect of Preliminary Cold Plastic Deformation on the Properties of Maraging Steels," Metallovedenie i Termicheskaya Obrabotka Metallov, September 1975, No. 9, pp. 15-18.

[73] Kondratov V.M. and Skvortsov A.I., "Dependence of Physicomechanical Properties of Maraging Steels on Aging Processes," Metallovedenie i Termicheskaya Obrabotka Metallov, September 1975, No. 9, pp. 11-15.

[74] Zaitseva R.D. and Perkas M.D. "Factors Determining the Ductility and Toughness of Maraging Steels," Metallovedenie i Termicheskaya Obrabotka Metallov, September 1975, No. 9, pp. 2-11.

[75] Jacobi H. and Hagedorn K.E., "Austenite-Reversion and Deformation Behavior of Steady State Unidirectionally Solidified Maraging Steel," Zeitschrift fur Metallkunde, January 1977, Band 68, Heft 1, pp. 44-46.

[76] Francis B., "Increasing the Fracture Toughness of a Maraging Steel Type Alloy," Metallurgical Transactions A, March 1976, Volume 7a, pp. 465-468.

[77] Thevenin J.P., Cizeron G. and Lacombe P., "Etude de la Reversion a Vitesse de Chauffage Rapide de la Martensite de l'Acier Maraging a 18Molybdene," Memoires Scientifiques Rev. Metallurg., LXVIII, No. 4, 1971, pp. 215-222.

[78] Colombarolli W., Metais D. and Murry G., "Contribution a l'Etude des Transformations de l'Austenite Residuelle de Deux Aciers a Outils," Memoires Scientifiques Rev. Metallurg., LXVIII, No. 6, 1971, pp. 375-383

[79] Thevenin J.P., Cizeron G. and Lacombe P., "Etude de la Stabilisation par Trempe Interrompue de l'Austenite des Aciers Maraging a 18Rev. Metallurg., LXVIII, No. 2, 1971, pp. 75-80.

[80] Thevenin J.P., Barreau G., Cizeron G. and Lacombe P., "Stabilite de la Phase Austenitique Obtenue par Cyclage des Acier Maraging a 18Metallurg., LXVIII, No. 12, 1971, pp. 827-835.

[81] Rack H.J., Beitscher S. and Kalish D., "The Strain-Rate and Temperature Dependence of 18Ni(350) Maraging Steel Tensile Properties," Journal of Engineering Materials and Technology, January 1979, vol. 101, pp. 91-97.

[82] Tobler R.L., Reed R.P. and Schramm R.E., "Cryogenic Tensile, Fatigue, and Fracture Parameters for a Solution- Annealed 18 Percent Nickel Maraging Steel," Journal of Engineering Materials and Technology, April 1978, Vol. 100, pp. 189-194.

[83] Kakeshita T. and Shimizu K., "Magnetic Effects on the Shift of Ms Temperature of Martensitic Transformation and their Quantitative Evaluation," Proceedings of the International Conference on Martensitic Transformations, (1986) pp. 230- 235, The Japan Institute of Metals.

[84] E.A. Owen and Y.H.Liu, "Further X-Ray Study of the Equilibrium Diagram of the Iron-Nickel System," Journal of the Iron and Steel Institute, Oct. 1949, pp. 132-136.

Chapter 2

Material Testing and Modelling

The purpose of the material tests performed in this thesis was to study the strength of maraging steel at temperatures above 755 K, where there have only been a few studies [1]. Above 755 K, the strength decreases rapidly with temperature, and plastic strain rate effects are important. The expected service temperature regime is between 298 and 1500 K with plastic strain rates which vary from 10^{-6} - 10^{2} s^{-1} and for plastic strains less than 2 %. Two different plastic strain rate equations (kinetic equation) were developed. The first one is phenomenological, and it uses an over-stress formulation with equations similar to Eqs. 1.10 and 1.11. The second kinetic equation combines an Arrhenius rate equation with a power law stress function to estimate the plastic strain rate. The phenomenological rate equation is best for the testing regime while the Arrhenius rate equation makes the best extrapolations outside the testing regime.

This chapter will study monotonic and cyclic strain hardening behavior. In addition, the effects of phase transformations on strain hardening are investigated. Finally, using data obtained from the work of A. Goldberg on phase transformations in maraging steel [2][3], a model which can predict the combined thermal expansion and phase transformation strain over a temperature range of 298 to 1500 K is proposed.

Tensile Tests

The material tests cover a temperature range of 773 to 1083 K at plastic strain rates between 10^{-6} - 10^{-2} s^{-1} and for plastic strains ε^p less than 2 %. The tensile tests were conducted on an Instron Tensile Machine (Model # TCM1-6.) Fig. 2.1 shows the experimental setup, and Fig. 2.2 the dimensions of the specimens. The data output from this machine is a strip chart recording of force versus time. The applied crosshead displacement speed is v_c. In the elastic regime, approximately $\frac{1}{6}$ of the crosshead displacement occurred in the specimen, and the rest was in the specimen holder. The specimens were placed into a hot resistance heater that surrounded the specimen, and a thermocouple was placed next to the specimen to provide feedback to the heater. The maximum heater

temperature was 1123 K. There was a waiting period of approximately 5 to 10 min before each test began. The temperature variation during the tests was approximately $\pm$ 3K.

There were no strain gages or extensometers attached to the specimens. The engineering strain ε was determined by integrating the output data. $\dot{P}$,L_0, C_{Mach} and t are time rate of change of force, original specimen gage length, machine compliance and time respectively.

$$\varepsilon = \frac{1}{L_0} \int \left(v_c - \dot{P} C_{Mach} \right) dt \tag{2.1}$$

The machine compliance ($C_{Mach} \approx 0.2$ m/MN) is found from the slope of the force versus total displacement curve in the elastic regime ϕ, the original specimen cross sectional area A_0 and the Young's modulus E.

$$C_{Mach} = (tan\phi)^{-1} - \frac{L_0}{A_0 E} \tag{2.2}$$

From these tests, an "elastic limit" strength at 0.01 % offset, the 0.2% offset yield strength, the tensile strength and strain, and the fracture strain were obtained for various temperatures and plastic strain rates (Table 2.1). Engineering stresses and strains are used in Table 2.1, and the plastic strain rates are given at the elastic limit strength. Tests results obtained at a crosshead speed of 20 in/min were discarded because the recording pen was not fast enough to record the peak forces reached during the tests. The strain hardening data obtained from these tests was unreliable due to a large machine compliance and local variations in the slope of the load.

Four observations can be made from an examination of the data in Table 2.1. As temperature increases, the material strength decreases for similar plastic strain rates. For a given temperature, increases in the plastic strain rate result in higher strengths. The influence of plastic strain rate on strength is less at 773 K than it is at higher temperatures. Finally, the uniform strain (at tensile strength) and fracture strains for most of the data increase as the plastic strain rate decreases.

Fig. 2.3 shows the 0.2 % offset yield strength data versus temperature. Included in this plot are yield strengths obtained from a literature search (see

Table 2.2) [4]-[6]. The large decrease in strength from 600 to 900 K is centered at a temperature approximately 200 K less than the martensite to austenite phase transformation temperature. Overaging contributes the most to this reduction in strength. For tests conducted at temperatures above the austenite start temperature (970 K), solutionizing will contribute to a decrease in strength.

The tensile test data covers a broad range of temperatures and material microstructures. This is especially true in the high temperature regime tested in this work. It took approximately 5 min to heat and prepare a specimen for tensile testing, and during this time the microstructure was changing. Depending on the crosshead velocity, the test times varied from 1 to 30 min. Below are estimates of the material condition in the specimens at each of the five test temperatures.

773 K For all temperatures less than or equal to 773 K, the material is in the aged condition, and its strength near room temperature is still near peak.

873 K The material is slightly overaged for the large strain rate tests (still near optimum strength) and overaged for the smaller strain rate tests.

923 K At this temperature, overaging is significant, and there is some austenite reversion.

983 K The material has mixed material phases at this temperature, and the precipitates are overaging and solutionizing.

1083 K The steel is entirely in the austenite phase and precipitates are dissolving back into solution.

For temperatures less than 800 K, the test data is for aged maraging steel, while at temperatures above 1010 K, the test data is for solutionized maraging steel. While the tensile tests provide important data on the strength of maraging steel at various strain rates; they fail to provide information about the evolution of material phase and microstructure. So, the material test data is used to model the material strength in the magnet with the following assumptions and conditions. In the previous Chapter, two thermal cycling zones were described. In the first zone, temperatures peaked at 1450 K in 250 μs, cooled to 690 K in 5 s and then slowly cooled to room temperature in 15 min. In the second zone, the temperature peaked at 690 K in 5 and slowly cooled to room temperature.

Initially, the material in the magnet is entirely in the aged condition. Eventually, the material in Zone 1 becomes solutionized, while the material in Zone 2 is slightly overaged. The tensile test data are used here to approximate the material strength of the magnet for these two zones under the condition that the material in Zone 1 is solutionized but does not evolve, and the material in Zone 2 is slightly overaged. In addition, for temperatures less than 800 K the material strength in Zone 1 is approximated by the strength of aged material (an overestimate.) This overestimate of strength occurs when the magnet is heating up and cooling down. The strength of material between the two zones is approximated by test data at 923 and 983 K.

Kinetic Equations

In the previous Chapter, relationships between plastic strain rate and flow strength were not discussed. However, the rate of plastic deformation is related to the applied stress. For the range of temperatures studied in this thesis, plastic strain rate effects have a significant influence on the flow strength. A kinetic equation relates the rate of plastic straining to the applied stress at a given temperature and microstructure.

In this work, the uniaxial stress strain data is used to model the strength of maraging steel. For the short pulse magnet, its mechanical behavior is nearly unidirectional; the largest stresses and plastic strain increments occur in the the hoop direction. A three dimensional formulation is required to model the electromagnetic and thermal loads. The short pulse magnet deformation behavior is also cyclic. The cyclic stress strain behavior of maraging steel shows a significant Bauschinger effect. A kinematic plasticity formulation is used to model this behavior. The equation shown below describes the variables which define the kinetic equations used in this thesis. S_{ij} is the deviatoric stress. Ω_{ij} is the back stress, and $\|S_{ij} - \Omega_{ij}\|$ is the equivalent effective stress ($\|S_{ij} - \Omega_{ij}\|$ is defined with Eq. 3.29 in Chapter 3)

$$\dot{\varepsilon}^p = \dot{\varepsilon}^p \left(\|S_{ij} - \Omega_{ij}\|, \theta, s \right) \tag{2.3}$$

Before specific forms of the kinetic equation are selected and modeled, some comments about the change in strain rate effects with temperature are necessary. Strain rate effects have been observed and measured for maraging

steel at cryogenic and room temperatures [7]. When the strain rate at room temperature is increased by a factor of 1000, the yield strength is increased by just 7% , while at 983 K, increasing the plastic strain rate from 9.1×10^{-6} to 1.0×10^{-2} s^{-1} (a factor of 1100) causes the elastic limit strength to increase 270%. The strain rate sensitivity ($d\, ln\dot{\epsilon}\ /\ d\, ln\sigma$) is of the order of 100 between room temperature and 773 K and of the order of 10 between 873 to 1083 K (see Table 2.2).

Phenomenological Rate Equation

In the previous chapter, flow strength equations (Eq. 1.3-1.12) were proposed to model the strength of maraging steel. The general form of those equations can now be used to formulate new equations which approximate the flow strength based upon the tensile test data. What follows is a step by step description of how Eq. 1.11 can be modified to form a new flow strength formula. Using Eq. 1.3, the flow strength is rewritten below using flow strength terms (Eq. 1.11.)

$$s = f_M \left(s^M_{\ell.s} + s^M_p + s^M_d\right) + (1 - f_M) \left(s^A_{\ell.s} + s^A_p + s^A_d\right) \tag{2.4}$$

The first step is to remove the dislocation strength term s_d from Eq. 2.4. A back stress Ω_{ij} would model dislocation polarization and a limited amount of strain hardening; omitting it and s_d means that this process is not adequately accounted for in this formulation. Next, the solution and lattice flow strength contributions and the precipitation flow strength contributions for both the martensite and austenite phases are replaced with linear approximations to the temperature effect with the resulting assumption that the precipitate flow strength is static and does not evolve. This assumption is valid in maraging steel, so long as the precipitates do not change in size, spacing or volume fraction. As expected, the martensite solution, lattice and precipitation strength constant s_1 from the tensile data is larger than the austenite constant s_2 (see Table 2.3.)

$$s = f_M (s_1 + s_3\theta) + (1 - f_M)(s_2 + s_3\theta) \tag{2.5}$$

The s_3 constant gives this equation a small negative strength versus temperature slope. The same s_3 constant is used for both the martensitic and austenitic

terms because this assumption results in a more "well behaved" strength formula (different constants were tried, but this led to unrealistic strength predictions).

The final change made to this formula (Eq. 2.5) affects the martensite volume fraction variable f_M. Upon heating from room temperature into the austenite temperature regime, this variable changes from 1 at 970 K to 0 at 1010 K. This change is centered at 990 K and occurs over a temperature span of just 40 K. The tensile test results suggest the flow strength decreases over a broader temperature range which is centered at a lower temperature. For this reason, f_M is replaced by a thermal variable f_θ (Eqs. 2.6 and 2.7.) θ_0 and n_θ are material constants. The f_θ variable goes from 0.99 at 370 K to 0.01 at 1030 K. An exponential function was selected for f_θ, because it gives a continuous and smooth change in value over a relatively small temperature range:

$$s = f_\theta\,(s_1 + s_3\theta) + (1 - f_\theta)\,(s_2 + s_3\theta)\,, \tag{2.6}$$

where

$$f_\theta = exp\left(-\left(\frac{\theta}{\theta_0}\right)^{n_\theta}\right). \tag{2.7}$$

Eq. 2.6 is the flow strength formula developed for the phenomenological rate equation. This flow strength equation does not depend on the plastic strain rate, while the tensile test data clearly shows a strong plastic strain rate dependence. In that context, the flow strength formula for s (Eq. 2.6) will now be called the threshold or initial yield strength, and is defined at a plastic strain offset of 0.01 % and a plastic strain rate of 1×10^{-8} s^{-1} [8][9]. For equivalent effective stresses less than s, the plastic strain rate is zero, and for effective stresses greater than s, a kinetic equation determines the resulting plastic strain rate. The evolution of s is not modeled.

In Fig. 2.3, a curve is drawn beneath the yield strength data. This curve is the threshold strength function. The material constants s_1, s_2, s_3, θ_0 and n_θ were determined using a least squares data fit to the estimated threshold strength at each of the tensile test temperatures (Table 2.3.). The estimated threshold strengths were determined by extrapolating the elastic limit strengths down to a plastic strain rate of 1×10^{-8} s^{-1}. Thus, the threshold strength function is beneath most of the data points in Fig. 2.3 because of strain hardening and plastic strain rate effects.

Three forms for the phenomenological rate (kinetic) equation were examined for this formulation, a power law, an exponential and an hyperbolic sine function [10]-[15]. The simpler power law formula is used in this study, because of the three it best approximated the tensile data. The phenomenological kinetic equation is shown below in Eqs. 2.9 and 2.10. $\dot{\varepsilon}_0^p$ and $n_{\dot{\varepsilon}^p}$ are material constants.

$$\dot{\varepsilon}^p = 0 \qquad For \quad \|S_{ij} - \Omega_{ij}\| \leq s \tag{2.8}$$

$$\dot{\varepsilon}^p = \dot{\varepsilon}_0^p \left(\frac{\|S_{ij} - \Omega_{ij}\| - s}{(s_2 - s_1)(1 - f_\theta)} \right)^{1/n_{\dot{\varepsilon}^p}} \qquad For \quad \|S_{ij} - \Omega_{ij}\| > s \tag{2.9}$$

As mentioned before, plastic strain rate effects are most important in the high temperature regime and less so at temperatures less than 800 K. This observation is used in the formulation of Eq. 2.9. Rearranging Eq. 2.9 for the equivalent effective stress shows that the plastic strain rate affects the equivalent effective stress in the high temperature regime only: low temperature (martensite) strain rate effects are neglected in this treatment.

$$\|S_{ij} - \Omega_{ij}\| = f_\theta (s_1 + s_3\theta) + (1 - f_\theta) \left[s_2 + s_3\theta + (s_2 - s_1) \left(\frac{\dot{\varepsilon}^p}{\dot{\varepsilon}_0^p} \right)^{n_{\dot{\varepsilon}^p}} \right] \tag{2.10}$$

During a tensile test of virgin material, the back stress Ω_{ij} is initially zero and increases as the stress σ_{ij} increases. It is assumed that $\Omega_{ij} = 0$ and $\dot{\Omega}_{ij} \neq 0$ at the elastic limit strength. Thus, at the elastic limit strength σ_{ij} and $\dot{\varepsilon}^p$ are known. Since the elastic limit strength is defined in this model at a plastic strain of 0.01%, the plastic strain rate is non zero for this elastic limit strength. The material constants for Eq. 2.10 are found by performing a least squares data fit with the elastic limit strength and plastic strain rate data with the results shown in Table 2.3. Fig. 2.4 shows the elastic limit strengths predicted by Eq. 2.10 plotted with the tensile test data. The average error between the data and Eq. 2.10 is 15%.

Although the fit of the elastic limit strength data to the curves is not exact, it is sufficiently close to conclude that Eqs. 2.6, 2.7 and 2.10 adequately predict the elastic limit strengths in the temperature, plastic strain (1 %) and plastic strain rate regimes tested. There are two objectives motivating this analysis of the test data. First, the large drop in flow strength centered around 800 K must be modeled with a smooth and continuous function. Secondly, the kinetic equation should give reasonable extrapolations for the plastic strain rate outside

the testing temperature regime. The phenomenological rate equation satisfies the first objective, but its extrapolations of plastic strain rate outside the testing temperature regime are smaller than expected.

Arrhenius Rate Equation

In the development of the phenomenological rate equation, very little of the "physics" of plastic deformation at high temperatures was incorporated into the equations. At high temperatures ($\theta/\theta_m > 0.5$,) the effect of thermal activation on the motion of dislocations is fundamental. In the high temperature regime, increases in temperature lower the equivalent effective stress necessary for plastic straining. This relationship is not predicted by the phenomenological rate equation. The kinetic equation shown below captures this effect. Δh is a stress dependent activation energy, and R is the universal gas constant. $\dot{\varepsilon}_0^p$, σ_0 and $n_{\dot{\varepsilon}^p}$ are material constants.

$$\dot{\varepsilon}^p = \dot{\varepsilon}_0^p \left(\frac{\frac{\|S_{ij}-\Omega_{ij}\|}{\sigma_0}}{G} \right)^{1/n_{\dot{\varepsilon}^p}} exp\left(\frac{-\Delta h \left(\frac{\|S_{ij}-\Omega_{ij}\|}{\sigma_0} \right)}{R\theta} \right) \tag{2.11}$$

There are four main features to this Arrhenius rate equation. First, an Arrhenius term $exp(-\Delta h/R\theta)$ is included in the equation to model thermal activation energy effects on the plastic strain rate. Secondly, the activation energy Δh is a function of stress. Third, the plastic strain rate is a function of the equivalent effective stress raised to the power $1/n_{\dot{\varepsilon}^p}$. This exponent is often a function of temperature, but this dependence was not studied. Lastly, the plastic strain rate is also a function of the shear modulus G. In other words, the flow strength is proportional to the shear modulus (see Eqs. 1.4 - 1.6.)

Fitting the experimental data to the Arrhenius rate equation is accomplished in two steps. For the first step, at constant stress Δh is assumed constant, and a least squares data fit is performed on Eq. 2.11 to determine Δh_0, $n_{\dot{\varepsilon}^p}$ and $\dot{\varepsilon}_0^p$. These constants are given in Table 2.4. For the second step, data from literature is used to analyze the change in activation with stress. Since the elastic limit strength and the plastic strain rate are not given in most published data, the yield strength is used for the elastic limit strength and a plastic strain rate of 10^{-4} s^{-1} is assumed. Using Δh versus σ data, a line is fitted to the data

points, and the stress σ_0 at zero activation energy is calculated. Then, a polynomial function of stress is used to model the activation energy. The constants A, B, n_1, n_2 and σ_0 are contained in Table 2.4, and the evolution of $\dot{\Omega}_{ij}$ is given by Eq. 2.14 below.

$$\Delta h = \Delta h_0 \, f\left(\frac{\|S_{ij} - \Omega_{ij}\|}{\sigma_0}\right) \tag{2.12}$$

$$f\left(\frac{\|S_{ij} - \Omega_{ij}\|}{\sigma_0}\right) = 1 + A\left(\frac{\|S_{ij} - \Omega_{ij}\|}{\sigma_0}\right)^{n_1} + B\left(\frac{\|S_{ij} - \Omega_{ij}\|}{\sigma_0}\right)^{n_2} \tag{2.13}$$

Fig. 2.5 shows the stress versus activation energy data and Eq. 2.12. The average error between the calculated and predicted activation energies is 7 %. An activation energy of 223 kJ/mole is reasonable, since the self diffusion energy for Fe varies between 239 and 270 kJ/mole for temperatures between room temperature and 1650 K, and the self diffusion energy for Ni is 284 kJ/mole [16].

Finally, it is possible to compare the experimental data to predictions made by the Arrhenius rate equation. Fig. 2.6 shows the strength predictions at the five test temperatures. The average error between the data points and the predicted strengths is 14 %. The strengths predicted with the Arrhenius kinetic equation at 773 K are too low for plastic strain rates less than 10^{-3} s^{-3}, but it gives more realistic predictions of strength than the phenomenological kinetic equation at 1083 K and higher.

Figs. 2.7 and 2.8 compare the elastic limit strengths predicted by the phenomenological rate equation and the Arrhenius rate equation. Fig 2.7 shows the strengths and weaknesses of these two equations. At 773 K, the phenomenological rate equation makes a better prediction of strength than the Arrhenius rate equation, while at 1400 K, the Arrhenius rate equation makes a smaller and more likely prediction of strength. In Fig. 2.8, the variation of strength with temperature at constant plastic strain rate shows that Arrhenius rate equation gives more conservative predictions of strength than the phenomenological rate equation.

Cyclic Fatigue Tests

Four cyclic fatigue tests ($\sigma_{min}/\sigma_{max} = -1$) at 873, 873, 973 and 1073 K provided important cyclic strain hardening and low cycle fatigue data. The

plastic strain range of interest is less than 1.0%. Table 2.6 lists the conditions and results of these tests. A discussion of the fatigue results is postponed until Chapter 6. For these tests, an 810 MTS machine was used. These tests were carried out by a fellow graduate student Glen Romanoski, and a more detailed description of this experimental setup can be found in [17]. Fig. 2.9 details the dimensions of the test specimens. Strain in the specimen was measured with ceramic extensometer probes. The specimens were heated with an induction heater, and a thermocouple spot welded to the specimen provided feedback to the induction heater. Temperature variations in these tests were approximately $\pm$ 1K, and the temperature variation along the gage section was about 3 K/mm. Feedback from the extensometry allowed the tests to be performed at a constant strain rate.

The first cycle of the cyclic stress strain test data (Figs. 2.10a to 2.10d) reveals the following observations. The Bauschinger effect is present during cyclic straining, and the amount of strain hardening decreases with increasing temperature. The shape of the first quarter cycle (monotonic) of the cyclic stress strain curve is similar to the "halved" tip-to-tip cyclic stress strain curve (described later below). The first half of the low cycle fatigue life exhibits neither cyclic strain hardening nor softening, beyond the first quarter cycle (the cyclic curves which followed Figs. 2.10a-d did not significantly change). The Bauschinger effect was an expected observation, but the lack of cyclic strain softening at high temperatures (maraging steel shows cyclically softens at room temperature) was not. The lack of cyclic strain hardening or softening exists over at least a 200 K temperature range.

For this work, the plastic straining is uniaxial and cyclic. The dislocation flow strength is modeled with a kinematic back stress or rest stress tensor Ω_{ij}, and the evolution of back stress is proportional to $h\dot{\epsilon}^p_{ij}$ (see also [18]-[20]).

$$\dot{\Omega}_{ij} = {}^2/_3 \, h \, \dot{\epsilon}^p_{ij} \tag{2.14}$$

It is worth mentioning here that for small strains (less than 1 %) Ω_{ij} is more associated with moving the easy parts of a dislocation distribution, and that at larger strains Ω_{ij} is for monotonic (isotropic) strain hardening. The parameters governing the evolution of the strain hardening coefficient h were discussed in the last chapter (Eqs. 1.11-1.12). The next section describes equations used to approximate this coefficient under uniaxial cyclic conditions.

Monotonic Strain Hardening

Fig. 2.11 shows the monotonic (first quarter cycle) stress strain curves at the three different test temperatures. Clearly more strain hardening occurs at the lower temperatures. While it is possible to model strain hardening as a function of temperature and plastic strain for these three curves, complex thermo plastic loading histories present several problems. For instance, plastic deformation at 873 K can substantially increase the flow strength, but subsequent deformation at 1073 K would likely be dominated by dynamic recovery mechanisms resulting in softening. Thus, determining the strain hardening coefficient h is a complex problem which requires extensive testing and modelling to make predictions for complex thermal loading histories.

For this work, the following assumptions have been made. First, a strain hardening coefficient for a monotonic stress strain curve, h_m, is explicitly defined in terms of the monotonic plastic strain ε_m^p and three material constants h_0, ε_0^p and n_h.

$$h_m = h_0\left(1 + \frac{\varepsilon_m^p}{\varepsilon_0^p}\right)^{-(n_h+1)} \tag{2.15}$$

This function was selected because it initially predicts a high strain hardening coefficient, but as the plastic strain increases, the coefficient goes to zero strain hardening (caused by dynamic recovery). This assumption means the change in flow strength due to plastic straining is a predetermined function of the plastic strain ε_m^p. The function is fitted to the plastic strain hardening data obtained at 1073 K. This particular data was selected because it has the smallest amount of strain hardening. This in turn increases the magnitude of the plastic straining and should lead to conservative estimates of material life. The constants are given in Table 2.6.

Cyclic Strain Hardening

Next, it is assumed the strain hardening behavior of maraging steel can be divided into two modes, monotonic and cyclic hardening. The next assumptions make use of the similarity between the monotonic stress strain curve and the tip-to-tip cyclic stress strain curve. As an example, consider the cyclic stress curve shown in Fig 2.10d and redrawn in Fig. 2.12a. If the top cyclic stress strain curve CB is translated to the origin and scaled by a factor of 1/2 on both

axes, then the resulting dashed curve $C'B'$ in Fig. 2.12b is very similar to the monotonic curve AB. Two conclusions are made from this observation. The size of the cyclic elastic regime is twice the size of the monotonic elastic regime, and the cyclic hardening coefficient h_c should predict twice as much hardening as the monotonic hardening coefficient at twice the monotonic plastic strain. This relationship is enough to define the following equation for the cyclic hardening coefficient. The variable ε_c^p is the plastic strain since reversal.

$$h_c = h_0 \left(1 + \frac{\varepsilon_c^p}{2\varepsilon_0^p} \right)^{-(n_h+1)} \tag{2.16}$$

To evaluate Eqs. 2.15 and 2.16, ε_m^p and ε_c^p must be determined. Initially, monotonic behavior is assumed and ε_m^p equals zero. During monotonic deformation, the plastic strain rate $\dot{\varepsilon}^p$ equals the monotonic plastic strain rate $\dot{\varepsilon}_m^p$.

$$\varepsilon_m^p \Big|_{t=0} = 0 \tag{2.17}$$

$$\dot{\varepsilon}_m^p = \dot{\varepsilon}^p \tag{2.18}$$

So, during monotonic hardening, $\dot{\varepsilon}_m^p$ is integrated to determine ε_m^p and then this is used to calculate h_m.

For cyclic behavior, a special set of rules is constructed to evaluate h_c. A maximum stress method is proposed here to differentiate between cyclic and monotonic strain hardening. When the back stress equals or exceeds the previous maximum magnitude of back stress Ω_{max} (determined from an integration of Eq. 2.14 and 2.15 from 0 to ε_m^p), monotonic strain hardening is assumed, otherwise cyclic hardening is assumed. When the direction of plastic straining reverses, ε_c^p is set to to zero. During cyclic strain hardening, the plastic strain rate $\dot{\varepsilon}^p$ equals the cyclic plastic strain rate $\dot{\varepsilon}_c^p$.

$$\dot{\varepsilon}_c^p = \dot{\varepsilon}^p \tag{2.19}$$

So, during cyclic hardening, $\dot{\varepsilon}_c^p$ is integrated to determine ε_c^p, and then this is used to calculate h_c. Fig. 2.13 depicts ε_m^p and ε_c^p during the first cycle of deformation. Between points A and B, monotonic hardening occurs and ε_m^p goes from zero to ε_1^p. Between B and C, cyclic hardening occurs and ε_c^p goes from

zero to $|\varepsilon_2^p - \varepsilon_1^p|$. Finally, between C and D, there is cyclic hardening, and ε_c^p goes from zero to $|\varepsilon_3^p$-$\varepsilon_2^p|$. The details describing the calculation of h_m and h_c are given in Appendix C.

Finally, Figs. 2.14a-2.14d show the cyclic stress strain data and the curves predicting their behavior (the predicted curves were generated by a finite element analysis of a single element using the material strength models described here; the implementation of these models is given in the next chapter). The phenomenological rate equation is used for the "predicted" phenomenological curves. The predicted elastic limit strengths are approximately 150 MPa greater than the elastic limit strengths measured in these tests. The elastic limit strengths predicted from the Arrhenius rate equation are also about 150 MPa larger than the measured strengths. Fig. 2.15 compares the predicted room temperature behavior and data obtained by Van Swam [21].

Phase Transformation Recovery

Two additional material strength tests were performed under strain control at 1073 and 973 K to determine the effect of phase transformations on the flow strength. In the first test (Fig. 2.16a) the tensile specimen was heated to 1073 K (13.3 K/s), loaded to 0.31% plastic strain, unloaded, cooled to room temperature (-3.3 K/s), reheated to 1073 K, and held for approximately 10 min while the extensometry was recalibrated. Thus, the tensile specimen underwent two phase transformations. The stress-strain slopes were smaller than expected (Young's modulus of 13 versus 17 GPa), and we have not been able to explain this. Reloading to 0.7% total strain showed some of the initial hardening to remain since the previous stress level was attained after only 0.14% rather than 0.31 % plastic strain. There is also a Bauschinger effect on reloading.

The second test was the same as the first test but at 973 K. In this test, the heating portion of the thermal cycling consisted of heating to 1073 K (about 1 min), to ensure a complete transformation from martensite to austenite, and then cooling to 973 K (also about 1 min). The first reloading showed more hardening (same elastic limit) than at 1073 K; as if there had not been phase transformations. After the second unloading (Fig. 2.16b), the specimen was thermally cycled for a second time. The next loading was done in compression to determine the Bauschinger effect. The specimen had plastically strained a total of 0.53% to achieve a stress level of 600 MPa, but upon reverse loading it took

0.49% reverse plastic strain to attain -600 MPa. These two strains are nearly the same, between isotropic and kinematic hardening. The reversed loading shows a Bauschinger effect reduced by a factor of about 2. Thus, phase transformations from austenite to martensite and back to austenite did not entirely eliminate the accumulated strain hardening in the specimen, and Bauschinger effects are reduced.

Other factors such as austenite reversion, grain boundary segregation, and solutionizing all may have influenced the flow strength during thermal cycling. When modelling the cyclic thermal behavior of maraging steel, it is assumed that phase transformations do not alter the strain hardening contribution to the flow strength. Figs. 2.16a and 2.16b show the stress strain results from these tests along with the predicted curves.

Phase Transformation Modeling

Modeling phase transformation straining requires several simplifying assumptions. The first assumptions concern the nature of phase transformations in a short pulse magnet application. The second set of assumptions deal with the linearization of phase transformation behavior.

For an initially homogeneous, polycrystalline microstructure in maraging steel, just dilatational phase transformation straining can be assumed (no distortional shear straining). In a short pulse magnet, the heating rate is extremely rapid, and an inner portion of the coil (Zone 1) is thermally cycled to temperatures greater than 968 K. In this zone aging and austenite reversion are insignificant, and the dilatation versus temperature curves are independent of the number of thermal cycles (see Chapter 1). Similarly, it is assumed that solutionizing, applied stress and magnetic fields do not affect the transformation curves (also see Chapter 1).

It is assumed here that the thermal expansion and transformation strains can be approximated with linear functions of temperature and material phase (Fig. 2.17). Next, an assumption is made about the transformation behavior when thermal cycling results in partially transformed material. Under these circumstances, new austenite and martensite transformation starting temperatures are interpolated using the intermediate phase composition. These new starting temperatures are determined with a linear scaling between the untransformed

start temperature and the completely transformed finish temperature, as shown in Fig. 2.18 for transformation between austenite and martensite.

The combined thermal expansion and phase transformation strain ε_t, has an important influence on mechanical behavior. The evolution of ε_t is a function of temperature θ, rate of temperature change $\dot{\theta}$ and the material phase volume fraction f_M as shown in Eq. 2.20.

$$\dot{\varepsilon}_t = \dot{\varepsilon}_t \left(\theta, \dot{\theta}, f_M\right) \tag{2.20}$$

Predictions for ε_t have been divided into the three temperature regimes (Fig. 2.19). In the first and third regime a linear function of temperature is adequate for ε_t, but in the second regime, a temperature and phase-dependent interpolation function h_i, discussed below, is used to determine ε_t. Fig. 2.19 graphically shows and Table 2.7 gives values for the 7 thermal expansion and phase transformation constants α_M, α_A, θ_{A_s}, θ_{A_f}, θ_{M_s}, θ_{M_f} and ϵ_0 needed to define the thermal cycling. θ_0 is the reference temperature for a thermally stress free structure, and ϵ_{t_i} are the combined thermal expansion and phase transformation strains for each of the interpolation functions.

$$\varepsilon_t = \alpha_M (\theta - \theta_0) \qquad \theta < \theta_{M_f} \tag{2.21}$$

$$\varepsilon_t = \sum_{i=1}^{4} h_i \epsilon_{t_i} \qquad \theta_{M_f} \leq \theta \leq \theta_{A_f} \tag{2.22}$$

$$\varepsilon_t = \alpha_A (\theta - \theta_0) - \varepsilon_0 \qquad \theta > \theta_{A_f} \tag{2.23}$$

The interpolation function can be visualized in Fig. 2.20 as a 4 node finite element. Nodes 1 and 2 correspond to the martensite finish and austenite start temperatures and strains respectively, where the material phase is entirely martensitic. Likewise, Nodes 3 and 4 are the austenite finish and martensite start temperatures and strains, where the material phase is entirely austenitic. The two interpolation variables are material phase χ and a normalized transformation

temperature variable r. For the martensitic and austenitic phases, χ is 1 and -1 respectively. Definitions for h_i, χ and r are given below.

$$h_1 = (1-r)(1+\chi)/4 \qquad h_3 = (1+r)(1-\chi)/4 \qquad (2.24a)(2.24c)$$

$$h_2 = (1+r)(1+\chi)/4 \qquad h_4 = (1-r)(1-\chi)/4 \qquad (2.24b)(2.24d)$$

$$\chi = 2f_m - 1 \qquad (2.25)$$

$$r = \frac{(2\theta - \theta_{A_s} - \theta_{M_f}) + \left(\frac{\chi-1}{2}\right)(\theta_{M_s} - \theta_{M_f} - \theta_{A_s} + \theta_{A_f})}{(\theta_{A_s} - \theta_{M_f}) + \left(\frac{\chi-1}{2}\right)(\theta_{M_s} - \theta_{M_f} + \theta_{A_s} - \theta_{A_f})} \qquad (2.26)$$

Thus, for a given temperature and material phase composition f_m, it is possible to determine ε_t. However, in the second regime, f_M changes with time, so an evolution equation for this variable is necessary. Based upon the assumptions already mentioned, a change in material phase only occurs when r equals -1 or 1. Eqs. 2.27 and 2.28 define $\dot{\chi}$ for these two cases.

When $r = 1$ and $\dot{\theta} > 0$ then

$$\dot{\chi} = \frac{-(1+\chi)}{(\theta_{A_f} - \theta_{A_s})}\dot{\theta}. \qquad (2.27)$$

When $r = -1$ and $\dot{\theta} < 0$ then

$$\dot{\chi} = \frac{(1-\chi)}{(\theta_{M_s} - \theta_{M_f})}\dot{\theta}. \qquad (2.28)$$

Otherwise

$$\dot{\chi} = 0 \qquad (2.29)$$

Conclusions

Tensile tests were performed on maraging steel to determine its strength at temperatures above 755 K and at plastic strain rates which varied from 10^{-6} to 10^{-2} s^{-1}. From these tests, the following conclusions are drawn.

1. As temperature increases, there is a large decrease in its strength from 2000 MPa at 300 K to approximately 200 MPa at 1100 K.

2. Plastic strain rate effects are more important at high temperatures than at low temperatures; the strain rate sensitivity ($d\ ln\dot{\varepsilon}\ /\ d\ ln\sigma$) is of order 100 between room temperature and 773 K and of order 10 between 873 and 1083 K.

3. In general, as temperature increases and plastic strain rates decrease, the fracture strain increases.

4. The decrease in strength is centered at a temperature 200 K lower than the martensite-to-austenite transformation temperatures.

5. The material strength data taken at temperatures less than 900 K is for material in the aged condition, while for temperatures greater than 1010 K, the material strength data is for solutionized maraging steel.

Two kinetic equations are proposed to model the plastic strain rate behavior of maraging steel over a temperature range of 298 to 1500 K. These equations must predict the large drop in strength observed at 900 K, and also give reasonable extrapolations of plastic strain rate for temperatures above 1083 K. The first kinetic equation is phenomenological, and it best predicts the decrease in strength at 900 K. This equation is based upon the flow strength formulation proposed in Chapter 1, and it uses an over-stress power law to predict the plastic strain rate. The second kinetic equation combines an Arrhenius activation energy function with a power law stress function. This kinetic equation best approximates the plastic strain rates outside the testing temperature regime.

Cyclic fatigue tests revealed that for a temperature range of 873 to 1073 K, maraging steel exhibits neither cyclic hardening nor softening through half its fatigue life. The Bauschinger effect is significant at all temperatures. The strain hardening behavior is modeled with a back stress variable which is a function of the strain hardening coefficient times the plastic strain rate. The strain hardening is divided into two modes, monotonic and cyclic. Neither cyclic hardening or softening is predicted. The strain hardening behavior is approximated with explicit equations for the monotonic and cyclic strain hardening coefficients, and the strain hardening data at 1073 K is used to determine the material constants

for these equations. Strain hardening is purposely underestimated to predict conservative (larger) plastic strains.

An investigation into the phase transformation effects on strain hardening gave mixed results. In the first test, at 1073K, phase transformations did not eliminate the accumulated strain hardening from a previous loading. For the second test, at 973 K, less than half the Bauschinger strain remained after phase transformations. The model used in this study ignores phase transformation effects on the strain hardening strength.

Finally, the combined thermal expansion and phase transformation strains are predicted with linear approximations to the dilatation versus temperature curves obtained from literature. The rate of evolution of the combined thermal and phase transformation strains is modeled as a function of temperature and the material phase volume fraction. The material strength and phase transformation behavior modeled in this chapter are incorporated into the finite element analysis described in the next chapter.

Table 2.1 Summary of tensile test experiments.

Temp. (K)	Pl. Strain Rate* (s^{-1})	El. Limit Strength (MPa)	Yield Strength (MPa)	Tensile Strength (MPa)	Tensile Strain (%)	Fracture Strain $\ln(A_i/A_f)$
773	3.66×10^{-5}	1243	**	1273	.84	1.28
	1.20×10^{-4}	1240	1282	1330	2.45	1.15
	1.46×10^{-3}	1285	1321	1354	1.96	0.94
	4.37×10^{-3}	1195	1320	1324	1.57	0.88
873	4.24×10^{-5}	450	472	511	2.08	4.57
	1.37×10^{-4}	636	684	707	1.52	2.64
	1.03×10^{-3}	719	810	842	1.58	1.83
	1.75×10^{-2}	833	869	881	1.34	1.14
923	8.84×10^{-6}	344	350	401	2.87	4.16
	1.22×10^{-4}	503	527	595	2.33	4.47
	1.29×10^{-3}	592	662	738	2.56	3.25
	1.42×10^{-2}	876	883	888	1.24	1.87
983	9.12×10^{-6}	218	219	242	14.74	2.79
	2.87×10^{-4}	242	274	328	2.83	3.87
	1.24×10^{-3}	363	421	484	3.77	1.53
	1.03×10^{-2}	586	592	598	0.98	2.15
1083	3.44×10^{-5}	217	231	236	1.28	2.96
	1.38×10^{-4}	230	252	257	2.96	2.57
	1.30×10^{-3}	334	344	366	2.50	2.19
	1.57×10^{-2}	417	419	421	0.98	1.93

* Plastic strain rate at the elastic limit strength (0.01 % offset, Eq. 2.1) assuming all the crosshead rate is applied to the specimen and holder.

** The test specimen reached its maximum (engineering) strength after a plastic strain offset less than 0.2 %.

Table 2.2 Temperature versus yield strength (0.2 % offset) data from literature.

Temperature (K)	Yield Strength (MPa)	Reference
200	2077	[4]
298	1931	
422	1771	
589	1626	
700	1517	
811	1110	
298	2027	[5]
589	1693	
700	1570	
754	1343	
783	1192	
811	1056	
173	2180	[6]
233	2010	
293	1930	
373	1790	
473	1710	
573	1650	
673	1510	
753	1380	

Table 2.3 Material constants for phenomenological rate equation.

s_1	1912.0	MPa
s_2	50.0	MPa
s_3	-0.017	MPa/K
θ_0	812.0	K
n_θ	6.43	
$\dot{\varepsilon}_0^p$	1.84	s^{-1}
$n_{\varepsilon_0^p}$	0.238	

Table 2.4 Material constants for Arrhenius rate equation.

A	3.39	
B	-4.39	
n_1	7	
n_2	6	
σ_0	2351	MPa
Δh_0	223	kJ/mole
$\dot{\varepsilon}_0^p$	1215	s^{-1}
$n_{\varepsilon_0^p}$	0.149	

Table 2.5 Summary of cyclic test experiments.

Test	Temp. (K)	Strain Rate (s^{-1})	El.Limit Strength (MPa)	Strain Range (%)	Stress Range (MPa)	Cycles to 90% Stress Range	Cycles to Failure N_f
1	873	4.0×10^{-3}	248	0.38	1222	650	830
2	873	5.2×10^{-3}	248	0.64	1282	420	475
3	973	3.6×10^{-3}	227	0.58	830	230	270
4	1073	3.6×10^{-3}	159	0.70	596	135	293

Table 2.6 Material constants for strain hardening behavior (Eq. 2.15 and 2.16).

h_0	454.82	GPa
ε_0^p	6.53×10^{-5}	
n_h	0.198	

Table 2.7 Thermal and phase transformation strain constants.

α_M	martensite thermal exp. coef.	10.1×10^{-6}	K^{-1}
α_A	austenite thermal exp. coef.	17.7×10^{-6}	K^{-1}
θ_{A_s}	austenite start temp.	968	K
θ_{A_f}	austenite finish temp.	1008	K
θ_{M_s}	martensite start temp.	473	K
θ_{A_s}	martensite finish temp.	373	K
ε_0	phase transf. strain	7.52×10^{-3}	

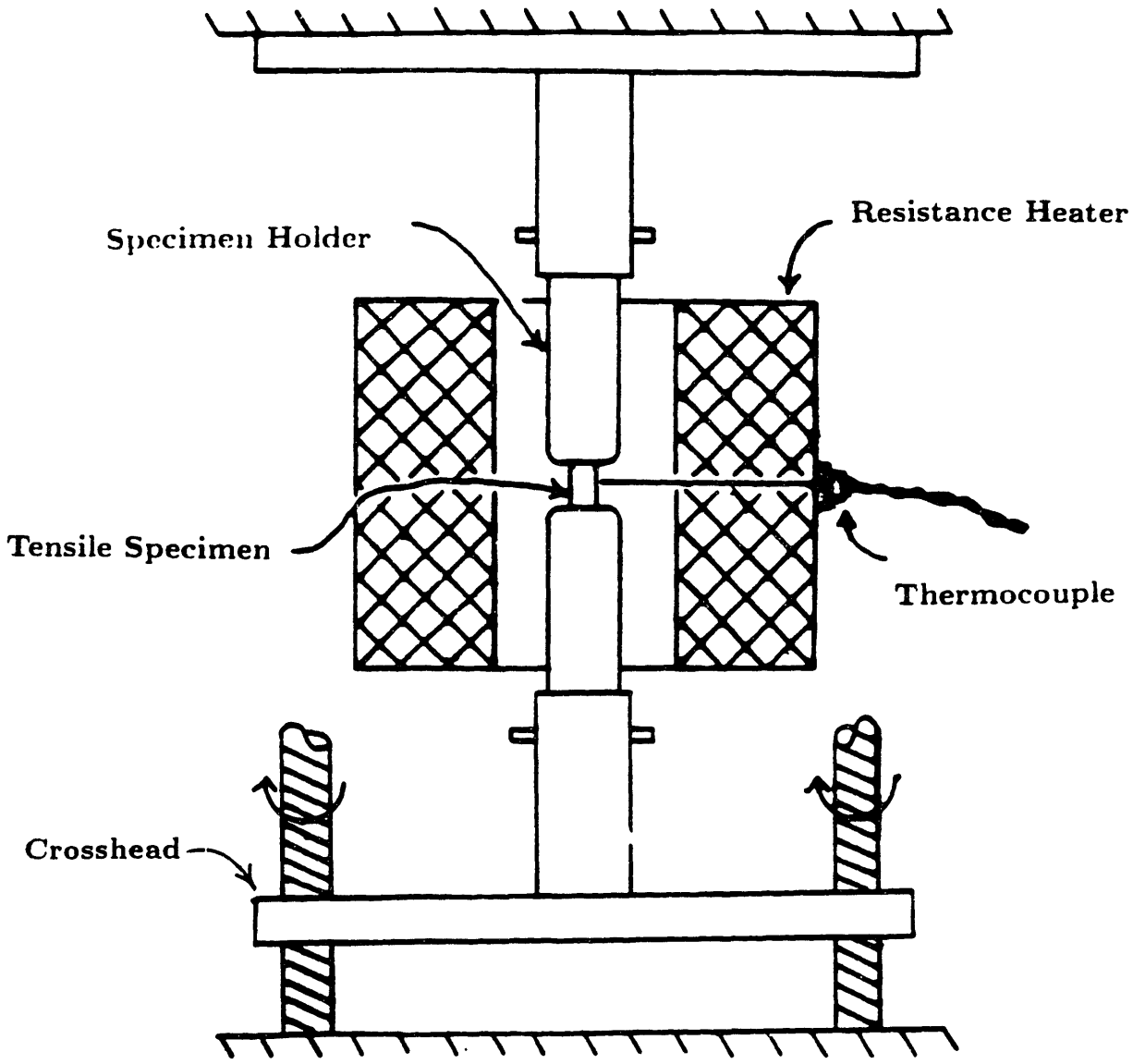

Fig. 2.1 Experimental setup for tensile tests.

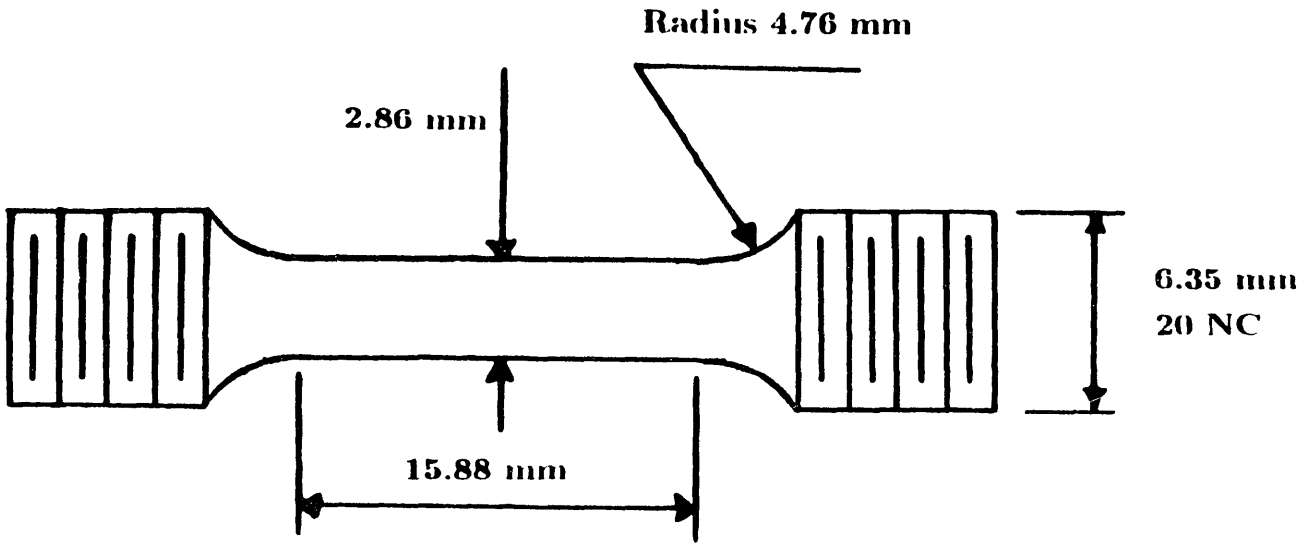

Fig. 2.2 Tensile test specimen.

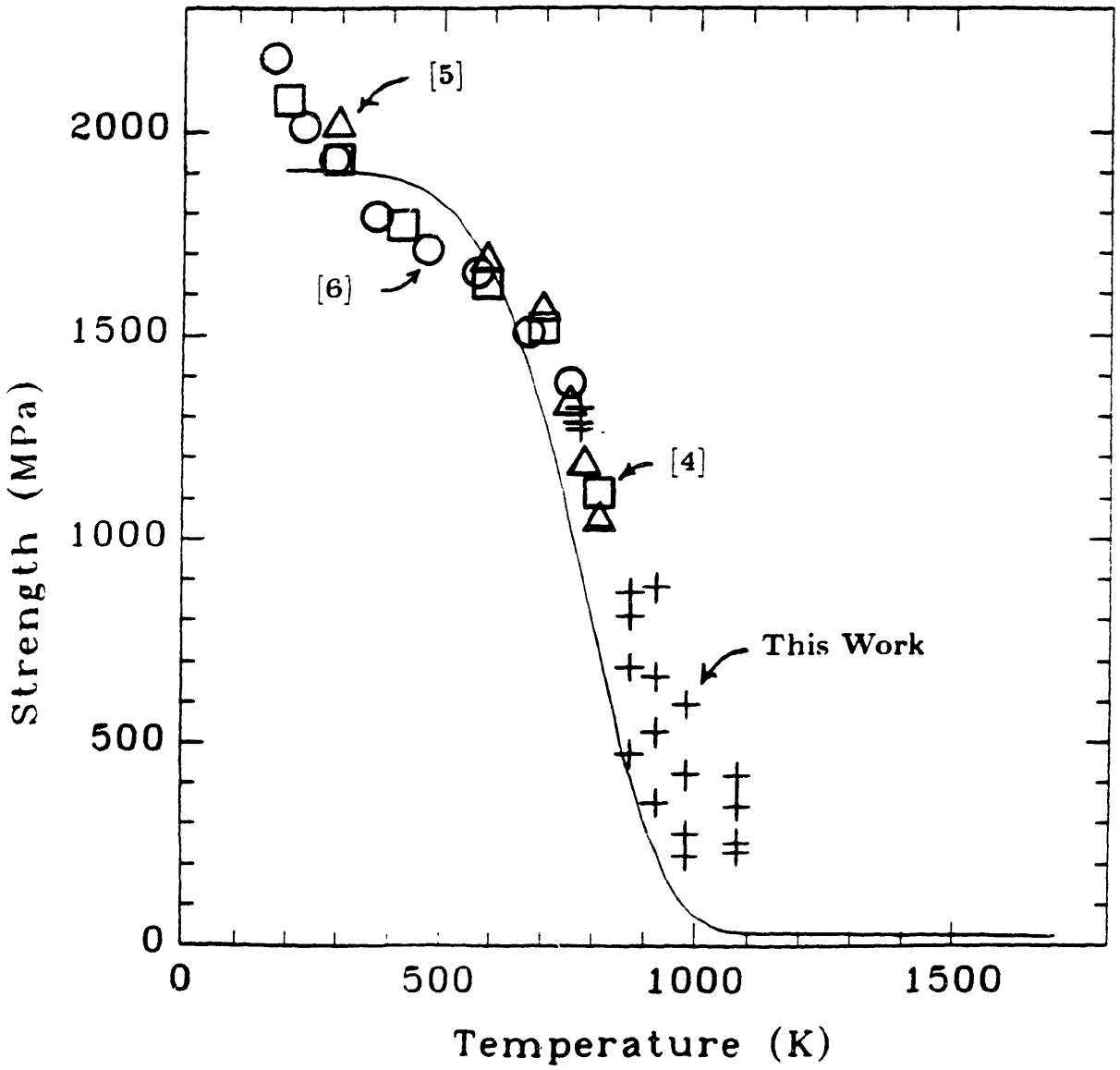

Fig. 2.3 Yield strength (0.2 % offset) versus temperature compared to the phenomenological rate equation Eq. 2.10 ($\dot{\epsilon}^p = 1 \times 10^{-8}$ s^{-1})

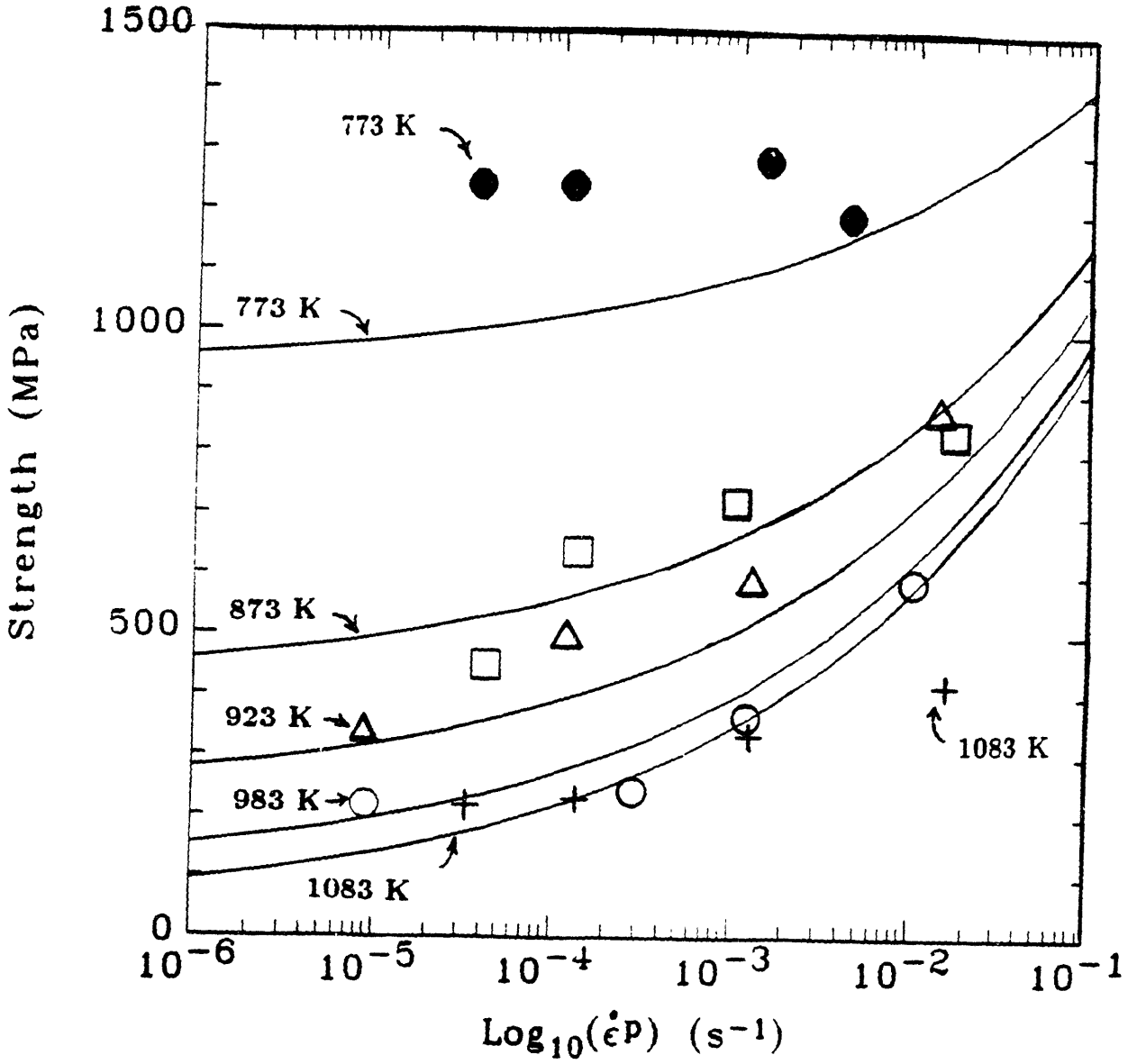

Fig. 2.4 Elastic limit strength data at different temperatures with varying plastic strain rate (phenomenological rate equation).

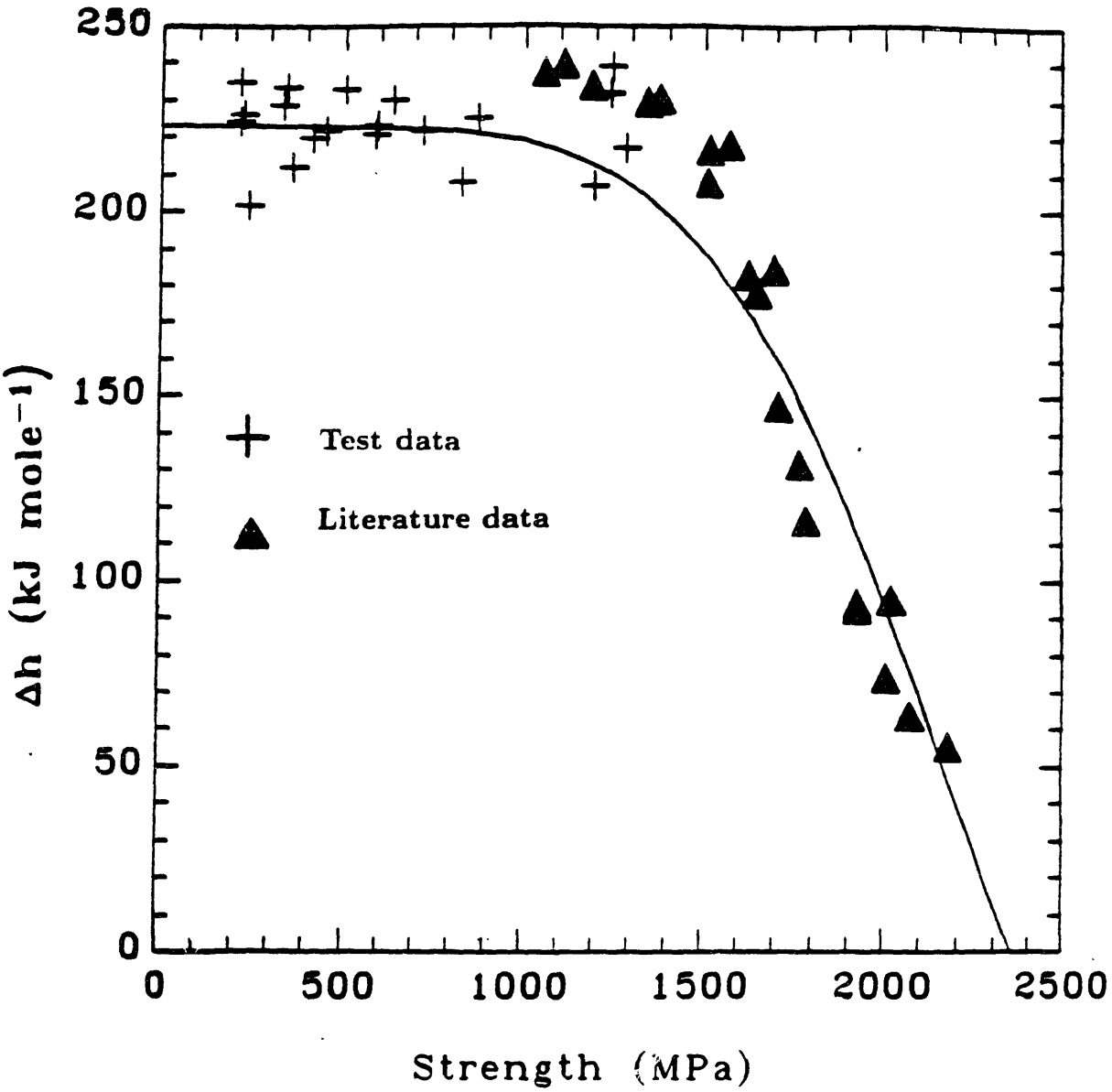

Fig. 2.5 Activation energy versus equivalent effective stress ($\|S_{ij} - \Omega_{ij}\|$). The literature data is calculated from yield strengths where $\dot{\varepsilon}^p = 10^{-4} s^{-1}$ is assumed. The test data is calculated from elastic limit strengths and plastic strain rates.

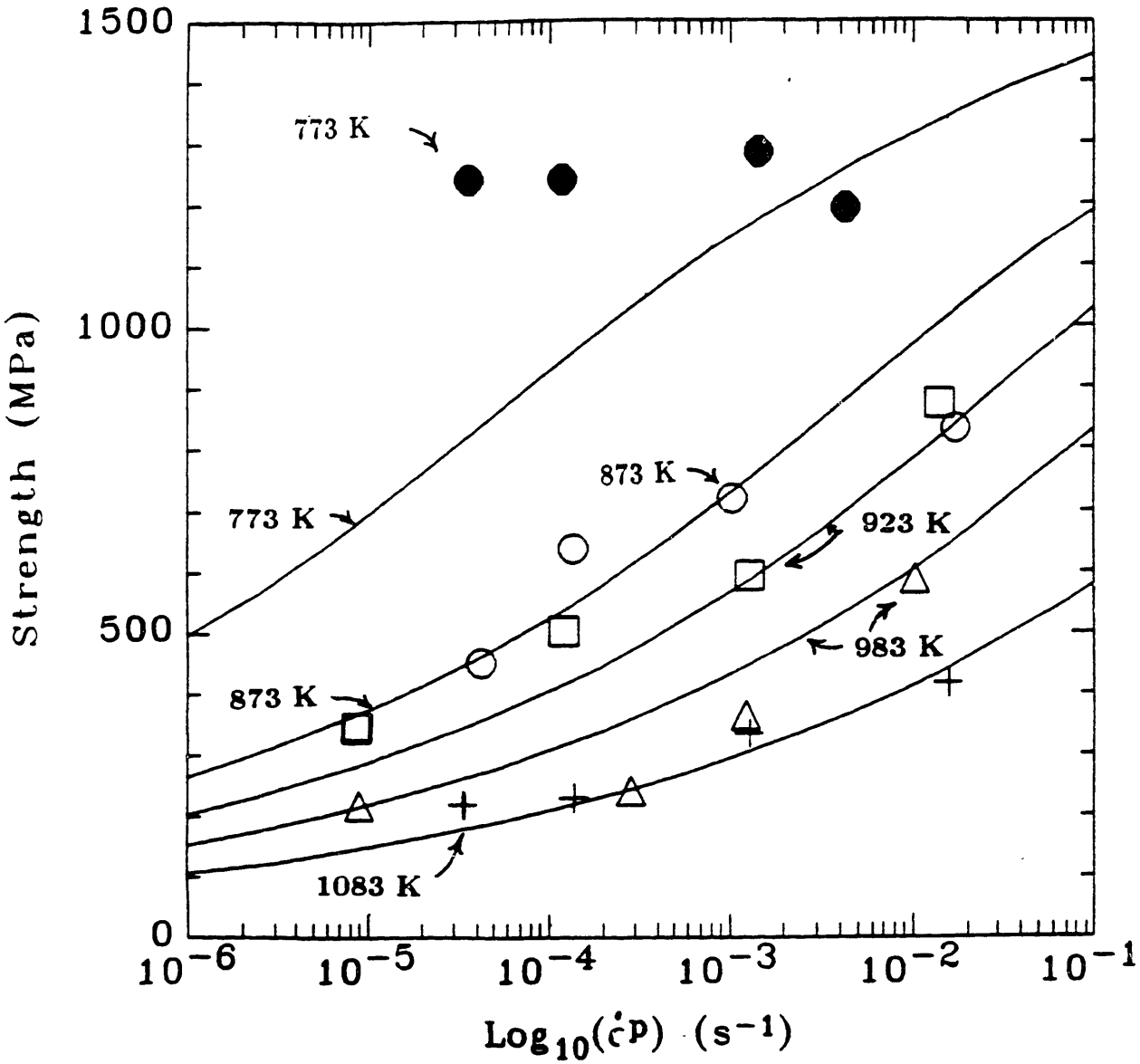

Fig. 2.6 **Elastic limit strength data at different temperatures with varying plastic strain rate (Arrhenius rate equation).**

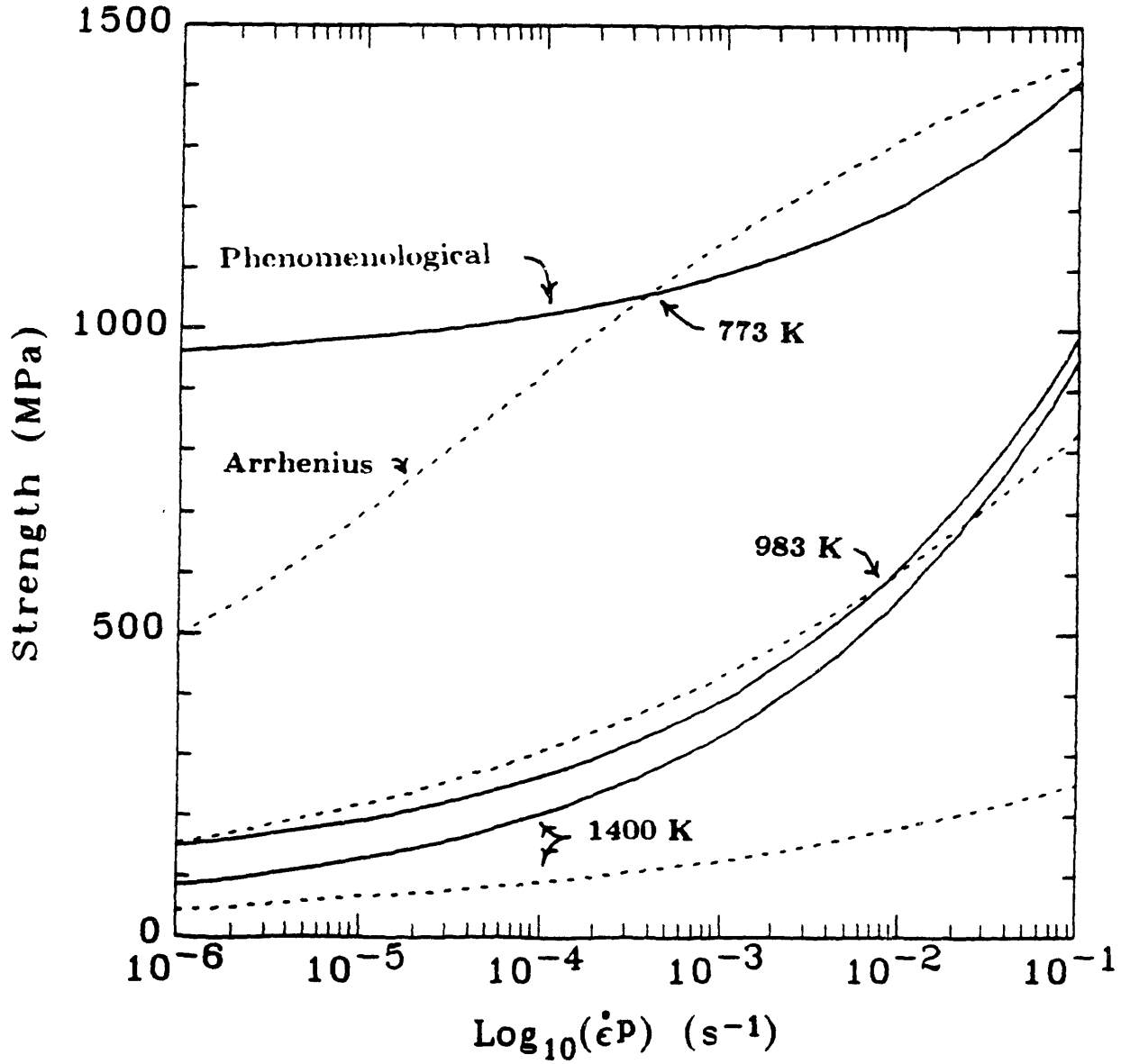

Fig. 2.7 Phenomenological versus Arrhenius predictions of elastic limit strength at different temperatures with varying plastic strain rate.

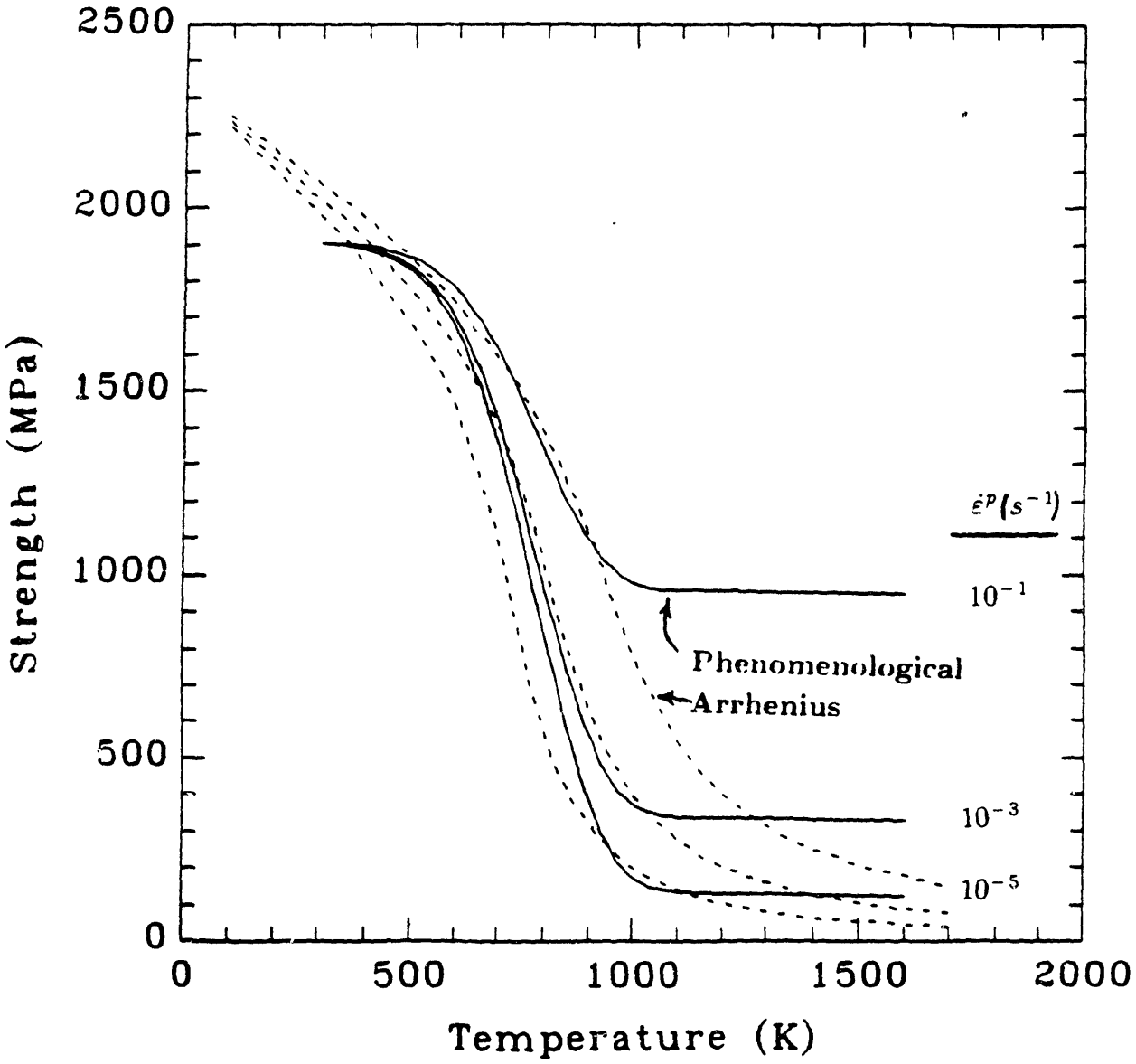

Fig. 2.8 Phenomenological versus Arrhenius predictions of elastic limit strength at different plastic strain rates with varying temperatures.

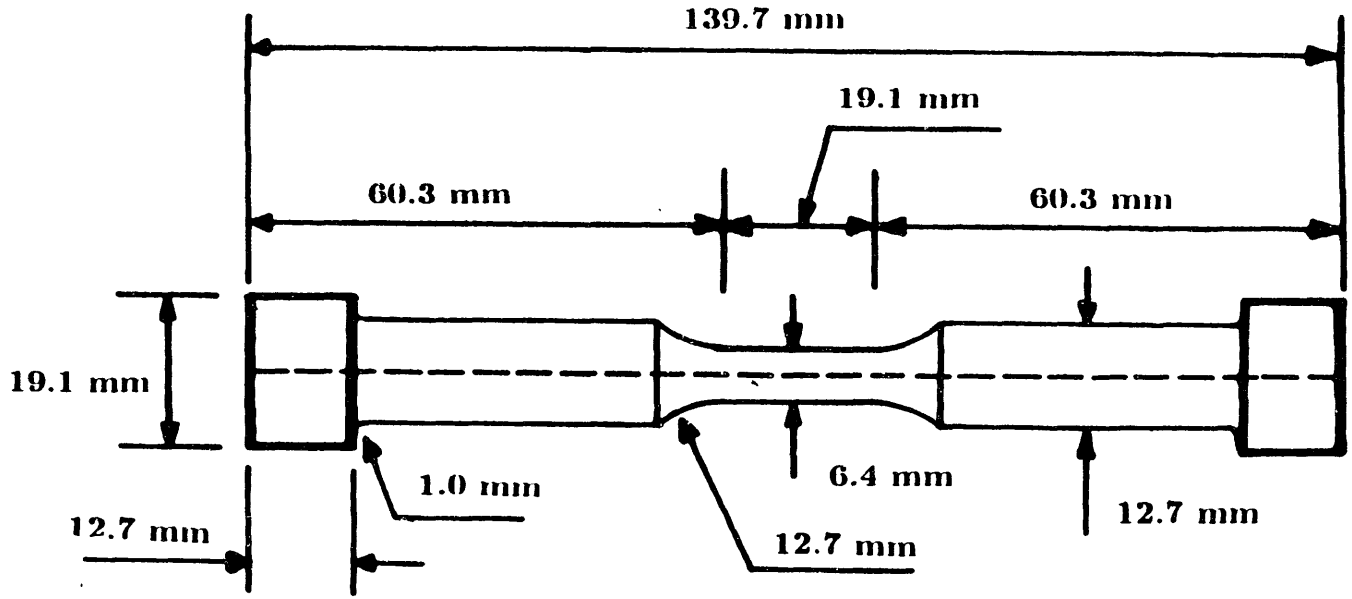

Fig. 2.9 Cyclic tensile specimen.

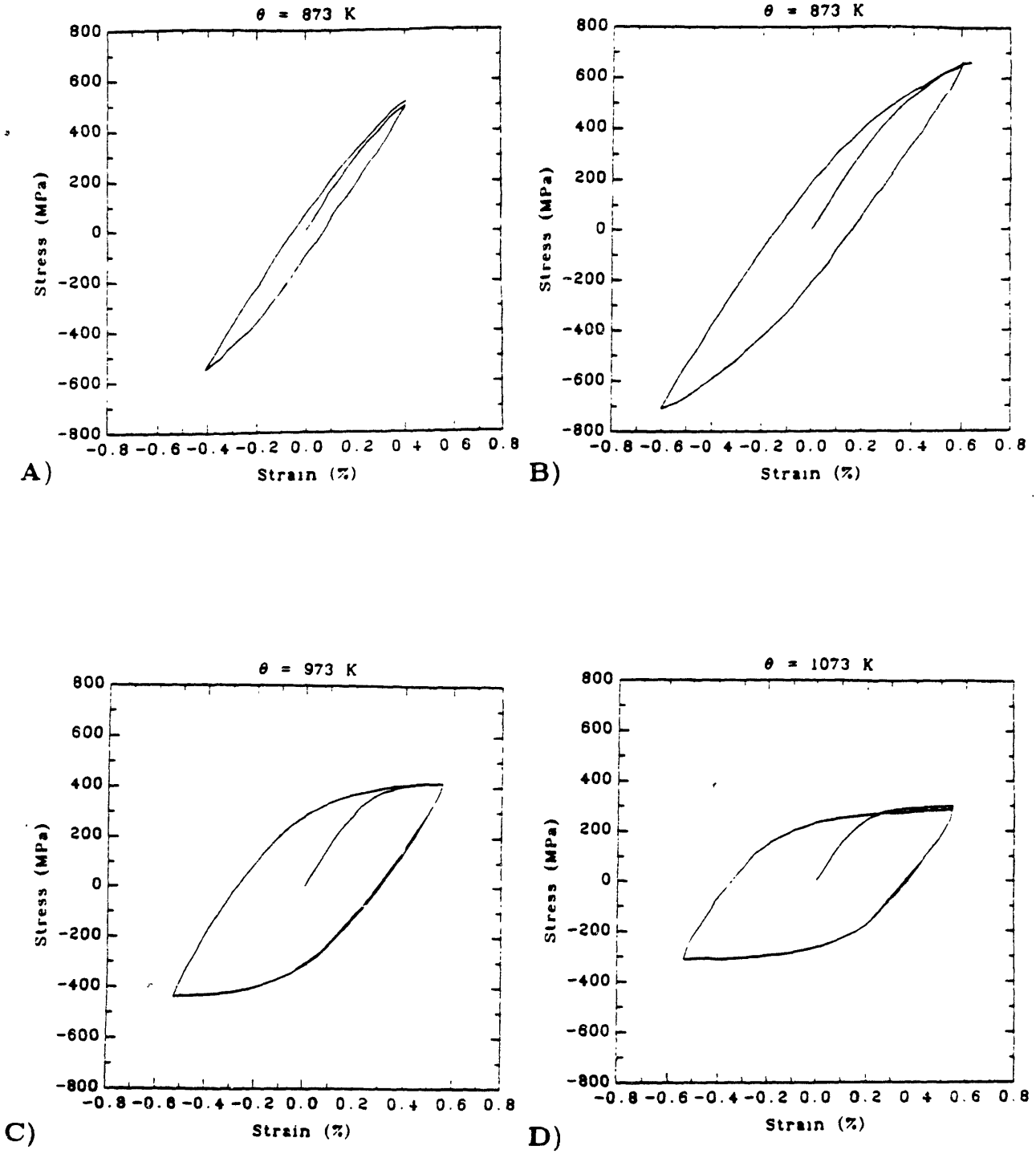

Fig. 2.10 First cycle of cyclic fatigue tests.

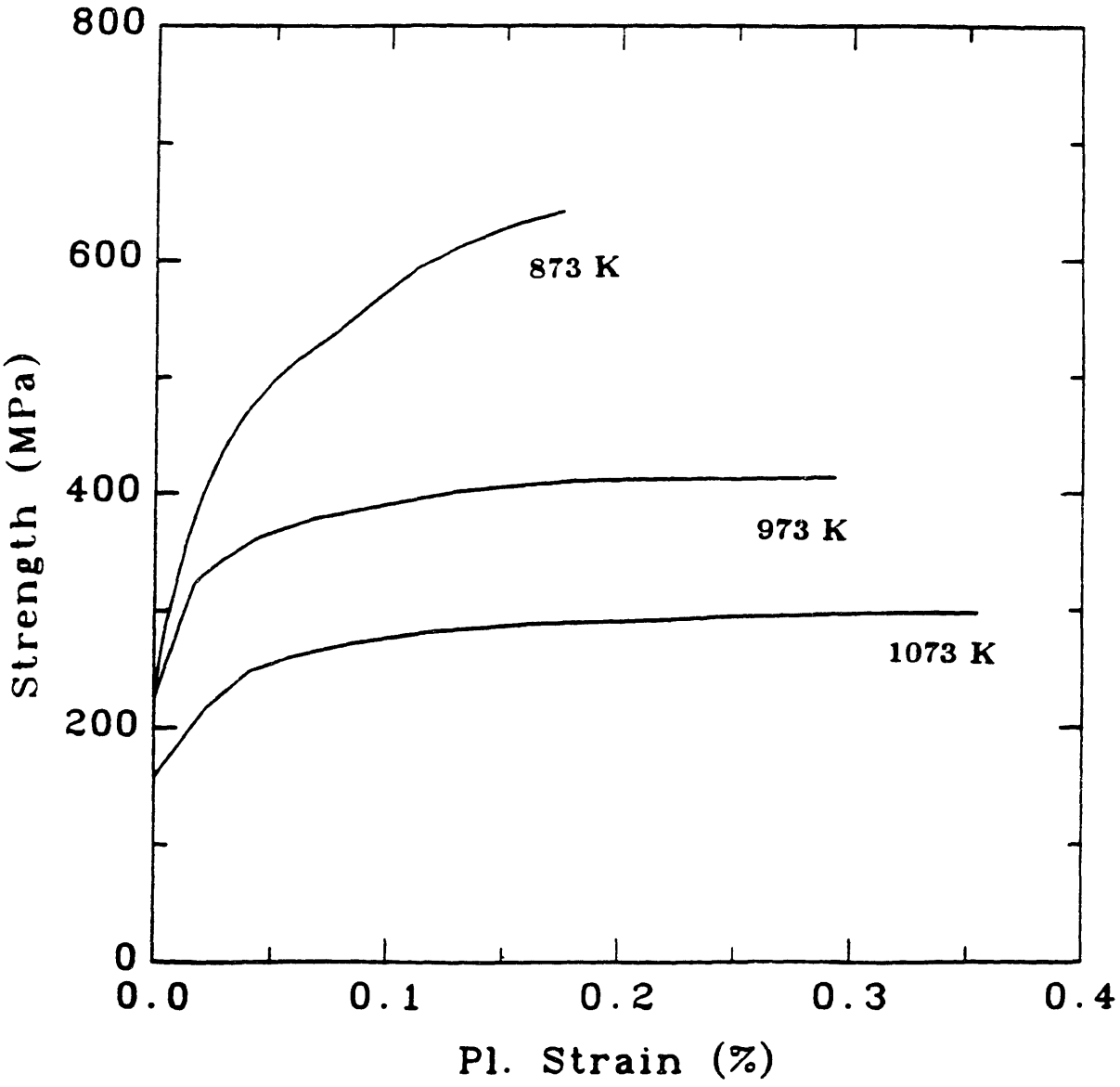

Fig. 2.11 Monotonic strain hardening data.

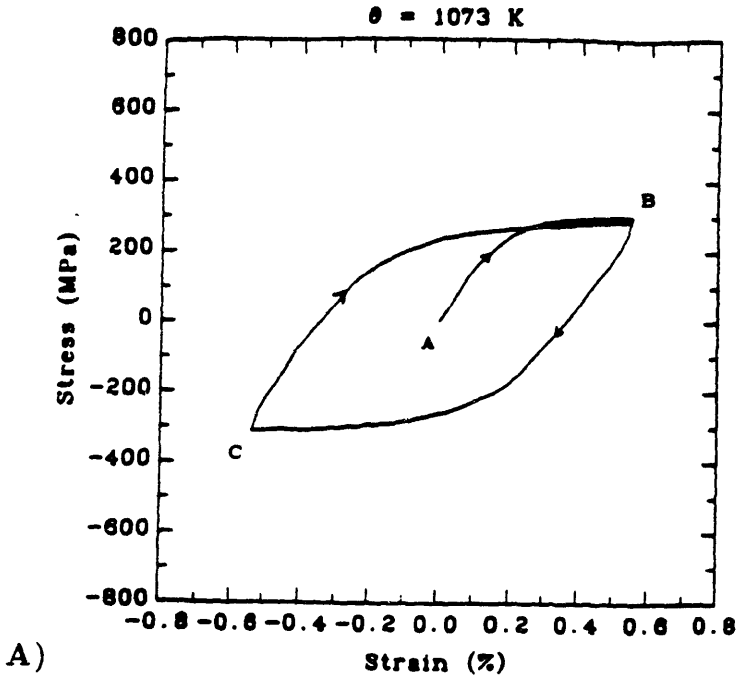

A)

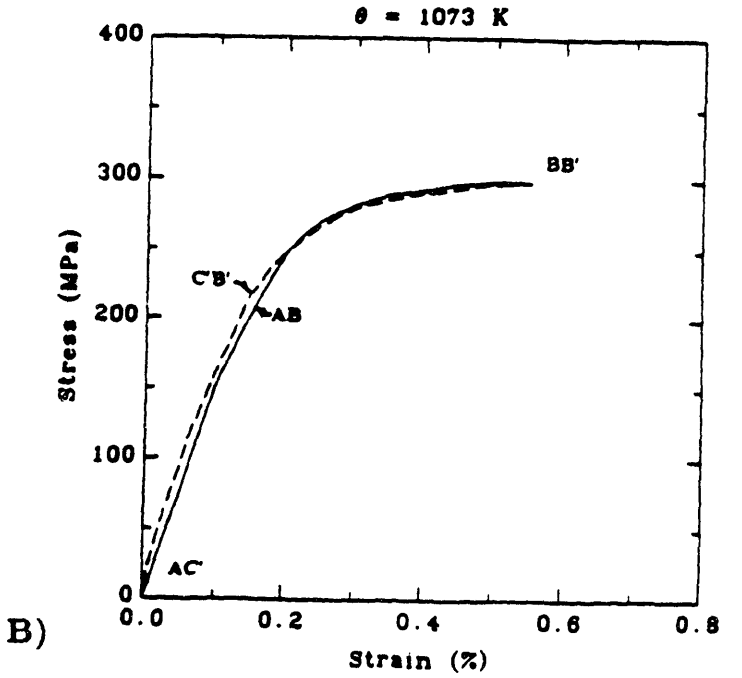

B)

Fig. 2.12 Similarity between monotonic and cyclic strain hardening curves. Curve CB is scaled by 1/2 and translated so that point C′ is at (0,0).

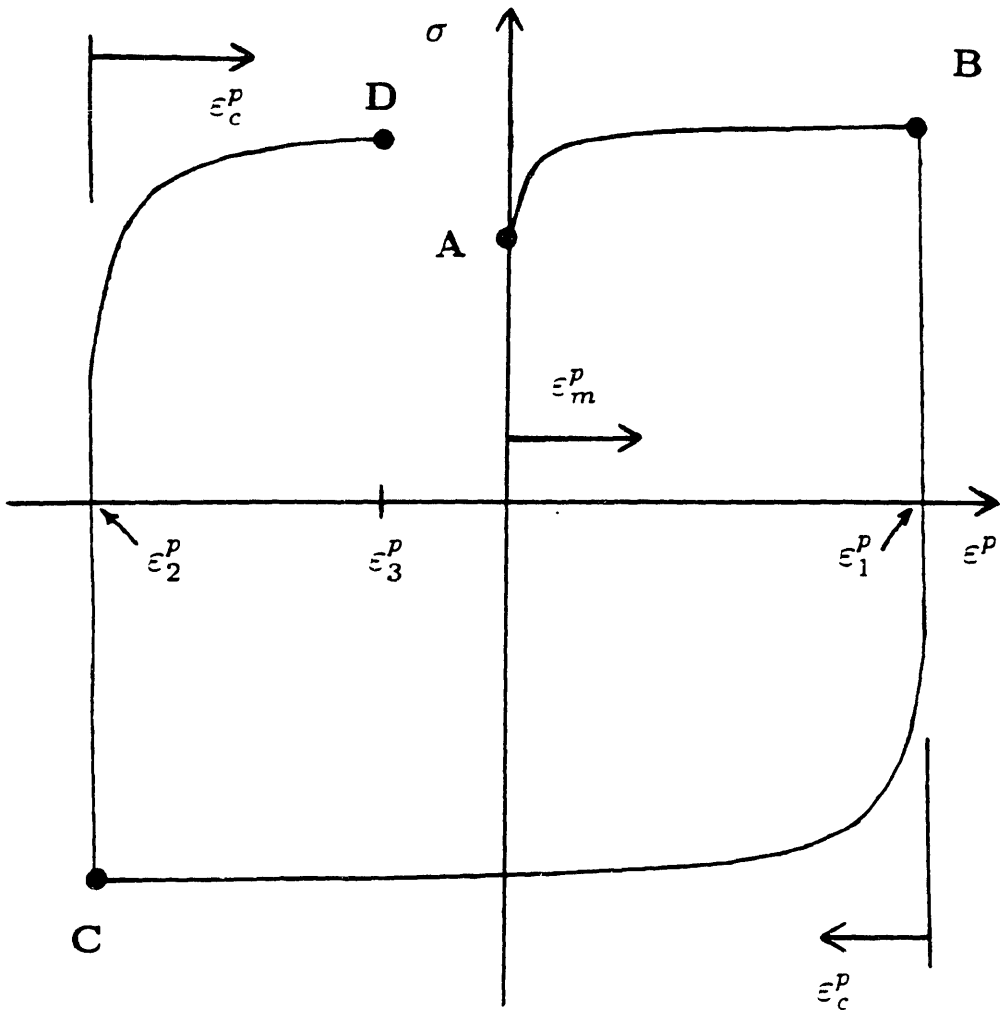

Fig. 2.13 Strain hardening diagram for the integrated strain history variables ε_m^p and ε_c^p.

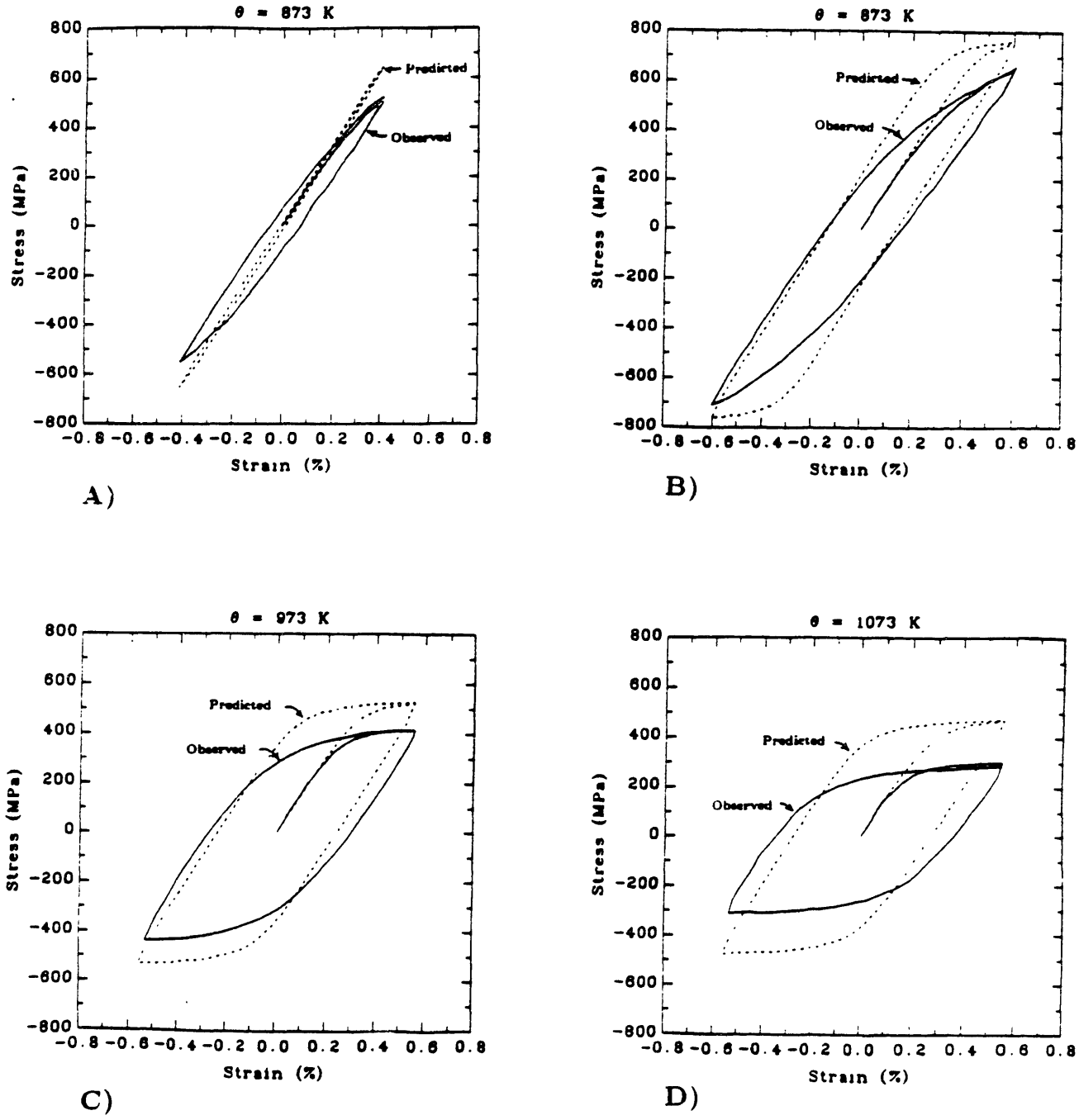

Fig. 2.14 Predicted and observed cyclic stress-strain curves (phenomenological rate equation).

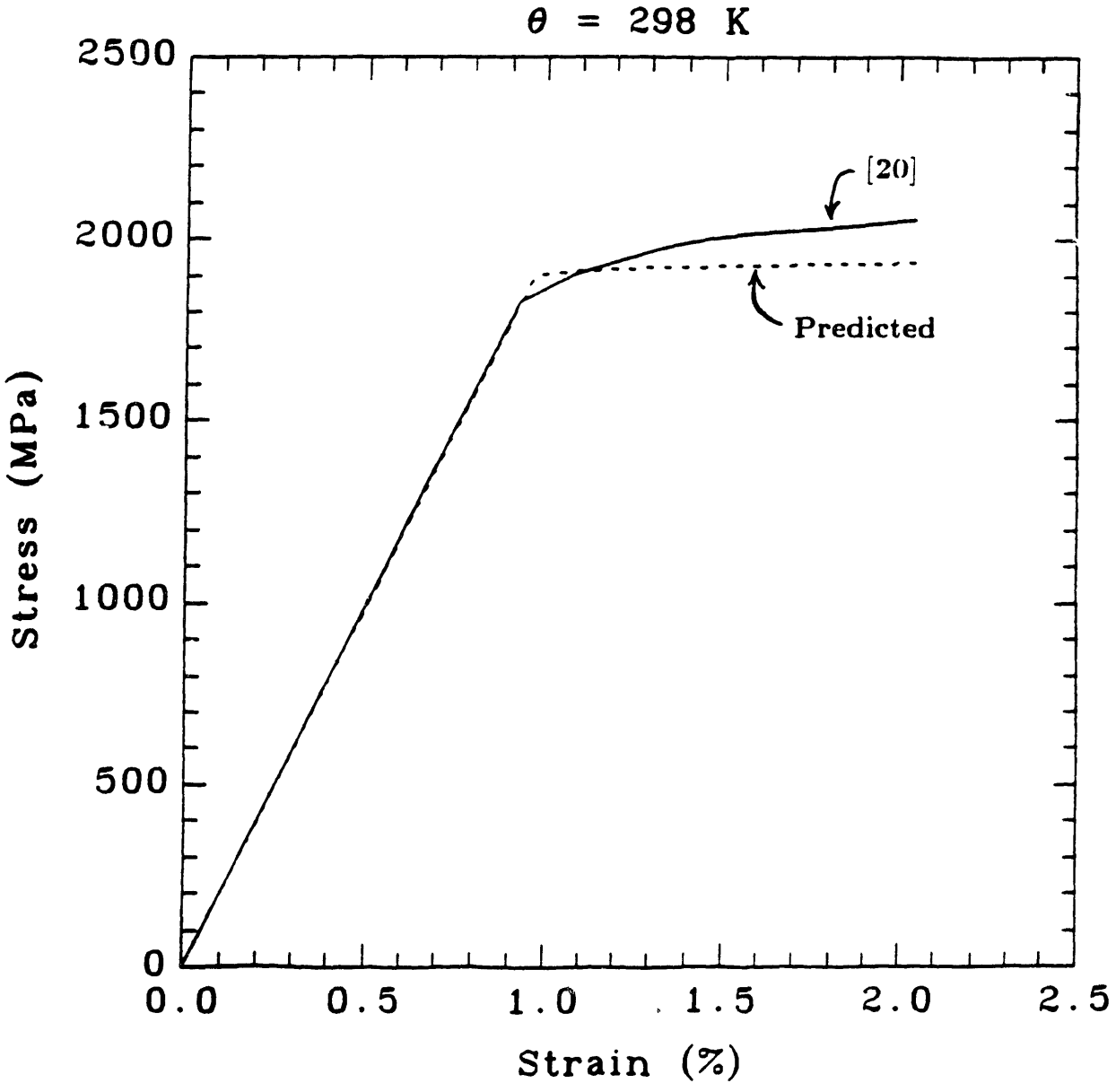

Fig. 2.15 Comparison between predicted (phenomenological) and observed [20] monotonic stress-strain curves at room temperature.

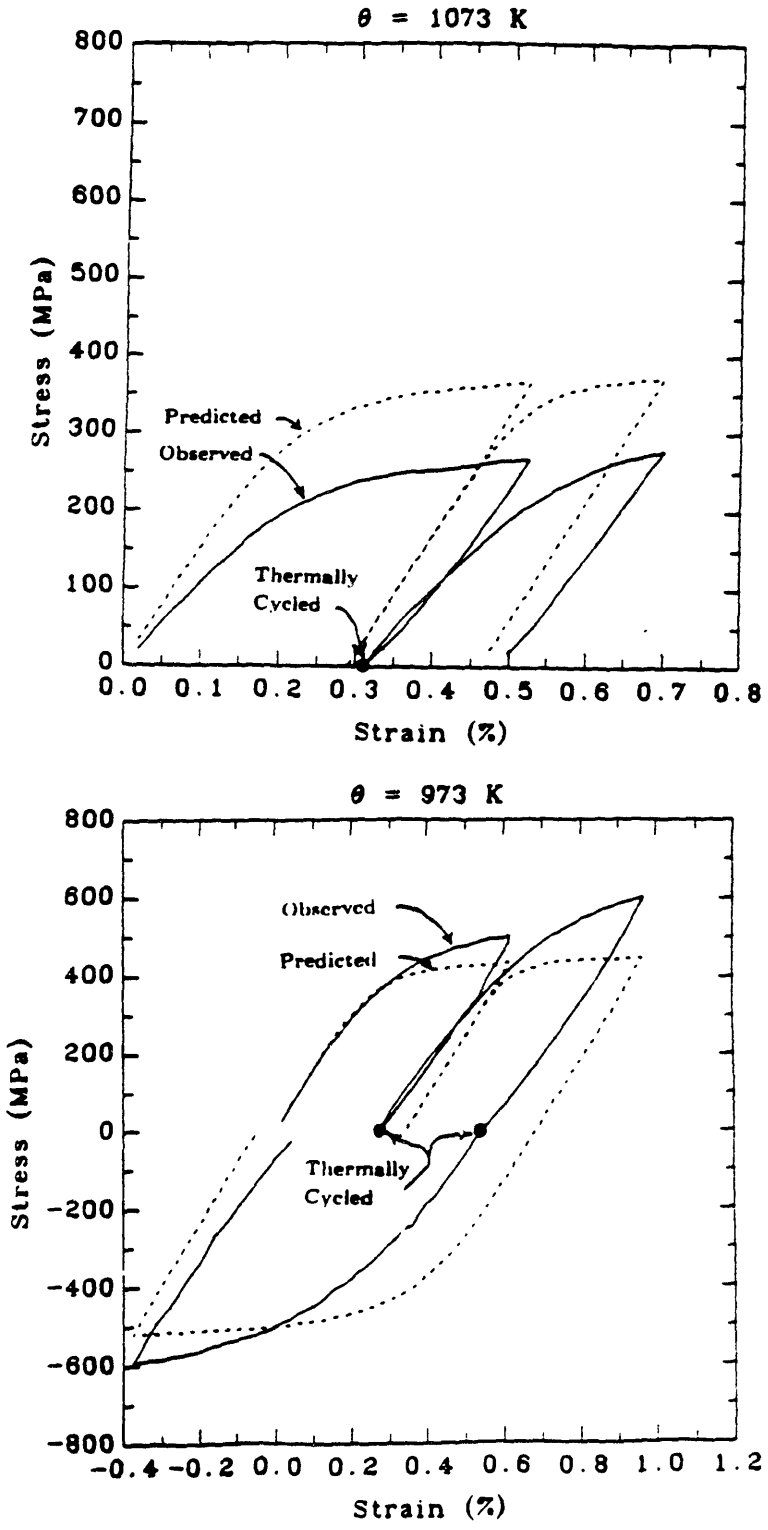

Fig. 2.16 Phase transformation effects on cyclic stress strain behavior.

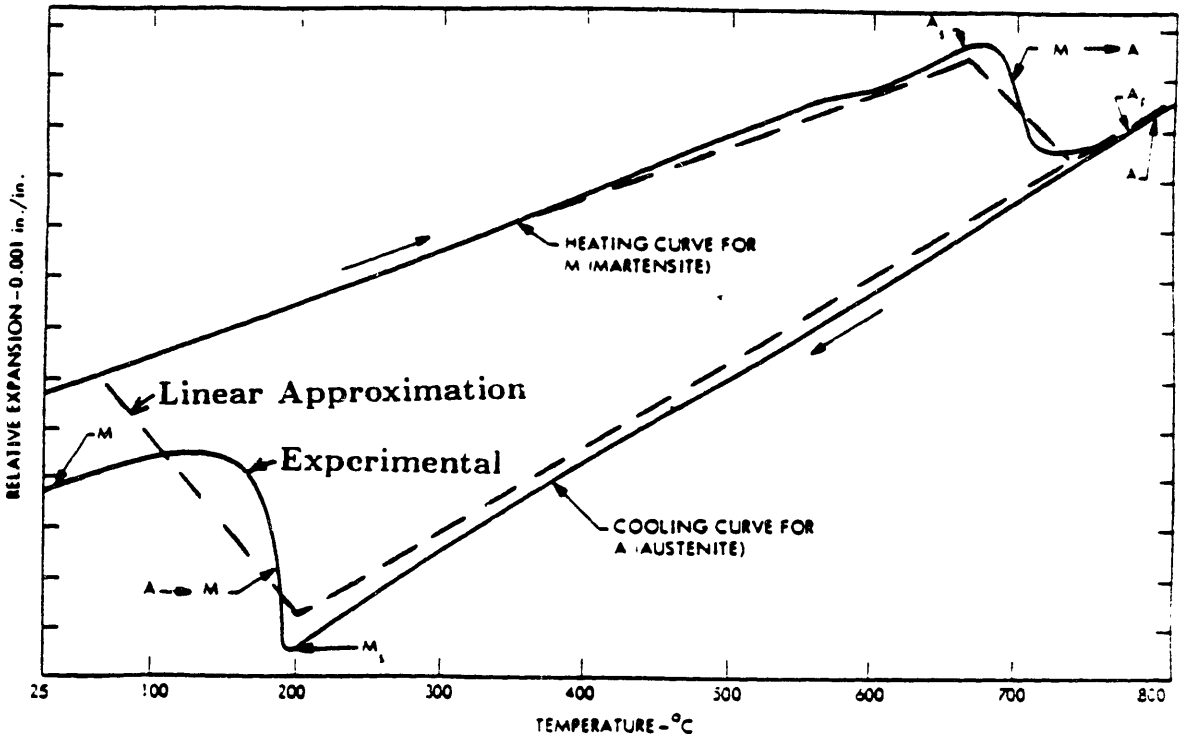

Fig. 2.17 Linear approximation to the thermal expansion and phase transformation strains.

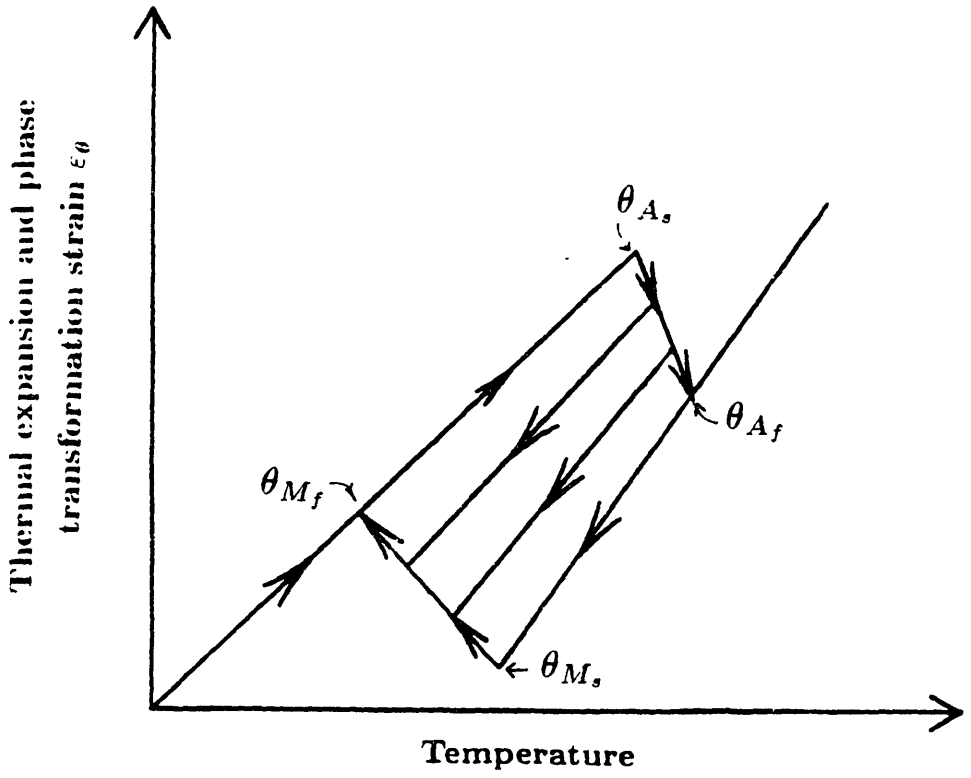

Fig. 2.18 Thermal expansion and phase transformation strain curves for partially transformed material.

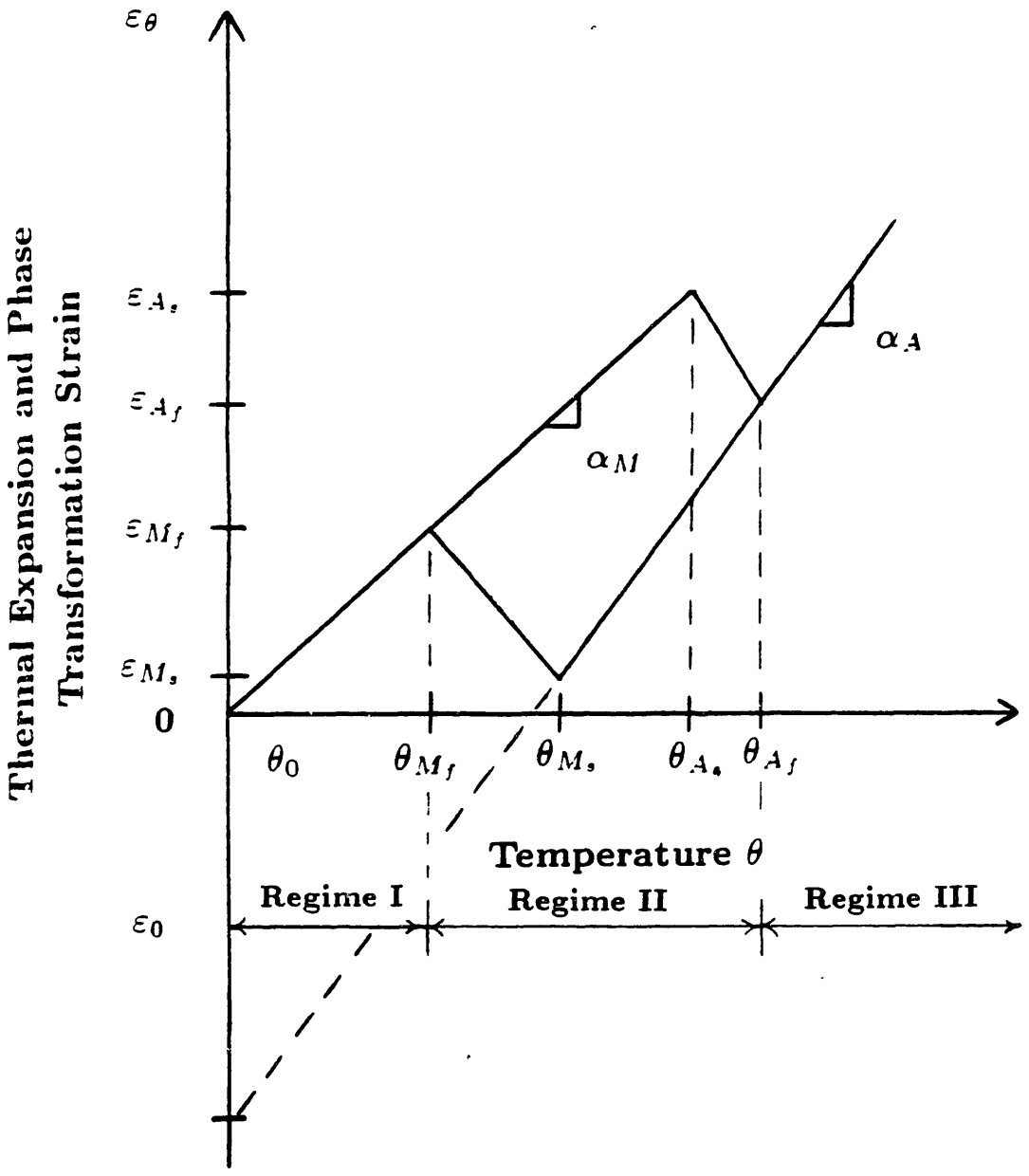

Fig. 2.19 Thermal expansion and phase transformation variables.

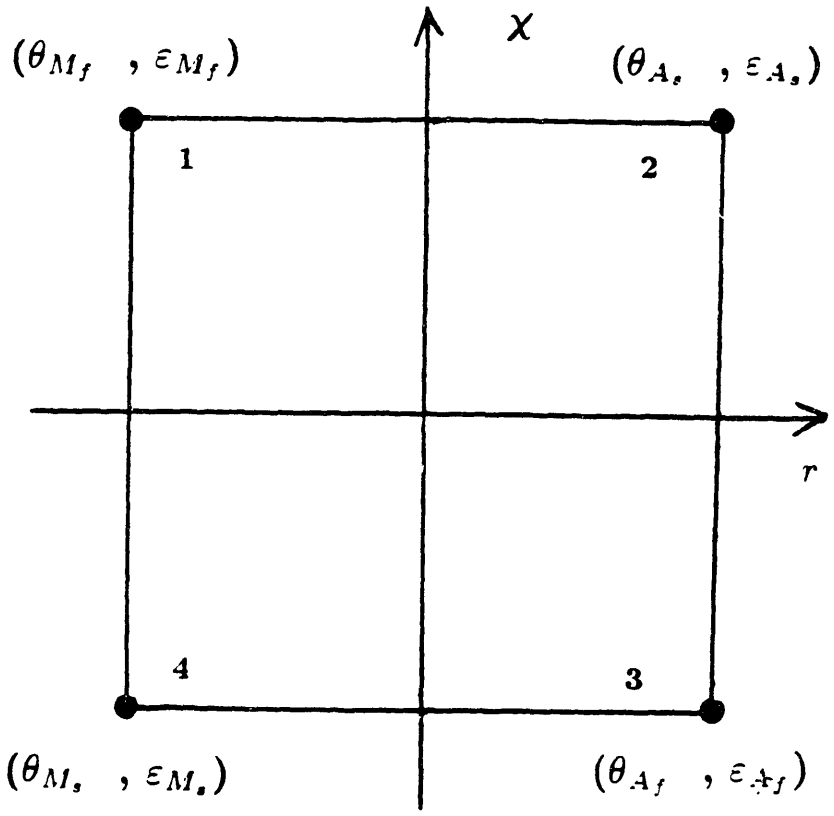

Fig. 2.20 Thermal expansion and phase transformation finite element model.

References

[1] Saul G., Roberson J.A. and Adair A.M., "The effects of Thermal Treatment on the Austenitic Grain Size and Mechanical Properties of 18 Pct Ni Maraging Steels," Metallurgical Transactions, Vol. 1, Feb. 1970.

[2] Goldberg A., "Effects of Repeated Thermal Cycling on the Microstructure of 300-Grade Maraging Steel", Transactions of ASM, Vol. 61, 1968, pp. 41-51.

[3] Thevenin J.P., Cizeron G. and Lacombe P., "Etude de la Reversion a Vitesse de Chauffage Rapide de la Martensite de l'Acier Maraging a 18Molybdene," Memoires Scientifiques Rev. Metallurg., LXVIII, No. 4, 1971, pp. 215-222.

[4] Wei R.P., *Aerospace Structural Metals Handbook,* 1972, Belfout Stulen Inc.

[5] Teledyne Vasco, Manufacturers Informational Brochure, 1982, Latrobe, Pa.

[6] "The 18 Per Cent Nickel Maraging Steels" (INCO Databook,) Source Book on Maraging Steels, American Society for Metals, R.F. Decker Editor, 1979, pp. 351-377.

[7] Rack H.J., Beitscher S. and Kalish D., "The Strain-Rate and Temperature Dependence of 18Ni(350) Maraging Steel Tensile Properties," Journal of Engineering Materials and Technology, January 1979, vol. 101, pp. 91-97.

[8] Anand L., "Constitutive Equations for the Rate-Dependent Deformation of Metals at Elevated Temperatures," Journal of Engineering Materials and Technology, Jan. 1982, Vol. 104, pp. 12-17.

[9] Bohun M.H. and Palazotto A.N., "Comparison of Two Viscoplastic Flow Laws as Applied to a problem of Crack Growth," Engineering Fracture Mechanics, 1985, Vol. 21, No. 3, pp. 503-519.

[10] Haisler W.E. and Imbrie P.K., "Numerical Considerations in the Development and Implementation of Constitutive Models," Nonlinear Constitutive Relations for High Temperature Application - 1984, Nasa Conf. June 1984, pp. 169-185.

[11] Lindholm U.S., "Unified Viscoplastic Constitutive Equations and Their Applications," Interdisciplinary Issues in Materials Processing and Manufacturing, Vol. 1, ASME, December 1987, pp. 77-93.

[12] Chan K.S., Lindholm U.S., Bodner S.R. and Walker K.P., "A Survey of Unified Constitutive Theories," Nonlinear Constitutive Relations for High Temperature Application, June 1984, Proc. of a Symposium held at NASA Lewis Research Center Cleveland, Ohio, pp. 1-23.

[13] Lowe T.C. and Miller A.K., "Improved Constitutive Equations for Modeling Strain Softening - Part 1: Conceptual Development," Journal of Engineering Materials and Technology, October 1984, Vol. 106, pp. 337-342.

[14] Chen Y., "Power-Formula Viscoplasticity, Its Modification and Some Applications," Journal of Engineering Materials and Technology, October 1984, Vol. 106, pp. 383-387.

[15] Chan K.S., Bodner S.R. and Lindholm U.S., "Phenomenological Modeling of Hardening and Thermal Recovery in Metals," Journal of Engineering Materials and Technology, Jan. 1988, Vol. 110, pp. 1-8.

[16] Frost H.J. and Ashby M.F., "Deformation-Mechanism Maps, The Plasticity and Creep of Metals and Ceramics," 1982, Pergamon Press, pp. 20-29,60-68.

[17] R.M. Pelloux, J. Feng and G. Romanoski, "A Study of the Fatigue Behavior of Small Cracks in Nickel-Base Superalloys," Air Force Office of Scientific Research, Grant # AFOSR-84-0075, Dept. of Mat. Sci. & Eng., M.I.T., Feb. 24, 1988.

[18] Naghdi P.M., "Stress-Strain Relations in Plasticity and Thermoplasticity," Proceedings of the Second Symposium on Naval Structural Mechanics, Pergamon Press, 1960, pp. 121-169.

[19] Krempl E., Cernocky E.P., Liu M.C.M., "The Representation of Viscoplastic Phenomena in Constitutive Equations," Constitutive Equations in Viscoplasticity: Computational and Engineering Aspects, The American Society of Mechanical Engineers, Dec. 5-11, 1976, pp. 95-114.

[20] Chaboche J.L., Rousselier G., "On the Plastic and Viscoplastic Constitutive Equations- Part 1: Rules Developed With Internal Variable Concept," Journal of Pressure Vessel Technology, Trans. of the ASME, May 1983, Vol. 105, pp. 153-158.

[21] L.F.P. Van Swam, "Fatigue Behavior of Maraging Steel 300," ScD Thesis at Mass. Inst. of Tech., Materials Science Dept., 1973.

Chapter 3

Thermo - Elastic - Plastic Analysis

In a previous analysis of short pulse magnets [1], a theoretical examination of the coil mechanics resulted in formulas predicting the elastic displacements, strains and stresses. The elastic constants of maraging steel were assumed not to change with temperature. This chapter focuses on using the measured and modeled plastic behavior of the material with a numerical approach to examine the coil mechanics.

The finite element method is selected for this study, because it is a versatile method for studying problems with rate-dependent plasticity and loading conditions. Specifically, the requirements for this analysis are

1. Time dependent finite element formulation
2. Temperatures which vary as a function of time and position
3. Body forces which vary as a function of time and position
4. Displacement boundary conditions
5. Force boundary conditions
6. Young's modulus (E) which is a function of temperature
7. Thermal expansion and phase transformation strains
8. Viscoplastic, rate dependent plasticity

Several commercial finite element packages were considered (PAFEC, ADINA, ABAQUS and NIKE2D,) but two difficulties arose. The first difficulty is data preparation. The temperature and body force data must be supplied at each element node for each of these codes. This might seem trivial but when considering models with hundreds of nodes, and up to 18 time steps, the data preparation becomes burdensome and unwieldy. The second difficulty is modeling the material nonlinearity. For some of these packages, modeling the material behavior of maraging steel would require changes in the program codes. Not surprisingly, access to most of these codes is prohibited, but even when allowed, the time required to understand the codes and implement changes is excessive. Given these two difficulties, a special purpose finite element code AFESA (Axisymmetric Finite Element Solenoid Analysis) was written to minimize the amount of data preparation and to implement the material behavior of maraging steel. The time saved in data preparation and studying a packaged code

was invested into the development of a code specific to the application being studied. Wherever possible, finite element subroutines from published sources were borrowed and incorporated into AFESA.

This chapter describes the program AFESA and the numerical methods used to implement the material behavior of maraging steel. The discussion which follows is intended for those familiar with the finite element method and plasticity. For basic information on this topic see [2]-[7].

Finite Element Formulation

The program AFESA is designed to handle axisymmetric finite element models. The selection of this geometry is necessary for analyzing the annular ring model which is used in the study of short pulse magnet mechanics [8]-[11]. In addition, tensile and cyclic fatigue test specimens are cylindrical, so these tests are also simulated with finite element models using AFESA. The geometry of the short pulse magnet structure prevents excessive deformation, and the accumulated plastic strains are less than 1.0% Thus, small displacements, strains and rotations are expected. AFESA is suitable for analyses which take into account only materially nonlinearities.

Eight node, quadrilateral elements are used in AFESA. This element type was selected because it offers good predictive capabilities for a reasonable cost [1]. The elements are integrated with a 3 by 3 Gauss-Legendre numerical integration scheme. The displacement interpolation functions are represented in matrix form as $\mathbf{H}$ and the nodal displacements are similarly represented with $\mathbf{U}$. The strain-displacement transformation matrix $\mathbf{B}$ relates the nodal displacements to the element strain matrix ϵ. Appendix A describes the $\mathbf{H}$ and $\mathbf{B}$ matrices used for these elements.

$$\epsilon = \mathbf{BU} \tag{3.1}$$

AFESA is a time-dependent finite element analysis program. The program uses time steps to discretize the analysis. Each time step must be defined with user-supplied boundary and loading conditions. Between time steps, the analysis is divided into subincrements for which the boundary and loading conditions are linearly interpolated.

In most finite element programs, external temperature and body force information is supplied (as input data) for each node. For a transient temperature field, this can pose a burden on the data preparation. This is especially true when different finite element meshes for the same structure are being scrutinized. AFESA simplifies the data input requirements by letting the user define a rectangular grid of temperatures and body forces spanning the coordinates of the finite element model. The spatial grid is defined for each time step by the user. During the finite element analysis, the temperatures and body forces are interpolated from the input grid for each integration point being analyzed. This is similar to what most commercial codes do, except they use nodal temperature or body force values for their interpolation grid. Between time steps, new temperature and body force grids are created with linear interpolations between the time steps. Testing different mesh geometries is made easier when just the mesh is refined and not the temperature and body force data.

Equilibrium Equation

In its simplest form, the equilibrium equation describes the balance between applied forces and nodal forces from element stresses. A time-dependent finite element analysis must continually satisfy the equilibrium equation. (Variables printed in bold face type represent matrix quantities, and unless otherwise noted, all other variables are scalar quantities). There are two kinds of applied forces in the short pulse application. The first is nodal forces $\mathbf{R}_b$ resulting from Lorentz electromagnetic body force loads f_b.

$$\mathbf{R}_b = \sum_e \int_V \mathbf{H} f_b \, dV \tag{3.2}$$

The second set of forces directly applied to the model is $\mathbf{R}_f$. These forces are used to model the compressive forces imposed on the short pulse magnet during operation. The element stresses σ generate the vector of nodal forces $\mathbf{F}$. The determination of σ provides the challenge for finite element plasticity.

$$\mathbf{F} = \sum_e \int_V \mathbf{B}^T \sigma \, dV \tag{3.3}$$

Equilibrium is satisfied when the sum of these forces Ψ is zero. The equilibrium equation shown below is in matrix form and represents a system of equations defining equilibrium for each finite element node.

$$\Psi = \mathbf{R}_b + \mathbf{R}_f - \mathbf{F} \tag{3.4}$$

Since the stresses σ are functions of $\mathbf{U}$, so is $\mathbf{F}$ and hence

$$\Psi(\mathbf{U}) = 0 \tag{3.5}$$

The equilibrium equation 3.5 is solved iteratively, and each iteration for the nodal displacements results in element stresses which must finally balance the applied forces and be in equilibrium themselves. Eq. 3.3 is the equilibrium form of the principle of virtual work.

Solution Procedures

There are three key components to the finite element solution procedure employed in AFESA. The first is the frontal solution technique which minimizes the storage requirements needed to save the finite element stiffness matrix. It also minimizes the time needed to solve for the nodal displacements. The method is described in [12][13]. Each nodal equilibrium equation depends on the adjacent element nodal displacement variables, and an efficient ordering of these nodal displacement variables minimizes the number of variables describing each nodal equilibrium equation. For AFESA, the implementation of the frontal method is accomplished with an automatic renumbering of both the elements and their node numbers. In this manner, the elements are integrated in an efficient order and the active front of nodal displacements is minimized.

The second component is the solution procedure used to determine the unknown equilibrium displacements. AFESA uses the Newton Raphson method combined with the Alpha-Constant stiffness method [14]. Applying the Newton Raphson iteration procedure to Eq. 3.2 gives equations for determining the displacements $\mathbf{U}^{n+1}$ at time t^{n+1}. This procedure assumes equilibrium is satisfied at time t^n with displacements $\mathbf{U}^n$. Moreover, it assumes the displacements $\mathbf{U}_0^{n+1}$ for the first iteration are initialized with the displacements $\mathbf{U}^n$. In these

equations, the superscript $n+1$ is understood, so it is not included in the formulations. The subscript i denotes the iteration count number during equilibrium iterations for time t^{n+1}.

$$-\Psi_i = \frac{\partial \Psi}{\partial \mathbf{U}} \Delta \mathbf{U}_i \tag{3.6}$$

$$\mathbf{U}_i = \mathbf{U}_{i-1} + \Delta \mathbf{U}_i \tag{3.7}$$

The partial derivative of Ψ with respect to $\mathbf{U}$ in Eq. 3.6 is called the tangent stiffness or Jacobian matrix $\mathbf{K}_T$. Many finite element codes expend a great deal of effort calculating accurate Jacobian matrices, because significant reductions in computing time can be realized. In a materially nonlinear, cyclic, thermo-elastic-plastic analysis, the Jacobian matrix is nonlinear and transient. During perfectly plastic deformation, components of the Jacobian matrix go to zero, while when unloading from a plastic state, components of the Jacobian matrix can be infinite. Most of the Jacobian nonlinearity is approximated by the alpha constant stiffness method. This numerical method trades the time necessary to formulate and invert a new stiffness matrix for the time required to iteratively solve with an elastic stiffness matrix. The elastic stiffness matrix depends on the Young's modulus and the Poisson's ratio, and this accounts for a small portion of the material nonlinearity. What follows is a short description of the alpha constant stiffness method and the assumptions which are necessary for its derivation.

In the alpha constant stiffness method, the tangent stiffness matrix is replaced with the finite difference approximation shown below. $\Delta\Psi'$ is the net nodal loads, and $\Delta\mathbf{U}'_i$ is the elastic displacement increment.

$$\mathbf{K}_T = \frac{\Delta \Psi'}{\Delta \mathbf{U}'} \tag{3.8}$$

where

$$\Delta \Psi' = \Psi' - \Psi_i \tag{3.9}$$

$$\Psi' = \Psi(\mathbf{U}'_i) \tag{3.10}$$

Next, three equations necessary for the derivation are defined. First, the tangent stiffness matrix is separated into a linear $\mathbf{K}_0$ and nonlinear component

$\mathbf{K}_C$ (Eq. 3.11.) The elastic displacement increment $\Delta\mathbf{U}'_i$ is determined with the inverted elastic stiffness matrix $\mathbf{K}_0^{-1}$ and the net nodal loads Ψ_i (Eq. 3.12). Then, the displacement increment $\Delta\mathbf{U}_i$ is defined with the product of a diagonal alpha matrix α_i and the elastic displacement increment $\Delta\mathbf{U}'_i$ (Eq. 3.13.) This method assumes the alpha matrix can correct the nodal displacements predicted by the elastic stiffness matrix, giving nodal displacements which will satisfy equilibrium.

$$\mathbf{K}_T = \mathbf{K}_0 - \mathbf{K}_C \tag{3.11}$$

$$\Delta\mathbf{U}'_i = -\mathbf{K}_0^{-1}\Psi_i \tag{3.12}$$

$$\Delta\mathbf{U}_i = \alpha_i\Delta\mathbf{U}'_i \tag{3.13}$$

Now substitute Eqs. 3.11 - 3.13 into Eq. 3.6 and pre-multiply both sides by $\mathbf{K}_0^{-1}$.

$$\Delta\mathbf{U}'_i = \alpha_i\Delta\mathbf{U}'_i - \mathbf{K}_0^{-1}\mathbf{K}_C\Delta\mathbf{U}_i \tag{3.14}$$

Next, substitute Eq, 3.8 into Eq. 3.11 and insert this into Eq. 3.14. Rearrange the equation and solve for the alpha matrix α_i. The matrix $\mathbf{I}$ is the identity matrix.

$$\alpha_i = \mathbf{I} + \frac{\Delta\mathbf{U}_i - \mathbf{K}_0^{-1}\Delta\Psi'_i}{\Delta\mathbf{U}'_i} \tag{3.15}$$

The iterative process is broken into two phases. This is done so that an estimate for $\mathbf{U}_i$ can be made. Namely, it is assumed the previous alpha matrix makes an adequate prediction (Eq. 3.16). Substituting Eq. 3.16 into Eq. 3.15 gives the final result shown in Eq. 3.17 .

$$\Delta\mathbf{U}_i = \alpha_{i-1}\Delta\mathbf{U}'_i \tag{3.16}$$

$$\alpha_i = \alpha_{i-1} - \frac{\mathbf{K}_0^{-1}\Psi'_i}{\Delta\mathbf{U}'_i} \tag{3.17}$$

In the first phase of the alpha constant stiffness method, an approximation to the equilibrium displacements is made with the elastic stiffness matrix. In the second phase, these displacements are used to determine the out-of-balance

equilibrium loads Ψ_i' and then using Eq. 3.17, the alpha matrix is calculated and substituted into Eq. 3.13 to determine the equilibrium displacements. When an entry inside the elastic displacement increment $\Delta \mathbf{U}_i'$ is zero, then the second term of Eq. 3.17 is dropped and that alpha matrix entry remains constant. When a material is unloading from a viscoplastic state and the total strain rate is approximately equal to zero ($\dot{\varepsilon}^p + \dot{\varepsilon}^c \approx 0$), most of the alpha matrix entries are constant and equal to 1. These two phases constitute one iteration, and the iterations continue until the net nodal loads are sufficiently small to terminate the process. The primary advantage of this technique is its use of a constant elastic stiffness matrix. The complete alpha constant stiffness procedure used in AFESA is listed in Appendix B.

The last important component of the solution procedure employed by AFESA is the subroutine COLSOL. This subroutine was written by K.-J. Bathe and is used in the finite element program ADINA [2]. Because of symmetry, this subroutine only stores the upper skyline of the stiffness matrix, and this minimizes the storage requirements. COLSOL also has the feature of dividing the solution of nodal displacements into two steps. The first steps triangularizes the stiffness matrix, and the second step reduces the load matrix and back substitutes for the output displacement increments. The second step is independent of the triangularizing step, so it is possible to continuously update the load matrix and solve for new displacements without having to repeat phase one calculations. This capability is an important feature when iterating with a constant stiffness matrix and varying load matrices as described in the alpha constant stiffness method.

Constitutive Equations

When a set of displacements $\mathbf{U}$ is determined from a solution of the net nodal loads Ψ, the new displacements are converted into strains using Eq. 3.1. These strains are then used to determine the stresses within the finite element model. This last step involves the constitutive equations which model the stress strain behavior of maraging steel. The constitutive equations must predict the thermo-elastic-plastic behavior for the time dependent material models described in Chapter 2. In addition, the evolution of back stress must be modeled for the cyclic conditions expected in this application.

Hooke's law defines the isotropic stress strain relationship.

$$\sigma_{ij} = 2\mu\epsilon^e_{ij} + \lambda\epsilon^e_{kk}\delta_{ij} \tag{3.18}$$

where:

σ_{ij} is the Cauchy stress

ϵ^e_{ij} is the elastic strain

δ_{ij} is the Kronecker delta

μ,λ are the Lamé material constants:

$$\mu = \frac{E}{2(1+\nu)} \tag{3.19}$$

$$\lambda = \frac{E\nu}{(1+\nu)(1-2\nu)} \tag{3.20}$$

For a time-dependent analysis, the stress rates are integrated over time. The rate form of the Cauchy stress is defined by taking the partial derivative of Eq. 3.18 with respect to time. All time derivative (rate) variables are designated by a raised dot ($\dot{}$). The material constants μ and λ are functions of temperature, so their rate of change is controlled by temperature changes.

$$\dot{\sigma}_{ij} = 2\mu\dot{\epsilon}^e_{ij} + 2\dot{\mu}\epsilon^e_{ij} + \left(\lambda\dot{\epsilon}^e_{kk} + \dot{\lambda}\epsilon^e_{kk}\right)\delta_{ij} \tag{3.21}$$

The total strain rate $\dot{\epsilon}_{ij}$ is defined as the sum of the elastic, plastic and the thermal and phase transformation strain rates, $\dot{\epsilon}^e_{ij}$, $\dot{\epsilon}^p_{ij}$ and $\dot{\varepsilon}_t$ respectively.

$$\dot{\epsilon}_{ij} = \dot{\epsilon}^e_{ij} + \dot{\epsilon}^p_{ij} + \dot{\varepsilon}_t\delta_{ij} \tag{3.22}$$

Eliminating $\dot{\epsilon}^e_{ij}$ in Eq. 3.21 with Eq. 3.22 gives the Cauchy stress rate:

$$\dot{\sigma}_{ij} = 2\mu\left(\dot{\epsilon}_{ij} - \dot{\epsilon}^p_{ij}\right) + 2\dot{\mu}\epsilon^e_{ij} + \left[\lambda\dot{\epsilon}_{kk} + \dot{\lambda}\epsilon^e_{kk} - (3\lambda+2\mu)\,\dot{\varepsilon}_t\right]\delta_{ij}. \tag{3.23}$$

The total strain rate is calculated from the displacements predicted by the equilibrium equations. Eq. 3.23 is the constitutive equation for stress used in this thesis. The next task is to determine the plastic strain rate, so the Cauchy stress rate in Eq. 3.23 can be calculated.

Flow Rule and Evolutionary Equations

There are several assumptions which are important to this formulation. Plastic deformation is assumed to occur in a direction normal to the yield surface and this deformation does not distort the shape of the yield surface (the loading was indeed nearly radial). The set of equations shown below are standard definitions used in classical kinematic plasticity theory to define the flow rule and the evolution of back stress. The flow rule is given in Eq. 3.24 and the evolution of back stress is given in Eq. 3.28.

$$\dot{\epsilon}^p_{ij} = \sqrt{3/2}\dot{\epsilon}^p N_{ij} \tag{3.24}$$

$$N_{ij} = \frac{\tilde{\sigma}_{ij}}{\sqrt{\tilde{\sigma}_{ij} \cdot \tilde{\sigma}_{ij}}} \tag{3.25}$$

$$\tilde{\sigma}_{ij} = S_{ij} - \Omega_{ij} \tag{3.26}$$

$$S_{ij} = \sigma_{ij} - \frac{1}{3}\sigma_{kk}\delta_{ij} \tag{3.27}$$

$$\dot{\Omega}_{ij} = \sqrt{2/3}h\ \dot{\epsilon}^p N_{ij} \tag{3.28}$$

where:

$\dot{\epsilon}^p$ is the equivalent plastic strain rate

N_{ij} is the unit vector normal to the yield surface

$\tilde{\sigma}_{ij}$ is the effective stress

S_{ij} is the deviatoric stress

h is the strain hardening coefficient

Numerical Solution

Four equations must be satisfied in order to determine the stress state in this time-dependent analysis. The first equation is the constitutive equation for stress (Eq. 3.23). The second equation is the flow rule (Eq. 3.24). The third is the evolution of back stress (Eq. 3.28), and the fourth is the kinetic equation for plastic strain rate (Eq. 2.9 or Eq. 2.11). Eqs. 3.23, 3.24 and 3.28 are tensor equations, while the kinetic equation is a scalar function. The kinetic equations of Chapter 2 functions of the equivalent effective stress $\|S_{ij} - \Omega_{ij}\|$. The equivalent effective stress Y is

$$Y = \sqrt{(3/2)\,(S_{ij} - \Omega_{ij}) \cdot (S_{ij} - \Omega_{ij})}. \tag{3.29}$$

The phenomenological rate equation is based on an over-stress formulation. When the equivalent effective stress Y is less than the threshold strength s, the resulting plastic strain rate is zero. For the Arrhenius rate equation, plastic straining occurs at all nonzero values of equivalent effective stress. In practice however, when predicted plastic strain rates are less than 10^{-12} s^{-1}, the stress behavior is assumed to be entirely elastic. For plastic behavior, a consistency equation (yield surface equation) is used to link the tensor equations (Eqs. 3.23, 3.24 and 3.28) to the scalar kinetic equations:

$$\Phi = (S_{ij} - \Omega_{ij}) \cdot (S_{ij} - \Omega_{ij}) - \frac{2}{3}Y^2 \quad \leq \quad 0 \tag{3.30}$$

Plastic deformation occurs when $\Phi \equiv 0$, and under these conditions, the consistency equation is identical to the definition of equivalent effective stress. The unknown variables in these equations are the plastic strain rate $\dot{\epsilon}^p$ and the equivalent effective stress Y. For plastic deformation, the task is to predict stress states which satisfy the kinetic and consistency equations and to predict plastic strains which obey the flow rule.

There are several approaches to this problem. One technique is the tangent modulus method [15][16] which uses a forward Euler integration scheme and a Taylor expansion of the plastic strain rate to predict a stress rate. The only restriction in this method is the maximum allowable time step. The method chosen for this work is a variation of the Radial Return Algorithm [17], adapted to viscoplasticity. The method is implicit and requires about 10 iterations for each sub-increment time step. It is less restrictive on the maximum time step size. Descriptions of other solution techniques can be found in [18].

One way to solve for $\dot{\epsilon}^p$ and Y is to use the following numerical approximations. First, assume the equilibrium and consistency equations are satisfied at time t^n. Require all rate variables be defined with finite difference approximations between times t^n and t^{n+1}. For example, the following equations are used to define the deviatoric stress and the back stress at time t^{n+1}.

$$S_{ij}^{n+1} = S_{ij}^n + \left(\Delta\sigma_{ij}^{Tr}\right)' - \sqrt{6}\mu\dot{\epsilon}^p N_{ij}\Delta t \tag{3.31}$$

$$\left(\Delta\sigma_{ij}^{Tr}\right)' = \left[2\mu^n\dot{\epsilon}_{ij} + 2\dot{\mu}\left(\epsilon_{ij}^e\right)^n\right]\Delta t \tag{3.32}$$

$$\Delta\sigma_{ij}^{Tr} = \Big[2\mu^n\dot{\epsilon}_{ij} + 2\dot{\mu}\left(\epsilon_{ij}^e\right)^n +$$

$$\left[\lambda^n \dot{\epsilon}_{kk} + \dot{\lambda}\left(\epsilon_{kk}\right)^n - \left(3\lambda + 2\mu\right)\left(\dot{\epsilon}_t\right)^n\right]\delta_{ij}\Bigg]\Delta t \tag{3.33}$$

$$\Omega_{ij}^{n+1} = \Omega_{ij}^n + \frac{2}{3}h\dot{\epsilon}^p N_{ij}\Delta t \tag{3.34}$$

$$\Delta t = t_{n+1} - t_n \tag{3.35}$$

The variable σ_{ij}^{Tr} is called the trial stress. If the plastic strain rate is zero, then the trial stress equals the final stress σ_{ij}^{n+1}. Next, the consistency equation is satisfied at time t^{n+1}. Substitute Eqs. 3.31-3.34 into Eq. 3.30, and let Φ equal zero to get

$$\left\| \left(S_{ij}^n + \left(\Delta\sigma_{ij}^{Tr}\right)' - \Omega_{ij}^n\right) - \sqrt{3/2}\left(2\mu + \frac{2}{3}h\right)\dot{\epsilon}^p N_{ij}\Delta t \right\| = \sqrt{\frac{3}{2}}Y^{n+1} \tag{3.36}$$

The principal assumption in the radial return algorithm requires the normal to the yield surface be approximated with the following equation.

$$\tilde{N}_{ij} = \frac{\left(S_{ij}^n + \left(\Delta\sigma_{ij}^{Tr}\right)' - \Omega_{ij}^n\right)}{\left\|S_{ij}^n + \left(\Delta\sigma_{ij}^{Tr}\right)' - \Omega_{ij}^n\right\|} \tag{3.37}$$

With this assumption, Eq. 3.36 is greatly simplified, and it is possible to write a direct solution for $\dot{\epsilon}^p$.

$$\dot{\epsilon}^p = \frac{\left\|S_{ij}^n + \left(\Delta\sigma_{ij}^{Tr}\right)' - \Omega_{ij}^n\right\| - \sqrt{\frac{2}{3}}Y^{n+1}}{\sqrt{3/2}\left(2\mu + \frac{2}{3}h\right)\Delta t} \tag{3.38}$$

There are now two equations with two unknowns, Y^{n+1} and $\dot{\epsilon}^p$. The first equation is given above in Eq. 3.38, and the second equation is either of the kinetic equations (Eqs. 2.9 and 2.11.) AFESA uses a numerical interpolation procedure to calculate Y^{n+1} and $\dot{\epsilon}^p$. Linear interpolations between predicted plastic strain rates (Eq. 3.38) and resultant plastic strain rates (kinetic equation) are used to make new predictions for the plastic strain rate. By eliminating predictions which are not close to the resultant plastic strain rates, it is possible to successively iterate until the predictions and resultants are the same. A more efficient numerical technique likely exists, but our procedure has proved reliable, and it takes approximately 10 iterations for convergence. Once $\dot{\epsilon}^p$ and Y^{n+1} are known, it is possible to calculate σ_{ij}^{n+1} Ω_{ij}^{n+1} and $(\epsilon_{ij}^p)^{n+1}$. Appendix C details the thermo-elastic-plastic equations used by AFESA. A listing of the AFESA

program, the input commands and two examples are given in Appendix E (this appendix is out of order; mea culpa).

It should be mentioned at this point that there is a significant difference in computer execution time between the phenomenological and Arrhenius rate equations. The Arrhenius rate equation takes approximately 9 times longer than the phenomenological rate equation to complete a plastic analysis. This difference is due primarily to the dependency of the activation energy on the equivalent effective stress. It is possible to rearrange the phenomenological rate equation to get an equivalent effective stress function which depends on temperature and plastic strain rate. This manipulation facilitates the numerical solution procedure. This same manipulation is not possible for the Arrhenius rate equation, so a subroutine is employed to iteratively determine the equivalent effective stress as a function of temperature and plastic strain rate.

Strain Hardening

In Chapter 2, the strain hardening coefficient h was described for monotonic and cyclic strain hardening modes. In the finite element implementation, h is determined under the same conditions. The strain hardening coefficient used in Eq. 3.38 is constant over the sub-increment time step, but the strain hardening coefficients described by Eqs. 2.15 and 2.16 are changing continuously with ε^p. To correct this discrepancy, the mean value theorem is used to approximate the average strain hardening coefficient (Eq. 3.39.) Therefore $\bar{h}$ replaces h in Eqs. 3.34 and 3.38. $\bar{h}$ is constant over each sub-increment time step, but it changes with each time step. Because $\dot{\varepsilon}^p$ is changing during the iterations for $\dot{\varepsilon}^p$ and Y^{n+1}, the strain hardening coefficient $\bar{h}$ is also changing.

$$\bar{h} \equiv \frac{\int_{t^n}^{t^{n+1}} h\dot{\varepsilon}^p dt}{\int_{t^n}^{t^{n+1}} \dot{\varepsilon}^p dt} \tag{3.39}$$

To evaluate Eq. 3.39, the rules governing whether the hardening mode is monotonic or cyclic are applied to determine which function for h (Eq. 2.12 or 2.13) should be used. A determination of the appropriate strain hardening mode is based upon an evaluation of the stress state at time t^n.

Fig. 3.1 shows the effect of the number of sub-increment time steps on the prediction of an elastic plastic stress strain curve. In this example, the total

strain rate is constant $2 \times 10^{-2} s^{-1}$ and the temperature is 900 K° . The finite element analysis uses one time step to reach a total strain of 2.0%. In the figure, three curves representing 5, 15 and 135 sub-increments are illustrated. As the number of sub-increments increases, the resulting stress strain curve rises and becomes smoother. Table 3.1 gives the stresses at strains of 0.4, 0.8, 1.2, 1.6 and 2.0% for varying number of sub-increments. The maximum deviation between 135 and 5 sub-increments is just 6.7 % The rise in the stress strain curves is attributed in part to the plastic strain rates which are rapidly changing between 0.4 and 0.12% strain. In any case, $\bar{h}$ does a satisfactory job approximating the stress strain curve, and the solution procedure employed in AFESA gives reasonable predictions of stress for a relatively small number of sub-increment time steps.

Conclusions

A finite element program, AFESA, has been written to analyze structures made of maraging steel subjected to extreme electromechanical and thermal loading conditions. The program uses a frontal method to compose the nodal equilibrium equations. The equilibrium equations balance the applied nodal and electromagnetic body forces with the equivalent nodal forces resulting from internal element stresses and strains. A Newton-Raphson solution method combined with the Alpha Constant stiffness method is used in combination with COLSOL to solve for the equilibrium displacements. These displacements define the strain conditions within the material, and they are used to determine the internal element strains. A constitutive stress rate equation, the flow rule, the evolution of back stress and a kinetic rate equation are used to determine the stress state under kinematic viscoplastic conditions. The consistency (yield surface) equation is used in the solution of these equations. Thus, the thermal and mechanical behavior of maraging steel is implemented into the finite element program AFESA.

Table 3.1 Stress-strain data of Fig. 3.1 for various subincrement quantities ($\dot{\epsilon} = 2 \times 10^{-2} s^{-1}$ and $\theta = 900K$).

	σ (MPa)			
ε (%)	N = 5	N = 15	N = 45	N = 135
0.4	566.1	585.7	596.7	600.5
0.8	776.9	802.3	811.6	814.3
1.2	827.6	833.7	835.0	835.2
1.6	840.8	841.3	841.5	841.5
2.0	845.6	845.1	845.2	845.2

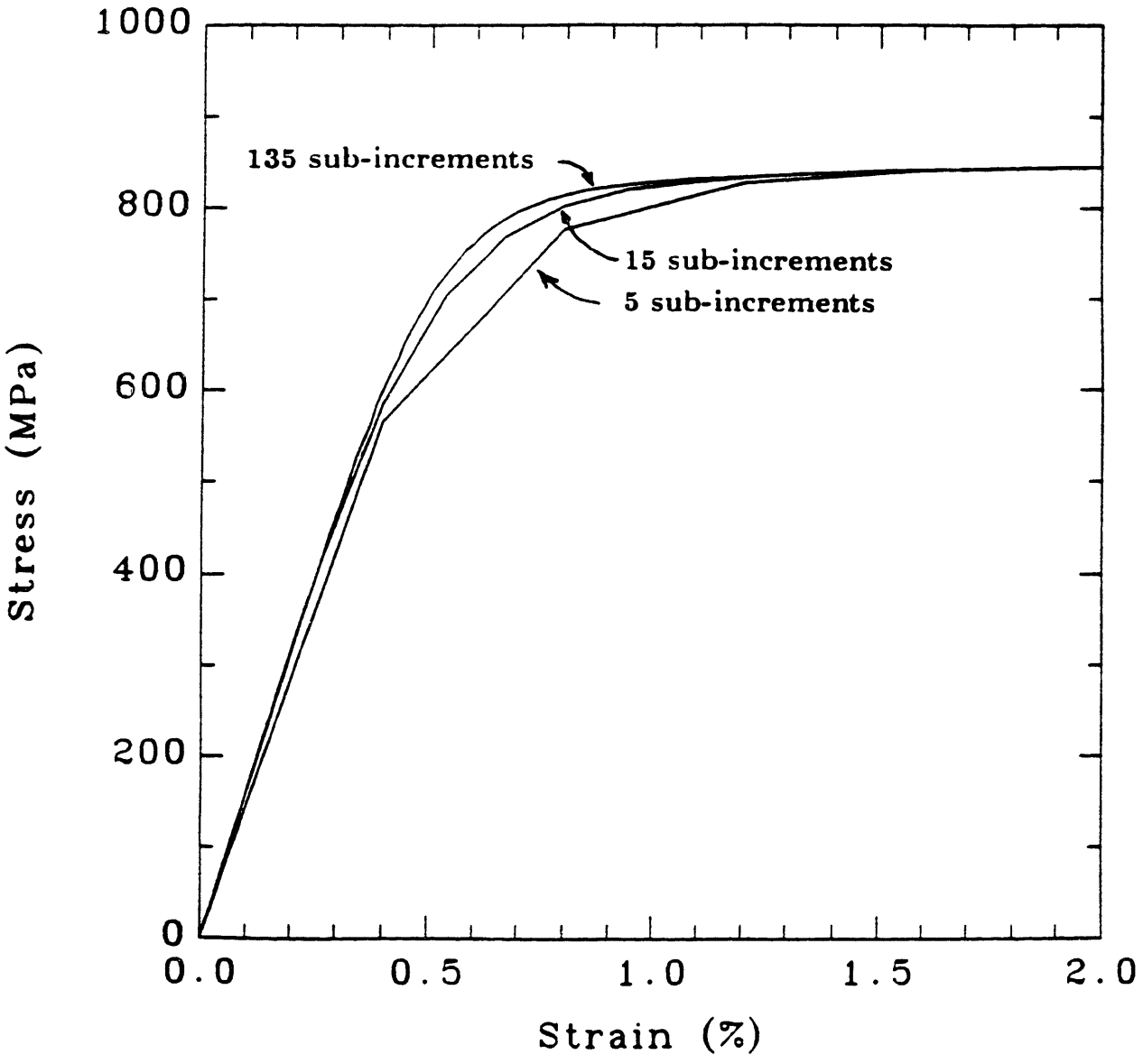

Fig. 3.1 **Effect of sub-increment size on stress strain curve at θ =900 k, $\dot{\varepsilon} = 2 \times 10^{-2}$ s^{-1}.**

References

[1] P.J. Raboin, "A High Magnetic Field Short Pulse Magnet System," S.M. Thesis, Mass. Inst. of Tech., Mech. Eng. Dept., 1985.

[2] K.-J. Bathe, *Finite Element Procedures in Engineering Analysis*, 1982, Englewood Cliffs, NJ: Prentice-Hall Inc., pp.290-294.

[3] O.C. Zienkiewicz, *The Finite Element Method in Structural and Continuum Mechanics*, 1967, New York: McGraw-Hill.

[4] C.S. Desai, *Elementary Finite Element Method*, 1979, Englewood Cliffs, NJ: Prentice-Hall Inc.

[5] D.R.J. Owen and E. Hinton, *Finite Elements in Plasticity*, 1980, Swansea: Pineridge Press.

[6] T.-R. Hsu, *The Finite Element Method in Thermomechanics*, 1986, Allen & Unwin, Inc.

[7] Snyder M.D. and Bathe K.J., "A Solution Procedure for Thermo-Elastic-Plastic and Creep Problems," Nuclear Engineering and Design, 1981, Vol. 64, pp. 49-80.

[8] M. Date, "A New Method of High Magnetic Field Generation," Journal of the Physical Society of Japan, Vol. 39 No. 4, Oct., 1975.

[9] W.F. Westendorp and R.W. Kilb, "Stresses in Magnetic Field Coils," The Proceedings of the 1968 Summer Study on Superconducting Devices and Accelerators, Part III, Brookhaven National Laboratory, June-July, 1968, pp. 714-726.

[10] D. Melville and P.G. Mattocks, "Stress Calculations for High Magnetic Field Coils," J. Phys. D: Appl. Phys., Vol. 5, 1972, pp. 139-153.

[11] B.E. Mulhall and D.H. Prothero, "Mechanical Stresses in Solenoid Coils," J. Phys. D: Appl. Phys., Vol. 6, 1973, pp. 177-181.

[12] B.M. Irons, "A Frontal Solution Problem for Finite Element Analysis," Int. Journal for Numerical Methods in Engineering, 2,5-32, (1970.)

[13] R.L. Taylor, E.L. Wilson and S.J. Sacket, "Direct Solution of Equations by Frontal and Variable Active Column Methods," Nonlinear Finite Element Analysis in Structural Mechanics, Proc. of the Europe-U.S. Workshop Ruhr-Universitat Bochum, Germany, July 1980, pp. 521-552.

[14] Nayak G.C. and Zienkiewicz O.C., "Note on the Alpha- Constant Stiffness Method for the Analysis of Non-Linear Problems," International Journal for Numerical Methods in Engineering, 1972, Vol. 4, pp. 579-582.

[15] Pierce D., Shih C.F., and Needleman A., "A Tangent Modulus Method for Rate Dependent Solids," Computers & Structures Vol. 18, No. 5, pp. 875-887, 1984.

[16] Kim K.H., Lush A.M., and Anand L., "Constitutive Equations and Computational Procedures for Hot Working of Metals," Manufacturing Processes, Machines & Systems, 13 Th. Conf. on Production Research & Tech. Conf. Proceedings, Nov. 18-21, 1986, pp. 231-241.

[17] Krieg R.D, and Key S.W., "Implementation of a Time Independent Plasticity Theory into Structural Computer Programs," Constitutive Equations in Viscoplasticity: Computational and Engineering Aspects, The Amer. Soc. of Mechanical Engineers, AMD-Vol. 20, Dec. 1976, pp. 125-137.

[18] Chan K.S., Lindholm U.S., Bodner S.R. and Walker K.P., "A Survey of Unified Constitutive Theories," Nonlinear Constitutive Relations for High Temperature Application, June 1984, Proc. of a Symposium held at NASA Lewis Research Center Cleveland, Ohio, pp. 1-23.

Chapter 4

Thermal Cycling

By simulating the thermal conditions of the short pulse magnet with inexpensive test specimens, it is possible to study the suitability of maraging steel as an electrical conductor. The specimens are heated with a discharge of electricity from a capacitor bank, and cooled by thermal conduction into a brass block. The heating takes place in about 500 μs, and cooling back down to room temperature takes approximately 3 min. The electrical heating causes thermal strains which stress the constrained specimens. There were unexpected catastrophic test specimen failures during the course of experiments, so the testing conditions were re-evaluated using a thermal finite difference analysis and a structural finite element analysis. The test specimens developed double (two distinct) necks in their gage sections, and the number of thermal cycles to failure was small (less than 50.) The double necking phenomenon is predicted by the finite element analysis, and an explanation of its presence is given. Using the results from these analyses, new test specimens were designed and tested. These specimens have an increased lifetime, but they still fail in less than 50 thermal cycles. A description of the mechanisms involved in these failures is given in Chapter 6.

Concept and Purpose

Capacitor banks have been used by various researchers to study rapid phase transformations in Cu-Zn alloys [1]. The intention of that research was to study material phase and microstructural changes in a material due to "up-quenching." The purpose of these thermal cycling tests is to study the mechanical behavior of maraging steel under extreme constrained thermal cycling conditions in the absence of magnetic body forces. At first, we believed it would be possible to thermally cycle tensile specimens with our capacitor bank, and then perform tensile tests on these specimens to determine their strength. When it became clear that mechanical deformation and other processes were causing the early failure of the specimens, we used the available information to show how temperature, current density and stresses (for given pulse characteristics) limit the use of maraging steel as a conductor.

The capacitor bank used for pulsing the short pulse magnet is also used for these tests. The discharge of electricity results in a current waveform similar to that of Fig. 4.1. This waveform is nearly identical to the one experienced by the short pulse magnet. Consequently, the electrical heating characteristics are also the same. The total current passing through the specimen can be varied to achieve a desired peak temperature. Because of the short period of the pulse, electrical skin depth effects are important. The skin depth refers to the characteristic depth δ for which the current density has attenuated to e^{-1} of its surface value. With this in mind, the test specimen diameters (2.9 mm) are smaller than the theoretical skin depth (3.3 mm,) and this results in a uniform current density through the test specimens. The waveform current I versus time (Fig. 4.1) is given in terms of a constant I_0, a damping factor ($b = 10200$ s^{-1}) and an angular pulse frequency ($\omega = 22000$ rad s^{-1}).

$$I = I_0 exp(-bt)\, sin(\omega t) \tag{4.1}$$

The skin depth δ is given in meters, and μ_0 is the magnetic permeability in a vacuum ($4\pi \times 10^{-7}$ H/m.)

$$\delta = \sqrt{\frac{2\rho}{\omega \mu_0}} \tag{4.2}$$

It was originally intended that after a certain number of thermal cycles, the specimens would be removed and tested on a tensile test machine to determine their strength. This plan was abandoned because thermal cycling caused significant damage to the test specimens. Removing the specimens from the testing apparatus often resulted in bending or breaking because the steel threads become welded and jammed with debris due to electrical arcing. Also, there was circumferential cracking in the gage section and a reduction of cross sectional area in the specimens. In addition, outright failure of the specimens (an electrical explosion which vaporized the specimen) occurred after just a few dozen thermal cycles. These results led to a reevaluation of the loading conditions and the specimen geometry.

The ends of the test specimens are constrained, so thermal expansion in the specimen compresses the alloy plastically at high temperatures. Cooling puts the alloy in tension. The largest deformations were expected in the center of the gage section. However, the first two showed double necking near the

ends of the gage section. A finite element analysis was performed to confirm this observation. The ends of the gage section shall be called the ends for convenience from now on.

At first, the excessive deformation observed in the ends was thought to be the result of specimen geometry, so the remaining specimens were sanded to a tapered gage section (Fig. 4.2). This specimen is hereafter called the tapered specimen. The purpose of this change was to maximize the temperature and stress at the center of the specimen and shift the necking behavior from the ends to the center of the gage section. However, tapering the specimen did not prevent double necking, and an additional buckling deformation was observed in the specimen after about 12 thermal cycles.

In these first tests, the ratio of gage length (15.88 mm) to minimum specimen diameter (2.46 mm) is 6.5. This parameter is important to this type of test, because as this ratio decreases the likelihood of buckling decreases. In the last tests, a new thermal cycling specimen was designed with a decreased gage length (8.76 mm) to diameter ratio of just 3.6. This specimen is called the hourglass specimen (Fig. 4.3.) Double necking and buckling deformations were not observed in the hourglass specimen. The hourglass specimens had a longer life than the tapered test specimens.

Experimental Setup

The capacitor bank, dummy load and experimental apparatus are shown in Fig. 4.4, and the specifications are given in Table 4.1. The dummy load is a single loop of sheet metal which provides an inductance more or less equivalent to that of the short pulse magnet for this simple RLC circuit (Fig. 4.5). Two test specimens are in parallel with each other and in series with the circuit. Two specimens are tested together for reasons of safety. Should one specimen fracture and separate during the test, the other specimen maintains a closed circuit. The electrical resistance of these specimens is negligible compared to the dummy load resistance, so they do not significantly affect the RLC circuit. The capacitor bank has a maximum charging voltage of 20 kV and a maximum current capacity of 400 kA. The charging voltage can be varied, and the maximum current scales linearly with the charging voltage. For these tests, the highest charging voltage was 6.4 kV with a maximum total current of 115 kA through the specimens.

A Rogowski coil measures the total current flowing through both specimens, and the data from this coil is integrated and measured on an oscilloscope. The current flowing through each specimen is half the total current. The temperature distribution within the thermal specimens is determined numerically with an integration of the resistive heating from the current versus time data. A thermocouple was not used to determine the temperature in the thermal test specimens, because it was not known how to safeguard against the high voltage dangers. In retrospect, it might have been possible to use a voltage limiting clipper circuit to interface between a thermocouple attached to the specimen and an oscilloscope, but this option was not known at the time.

As previously mentioned, the thermal cycling tests were performed with the uniform, tapered and hourglass specimens shown in Figs. 2.2, 4.2 and 4.3. All were made with Vasco Max 300 grade maraging steel, and heat treated as described in Chapter 1. Each specimen was ground with a 640 grit sandpaper prior to testing.

Fig. 4.6 illustrates the holding assembly for the thermal test specimens. The two specimens are screwed directly into the top brass block. Brass holding pieces are screwed onto the bottom of the specimens, and then the bottom brass block slides over the brass holding pieces. Two set screws firmly fix the brass holding pieces to the bottom brass blocks. Next, two 1/4 inch G-10 plates are bolted to the upper and lower brass blocks. These plates restrain the movement of the brass blocks with respect to one another, and this constrains the ends of the thermal test specimens (the ratio of G-10 to specimen stiffness is approximately 11).

Thermal Analysis

The temperature profiles for the thermal cycling specimens are predicted with a thermal finite difference method. The resistive heating rate per unit volume is equal to the electrical resistivity ρ times the square of the current density J. For a given current passing through the specimen, the cross sectional area of the specimen is the single most important factor determining the heating rate. Resistive heating dominates for the first 500 μs, and then thermal conduction cools the specimen to room temperature in about 3 min. Thermal convection between the specimen and the air is small and can be neglected ($2\ \mathrm{Nu}\ (l/d)^2 = 0.16$). The details of the finite difference method used for this problem are

given in Appendix D. The radial and circumferential temperature gradients are assumed negligible. Hence, the temperature only varies along the Z axis of the specimens. The salient feature of the thermal analysis is the initial dominance of resistive heating followed by the conduction of heat from the specimens into the large brass blocks holding the specimens.

Fig. 4.7 shows the axial temperature distribution in the uniform tensile specimen at 6 different times during the thermal cycling. These curves correspond to a charging voltage of 5.0 kV, and a peak current density of 7.54 kA/mm^2. The gage section has a uniform cross section, so the resulting temperature profiles are constant during the first 500 μs in this region. After this time, a temperature gradient develops, largest at the ends of the test specimen.

The temperature profiles for the tapered test specimen are given in Fig. 4.8. These curves are for a charging voltage of 4.1 kV and a maximum current density of 7.97 kA / mm^2. The temperatures vary by 50 K across the gage section for this specimen because of the tapered cross sectional area. Again, the largest temperature gradient is in the end of the specimen. The temperature profiles for the hourglass specimen are shown in Fig 4.9. The charging voltage for these curves is 4.5 kV, and the peak current density is 8.48 kA / mm^2. This specimen has a cross sectional area which varies the most in its gage section, and consequently, it has the largest temperature gradients in the gage section of the three specimen geometries. The temperature gradients in the ends of this specimen are not as large as the other specimens.

Experimental Results

The results of the thermal cycling tests are summarized in Table 4.2 . This table lists the specimen type, the maximum temperature, the maximum current density and the number of thermal cycles tested. The first test demonstrates the inability of the maraging steel specimens to survive intact under the very high current density and extreme thermal conditions. It also shows that higher current densities result in higher temperatures and a lower number of thermal cycles to failure. Finally, the hourglass specimen shape is better able to withstand higher current densities than the tapered specimen shape.

All of the specimens which were pulsed to temperatures between 1000 and 1200 K shared some common characteristics. The first pulse leaves a bluish

discoloration on the specimen gage length. Between the 2nd and 10th pulse, there is a gradual change in specimen color to dull gray. The surfaces appear smooth and there is some visual indication of deformation in the specimen. After about the 10th pulse, the surface texture and shape of the gage section change more rapidly. The surface becomes rough and circumferential cracks develop (same as polishing direction). The color and texture changes observed for each specimen type are similar, but the deformation observed among the different specimen types is different.

The geometry of the test specimen plays an important role in the extent and type of deformation which occurs. What follows are short descriptions of the kinds of deformation observed and the testing failures for each specimen type.

The first thermal cycling test began with the expectation that the specimens could be cycled to a peak temperature greater than 1400 K. For the first pulse, a red glow was observed immediately after the discharge of the capacitor bank, and then the specimen very quickly turned to a dull gray. When the tensile specimen was pulsed a second time, there was a bright flash and a load bang was heard. An examination of both specimens revealed that the gage sections had completely vaporized. There were threaded stubs still screwed into the brass blocks, but where the gage sections had been, nothing was left. Metal splashes were visible on the surfaces of the brass, but after a search, no metal fragments were found.

With Test 2, the specimens were thermally cycled to a smaller peak temperature of 931 K. At this temperature, the material did not transform to austenite and remained entirely in the martensitic phase. After 25 thermal cycles, the specimen surfaces were gray, and had circumferential as well as longitudinal markings on their gage sections. The test was terminated, so the test specimens could be examined more closely. One of the specimens was examined under an electron microscope, and the markings were found to be cracks and flaking in an oxide coating. A search of the specimen surface did not turn up any cracks extending through the oxide into the specimen.

Tests 3 - 5 were all conducted on tapered specimens to the same predicted peak temperature of 1047 K. The first of these tests resulted in the failure of the specimen after 33 thermal cycles. Failure again occurred with a bright flash

and a load bang. One of the specimen gage sections vaporized, and the other showed severe deformation and some melting in the gage section. For Test 4, the specimen was thermally cycled 16 times. The test was then halted so the specimens could be examined in more detail. For the third test with a tapered specimen, the thermal cycling was continued until failure seemed imminent (25 cycles), and then the specimens were removed.

For the peak temperatures being predicted, the central portion of the gage section transforms to austenite. All three tests showed double necking in the ends after the 10th pulse. In the ends, there is an additional sharp reduction in cross sectional area due to plastic deformation. Figs. 4.10a and 4.10b illustrate this deformation in the test specimen from Test 5. The length of the sharp transition in Fig. 4.10b is approximately 1 mm. Fig. 4.11 shows a prediction of material phase at the moment of peak temperature. There are three regions in this picture, and they correspond to a martensitic, austenitic, and a martensite to austenite transition region. By comparing Fig. 4.10b with Fig. 4.11, it is easy to see that the deformation observed in the specimen corresponds to the predicted region of phase transformations. Based upon this association, it appears that phase transformations in the ends contributes to double necking.

A measurement of the minimum diameter in the necked region of the test specimen from Test 5 indicates a reduction in cross sectional area of 19 %. The gage center on the other hand showed an increase of cross sectional area of 9 % Using this fact, the new peak temperature prediction is 1307 K, rather than 1000 K at $z = 0$ from Fig. 4.8. Thus, there is a shift in the peak temperature from the gage center to the ends.

All six tapered specimens showed signs of buckling in the austenite region between the double necks. Buckling was first observed between the 12th and 18th thermal cycles. The ends of the specimens remain fixed during these tests, and this limits the buckling. The gage section between the double necks is austenitic at the moment of peak temperature, and in this phase the material is not as strong as in the martensitic phase. Thus, primarily this portion buckled plastically. The failed test specimen vaporized between the double necks.

One of the specimens from Test 5 was mounted and polished to expose the sectioned half of the specimen. The outline of the sectioned specimen and the tapered specimen of Fig. 4.2 are the same. Close examination of the sectioned

specimen reveals an oxide coating on the outline of the specimen which is 20-30 μm thick. The thickness of the oxide coating was largest on the high temperature portions of the specimen and was not even visible at the ends. Microhardness measurements along the centerline of the specimen (Fig. 4.12), show a sharp transition in material strength. Those portions of the thermal cycling specimen which were pulsed into the austenite regime show a drop in Rockwell C hardness from 59 to 34.

There were two thermal cycling tests of the hourglass specimen. The first, Test 6, reached a predicted peak temperature of 1063 K, and was pulsed 45 times before it failed. Figs. 4.13a and 4.13b show one of the specimens. These photographs reveal several important features. First, there is a banded region of discoloration in the ends. Secondly, there is a sharp transition region where the cross sectional area decreases because of plastic deformation. Fig 4.14 shows the material phases predicted at the moment of peak temperature. The temperature gradient for the hourglass specimen is larger, so the transition from martensite to austenite occurs over a shorter distance. The measured distance of the sharp transition shown in Figs. 4.13a and 4.13b is 0.3 mm .

The gage sections of these specimens are much shorter than the tapered specimens, and there is no evidence of double necking or buckling. Instead, the austenite center of the gage section developed a barrel shape. There is a sharp change in shape where the material at the edge of the phase transformation transition is entirely martensitic during the thermal cycles. The maximum diameter of the barrel section increased to 1.29 mm, an increase in cross sectional area of 10 %. At the sharp transition, the diameter had decreased to 1.23 mm. Again, the peak temperature during a thermal cycle had shifted from the center towards the ends.

A specimen from the first hourglass test was also sectioned, mounted and polished for a closer examination. With a higher peak temperature and more thermal cycles, the oxide coating measured 50 - 70 μm thick. This is a 40 μm increase in thickness over the tapered specimen oxide coating. The change in oxide thickness occurs over a shorter distance for this specimen because the temperature gradient is larger. The temperature gradient for this test has an even more dramatic effect on the microhardness measurements taken along the Z axis (Fig. 4.15). Again, those portions of the thermal cycling specimen which

are pulsed into the austenite regime show a drop in Rockwell C hardness from 57 to 37.

The second thermal cycling test with the hourglass specimens was pulsed to a predicted peak temperature of 1133 K, and its lifetime was 20 cycles. These specimens had the same features as those mentioned above. The barreling of the gage section was visible after the 14th thermal cycle. Unlike the tapered specimens, the hourglass specimens showed few signs of imminent failure. The surfaces of the hourglass specimens were darkened after just a couple of thermal cycles, and they became rough in the gage section at the same time the sharp transition region became evident. Once the barrel shape is formed, there is no visible (as seen with the naked eye and measured with a micrometer) sign of further change until the electrical explosion.

Finite Element Analysis

A finite element study was undertaken to verify the mechanical behavior observed in the thermal cycling tests. The material model of Chapter 2 and the finite element implementation described in Chapter 3 are used here for this analysis. The phenomenological kinetic equation is used in these finite element analyses. In Chapter 1, two thermal cycling zones in the short pulse magnet were described. The thermal cycling specimen can also be divided into two zones. The gage length corresponds to Zone 1, and it is heated to the highest temperature in the specimen. The ends of the specimen correspond to Zone 2, and they heat to less than half the peak temperature. The assumptions and conditions made in developing the kinetic equations for the two zones are also applied here. Thus, the strength in the gage length is approximated by the strength of solutionized steel (high temperatures,) while the strength in the ends is approximated by the strength of aged maraging steel (low temperature.)

Each of the specimen geometries with its associated temperature profiles is examined, and the deformation shapes and stress contours predicted by these models are plotted and discussed. In addition, several thermal cycles are modeled with the tapered and hourglass meshes. With the multiple cycle data, it is possible to draw a hysteresis plot of the stress-strain response to the thermal loadings. Finally, an effective plastic strain increment per thermal cycle is predicted from the finite element analysis. The results from all the finite analyses

are compiled into Table 4.3 showing some aspects of the usefulness of maraging steel as an electrical conductor.

The boundary and loading conditions applied to the three different thermal cycling specimens are similar. The ends of the finite element models are constrained from axial movement. The original temperature profiles shown in Figs. 4.7-4.9 are applied to their respective models for up to 3 cycles. There are 8 time steps used in the analyses, and they are 50, 100 and 500 μs, 0.005, 0.05, 1.0, 4.0 and 180 s. The 0.005 and 0.05 s time steps are important to the finite element analysis, because they serve as a bridge for changing the time step size. The number of sub-increment time steps chosen for all these analyses is 15. Between each time interval, the time step size increases. The changing time step size should not be too dramatic, so the intermediate time steps of 0.005 and 0.05 are included.

Uniform Test Specimen

Fig. 4.16 shows the finite element mesh used to model the uniform test specimen. For reasons of symmetry, just the top half of the test specimen is modeled, and since it is axisymmetric, a two dimensional finite element mesh is used. There are 72 elements and 271 nodes in the finite element mesh. The maximum element aspect ratio (the radial dimension divided by the axial dimension of an element) is 1.8 . In the ends of the mesh, the minimum element interior angle is 49.1° . The aspect ratio and its inverse should not be greater than 3, and the interior angle should not be less than 30° or greater than 150° for finite element analyses [2].

Figs. 4.17a and 4.17b are plots of the original and deformed mesh outline at the end of the first and second thermal cycles (displacements are magnified by 100, and the distorted outline is dashed). A double neck is predicted by the finite element model in the ends of the specimen. The center of the gage section has increased in diameter, while near the ends, the cross sectional area has decreased. The change in shape predicted here is the result of plastic deformation during the thermal pulse.

The maximum temperature of this test did not cause any phase transformations in the steel. The double necking predicted here is the result of the

temperature gradient present in the ends, because with a given uniform temperature change, with the same boundary conditions, and with plastic deformation, the double necking is absent. Thus, three factors contribute to double necking at the ends: the temperature gradient, the geometry of the ends which affects the state of stress and strain and the interactions between temperature, stress and the flow strength of maraging steel.

Two times are examined in this review of the finite element results; the first is 500 μs when the ohmic heating has ended, and the second is 3 min, at the end of the thermal cycle. Fig. 4.18 shows the radial, hoop, and axial stresses on the Z axis of the thermal cycling specimen at 500 μs (starting at the center of the specimen R=0 and Z=0, and going up the Z axis to the top of the specimen R=0 and Z=12mm.) The radial and hoop stresses predicted by AFESA are equal to each other because the radius is zero all along these curves. The radial and hoop stresses are zero everywhere except near the ends of the specimen. The axial stress is constant in the gage section, peaks near the fillets and decreases through the ends.

Fig. 4.19a shows the von Mises stress on the Z axis of the specimen at 500 μs. This curve predicts a uniform stress of 830 MPa in the gage section, a peak stress of 900 MPa in the ends and then a decrease to 180 MPa beyond the ends. The stresses predicted in each finite element are linear over the domain of that element, so the smoothness of the stress distribution is a measure of the finite element mesh's modeling accuracy.

Fig. 4.19b plots von Mises contour bands in the specimen at 500 μs. Each contour band is identified with a mean stress. The edge between two stress bands corresponds to the mean of the two adjacent stress band levels. In other words, the edge between a black and white contour band is actually a contour line with a stress level equal to the mean of the two adjacent stress bands. It is helpful to refer to Fig. 4.19a, since it describes the von Mises stress on the left edge of the plot. Stress bands are useful in identifying where the largest gradients in stress are located [3]. When there are more stress bands in a region, the stress gradient for that region is larger. As expected, there are more stress bands in the ends, and the center gage section is uniformly stressed.

Fig. 4.20a shows the von Mises stress on the Z axis of specimen at the end of the first pulse, and Fig. 4.20b shows the von Mises stress contours at the end

of the first pulse. The specimens remain constrained at the end of the pulse, so the specimens are in tension until the next pulse. The region of peak stress has broadened by the end of the first pulse and is located where the diameter of the specimen has decreased.

Figs. 4.21a and 4.21b are the deviatoric axial stress and strain hysteresis loops for the first thermal cycle, and then for the first and second thermal cycle at an integration point near the center of the specimen (1st integration point of Fig. 4.16). The deviatoric component was chosen because it eliminates the thermal and phase transformation strain (dilatational), and makes it easier to comprehend the hysteresis histories. Fig. 4.21a is labelled with times and temperatures to give a better understanding of dynamics of the thermal cycling. Very little plastic deformation occurs during the heating of the specimen, only after the pulse. For the first thermal cycle, the effective plastic strain increment is 0.34% and for the second pulse it is 0.11%. The von Mises stress at this integration point at the end of the first pulse is 217 MPa, and at the end of the second pulse, it is 273 MPa. The information at this integration point indicates that the stress-strain response in the tensile specimen does not shake out in the first pulse, and each thermal cycle predicts further plastic straining.

A plot of plastic strain rate versus time is given in Fig. 4.22. During the initial heating, the plastic strain rates are high, but the time available for deformation is short. Conversely, after the end of the heating, the plastic strain rates are decreasing, and the time available for deformation is increasing. This interaction of plastic strain rate and time shows the time-dependent (pulsed) nature of the plastic deformation.

A second integration point, near the fillet region is also examined (Integration Point 2 of Fig. 4.16). The deviatoric axial stress-strain hysteresis loop for the first thermal cycle is shown in Fig. 4.23. The plastic strains at this point and elsewhere are all smaller than those at the center of the specimen. This is true for all the specimen geometries.

Tapered Test Specimen

The finite element mesh used to model the tapered specimen is shown in Fig. 4.24. It is essentially the same mesh as used before, just different radii in the gage section. The thermal loading conditions for this specimen cause phase transformation in the material. The transformation from martensite to austenite occurs over a temperature span of just 40 K. The finite element mesh used here maintains at least two elements across the region of phase transformation. All other boundary conditions and time steps are the same as the uniform specimen analysis.

The outlines of the deformed meshes after one and two thermal cycles are shown in Figs. 4.25a and 4.25b. The nodal displacements are magnified 100 times. What these figures show is a broadened region of necking in the ends. The center of the specimen is increasing in diameter. The specimen diameter is unchanged 3.7 mm away from the center.

Fig. 4.26 gives the radial, hoop and axial stress on the Z axis of the tapered specimen 500 μs into the first pulse. This plot shows an important result; the radial and hoop stresses are near zero everywhere, except in the ends and the phase transformation transition region. In the previous analysis, these two stresses were nonzero only in the ends. The axial stress (which is strongly influenced by the tapered cross sectional area), increases from the end of the specimen towards the center, shows a peak stress at Z=3.6 mm, decreases across the phase transformation transition and then increases towards the center. The stress distribution for the tapered specimen is not smooth, and more elements should probably be used for this analysis.

Figs. 4.27a shows the von Mises stress on the Z axis of the specimen and Fig. 4.27b shows the von Mises stress contour plots 500 μs into the first pulse. The maximum stress is in the center portion of the specimen and fluctuates across the phase transition and the ends. These stress variations are clearly shown by the stress bands. Figs 4.28a and 4.28b show similar results for the end of the pulse. The residual stresses through the prior phase transition region fluctuate, while they vary steadily across the ends.

The hysteresis loops for the tapered specimen are given in Figs. 4.29a and 4.29b. As before, the axes are deviatoric axial strain and stress, and Integration

Point 1 of Fig. 4.16 (closest to the center of the specimen) is analyzed. In addition to the time and temperature labels in Fig 4.29a, the positions of the phase transformation start and finish temperatures are indicated. Upon heating, the martensite to austenite phase transformation effect is visible on the curve. During the phase transformation, the increment of plastic deformation is not large. The interaction between plastic strain rate and time observed in the uniform specimen analysis also happens here. Most of the plastic deformation occurs after the heating. The final transformation from austenite back to martensite occurs elastically and causes a fluctuation in stresses at the very end of the thermal cycle.

The finite element analysis of the tapered specimen was continued over three thermal cycles. The effective plastic strain increments for these three cycles were 0.59, 0.16 and 0.08%. The final von Mises stresses for these cycles were 307, 395 and 450 MPa. The deformation occurring in the tapered specimens is larger than that predicted for the uniform specimen. The effective plastic strain increments are decreasing substantially with each pulse, and the residual stresses are increasing.

Hourglass Test Specimen

A finite element analysis of the hourglass specimen was performed for Tests 6 and 7. The conditions are nearly identical, so only the results of Test 6 are reported. The temperature gradient in the hourglass specimen is larger than that found in previous analyses, so a finer element mesh is required. After several models were examined, the finite element mesh shown in Fig. 4.30 was selected. This mesh maintains 3 elements across the phase transformation transition. The maximum element aspect ratio is 1.9 and the worst interior angle is 71°. There are 613 nodes and 180 elements. The time steps for this analysis are unchanged.

The deformed mesh outlines are shown in Fig. 4.31a and 4.31b for the first and second pulse. The displacements have been magnified 100 times. The finite element analysis predicts a barrel-shaped center for the specimen. The bulk of the specimen seems unaffected by the thermal cycle, and just the center shows permanent deformation. Between the first and second pulse, the curvature of the barrel increases. In Fig. 4.31b, the beginning (top) of the barrel is sharper and the center of the barrel is rounder.

For the radial, hoop and axial stresses on the Z axis of the specimen at 500 μs (Fig. 4.32,) the results are similar to Fig. 4.26. The difference is that the phase transformations at $Z = 1$ mm have a more pronounced effect on the radial and hoop stress, while at the ends, $Z = 4$ mm, the deviation from zero stress is broader and smaller. The variation in axial stress is smooth through the ends, increases as the cross section decreases, is nearly discontinuous through the phase transition zone, and then increases to the center. More finite elements are needed in this phase transition region to obtain a smoother variation in stresses. Even so, the results show that the stress state and material phase change over a very short distance,

The von Mises stress on the Z axis of the specimen and the von Mises stress contour plots at 500 μs are given in Figs. 4.33a and 4.33b. The graph indicates a peak stress in the phase transition region and decreasing stress levels on both sides. The contour plots show a gradual change in stress through the ends with very thin contour bands at the phase transition indicating high gradients in stress. At the end of the pulse (Figs. 4.34a and 4.34b), the peak stress in the specimen is still in the phase transition region, and all of the stress contour bands are positioned near there.

The deviatoric axial stress and strain hysteresis loops at the center of the hourglass specimen are given in Figs. 4.35a and 4.35b. The comments concerning the hysteresis loops for the tapered specimen also apply here. The major difference is the extent to which the phase transformations affect the curves. The plastic strain increments during the transformation did not increase, but a larger elastic stress-strain response is observed.

The effective plastic strain increments for this integration point are 0.43 and 0.18% for the first and second pulse respectively. The residual von Mises stresses were 125 MPa for the first pulse and 200 MPa at the end of the second pulse. For Test 7 the effective plastic strain increments and the final von Mises stresses in the same order were 0.30, 0.17% and 52, 98 MPa. The peak temperature difference between these two tests is 70 K.

Conclusions

The thermal cycling tests show the mechanical behavior of maraging steel under extreme thermal cycling conditions in the absence of magnetic body forces. The agreement of the analysis with the thermal cycling tests indicates that the analyses and underlying materials data will be useful to the design of short pulse magnets. That is, the results from these tests confirm the mechanical behavior being predicted by AFESA for maraging steel under short pulse conditions.

Thermal cycling consists of ohmic heating to temperatures greater than 900 K in 500 μs, followed by conduction cooling back to room temperature in about 3 min. The thermal cycling test specimens are similar in shape to the tensile test specimens. The temperature profiles within the specimen are defined mostly by the cross sectional area of the test specimen. The largest temperature gradients are in the ends. During cooldown, the temperature gradient extends across the entire specimen length.

Three different shapes of thermal cycling specimens were tested to failure. These test specimens had a uniform, tapered and an hourglass gage section shape. Thermal cycling to temperatures greater than 1000 K causes significant damage to the test specimens. The test data shows that thermal cycling to temperatures above 1400 K for just a few pulses leads to an electrical explosion which destroys the test specimens. Cracks were found with a stereomicroscope in the 20 - 70 μm thick oxide coating which covered some specimens, but no cracks were found beneath these oxides, using SEM or sectioning. The data indicate that higher current densities and higher temperatures lower the number of cycles to failure. Changes in specimen geometry which decrease the plastic strain increments and stress levels do increase the number of cycles to failure.

All of the tapered test specimens showed signs of double necking (necking in both ends). The location of the double necks corresponds to the predicted position of the martensite to austenite phase transformation transition region. The centers of these specimens increase in diameter, while the double necks decrease in diameter. The double necks cause an increased local current density, leading to higher temperatures and increased plastic deformation in this region. The tapered specimens showed signs of buckling between double necks.

Microhardness measurements show a significant drop in Rockwell C hardness from 59 to 34 after 16 and 45 thermal cycles for the tapered and hourglass

test specimens respectively. This result is very important, since it means that 16 thermal cycles reduced the material hardness 50%. More importantly, the decrease in strength measured here will occur in those portions of the short pulse magnet exposed to similar thermal cycling conditions.

The events preceding failure in the uniform and tapered test specimens were a roughening of the surface texture, the formation of double necks and some buckling between the double necks. For the hourglass specimens, failure was preceded by a roughening of the surface and the gradual formation of a barrel shape in the center of the gage section. Failure occurred at the top of the barrel, which also corresponds to the position of the phase transition between martensite and austenite.

A finite element analysis of the three specimen geometries reveals some additional information. The analysis of the uniform test specimen shows that the temperature gradient, the stress and strain state (influenced by end geometry) and the flow strength interactions cause double necking. The von Mises stresses are largest in the ends, but the plastic strain increments are greatest at the center of the specimen.

For all three specimens, very little plastic deformation occurs during the heating of the specimen. The plastic strain rates are large (10^{-2} s^{-1},) but the time available for deformation is short. Most of the plastic strain is accumulated after the pulse, during the specimen cooling. The stress-strain hysteresis results indicate the stress strain response does not shake out after a few pulses, and that each thermal cycle will result in further plastic straining.

The finite element results for the tapered test specimen show a broadened region of necking in the ends. This is due to the combined effects of a temperature gradient in the ends and the transition from martensite to austenite phase which occurs in this same location. The predicted plastic strain increments at the center of the specimen are 0.59, 0.16 and 0.08 % for the first three cycles, and the corresponding residual stress at the end of these pulses is 307, 395 and 450 MPa.

For the hourglass specimen, a barrel-shaped deformation is predicted. The largest plastic deformations are concentrated in the center of the specimen. The variation in von Mises stress is smooth across the ends, but it is nearly discontinuous across the phase transition zone. The position of this zone is at the top of the barrel-shaped deformation in the specimen. Compared to the tapered

specimen, the hysteresis loops for the hourglass specimen show a decrease in the plastic strain increments (0.30 and 0.17 %) and the residual stresses (52 and 98 MPa.)

Table 4.3 shows the results of the thermal cycling experiments. Included in this table are the maximum current density, the peak temperature achieved, the predicted plastic strain increment for the first pulse $\Delta\varepsilon^{p_1}$, the residual von Mises stress at the end of the first pulse and the number of cycles to failure. The number of cycles to failure is influenced most by the peak current density and temperature. A comparison between Tests 3 and 6 shows that for similar peak current densities and temperatures, the number of cycles to failure is also influenced by the amount of plastic deformation per pulse. Test 6 had a higher peak temperature and a longer life than Test 3, because its effective plastic strain increment was smaller.

The results of the finite element analyses for all three specimens confirm the behavior observed experimentally. The uniform specimen analysis shows that the thermal gradient in the ends is high enough to cause double necking. The tapered specimen analysis predicts a larger double neck region that is the result of the thermal gradient in the ends and the transition from the martensite to austenite phases. Finally, the hourglass analysis correctly predicts the barrel shape in the center of the specimen.

The kinetic equation used to model plastic straining in the thermal cycling specimens assumed a static microstructure. The thermal cycles modeled in the finite element analysis used the same temperature distributions for each cycle. In reality, the microstructure in the specimen is evolving. The changing specimen shape will alter the temperature distributions, and phase transformation strains will become anisotropic. These processes are not modeled by the finite element analysis, but the initial deformed shapes predicted here do match the observed deformed specimen shapes. Just as important, the predicted deformation shapes will change the temperature profiles of subsequent pulses, due to metallurgical and geometrical changes. This leads to an unstable situation where each thermal cycle causes deformations which increase the peak temperature of the next thermal cycle and so on.

Table 4.1 Capacitor bank and dummy load electrical specifications

Energy Storage	273 kJ
Operating Voltage	1-20 kV
Peak Current	400 kA
Inductance	1.25 μH
Capacitance	1.37 mF
Resistance	25.4 mΩ

Table 4.2 Thermal cycling test data.

Spec. Type	Test #	Max Current (kA)	Max Cur. Density (kA/mm^2)	Peak Temp. (K)	No. Cycles	Remaks
Uniform	1	59.2	9.65	1413	2[i]	Vaporized
Uniform	2	46.2	7.54	974	25	OxideCracks
Tapered	3	37.9	7.97	1047	33[i]	Vaporized, DN[ii], B[iii]
Tapered	4	37.9	7.97	1047	16	DN, B
Tapered	5	37.9	7.97	1047	25	DN, B
Hourglass	6	39.1	8.23	1063	45[i]	Vaporized, BS[iv]
Hourglass	7	40.3	8.48	1133	20[i]	Vaporized (1 spec.), BS

[i] Tests which ended with specimen failures.
[ii] Double Necking.
[iii] Buckling.
[iv] Barrel-Shaped.

Table 4.3 Thermal cycling test results

Test #	MaxCurrent Density (kA/mm^2)	Peak Temp. (K)	$\Delta\varepsilon^{p_1}$ (%)	Residual Stress (MPa)	Cycles to Failure
1 (Unif.)	9.65	1413	-	-	2
3 (Tap.)	7.97	1047	0.59	307	33
6 (Hr-Gl)	8.23	1063	0.30	52	45
7 (Hr-Gl)	8.48	1133	0.43	125	20

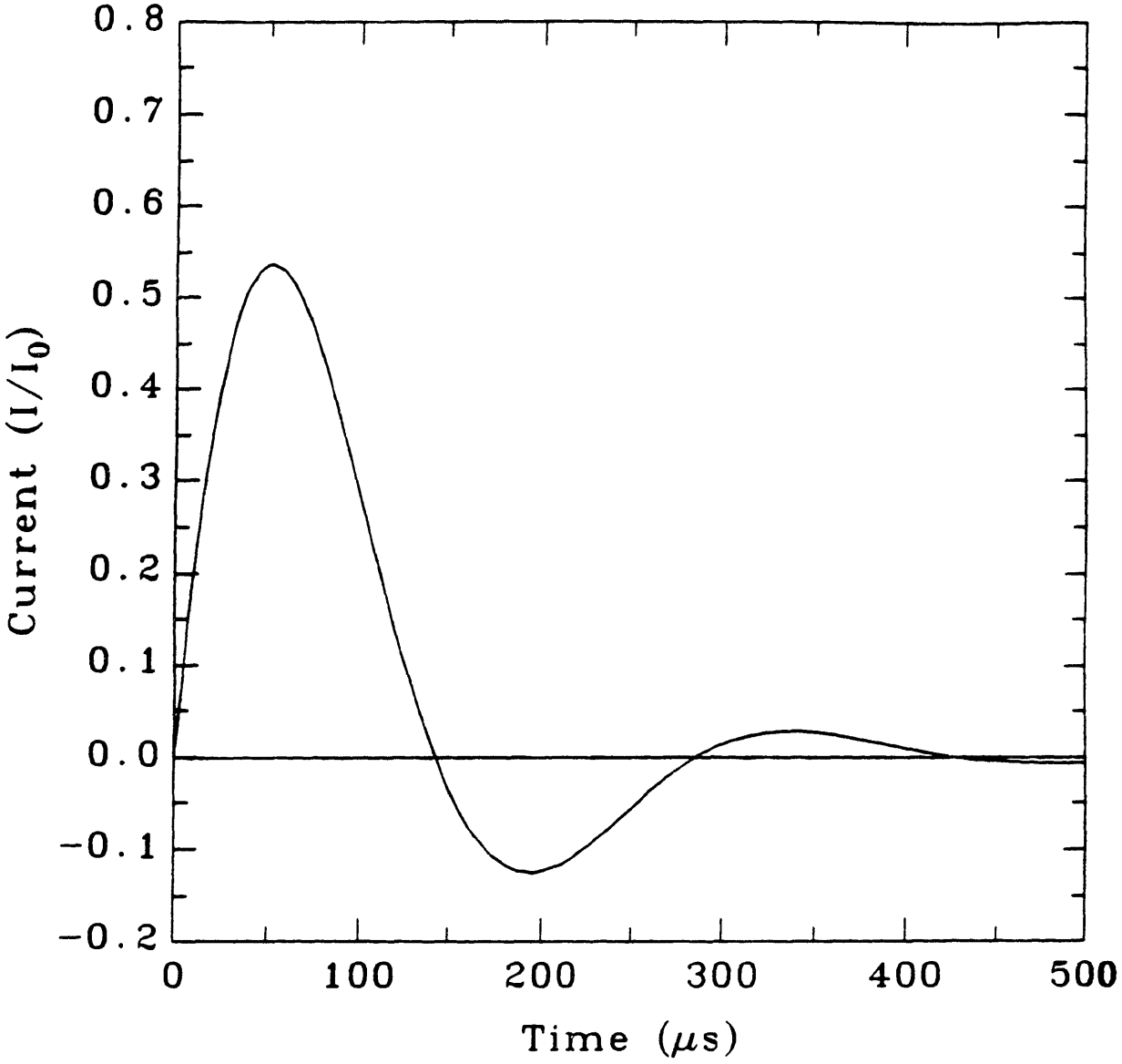

Fig. 4.1 Current waveform for thermal cycling specimens.

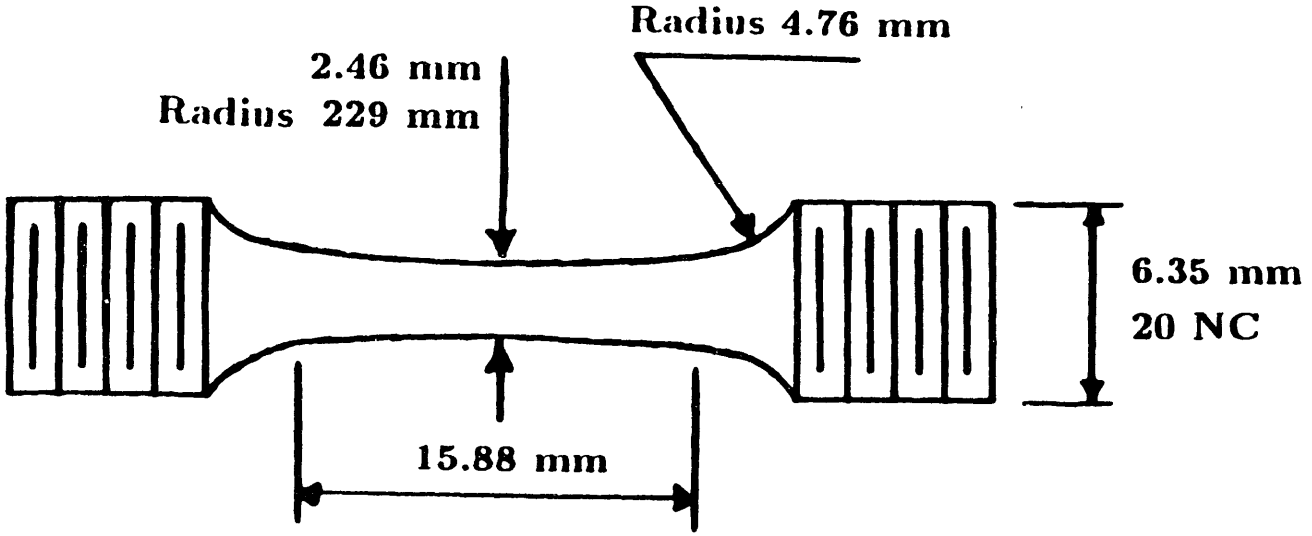

Fig. 4.2 Tapered test specimen.

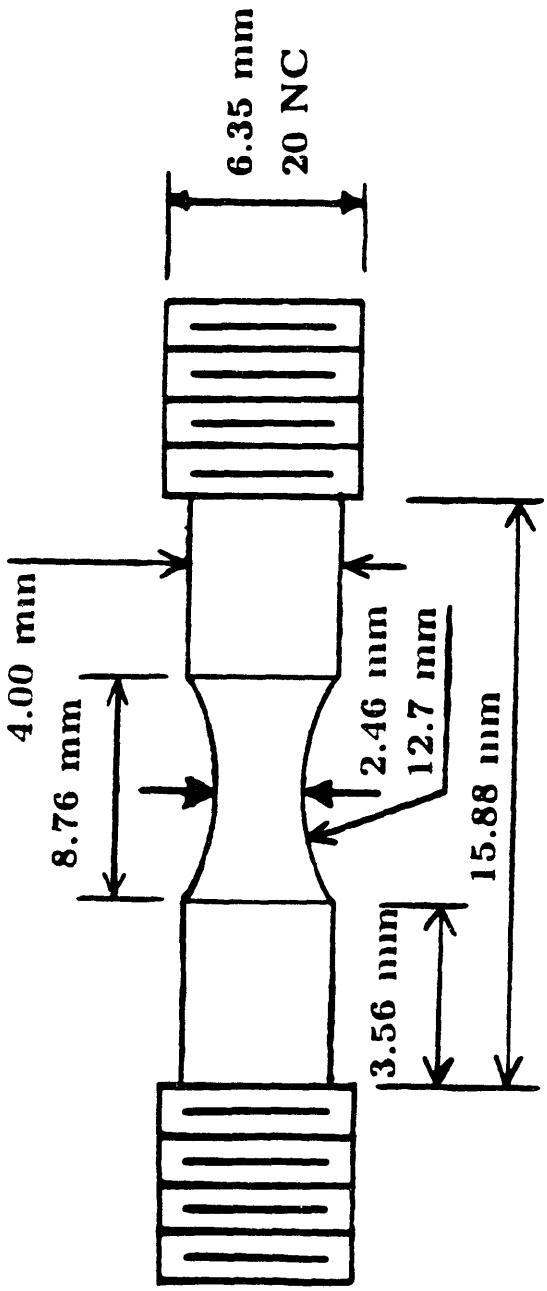

Fig. 4.3 Houglass test specimen.

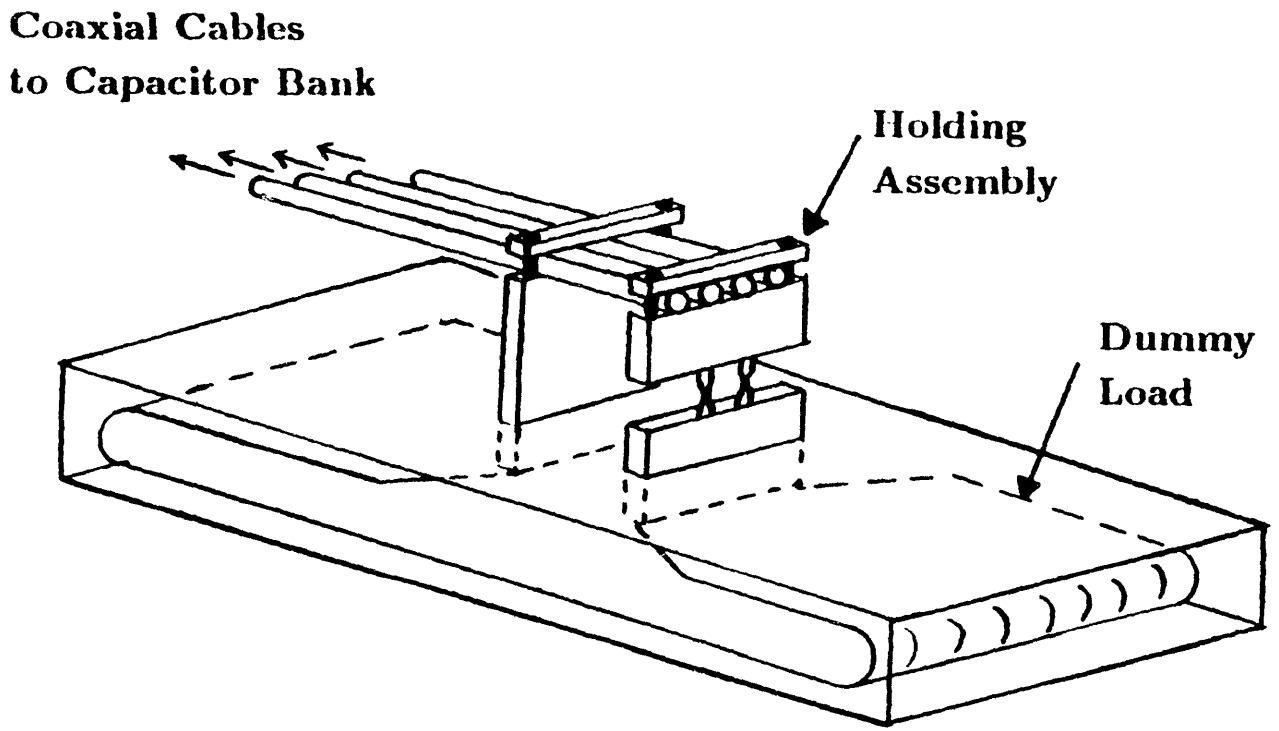

Fig. 4.4 Thermal cycling testing apparatus and dummy load.

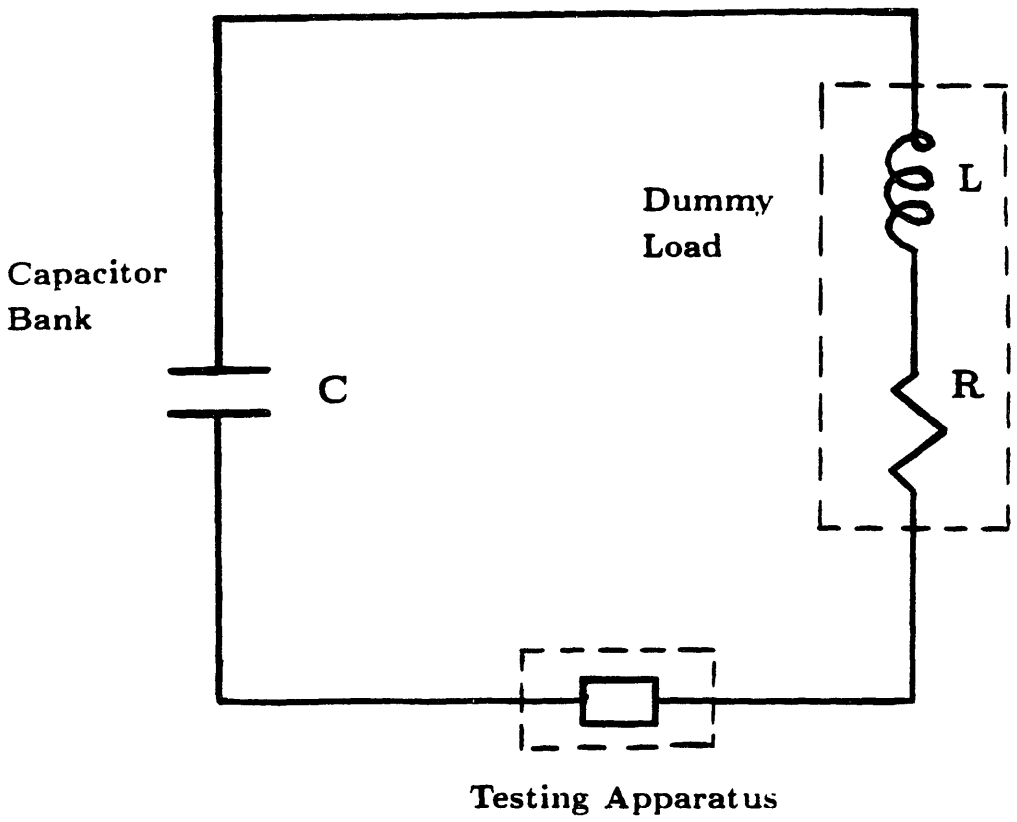

Fig. 4.5 Thermal cycling experimental setup.

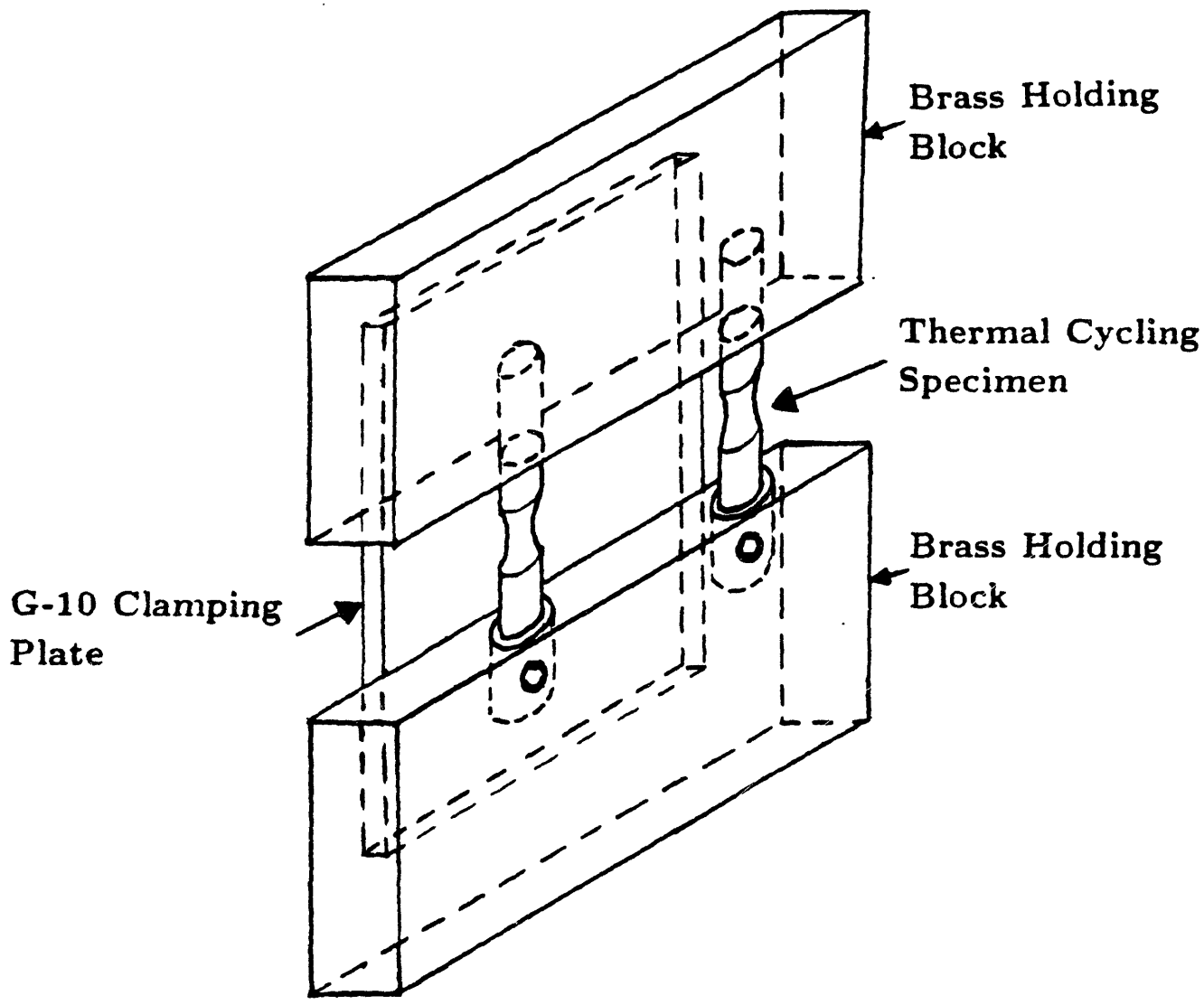

Fig. 4.6 Thermal cycling holding assembly.

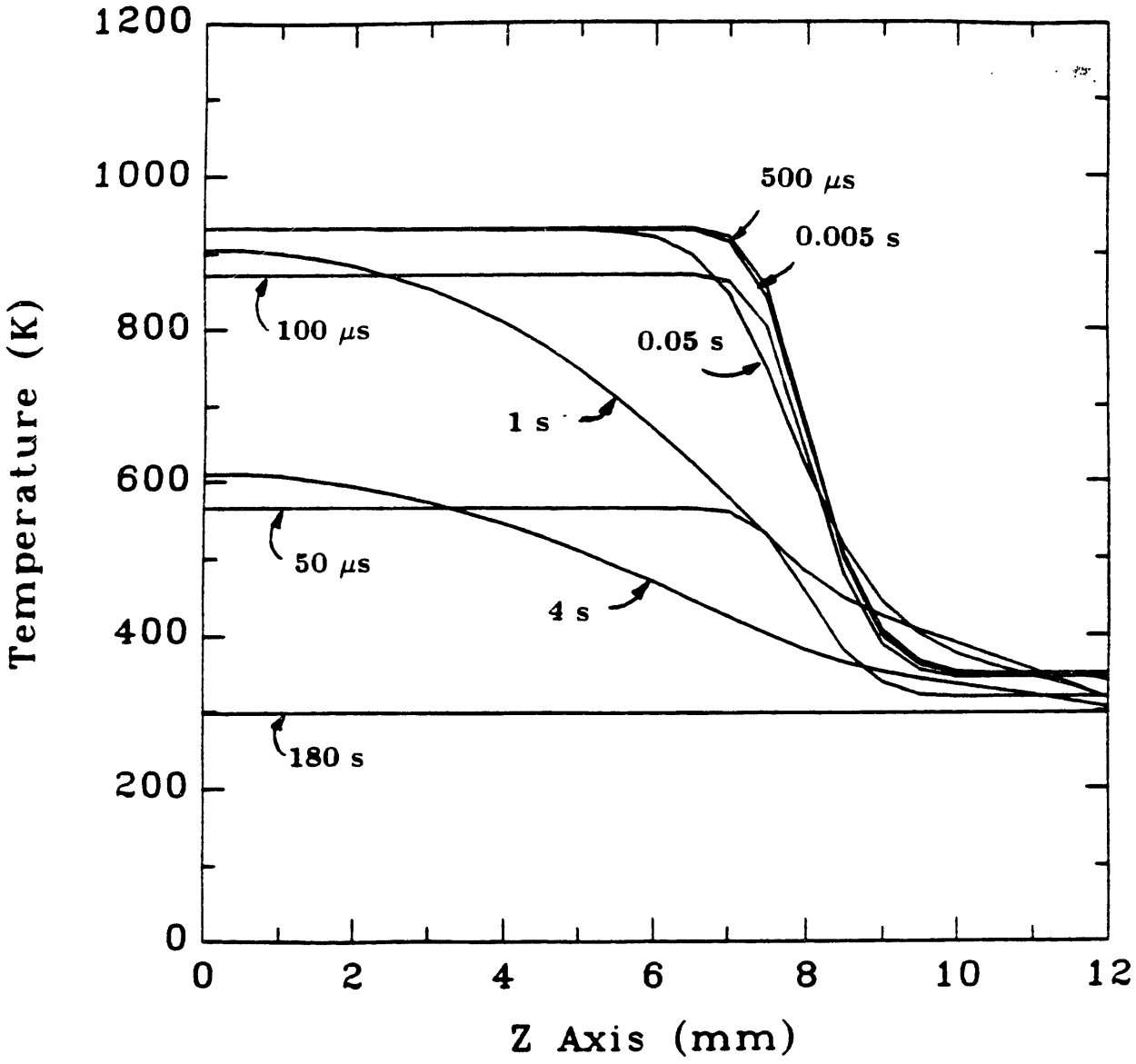

Fig. 4.7 Temperature distributions in uniform (tensile) test specimen.

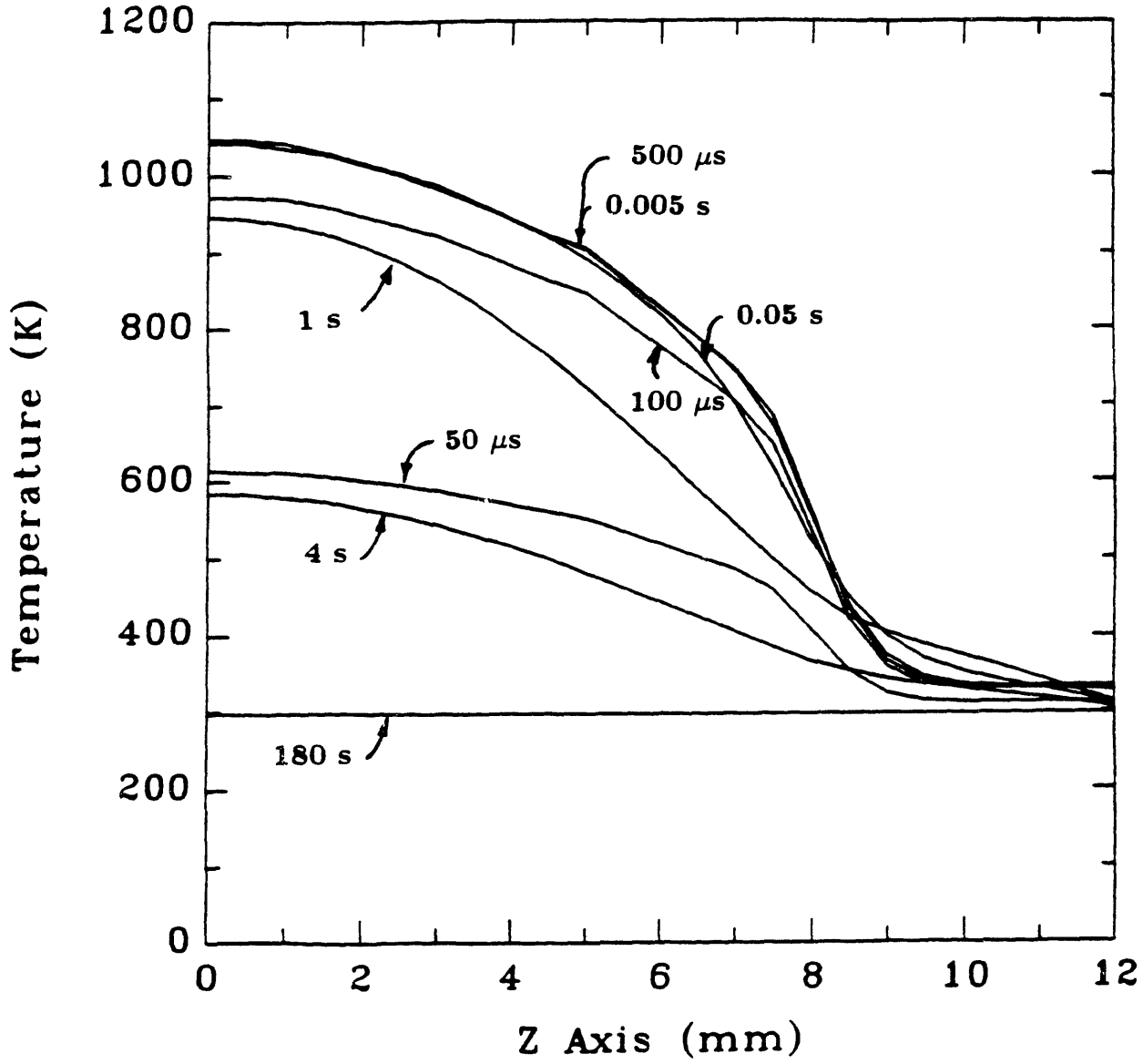

Fig. 4.8 Temperature distributions for tapered test specimen.

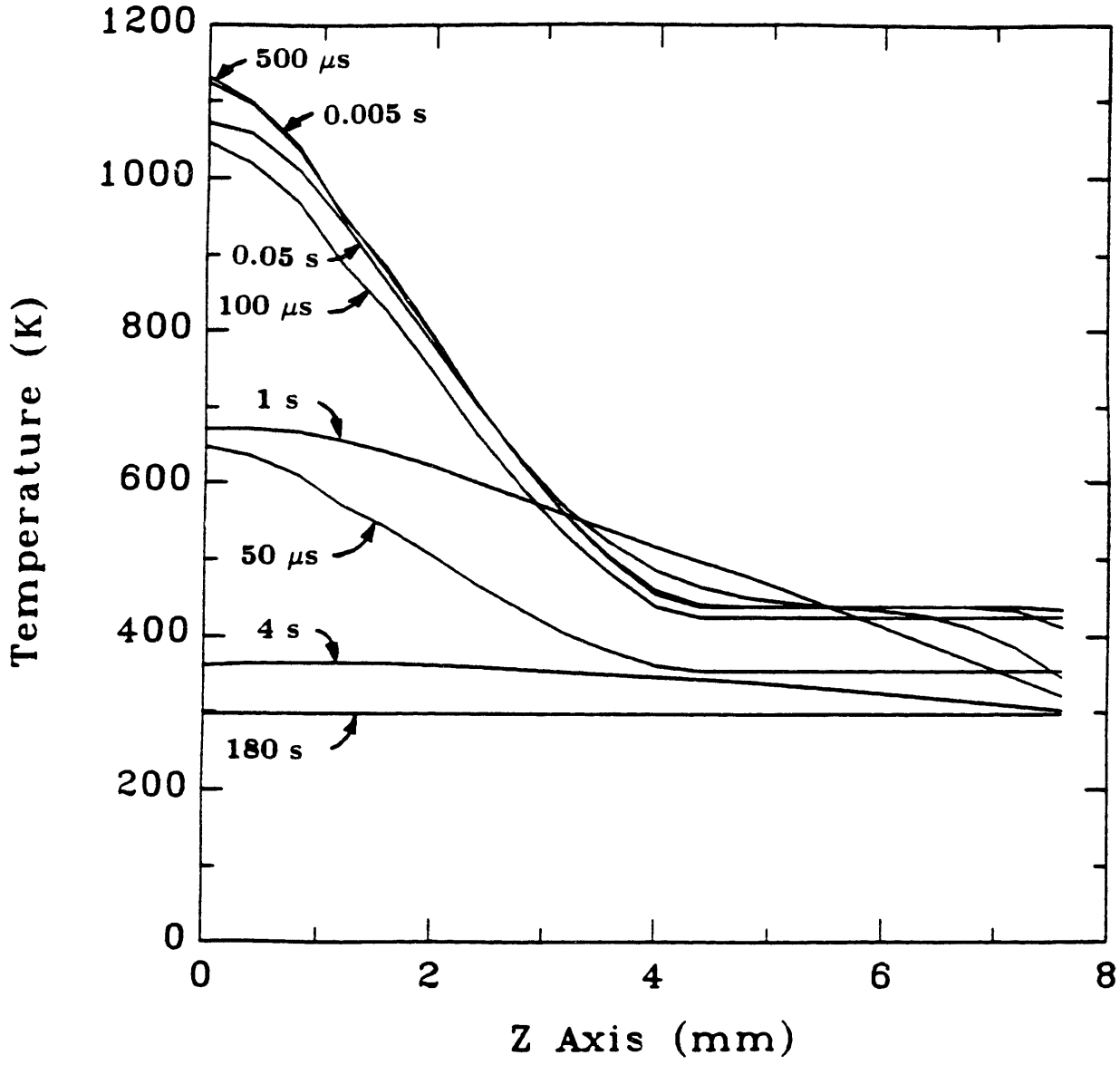

Fig. 4.9 Temperature distributions for hourglass test specimen.

A)

B)

Fig. 4.10 Tapered test specimen from Test 5 after 25 pulses.

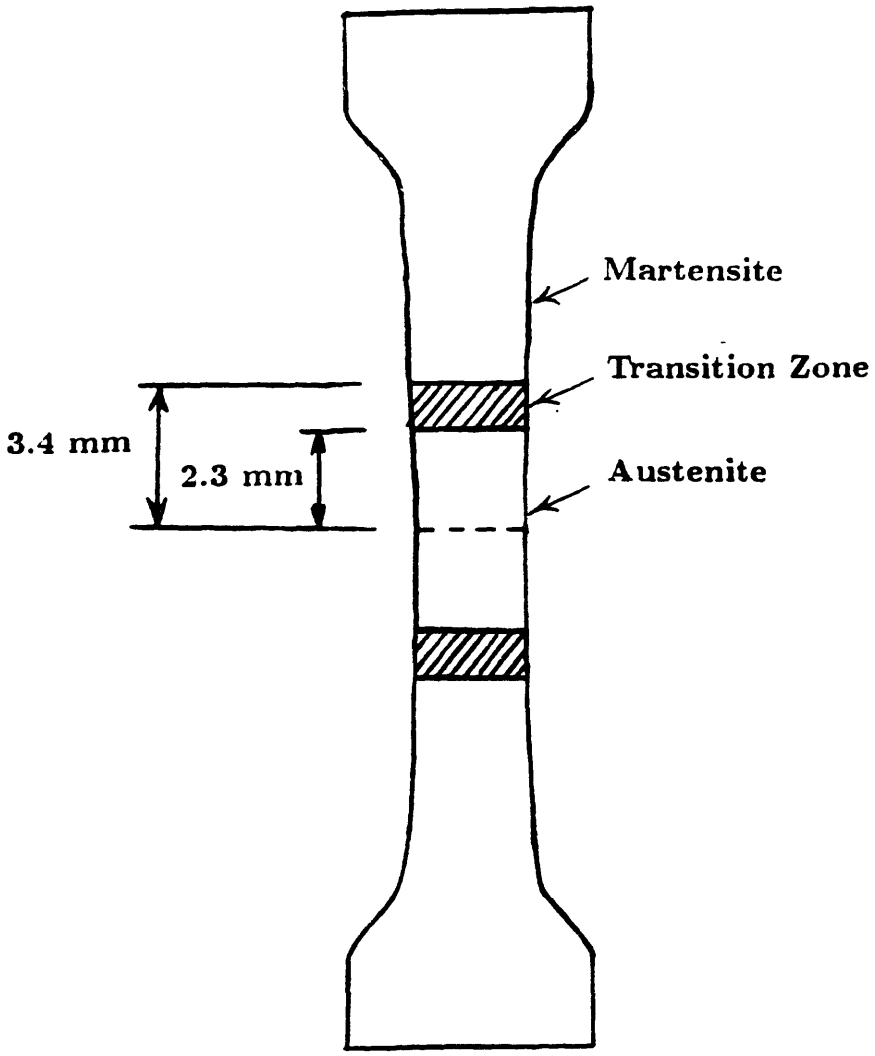

Fig. 4.11 Prediction of material phase at 500 μs in the tapered test specimen.

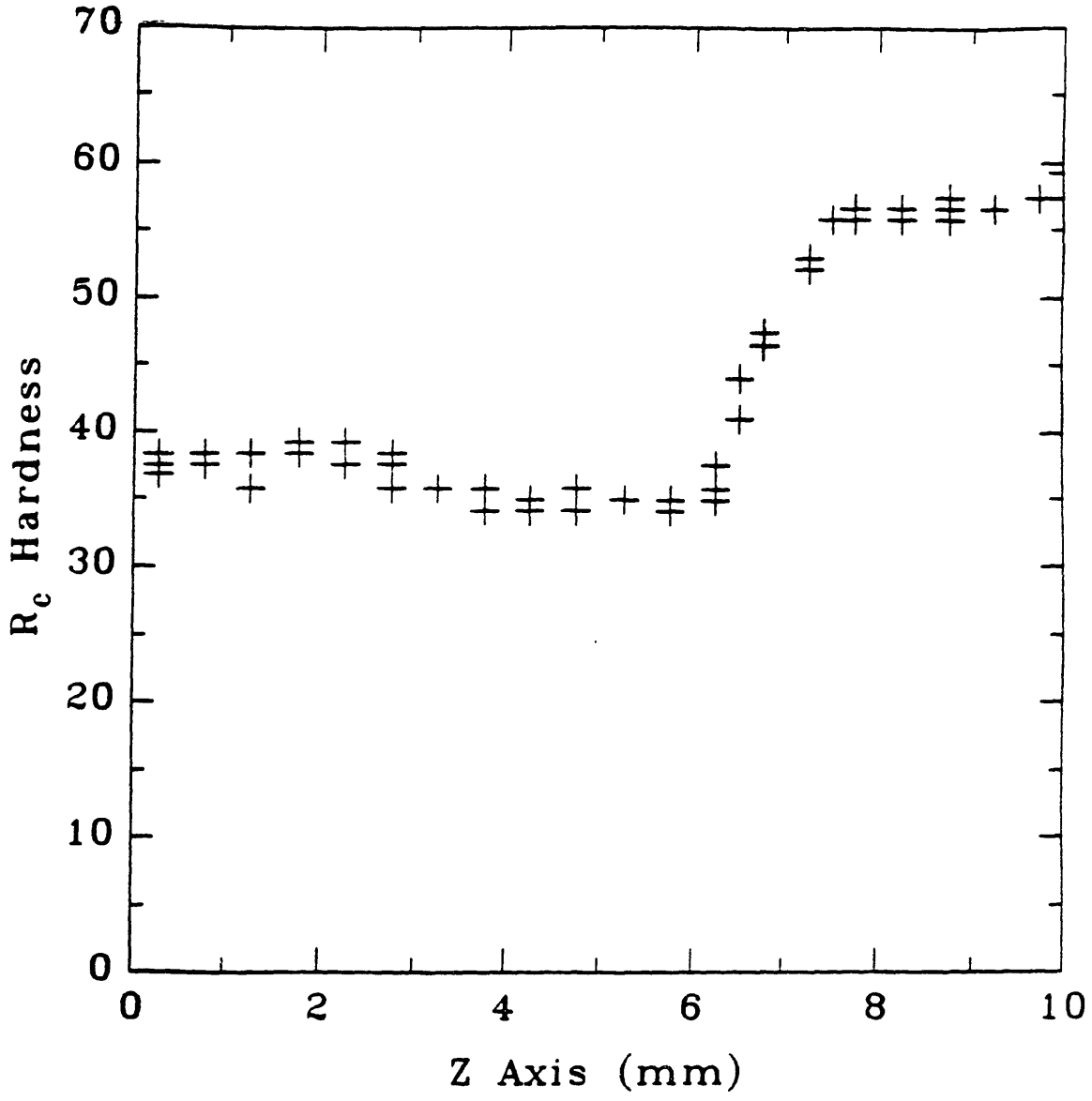

Fig. 4.12 Rockwell C hardness in the tapered test specimen after 25 pulses.

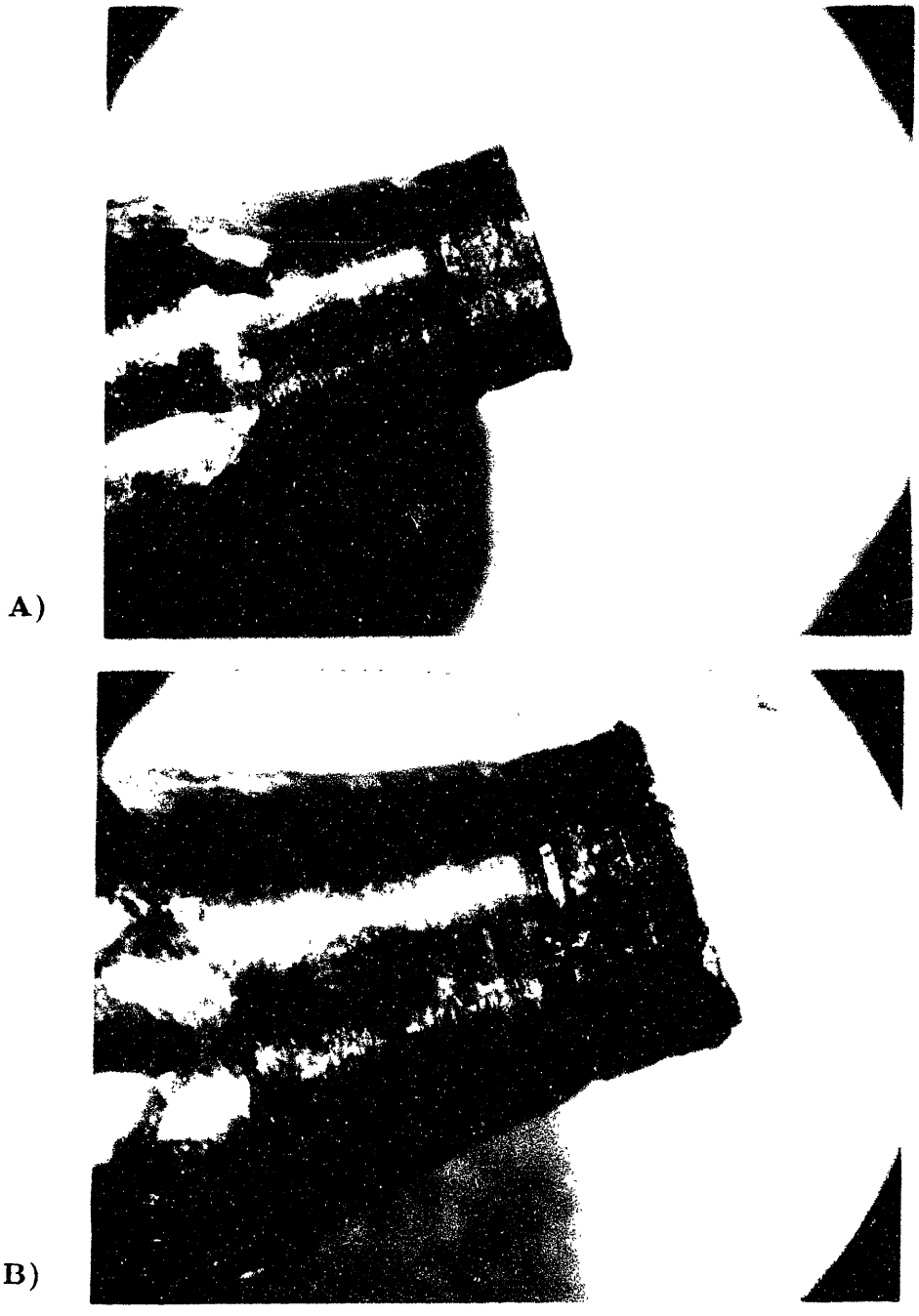

Fig. 4.13 Hourglass test specimen from Test 6 after 45 pulses.

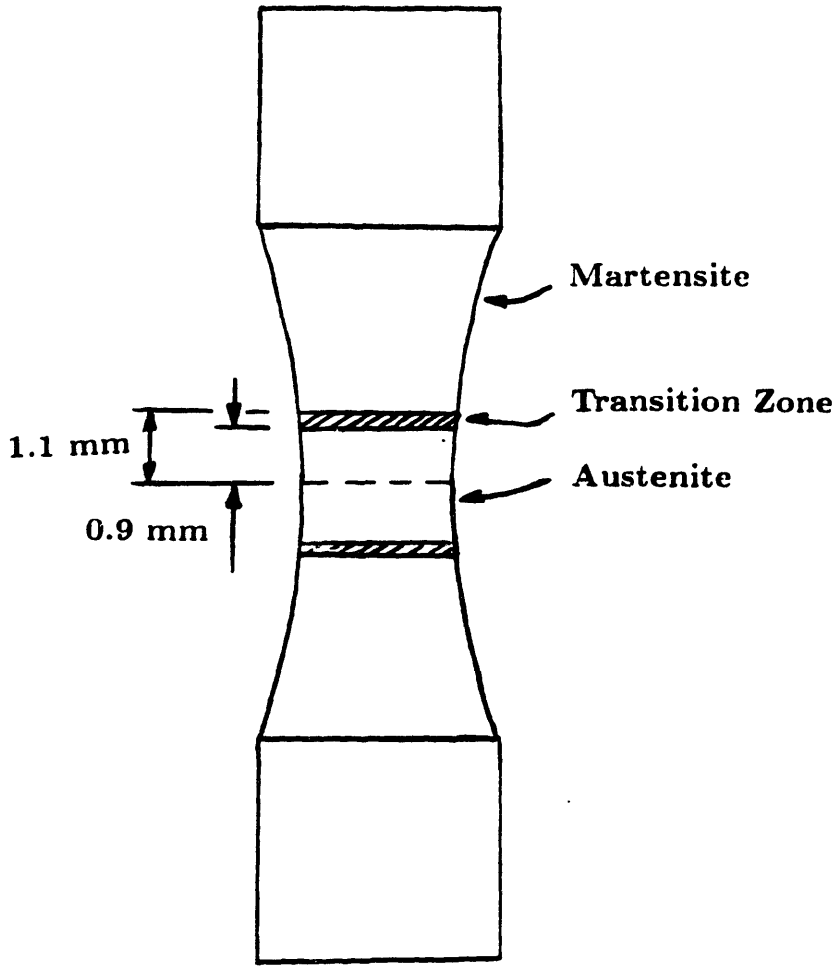

Fig. 4.14 Prediction of material phase at 500 μs in the hourglass specimen.

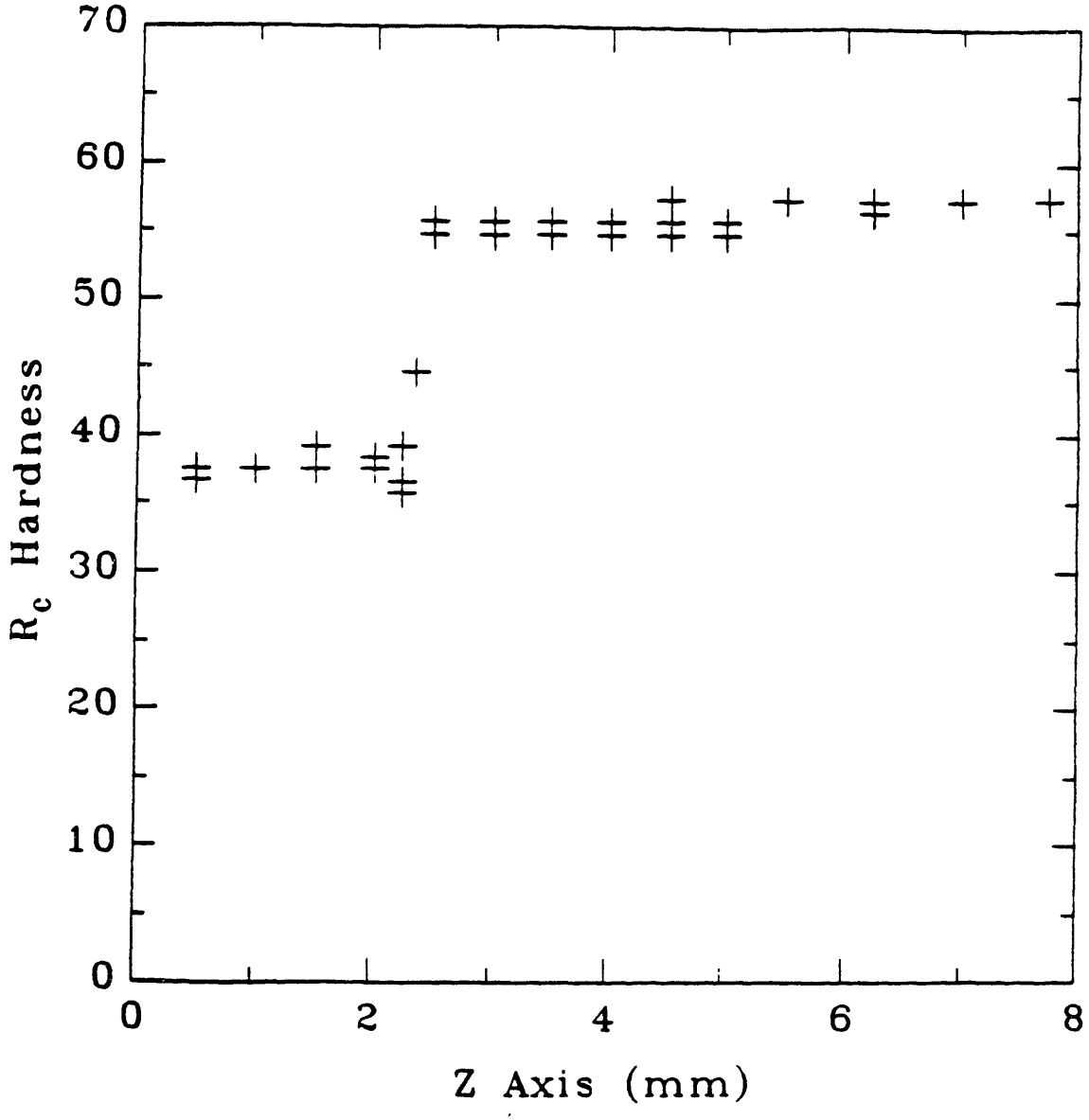

Fig. 4.15 Rockwell C hardness in the Hourglass test specimen after 45 pulses to 1063 K.

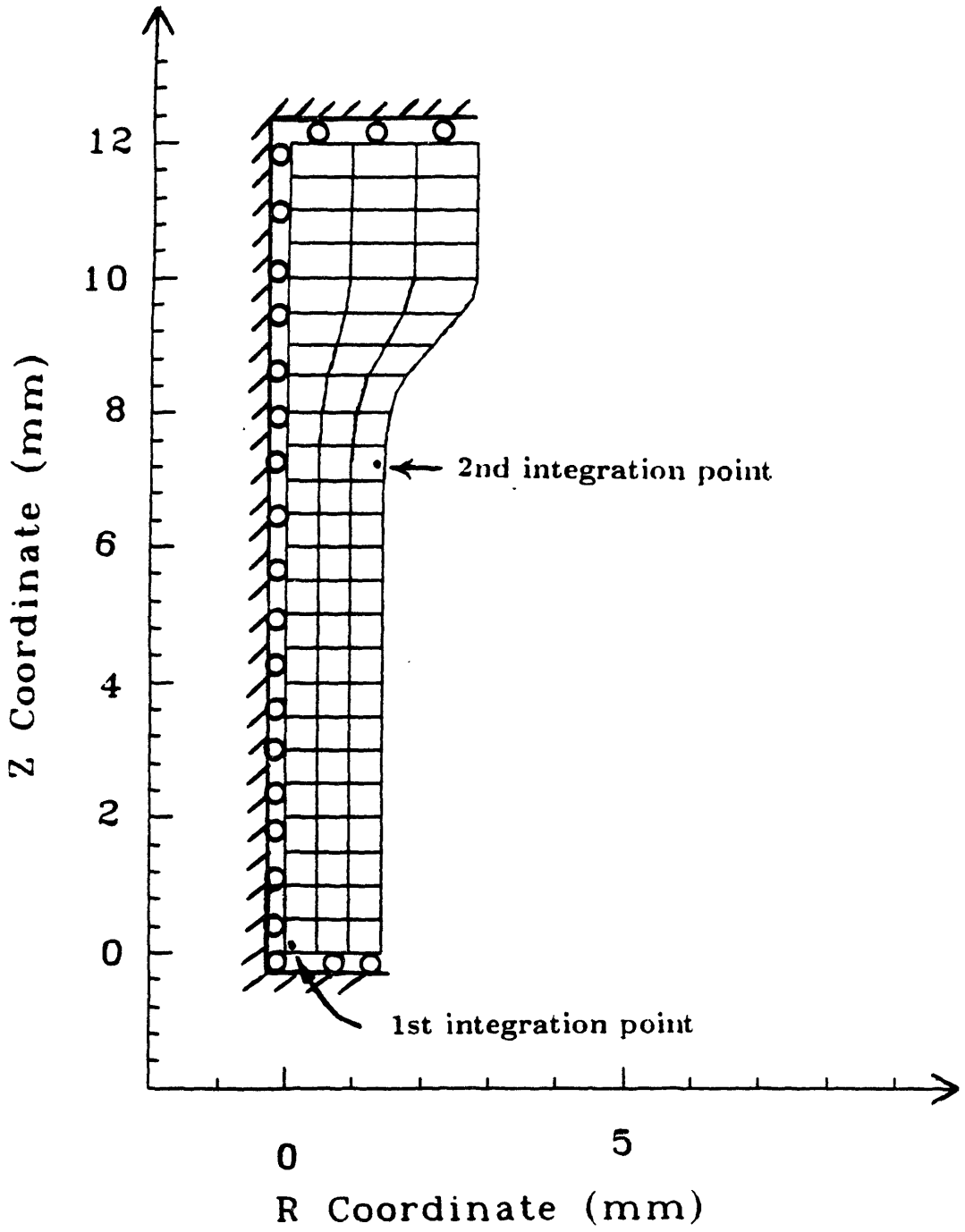

Fig. 4.16 Finite element model for uniform test specimen.

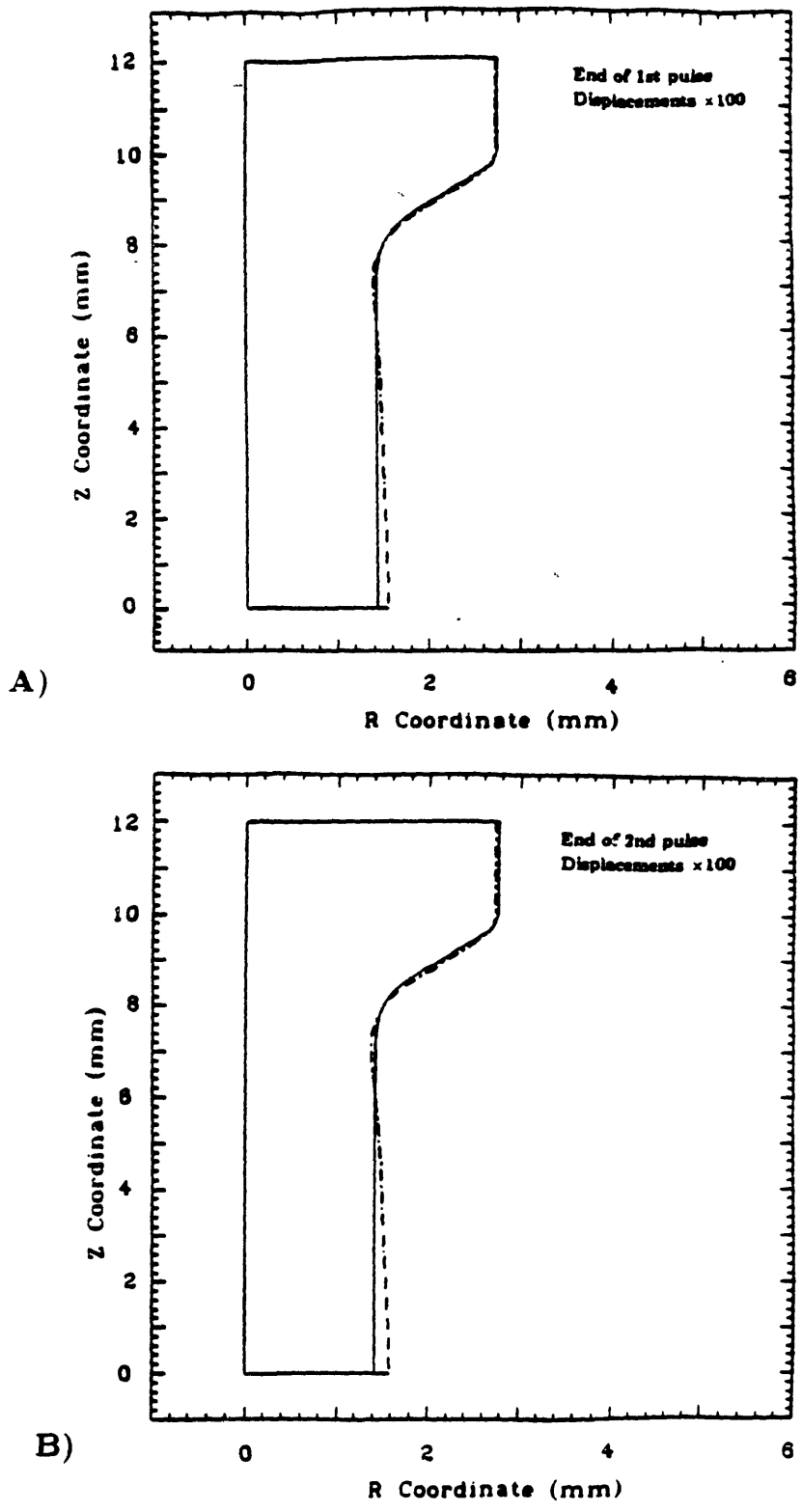

Fig. 4.17 Deformed mesh outlines for uniform test specimen.

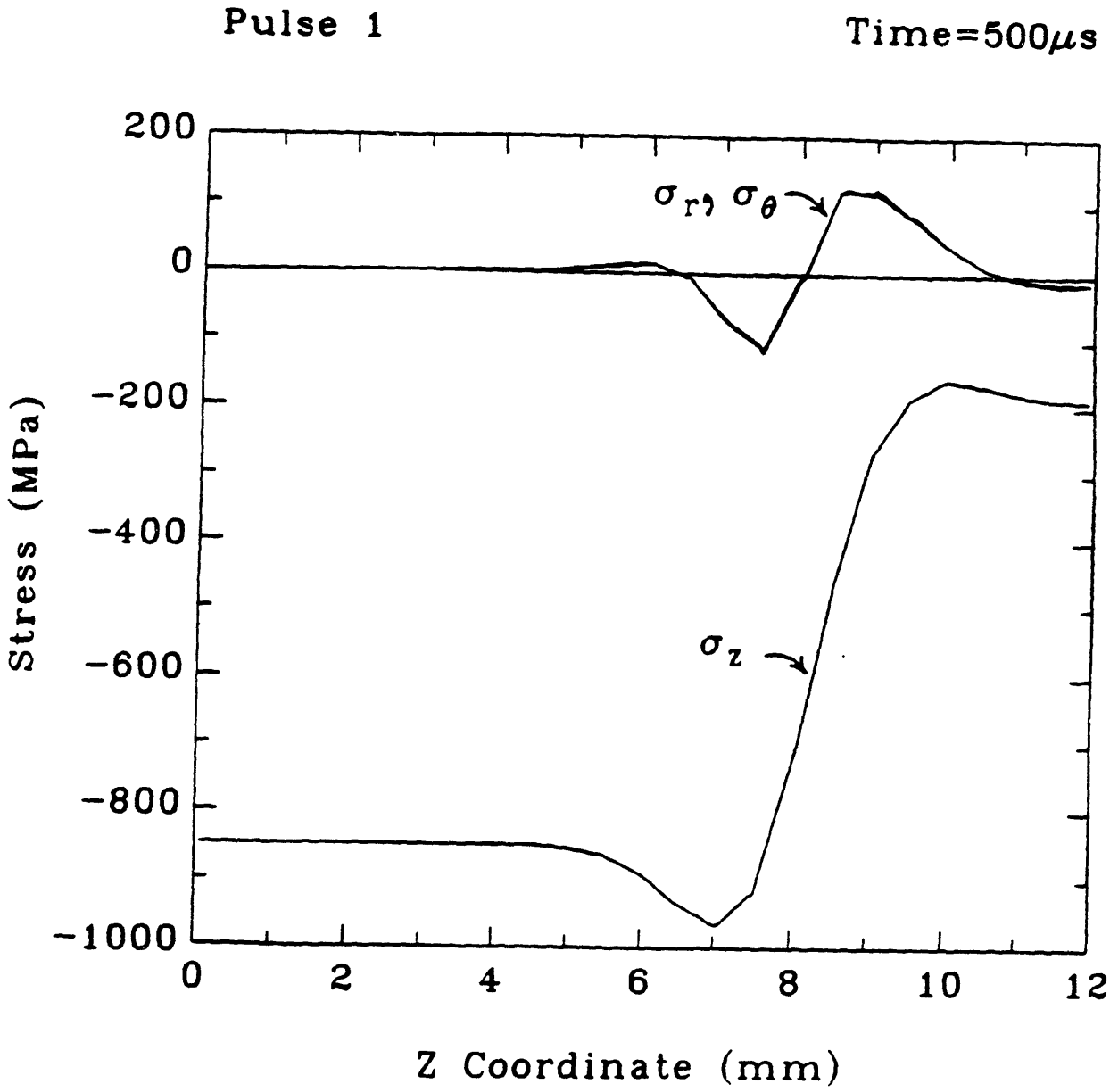

Fig. 4.18 **Radial, hoop and axial stress on the Z Axis of the uniform test specimen.**

Fig. 4.19a
Von Mises stress on the Z Axis of the uniform test specimen.

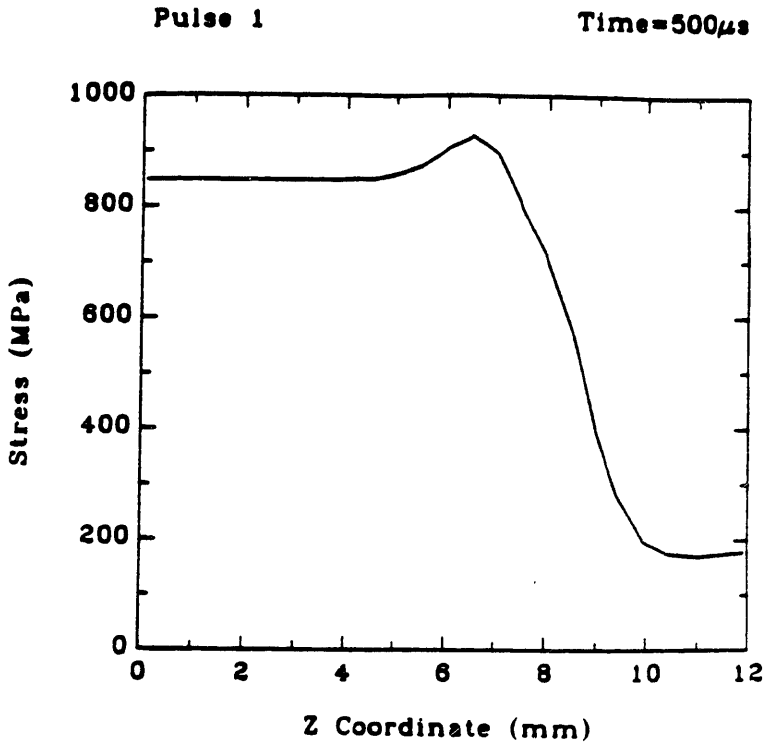

Fig. 4.19b
Von Miscs stress contour bands in uniform test specimen.

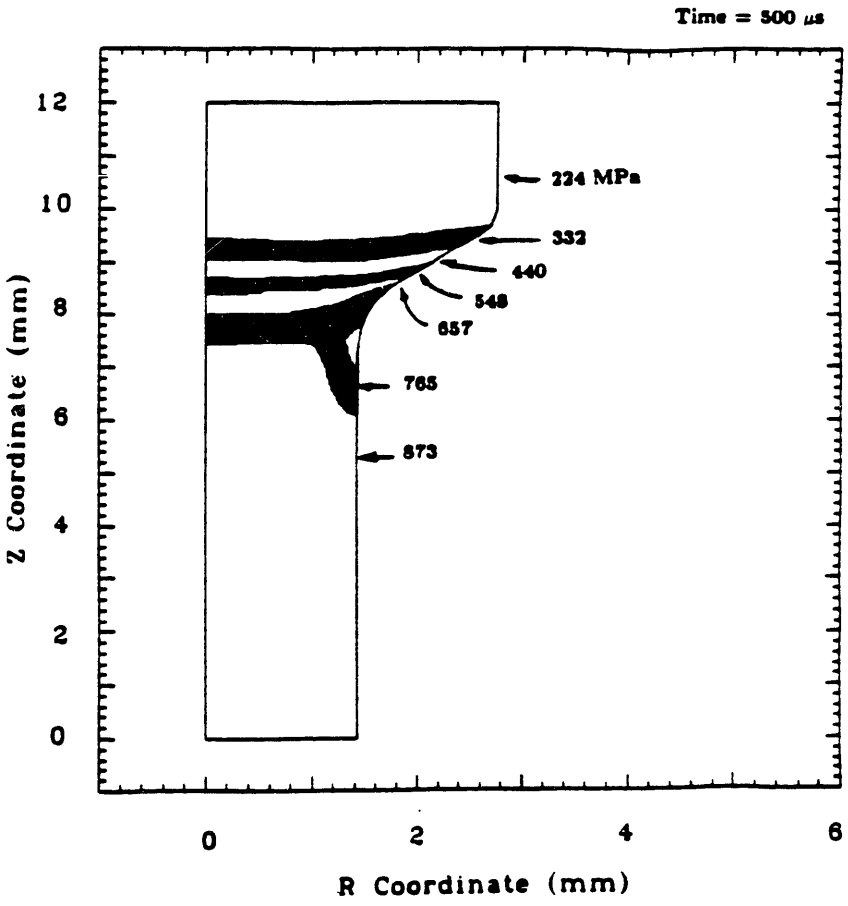

Fig. 4.20a
Von Mises stress on the Z Axis of the uniform test specimen.

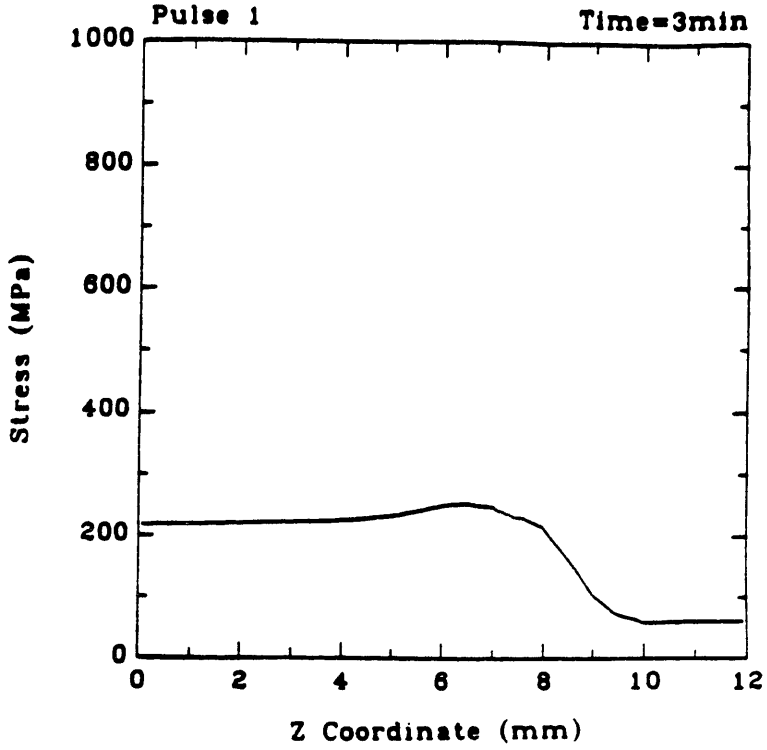

Fig. 4.20b
Von Mises stress contour bands in uniform test specimen.

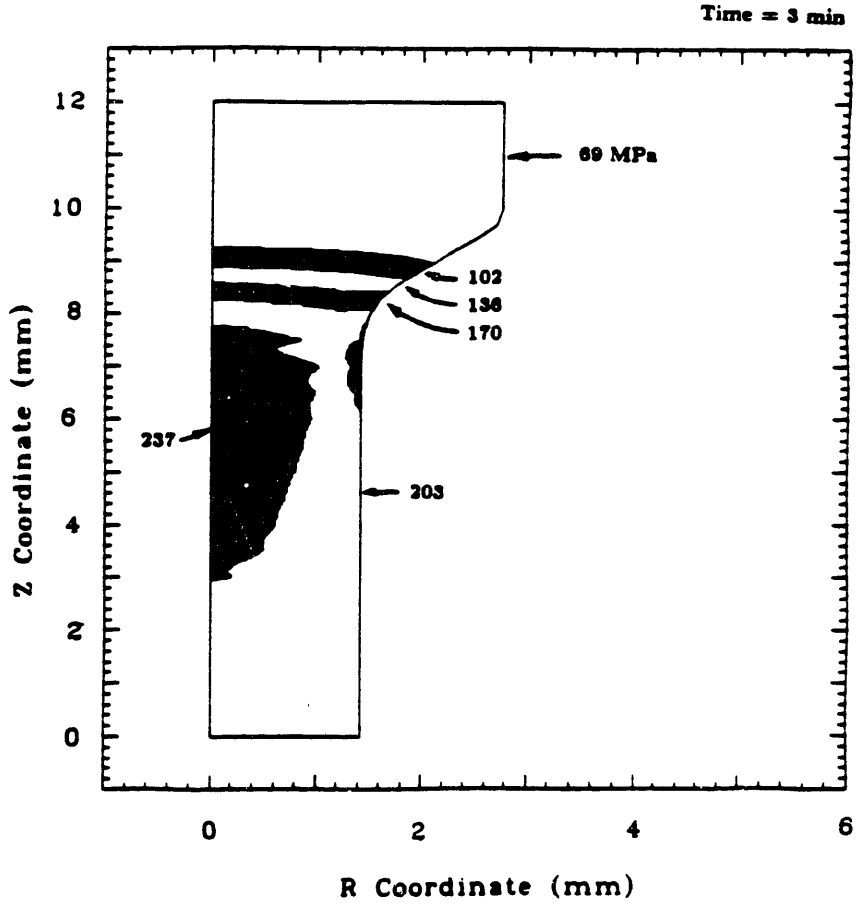

Fig. 4.21a
Deviatoric axial stress-strain hysteresis plot of 1st thermal cycle in uniform test specimen at Int. Pt. 1 (Fig. 4.16).

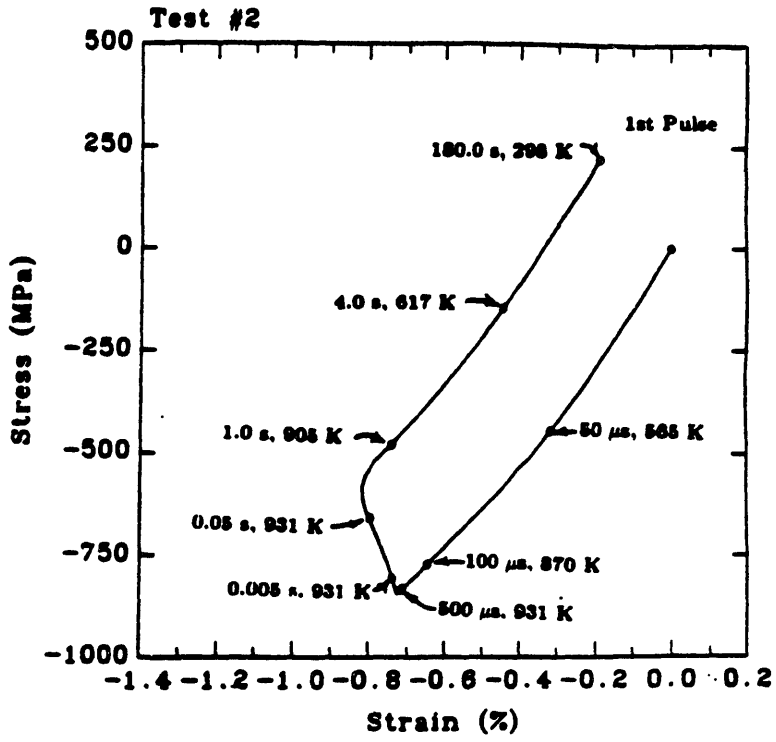

Fig. 4.21b
Deviatoric axial stress-strain hysteresis plot of 1st and 2nd thermal cycle in uniform test specimen.

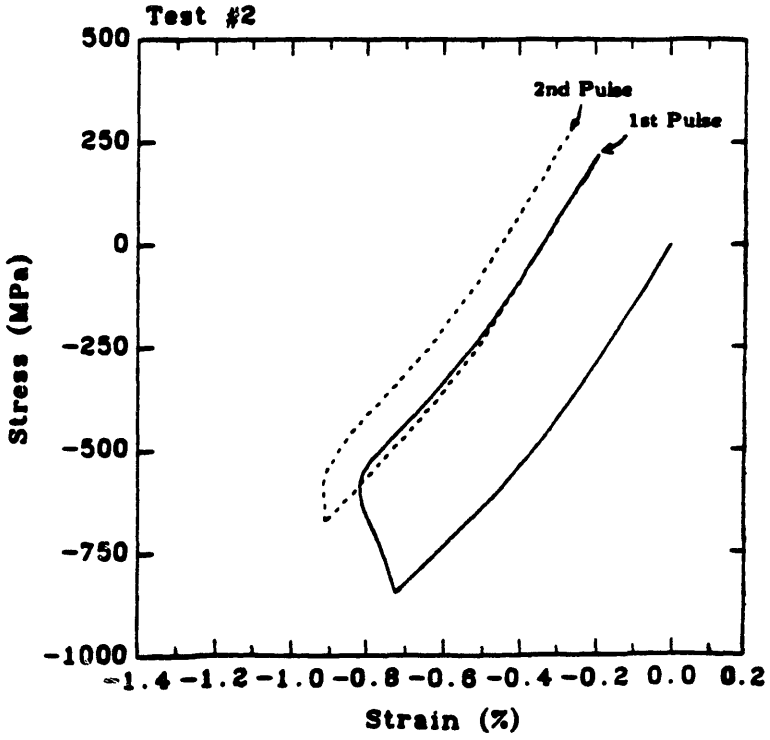

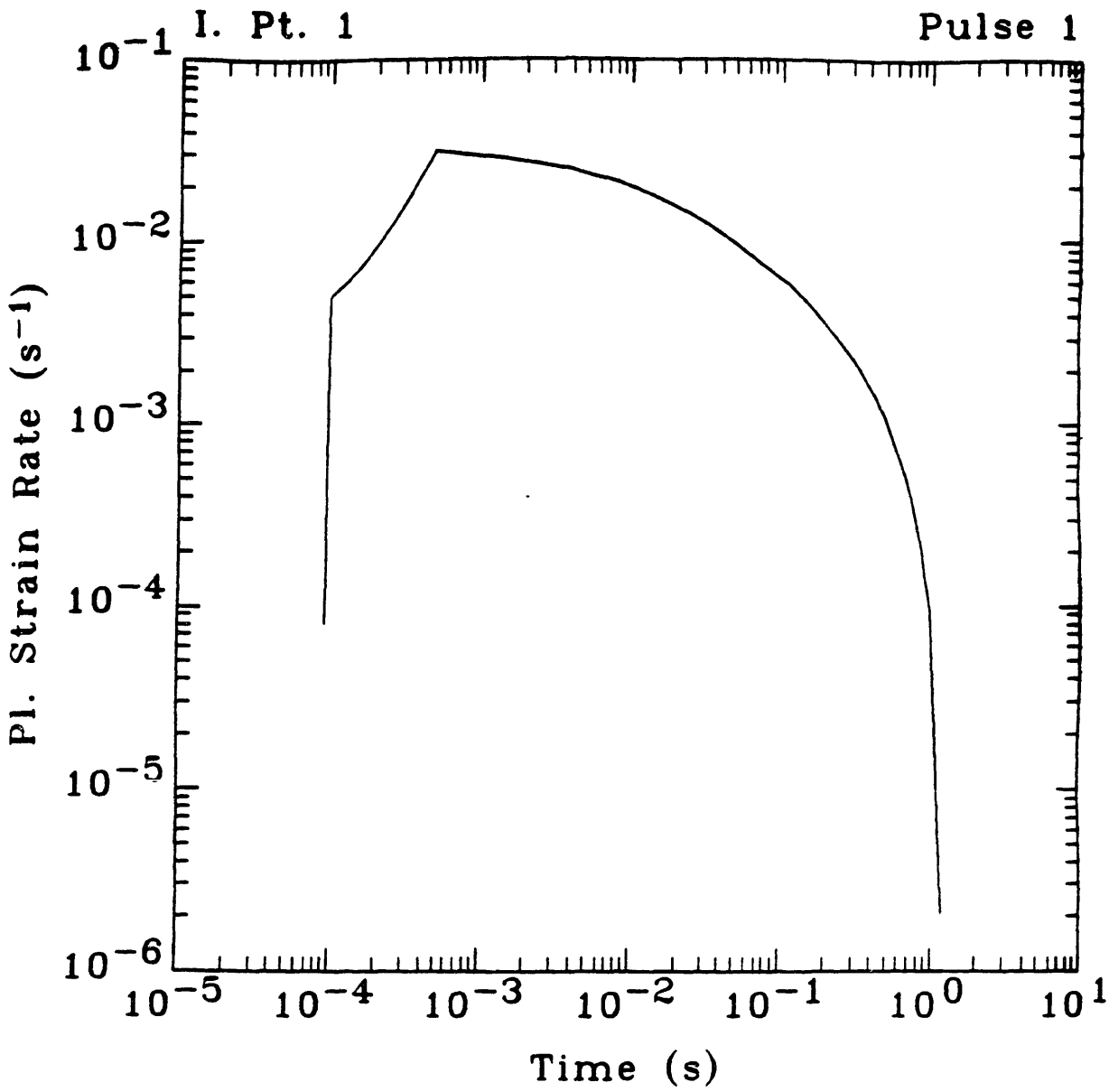

Fig. 4.22 Plastic strain rate versus time for the 1st integration point during the 1st pulse of the uniform test specimen.

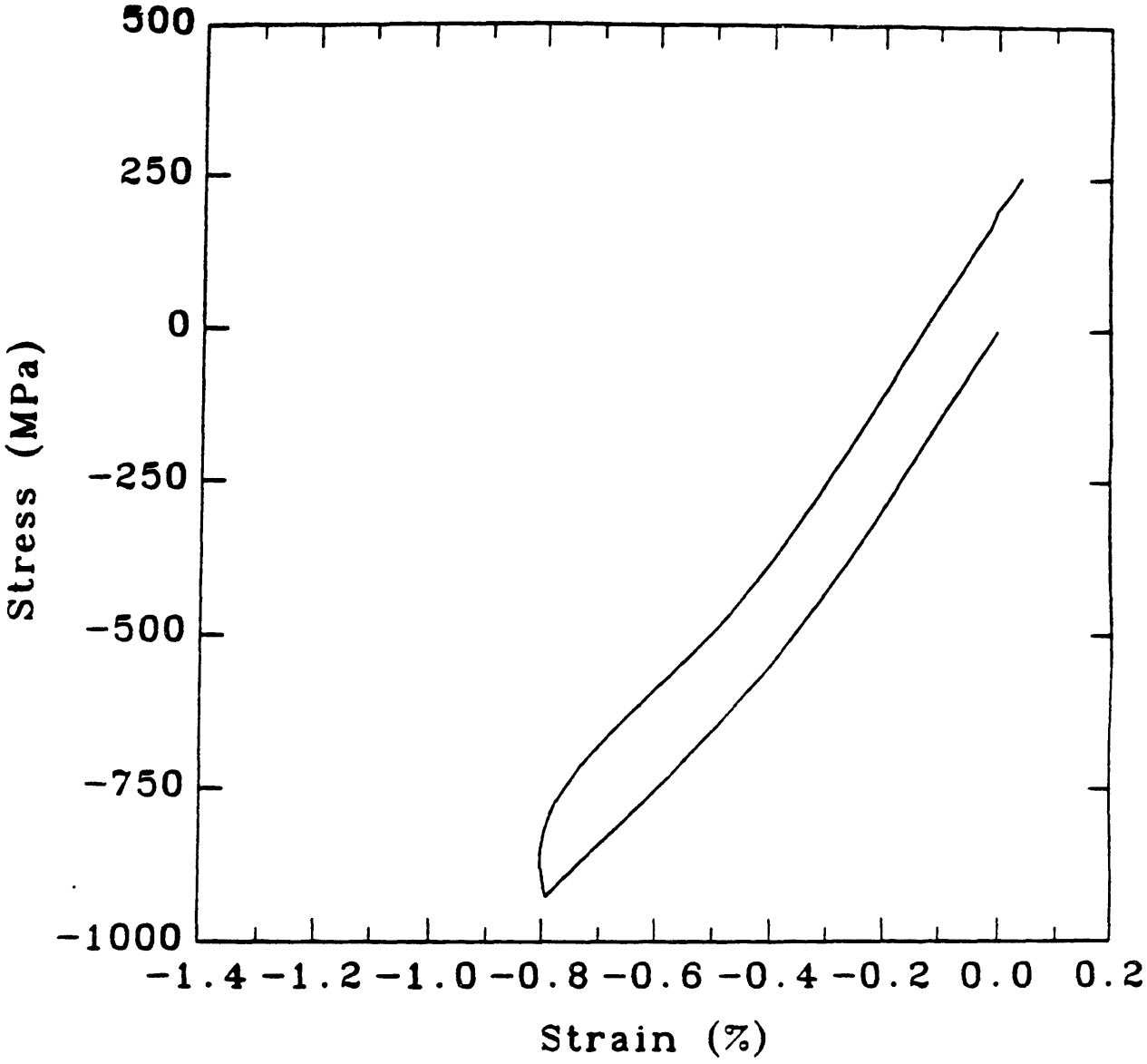

Fig. 4.23 Deviatoric axial stress-strain hysteresis plot at the 2nd integration point during the 1st pulse of the uniform test specimen.

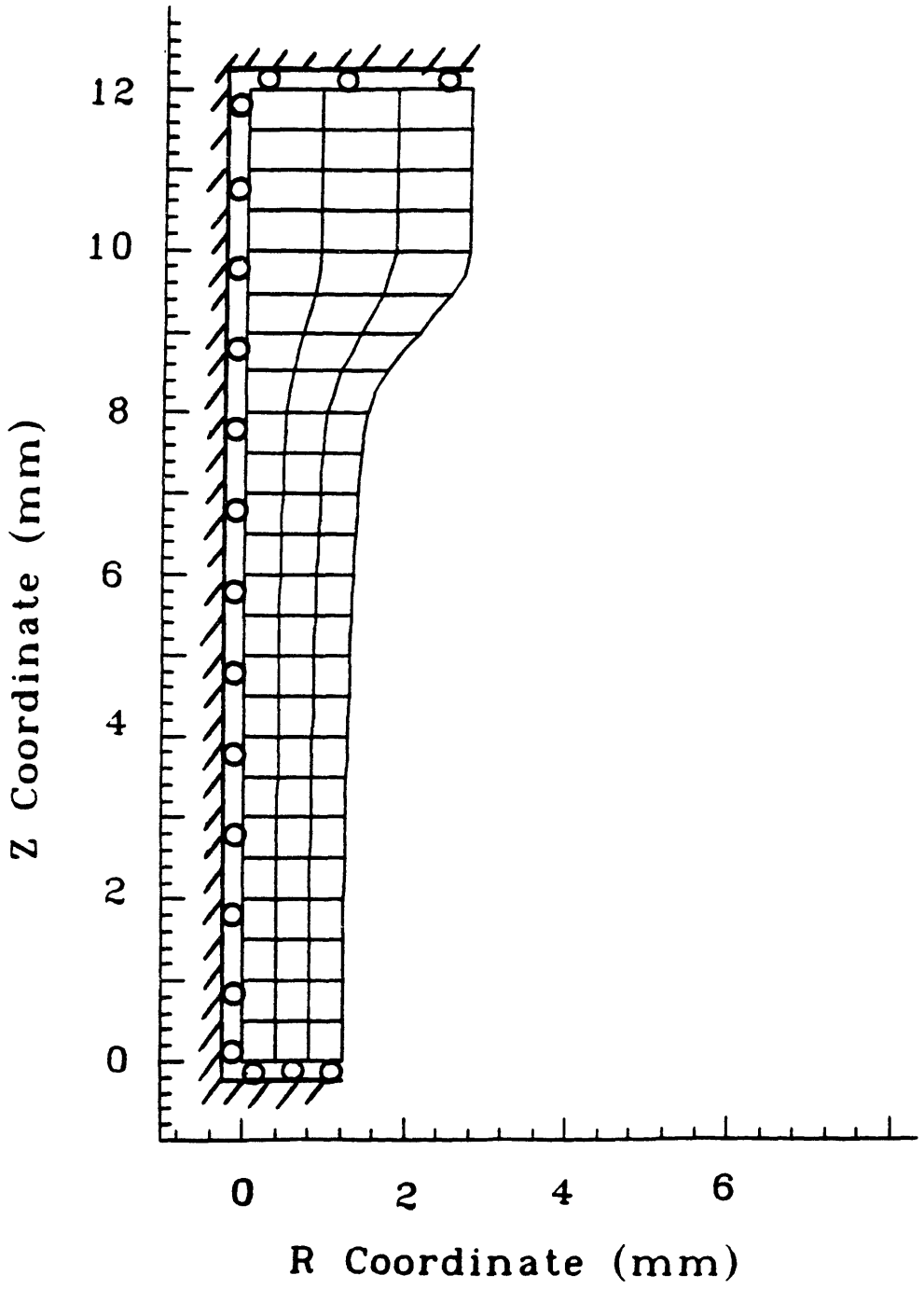

Fig. 4.24 Finite element model for tapered test specimen.

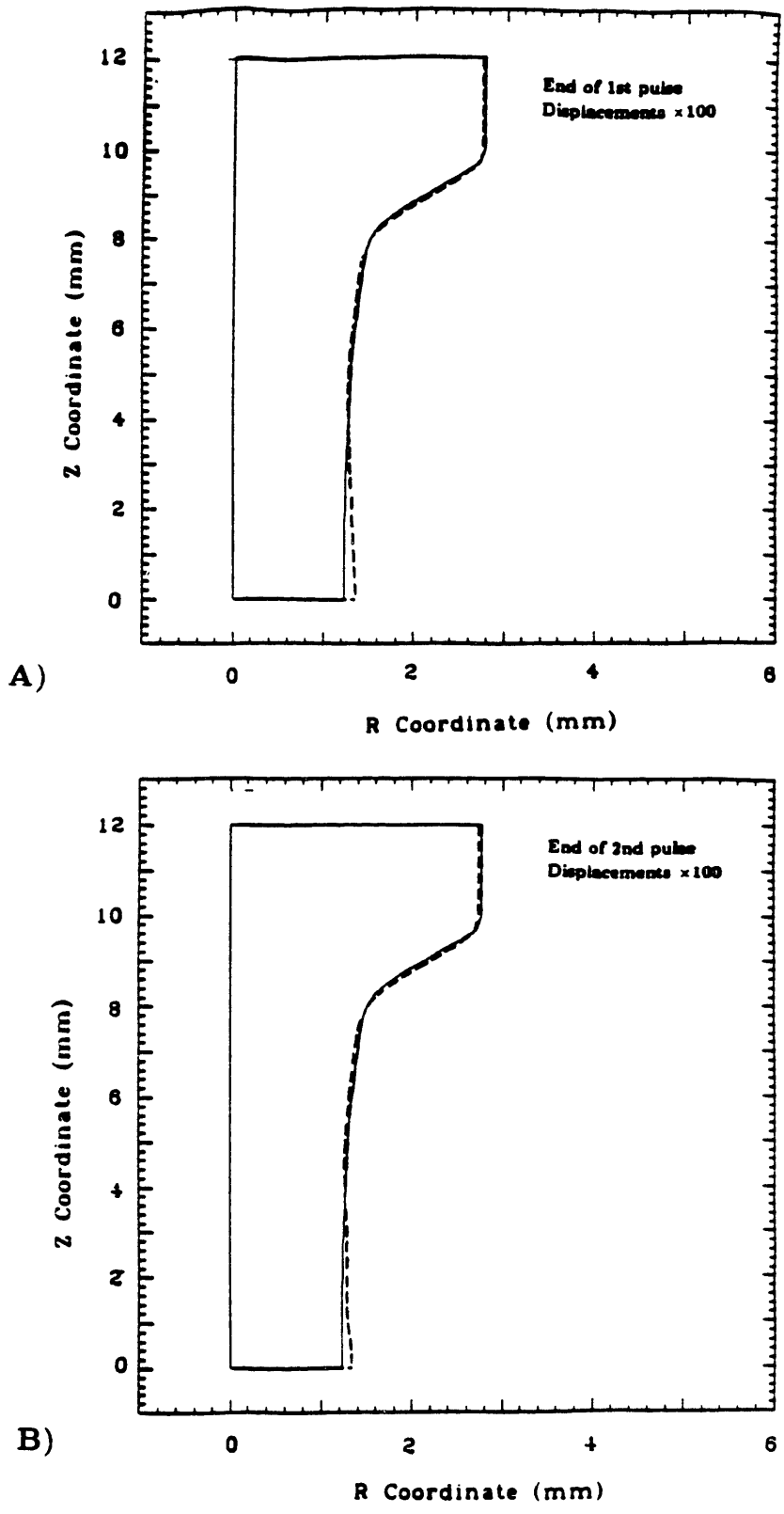

Fig. 4.25 Deformed mesh outlines for tapered test specimen.

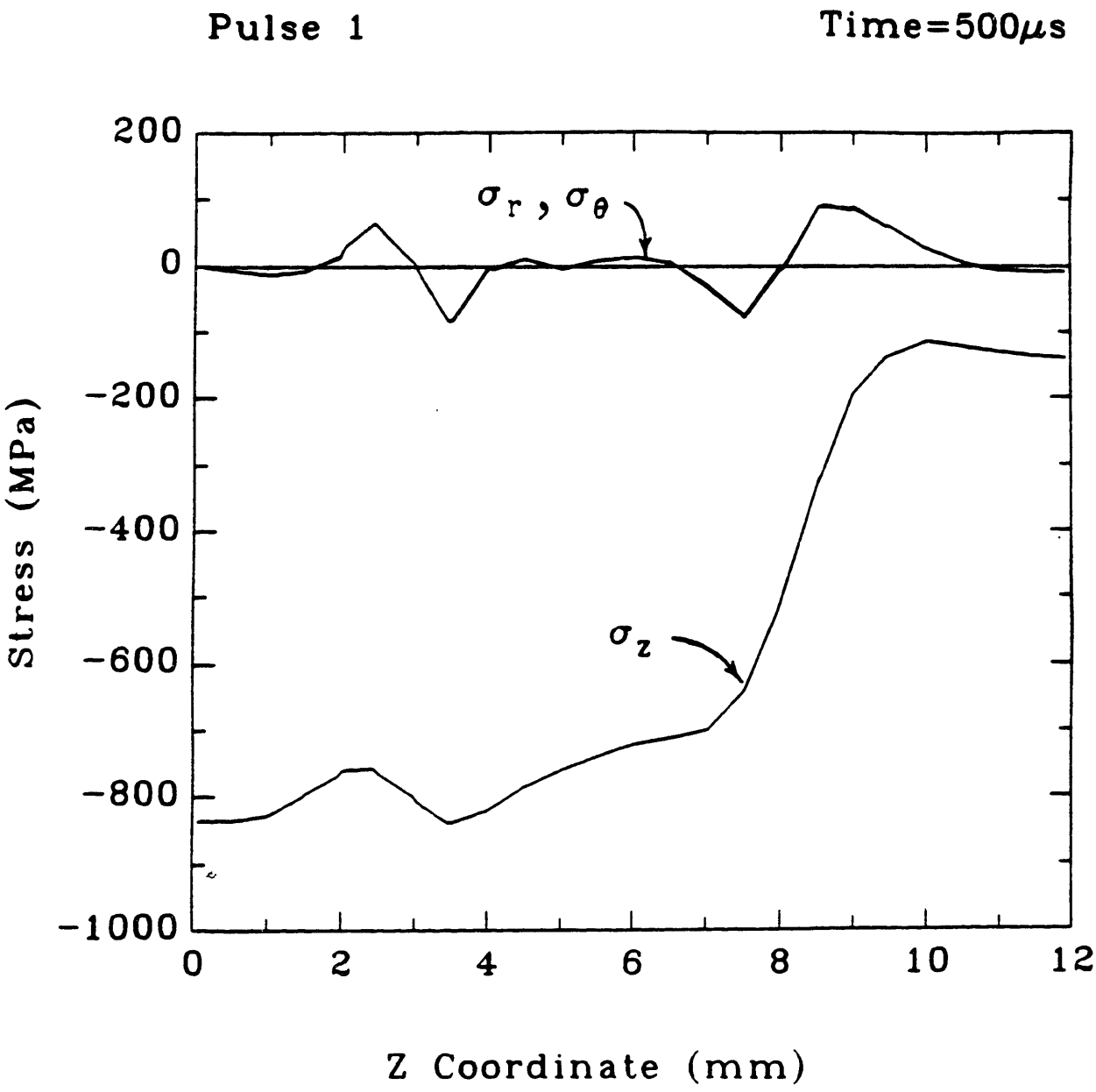

Fig. 4.26 **Radial, hoop and axial stress on the Z Axis of the tapered test specimen.**

Fig. 4.27a
Von Mises stress on the Z Axis of the tapered test specimen.

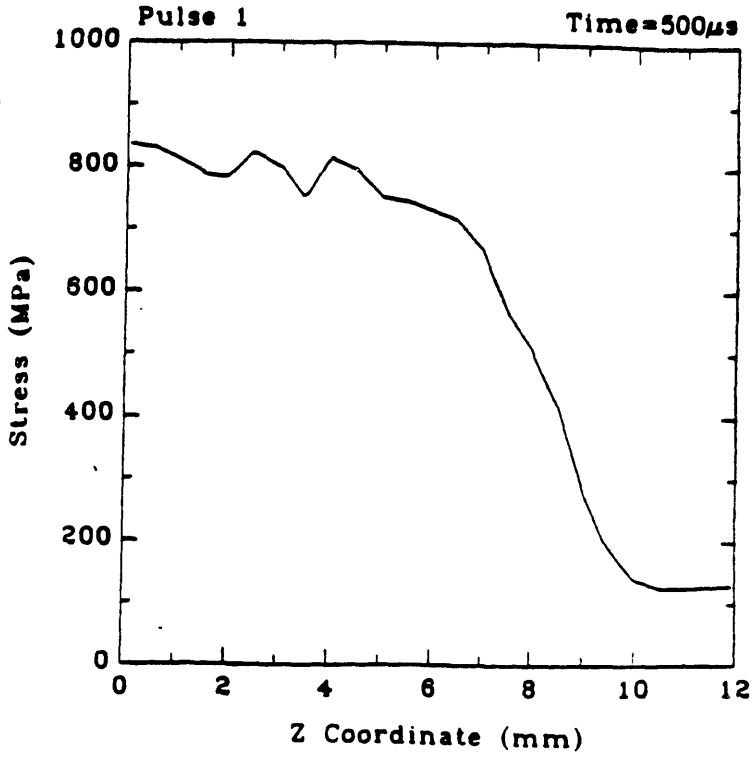

Fig. 4.27b
Von Misces stress contour bands in tapered test specimen.

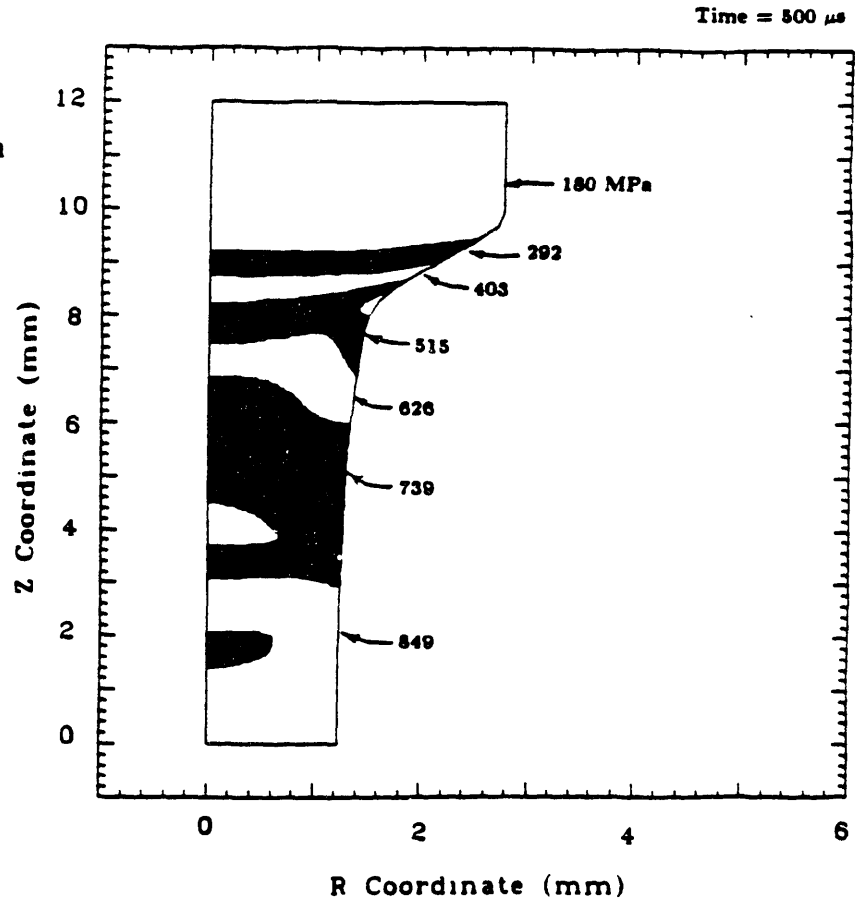

Fig. 4.28a
Von Mises stress on the Z Axis of the tapered test specimen.

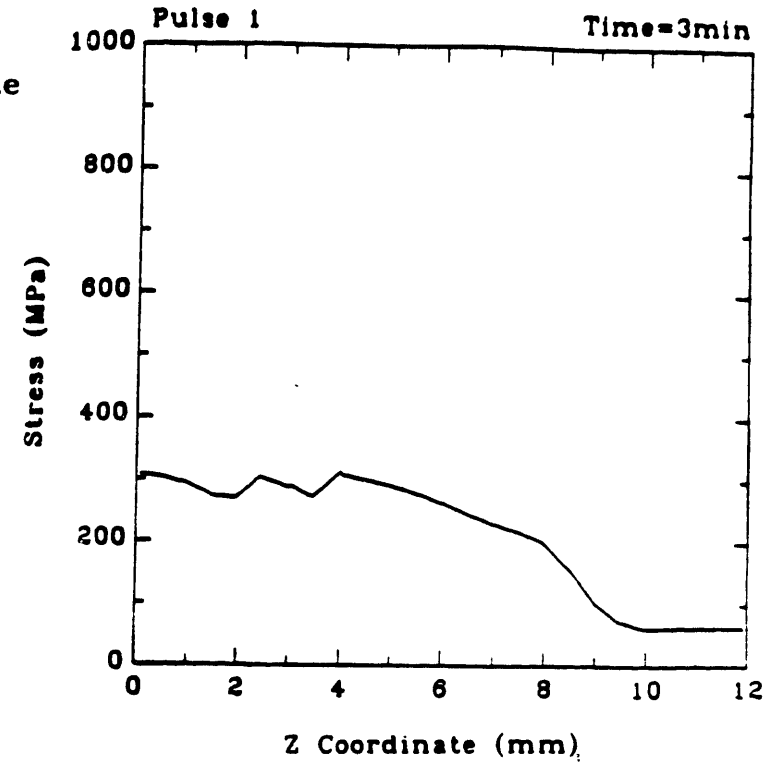

Fig. 4.28b
Von Mises stress contour bands in tapered test specimen.

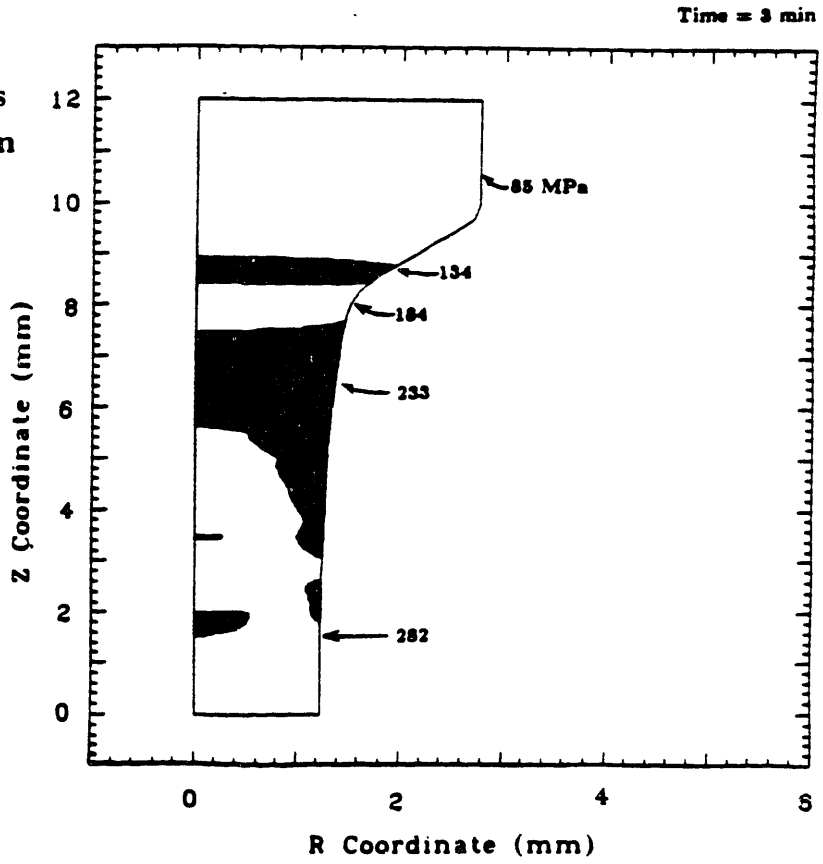

Fig. 4.29a
Deviatoric axial stress-strain hysteresis plot of 1st thermal cycle in tapered test specimen.

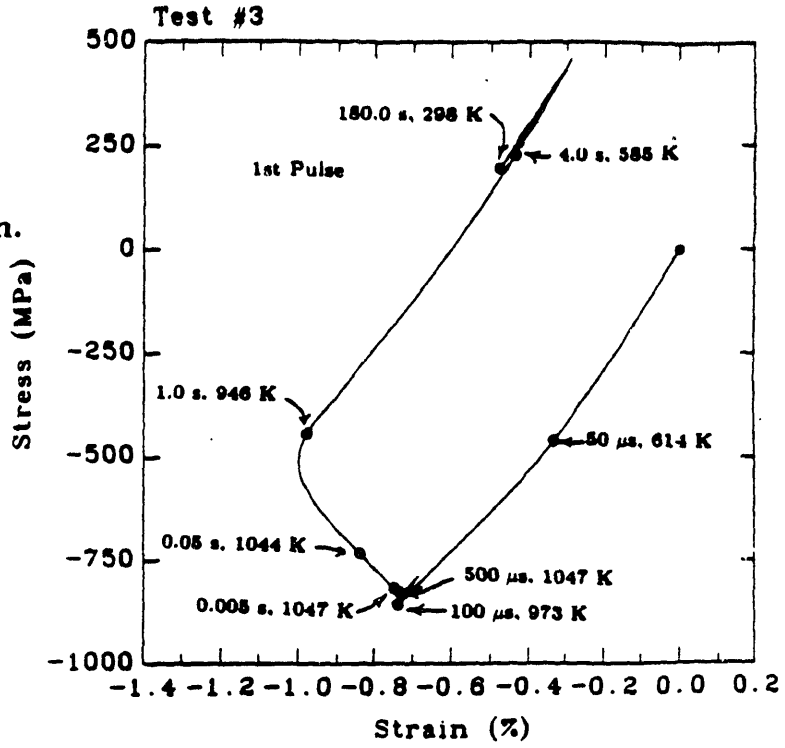

Fig. 4.29b
Deviatoric axial stress-strain hysteresis plot of 1st, 2nd and 3rd thermal cycle in tapered test specimen.

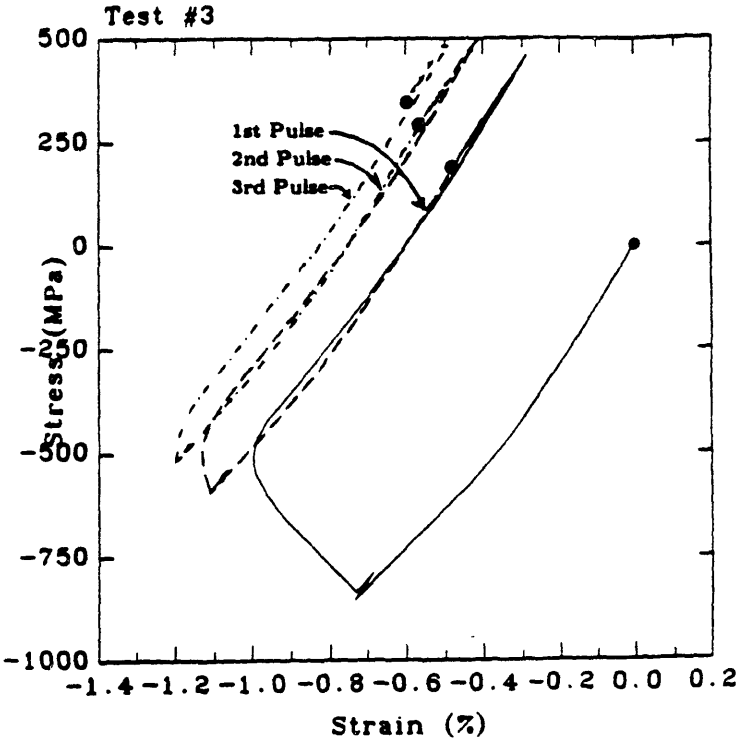

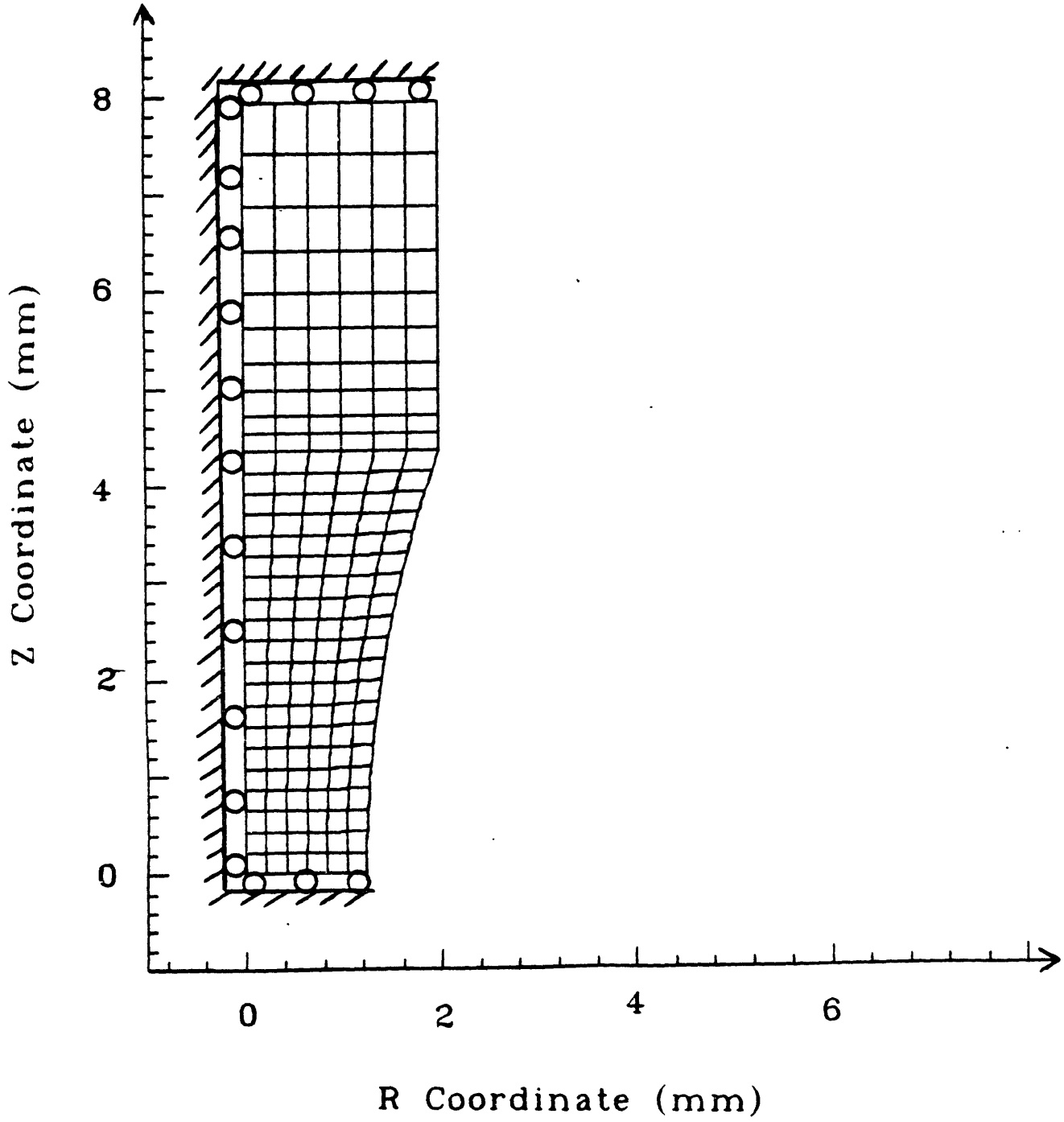

Fig. 4.30 Finite element model for hourglass test specimen.

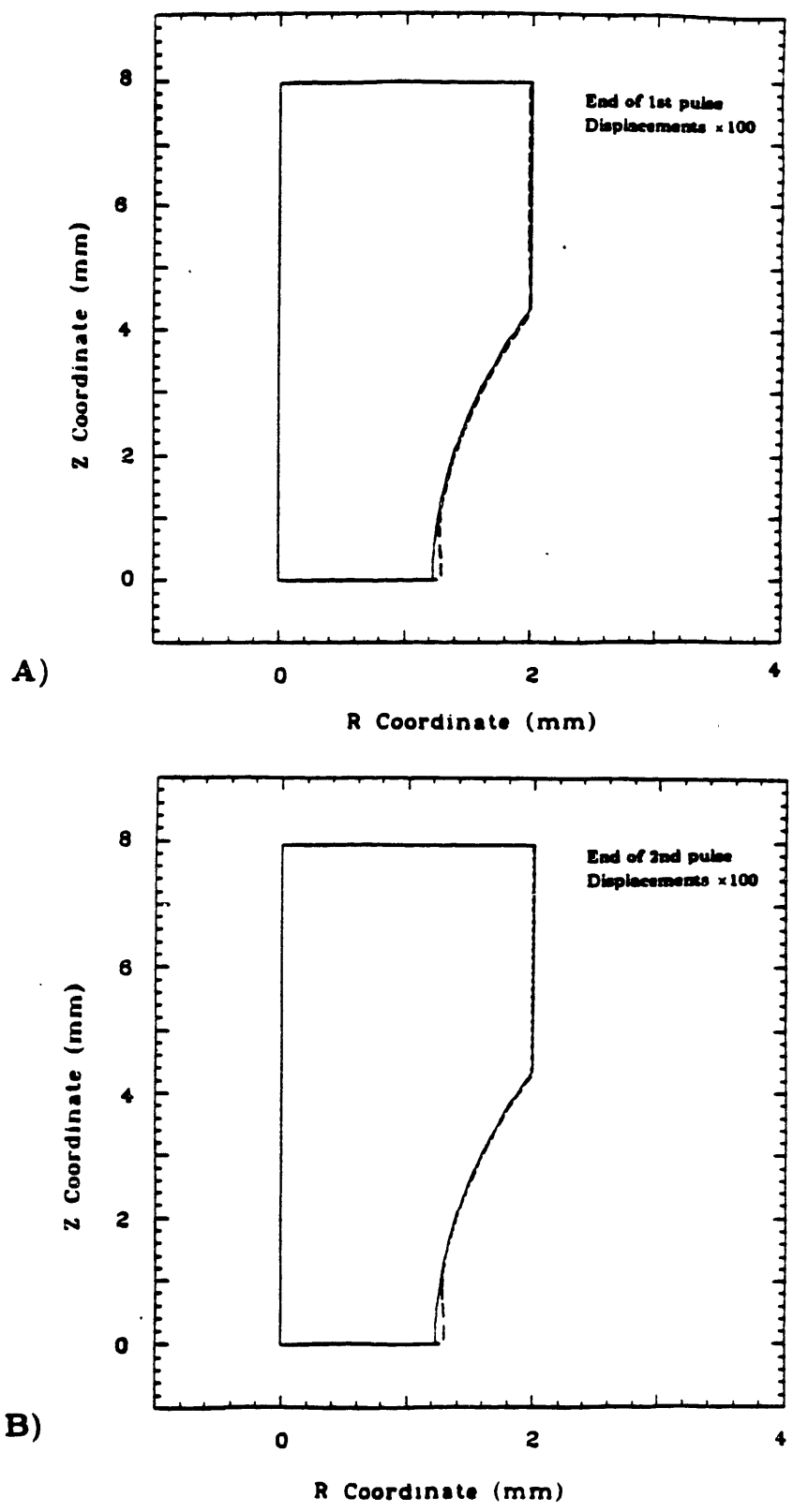

Fig. 4.31 Deformed mesh outlines for hourglass test specimen.

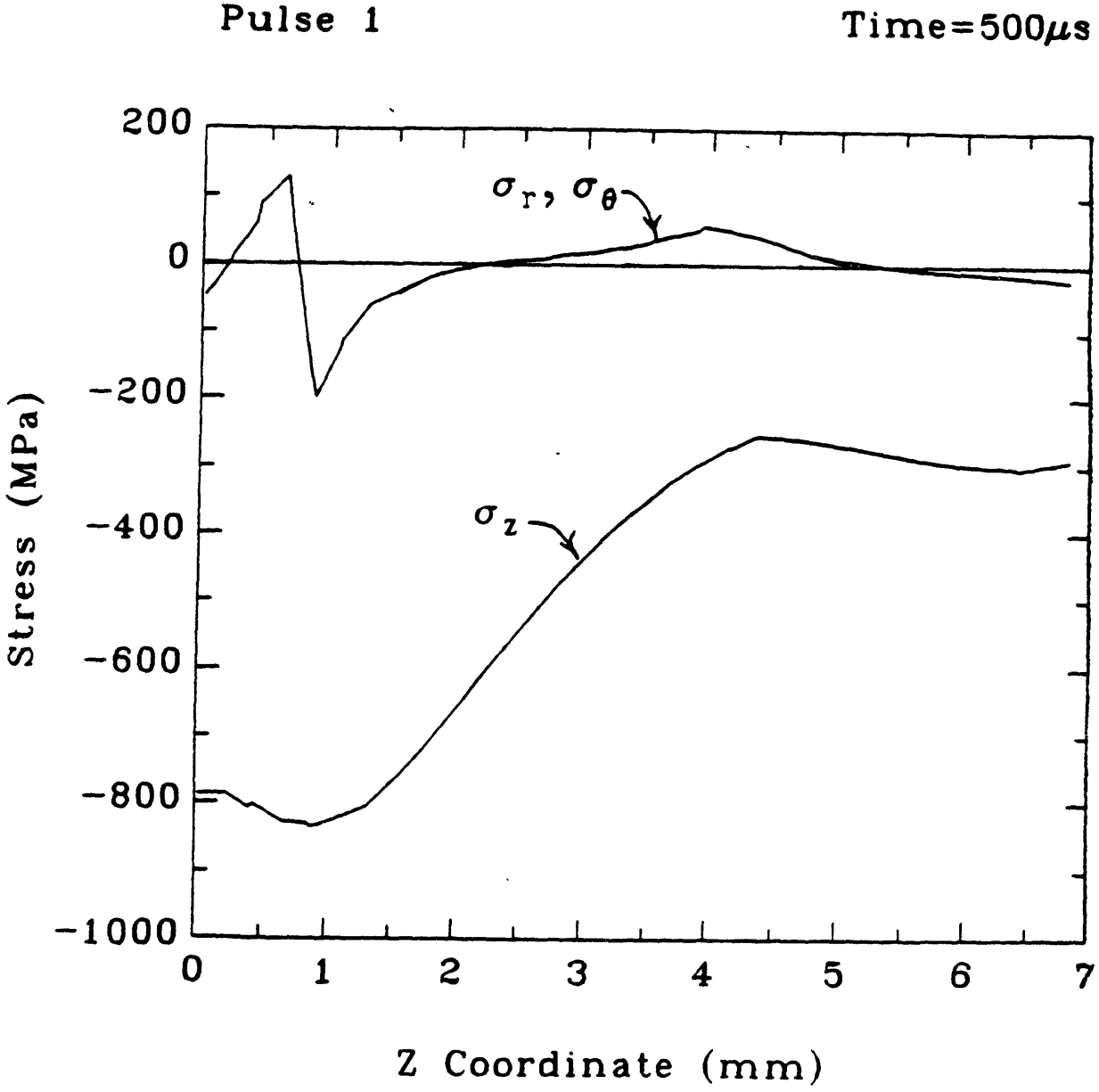

Fig. 4.32 **Radial, hoop and axial stress on the Z Axis of the hourglass test specimen.**

Fig. 4.33a

Von Mises stress on the Z Axis of the hourglass test specimen.

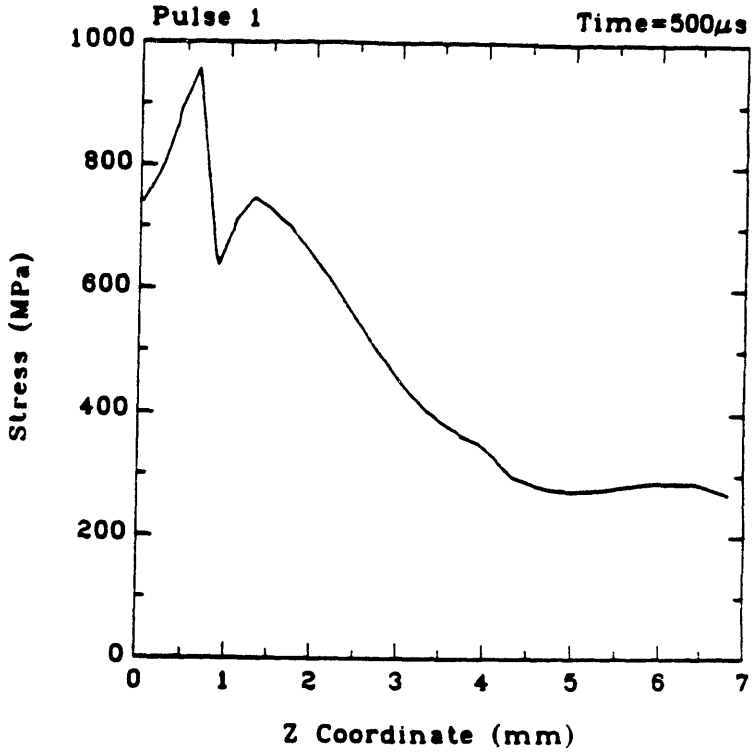

Fig. 4.33b

Von Mises stress contour bands in hourglass test specimen.

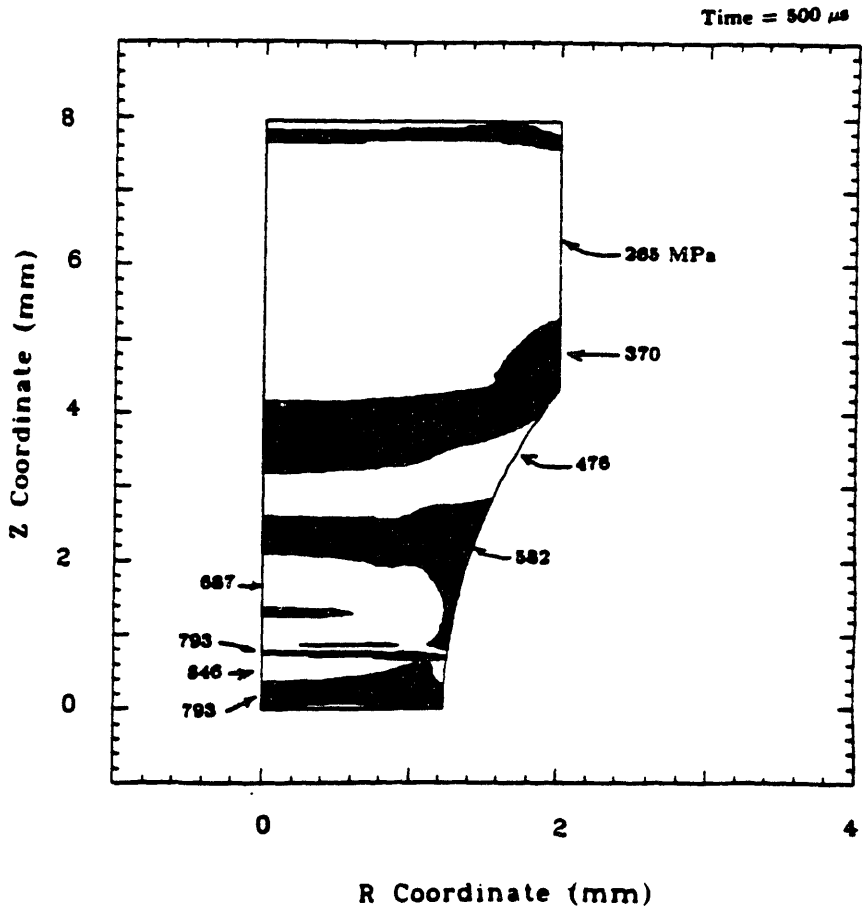

Fig. 4.34a
Von Mises stress on the Z Axis of the hourglass test specimen.

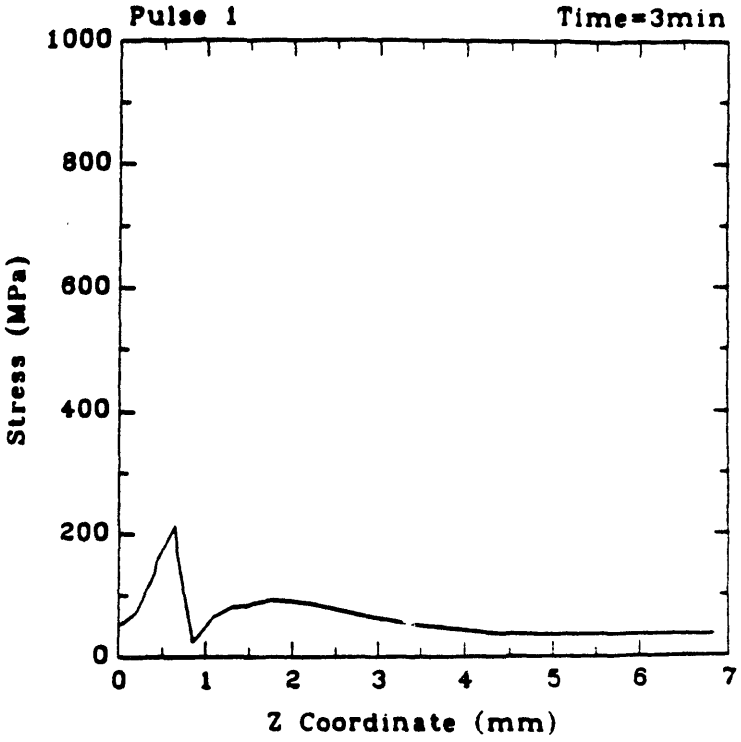

Fig. 4.34b
Von Misces stress contour bands in hourglass test specimen.

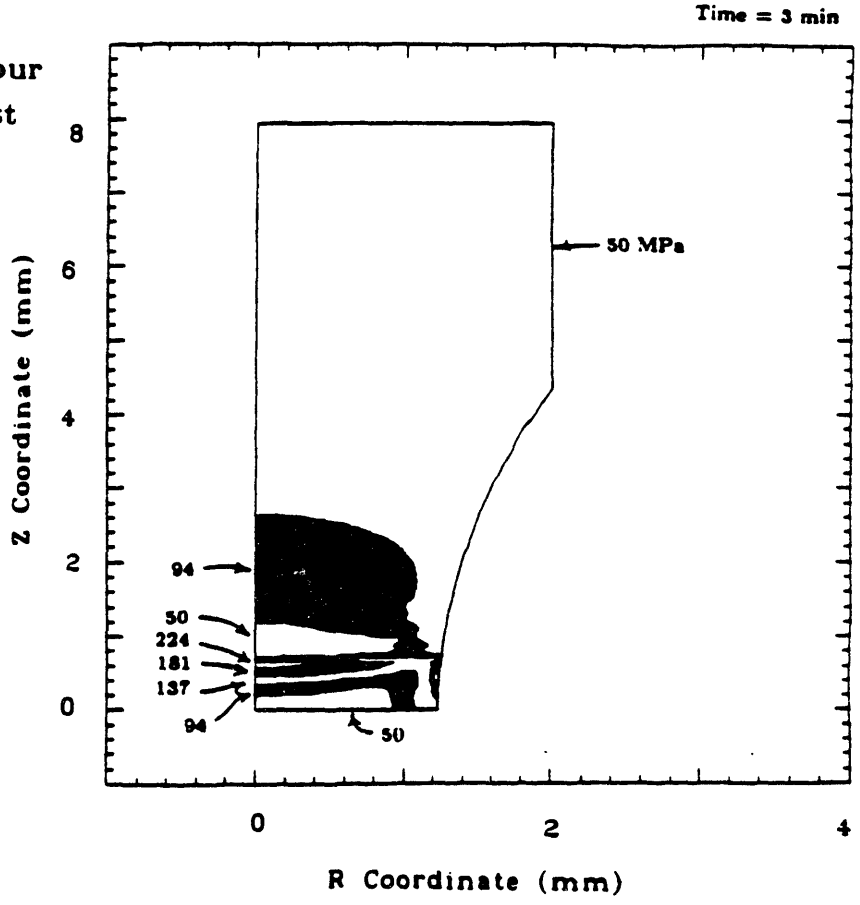

Fig. 4.35a
Deviatoric axial stress-strain hysteresis plot of 1st thermal cycle in hourglass test specimen.

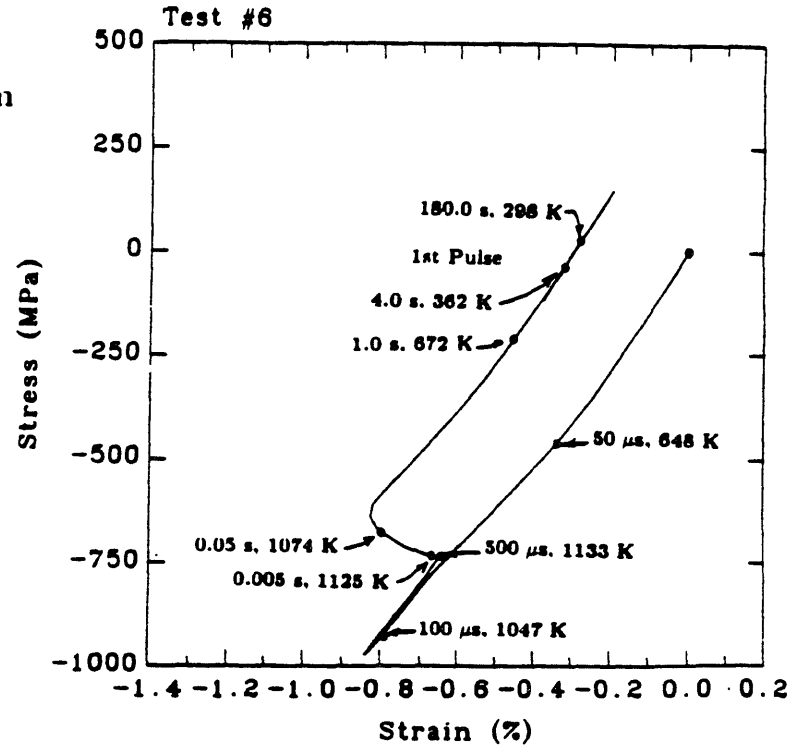

Fig. 4.35b
Deviatoric axial stress-strain hysteresis plot of 1st and 2nd thermal cycle in hourglass test specimen.

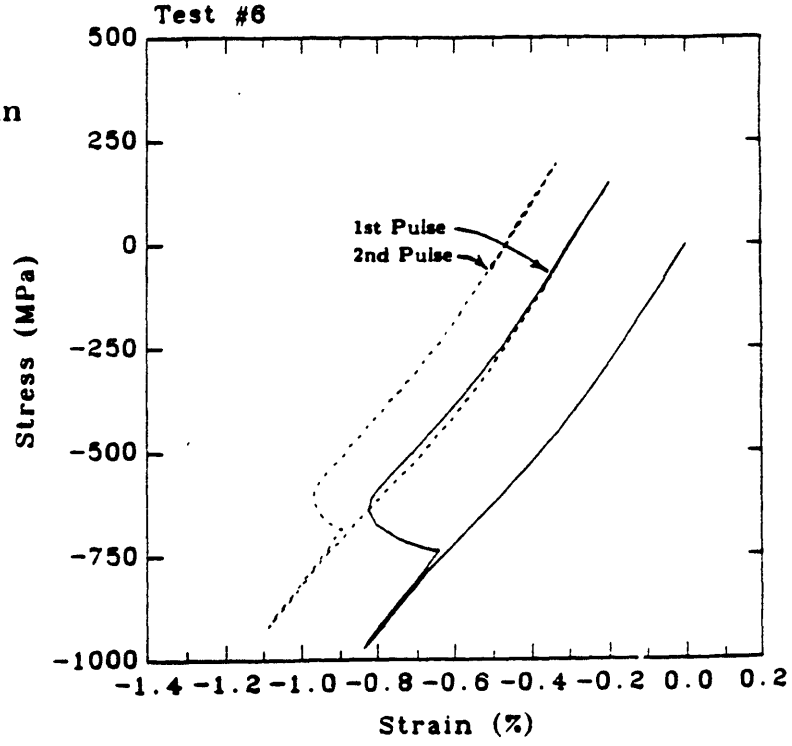

References

[1] D.A. Karlyn, "Capacitor - Discharge Pulse Heating," Transactions of the ASM, Vol. 62, 1969, pp. 288-291.

[2] R.D. Cook, *Concepts and Application of Finite Element Analysis*, 1981, John Wiley and Sons Inc., pg. 211.

[3] Sussman T. and Bathe K.J., "Studies of Finite Element Procedures - Stress Band Plots and the Evaluation of Finite Element Meshes," J. Engineering Computations, To Appear.

Chapter 5

Short Pulse Magnets

The purpose of research into the mechanical behavior of maraging steel is to predict the behavior of short pulse magnets built of that material. Initially, this Chapter discusses the motivations behind the use of maraging steel, describes the design parameters which affect short pulse magnet design and examines the equations which govern the electrical behavior. Then, the Chapter focuses on a short pulse, destructible test coil (DTC) which was designed, built and tested to failure for this research. This magnet provides important information about the number of pulses to failure, and the mode of short pulse magnet failure. Using the results of an electromagnetic and thermal analysis, a finite element analysis of the DTC is performed to determine its mechanical behavior. The material models developed for maraging steel developed in Chapter 2 are used in the mechanical analysis. From this work, the displacements, strains and stresses within the magnet are predicted for two pulses.

Short Pulse, High Magnetic Field Magnets

Short pulse, high magnetic field magnets are used around the world by scientists to generate large magnetic fields (> 50 T) in a non destructive way [1]-[3]. Steady state magnets do not (currently) generate magnetic fields in this regime because of power constraints. The strategy for short pulse magnets is to produce a large magnetic field in a short period of time. The energy requirements are reduced, and there are no requirements to remove the heat generated during the pulse. By using a pulse of electricity, it is possible to generate magnetic fields between 40 and 100 T. For fields greater than 100 T, electrical explosions in the magnet are common, destroying experiments and the magnet.

The impetus behind this work is the production of ever higher magnetic fields (above 50 T), for long times, in a safe manner. The pulses are short to minimize the heat generated during the pulse. The limiting design criteria for these magnets are their strength at elevated temperature versus electrical resistivity. The resistivity of maraging steel is about 32 times larger than the resistivity of copper, and its strength is approximately 5 times larger. By reducing the time available for heating, the superior strength properties of steel can be utilized. Steel was first used in a short pulse magnet by Simon Foner and Henry Kolm

[4] in 1957. Later, M. Date [5] used maraging steel to construct a short pulse magnet, and they have reportedly achieved peak magnetic fields of 70T with a multiple magnet combination.

In 1982 the Francis Bitter National Magnet Laboratory, with the support of the National Science Foundation, undertook the study of short pulse magnets with the goal of generating 50 T with a single magnet and then 70 T with a pair of concentric magnets. The first goal was realized in March 1985, and this has been reported in this author's master thesis [6] and in a paper published at the Megagauss Magnetic Field Production Conference [7]. The 50 T magnet was designed and built 3 years ago, and it has been pulsed over 20 times at full field. This magnet is called the 50T coil for the remainder of this paper.

Maraging steel was chosen for this application because of its high strength and its machinability prior to aging. Constructing the helical shape of the short pulse magnet requires extensive machining ($\approx$ 100 hr), and this is performed in the unaged condition. In a short pulse magnet, maraging steel experiences magnetic and thermal loads which cause plastic deformation. The selection of this steel by M. Date was made on the basis of its room temperature strength. When this work began, the material behavior of maraging steel under extreme thermal and electromagnetic conditions was not known. Thus, this thesis also examines the suitability of maraging steel as a magnet material.

Although the DTC and 50T coil are both capable of generating a peak magnetic field of 50 T, they are different in most other aspects. The 50T coil is designed with safety as a major concern. The build of a magnet is the difference between the outer radius and the inner radius and a build is considered large when the ratio of build to skin depth (see Eq. 4.2) is greater than 5 (the skin depth for both these coils is 6 mm). The 50T magnet has a large build 46 mm, and its peak temperature (1300K) is minimized for the given design field and capacitor bank. The purpose of the DTC on the other hand is to learn how these magnets fail, and to determine if the methods being employed in the design of these magnets are valid. The DTC has a small build (15 mm), and the peak temperatures are 150 K higher than those in the 50T coil. The 50T coil has an expected life of approximately 1-2000 pulses, while the expected life for the DTC was less than 200 pulses.

Magnet Design

The three design specifications which most affect the design of a short pulse magnet are its peak magnetic field, the peak temperature, and the build of the magnet. The build affects the stress levels, magnet temperature, and clearance for multiple magnet systems. The variables which most affect the peak magnetic field and temperature in descending importance are the charging energy (voltage, limited by the capacitor bank), the inner radius, the turn thickness and the number of turns. Several computer codes are used in the design and analyses of short pulse magnets. These codes analyze various magnet designs and are used to determine the optimum coil geometry. From this work, several important insights into the art of magnet design have been learned.

The inner radius of a pulse magnet has the biggest effect on the peak magnetic field and temperatures. The peak magnetic field is measured at the center of the magnet bore. For uniform current density solenoids, the peak magnetic field is proportional to the inverse of the inner radius. A similar relationship holds for the short pulse magnet. In addition, decreasing the inner radius increases the current density gradients. The coil temperatures depend on the integral of the current density squared, so as the inner radius decreases, the peak temperatures increase.

The turn thickness and number of turns affect the peak magnetic field and temperatures in a more complex manner. For a fixed interspace distance between the magnet turns, a constant peak current, and a fixed pulse length, the following relationships hold. Increasing the turn thickness decreases the current density which lowers the magnetic field, and increases the spacing factor (ratio of active conductor section to the total magnet section) which increases the magnetic field. Increasing the turn thickness lowers the electrical resistance. Increasing the number of coil turns increases the magnetic field and the electrical resistance. The magnet temperatures depend on the current densities, so anything that raises the current densities raises the coil temperatures. Thus, the turn thickness and the number of coil turns are varied to maximize the peak magnetic field and minimize the peak temperature. For more information on magnet design see [8].

In general, as the build of a magnet increases, it is likely to be a safer magnet, and its lifetime increases. This is because a larger build lowers the effective stress level in the magnet during its operation, and a larger build also

gives the magnet a larger thermal mass. The first point is seen from the fact that when the build of a magnet exceeds the skin depth, there is material not loaded by Lorentz body forces which can support material being loaded in the skin depth region. The second point means that after the electrical pulse when the temperature distribution is nearly uniform, the mean temperature in the magnetic is smaller for larger builds. Safety in this context means that a magnet failure results in less damage to experiments and equipment near the magnet.

When a magnet fails during a pulse, the principal point to consider is the electrical consequence of the failure. Very large currents are passing through the magnet (300 kA), and a continuous path of electrical conduction is maintained during the failure. When a magnet fails, and there is a loss of structural integrity, the regions most affected are at or near the inside radius. This corresponds to the region through which most of the current is flowing. It is highly unlikely, if not impossible for a magnet failure to interrupt these currents. Thus, a potentially large electrical explosion can occur when 250 kJ of energy are discharged through the magnet. The build of the magnet must contain any failure occurring at or near the inner radius of its turns. If the electrical explosion is not confined by the build of the magnet, flying shrapnel could cause serious damage to the surroundings.

The specifications for the 50T coil are summarized in Table 5.1. The 50T coil generates 50 T of peak field in a 34 mm bore with a coil build of 48 mm, and it requires the entire stored energy of the capacitor bank 273 kJ. This magnet reaches a peak temperature of 1300 K and cools to a post-pulse temperature of 413 K (t = 300 μs). Likewise, the specifications for the destructible test coil are given in Table 5.2. This coil is pictured in Fig. 5.1. The DTC generates 50 T of peak field in a 18.5 mm bore, and it requires just 93 kJ of capacitor bank energy. The magnet build is 15 mm and the turn thickness is 4.6 mm. The destructible test coil heats to a peak temperature of 1460 K and cools to an immediate post-pulse temperature of 690 K.

Magnet Construction

A brief description of the magnet assembly is necessary here to introduce some terminology and concepts to this discussion. Fig. 5.2a shows the DTC magnet assembly. Two layers of 1/16 inch thick G-7 insulation are inserted between the turns of the magnet to prevent electrical arcing. The magnet is

bolted to two large brass conductor plates. Attached to the brass conductor plates are rings of G-10 insulation. An oak safety ring slides over both G-10 rings, and should a catastrophic failure occur, the oak ring will slow any shrapnel. The magnet assembly is surrounded with 6 threaded A-286 steel tie rods which compress the magnet, reducing coil movement during a pulse. Using a torque wrench, it is possible to apply up to 70 tons of compression on the magnet assembly. The G-10 plates insulate the steel plates from the brass conductor plates. Coaxial cables from the capacitor bank are attached to both brass conductor plates, closing the electrical circuit.

The construction methods for the 50T and the destructible coil magnets are similar. The coils are cut from round billets of maraging steel. The cutter for the 50T coil is an 8 inch diameter, 1/8 inch thick high speed steel circular saw blade. The cutter for the destructible test coil is a 4 inch diameter, 1/16 thick abrasive circular blade. In both cases, the cutter rotates about a stationary axis. The steel billet is rotated and moved along its Z axis. The saws cut a helical groove into the billet. Up to 10 passes of the cutter are necessary to cut a groove deep enough to exceed the build of the magnet. The beginning and the end of the magnet turns are cut with an EDM (Electrode Discharge Machining) electrode. Next, the center of the billet is bored out to the inner radius dimension.

One unfortunate consequence of using a circular saw to cut the helical magnet is the resulting shape of the magnet turn cross section. Fig. 5.3 shows the turn cross section which results from machining the DTC coil. This profile damages the electrical insulation which separates the turns [7]. During a pulse, the combined thermal expansion and axial Lorentz forces cause adjacent coil turns to pinch the insulation which separates them. The corners of previous coil turns (the 50T coil) are rounded with sandpaper, but this does not prevent the turns from damaging the insulation. One of the design goals for the DTC is a turn profile which does not cut into the insulation. Therefore, the DTC coil turn shape was altered with a hand grinder. Fig 5.3 shows a before and after cross section of the DTC turn. The purpose of this alteration is to reduce the turn thickness at the inner radius 15 % from 4.6 to 3.9 mm, thereby separating the G-7 insulation from the magnet. After grinding, the surface is smoothed with a 640 grit sandpaper. The small build of the DTC makes this manufacturing step feasible.

The heat treatment for both coils is the same. Spacers are inserted between the turns, and the coil is compressed in a holding fixture. The magnet and holding fixture are placed in a dewar, and the dewar is placed into a furnace. A nitrogen atmosphere is introduced into the dewar and the entire assembly is heated to 755 K. After 4 hr, the doors to the furnace are opened and the dewar is air cooled. Except for the longer cooling times (1 hr versus 15 min), this is the same heat treatment described in Chapters 1 and 2.

Electromagnetic Analysis

The purpose of an electromagnetic analysis is to determine the current densities, temperatures, magnetic fields and Lorentz body forces within the short pulse magnet as a function of time and position. The most important unknown in this analysis is the current density distribution, since it defines the magnetic field and the heat generation within the magnet. The magnetic field distribution is calculated with the program SOLDESIGN, written by R.J. Pillsbury. Based upon input current densities, SOLDESIGN calculates the magnetic field vector for specified points. The Lorentz body forces are found by calculating the cross product of the current density vector with the magnetic field vector.

The current density distributions for the short pulse magnet are determined using a nonlinear numerical integration of the electrical circuit equations. Previous modeling of the discharge of electricity into the short pulse magnet either relied on skin depth assumptions, or was restricted to the first half period of the electromagnetic pulse [6]. The method described here does not have these restrictions, and its predictions of current and magnetic field versus time agree with experimental results to within 7 %. Indeed, this method is used to solve more complicated multiple magnet, short pulse analyses.

The electromagnetic analysis is a part of a larger program called MESPA, which stands for Mechanical, Electromagnetic Short Pulse Analysis. The program MESPA calculates the current density profiles, uses SOLDESIGN to find the magnetic fields, calculates the radial body force and temperature distribution and then performs an elastic structural analysis for the short pulse magnet(s). The elastic analysis is not valid for the range of temperatures and body forces being considered here, so this portion of MESPA is not described. MESPA provides the body force and temperature information for the finite element analysis.

A program listing of MESPA is kept at the Francis Bitter National Magnet Laboratory.

The Model

For a solid helix, each turn occupies the entire build of the magnet and is a single conductor. Thus, the turns of a solid helix can be stacked up on top of one another (Fig. 5.4). The voltage along a radius of a solid helix coil is constant and the current density J varies in the radial direction only.

In the program MESPA, the short pulse magnet is divided into parallel, helical sub-coils (magnets), and then each of these sub-coils is assumed to consist of n stacked turns. A single electrical conductor can be replaced by a system of conductors, so long as the overall electrical characteristics (resistance, inductance and capacitance) remain constant. The model shown in Fig. 5.5 replaces the single solid turn of the helical conductor with 3 parallel sub-coils. The next assumption for this model states that the current density within each sub-coil is constant and does not vary along its length. Thus, a nonlinear current density distribution is approximated with numerous constant-current sub-coils (30 sub-coils are used in the DTC analysis).

Governing Electrical Equation

The governing electrical equation for this problem is the the standard RLC circuit equation. However, the system inductance L and resistance R are variable. The inductance of a short pulse magnet is a function of the current path geometry. The current diffuses into the solid helix from the inner radius, and this penetration is a function of temperature, time and position (a radial component of current density is not necessary for radial diffusion, because the inductances of the sub-coils and the rate of current change within the sub-coils create voltage potentials for current flow in adjacent sub-coils). The electrical resistance of a magnet is a function of the current and temperature distributions. C is the capacitance of the capacitor bank described in Chapter 4. The initial conditions for this problem are given in Eqs. 5.2 and 5.3. The capacitor is

charged to an initial voltage V_0 at time τ_0, and then the capacitor bank is discharged.

$$L\frac{\partial I}{\partial t} + RI + \frac{1}{C}\int_{\tau_0}^{\tau} I\ dt = 0 \tag{5.1}$$

$$I\Big|_{\tau_0} = 0 \tag{5.2}$$

$$\frac{1}{C}\int_{0}^{\tau_0} I\ dt = V_0 \tag{5.3}$$

The governing equation must be modified and expanded to represent the governing equations for the sub-coil in the model. This modification is best demonstrated by considering an example divided into 3 rather than 30 sub-coils and deriving the governing equations. The short pulse coil is divided into 3 parallel sub-coils. Fig. 5.6 is the electrical circuit for this system. The magnet inductance is defined with a 3 by 3 inductance matrix $[L]$, and each sub-coil has its own resistance which is stored on the diagonal of a 3 by 3 resistance matrix $[R]$. The inductance matrix is calculated by the program SOLDESIGN, and the resistance matrix is calculated directly from the electrical resistivity and the conductor geometry. In addition to the magnet variables, there is a constant system inductance L_c of 0.47 μh, and a constant system resistance R_c of 9.7 mΩ.

Examining the voltage potentials of the model gives two sets of simultaneous equations. The first set of equations describes the voltage across each sub-coil, and they all equal V'. For this problem, there are three current variables, one for each sub-coil. I^T is the total current flowing through the magnet and capacitor bank, and it is equal to the sum of the sub-coil currents.

$$\begin{bmatrix} L_{11} & L_{12} & L_{13} \\ L_{21} & L_{22} & L_{23} \\ L_{31} & L_{32} & L_{33} \end{bmatrix} \frac{d}{dt} \begin{bmatrix} I_1 \\ I_2 \\ I_3 \end{bmatrix} + \begin{bmatrix} R_1 & 0 & 0 \\ 0 & R_2 & 0 \\ 0 & 0 & R_3 \end{bmatrix} \begin{bmatrix} I_1 \\ I_2 \\ I_3 \end{bmatrix} = V' \begin{bmatrix} 1 \\ 1 \\ 1 \end{bmatrix} \tag{5.4}$$

where

$$V' = V - R_c I^T - L_c \frac{dI^T}{dt} \tag{5.5}$$

The next equation describes the voltage V across the capacitor bank, and there is only one equation for this single magnet system.

$$\frac{dV}{dt} = \frac{-I^T}{C} \tag{5.6}$$

It is helpful to rewrite Eq. 5.4 in matrix notation, so the convention of brackets is adopted to designate matrix variables. The currents flowing through the sub-coils are described with a column matrix $[I]$. The variable [1] is a column vector of 1's. Using this notation, Eq. 5.4 is re-written as

$$[L]\frac{d[I]}{dt} + [R][I] = V'[1] \quad . \tag{5.7}$$

The $[R]$ matrix employed in this problem is a function of temperature. Each sub-coil has its own temperature, so during a pulse, the electrical resistivity changes as ohmic heat generation raises the sub-coil temperatures. The $[L]$ matrix is a function of geometry and is constant for all the sub-coils. The system inductance L_s is a function of $[L]$ and $[I]$, so it changes during the pulse.

$$L_s = \frac{[I]^T[L][I]}{(I^T)^2} \tag{5.8}$$

Mechanical displacements of the sub-coils do not significantly affect the coil geometry, hence the assumption of a constant $[L]$ matrix is valid.

Eqs. 5.4-5.6 predict the electromagnetic behavior of this simple system. The prediction of eddy currents at the outer radii, induced voltages, and skin effects are contained in these equations. More specifically, the $[L]$ matrix is principally responsible for capturing these effects. The derivation and calculation of the $[L]$ matrix uses Maxwell's equations of electromagnetism. It is the calculation of $[L]$ (SOLDESIGN) which underlies the success of this method.

Solution Procedures

A numerical solution procedure is employed to determine the current densities for the sub-coils. For reasons of stability, this problem is solved iteratively with an implicit finite difference (Euler) method. The derivatives of current and

voltage are approximated with a finite difference equations. The implicit formulation for Eqs. 5.5-5.7 requires their being satisfied at time $t + \Delta t$. The times for each variable are denoted with an upper right superscript. Using a simple finite difference approximation for Eq. 5.9, Eq. 5.10 defines a set of equations which when solved determine the unknown currents at time $t + \Delta t$. Eq. 5.11 defines the sub-coil voltages, and Eq. 5.12 defines the capacitor bank voltage.

$$\frac{d[I]}{dt} = \frac{[I]^{t+\Delta t} - [I]^t}{\Delta t} \tag{5.9}$$

$$\left(\frac{1}{\Delta t}[L] + [R]^{t+\Delta t}\right)[I]^{t+\Delta t} = (V')^{t+\Delta t}[1] + \frac{1}{\Delta t}[L][I]^t \tag{5.10}$$

$$(V')^{t+\Delta t} = V^{t+\Delta t} - R_c\left(I^T\right)^{t+\Delta t} - \frac{L_c}{\Delta t}\left[\left(I^T\right)^{t+\Delta t} - \left(I^T\right)^t\right] \tag{5.11}$$

$$V^{t+\Delta t} = V^t - \left(I^T\right)^{t+\Delta t}\frac{\Delta t}{C} \tag{5.12}$$

The initial conditions for this problem are the applied voltage of the capacitor bank, and zero current flowing in the coil. Since the voltage $(V')^{t+\Delta t}$ cannot be known at time t, and because the total current $(I^T)^{t+\Delta t}$ is also unknown, the solution to these equations must be determined iteratively.

From experience, it has been found that $[R]$ does not change significantly during the iterations at each time step. So it is assumed that $[K]_e$ only changes between time steps and not during the iterative solution for that time step.

$$[K]_e = \frac{1}{\Delta t}[L] + [R]^t \tag{5.13}$$

$$[K]_e[I]^{t+\Delta t} = (V')^{t+\Delta t}[1] + \frac{1}{\Delta t}[L][I]^t \tag{5.14}$$

Thus, $[K]_e$ is not solved at time $t + \Delta t$, but instead at time t. The $[K]_e$ matrix is symmetric, and this property allows an efficient matrix solver to be employed (COLSOL). Since $[K]_e$ does not change during iterations at each time step, it is

triangularized and stored just once at each time step. For each iteration, only a reduction and back substitution of the load vector (right hand side of Eq. 5.14) is necessary to obtain $[I]^{t+\Delta t}$. By successively substituting the results of Eqs. 5.12, 5.11 and 5.13 into each other, solutions for $(I^T)^{t+\Delta t}$,$V^{t+\Delta t}$ and $[I]^{t+\Delta t}$ converge.

The $[K]_e$ matrix has additional significance in the solution to the short pulse equations. An examination of the $[K]_e$ matrix reveals important time convergence limits for these systems. When $\Delta t \rightarrow \infty$, the problem converges to a steady state solution where only $[R]$ is important. When $\Delta t \rightarrow 0$, the problem is time-dependent, and $[L]$ dominates the solution. Because this is an implicit solution scheme, $[R]$ is a part of the $[K]_e$ matrix. Its inclusion is responsible for the stability of this solution procedure. For the short pulse analyses $\frac{1}{\Delta t}[L]$ and $[R]$ are of the same order of magnitude ($\approx$ 0.4 and 0.1 Ohm respectively.)

Thermal Analysis

The thermal analysis for the short pulse magnet is patterned after the electromagnetic analysis. A finite difference method is used to determine the temperature distribution within the magnet. The same sub-coil model is used for both analyses, and the time steps are identical. During the pulse, thermal conduction and convection are not significant, but ohmic heating is significant. Immediately after the pulse (260 μs), there are extreme temperature gradients inside the magnet, and thermal conduction is important in reducing the temperature differences. The magnet cools to room temperature by thermal convection to the air and by heat conduction out the ends of the magnet into the magnet assembly.

The finite difference heat transfer equations for an axisymmetric coordinate system have been derived previously [7]. The equation for the temperature at the next time step in a finite difference formulation is given in terms of the sub-coil build Δr and mean sub-coil radius r_i.

$$\theta_i^{t+\Delta t} = \theta_i^t + \left(\frac{\kappa \Delta t}{dC_p \Delta r^2}\right)\left[\left(1+\frac{\Delta r}{2r_i}\right)\theta_{i+1}^t + \left(1-\frac{\Delta r}{2r_i}\right)\theta_{i-1}^t - 2\theta_i^t\right] + \frac{\rho J^2 \Delta t}{dC_p} \qquad (5.15)$$

The boundary conditions for this model are determined by defining the convective heat transfer rate at the inside and outside radius of the model (Eq. 5.16). $\hbar$ is the convective heat transfer coefficient, and θ_∞ is the air temperature. By creating fictitious grid temperatures on the boundary of the finite difference model it is possible to impose the boundary condition relationship.

$$\frac{\partial \theta}{\partial r} = \frac{\hbar}{\kappa}(\theta_\infty - \theta) \tag{5.16}$$

By using Eq. 5.15 in a standard finite difference formulation, it is possible to determine the temperature profile in each sub-coil during and after the pulse. The thermal analysis of the short pulse magnet is coupled to the electromagnetic analysis.

Changes in temperature affect the electrical resistivity, which affects the current densities which in turn affect the temperatures. To study the importance of a coupled electromagnetic and thermal analysis, an analysis was performed with a constant electrical resistivity. The resulting currents did not diffuse as deeply into the the build of the magnet. The difference in current penetration between this example and the temperature dependent resistivity case is about equal to the difference between their respective skin depths (Eq. 4.2).

Short Pulse Test Results

The 50T coil has been pulsed over 20 times to magnetic fields greater than 40 T without any visible damage to the magnet itself. However, the interspace insulation which separates the turns has been cut and damaged by the magnet. The insulation lasts about 8 pulses before it must be replaced. Results from the 50T tests have already been reported, so this discussion concentrates on the predictions and results obtained from the DTC tests.

The DTC was pulsed 16 times to magnetic fields between 48 and 54 T before crack growth on the inside radius caused it to fail. A coil failure analysis is postponed to Chapter 6. The short pulse tests were halted after the 12th test to examine the coil and interspace insulation. The magnet appeared undamaged in its assembly, but after removing it from the assembly, eight cracks were found on the inner radii. The insulation was in very good shape. There was none of the damage observed in the 50T coil insulation. The modification to the turn cross

section (a gap between the coil and insulation at the inner radius) successfully prevents insulation damage.

The program MESPA makes the following predictions for the loading conditions of the DTC. Figs. 5.7a and 5.7b show the magnetic field and total current flowing through the magnet as a function of time. Figure 5.7c shows the actual total current which was measured during the first 50 T pulse of the magnet. Traces of magnetic field versus time were measured at low voltages to correlate the current with the peak magnetic field. For safety reasons, traces of the magnetic field were not measured at 50 T. A magnet failure would destroy the pickup coil used to measure the field, creating a serious high voltage danger. Instead, field measurements were made at 8.6 T (2 kV) to correlate the peak magnetic field with the peak current in the magnet. The ratio between the peak field and current is constant for short pulse magnets. Using this correlation, it is possible to determine the peak magnetic field based upon a measured peak current. The peak magnetic field predicted by MESPA is 45.5 T at 42 μs, while the scaled peak magnetic field is 48.8 T at 46.0 μs. The predicted peak current is 278 kA at 45.0 μs, while the actual measured peak current is 272 kA at 49.0 μs.

Within the magnet, the current density profiles are given in Figs. 5.8a and 5.8b. 30 sub-coils were used by MESPA to determine these profiles. Initially, the largest current densities are at the inside radius. With time, the current diffuses into the build of the magnet (again by a constant amount along the length of the sub-coil). The slight rise in current densities at the outer radius of the magnet is due to eddy currents generated by the return field as it flows back around the magnet.

The temperature distributions within the magnet during the electromagnetic pulse are given in Figs. 5.9 and 5.10. Clearly, the temperature profiles reflect the high current density profiles predicted during the pulse. Fig. 5.11 shows the temperature profiles at different times during the magnet cooling. The temperatures predicted here are used later in the finite element analysis.

Mechanical Analysis

The mechanical analysis of the short pulse magnet is simplified with approximations to the geometry and loading. The primary geometrical assumption

is that an annular ring model can be used to analyze the problem. The axisymmetry of the annular ring replaces the helical geometry of the magnet. The annular ring is also assumed to represent the center turn of the magnet where the turn is symmetric along the R axis (Fig 5.12). An axisymmetric finite element analysis is performed on the annular ring model. The material models developed for maraging steel in Chapter 2, and incorporated into the finite element program AFESA, are used to study the mechanical behavior of the DTC.

The short pulse magnet is subjected to two kinds of mechanical loads, axial compression from the magnet assembly and Lorentz body forces. The Lorentz body forces (N / mm^3) are derived from the cross product of the current density and the magnetic field. When the helical geometry of the current path is considered, there are three components to the Lorentz body force, radial, axial and angular. At the ends of the magnet where the radial component of the magnetic field is largest, the axial and angular body force components are also largest. The axial component of the body force compresses the magnet, while the angular component of the body force winds the magnet tighter. An analysis of the end of the magnet is complicated by the geometry of the transition regions and the lack of an electromagnetic analysis which can predict the current densities and magnetic fields in this region. At the center of the magnet there is no radial component of magnetic field, thus the axial and angular body forces are zero here. The axial magnetic field is largest at the center turn; thus the radial body force is largest body force component. The radial body force in the center turn is larger than either of the other two body force components anywhere in the magnet by a factor of at least 10.

The program SOLDESIGN calculates the axial magnetic field within the build of the magnet. The fields are multiplied by the current densities to get the radial body force profiles shown in Figs. 5.13 and 5.14. The curves in Fig 5.13 show a concentration of body force within the skin depth region, with a decrease in magnitude going into the build of the magnet. The maximum body force during the pulse is 345 N/mm^3 at 30 μs. The gradient of body force in the magnet is 90 $N/mm^3/mm$. The scale of the body force axis is reduced by a factor of 10 in Fig. 5.14. The body forces in this figure occur during the reverse magnetic fields. Note the complete penetration of body forces into the build of the magnet, and the negative body forces at the time (120 μs) of zero total current in the magnet.

The maximum axial compression imposed by the magnet assembly on the magnet is determined from an integrated estimate of the maximum axial body force during a pulse. The estimate is made by determining the radial component of the magnetic field in the center of the skin depth region, along the length of the magnet. The axial body force is calculated from the radial field and the current density, and then integrating over the skin depth from the center of the magnet to its end. Using this method gives a total axial compressive force on the magnet of about 30 tons (0.27 MN). The purpose of the imposed axial compression by the magnet assembly on the short pulse magnet is to prevent movement of the magnet. Under a sufficiently large axial pre-compression and loading compliance, the center turn of the magnet does not experience an appreciable change in axial loads during a pulse.

The actual shape of the magnet turn cross section is used to define the shape of the annular ring model. Since the center turn of the magnet is being analyzed, symmetry allows the finite element model to span just half the magnet turn (Fig. 5.15). There are 90 elements and 271 nodes in this mesh. A high density of elements is used at the inner radius of the mesh to model the steep gradients of body force and temperature. There are 2 elements in the phase transformation transition region at all times during the pulse.

The axial compressive force on the magnet is included in the finite element analyses. To find it, a separate finite element analysis was performed. The G-7 insulation has a compressive yield strength under uniaxial strain of 234 MPa. The insulation was modeled with nodal springs that can only transmit a compressive force, and the maximum force they can transmit is equivalent to a stress of 234 MPa. Because the G-7 is in uniaxial strain, it might withstand larger stresses than assumed here, for a few cycles. The nodal springs are attached to the top surface of the finite element mesh (see Fig 5.16), and the bottom surface of the model is displaced ($\Delta u = 0.015$ mm) upward until the total axial force on the model is 30 tons (0.27 MN). The spring stiffnesses are determined by integrating a quadratic interpolation function to find the area associated with each node and then multiplying the result by the ratio of the measured G-7 Young's modulus (12.4 GPa) to the insulation thickness (0.794 mm). From the analysis, the resulting nodal force from each axial spring is determined. These axial node forces are then used as an applied force (constant) for the finite element analysis of the magnet pulse. Thus, no attempt is made to study the interface between

G-7 and the maraging steel, and the only objective here is to include the 30 ton (0.27 MN) compressive force on the center turn model.

Figs. 5.16a and 5.16b show the axial stress and contour plot in the DTC prior to pulsing. The stresses in Fig. 5.16a are taken along the R axis, and they show a smooth variation in axial stress at r = 13 mm (6 elements between r = 12 and 14 mm). The stresses could be nearly discontinuous at the top surface, but they are smooth along the Z axis.

The electromagnetic pulse is broken into three phases, each with 6 time steps. Each time step is broken up into 15 sub-increments. The time steps for the first phase are 20, 30, 40, 50, 60 and 80 μs, and they span the largest magnetic fields and current densities. The second phase spans the reverse magnetic fields, and the time steps are 120, 140, 160, 180, 200 and 260 μs. The last phase covers the cooling of the magnet back down to room temperature, with time steps of 0.001, 0.01, 0.25, 5, 60 and 900 s. Fig. 5.17 shows the magnetic field versus time with the time step positions marked on the curve. There are Lorentz body forces for the first 2 phases only, and temperature profiles for all three phases.

The boundary conditions for the finite element mesh are very simple. The bottom edge of the model is restricted from any axial displacement, due to modeling just the top half of the center turn, and the necessity of preventing the model from moving in the Z direction. The entire model is free to move in the radial direction.

A dynamic finite element analysis of the DTC was performed to investigate the importance of dynamic body forces on the mechanical behavior. The phenomenological rate equation was used for these analyses, because it was developed first, and its computer execution time is shorter. To study dynamic body force effects, the body forces are calculated from nodal displacements and added to the equilibrium equation (Eq. 3.4). A comparison between finite element results with and without dynamic body forces show that these forces are not significant. The Lorentz body forces are approximately 100 times larger than the dynamic body forces.

The phenomenological rate equation is best suited for temperatures between 298 and 1100 K. For temperatures above 1100 K, the Arrhenius rate

equation best predicts plastic straining in maraging steel. A second finite element analysis was performed on the DTC, and these results are compared to the phenomenological finite element results. The phenomenological and Arrhenius displacements are nearly identical, but the stress distributions and stress-strain hysteresis loops for these two analyses differ (being derivatives) as discussed below.

The finite element results are broken into three categories: nodal displacements, stresses, and stress-strain hysteresis loops. The stress plots for the DTC show little variation in the Z direction anywhere inside the magnet turn (see Fig. 5.16b). Thus, graphs of displacement and stress are described with plots along the R axis alone. The RZ shear stresses are smaller than the hoop stresses by a factor of 1000 everywhere inside the magnet. This means the radial, hoop and axial stresses are also the principal components for this model.

Displacements

All of the results for displacements are for the phenomenological rate equation analysis (valid below 1100 K; even above, the difference between that and the Arrhenius rate equation analysis are not noticeable). Figs. 5.18-5.20 show the finite element mesh deformation outlines before, during, and after the first pulse. In the first and last plot, the displacements have been magnified 100 times. The second plot, Fig. 5.19 is at 260 μs, and its displacements are magnified 10 times. Initially, the coil turn deformation shows the effect of axial pre-compression. Beginning at a radius of 14mm, the coil turn is deformed downward and this deformation extends to the outer radius. The surface at the inner radius is displaced outward. At 260 μs, the Lorentz body forces have subsided and the coil is at its peak temperature. The important deformation features at this time are outward expansion of the magnet turn and axial expansion of the magnet, especially at the inner radius. The dotted deformation outline is more boxlike, and the effects of axial pre-compression are not visible in the plot. The top left corner of the deformed outline has risen and is closer to the insulation. If the shape of the magnet turn is not altered, then the corner pinches into the insulation during the pulse. After the pulse, the deformation outline has changed in two ways. The inner radius coil surface is radially displaced inward and the top surface of the coil turn at r = 11 mm is slightly depressed. The effects of axial compression are evident again.

A finite element analysis of a second electromagnetic pulse does not show significant deviations in the deformation outlines of Figs. 5.19 and 5.20. For the short pulse magnet, the turn width and inner radius change very little between cycles, and the heating characteristics of subsequent pulses do not change. For the thermal cycling tests, each thermal cycle caused a change in the specimen shape which influenced the heating characteristics of the next pulse.

Figs. 5.21a-5.21c show the radial displacements in the magnet as a function of time and position. Initially, the magnetic body forces cause a rapid radial expansion of the magnet. During a pulse, the peak displacements are between a radius of 10 to 12 mm, and decrease on both sides. The peak field is at 42 μs, but the analysis predicts larger displacements at 50 μs than at 40 μs. By 80 μs, the magnetic body forces diminish, and the thermal loads dominate. For the remainder of the pulse, the maximum displacements are at the outer radius. Fig. 5.21b shows the radial displacements during the reverse magnet fields. The times listed above the curves correspond in the same order to the curves below. The reverse magnetic fields have the effect of increasing the overall radial displacements in the magnet but they do not change the general shape of the displacement curves. The thermal loads overwhelm the reverse magnetic field loads.

The radial displacement curves (Fig. 5.21c) show the influence of temperature distributions in the magnet. At 0.001, 0.01 and 0.25s, the temperature gradients are still nonlinear, and the curves have the same shape as those in Fig. 5.21b. At 5, 60 and 900 s, the temperature gradients are nearly constant, and the resulting radial displacements are linear. The sharp changes in the linear slopes of these curves at r = 12 mm reflect the material phase transition between austenite and martensite. For r < 12 mm, the coil material has transformed to austenite, while for r > 12 mm, the material remains elastic throughout the pulse. The thermal strains in these these two phases are different, and this accounts for the change in displacement slope. By the end of the pulse, the radial displacements are negative at the inner radius and positive at the outer radius.

Stresses

The radial, hoop and axial stresses for the phenomenological rate equation analysis are shown in Figs 5.22 - 5.35, and the same set of results are shown for the Arrhenius finite element analysis in Figs. 5.36-5.49. The 120, 140, 160, 180

and 200 μs time steps are not included here, because they are all very similar to Fig. 5.29. The large change in hoop stress between Figs. 5.28 and 5.29 occurs between 80 and 120 μs. Two observations should be made about the radial and axial stresses in these plots. The radial stress is zero at the inner and outer radius of the magnet turn. The radial Lorentz forces are greatest at the inside radius, yet the radial stress is zero. The second observation is that during a pulse, the axial stress is nearly constant at -234 MPa between r = 16 mm and 21 mm. This corresponds to the yield strength of G-7 (although the stress could rise higher under uniaxial strain conditions).

During the first 20 μs of a pulse, the stress distributions in a virgin coil are elastic. Starting at 30 μs, phase transformations begin at the inner radius, and they cause steep gradients in the axial and hoop stresses. By 50 μs, the phase transformation transition region has moved further into the magnet build. The hoop stress is the largest stress component, and it has two maxima. The first maximum is at the austenite edge of the phase transition, and the second is in the interior of the magnet at r = 15 mm. The radial stress seems unaffected by phase transformation strains and its maximum is at r = 13 mm. The lack of phase transformation effects on the radial stress is likely due to the fact that the radial stress is normal to the phase transition zone. Unlike the thermal test specimens which were restricted from displacing in the Z direction, the magnet is not restricted from displacing in the R direction, but more restricted in the θ direction.

Elastic analyses of this problem type show that magnetic body forces cause a positive hoop stress at the inner radius, and thermal gradients cause a negative hoop stress at the inner radius. The combination of these loads result in a shift of the maximum hoop stress from the inner radius into the the build of the magnet (the second maxima). Fortunately for the magnet, this maximum hoop stress occurs in the lower temperature, higher strength martensite phase.

At the end of the magnetic field pulse, thermal gradients dominate the loading, and the maximum stress shifts to the inner radius. The radial stress inside the magnet build is large during the field pulse, but it is diminished during cooling. The hoop stress however reaches its maximum negative magnitude at 260 μs (see Figs. 5.29 and 5.42). The largest positive stress at this moment is also the hoop stress, 400 MPa at the outer radius of the coil.

As the magnet cools uniformly from 690 K at 1 min to 298 K at 15 min, the stress distributions in the magnet change, and there are steep gradients in stress near the inner radius. This is due to the two different material phases in the coil at the same time, and the uniform temperature profile. Plastic hoop strains (developed at the time of peak temperature) force the hoop stress into tension as the magnet cools. By the end of the cycle, there is a positive residual hoop stress at the inner radius. The stress distribution varies within the prior austenite region, but is nearly constant in the martensitic region. A large stress gradient exists near r = 12 mm, and this position corresponds to the maximum penetration of the austenite phase.

For the phenomenological and Arrhenius analyses, the predicted stresses are similar for the first 80 μs of a pulse but differ for the remainder. At 260 μs, the hoop stress predicted by the phenomenological analysis is twice as large as the hoop stress predicted by the Arrhenius analysis. Both finite element analyses predict steep gradients in stress at a radius of 12 mm, and the stress distributions at 60 and 900 s are similar in shape. The Arrhenius results differ most from the phenomenological results in those portions of the magnet where the temperature exceeds 1100 K.

Figs. 5.49 - 5.50 show the von Mises stress along the R axis of the magnet turn between 20 and 80 μs. With these figures it is possible to visualize the effects of magnetic and thermal loading on the magnet. The peak stress increases in magnitude as the magnetic field increases. The location of the peak stress moves into the build in a manner similar to the current density penetration. The phase transformation between martensite and austenite begins at the inner radius and penetrates into the build of the magnet. As magnetic body forces decline, the stress at the inside radius decreases, and then increases again as thermal loads start to dominate. It is important to note the very high stresses (> 1000 MPa) which occur between r = 12 and 22 mm. The stress distribution in this region is entirely elastic, because the material strength is greater than 1500 MPa, and the temperatures are less than 690 K. Increasing the build of this magnet would definitely decrease the stress levels and make a safer magnet. A larger magnet build increases the volume of material which is elastically stressed at levels less than 1000 MPa.

While the shape of the deformed finite element model outline does not change significantly after the second electromagnetic pulse, there are changes in

the stress distributions. The von Mises stress plots for the second pulse between 0 and 80 μs are shown in Figs. 5.51 and 5.52. A comparison of these plots to Figs. 5.49 and 5.50 shows the effects of residual stresses. During the the first 50 μs of the second pulse, the maximum stress shifts to the inside radius. The advance of the phase transition region is visible again, and there is a gap (decrease in stress) between the current phase transition position and the previous maximum phase transition depth. This gap shrinks during the heating of the magnet.

Stress-Strain Hysteresis Loops

The stress-strain behavior at four element integration points are studied. Their radial positions are 9.3, 10.5, 12.0 and 18.2 mm and they are all 0.13 mm away from the R axis. At these integration points, the equivalent plastic strain rate $\dot{\varepsilon}^p$ versus time and the deviatoric hoop strain versus stress are plotted. The majority of this section of the chapter is spent discussing the results at the first integration point. The inside radius of the magnet has the largest increments in plastic strain, and the plastic strains decrease in magnitude as the radius increases. The hoop component of stress and strain is selected here for the hysteresis loops, because it is the largest in magnitude.

Figs. 5.53a and 5.53b show the equivalent plastic strain rate $\dot{\varepsilon}^p$ from the phenomenological finite element analysis for the first and second pulses at the first integration point (r = 9.3 mm). Figs. 5.54a and 5.54b show the deviatoric hoop stress-strain hysteresis histories during the first and second pulse from the same analysis at the same point. From these plots, three stages of plastic deformation are identified. The first stage occurs during the peak magnetic body forces, the second stage after the magnet is heated and large thermal gradients exist in the magnet, and the third stage occurs when the temperature in the coil has cooled to a uniformly high temperature of 690 K. This temperature will be called the post-pulse temperature. The hoop stress alternates between tension, compression and tension during the three stages of plastic straining.

The integrated plastic strain increments during these three stages are 8.5 $\times 10^{-5}$, 0.56 and 0.28 % respectively. For the second pulse, the plastic strain increments for these three stages are 5.4 $\times 10^{-4}$, 0.24 and 0.33 %. The final von Mises stress after the first and second pulse are 600 and 580 MPa. The stress-strain hysteresis loop for the first pulse encloses the loop for the second pulse. This suggests a final shakedown loop which is also within the first hysteresis loop.

Thus, the maximum plastic strain range predicted by the phenomenological finite element analysis for the DTC is 0.56 %.

The plastic strain rate versus time for the Arrhenius finite element analysis is shown in Fig. 5.55. The peak plastic strain rates for this analysis are about 100 times larger than those in the previous analysis. Plastic straining in the second stage occurs at a higher rate, but it only lasts until 0.007 s. In the third stage, plastic straining occurs over a longer time interval than the third stage in the phenomenological analysis. Fig. 5.56 compares the stress-strain hysteresis loops from the phenomenological and Arrhenius analyses. The two curves are similar through stage one, but the plastic strain increments for the second and third stage are larger for the Arrhenius analysis. The stress levels are smaller for the Arrhenius analysis, and this is consistent with the discussion in Chapter 2 about predictions of strength at temperatures above 1100 K. The maximum plastic strain range predicted by the Arrhenius finite element analysis for the DTC is 0.99 %. Thus, predictions of coil life should be made with the Arrhenius rate equation, since it will predict larger plastic strain ranges, hence a shorter coil life.

Figs. 5.57 - 5.59 are the deviatoric hoop strain versus stress hysteresis loops for the first pulse at the second, third and fourth integration points. These plots come from the Arrhenius analysis, and they show a decrease in plastic strains away from the inner radius of the magnet turn. For the second integration point, the maximum plastic strain range is 0.40 %. The plastic strains at the third and fourth integration points are very small (< 0.03 %), so their behavior is mostly elastic.

Conclusions

For magnetic fields greater than 50 T, the requirements of magnet strength versus available energy and allowable temperature dictate a pulsed field approach. Short pulse magnets sacrifice electrical conductance for a gain in magnet strength. Maraging steel is used in these magnets, because it fits the high strength requirement and is machinable in the unaged condition. The design of short pulse magnets is dictated by the available energy, bore size, peak magnetic field and maximum allowable temperature.

Predicting the current densities within a short pulse magnet is the critical task, because with this information, the magnetic fields, Lorentz body forces and temperatures are determined. The current densities are found by applying the RLC circuit equation to the magnet and capacitor bank system. The magnet is discretized into many sub-coils, and RLC circuit equations are applied to each sub-coil. By simultaneously solving the set of equations with an implicit numerical procedures, the currents within each sub-coil are found. The results from this analysis show the current density, magnetic field and Lorentz body forces diffusing into the build of the magnet. The temperature profile resulting from a short pulse has the highest temperatures at the inside radius, and an extreme temperature gradient (200 K/mm) extending into the build.

A short pulse high magnetic field, destructible test coil (DTC) was designed, built and pulsed to magnetic fields of 50 T. The purpose of this magnet was to predict its behavior and to observe how it failed. A special magnet assembly was designed and built to limit the potential danger of flying shrapnel from a magnet failure. Using the experience of previous magnet designs, the cross sectional turn shape of the DTC was successfully altered to prevent G-7 insulation damage. An electromagnetic and thermal analysis of the DTC was used in the design of this magnet. The predicted magnetic field was 45.5 T, while the observed field was 48.8 T. The expected design life of the magnet was 200 pulses, and the coil lasted 16 pulses before it failed.

The Lorentz body forces and temperature profiles predicted by the electromagnetic and thermal analysis are used in finite element analyses to study the mechanical behavior of the DTC. An annular ring models the center turn of the coil. The finite element analysis uses 18 time steps with 15 sub-increment time steps to discretize each pulse. The results of the finite element analyses are summarized below.

1. Dynamic body forces resulting do not play a significant role in the mechanical behavior of the short pulse magnet.

2. During a pulse, thermal expansion in the coil causes the top surface of the turn at the inner radius to rise significantly. This expansion can pinch G-7 insulation if the turn shape is not altered by reducing the turn thickness at the inside radius 15 % from 4.6 to 3.9 mm.

3. After a pulse, the shape of the DTC has not changed significantly. Thus, the heating characteristics of subsequent pulses are not affected by deformation from previous pulses.

4. The magnet radially expands all during the pulse, with the peak displacements occurring at the time of peak magnetic fields.

5. After the pulse (5 s - 1 min), when the coil is still hot ($\approx$ 690K) and the temperatures are nearly constant, the radial displacements in the coil are linear with r. The radial displacement slope is negative in the austenite regime and positive in martensite regime.

6. The axial stress resulting from the axial compression on the DTC does not change significantly during a pulse.

7. The hoop stress is the largest of the stress components, and it changes the most during a pulse. Along the R axis, all the shear stresses are zero making all normal components principal ones.

8. The variation in radial, axial and hoop stresses in the the axial direction of the coil turn is small; the significant variations in stress occur in the radial direction.

9. The stress-strain response is elastic for the first 30 μs, and then plastic straining begins at the inside radius.

10. A material phase transformation from martensite to austenite begins at the inside radius and travels into the build of the coil. The austenite phase extends a maximum of 2.7 mm into build of the magnet (r = 12 mm).

11. Across the material phase transition from austenite to martensite, the hoop and axial stresses change abruptly. Both stresses peak on the austentite side and dip on the martensite side. A similar change in radial stress does not appear.

12. The maximum positive hoop stress occurs during the peak magnetic fields, and the maximum negative hoop stress occurs immediately after the magnetic field pulse.

13. The reverse magnetic fields, and Lorentz body forces do not significantly change the stresses in the coil. After 80 μs, the temperature gradients in the magnet dominate the problem.

14. Plots of the von Mises stress during a pulse indicate very high stress levels ($>$ 1000 MPa) over most of the coil build. This is true for both the phenomenological and Arrhenius rate equation analyses.

15. Plastic straining during a pulse is separated into three stages. The first stage occurs during the peak magnetic fields, when the hoop stress is in tension. The second occurs after the Lorentz body forces have subsided, and the hoop stress is in compression. The third stage results from the magnet cooling to its post-pulse temperature when the hoop stresses are positive.

16. The largest plastic strain increments occur at the inner radius and decrease into the magnet build.

17. Although the plastic strain rates are large during the magnetic field pulse, the largest predicted plastic strain increment is 1 %.

18. The first pulse results in the largest stress-strain hysteresis loop, and the second hysteresis loop is within the first. For the phenomenological analysis, the residual von Mises stresses on the inside radius at the end of the first and second pulse are 600 and 580 MPa respectively. The maximum plastic strain range predicted for these pulses is 0.56 %. For the Arrhenius analysis, the residual von Mises stress on the inside radius is 389 MPa after the first pulse, and the maximum plastic strain range is 0.99 %.

In summation, the mechanical behavior of the short pulse coil is influenced most by the thermal loading. The Lorentz body forces are large enough to cause plastic straining, but because they occur in such a brief time span, they do not cause significant plastic deformation. The thermal loading however causes the largest plastic strain increments. Phase transformations caused by the temperature change affect the stress distribution, but they do not interact with the plastic deformation to change the turn shape. Such was the case for the thermal cycling specimens. The imposition of a large temperature gradient followed by a high uniform post-pulse temperature is the primary cause of plastic deformation in the short pulse magnet. Thus, the maximum coil temperature, the post pulse temperature, and the temperature profiles are important design factors when considering the mechanical behavior of short pulse magnets.

Table 5.1 50T magnet specifications

Inner Radius	17 mm	
Outer Radius	65 mm	
Turn Thickness	5.6 mm	
Insulation Thickness	3.75 mm	
Number of Turns	8	
Capacitor Bank Energy	273 kJ	
Charging Voltage	19.2 kV	
Max. Coil Temperature	1300 K	
	Predicted	Actual
Peak Magnetic Field	51.8 T	49.7 T
Peak Current	372 kA	348 kA
Peak Time	60 μs	65 μs

Table 5.2 Destructible test coil specifications

Inner Radius	9.27 mm	
Outer Radius	24.00 mm	
Turn Thickness	4.60 mm	
Insulation Thickness	3.75 mm	
Number of Turns	6.5	
Capacitor Bank Energy	91 kJ	
Charging Voltage	11.5 kV	
Max. Coil Temperature	1457 K	
	Predicted	Actual
Peak Magnetic Field	45.5 T	48.8 T
Peak Current	278 kA	272 kA
Peak Time	45 μs	49 μs

Fig. 5.1 Destructive test coil.

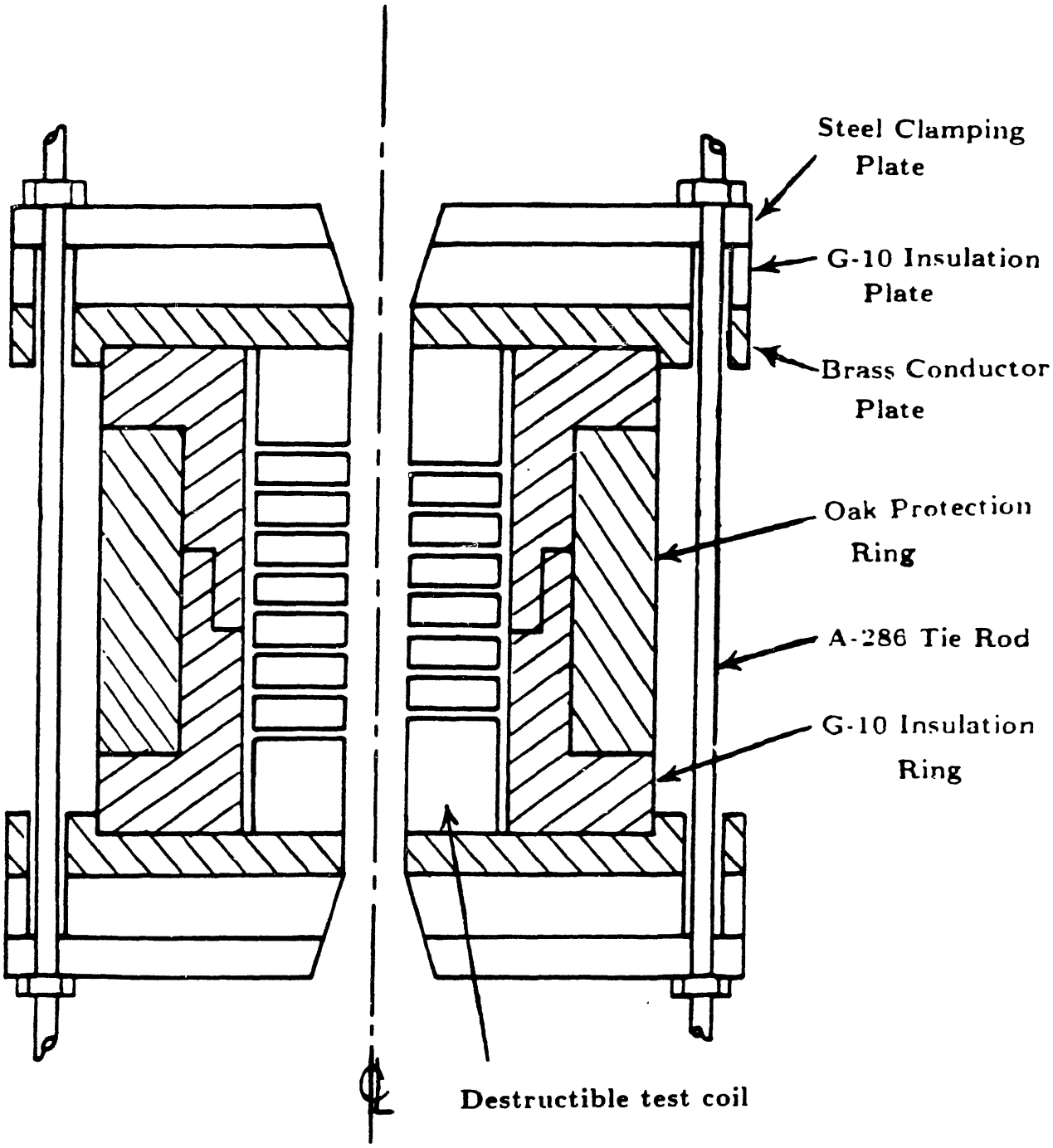

Fig 5.2 Destructible test coil assembly.

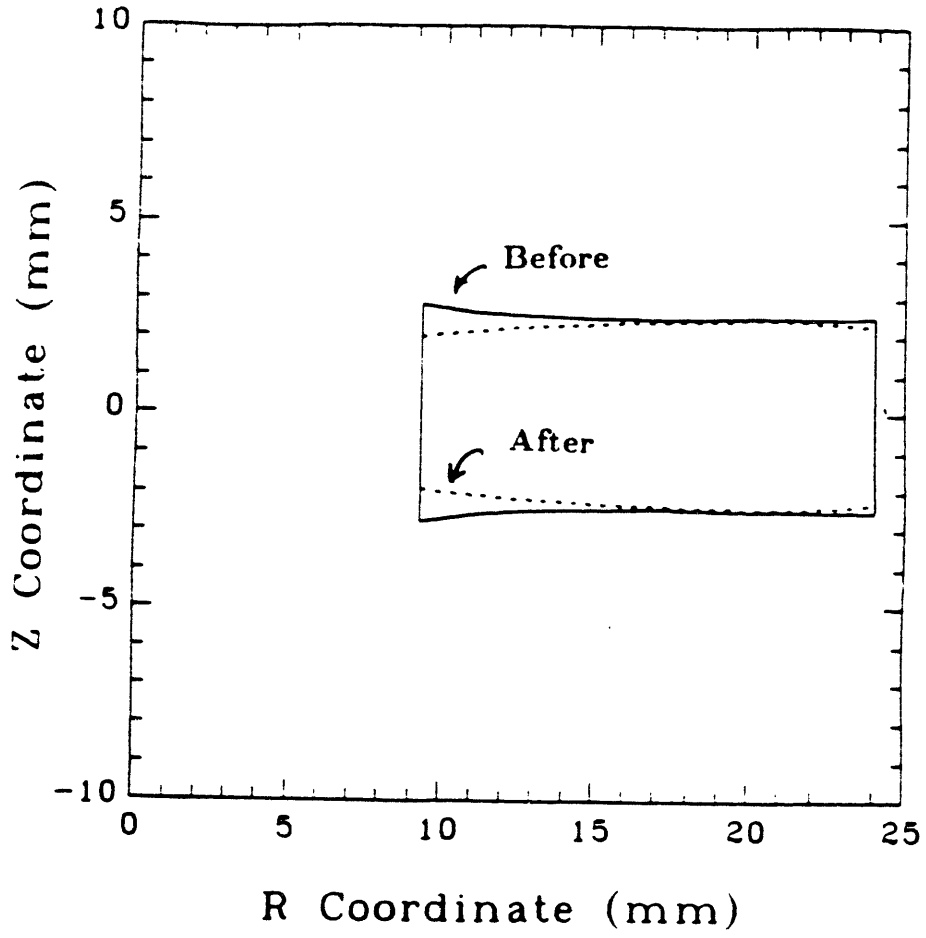

Fig. 5.3 DTC turn cross section before and after alteration with hand grinder.

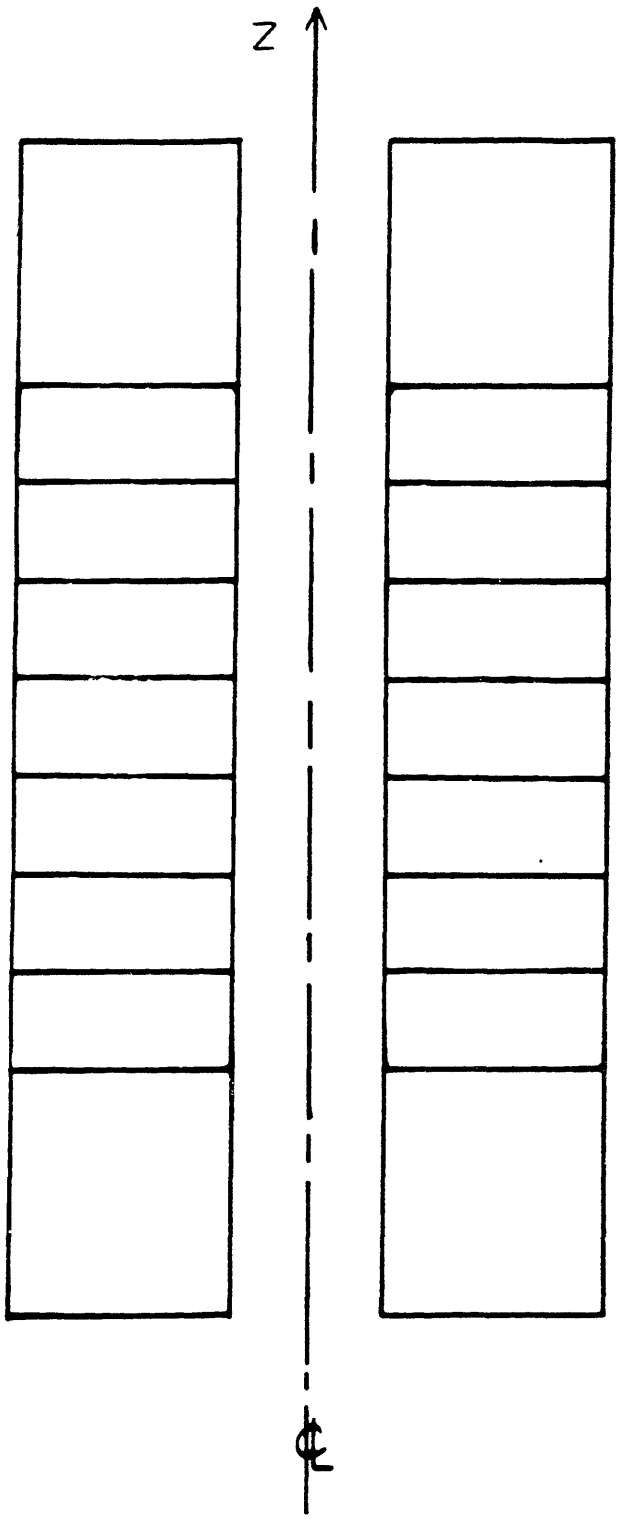

Fig 5.4 Solid helix model with 7 stacked turns.

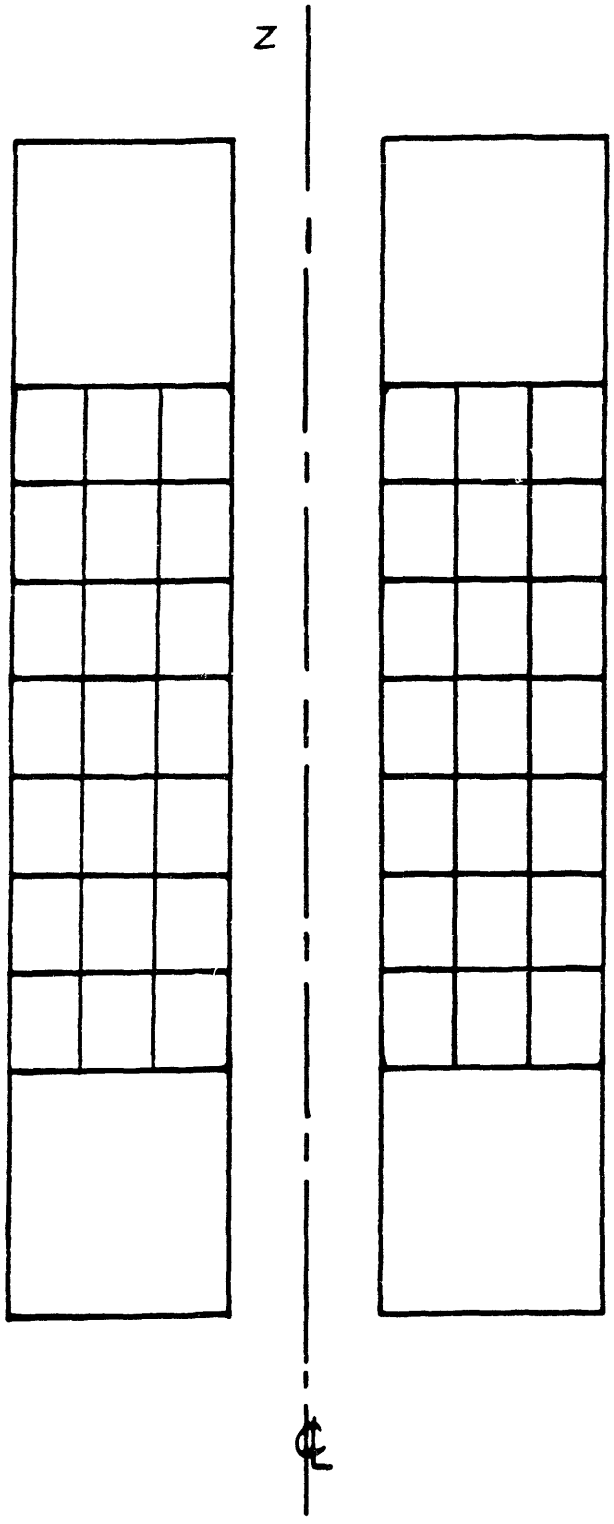

Fig 5.5 Sub-Coil model for electromagnetic analysis. There are 3 sub-coils, and each has 7 stacked turns.

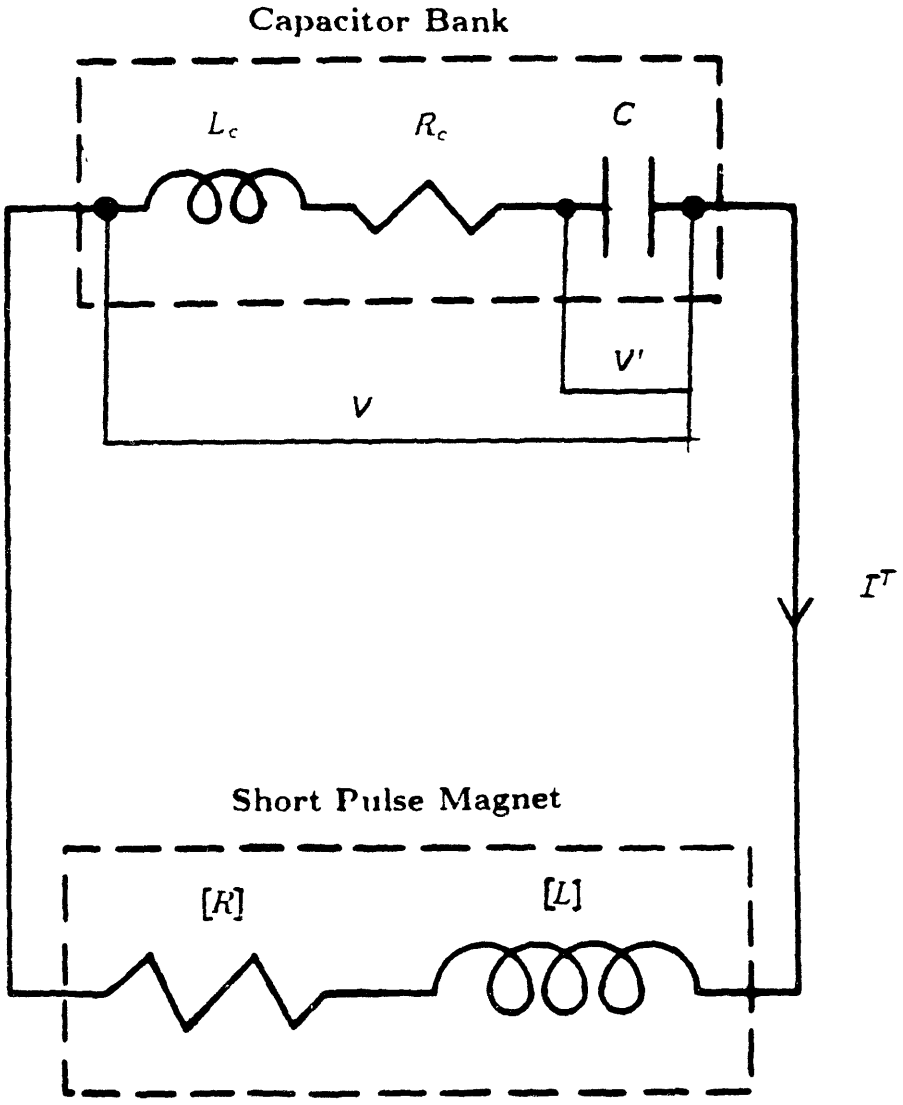

Fig. 5.6 Electrical circuit for short pulse magnet.

Fig. 5.7a
Predicted magnetic field plot for DTC pulsed at 11.5 kV.

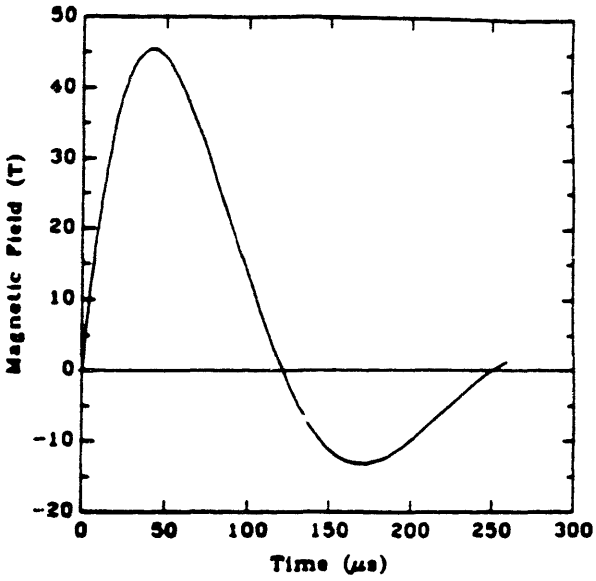

Fig. 5.7b
Measured current waveform for DTC pulsed at 11.5 kV. The abscissa scale is 50 μs/Div. and the ordinate scale is 100 kA/Div.

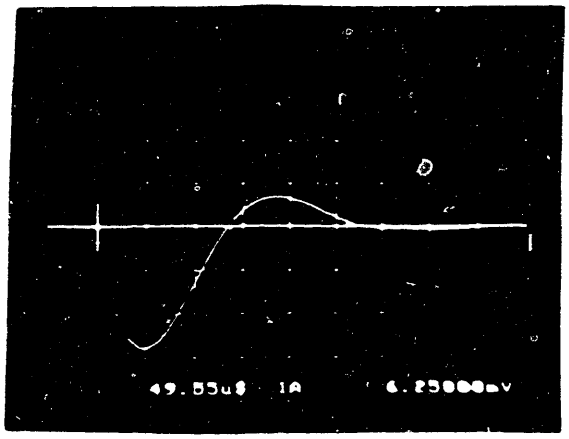

Fig. 5.7c
Predicted and observed current waveform for DTC pulsed at 11.5 kV.

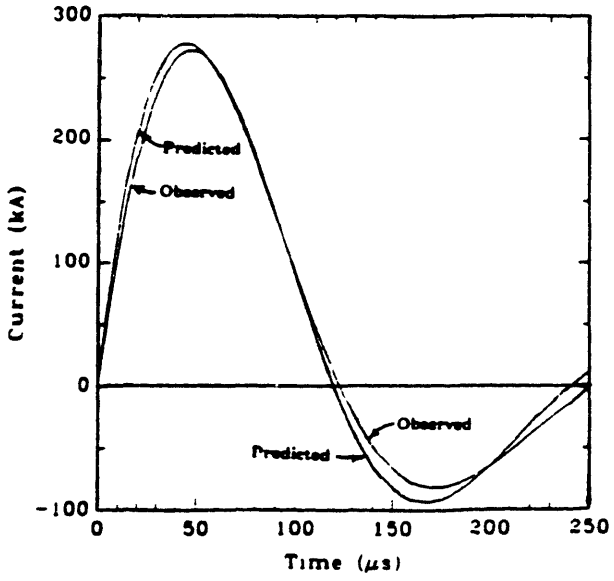

Fig. 5.8a

DTC current density profiles for an 11.5 kV pulse between 20 and 80 μs.

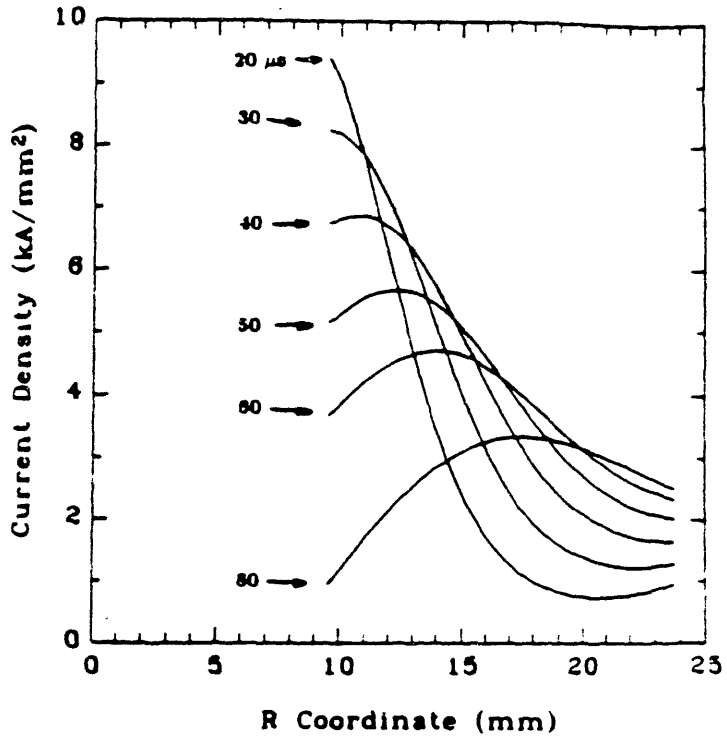

Fig. 5.8b

DTC current density profiles for an 11.5 kV pulse between 120 and 260 μs.

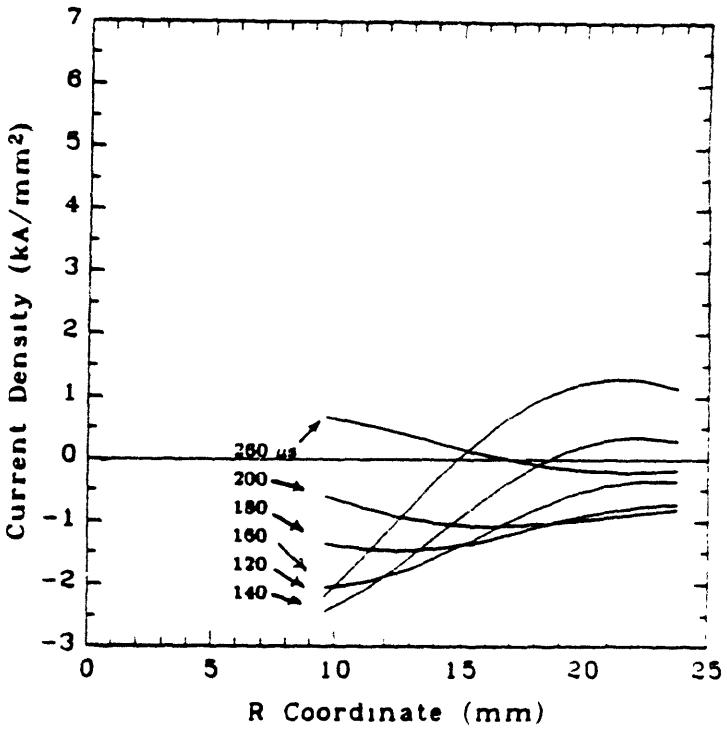

Fig. 5.9a
DTC temperature profiles for an 11.5 kV pulse between 20 and 80 μs.

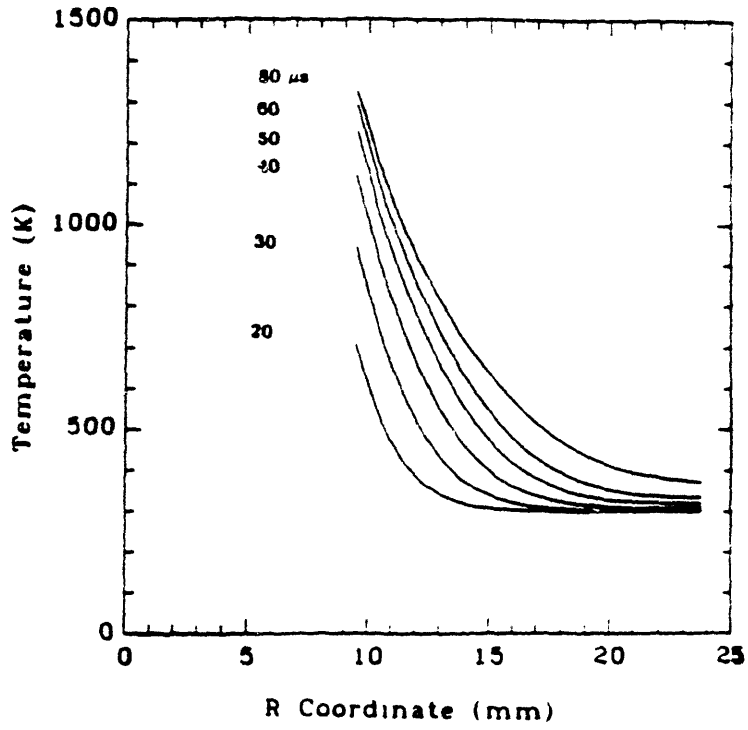

Fig. 5.9b
DTC temperature profiles for an 11.5 kV pulse between 120 and 260 μs.

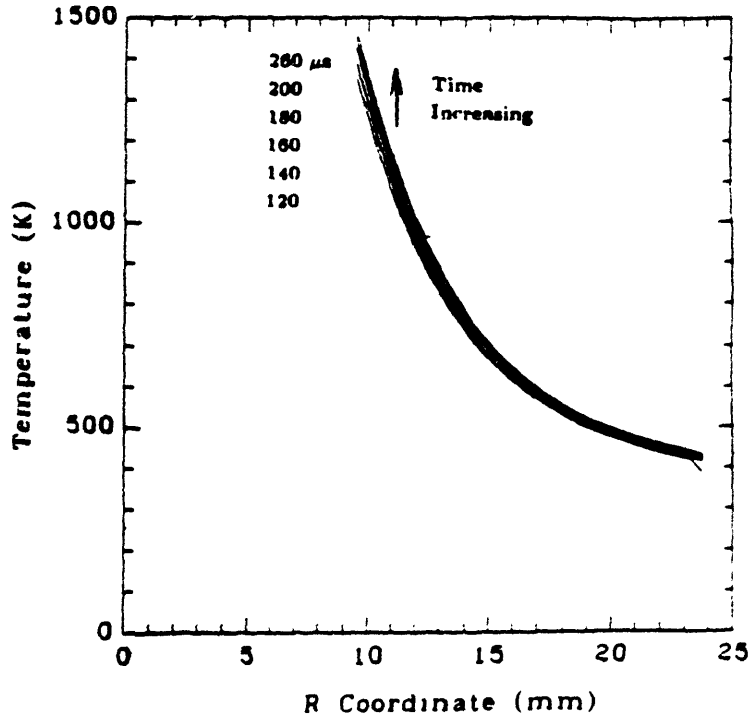

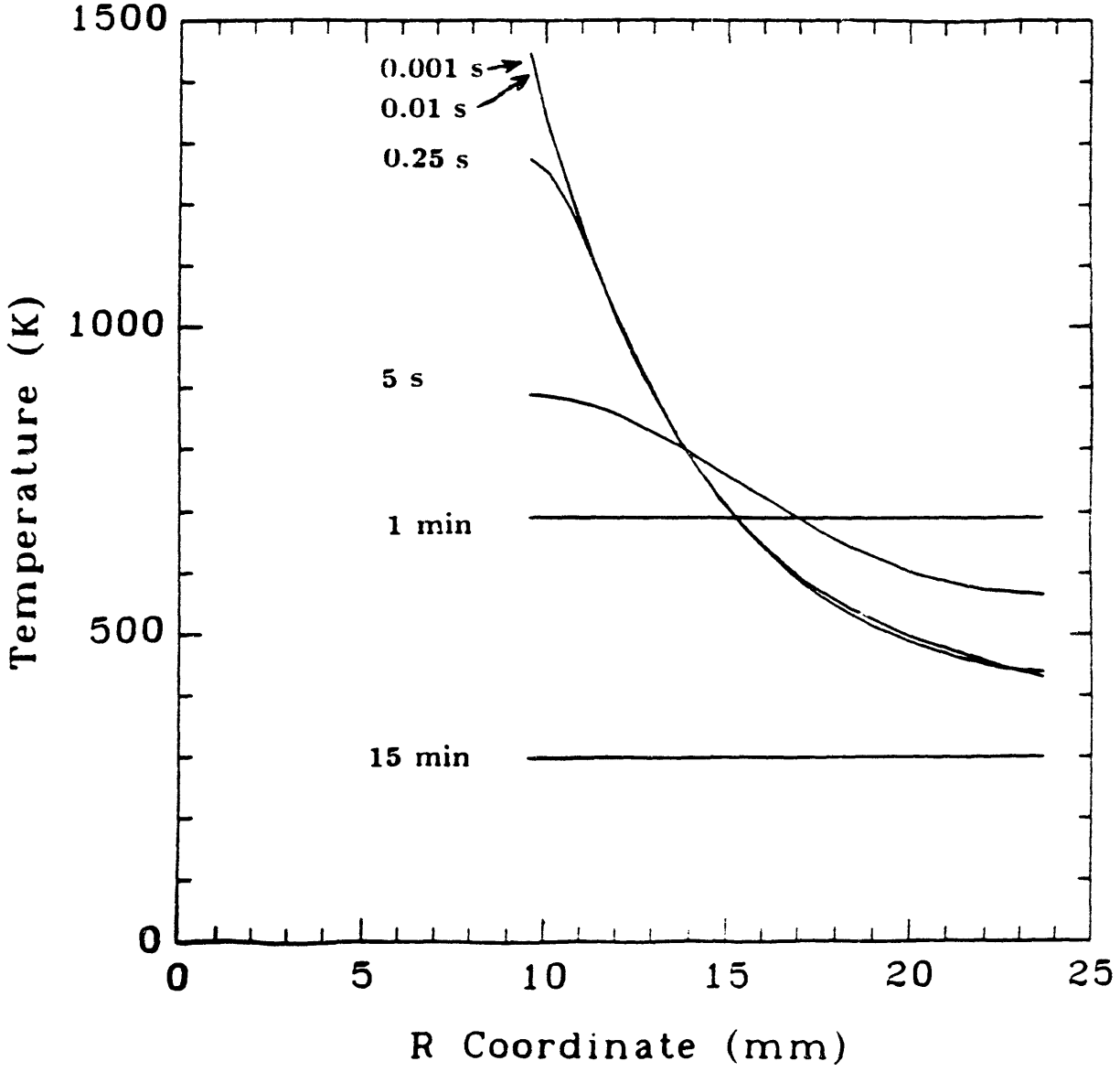

Fig. 5.10 DTC temperature profiles for an 11.5 kV pulse after 0.001 s.

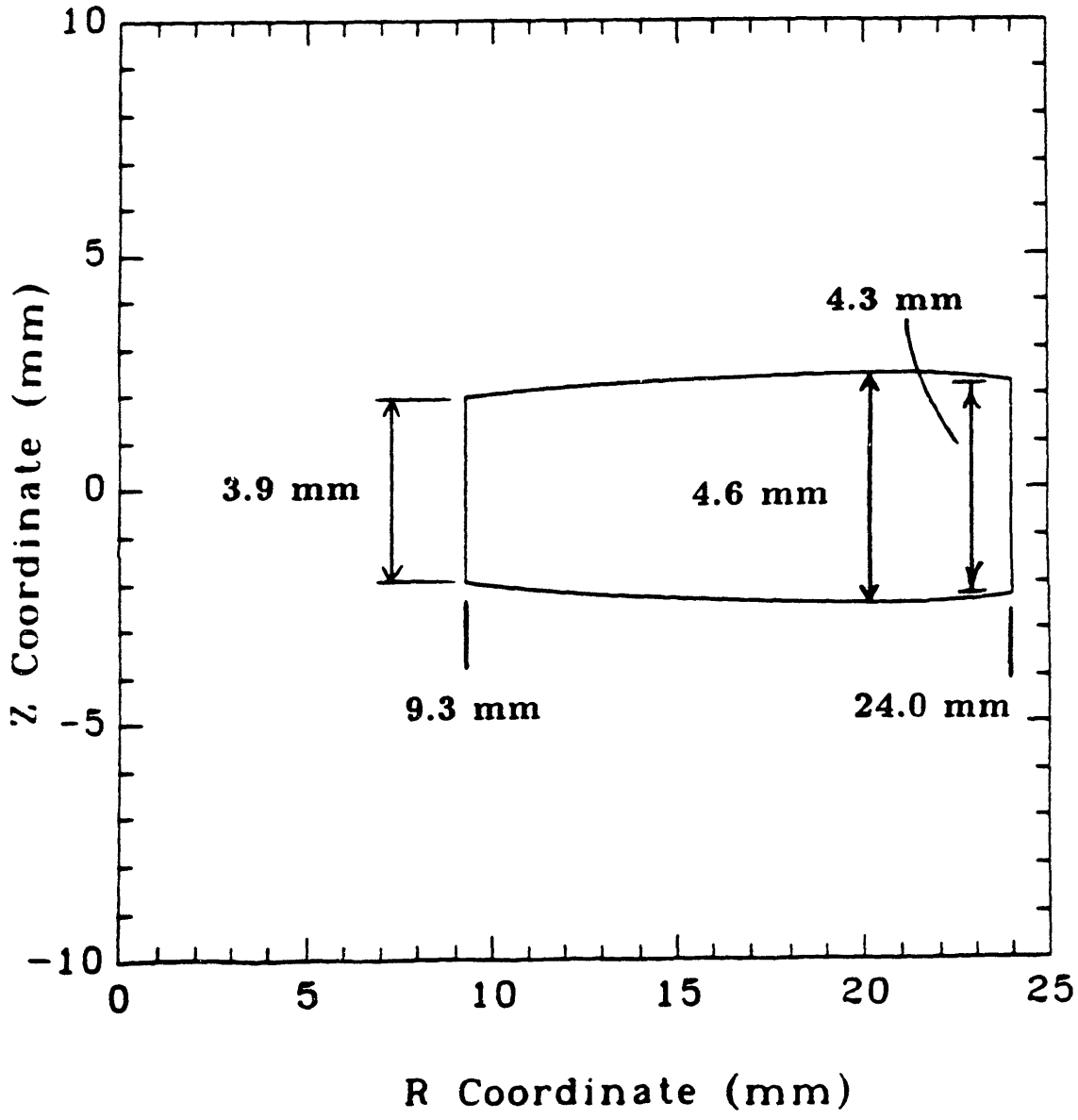

Fig. 5.11 Axisymmetric model dimensions for center turn of DTC.

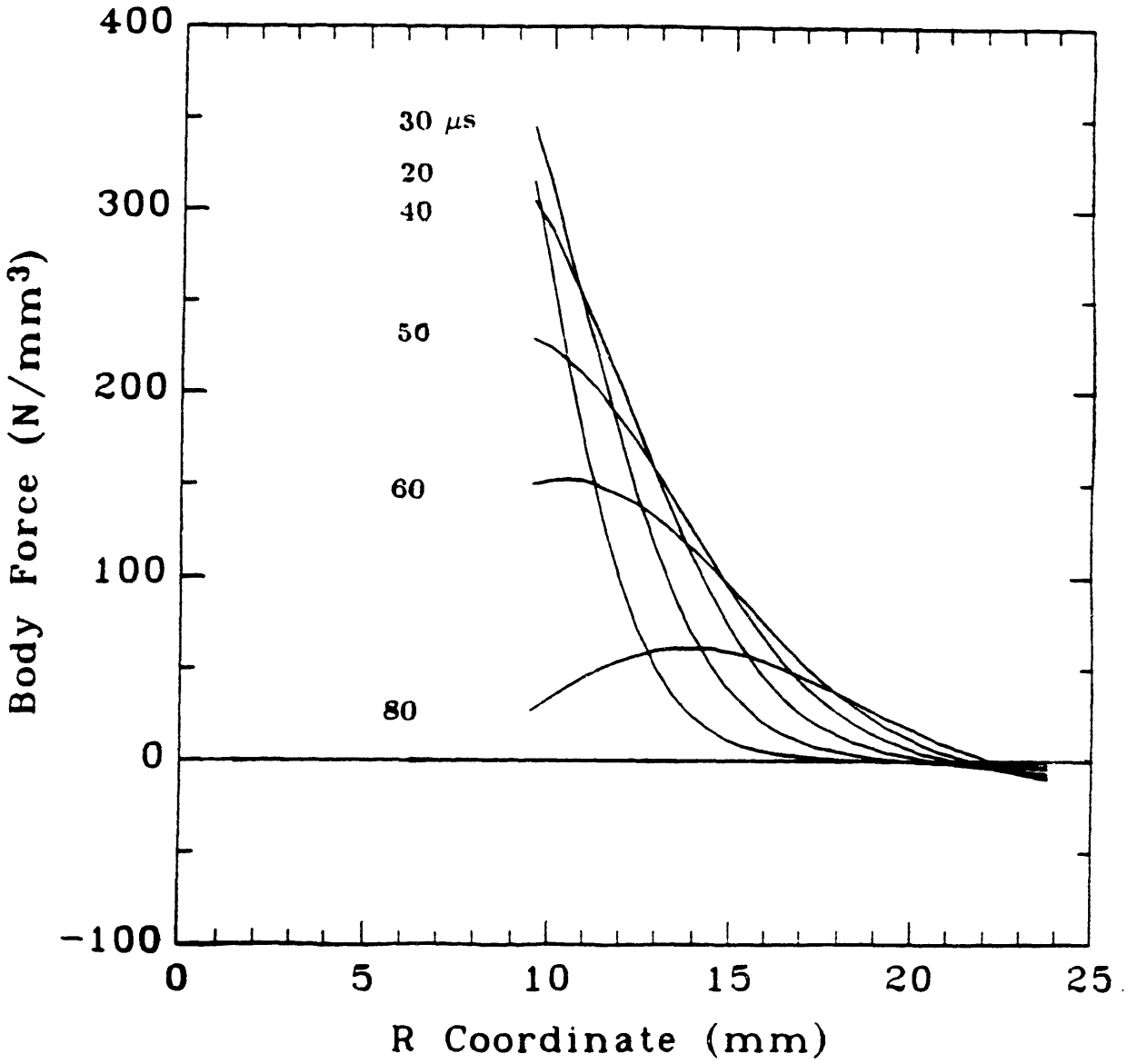

Fig. 5.12 Body force profiles in DTC for an 11.5 kV pulse ($t \leq 80$ μs).

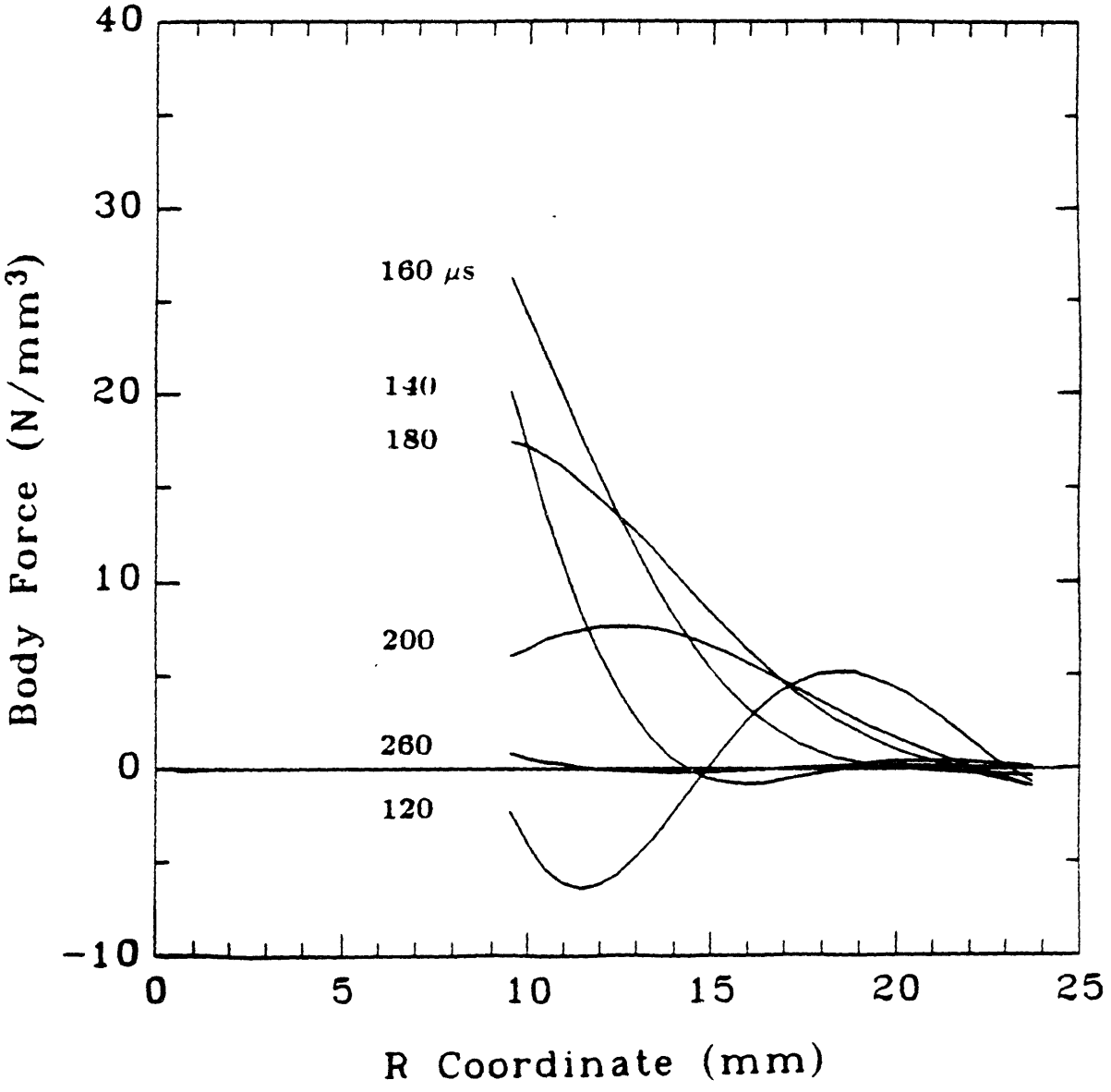

Fig. 5.13 Body force profiles in DTC for an 11.5 kV pulse between 120 and 260 μs.

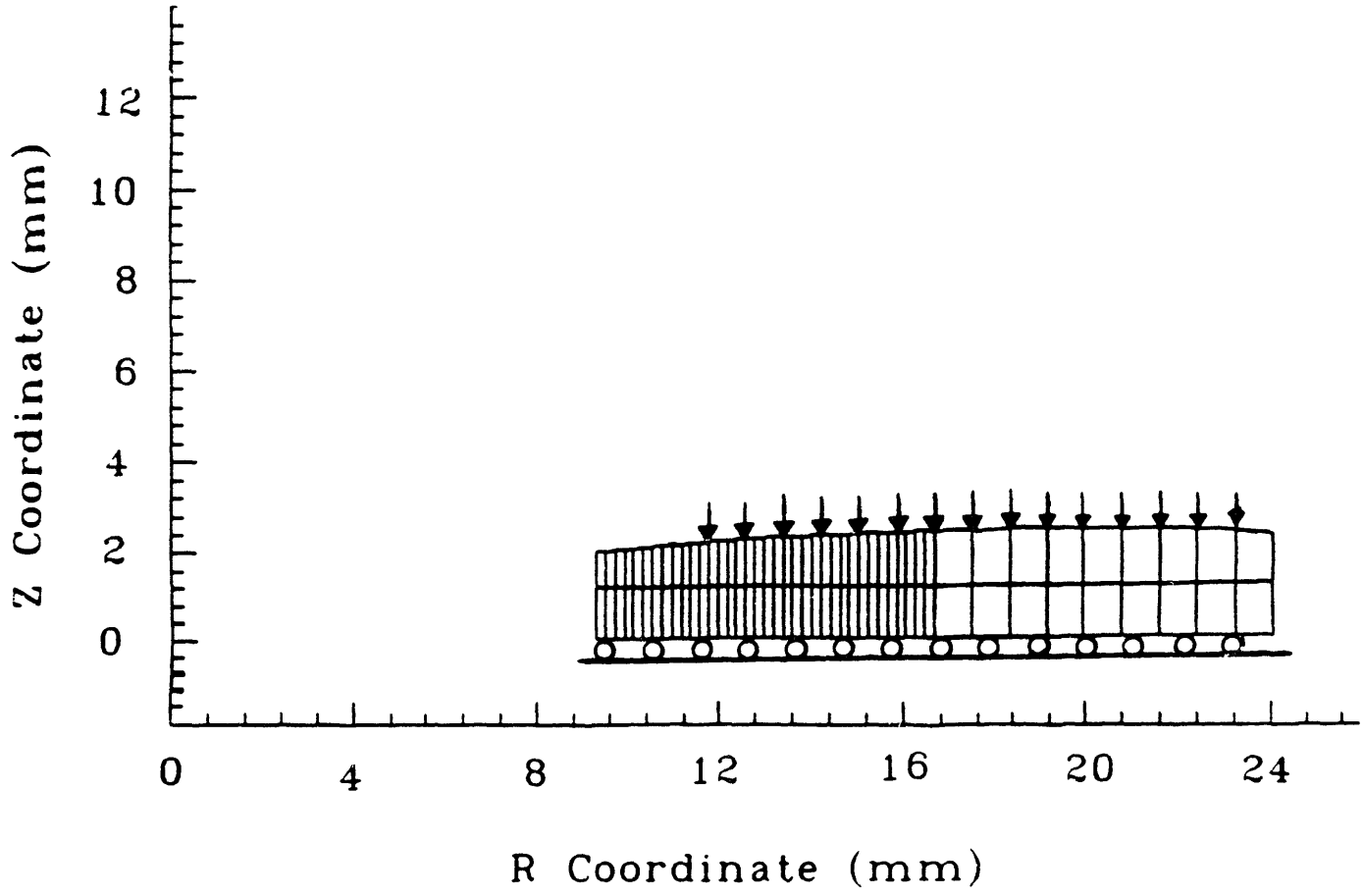

Fig. 5.14 Finite element model for center turn of DTC.

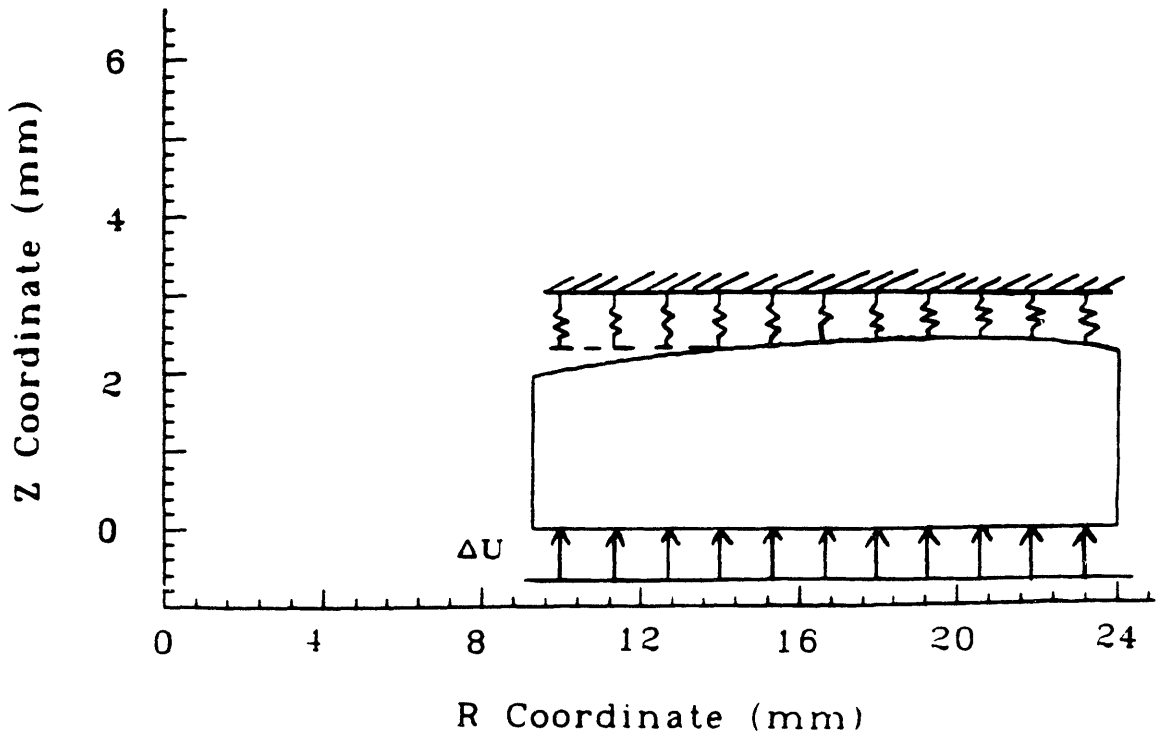

Fig. 5.15 G-7 insulation spring model for DTC.

Fig. 5.16a

Initial axial stress along symmetry plane of center turn.

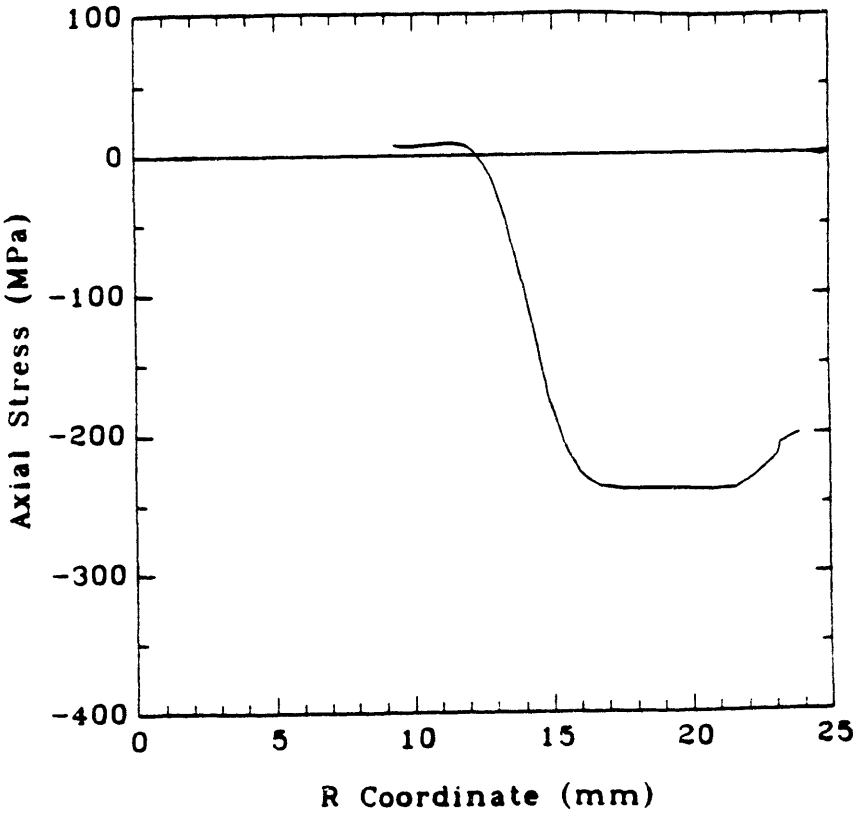

Fig. 5.16b

Initial axial stress contour bands in the center turn.

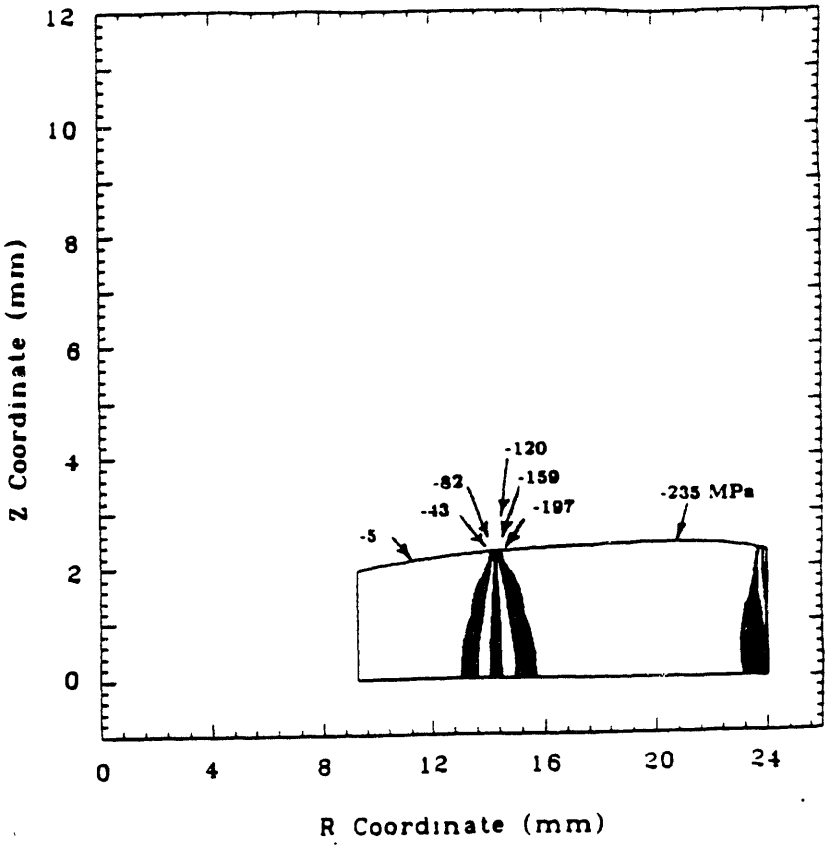

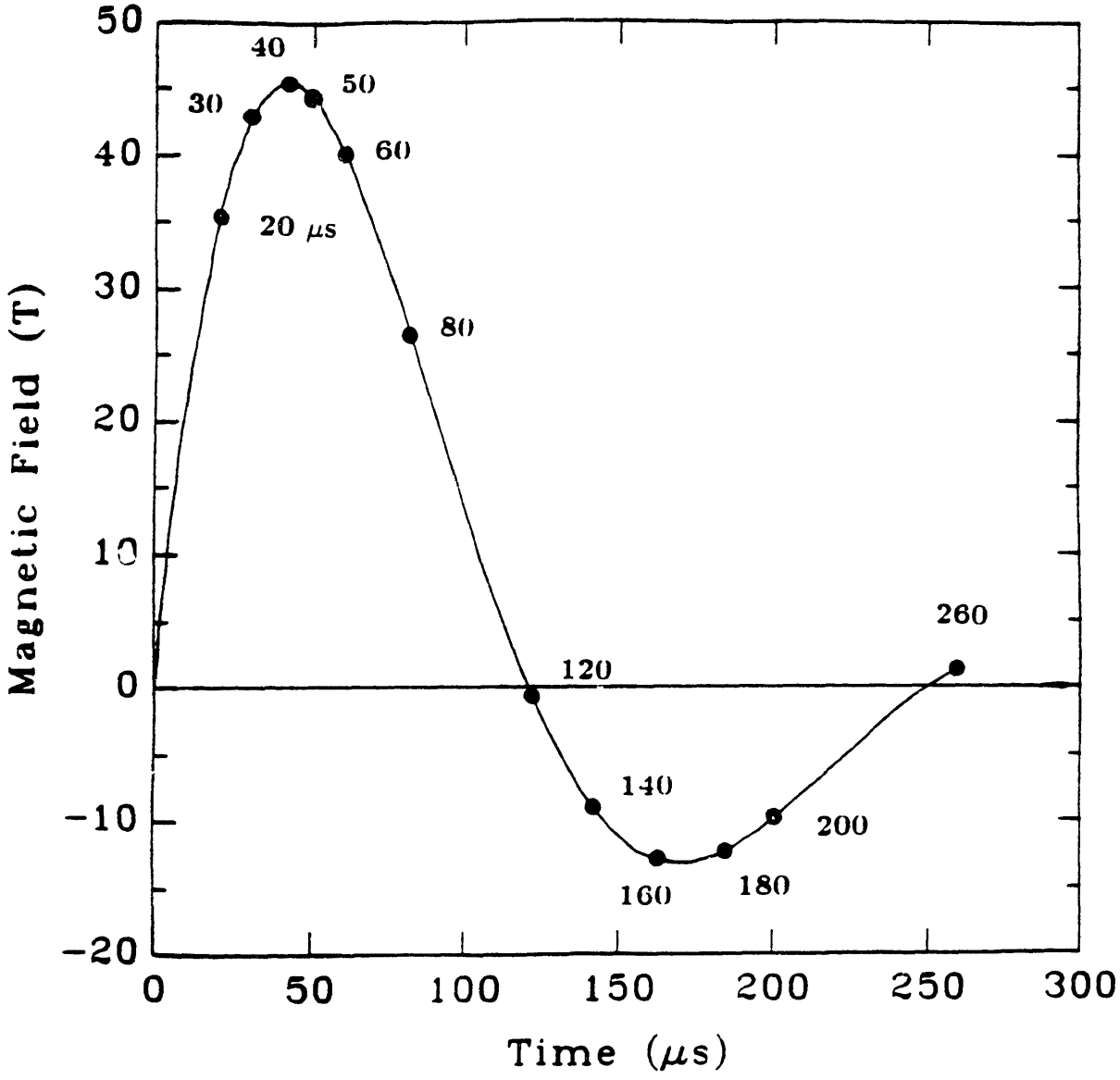

Fig. 5.17 Time step times for finite element analysis of DTC.

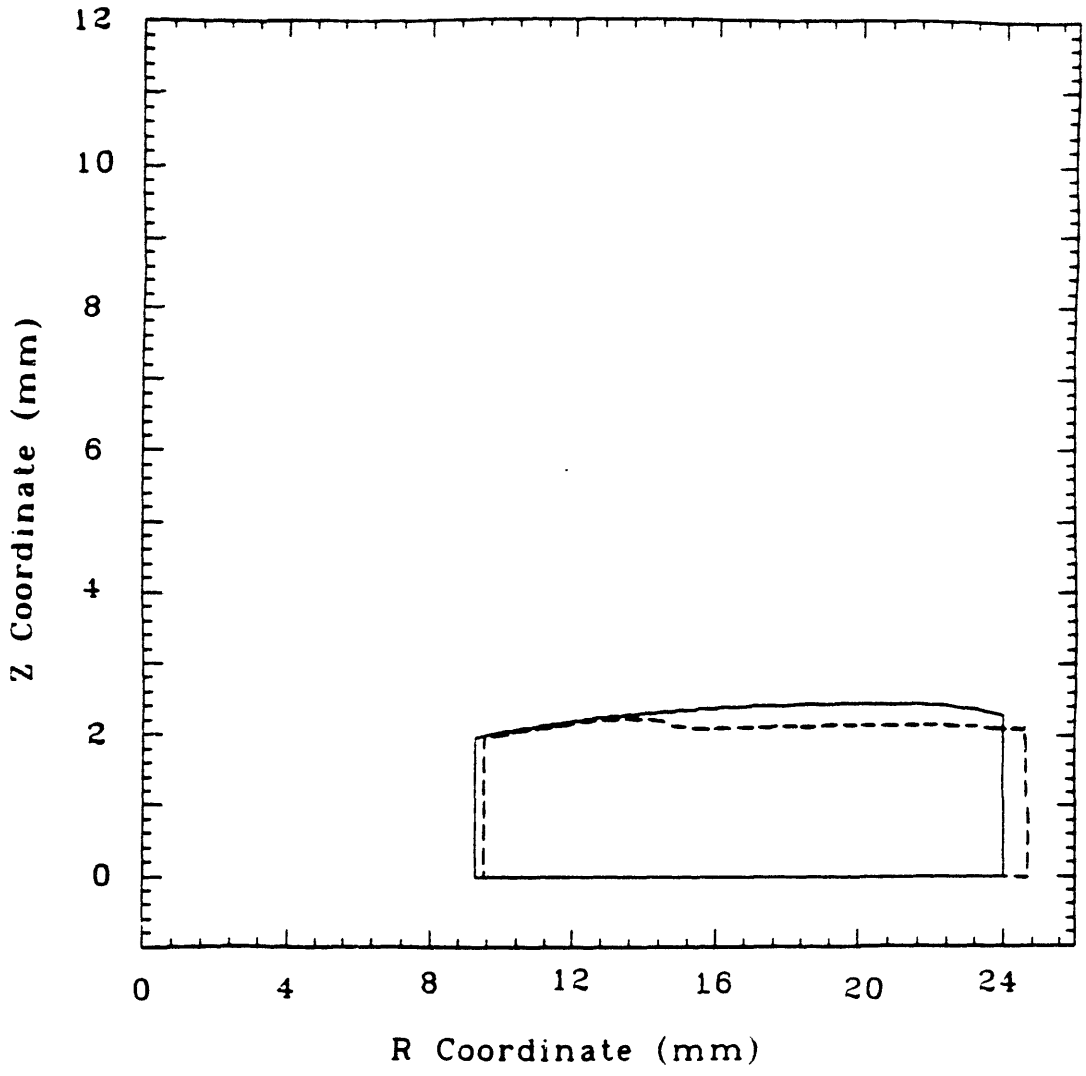

Fig. 5.18 **DTC deformed mesh outline at the beginning of the 1st pulse (Displacements $\times 100$).**

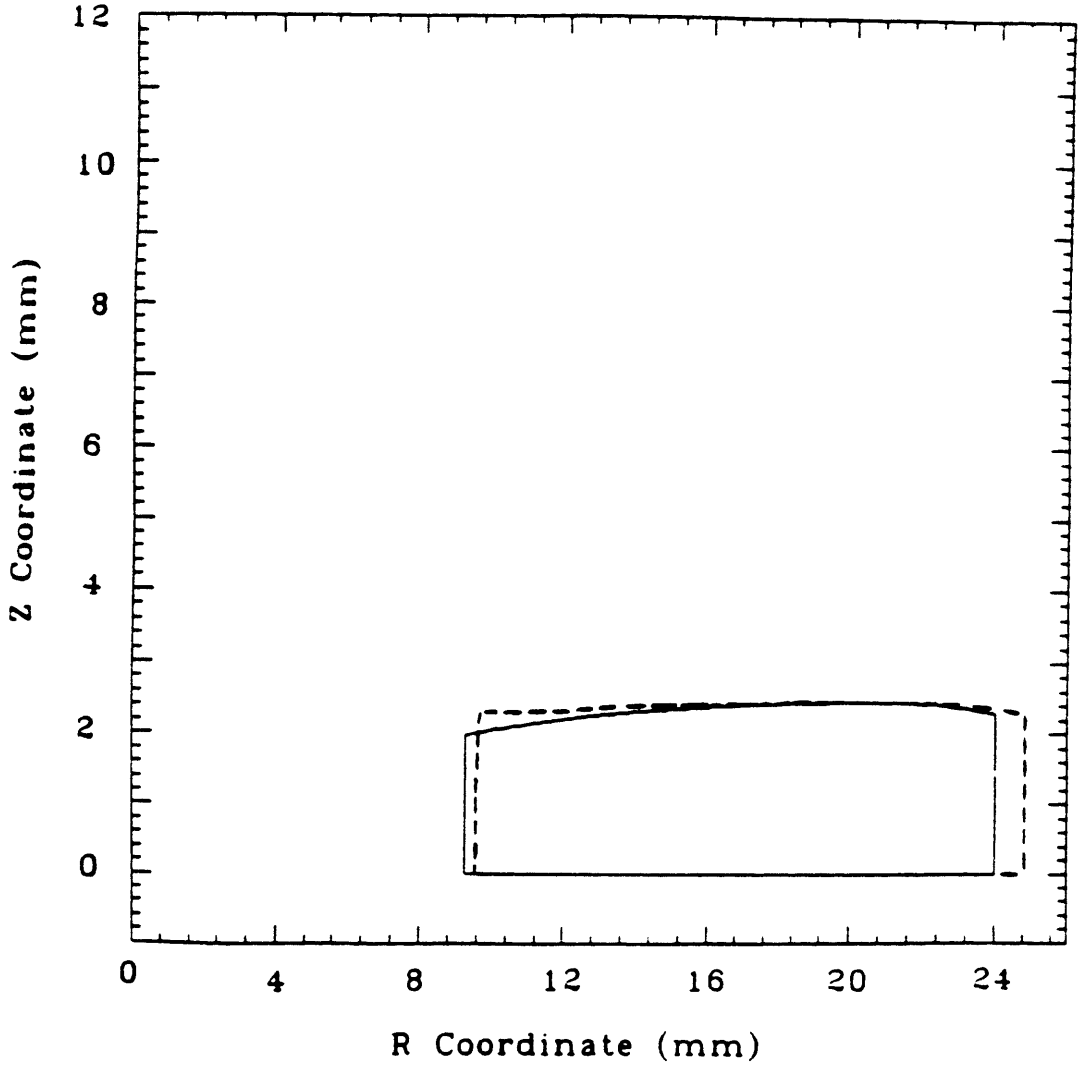

Fig. 5.19 DTC deformed mesh outline after 260 μs (Displacements $\times$10).

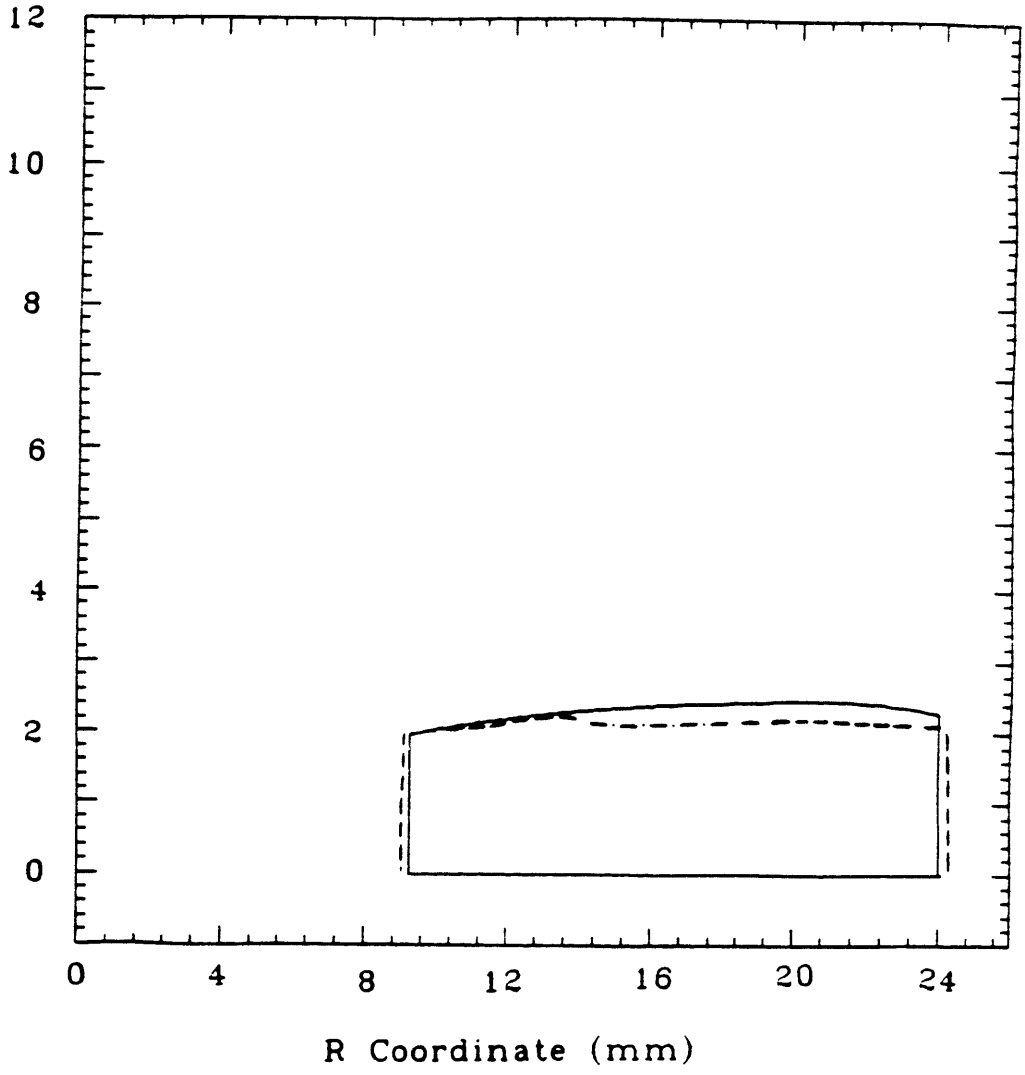

Fig. 5.20 DTC deformed mesh outline at the end of the first pulse (Displacements $\times 10$).

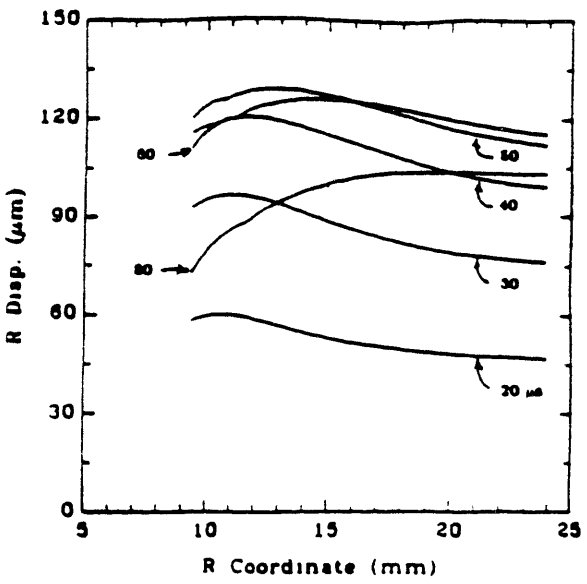

Fig. 5.21a
Radial displacements along symmetry plane of center turn between 20 and 80 μs (phenomenological rate equation analysis).

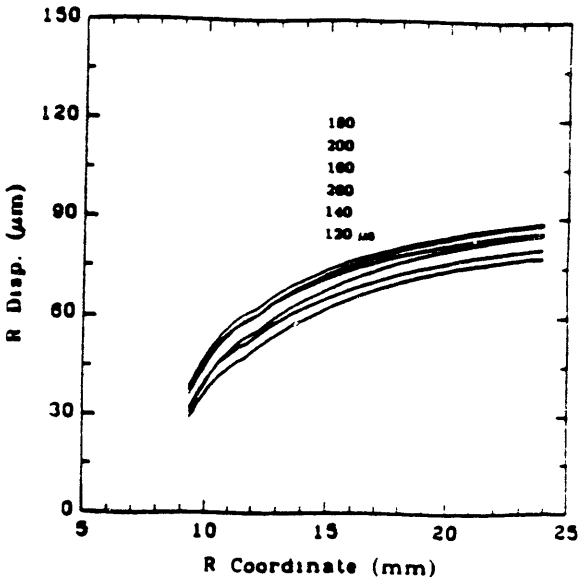

Fig. 5.21b
Radial displacements along symmetry plane of center turn between 120 and 260 μs (phenomenological rate equation analysis).

Fig. 5.21c
Radial displacements along symmetry plane of center turn between 0.001 s and 15 min (phenomenological rate equation analysis).

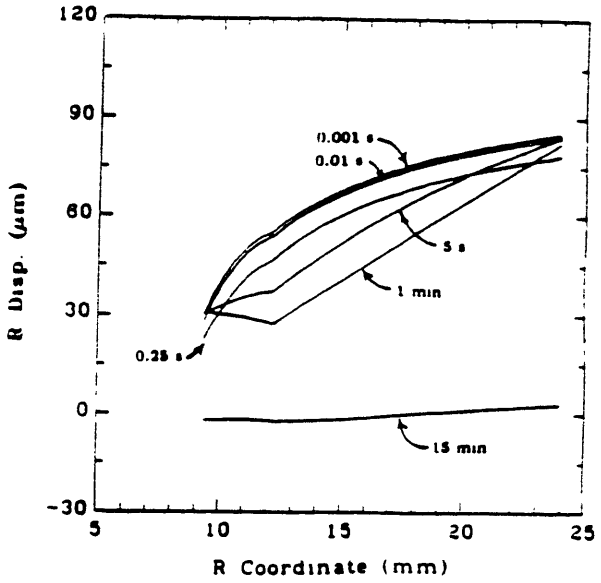

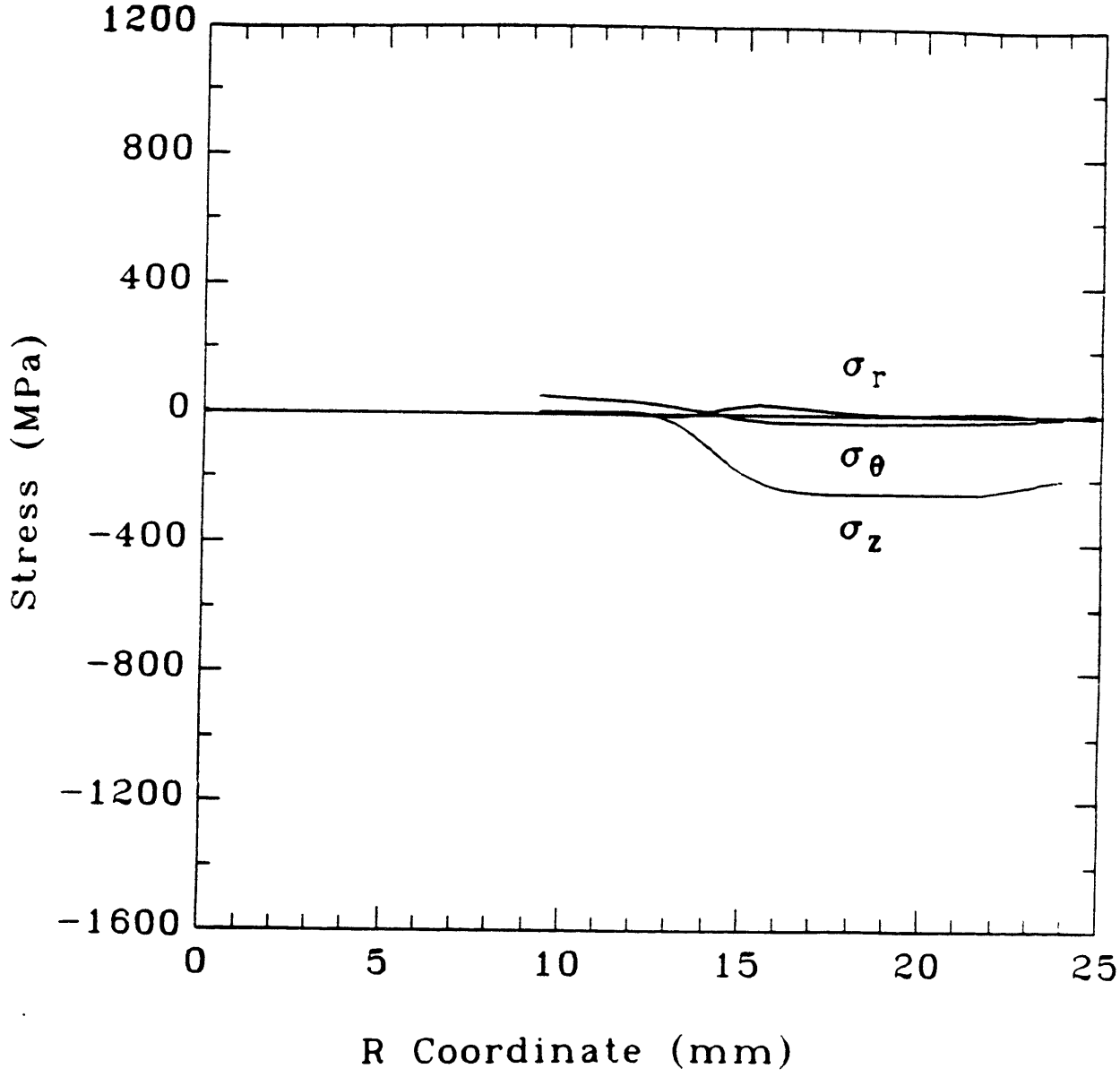

Fig. 5.22 Normal stresses from phenomenological rate equation analysis of DTC at 0 s.

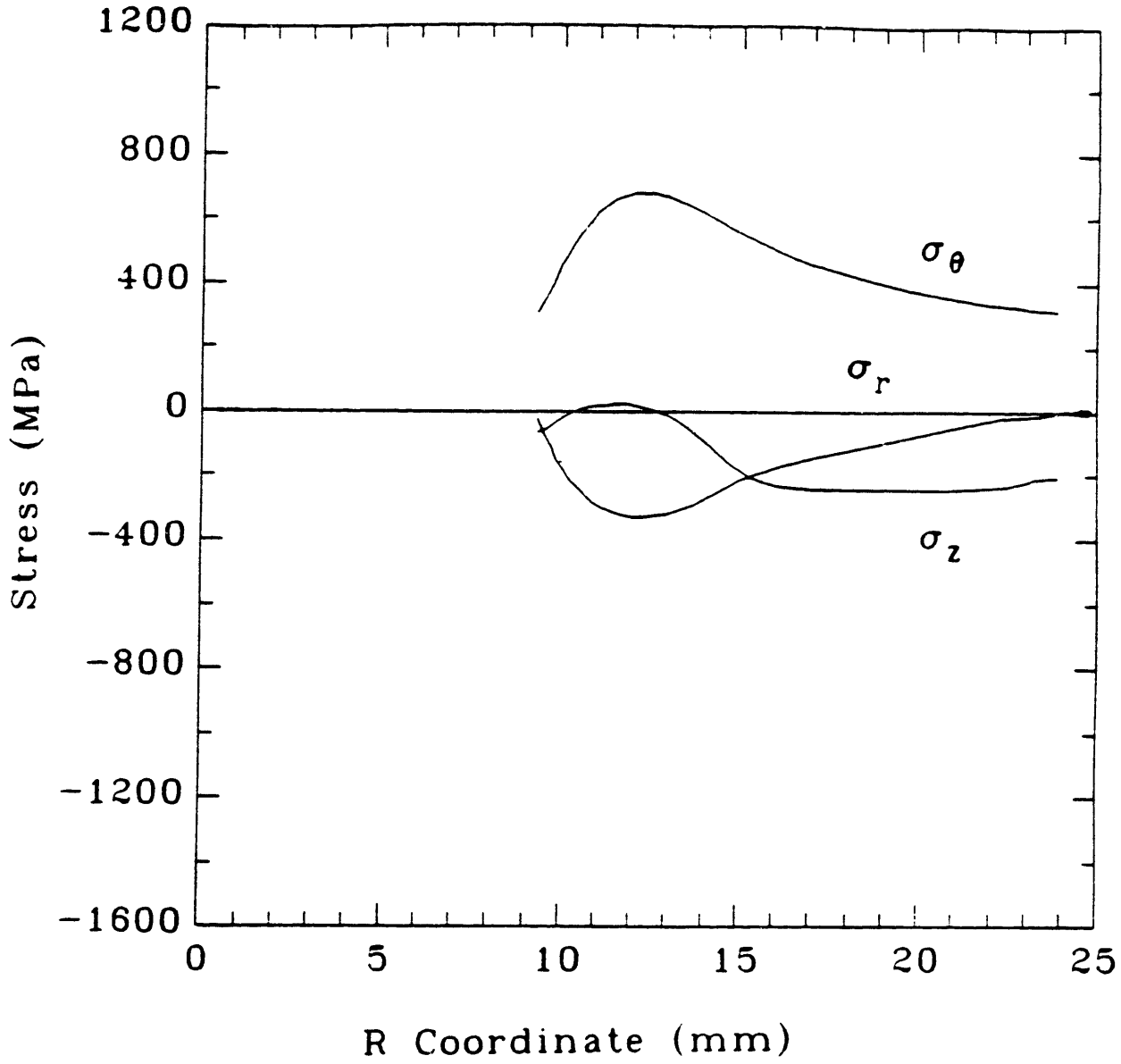

Fig. 5.23 Normal stresses from phenomenological rate equation analysis of DTC at 20 μs.

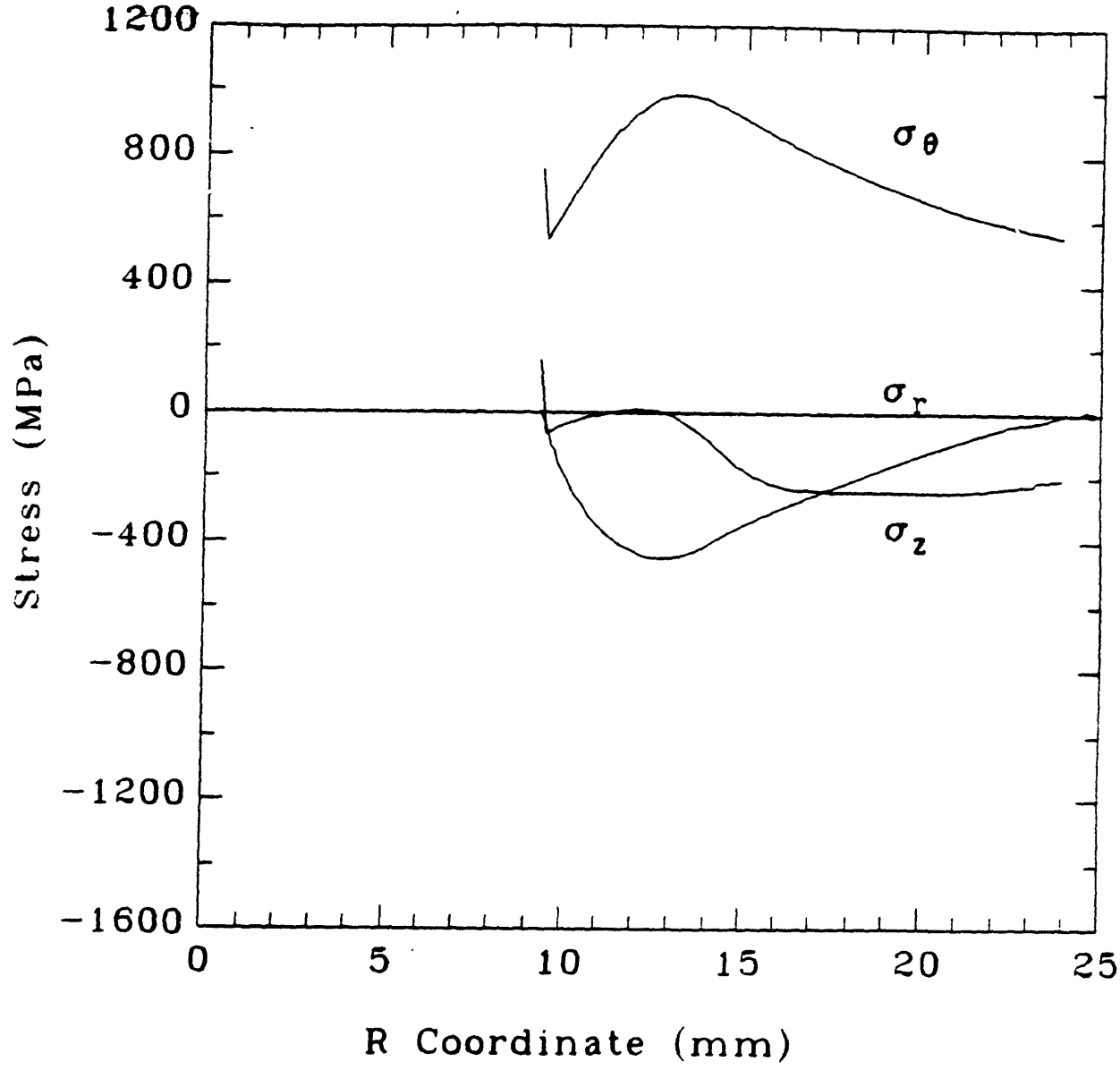

Fig. 5.24 **Normal stresses from phenomenological rate equation analysis of DTC at 30 μs.**

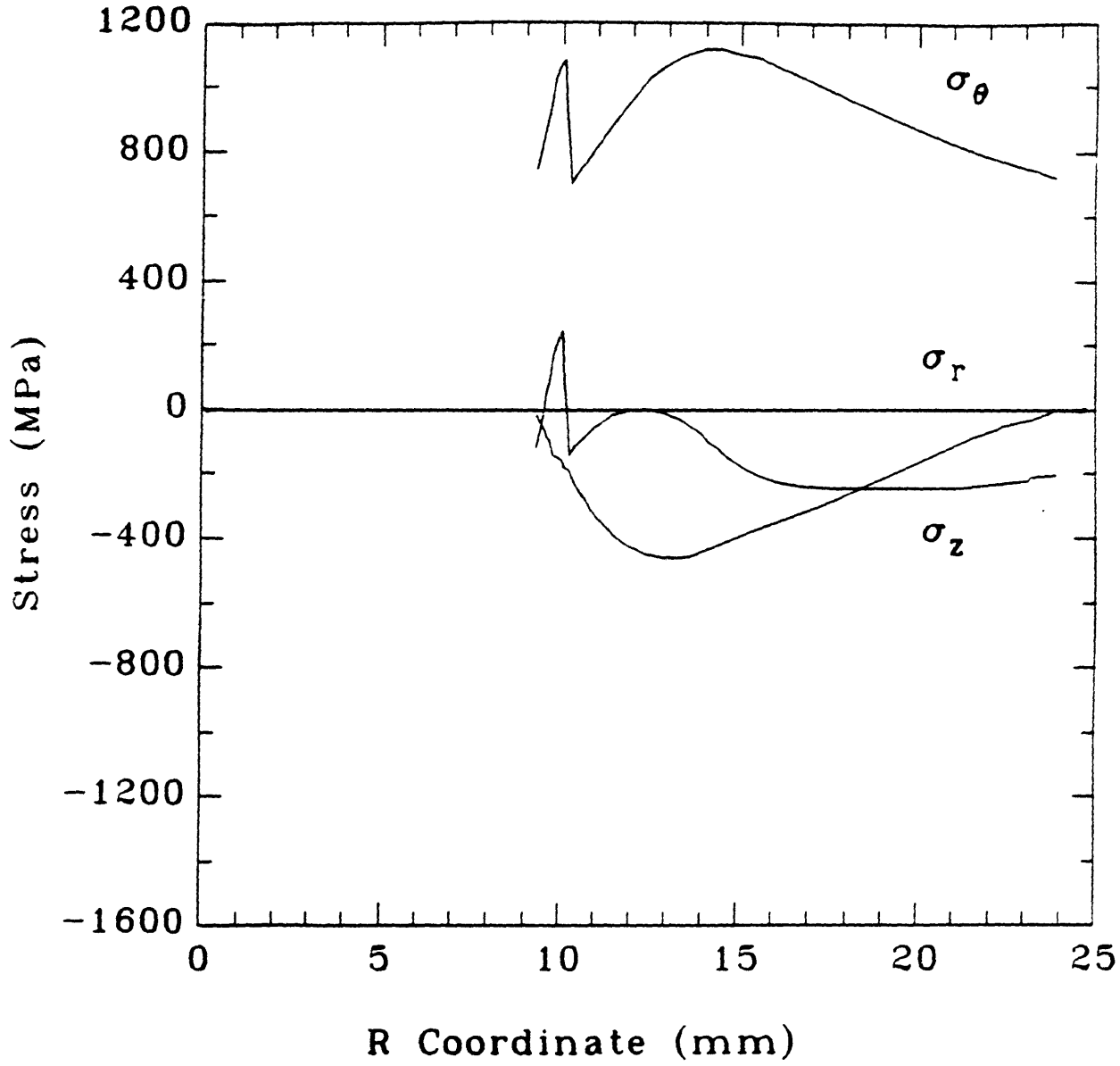

Fig. 5.25 **Normal stresses from phenomenological rate equation analysis of DTC at 40 μs.**

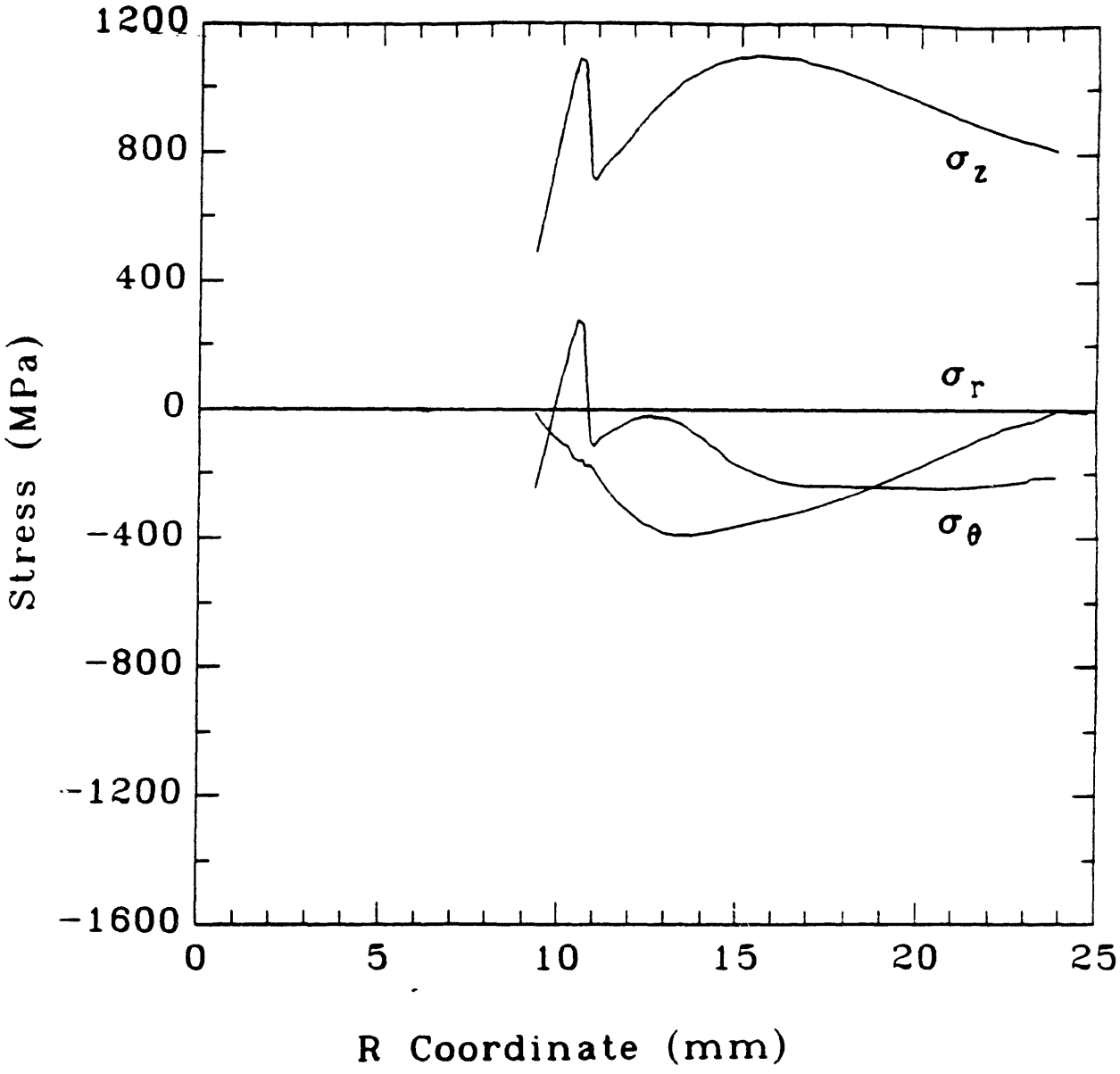

Fig. 5.26 **Normal stresses from phenomenological rate equation analysis of DTC at 50 μs.**

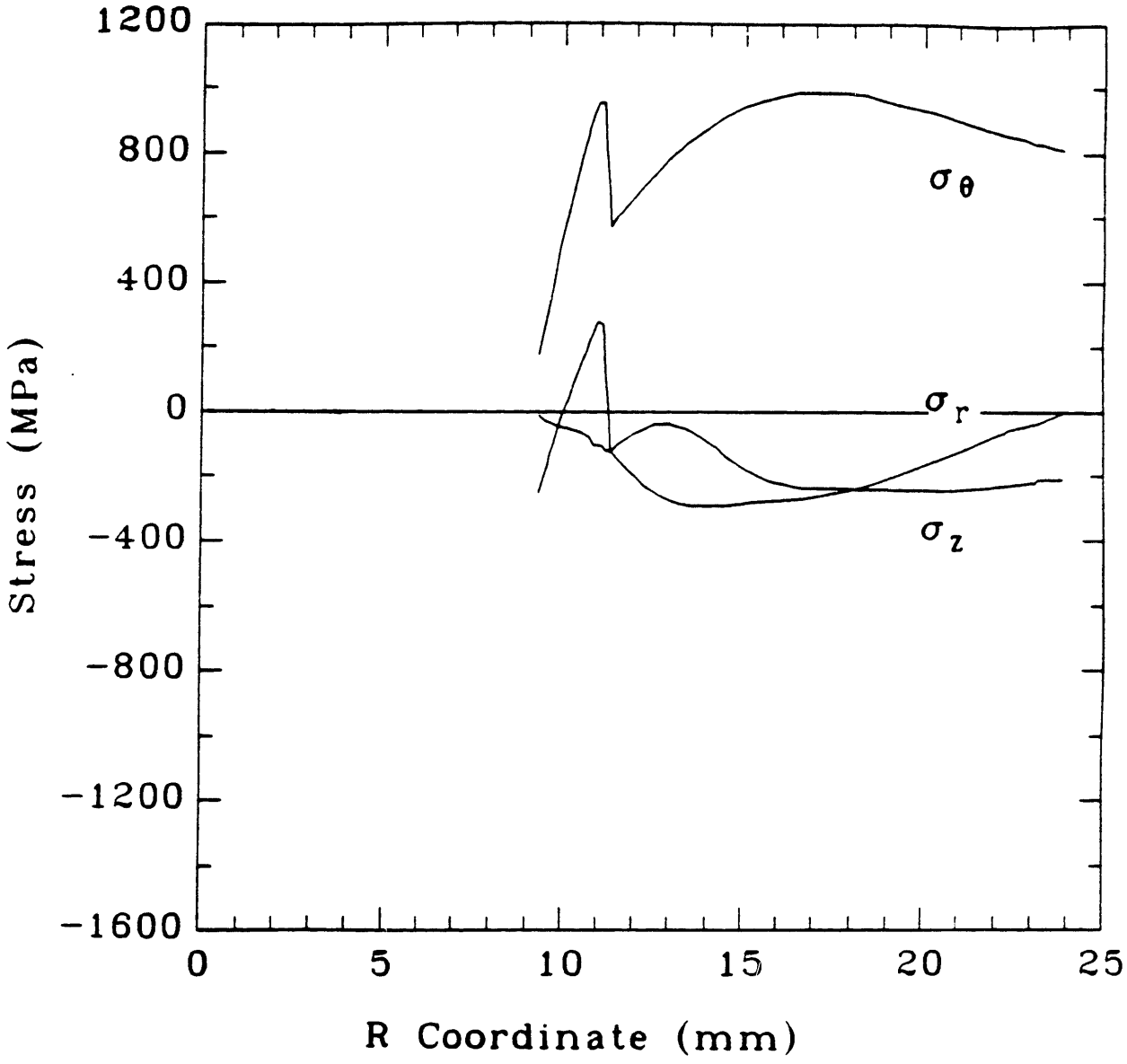

Fig. 5.27 **Normal stresses from phenomenological rate equation analysis of DTC at 60 μs.**

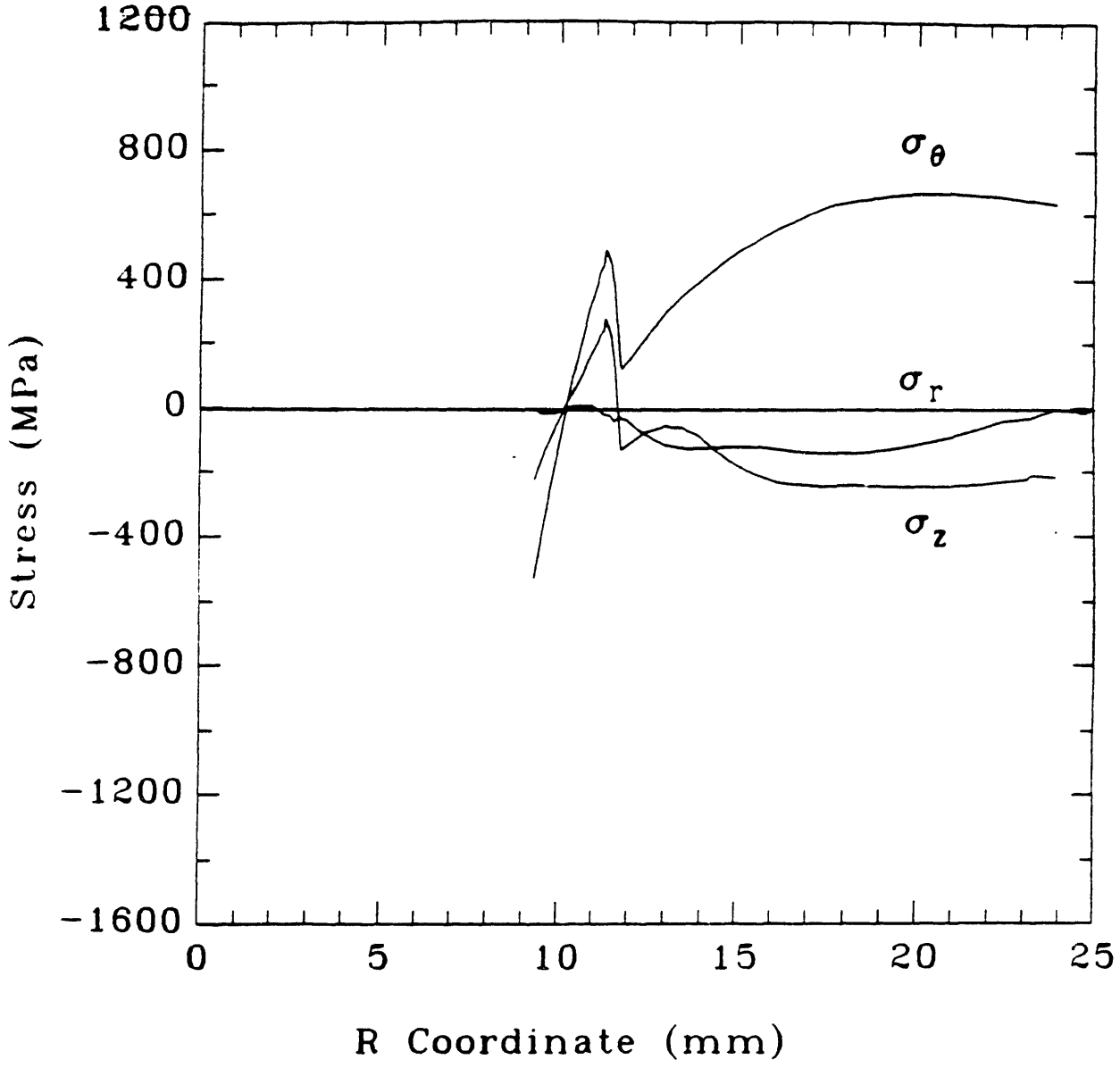

Fig. 5.28 Normal stresses from phenomenological rate equation analysis of DTC at 80 μs.

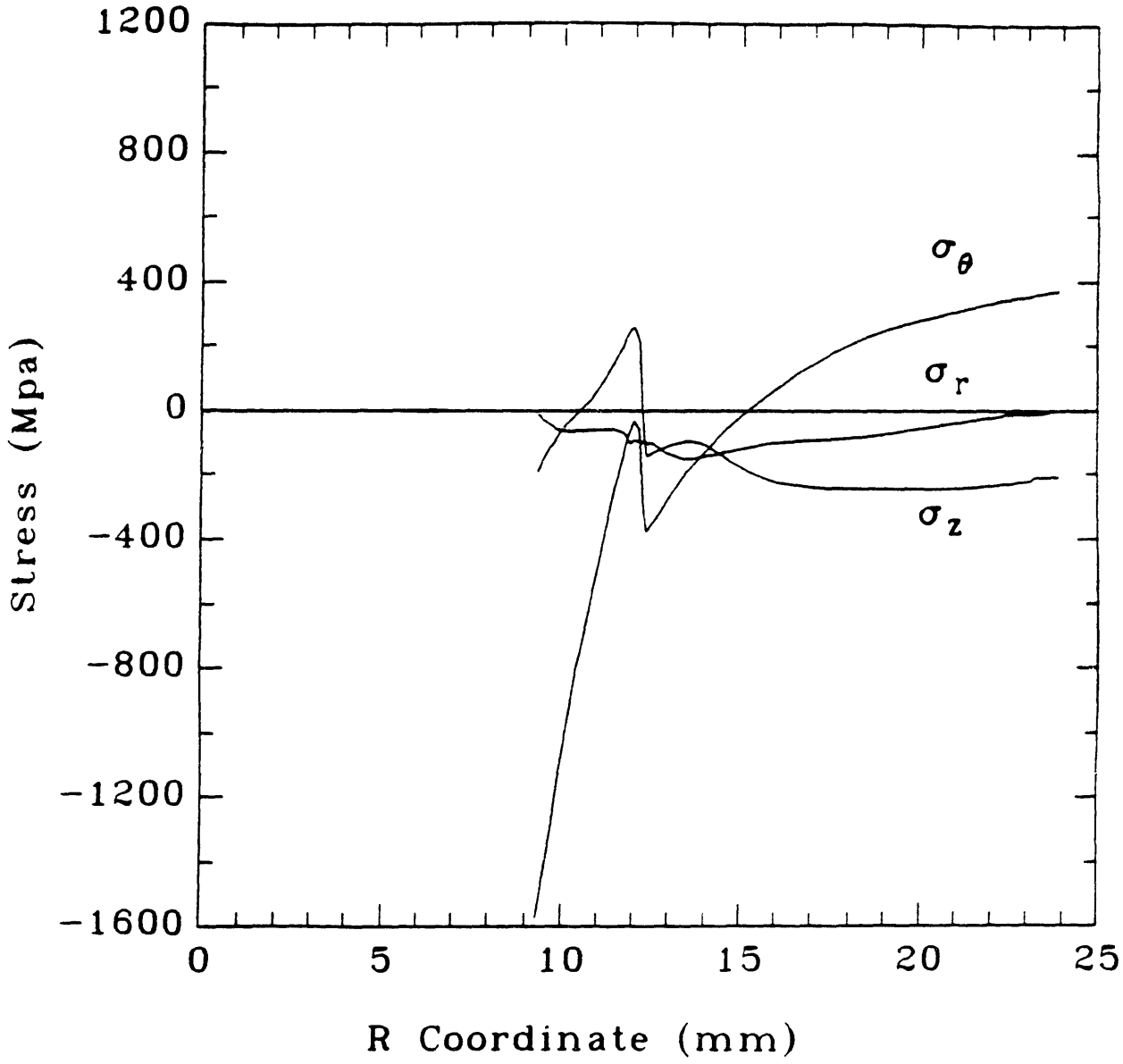

Fig. 5.29 Normal stresses from phenomenological rate equation analysis of DTC at 260 μs.

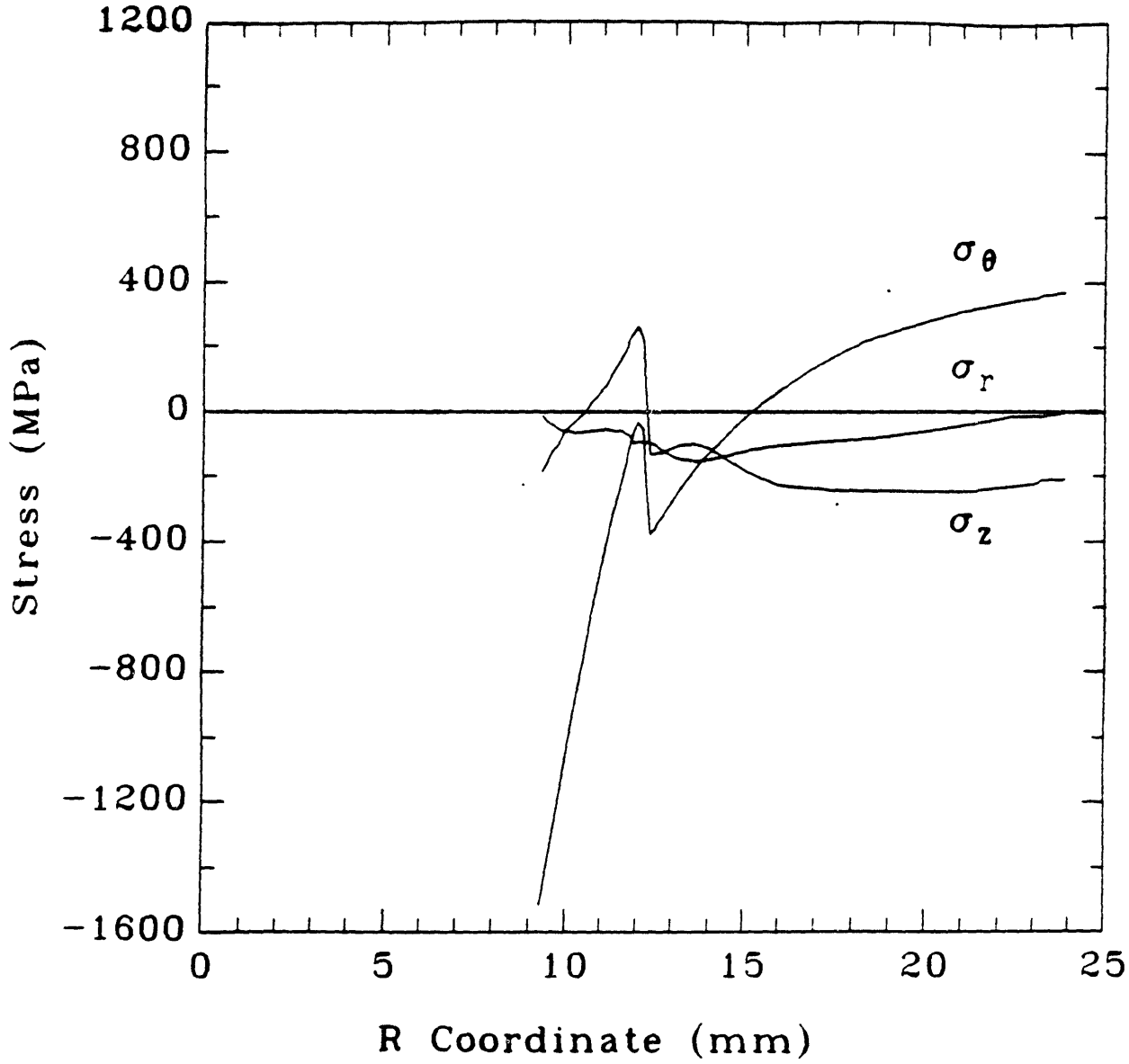

Fig. 5.30 Normal stresses from phenomenological rate equation analysis of DTC at 0.001 s.

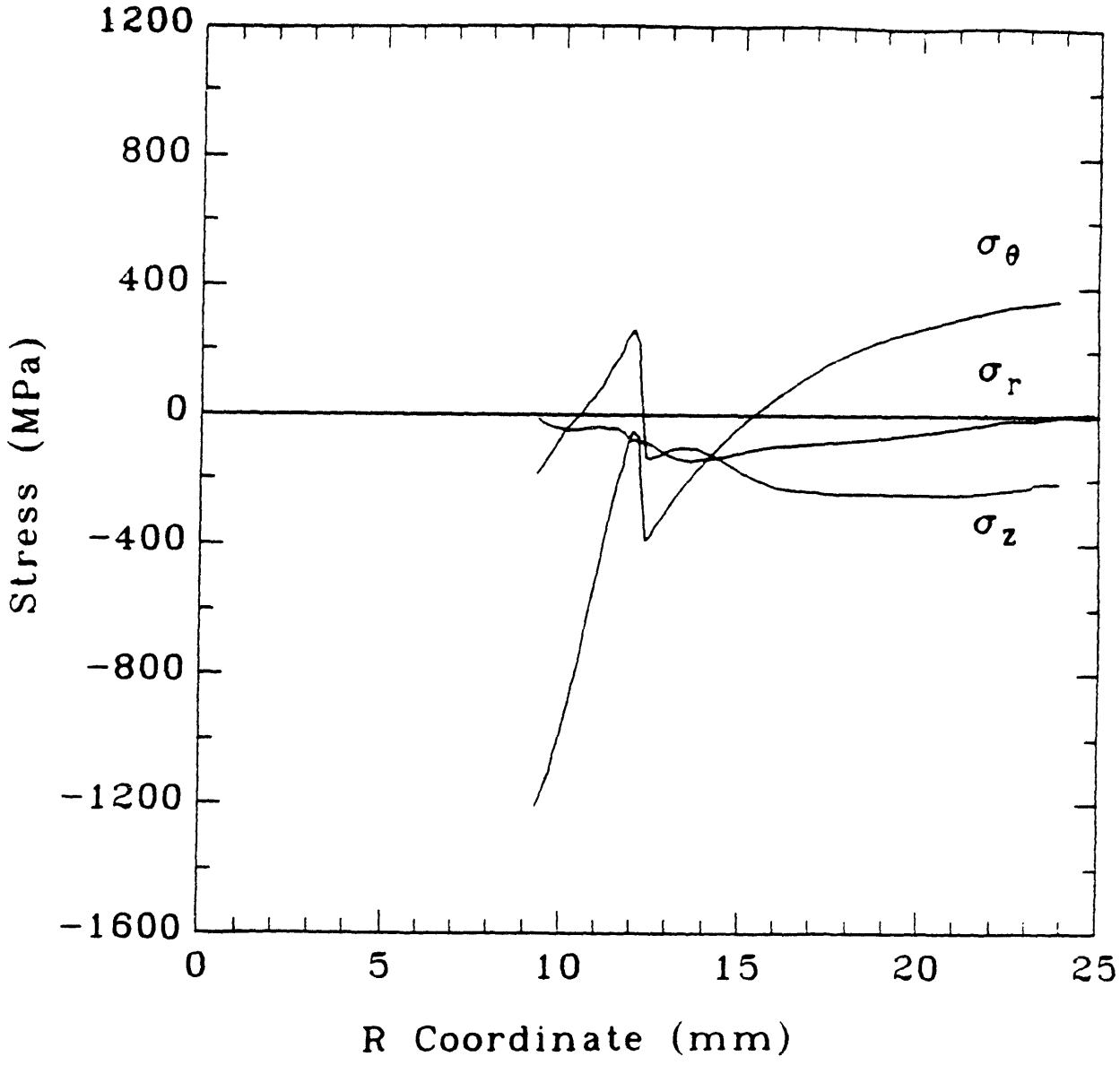

Fig. 5.31 Normal stresses from phenomenological rate equation analysis of DTC at 0.01 s.

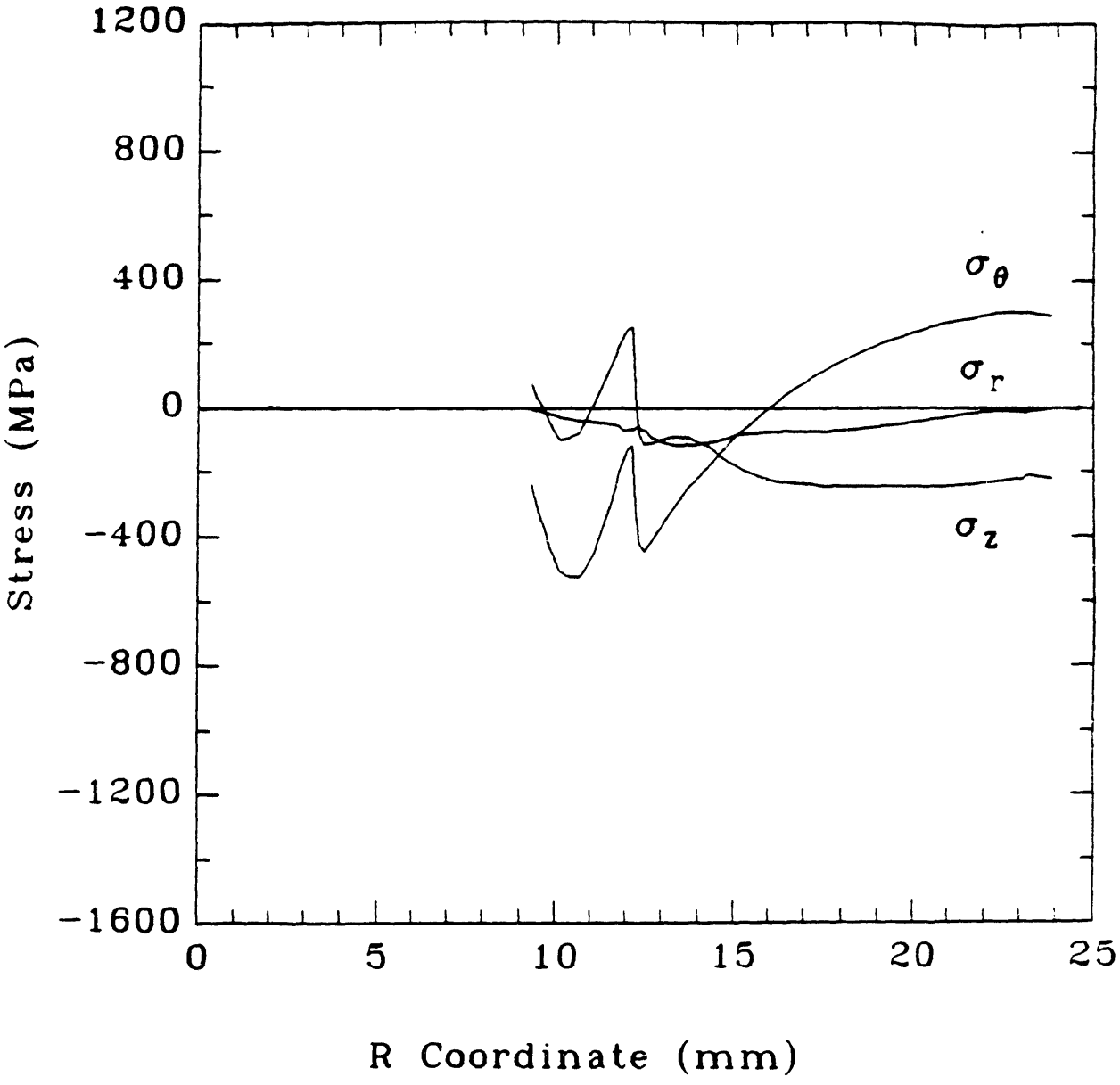

Fig. 5.32 Normal stresses from phenomenological rate equation analysis of DTC at 0.25 s.

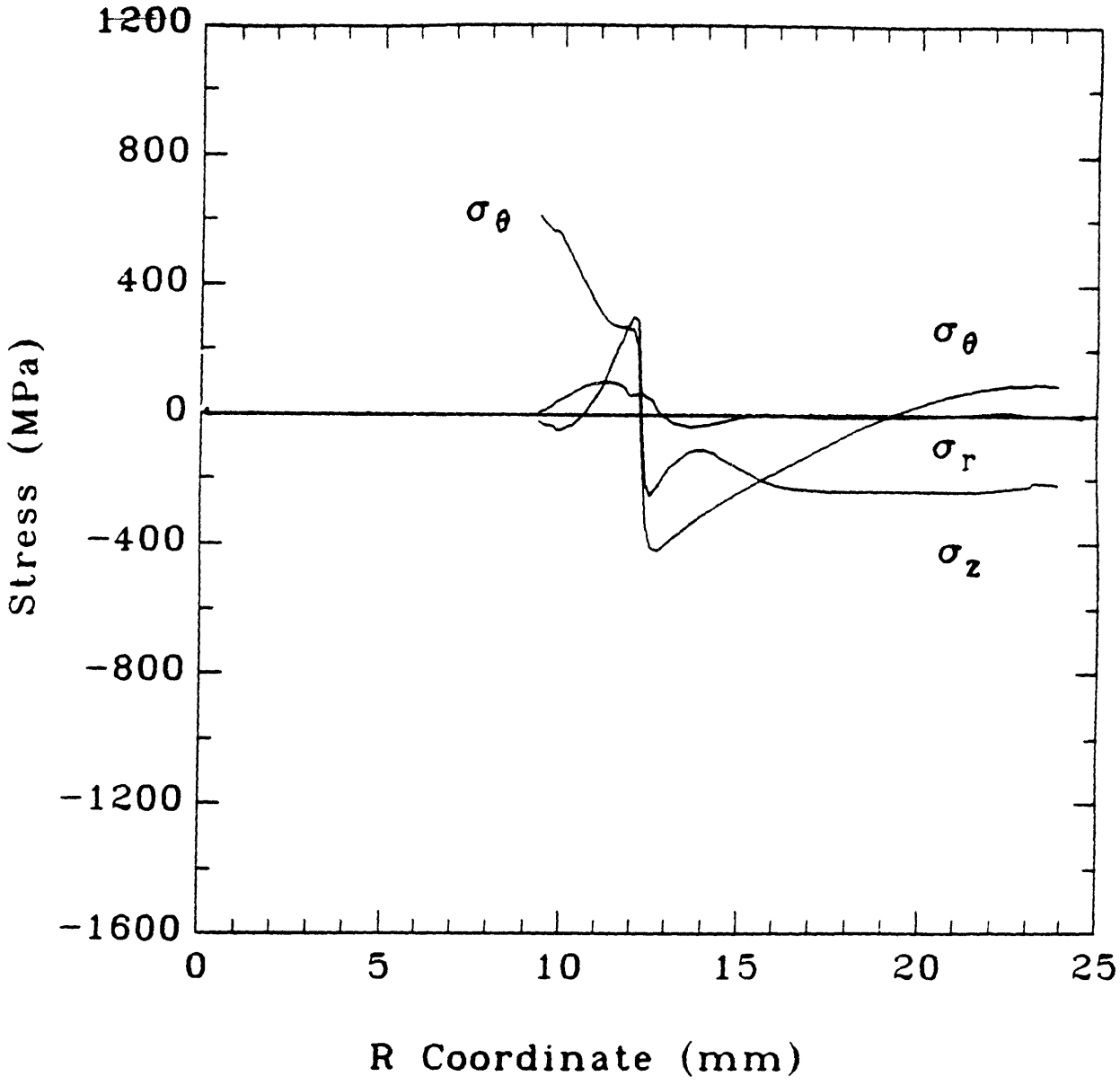

Fig. 5.33 Normal stresses from phenomenological rate equation analysis of DTC at 5 s.

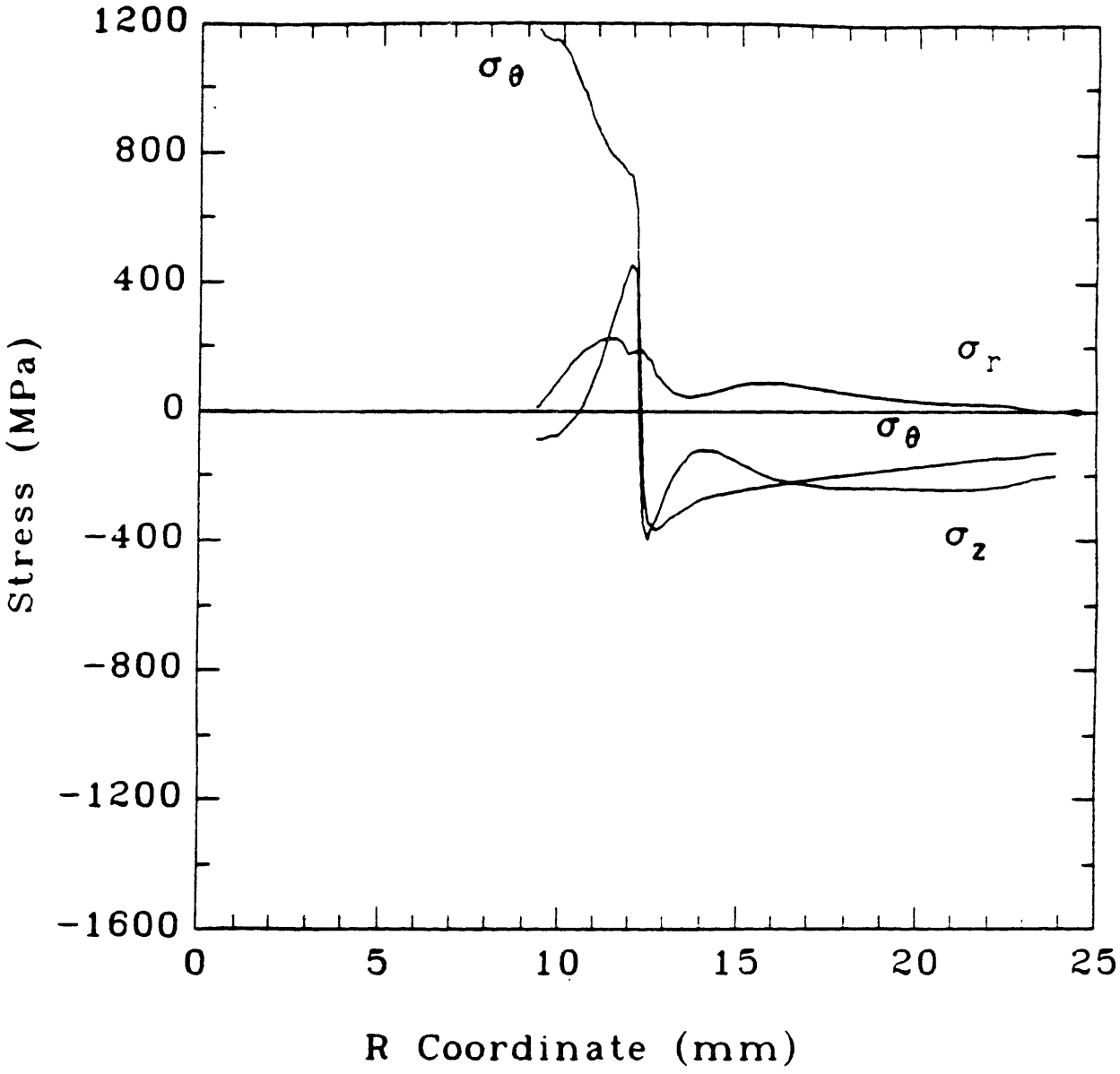

Fig. 5.34 Normal stresses from phenomenological rate equation analysis of DTC at 1 min.

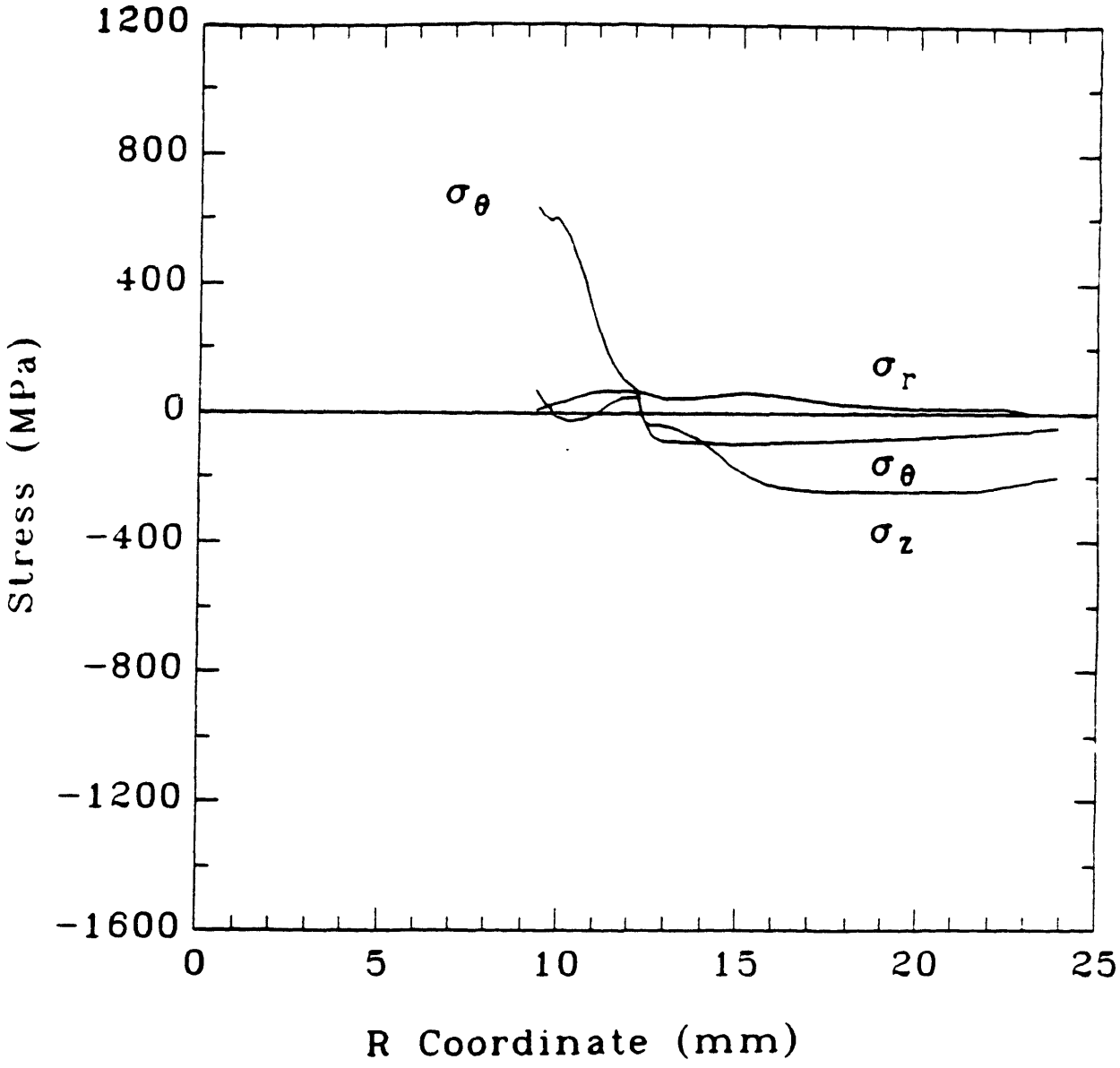

Fig. 5.35 Normal stresses from phenomenological rate equation analysis of DTC at 15 min.

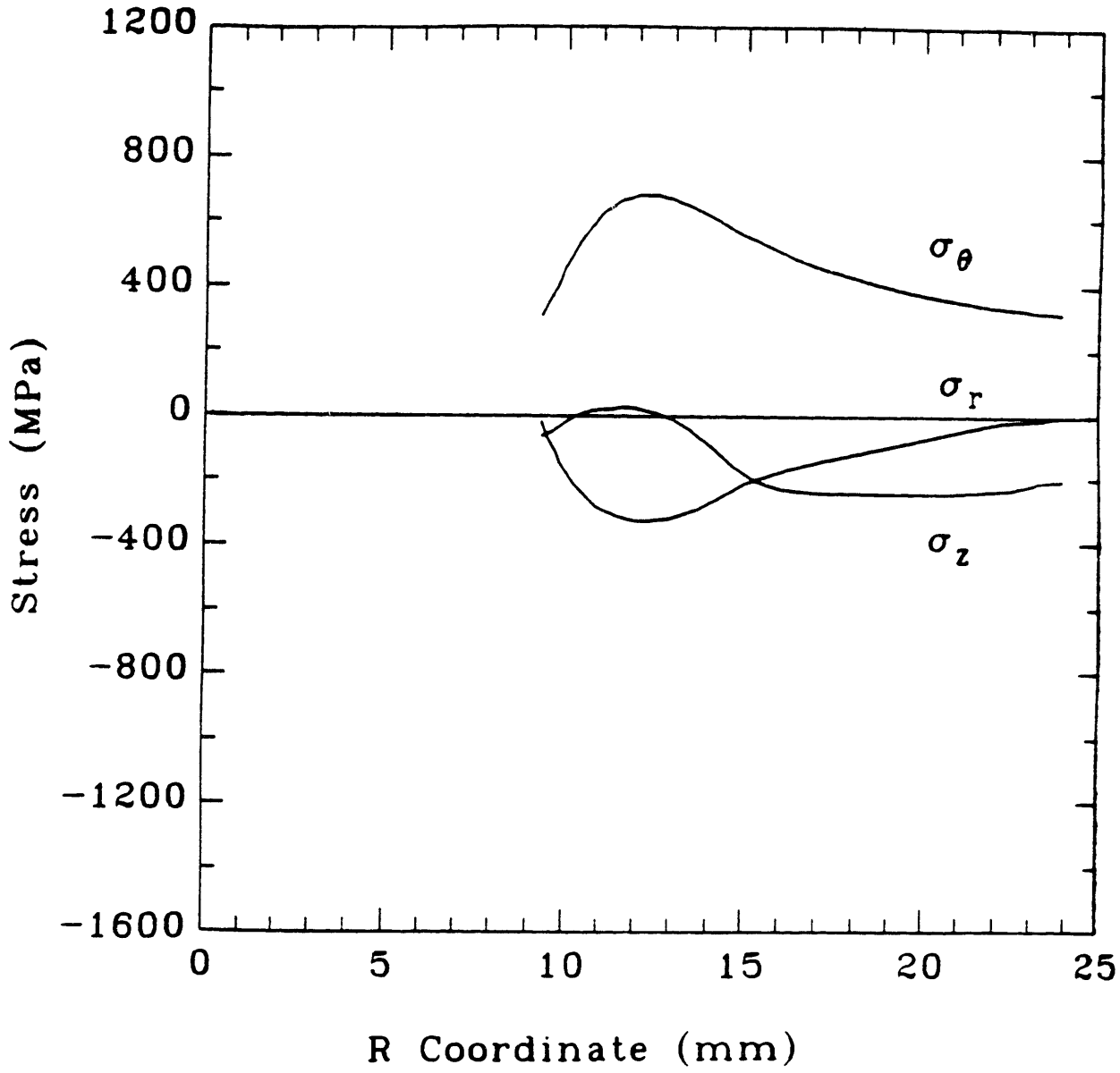

Fig. 5.36 Normal stresses from Arrhenius rate equation analysis of DTC at 20 μs.

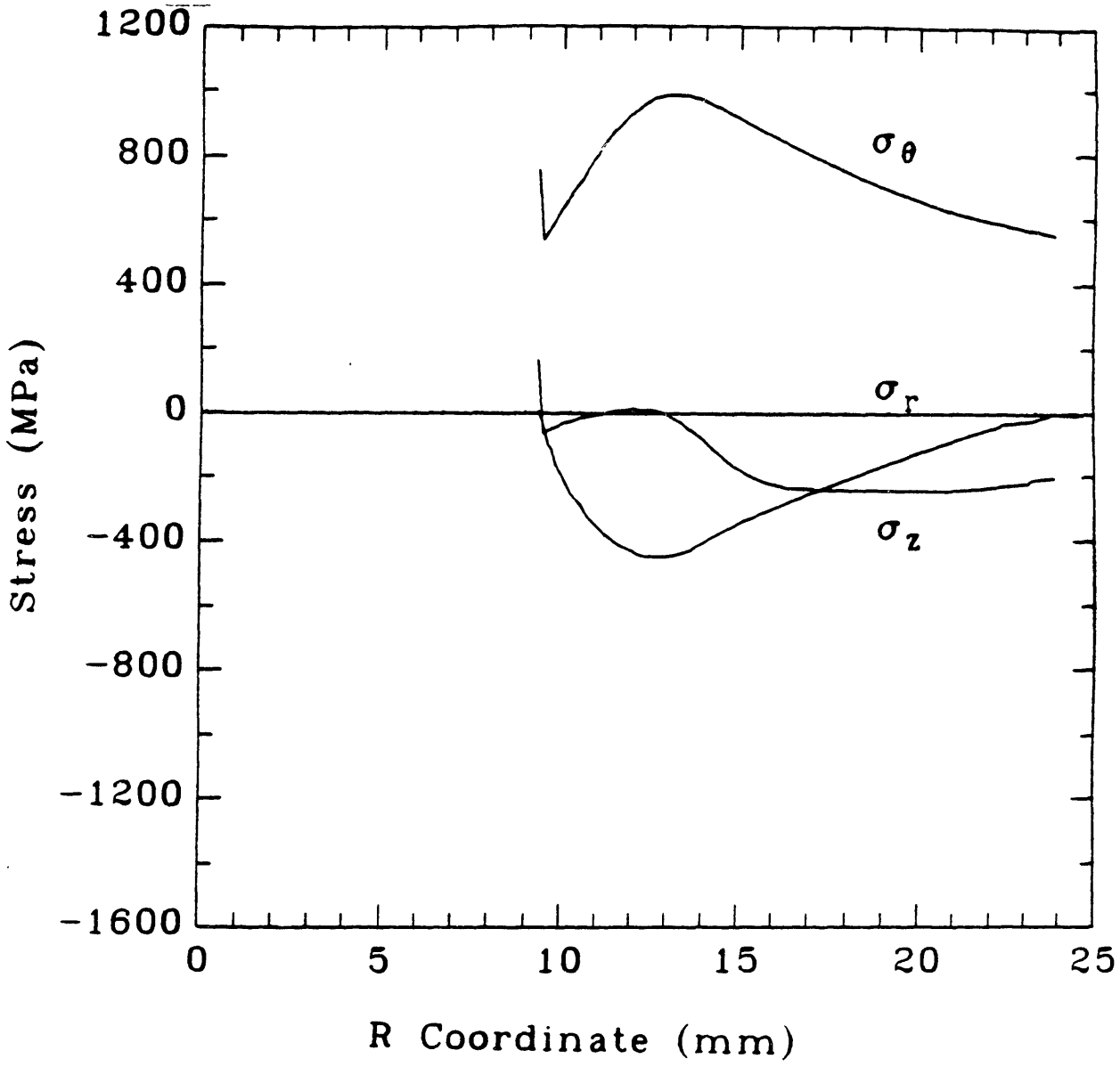

Fig. 5.37 Normal stresses from Arrhenius rate equation analysis of DTC at 30 μs.

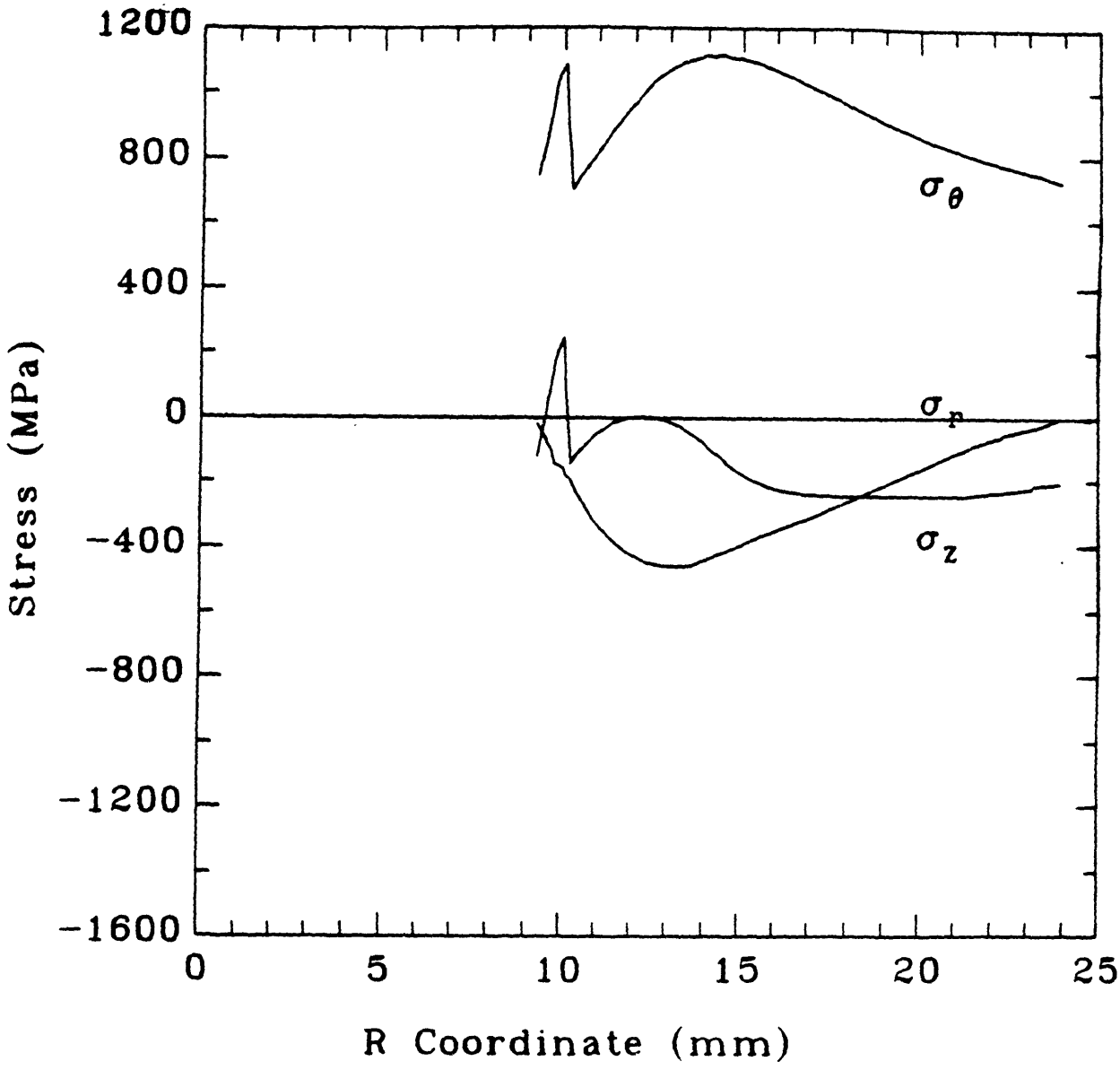

Fig. 5.38 Normal stresses from Arrhenius rate equation analysis of DTC at 40 μs.

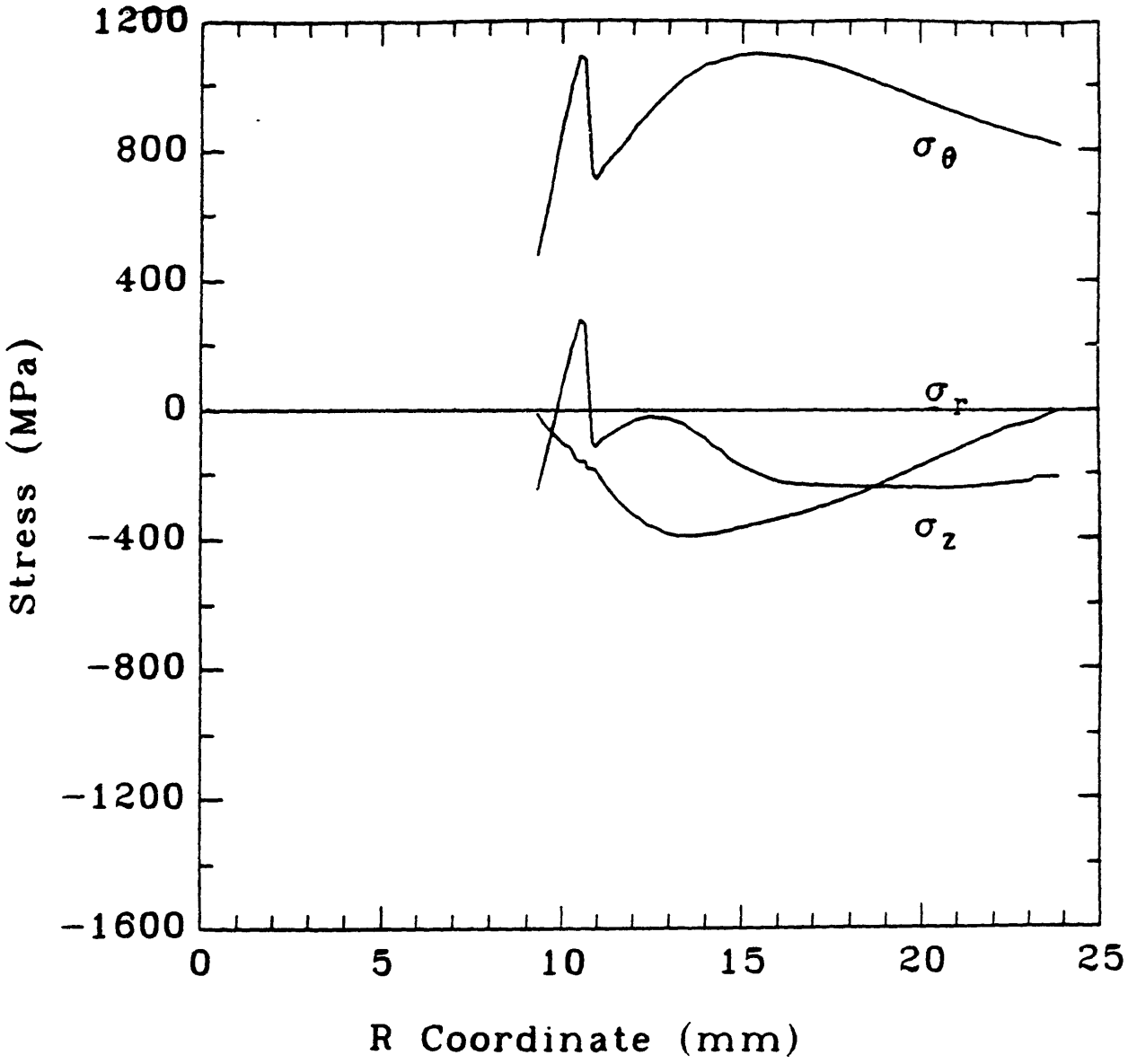

Fig. 5.39 Normal stresses from Arrhenius rate equation analysis of DTC at 50 μs.

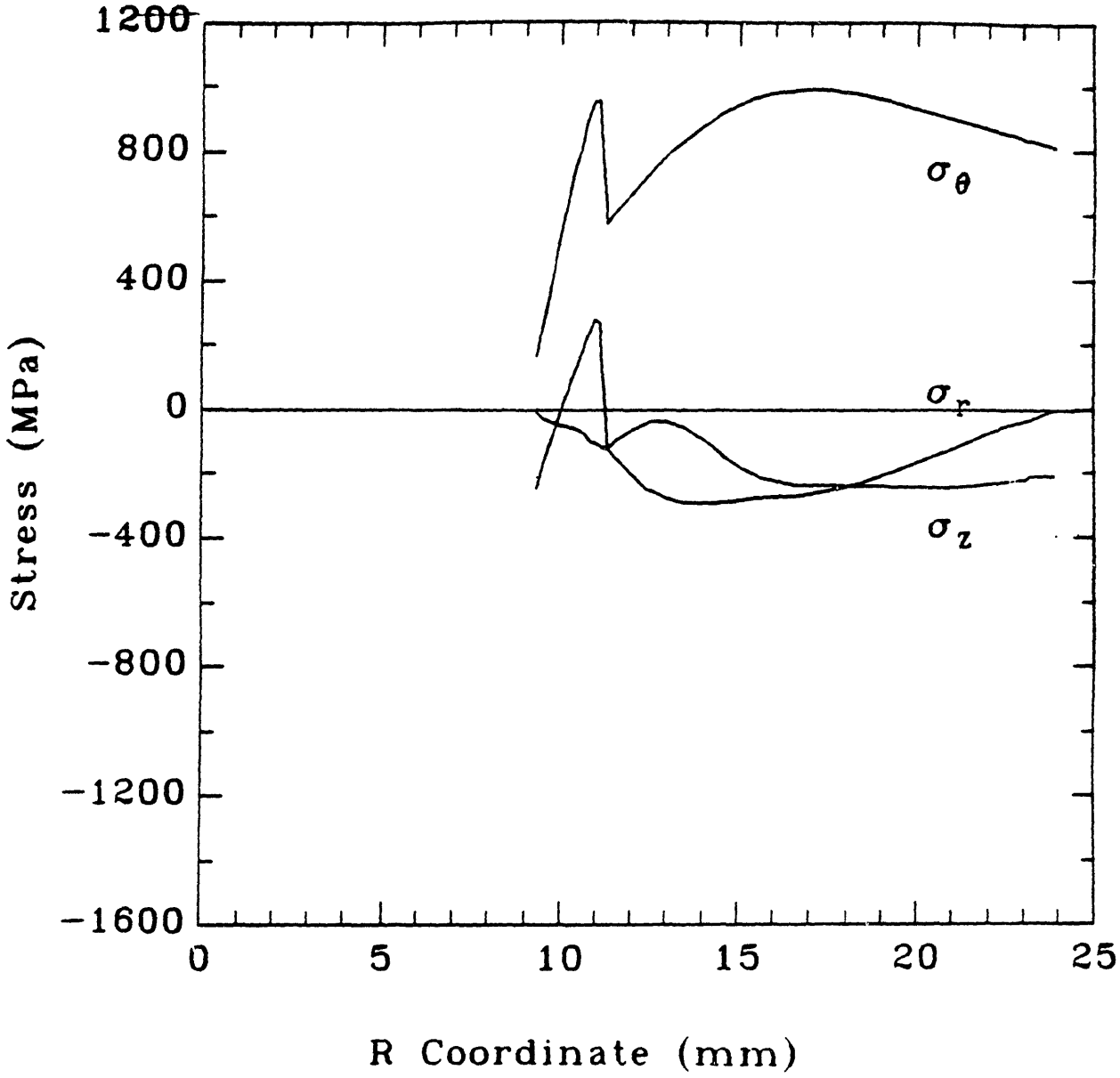

Fig. 5.40 **Normal stresses from Arrhenius rate equation analysis of DTC at 60 μs.**

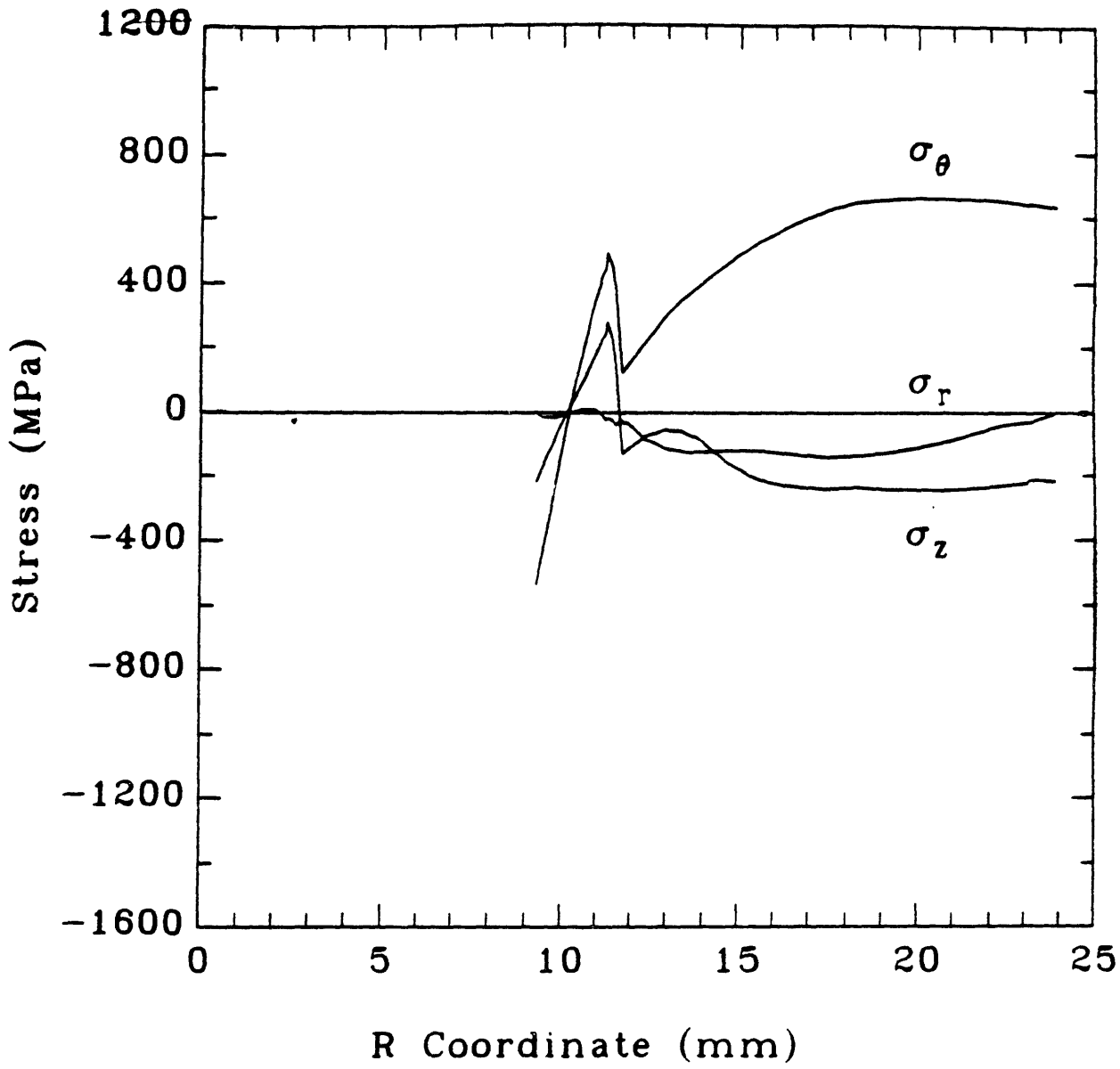

Fig. 5.41 Normal stresses from Arrhenius rate equation analysis of DTC at 80 μs.

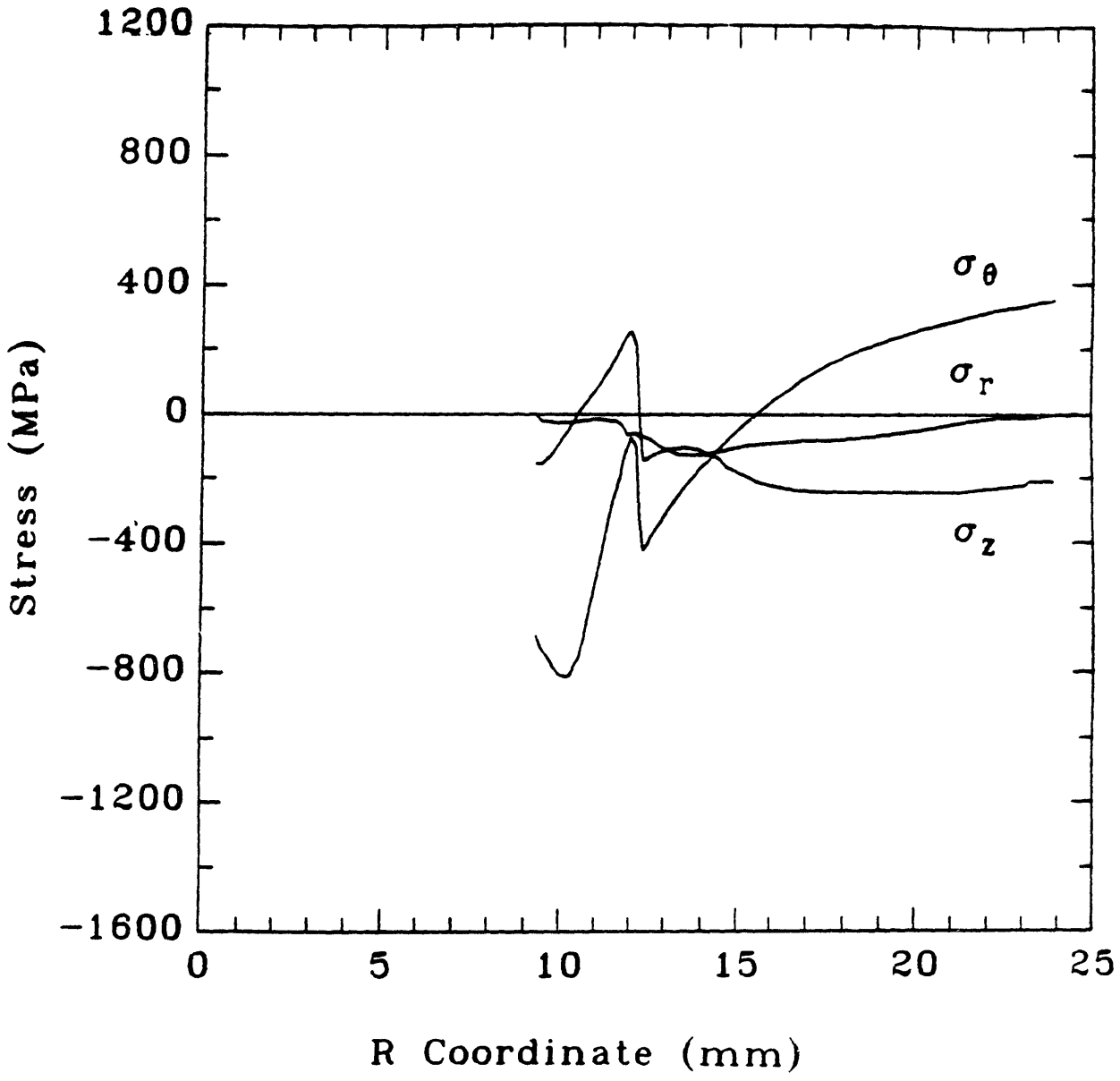

Fig. 5.42 Normal stresses from Arrhenius rate equation analysis of DTC at 260 μs.

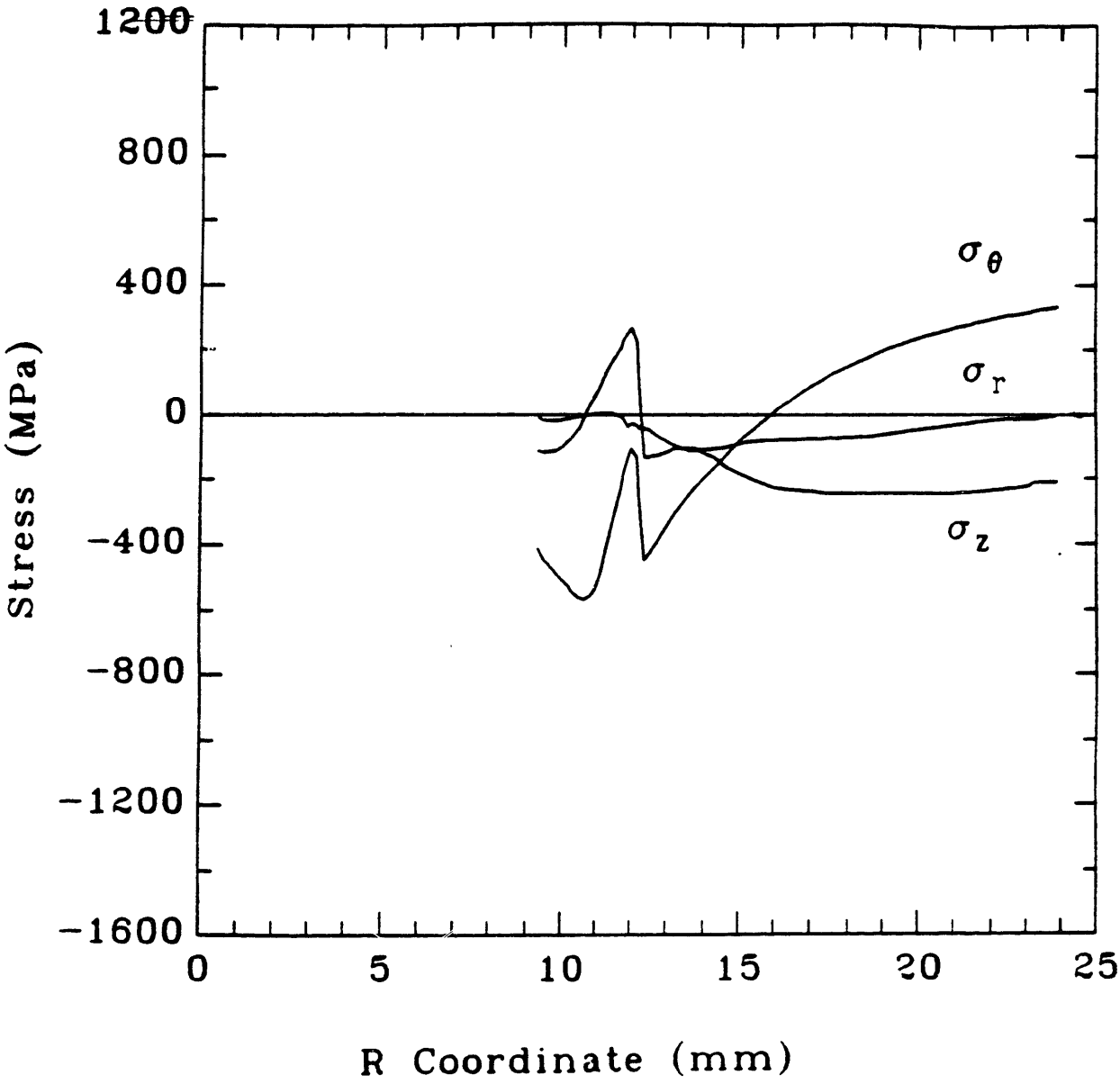

Fig. 5.43 Normal stresses from Arrhenius rate equation analysis of DTC at 0.001 s.

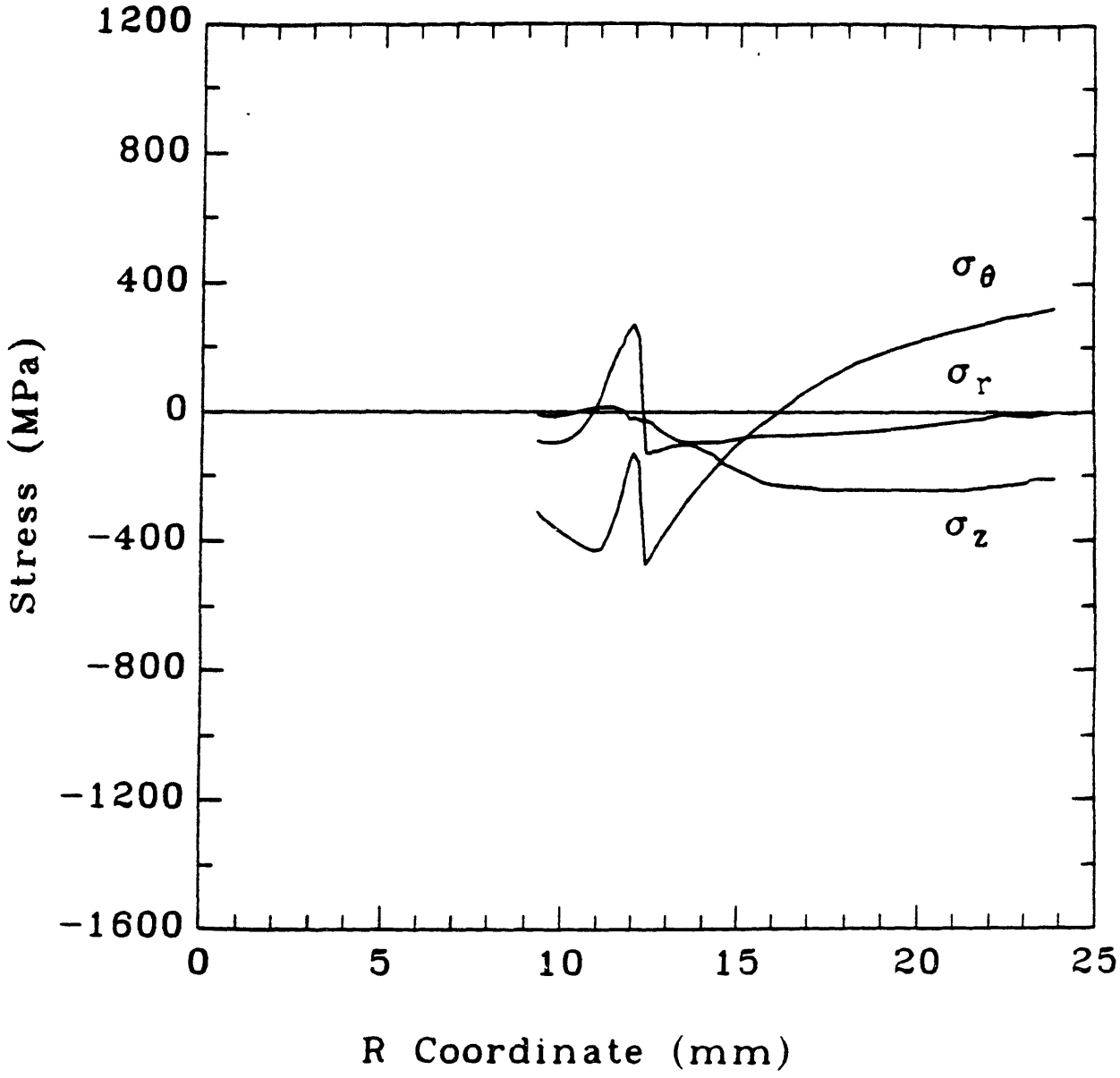

Fig. 5.44 Normal stresses from Arrhenius rate equation analysis of DTC at 0.01 s.

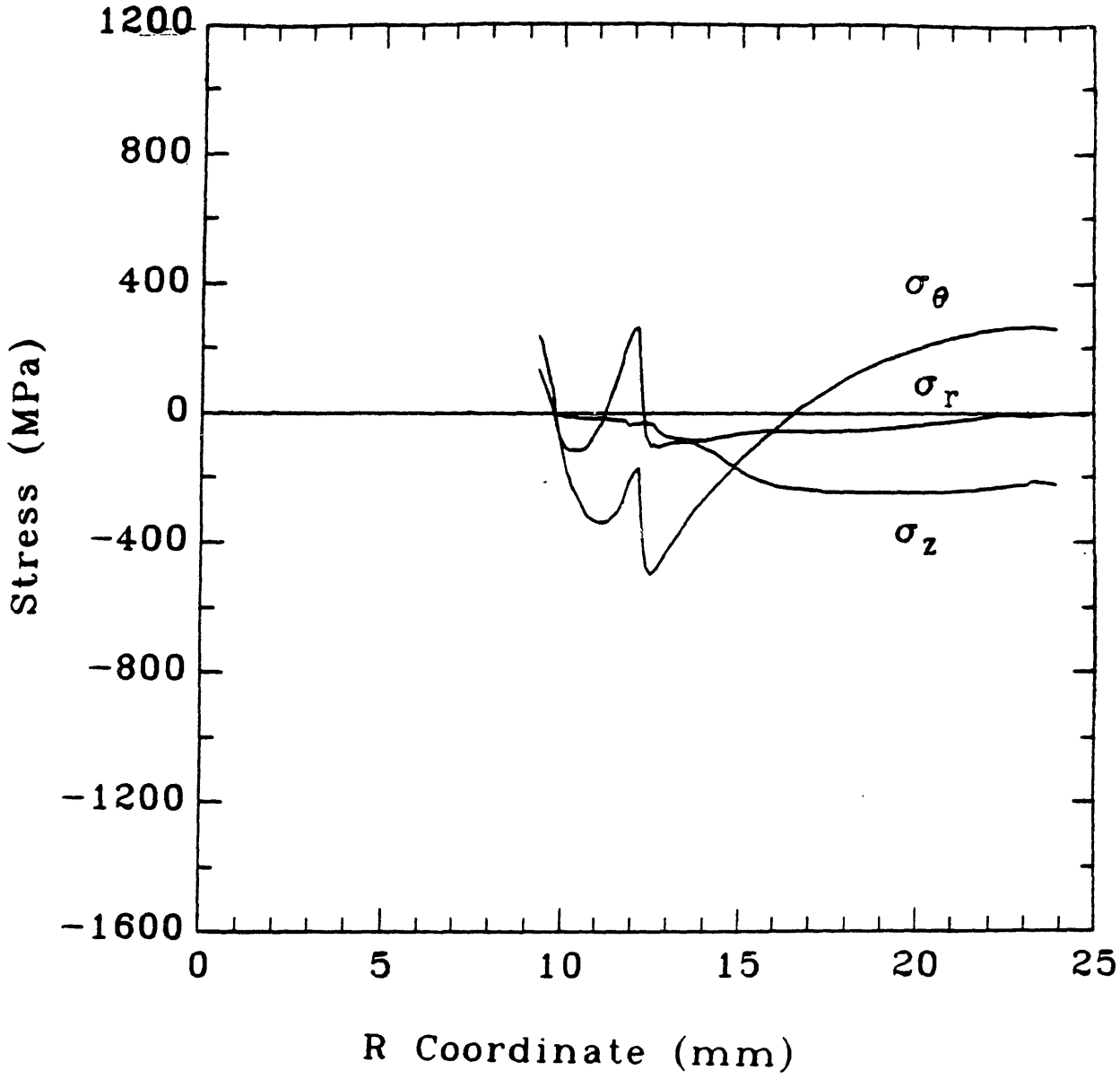

Fig. 5.45 Normal stresses from Arrhenius rate equation analysis of DTC at 0.25 s.

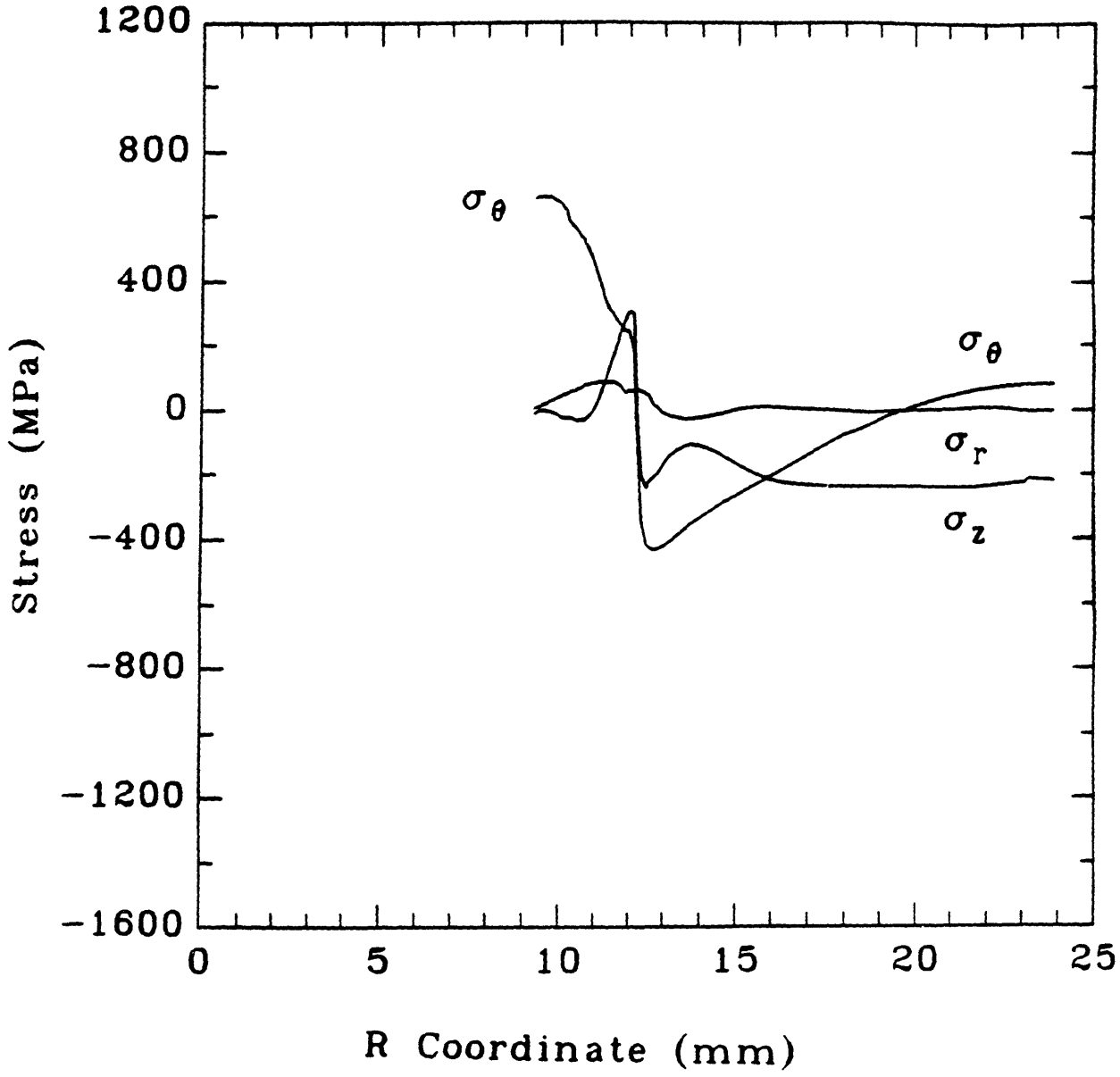

Fig. 5.46 Normal stresses from Arrhenius rate equation analysis of DTC at 5 s.

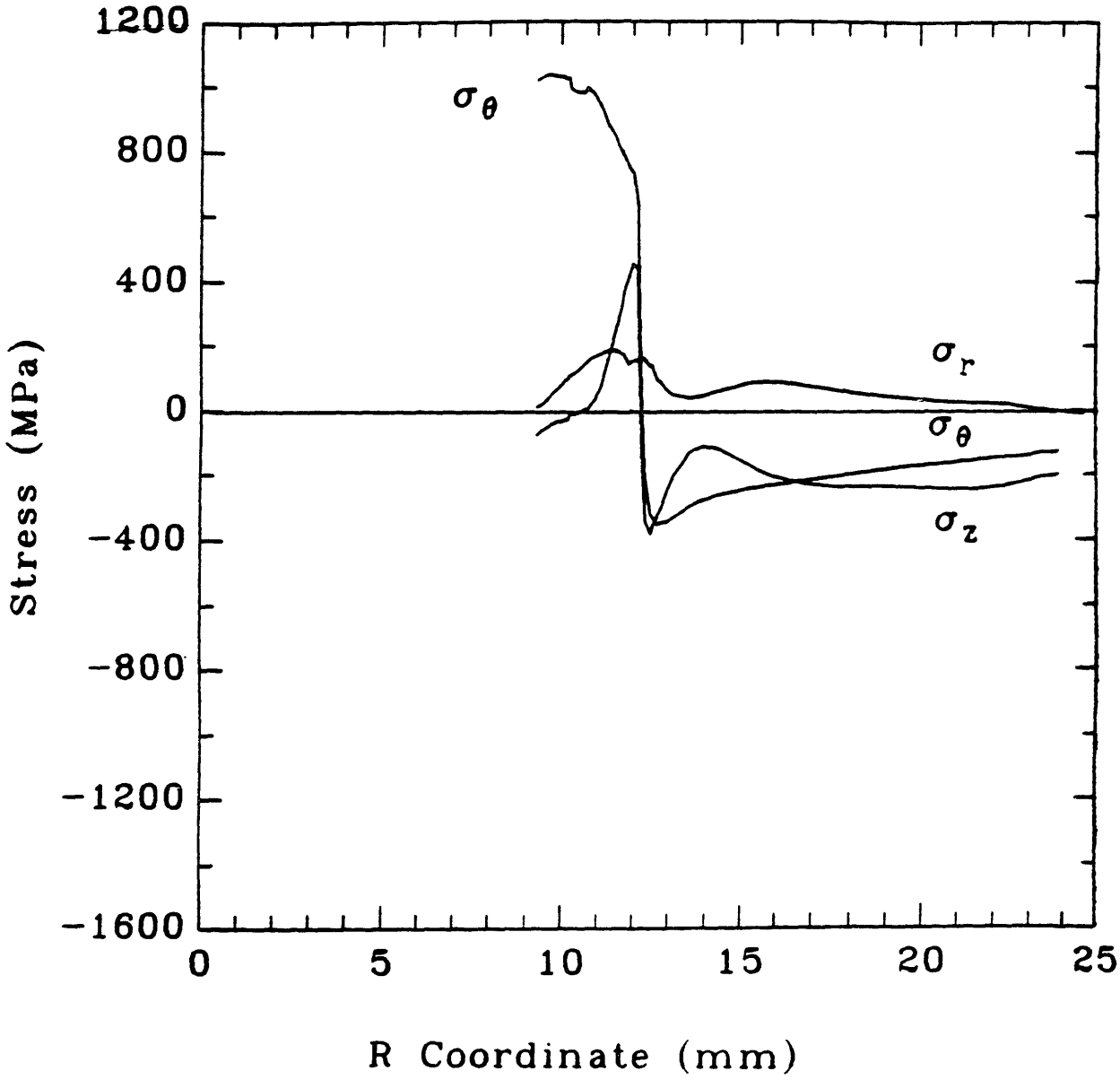

Fig. 5.47 **Normal stresses from Arrhenius rate equation analysis of DTC at 1 min.**

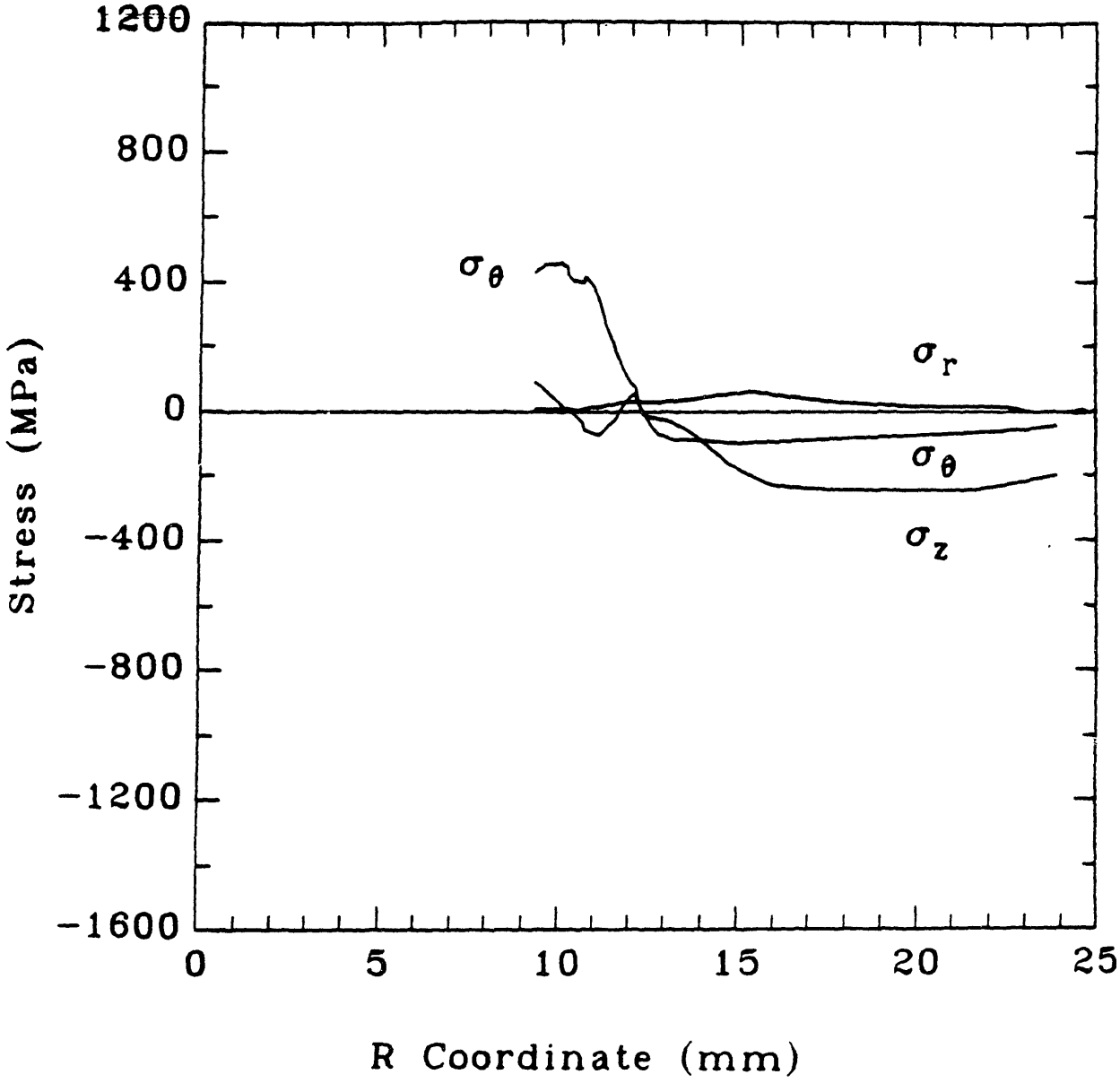

Fig. 5.48 Normal stresses from Arrhenius rate equation analysis of DTC at 15 min.

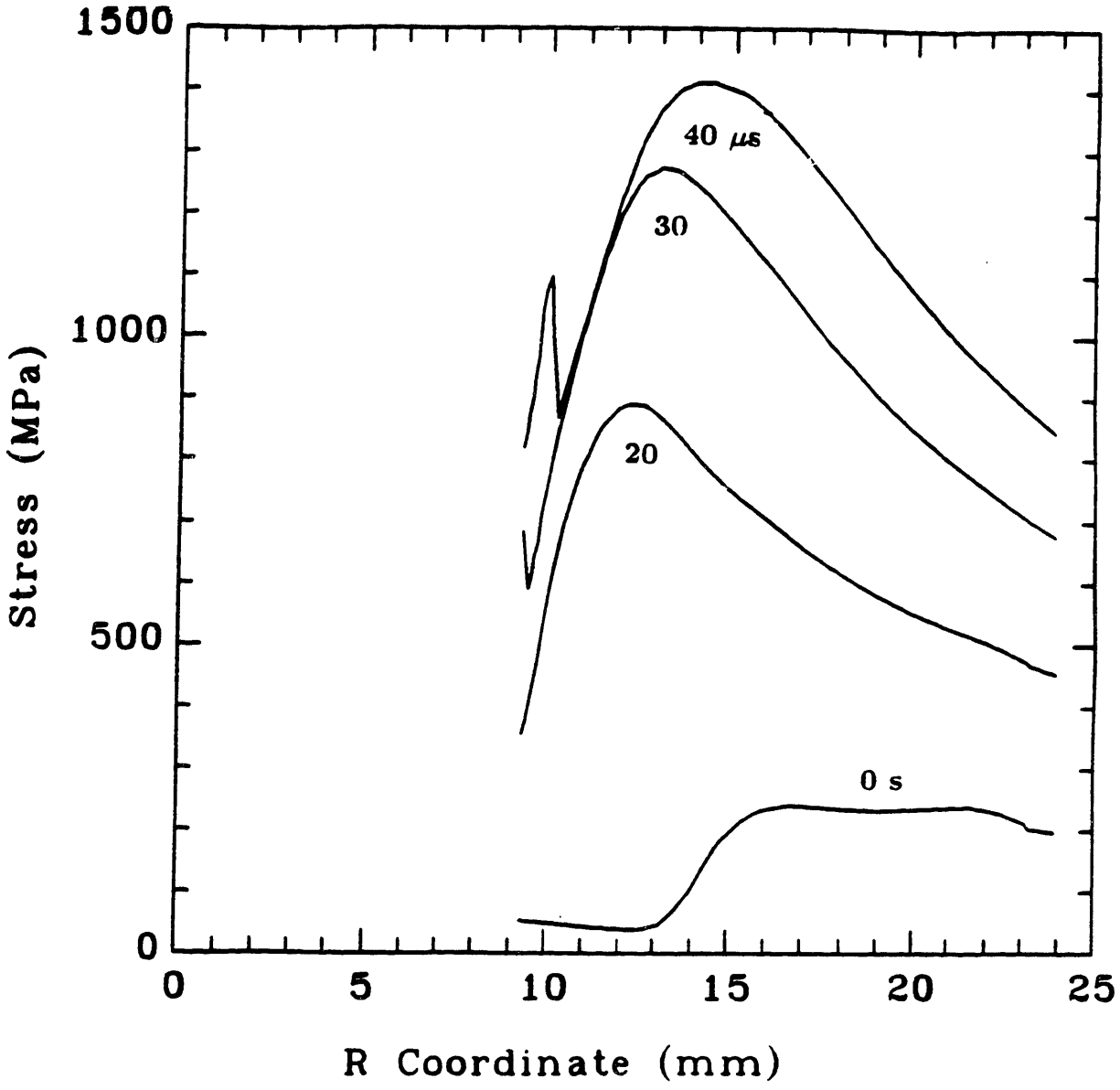

Fig. 5.49 Von Mises stresses from a phenomenological rate equation analysis of the first pulse at 0, 20, 30 and 40μs.

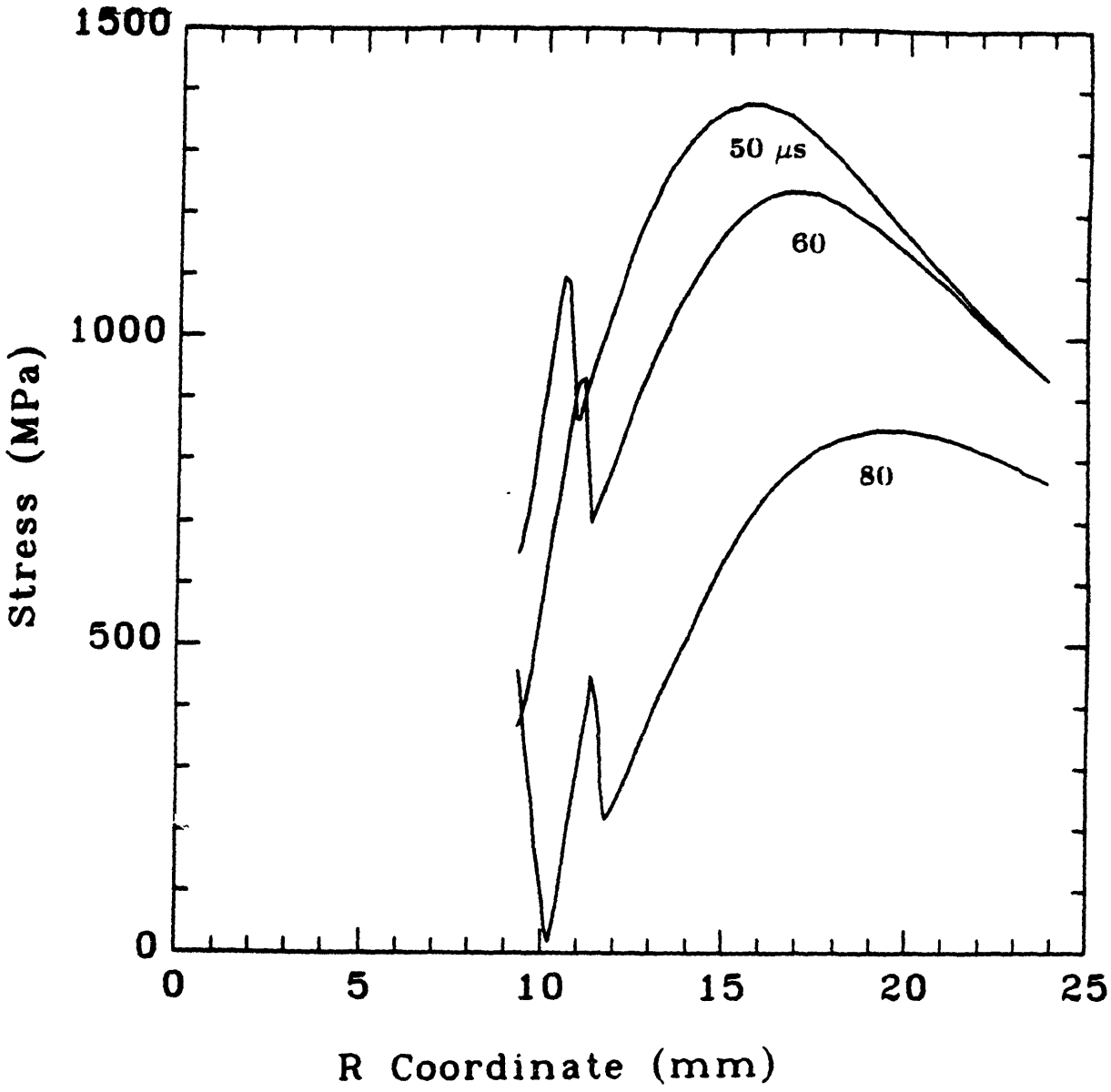

Fig. 5.50 Von Mises stresses from a phenomenological rate equation analysis of the first pulse at 50, 60 and 80μs.

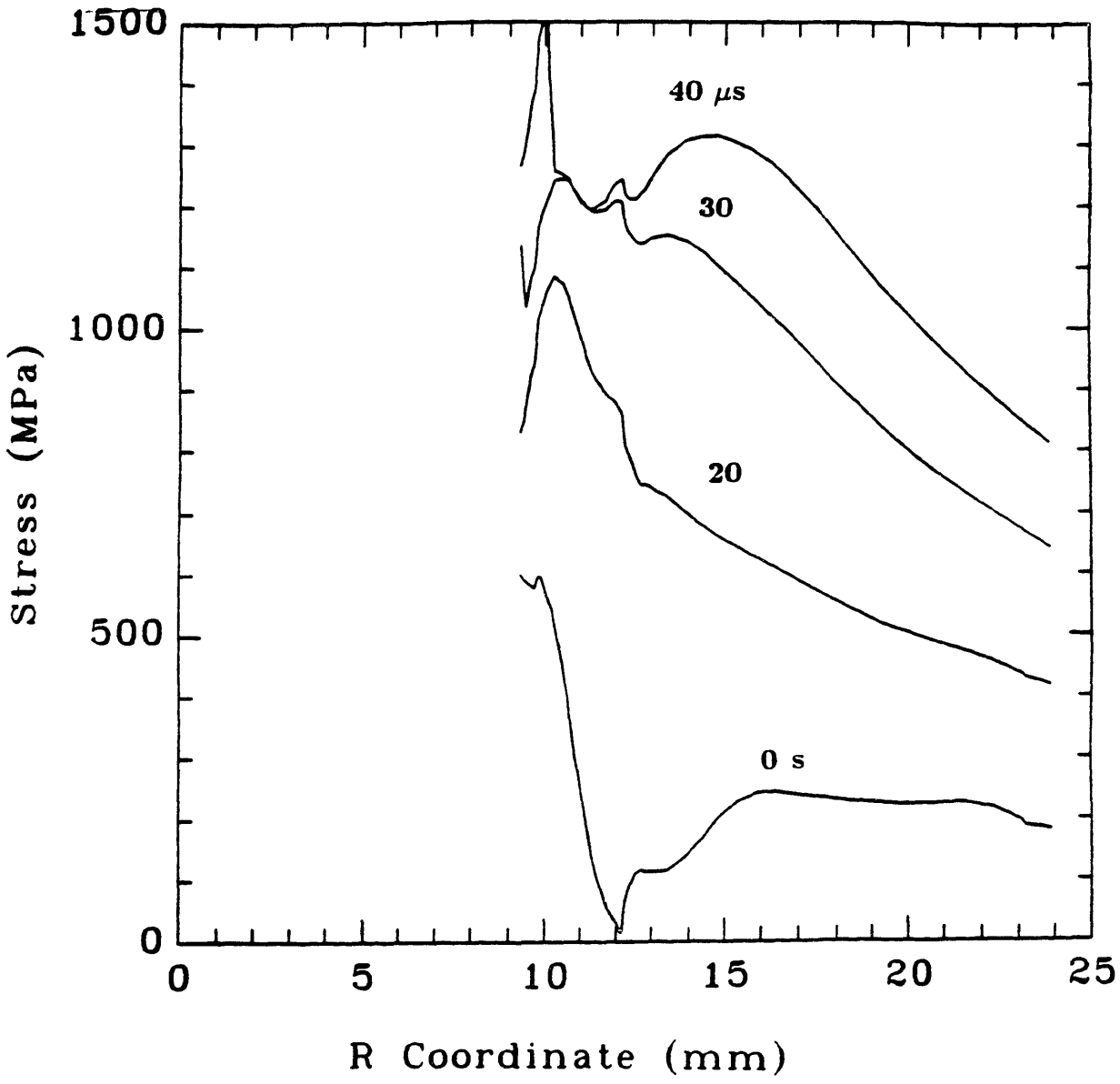

Fig. 5.51 Von Mises stresses from a phenomenological rate equation analysis of the second pulse at 0, 20, 30 and 40μs.

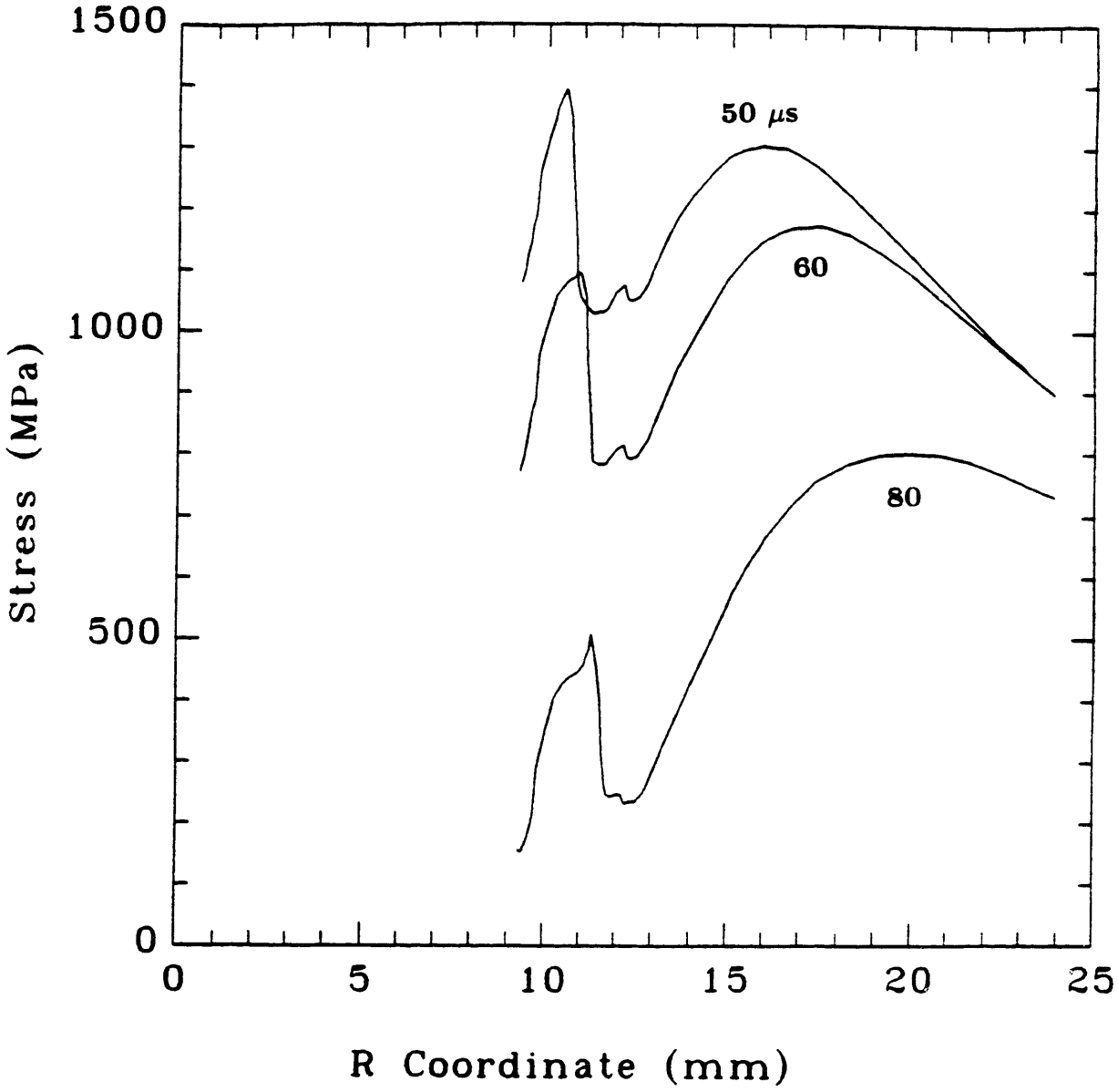

Fig. 5.52 Von Mises stresses from a phenomenological rate equation analysis of the second pulse at 50, 60 and 80μs.

Fig. 5.53a

Plastic strain rate versus time for the phenomenological rate equation analysis of the first pulse.

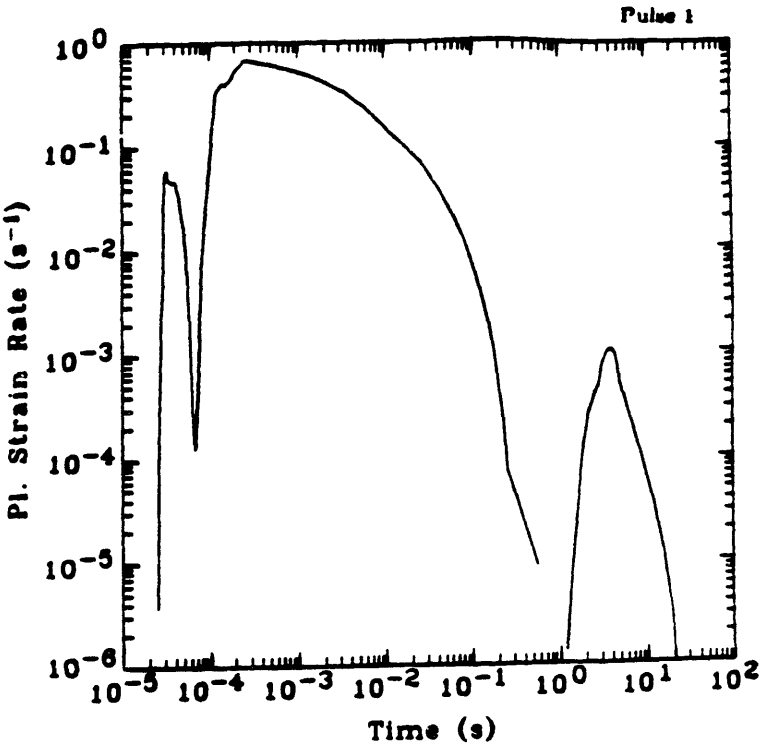

Fig. 5.53b

Plastic strain rate versus time for the phenomenological rate equation analysis of the second pulse.

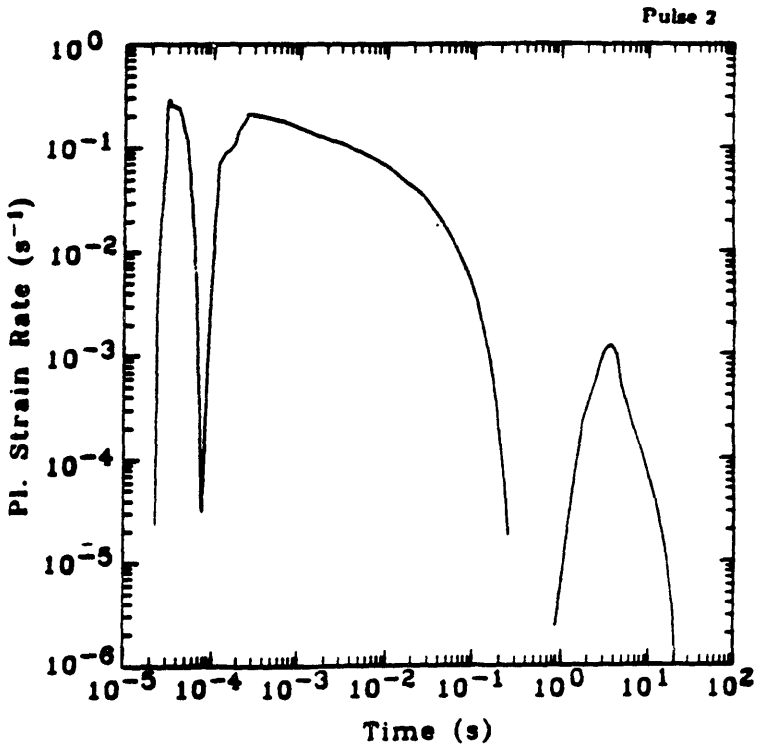

Fig. 5.54a

Deviatoric hoop stress-strain hysteresis plot of the 1st pulse at the 1st integration point from the phenomenological rate equation analysis.

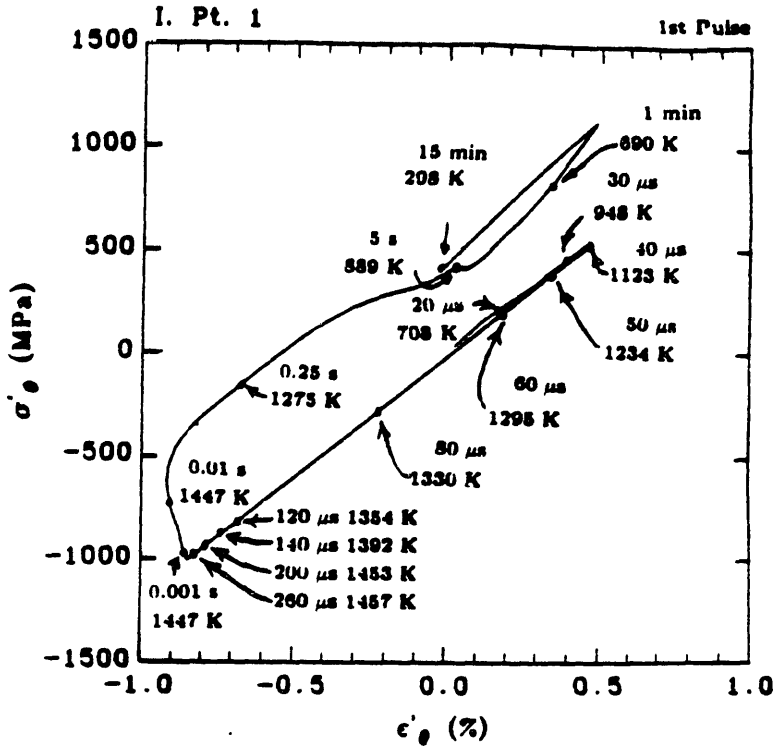

Fig. 5.54b

Deviatoric hoop stress-strain hysteresis plot of 1st and 2nd pulse at the 1st integration point from the phenomenological rate equation analysis.

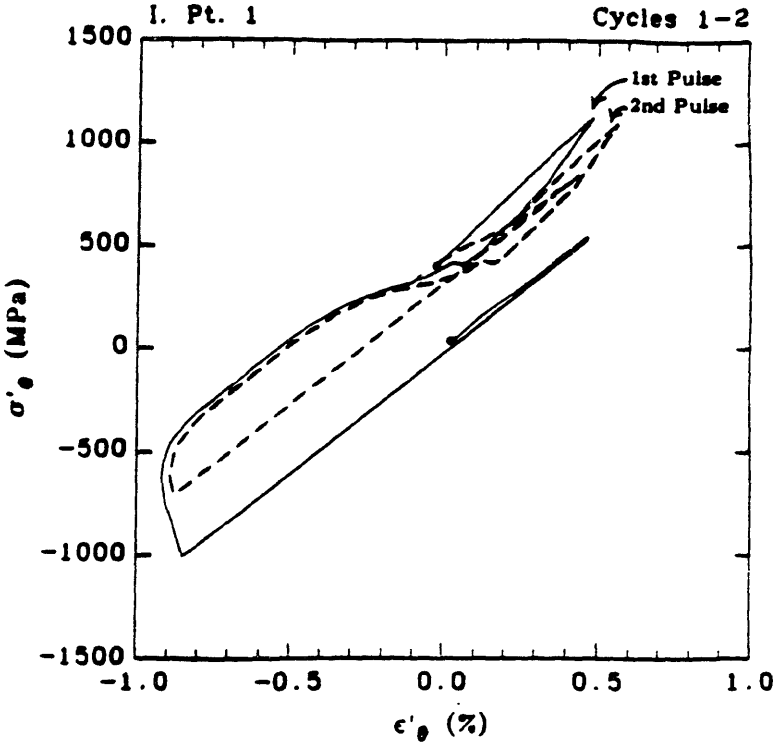

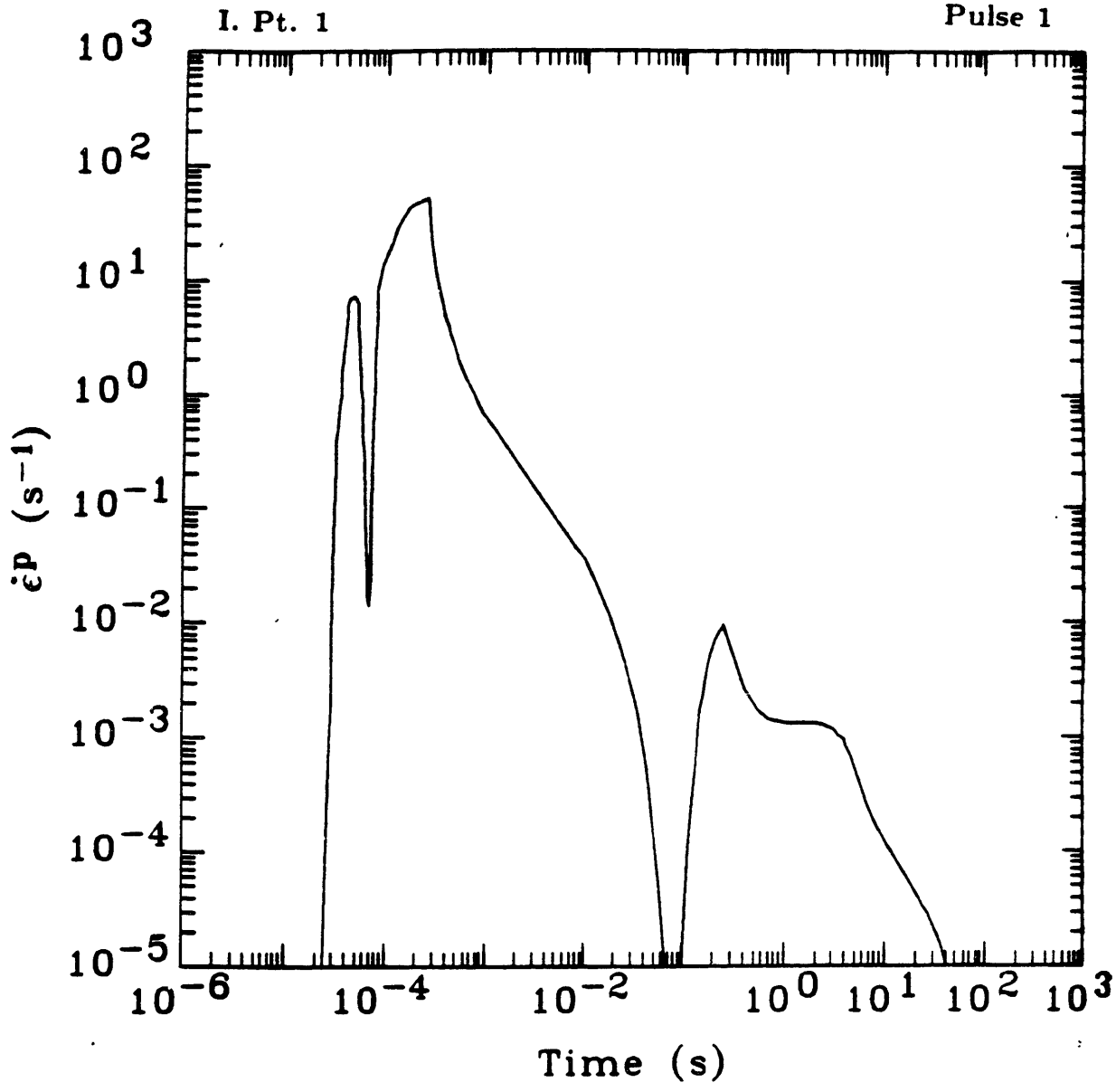

Fig. 5.55 Plastic strain rate versus time for the Arrhenius rate equation analysis of the first pulse.

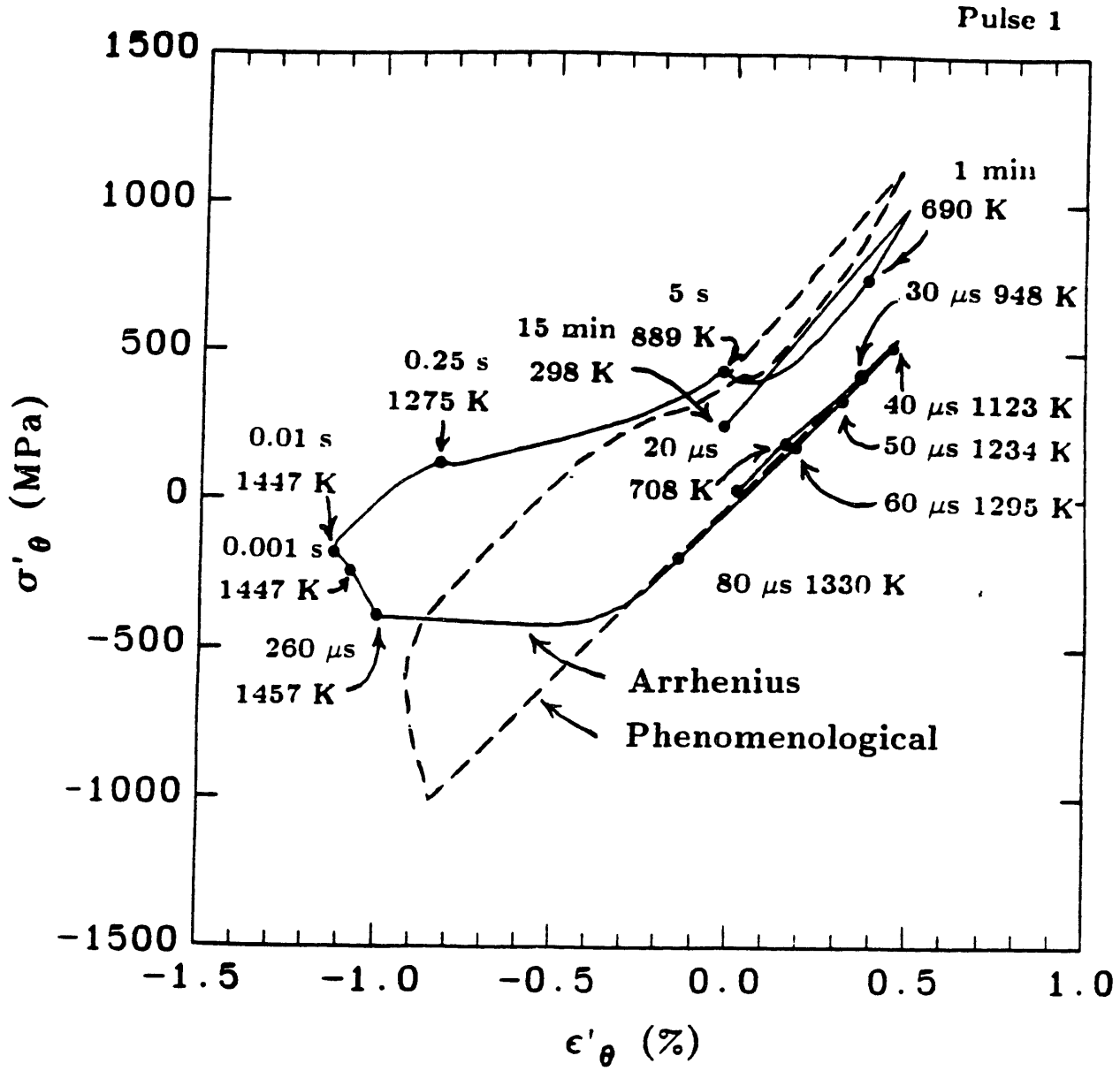

Fig. 5.56 Comparison between phenomenological and Arrhenius rate equation analyses of deviatoric hoop stress-strain hysteresis loops.

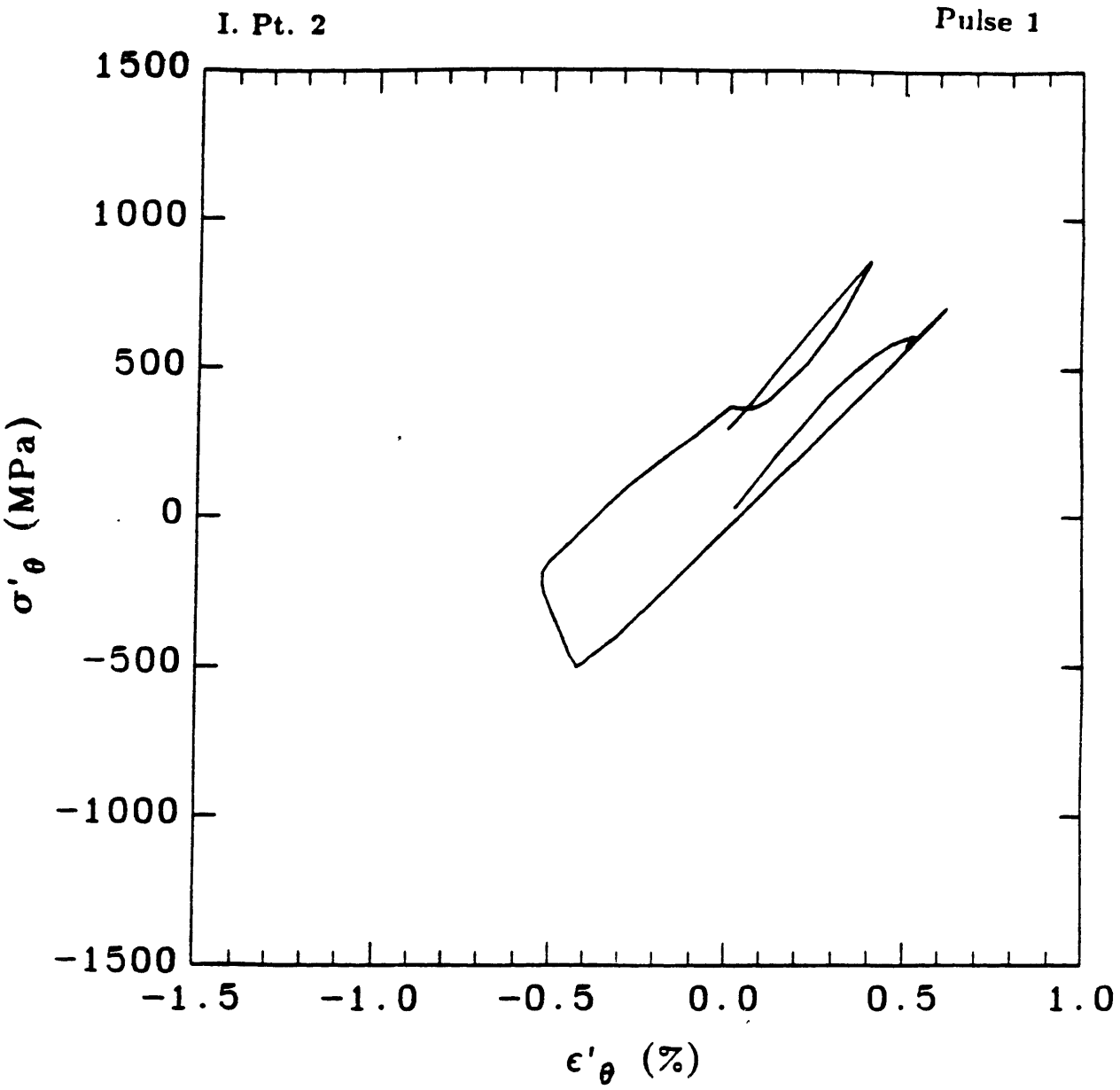

Fig. 5.57 Deviatoric hoop stress-strain hysteresis plot of the 1st pulse at the 2nd integration point from the Arrhenius rate equation analysis.

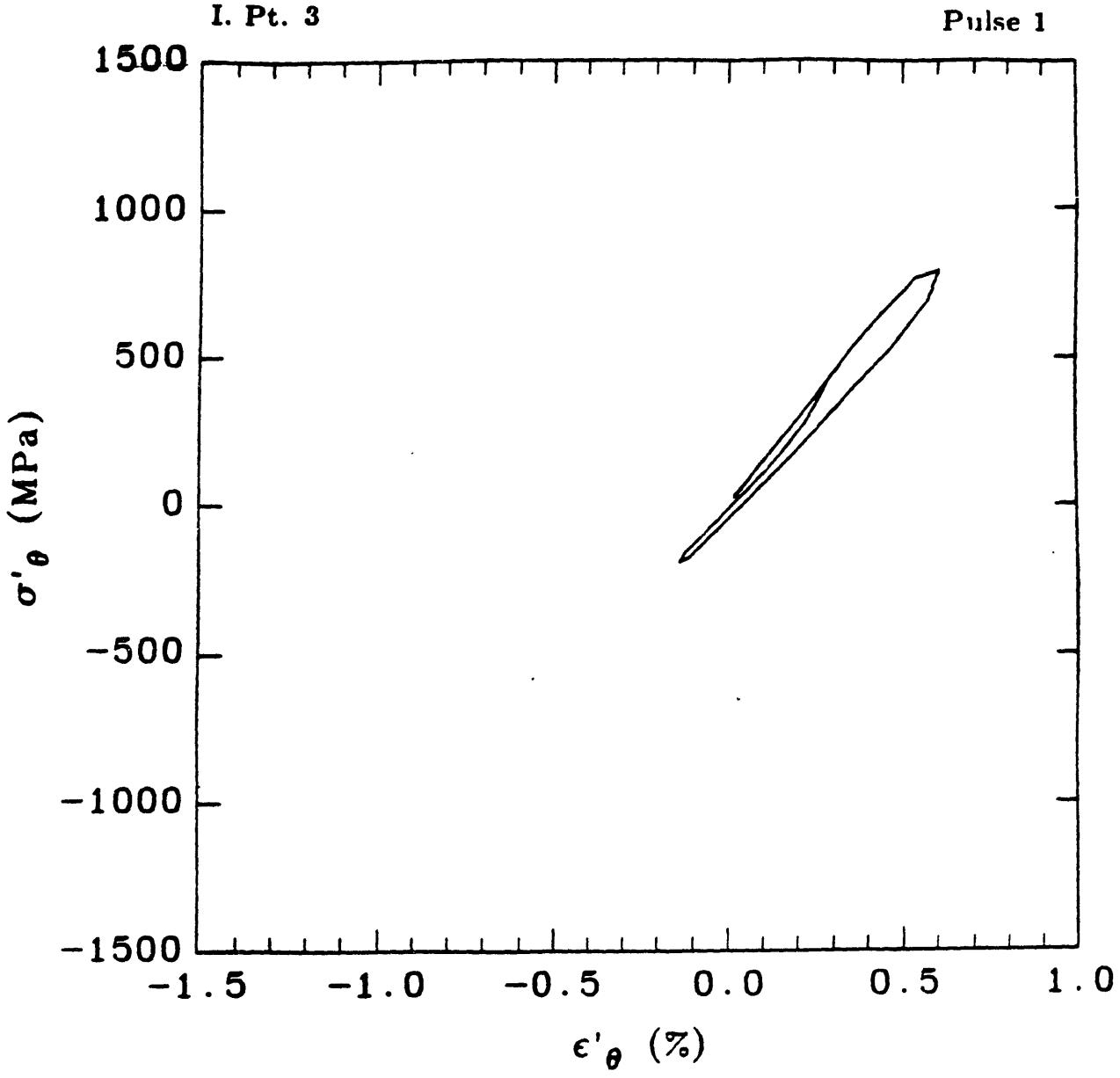

Fig. 5.58 Deviatoric hoop stress-strain hysteresis plot of the 1st pulse at the 3rd integration point from the Arrhenius rate equation analysis.

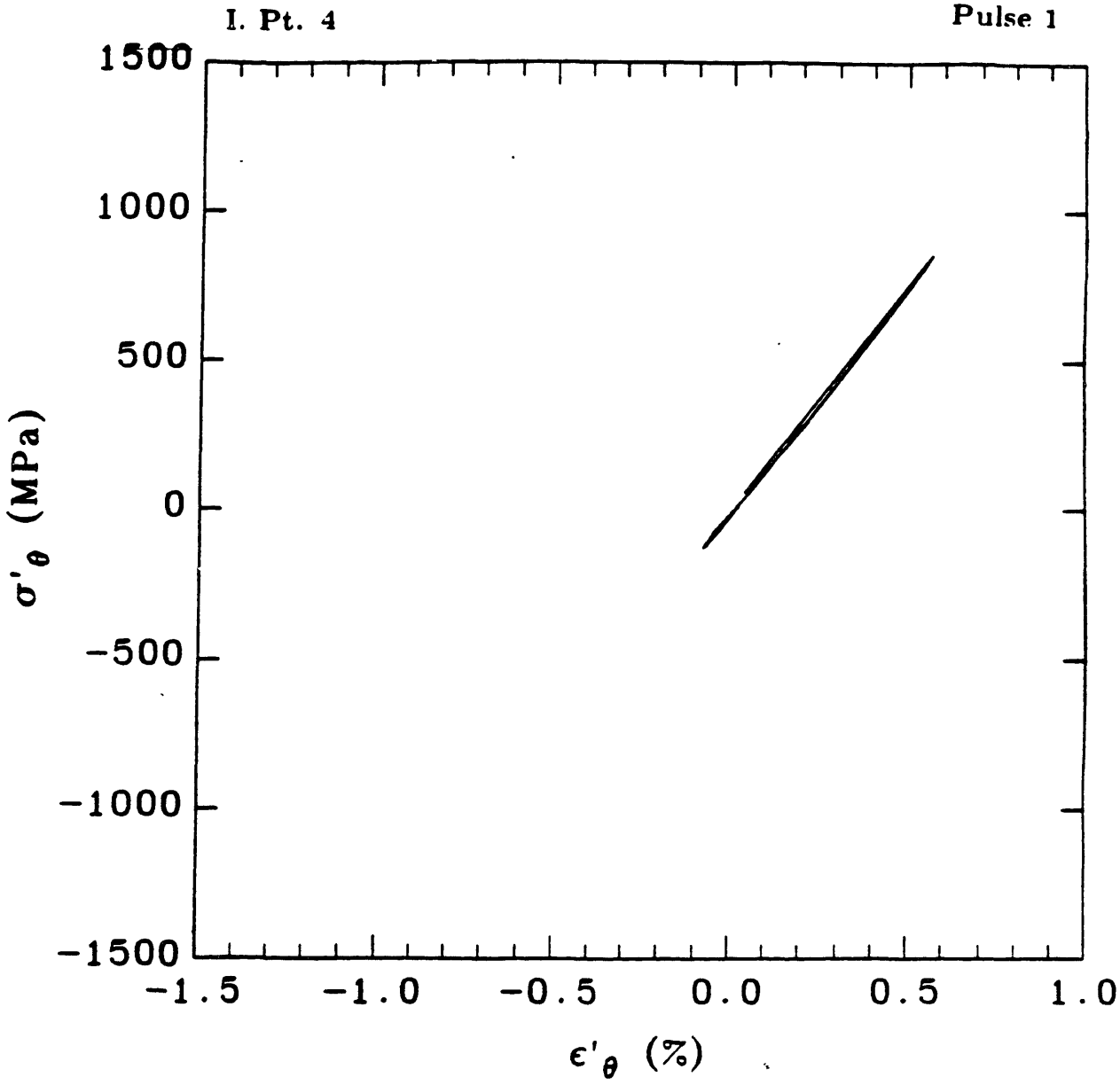

Fig. 5.59 Deviatoric hoop stress-strain hysteresis plot of the 1st pulse at the 4th integration point from the Arrhenius rate equation analysis.

References

[1] A. Yamagishi and M. Date, "High Magnetic Field Facility in Osaka University," Proceedings of the Int. Symposium on High Magnetic Field Magnetism, 1976.

[2] H.-J. Schneider-Muntau,"The Generation of Quasistationary Fields Up To 100T," IEEE Transactions on Magnetics, Vol. 24, No. 2, March 1988

[3] F. Herlach, "The Technology of Pulsed High Field Magnets," IEEE Transactions on Magnetics, Vol. 24, No. 2, March 1988.

[4] S. Foner and H.H. Kolm, "Coils for the Production of High Intensity Pulsed Magnetic Fields," The Review of Scientific Instruments, Vol. 28, No. 10, Oct. 1957, pp. 799-807.

[5] M. Date, "A New Method of High Magnetic Field Generation," Journal of the Physical Society of Japan, Vol. 39, No. 4, Oct. 1975.

[6] P.J. Raboin, "A High Magnetic Field Short Pulse System," Masters Thesis, 1985, Mass. Inst. of Technology.

[7] E.S. Bobrov, J.E.C. Williams and P.J. Raboin, "Development of a Short-Pulse High Field Magnet System at FBNML," Megagauss Technology and Pulsed Power Applications, Fourth Int. Conf. on Megagauss Magnetic Field Generation and Related Topics, July 1986, Santa Fe NM, Plenum Press.

[8] D. B. Montgomery and R.J. Weggel, *Solenoid Magnet Design*, 1980, R.E. Krieger Publishing Co., Huntington, New York, pg. 4.

Chapter 6

Failure and Fatigue Analysis for Short Pulse Magnets

This chapter brings together the diverse topics covered in this thesis. Beginning with a description and discussion of the destructible test coil (DTC) tests, the kind of deformation and destruction observed during the tests are explained. The short lifetime of the thermal cycling specimens and the test coil are discussed and compared to data from the low cycle fatigue results mentioned in Chapter 2. The mechanical analysis of maraging steel under these extreme conditions is important to the predictive capabilities of coil lifetime along with an understanding of the resulting deformation shapes. The fatigue behavior of the DTC is divided into two stages of crack growth. The first stage is governed by crack initiation and growth, and the second stage is controlled by geometric saw tooth crack growth. Finally, a discussion of the coil failure leads to recommendations for the design and safe operation of future short pulse magnets.

The Destructible Test Coil Failure

The first five pulses of the DTC were performed at 2.0 kV to determine the ratios of peak current and peak magnetic field to charging voltage, and to properly position the pick-up coil (a device to measure magnetic field) in the center of the magnet. The measured ratios were 23.7 kA/kV and 4.25 T/kV and compared to predicted ratios of 23.8 kA/kV and 3.90 T/kV. The charging voltage was increased to 6, 9 and finally 11.5 kV with the pick-up coil in the magnetic center of the bore to measure the current and field ratios. The pick-up coil was not used for the remainder of the tests because of safety concerns.

Over a two day period, the DTC was pulsed with a charging voltage between 11.5 and 11.7 kV. The largest current measured was 303 kA with an average peak current over charging voltage ratio of 24.6. Using a peak field to peak current ratio of 0.18, the largest measured current scales to a peak magnetic field of 54.3 T. A minimum of 45 min was allowed for magnet cooling. The bore of the magnet was searched periodically, for damaged insulation, but none was found. After 12 pulses, the magnet was disassembled to examine the insulation more closely.

Under close observation, numerous cracks were found on the inner radius of the DTC. The coil transition turns at the ends of the magnet were axially deformed towards the center of the magnet by about 1 mm. There were 8 cracks detected on the inner radius, and all of the crack fronts were parallel to the Z axis of the magnet. Two of the cracks extended across the entire width of the coil turn while the six others began from either of the inner radii turn corners, and extended towards the other corner. On three successive magnet turns there were two cracks about 10 mm apart which were aligned over two similar cracks on the next turn. Some faint, almost undetectable ridges were also seen on the inner radius of the magnet. The ridge lines were grouped in batches taking up half a turn, and they were separated by a smooth coil surface. There were 4 metal droplets or spatters on the center turn of magnet near the cracks. The top and bottom surfaces of the magnet turns were rough with metal spatters. The largest crack had penetrated approximately 2 mm into the build of magnet.

Close examination of the G-7 insulation revealed little to no damage; the modification to the coil turn cross section described in Chapter 5 prevented any pinching and cutting of insulation at the inner radius. Unlike the 50T coil, the DTC insulation was not burnt through, and it did not have the whitened discoloration which comes from overheating. The insulation over the cracks had metal spatters on its surface, but had not itself been damaged. After the inspections, new insulation was placed between the turns, and the magnet was reassembled for further testing. Even though the coil under normal laboratory conditions would have to be considered spent, the destructive nature of a short pulse failure had not been realized.

The DTC was pulsed 4 more times. On the sixteenth pulse, there was a powerful electrical explosion in the bore of the magnet. Demich [1] has defined an electrical explosion as the metal evaporation of a conductor which results from ohmic heating. There are 3/16 inch thick G-10 annular plates (center hole is 3/4 inch diameter) which are glued to the steel plates on the ends of the magnet assembly. The purpose of these plates is to guide the pick-up coil into the bore of the magnet and to keep it aligned in the center. The pick-up coil was not used during the final test, so there were 3/4 inch diameter openings to the bore of the magnet. The electrical explosion, with its rapid expansion of hot gases and molten metal, hurled the plates several feet away from the assembly. If there had been an experiment or any other object in the bore, it could have been seriously damaged.

The final inspection of the magnet and insulation revealed more useful information. The number of cracks visible with the naked eye increased to 14, and all of the cracks detected after 12 pulses had grown across the entire width of the coil turn and into the build of the magnet. The entire bore of the magnet was covered with metal spatters and ridge lines. These ridge lines appear to precede the development of cracks. They are similar in texture to the roughening of the surface which is observed in the thermal cycling tests.

The most interesting observation concerns the cracks which developed into axial holes in the conductor (Fig 6.1). These elliptically shaped holes extend 5 mm into the build of the magnet, and they are about 2 mm wide. These holes will be called crack-tip cavities. To obtain the Fig. 6.1 photograph, whole turns of the DTC were cut free with a hand grinder. Because of the crack alignment, it was possible to look down through three magnet turns. A crack similar to the one shown in Fig. 6.1 was opened to examine the inside surface of the crack-tip cavity. Fig. 6.2 is a photograph of this surface. This surface is clear evidence for the phenomenon of crack-tip melting and vaporization. The surface is porous, and it appears to be the source of metal which was spattered on the bore surface. Crack-tip melting occurs when the current must flow around a crack extending out from the inner radius. The discoloration of the coil surface in Fig. 6.1 illustrates the fact that the current density had to flow around the crack hole.

The center turn of the DTC was cut, sectioned and mounted in two different ways so the turn could be examined in more detail. Some specimens were taken from the surface of the turn build, and several other specimens were taken from cross sections of the turn. The mounted specimens were ground and polished to a 0.3 μm finish. Under a microscope, a 0.3 mm crack-tip cavity with the same general shape as the one in Fig. 6.1 was found just 2 mm away from a larger 5 mm crack-tip cavity. This crack was discovered on a surface specimen, and it was located on the inner radius.

The cross section specimens were tested for Rockwell C hardness. The hardness profile for the DTC build is shown in Fig. 6.3. This plot shows a sharp decrease in hardness in the skin depth region near the inner radius. The drop in hardness is similar to the drop observed in the thermal cycling specimens. From Fig. 6.3, the drop in hardness occurs at a radius of 10.8 mm. The largest radius of the austenite finish temperature (1070 K) predicted by MESPA during a pulse is 11.2 mm.

The DTC had been pulsed 12 times without any external indication of crack growth in the coil. The pulse length and shape of the current waveform did not change, and the ratio of peak current to charging voltage was also unchanged. The implication here is that a change in coil inductance due to radial cracking was not sufficiently large enough to detect with our instruments. Hence, the ratio of peak current to charging voltage did not change. The phenomenon of changing inductance has been observed in other coils of this magnetic field strength [1][2]. The mechanism which causes the change in coil inductance is the deformation (change in current path) occurring in the magnet during the pulse. When the displacement of a conductor is large, the change in current path will change the coil inductance. For a pulsed discharge of current through a magnet, there is an $I(\partial L/\partial t)$ voltage drop across the coil. This term is insignificant for the DTC, but for single turn solenoids, it important enough to limit the amount of magnetic field a coil is capable of producing. The fact that this magnet did not show any significant deviation (greater than 10%) in the ratio of peak current to charging voltage means that the build of the magnet supported the skin depth of current and the overall distortion of the magnet was not large. While the peak current to charging voltage was unchanged, it is not known if the peak current to peak field ratio was also unchanged.

As mentioned before, a closer examination of the DTC after 12 pulses revealed 8 cracks on the inside radius of the magnet. The type of cracks observed in these tests have been observed by other researchers [3]-[5]. The term which describes these cracks and their growth is the "saw tooth" effect. F. Herlach [6] has best described this phenomenon, and what follows is his description of the magnetic saw effect. "In coils with massive conductors, a 'saw effect' has been observed: it looks as if the magnetic stress were 'sawing' slits into the conductor from the inside surface. The explanation goes as follows: Once a tiny crack develops at the inside where the strain is largest, the current is forced to go around it in a sharp bend; this results in increased local stress and arcing which tends to open up the gap." The magnetic stress mentioned above refers to the frequently used method of modeling extreme Lorentz body forces inside the skin depth region with an equivalent magnetic stress (pressure) on the inside radius. The magnetic saw effect is a combination of crack growth and electromagnetic melting of coil material.

H.P. Furth [3] made some valuable observations on the behavior of short pulse helical coils over 30 years ago. He suggested that the melting temperature

of a material be used to determine the safe operating limits for helices. He observed that the electrical breakdown of coils during the pulse is not due to a failure in the electrical insulation but instead to metal vapor arcs along the inside surface of the magnet. The source of metal vapor is the magnetic saw effect. Finally, he commented that the consequence of the saw effect is short circuit conditions inside the bore of the magnet, while the current continues to circulate. The magnetic energy is dissipated into the saw cuts. He claims this failure scenario is substantiated by the alignment of saw cuts in the axial direction, even when the interspace insulation between the saw cuts is not damaged. The observations and conclusions made by Furth are supported by this work.

The saw tooth effect has a very important consequence on the life of short pulse magnets. The saw tooth crack growth rate for the DTC was approximately 1 mm per pulse over the last 4 pulses. Crack-tip cavities were found on all the radial cracks (large and small). Melted material is ejected away from the crack-tips (Lorentz body forces), so the radial cracks grow as new material ahead of the crack-tips melt and vaporize with each pulse. The point here is that the saw tooth crack growth rate is large, and the time spent initiating and growing a crack which then becomes a saw tooth crack, should occupy most of the magnet life. To judge whether this is in fact true, it is helpful to consider the dimensional scale for significant saw tooth crack growth.

Crack-Tip Melting

The purpose of this section is to determine what minimum crack size will result in crack-tip melting during a full field pulse. The crack geometry being considered here is a crack on the inner radius of a magnet where the crack surface obstructs the current flow (Fig 6.4). Because of current density concentrations, the temperature at the crack-tip is greater than the surrounding material. As the crack length increases, the size of a region (thermal zone) affected by current density concentrations increases. When the crack length is very small ($< 1\ \mu m$), heat conduction away from the crack-tip prevents crack-tip melting. Conversely, as the crack length increases to an "adiabatic" crack size, crack-tip melting occurs, and each subsequent pulse will cause crack-tip melting. The term adiabatic refers to thermal conditions at the crack-tip and the small influence of heat conduction at the crack-tip. The adiabatic crack size is also the critical crack size, because the magnet life is over when crack-tip melting (saw tooth crack growth) begins.

A lumped crack-tip thermal analysis is used to approximate the the adiabatic crack size c_a and the thermal zone size $2R$ (Fig 6.5). The circle of material ahead of the crack-tip (per unit thickness) is called the thermal zone, and a single lump temperature θ is assumed for this zone. The adiabatic crack size is the crack length which causes melting in the thermal zone by the end of a pulse. The material temperature surrounding the thermal zone is θ_∞. The strategy here is to first approximate the current density in and around the thermal zone, second to predict the thermal zone temperature change, and third to find the smallest crack length which results in the thermal zone heating to a melting temperature by the end of a pulse.

The current density in the DTC changes as a function of time and position. For this problem, the current density in the surrounding material is uniform and its magnitude changes according to the step function shown in Fig. 6.6. The current density magnitude J_∞ and time duration (50 μs) of this current density pulse are chosen so that the surrounding material heats to a peak temperature of 1460 K.

Inside the thermal zone, the current density is largest at the crack tip and decreases as the distance r from the crack-tip increases. There is an analogy through Laplace's equation between the current density increase at a crack-tip and the shear stress increase at a Mode III crack-tip. For more information on Mode III crack-tip stress analysis and solutions, see the following references [7]-[11]. At a crack-tip, the voltage potential analog is the displacement field. The current densities are proportional to the voltage gradients, and the shear stresses are proportional to the displacement gradients. A Laplacian differential equation describes the electrical and stress equilibrium, and the boundary conditions for the two problems are analogous. The stress distribution solution for a Mode III crack on a free surface is rewritten with the electrical analogy to give the following current density distribution around a crack-tip.

$$J_z = J_\infty \sqrt{\frac{c}{2r}} \cos\left(\frac{\alpha}{2}\right) \tag{6.1}$$

$$J_y = -J_\infty \sqrt{\frac{c}{2r}} \sin\left(\frac{\alpha}{2}\right) \tag{6.2}$$

This solution assumes the crack length c is much greater than the radius r away from the crack-tip. These equations predict infinite current densities as r goes to zero.

The second step in this strategy is to predict the temperature change in the thermal zone during a pulse. The adiabatic rate of temperature change for far-field material surrounding the thermal zone is

$$\frac{d\theta_\infty}{dt} = \frac{\rho J_\infty^2}{c_p d}. \tag{6.3}$$

The heat capacity c_p, density d and electrical resistivity ρ are assumed constant at 862 J kg^{-1} K^{-1}, 8000 kg m^{-3} and 1.0 $\mu\Omega$m respectively. With the current density assumption already made, Eq. 6.3 can be integrated, and the far-field temperature linearly increases as a function of time.

In the thermal zone, heat is added by ohmic heating and removed by thermal conduction to the surrounding material. When the current density equations (Eq. 6.1 and 6.2) are squared, added, integrated over the thermal zone area of radius R and multiplied by ρ, they contribute the following input heat per unit thickness.

$$Q_{in} = \rho J_\infty^2 (2cR) \tag{6.4}$$

Heat is removed from the thermal zone by conduction across an area $2\pi R$ with a temperature difference $(\theta - \theta_\infty)$ over a distance R. Output heat is given by

$$Q_{out} = 2\pi\kappa(\theta - \theta_\infty). \tag{6.5}$$

The thermal conductivity κ is assumed constant at 28.0 W m^{-1} K^{-1}. The rate of temperature change in the thermal zone πR^2 depends on the difference between the Q_{in} and Q_{out} heat terms.

$$\frac{d\theta}{dt} = \left(\frac{\rho J_\infty^2}{c_p d}\right)\left(\frac{2c}{\pi R}\right) - \frac{2D}{R^2}(\theta - \theta_\infty) \tag{6.6}$$

D is the thermal diffusivity (4.0×10^{-6}m^{2}s^{-1}). The homogeneous and particular solutions to this differential equation are combined to give the thermal zone temperature as a function of time, crack length and a dimensionless parameter χ which changes from infinity to a finite value during a pulse. The initial temperature is θ_0.

$$\frac{\theta - \theta_\infty}{\theta_\infty - \theta_0} = \left(\frac{2}{\pi}\frac{c}{\sqrt{2Dt}}\chi - \chi^2\right)\left(1 - exp\left(-1/\chi^2\right)\right) \tag{6.7}$$

$$\chi = \sqrt{\frac{R^2}{2Dt}} \tag{6.8}$$

The third and last step in determining the adiabatic (critical) crack size is maximizing Eq. 6.7 so that $\theta = \theta_m$ at the end of a pulse, $t = t^*$. A numerical search procedure was used to find the the χ (0.88) which maximizes the thermal zone temperature. Using this χ, the critical crack size can be expressed as

$$c_a = 3.48\sqrt{Dt^*}\left[\left(\frac{\theta_m - \theta_\infty}{\theta_\infty - \theta_0}\right) + 0.56\right]. \tag{6.9}$$

When the pulse time for the DTC experiment and the melting temperature of maraging steel are used in this equation, the predicted adiabatic crack size and the thermal zone size are 39 and 35 μm respectively. This result contradicts a current density assumption made earlier ($c \gg 2R$). To correct this, the current density functions are modified to predict a current density which goes to J_∞ as r goes to infinity. This will predict a smaller adiabatic crack size since the current density approximations are larger.

$$J_z = J_\infty\sqrt{\frac{c}{2r} + 1}\ cos\left(\frac{\alpha}{2}\right) \tag{6.10}$$

$$J_y = -J_\infty\sqrt{\frac{c}{2r} + 1}\ sin\left(\frac{\alpha}{2}\right) \tag{6.11}$$

By substituting these equations for Eqs. 6.1 and 6.2 and repeating the derivation just described, the critical crack size formula reduces to

$$c_a = 3.48\sqrt{Dt^*}\left(\frac{\theta_m - \theta_\infty}{\theta_\infty - \theta_0}\right). \tag{6.12}$$

Using Eq. 6.12, the adiabatic crack size of the DTC is just 11 μm and the thermal zone size is 35 μm. For thermal cycling Test 7, the pulse length was about 50 μs, the peak temperature was 1133 K and this results in an adiabatic crack length of 35 μm.

The exact adiabatic crack size is not as important here as the adiabatic crack size order of magnitude (10 μm). The grain size of maraging steel (about 50 μm) is of the same order of magnitude. The adiabatic crack size should be made as large as possible to increase coil life. Crack-tip melting was significant through most of the DTC life. If crack-tip melting causes cracks to grow by a thermal zone size with each pulse, then the resulting initial crack growth rate

is geometric. This supports the idea that the coil life is over when crack-tip melting begins.

The adiabatic crack size formula contains two parameters critical towards magnet design. The first is the pulse length t^*, and the second is the peak coil temperature. The pulse length should be made as large as possible without increasing the peak temperature. Minimizing the peak coil temperature for a desired magnetic field is accomplished by varying the coil geometry. The adiabatic crack size formula can also be used as a guide to magnet material selection, since increased thermal diffusivity and melting temperature increase the adiabatic crack size.

The important conclusions for this section are that using a conductor near its melting temperature decreases the service life, and the adiabatic (critical) crack size can be used predict coil life. The safe use of an electrical conductor must allow for current density concentrations so that crack-tip melting is not significant.

Fatigue Life Analysis

There were three different types of fatigue tests performed for this thesis, low cycle fatigue tests at elevated temperatures under strain control, thermal cycling tests with rapidly varying temperatures and mechanical loading, and the DTC tests with combined electromagnetic and thermal loading. Each of these tests exhibited unique behavior characteristic to the geometry and loading of the test. The high temperature low cycle fatigue tests predict over 250 cycles to failure at high temperatures and strain rates. The thermal cycling tests show less than 50 cycles to failure and a mode of deformation peculiar to the specimen geometry and the phase transformations which are occurring during the tests. The DTC had just 16 cycles to failure, and it displayed the saw tooth crack type of failure. What these different kinds of fatigue tests have in common is the range of temperature and plastic strains which are being measured and predicted.

The low cycle fatigue test results are listed in Table 2.2 and plotted in Fig. 6.7. The number of cycles to failure was determined when the tensile loads during the test decreased 80 %. The cracks in these specimens were 1 to 3 mm long at failure. Using Tomkin's theory and the parameters for annealed

maraging steel in Table 1.3, the number of predicted cycles to failure is 2 to 4 times larger than the observed number of cycles to failure. Included in Fig. 6.7 are two curves from Tomkin's equation (Eq. 1.15) with final crack lengths of 33 and 2500 μm. The difference between the low cycle fatigue tests and the predictions from Tomkin's theory is explained by the following factors. The high temperature environment is the most important factor since it accelerates crack surface oxidation. Also important are the microstructure changes such as overaging, the formation of austenite and grain boundary segregation. None of these parameters were controlled or measured during the tests, so an estimate of their importance is difficult. A simple estimate of their effect is a factor of 4 reduction in fatigue life from room temperature data.

The thermal cycling test results were unexpected because of the few number of cycles to failure (less than 50.) The plastic strain ranges were all less than 0.7%, and 6 of the 7 test temperatures were within the temperature range of the low cycle fatigue tests. There are two reasons for the low number of cycles to failure in the thermal cycling tests. After approximately a dozen thermal cycles, temperature gradients in the shoulders of the specimen and phase transformations in the gage section cause a sharp change or decrease in the cross sectional area of the thermal cycling specimen. This change causes double necking and the barrel shape which increased temperatures and stress concentrations in the specimens. Secondly, oxidation cracks on the surface of the specimens will cause crack-tip melting, and this leads to the sudden failure observed in these tests.

There are some important differences between the thermal cycling tests and the DTC test. Structural analyses of thermal cycling specimens predict deformations which lead to shorter specimen lifetimes. The structural analysis of the DTC does not predict any localized deformation in the magnet, and this is in agreement with observations of the coil after the final failure. Unlike the thermal cycling specimens, the phase transformations and significant plastic deformations do not occur simultaneously in the same location. Both are occurring within the magnet, but not in the same location. Another major difference between the two tests is the absence or presence of magnetic fields. According to the theory advanced by Furth, the magnetic field diffuses into the crack-tip cavities and this influences the crack alignment and its shape. There are no large magnetic fields for the thermal tests, and there were no crack-tip cavities. However, cracks in thermal cycling specimens are more likely to result

in catastrophic failure, since there is less material supporting the cracks (the magnet build supports cracks on the inner radius).

The fatigue life analysis of the DTC divides the life of the magnet into two stages of crack behavior. The first stage is crack initiation and growth to an adiabatic crack size. The second stage is geometric saw tooth crack growth until electrical failure. Before the viscoplastic finite element analyses of the DTC, the estimated plastic strain range per pulse was 2%, and 200 pulses were necessary to grow a crack to 0.5 mm using Tomkin's equation (Eq. 1.15.) The estimate of the plastic strain range was too high because the previous finite element analysis of the DTC (not discussed in this thesis) underestimated the material strength in the high temperature regime and did not include plastic strain rate effects. The number of cycles to failure was also too high because the data for Tomkin's equations are not in the high temperature regime, and the fatigue analysis did not take into account saw tooth crack growth rates.

The estimated second stage fatigue life for the DTC is 5-9 pulses, leaving just 7-3 pulses for possible crack initiation and growth to an adiabatic crack size of 11 μm. According to Tomkin's equation, the initial crack size is 10 μm, and with a plastic strain range of 0.99 %, 11 pulses are needed to grow a crack to 11 μm. With a factor of 4 reduction (high temperature effects) in the number of pulses to grow this crack, the estimated first stage life is 3 pulses. However, Tomkin's equation should not be used to predict the fatigue life for such small cracks. Instead, the Paris law (Eq. 1.14) and the stress intensity formula shown below should be used to integrate the crack length from an initial crack size to an adiabatic (critical) crack size.

$$\Delta K = 1.12\ \Delta\sigma\sqrt{\pi a} \tag{6.13}$$

There are three sources of error in predicting the fatigue life of the DTC. One, if the adiabatic crack size is smaller than 11 μm, then this would reduce the number of cycles spent in stage one crack growth. Two, the crack growth rate predictions are known to be too small under these high temperature conditions. Three, the initial crack size in the DTC might actually be larger than 11 μm. More research is needed to determine initial crack sizes and to measure short crack growth rates. The conclusion of this section is that the initial crack size

is probable 5 to 15 μm in size, and that within 3 to 7 pulses saw tooth crack growth dominates.

Failure Modes and Recommendations

The failure of the DTC has mixed implications towards the safety concerns of short pulse magnets. On the one hand, the magnet was pulsed with 300 kA of current with cracks 5 mm long on the inside radius and the outer build of the magnet did not crack or burst. The coil contained the pressure wave of the electrical explosion. On the other hand, without visual observations, the imminent failure of the magnet was not detected. The safe operation of a short pulse magnet requires some means of detecting an imminent electrical explosion.

Delaying and preventing dangerous electrical failures might be accomplished with the following recommendations.

1. In the magnet design stage, make a maximum allowable current density (peak temperature) a design criterion. Unavoidable micro-cracks in the material can cause crack-tip melting, reducing coil life. Improved thermal cycling tests should be employed to simulate the thermal and mechanical loading conditions of short pulse magnets.
2. The coil construction method should be altered to minimize the initiation of small cracks in the finished coil. The coil turns should be cut with the wire EDM method. After aging, the coil could be polished with a diamond paste and then electro-polished in an acid solution to remove any residual stresses and cracks near the surface of the magnet.
3. The ratio of magnetic field over current should be monitored during and between tests to detect the presence of saw tooth cracks. By placing a pick-up coil at the end of the bore near the inside radius, the radial component of magnetic field could be measured without interfering with any experiment occupying the bore of the magnet. As mentioned previously, even when the charging voltage is varied, the ratio of magnetic field to current should remain constant.
4. Using a magnetic probe (a small test coil), the magnetic characteristics of the magnet bore could be measured and mapped for a small DC current in the magnet between test runs. Cracks in the magnet turns might be detected from the mapped magnetic characteristics.
5. Using a bore-scope, the bore of the magnet should be examined every 5 pulses for saw tooth cracks on the inner radius. An alternative to the visual examination would be to place an insulated tube next to the inner

radius, and then just remove and inspect the tube for metal spitting or other metallic residue. A third alternative is some gaseous metal detector at the end of the of the bore which can detect metal vapor from the pulses. All of these proposals are trying to detect the occurrence of crack-tip melting and the magnetic saw effect.

6. Periodically (several dozen pulses), a magnet should be electro-polished to remove micro-cracks from the coil surface. If a crack is removed before it reaches an adiabatic size, the life of the coil would be increased.

The serious drop in material hardness observed in the thermal cycling specimens and the DTC tests show that the increased strength of maraging steel in its aged condition is lost after more than a dozen thermal cycles to temperatures greater than the austenite start temperature. It is the recommendation of this thesis that maraging steel not be used at temperatures greater than 950 K. For the DTC, this would limit the peak magnetic field to 40T. Different magnet designs could generate fields of greater than 40 T, while still limiting the peak coil temperature to 950 K. At this temperature, the processes of overaging and austenite reversion are still significant, but the decrease in strength is not as rapid. The kinematic phase transformation from martensite to austenite along with the potential for anisotropic phase transformation strains is eliminated.

The most important effect of a lower operating temperature is the increase in the adiabatic crack length from 11 to 38 μm. The number of cycles spent initiating and growing a crack to this size with the smaller 40 T electromagnetic loads, would certainly dominate the life of the coil. Assuming a plastic strain range of 0.25 %, the predicted first stage life is 181 pulses (this comes from Tomkin's equation with a factor of 4 reduction in coil life due to thermal effects). Future research on short pulse magnet design should concentrate on determining the number of cycles needed to initiate and grow cracks to 100 μm.

Two additional recommendations for the short pulse magnet design should be mentioned. The experience of the DTC is similar to that reported for single turn coils. The DTC has pushed maraging steel to its limit as an electrical conductor. Further increases in non-destructive short pulse magnetic fields will be made by two changes. First and most important, multiple coil designs must be employed to increase the efficiency of magnetic field production. By employing several concentric coils, it is possible to generate the same magnetic field as a single coil magnet with smaller current densities and lower temperatures.

Secondly, the experience of this research suggests that different high strength, high temperature alloys would make better magnet materials. The criteria for selecting a material should be a large thermal diffusivity, a high melting temperature and a stable microstructure over a large temperature regime (no phase changes.) It should also have superior high temperature strength and fatigue properties.

Conclusions

A failure and fatigue analysis of the DTC reveals several important facts. The DTC electrically exploded after 16 pulses, and the explosion was caused by arcing in the bore of the magnet. The arcing was due to metal vapor ejected from the crack-tip cavities. This mode of failure has been observed before and is common in single turn destructible coils. Due to the high operating current densities and temperatures, maraging steel as a conductor is at its operational limit in this application. Under these conditions cracks need only grow to 11 μm before the thermal conditions at the crack-tip become adiabatic and the crack growth rate becomes geometric.

Data from the high temperature low cycle fatigue tests of this thesis show a factor of 4 decrease in life from the room temperature fatigue life predictions. The thermal cycling test results show that high current densities, temperatures and mechanical loads can reduce the fatigue life. In these tests, plastic deformation increases the peak temperatures, and when this is combined with crack-tip melting, the fatigue life is shortened. Because of the similar number of cycles to failure between these tests and the DTC, thermal cycling tests should be used in the future to test the current carrying capacity of a conductor.

Recommendations for a safer operation of short pulse magnets include lowering the peak current densities and temperatures, modifying the magnet construction method to minimize micro-cracks, monitoring the field over current ratio, and devising a crack detection method. Finally, the magnet can be periodically electro-polished to remove a thin surface layer of the magnet which contains the micro-cracks.

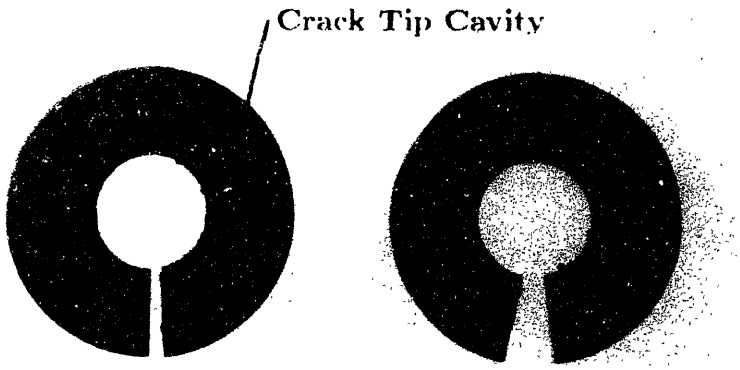

Fig. 6.1 Two adjacent turns from the destructive test coil.

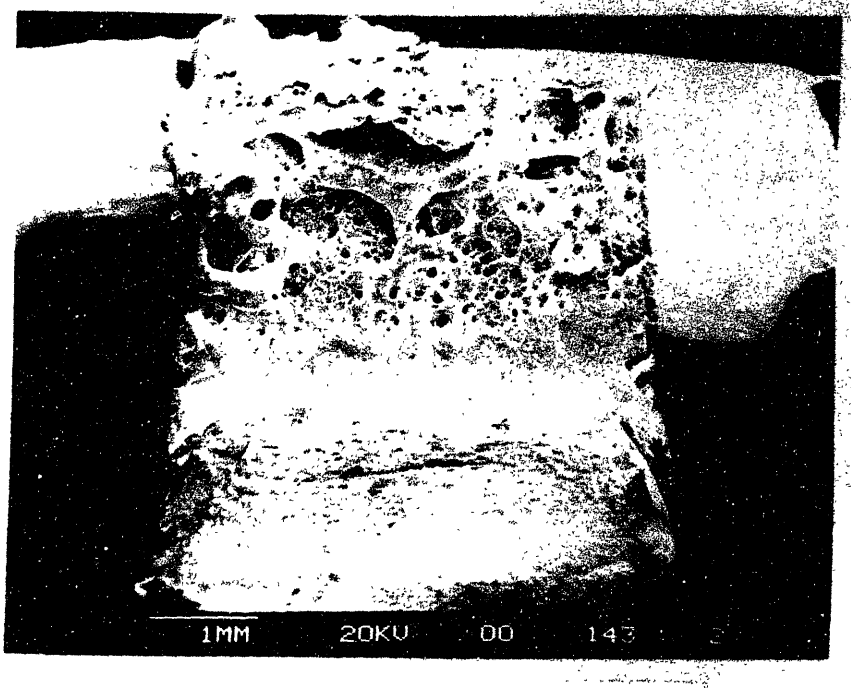

Fig. 6.2 Crack tip cavity surface.

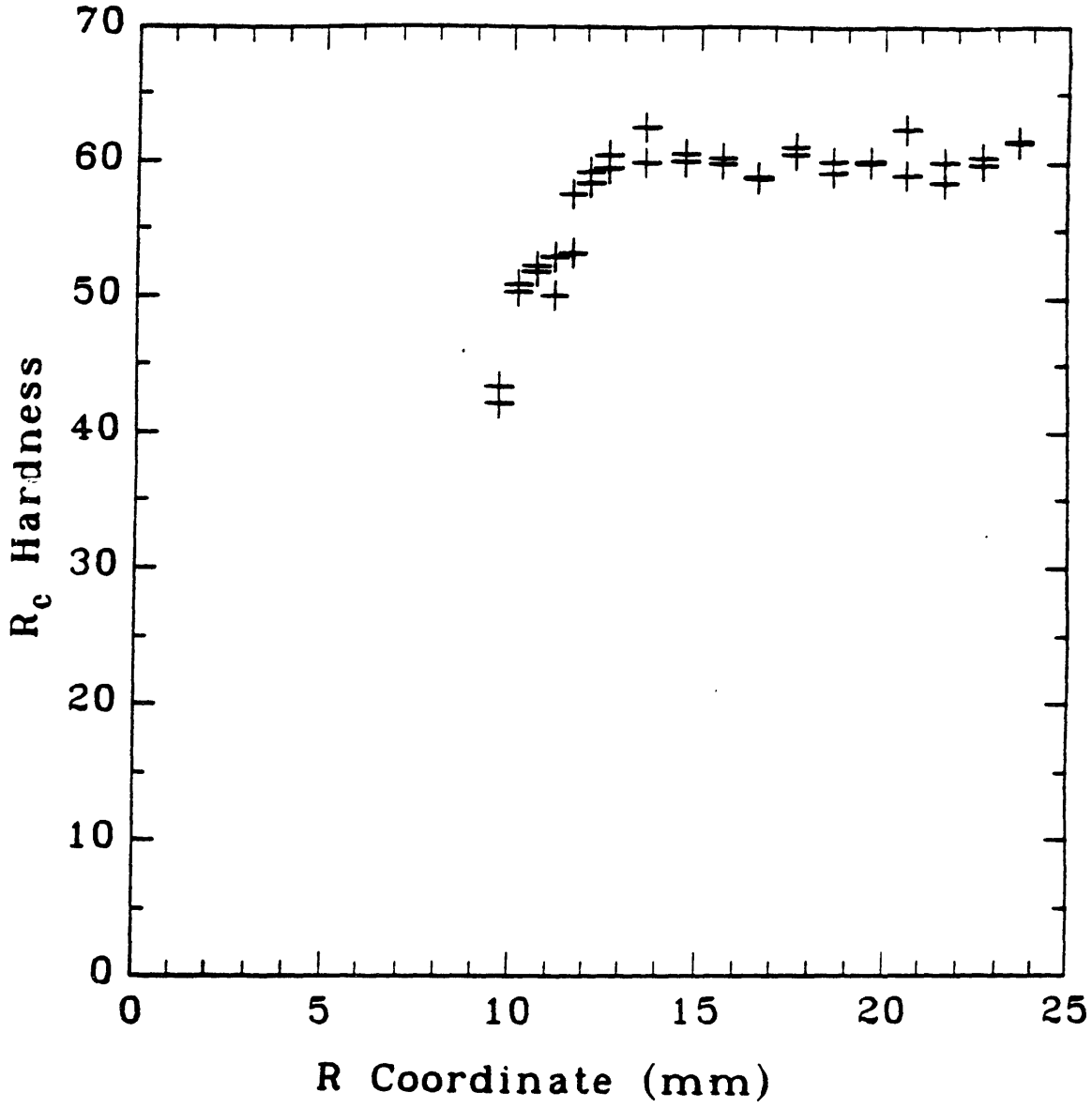

Fig. 6.3 Rockwell C hardness of DTC after 16 pulses.

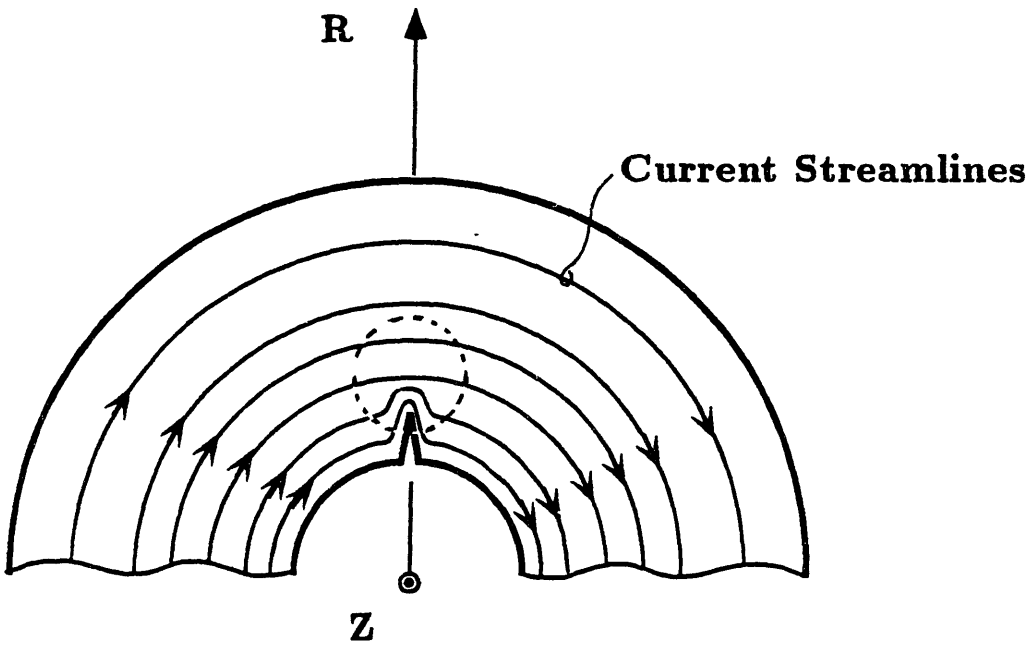

Fig. 6.4 Current density concentration at a crack-tip.

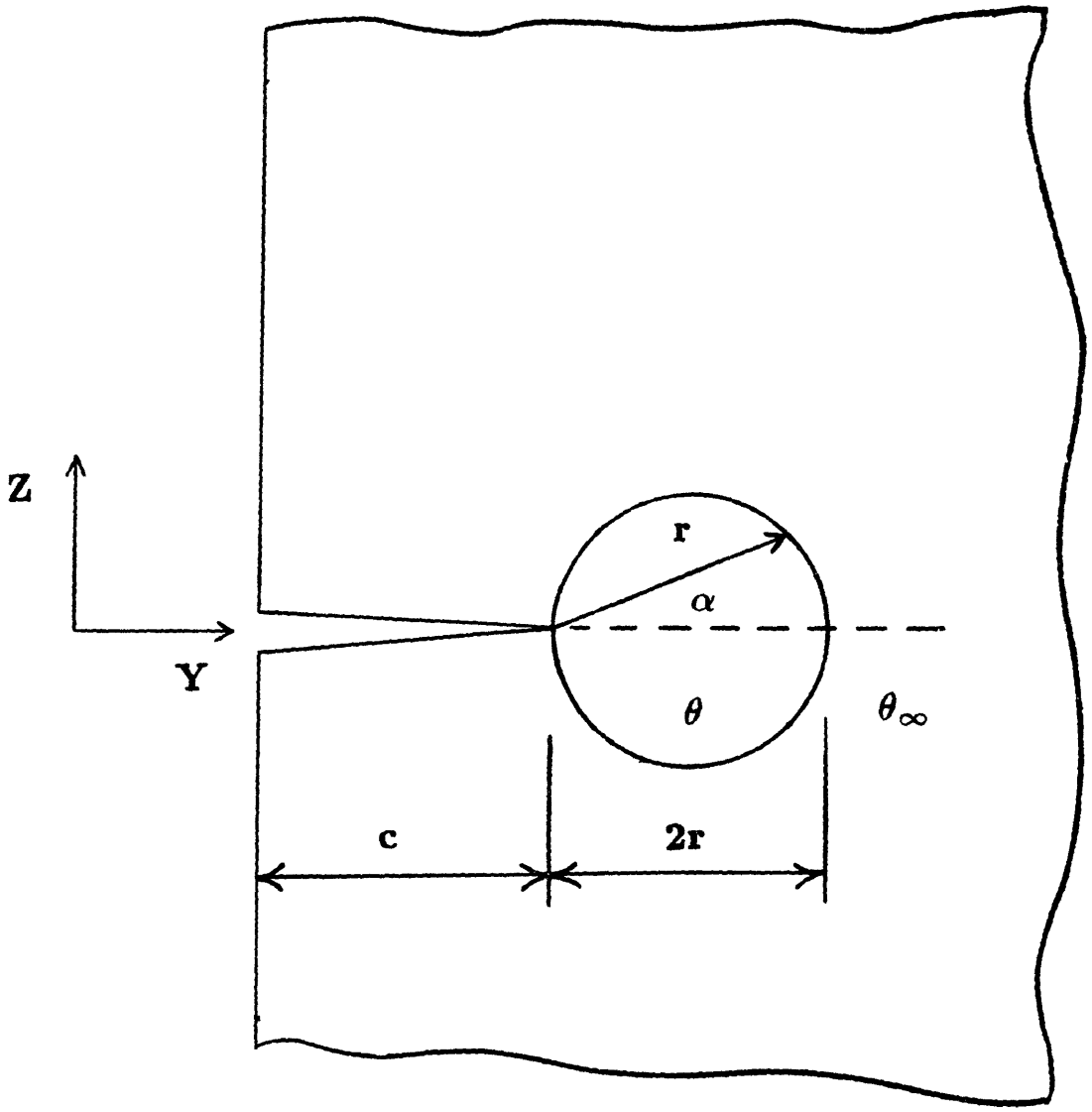

Fig. 6.5 The lumped crack-tip thermal analysis model.

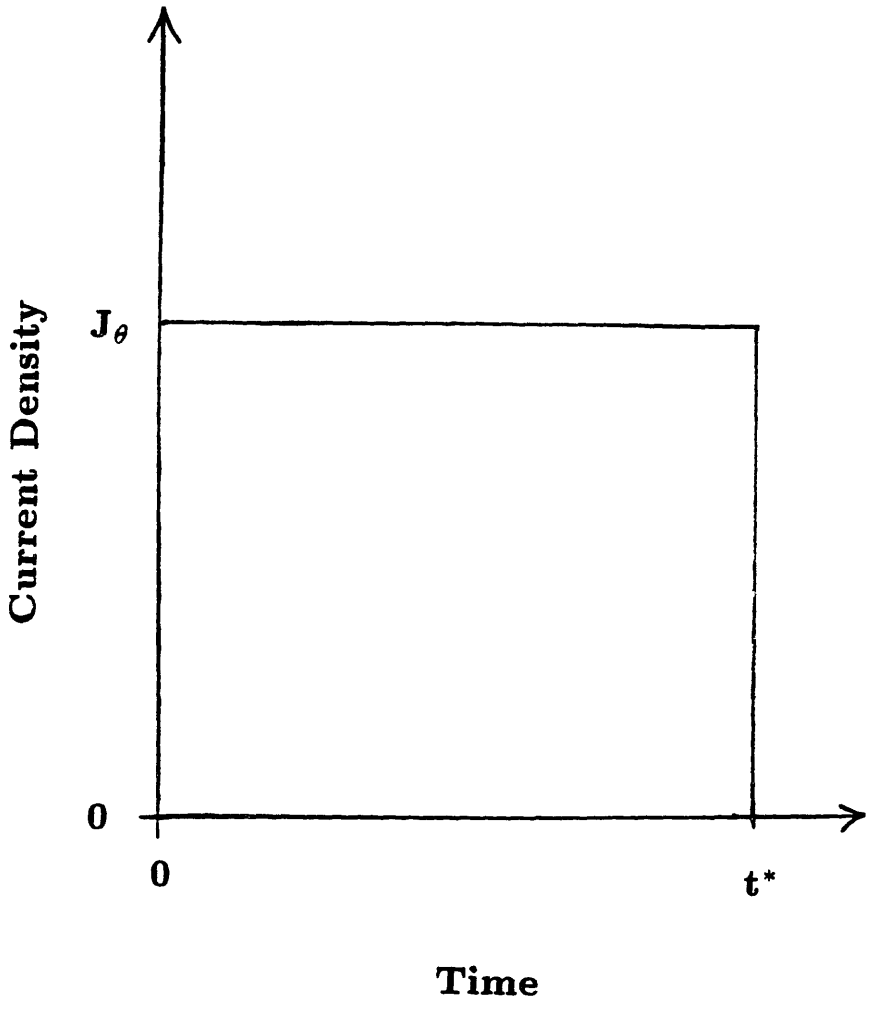

Fig. 6.6 Current density pulse approximation for material surrounding the crack-tip thermal zone.

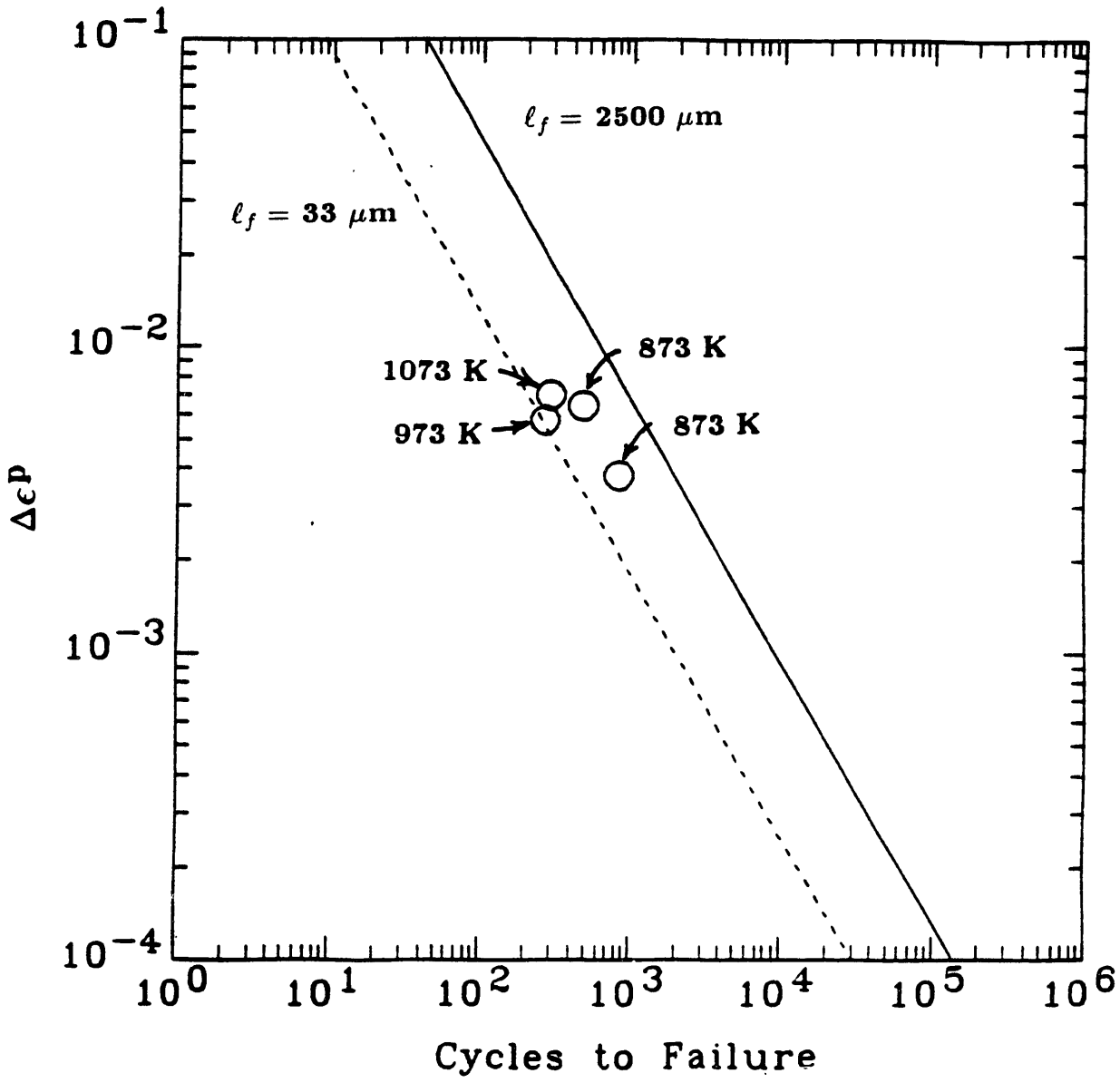

Fig. 6.7 Low cycle fatigue data from Chap. 2 and Tomkin's equation for annealed 300 grade maraging steel.

References

[1] V.F. Demichev and G.A. Shneerson, "Megagauss Magnetic Field Production by the Capacitor Bank Discharges," Megagauss Technology and Pulsed Poser Applications, Fourth Int. Conf. on Megagauss Magnetic Field Generation and Related Topics, July 1986, Santa Fe NM, Plenum Press.

[2] H. Jones, F. Herlach and J.A. Lee, "50 Tesla Pulsed Magnets Using a Copper Conductor Externally Reinforced With Stainless," IEEE Transactions on Magnetics, Vol. 24, No. 2, March 1988.

[3] H.P. Furth, M.A. Levine and R.W. Waniek, "Production and Use of High Transient Magnetic Fields. II," The Review of Scientific Instruments, Vol. 28, No. 11, Nov. 1957, pp. 949-958.

[4] A.M. Andrianov, V.F. Demichev, G.A.Eliseev and P.A. Levit, "Stability of Single-Turn Coils in Pulsed Magnetic Fields up to 1 MGs," Proceedings of the 6th Symposium on Fusion Technology, Aachen Germany, Sept. 1970, pp. 25-32.

[5] H. Knoepfel and R. Luppi, "Very High Magnetic Fields Generated in Single-Turn Solenoids, Journal of Physics E: Scientific Instruments 1972, Vol. 5, pp. 1133-1141.

[6] F. Herlach, "The Technology of Pulsed High Field Magnets," IEEE Transactions on Magnetics, Vol. 24, No. 2, March 1988.

[7] J.A.H. Hult and F.A.McClintock, "Elastic-Plastic Stress and Strain Distributions around Sharp Notches under Repeated Shear," Proc. IX Int. Conf. Appl. Mech., Brussels, 8, 1956, pp. 51-58.

[8] J.A.H. Hult, "Elastic Plastic Torsion of Sharply Notched Bars," Air Force Office of Scientific Research, Contract No. AF 18 (600) - 957, Div. File No. 10-12, July 1957.

[9] H.Tada, P.C.Paris and G.E.Irwin, "The Stress Analysis of Cracks Handbook," Del Research Corp., Hellertown PA, 1973 pp. 8.1.

[10] K. Hellan, *Introduction to Fracture Mechanics*, McGraw-Hill Book Co., 1984, pp. 7-48.

[11] H. Neuber, *Kerbspannungleshre* Springer, Berlin, 1937.

CONCLUSIONS

1. The electromechanical loads in this magnet cause a 350 N/mm^3 pulse of Lorentz body forces. Electrical resistance causes the temperature to rise from 298 to 1450 K in 250 μs, with a temperature gradient of 200 K/mm. After 1 min, the temperature of the magnet becomes nearly uniform at 690 K, and it then cools down to room temperature in 15 min. Under these extreme electromechanical and thermal conditions, there are microstructural changes, plastic deformation and crack growth in the maraging steel.

2. The most significant processes which affect the microstructure of maraging steel during its life in a short pulse magnet are phase transformations, aging and solutionizing, but not austenite reversion. At room temperature, maraging steel has a BCC martensite microstructure. Upon heating from 968 to 1008 K, maraging steel transforms to FCC austenite. The steel remains austenitic until it cools from 470 to 370 K. Phase transformations in maraging steel are time-independent, diffusionless and predominantly temperature-dependent. During a phase transformation from martensite to austenite, there is a macroscopic dilatational compression of 0.18 %, and for the austenite to martensite transformation, an expansion of 0.52 %. There are four major alloying elements in maraging steel: Ni, Mo, Co and Ti. In the annealed condition at room temperature, these elements are in solution. When the steel is held at 755 K for 4 hr, particles of Ni_3Mo and FeTi precipitate out of solution. These precipitates increase the tensile strength from 1000 to 2070 MPa. Should the precipitates grow too large and become widely spaced (overaging), the aged strength decreases. Solutionizing occurs in the austenite phase, dissolves precipitates and decreases the strength of aged maraging steel. Grain boundary segregation, and the formation of high nickel austenite and low nickel martensite by austenite reversion, occur too slowly to affect the microstructure under these conditions.

3. Four mechanisms contribute to the flow strength of maraging steel. In decreasing importance they are the precipitate shear resistance, the lattice and solution shear resistance, the dislocation shear resistance and a grain boundary contribution. The last one is less than 10 % of the tensile strength at room temperature. In summary, a physical description of the evolution of flow strength would primarily depend on the applied stress, temperature, volume fraction of martensite, precipitate sizes and spacings, and the dislocation density. The

flow strength evolves because phase transformations, aging, solutionizing and inelastic deformations affect the microstructure.

4. Large current density gradients exist near the inside radius of the magnet during an electromagnetic pulse. This creates two zones of essentially different electromagnetic and thermal conditions. Zone 1 extends 3 mm out from the inner radius, and in this zone, the largest body forces (350 N/mm^3) and temperatures (1460 K) are found. Zone 2 extends from the middle of the coil build to the outer radius, and in this zone both the peak Lorentz body forces (150 N/mm^3) and the peak temperatures are smaller (690 K). Initially, the maraging steel in the coil is in the aged condition, but after 16 pulses, the material in Zone 1 solutionizes and that in Zone 2 remains aged. Where the two zones meet, the alloy goes from the solutionized to overaged to aged condition in a span of about 0.3 mm. The mechanical behavior of the short pulse magnet is studied with a general material model which includes the behavior in the two zones.

5. An investigation of the flow strength of maraging steel was carried out with 23 tensile tests and 6 low cycle fatigue tests. These tests were performed at temperatures between 773 and 1083 K, and at plastic strain rates between 10^{-5} and 10^{-2} s^{-1}. The results show that the flow strength decreases 1000 MPa between 773 and 1083 K. Strain rate effects can more than double the flow strength at temperatures above 850 K.

6. Flow strength equations are incorporated into a time and temperature-dependent finite element analysis. This is done with a kinetic equation which predicts a rate of plastic straining as a function of the applied stress, a back stress and temperature. Material constants for the kinetic equation are found with a best fit to the tensile test data. The evolution of back stress is integrated with a nonlinear strain hardening coefficient function which approximates the strain hardening behavior observed in the low cycle fatigue tests.

7. Two kinetic equations have been studied and modeled in this thesis. The first is a phenomenological rate equation which uses a power law stress formula and can be derived from the rule of mixtures formulation of flow strength. The second is an Arrhenius rate equation which also has a power law stress term, but it includes a stress-dependent activation energy term. A comparison between these two kinetic equations shows that the phenomenological rate

equation better correlates with the large decrease in strength between 773 and 873 K (due to overaging and possible dynamic recovery), while the Arrhenius function makes a better prediction of material strength at temperatures greater than 1083 K.

8. The strain hardening behavior in the low cycle fatigue tests shows a Bauschinger effect, and neither strain hardening nor strain softening through half of the cyclic lives. There is not enough experimental data for this thesis to develop and model the evolutionary strain hardening behavior for complex thermal and mechanical loading histories. Instead, this model assumes an explicit function for the strain hardening coefficient and fits this to strain hardening data taken from the low cycle fatigue results at 1073 K. The strain hardening coefficient is nearly zero for plastic strains greater than 2 % (dynamic recovery effects are significant at this temperature).

9. During a pulse, the thermal history in Zone 1 of the magnet causes the material to undergo phase transformations between martensite and austenite and back again. The changes in temperature and material phase cause thermal and phase transformation strains. A linear model predicts these strains from the temperature and current material phase.

10. The finite element structural analysis of the short pulse magnet meets three major requirements. First, the analysis includes the Lorentz body forces which vary as a function of time and position within the magnet. Second, the analysis models the thermal and phase transformation strains which also vary as a function of time and position. Lastly, the kinetic and strain hardening equations are included to model the flow strength of maraging steel. To meet these requirements, a time dependent finite element program has been written to study the mechanical behavior of the short pulse magnet. The program is called AFESA for Axisymmetric Finite Element Solenoid Analysis. The code uses 8 - node axisymmetric elements and the frontal solution technique to minimize the stiffness matrix size. A modified Newton Raphson method is combined with the Alpha Constant Stiffness method to satisfy the the finite element equilibrium equations. The subroutine COLSOL written by K.J. Bathe solves the system of equations for the equilibrium displacements. The stress states within each element are integrated throughout the analysis. The radial return algorithm has been modified for this time-dependent analysis and is used with the kinetic equation to predict the plastic strain rates for the stress rate evaluation.

11. Thermal cycling tests were performed on different tensile specimen geometries to investigate the effects of extreme thermal cycling conditions in the absence of Lorentz body forces. The tensile specimen was constrained from movement at its ends, while a capacitor bank discharged a large current (20 kA) through the specimen, heating it to between 970 and 1410 K. The thermo - mechanical loading caused plastic deformation which led to specimen failure in less than 50 cycles.

12. Two observations dominate a discussion of the thermal cycling tests. First, localized thinning after a pulse increases the temperatures and temperature gradients for subsequent pulses. This reduces the specimen life. For the tapered specimens, a double necking phenomenon is observed after about 10 pulses. The necking occurs at the ends of the specimen gage length. Three factors contribute to this necking: the temperature gradient at the ends, the geometry of the ends which affects the stress-strain state and the strength (temperature-dependent) and phase transformation (there is a phase transition from martensite to austenite at the ends) behavior of maraging steel. For the hourglass specimen, a barrel-shaped deformation forms in the center of the gage section where the specimen transforms to austenite. The second major observation concerns the decrease in specimen hardness. The Rockwell C hardness decreases from 55 to 35 in the tapered and hourglass specimens after 16 and 25 cycles respectively. The hardness decreases between the austenite start and finish transformation temperatures.

13. Structural analysis of the tapered and hourglass specimens over several thermal cycles with AFESA predicts the observed double necking and the barrel shaped deformation. The analysis shows the plastic plastic deformation to be so localized that it absorbs the increased residual stress on cooling. The deformed shapes increase the peak temperatures and thermal gradients, the specimen life is strongly reduced. Thermal cycling shows that specimen life is decreased most by increased peak temperature. Decreasing the stress levels by altering the specimen geometry will increase the specimen life to a lesser extent. Thermal cycling has tested and verified the results predicted by AFESA.

14. The motivation for understanding the mechanical behavior of maraging steel is to produce the highest possible magnetic field with a short pulse magnet. The central achievement of this thesis is the successful design and construction of a 50 T, short pulse magnet (the destructible test coil, DTC). Design

methods, ideas and computer codes were tested and verified with this coil. Several important goals were achieved, as elaborated in the remaining conclusions.

A) Writing a program MESPA which predicts currents, temperatures, magnetic fields and Lorentz body forces within the magnet as a function of time.

B) Prevention of insulation failure by altering the shape of the DTC turn profile.

C) Developing an understanding of short pulse magnet failure which can aid future short pulse magnet design.

15. The program MESPA (Mechanical and Electromagnetic Short Pulse Analysis) solves the governing circuit equations for the short pulse magnet. It predicts the current density, temperature, magnetic field and body force profiles within the short pulse magnet as a function of time. With this code, the magnet design can be optimized for a given magnetic field and peak temperature. This is done by varying design parameters such as inner radius, turn thickness, number of coil turns and capacitor bank charging voltage.

16. A common problem for short pulse magnets of this type is pinched insulation at the inner radius of the magnet, due to thermal expansion and axial Lorentz body forces. The cross section of the DTC magnet turn was altered to create an air gap between the insulation and the coil turn at the inner radius. Thus, the insulation was not pinched and survived intact throughout the life of the magnet.

17. Finite element analysis with the phenomenological and Arrhenius rate equations were performed on the DTC. From these analyses, the following comments can be made. Dynamic body forces are insignificant. Permanent deformation resulting from Lorentz body forces are not large ($< 0.01\%$.) The thermal loading conditions dominate the plastic straining in this problem. Results from the phenomenological and Arrhenius analyses predict plastic strain ranges of 0.56 and 0.99 % respectively. Unlike the thermal cycling tests, the changes in cross-sectional shape of the coil turn do not change the thermal loading conditions for subsequent pulses. Phase transformations extend a maximum of 2.7 mm into the 15 mm magnet build. The hoop and axial stresses decrease by

about 400 MPa across the material phase transition from austenite to martensite. Most of the coil build is subjected to a stress range of greater than 1000 MPa per pulse.

18. A hysteresis plot of the deviatoric hoop strain versus stress at the inside radius indicates that most of the plastic straining occurs immediately after the electromagnetic pulse when high temperatures exist near the inside radius. Reverse plastic deformation occurs during cooling when the temperatures in the coil are nearly uniform. A hysteresis loop for the second pulse is contained within that for the first pulse, so the largest predicted strain increment is for the first pulse. The largest plastic strains occur at the inner radius and decrease into the build of the magnet. There is no plastic deformation predicted in the outer zone.

19. The DTC was pulsed 16 times to magnetic fields greater than 48 T. After 12 such pulses, 8 cracks were detected on the inside radius of the magnet along with some metal spatters. On the 16th pulse, a powerful electrical explosion occurred in the bore of the magnet. The cracks had developed crack-tip cavities, and material ejected from these cavities electrically shorted the turns of the magnet, causing an explosion. The crack-tip cavities form because the electric current must flow around cracks formed on the inside radius, and this concentrates the current density which melts material at the crack-tip. Crack growth due to crack-tip melting is called "saw-tooth" crack growth because externally, it resembles a rough saw cut.

20. An analysis of crack-tip melting shows that cracks smaller than a calculated adiabatic crack size will not develop crack-tip cavities. Instead, the additional heat generated by crack-tip current density concentrations is transported away from the crack-tip by thermal conduction. For cracks larger than the adiabatic crack size, melting occurs at the crack-tip and the resulting crack growth rate is geometric. The adiabatic crack size for the DTC was 11 μm and it took between 5 and 9 pulses (50 T) to grow a crack of this size to 2 mm. Judging from this estimate, it took the DTC 7 to 3 cycles to grow cracks to the adiabatic crack size. Thus, crack growth in high magnetic field short pulse magnets can be divided into two stages, crack initiation and growth to an adiabatic crack length and then saw tooth crack growth to failure. The DTC probably spent an equal amount time in the two stages. Because saw-tooth crack growth is geometric, a

magnet design should have a large adiabatic crack size to increase the number of cycles spent initiating and growing a crack to the adiabatic crack size.

21. Short pulse magnet design should use an adiabatic crack size as a criterion for predicting magnet life. Increasing this parameter will increase the magnet life and is best accomplished by decreasing the peak coil temperature. It is the recommendation of this thesis that maraging steel coil temperatures not exceed 950 K. This will lower the peak magnetic field and decrease the stress range during a pulse. To compensate, multiple magnet coils should be used to increase the magnetic field. Although maraging steel has a high tensile strength, its endurance limit is less than half its tensile strength and its strength is greatly decreased (from 2000 to 200 MPa) at high temperatures (above 1000 K). Different high-strength, high-temperature materials may be better suited for this application, but this needs more study. These coils should be machined using electrode discharge machining (EDM), and increased effort should be put into polishing. This should delay crack initiation to more nearly what would be expected from low cycle fatigue with a 1 % plastic strain range. Crack detection methods such as bore-scopic inspection, magnetic field monitoring, and crack-tip melting detection methods should also be investigated to ensure safer magnet operation.

In summary, this thesis has investigated the mechanical behavior of maraging steel and applied this knowledge to high magnetic field, short pulse magnets. From this study two flow strength models, and a thermal and phase transformation strain model were developed. Programs have been written to predict and analyze the electromagnetic, thermal and structural behavior of short pulse magnets. The design, construction and testing of the DTC yielded information which supports the design methods and ideas discussed here. Furthermore, the DTC experiment gave insight into the causes of short pulse magnet failure. As a result, limitations on the use of maraging steel as an electrical conductor were identified and correlated to important design parameters such as peak magnetic field and peak temperature.

Appendix A

Interpolation Functions

The interpolation functions given below correspond to the node numbers shown in Fig. A.1. These are standard quadrilateral isoparametric interpolation functions, and they are included in this thesis to define the basis of the element geometry and interpolation functions.

$$h_1 = \frac{1}{4}(1-r)(1-s)(-r-s-1) \tag{A.1}$$

$$h_2 = \frac{1}{2}(1-r^2)(1-s) \tag{A.2}$$

$$h_3 = \frac{1}{4}(1+r)(1-s)(r-s-1) \tag{A.3}$$

$$h_4 = \frac{1}{2}(1-s^2)(1+r) \tag{A.4}$$

$$h_5 = \frac{1}{4}(1+r)(1+s)(r+s-1) \tag{A.5}$$

$$h_6 = \frac{1}{2}(1-r^2)(1+s) \tag{A.6}$$

$$h_7 = \frac{1}{4}(1-r)(1+s)(-r+s-1) \tag{A.7}$$

$$h_8 = \frac{1}{2}(1-s^2)(1-r) \tag{A.8}$$

Strain-Displacement Matrix Entries

The notation for individual entries within the strain-displacement (**B**) matrix is shown below. The first subscript refers to the interpolation function, and the second subscript refers to the variable over which the derivative is taken.

$$b_{1,r} = \frac{\partial h_1}{\partial r} \tag{A.9}$$

It is obvious that the derivation of each strain-displacement matrix entry is a trivial matter of differentiation of the interpolation functions. However, the equations are rarely defined explicitly, and they are shown here for the benefit of the author.

$$b_{1,r} = \frac{1}{4}(1-s)(2r+s) \tag{A.10}$$

$$b_{1,s} = \frac{1}{4}(1-r)(r+2s) \tag{A.11}$$

$$b_{2,r} = -r(1-s) \tag{A.12}$$

$$b_{2,s} = -\frac{1}{2}(1-r^2) \tag{A.13}$$

$$b_{3,r} = \frac{1}{4}(1-s)(2r-s) \tag{A.14}$$

$$b_{3,s} = \frac{1}{4}(1+r)(2s-r) \tag{A.15}$$

$$b_{4,r} = \frac{1}{2}(1-s^2) \tag{A.16}$$

$$b_{4,s} = -(1+r)s \tag{A.17}$$

$$b_{5,r} = \frac{1}{4}(1+s)(2r+s) \tag{A.18}$$

$$b_{5,s} = \frac{1}{4}(1+r)(r+2s) \tag{A.19}$$

$$b_{6,r} = -r(1+s) \tag{A.20}$$

$$b_{6,s} = \frac{1}{2}(1-r^2) \tag{A.21}$$

$$b_{7,r} = \frac{1}{4}(1+s)(2r-s) \tag{A.22}$$

$$b_{7,s} = \frac{1}{4}(1-r)(2s-r) \tag{A.23}$$

$$b_{8,r} = -\frac{1}{2}(1-s^2) \tag{A.24}$$

$$b_{8,s} = -(1-r)s \tag{A.25}$$

The construction of the **H** and **B** matrices is dependent on the conventions used in the description of the nodal displacements and element stresses. The interpolation and strain-displacement entries listed here are the key components necessary to form **H** and **B** matrices.

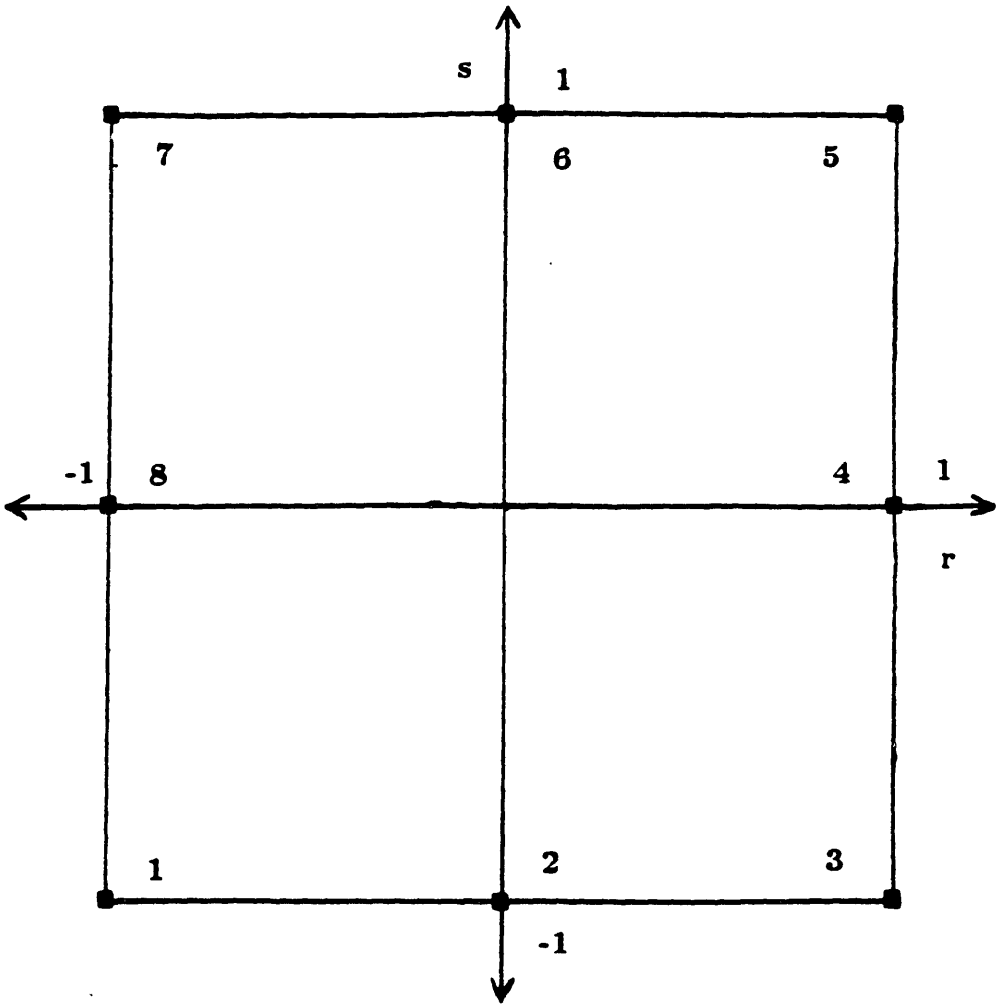

Fig. A.1 Finite element node numbering scheme.

Appendix B

Alpha Constant Stiffness Procedure

Initialize:

$$\mathbf{U}_0^{n+1} = \mathbf{U}^n \tag{B.1}$$

$$\alpha_0 = \mathbf{I} \tag{B.2}$$

Phase One :

$$\Psi_i = \Psi(\mathbf{U}_{i-1}) \tag{B.3}$$

$$\Delta\mathbf{U}_i' = -\mathbf{K}_0^{-1}\Psi_i \tag{B.4}$$

$$\mathbf{U}_i' = \mathbf{U}_{i-1} + \Delta\mathbf{U}_i' \tag{B.5}$$

Phase Two :

$$\Psi_i' = \Psi(\mathbf{U}_i') \tag{B.6}$$

$$\Delta\mathbf{U}_i' = -\mathbf{K}_0^{-1}\Psi_i \tag{B.7}$$

$$If \quad \Delta u_i' = 0 \quad Then \quad \alpha_i = \alpha_{i-1} \tag{B.8}$$

$$Else \quad If \quad \Delta u_i' \neq 0 \quad Then \quad \alpha_i = \alpha_{i-1} - \frac{\mathbf{K}_0^{-1}\Psi_i'}{\Delta u_i'} \tag{B.9}$$

$$\mathbf{U}_i = \mathbf{U}_{i-1} + \alpha_i\Delta\mathbf{U}_i' \tag{B.10}$$

Test for Convergence :

$$if \quad abs\left(\frac{\Psi_i}{\Psi_0}\right) > 10^{-16} \quad Then \tag{B.11}$$

$$\mathbf{U}_{i-1} = \mathbf{U}_i \tag{B.12}$$

$$\alpha_{i-1} = \alpha_i \tag{B.13}$$

GO TO PHASE ONE

End:

$$\mathbf{U}^{n+1} = \mathbf{U}_i \tag{B.14}$$

APPENDIX C

AFESA Plasticity Flow Chart

Based upon equilibrium values for the following variables; $(\epsilon_{ij})^n$, $(\epsilon^p_{ij})^n$, σ^n_{ij}, μ^n, λ^n, ϵ^n_θ, Ω^n_{ij}, ε^p_c and ε^p_m, new equilibrium values for ϵ^{n+1}_θ, σ^{n+1}_{ij}, $(\epsilon^p_{ij})^{n+1}$, Ω^{n+1}_{ij}, ε^p_c and ε^p_m are predicted based upon the input variables θ^{n+1} and $(\epsilon_{ij})^{n+1}$.

In Step 4, a test for plastic deformation is made, and if none is predicted, then the process is elastic and the flow chart branches to Step 12. For a plastic process, Step 5 determines whether a monotonic or cyclic hardening coefficient is used. This is accomplished by examining the stress state at time t^n and comparing it to the maximum back stress predicted with ε^p_m. If the back stress is equal to or greater than the maximum stress, then monotonic hardening is assumed. Next, a determination is made as to whether the stress increment crosses an elastic zone. Whenever a stress increment steps into or across the elastic regime, the cyclic plastic strain variable ε^p_c is set to zero and cyclic hardening is assumed.

Steps 7 through 11 outline the iterative procedures used to reconcile the kinetic equation with Eq. 3.38. Step 7 uses a predicted plastic strain rate $\dot{\varepsilon}^p_p$ to calculate Y^{n+1}. During the iterative process, the predicted plastic strain rate $\dot{\varepsilon}^p_p$ may be too large and the resulting Y^{n+1} is negative. To correct this, Y^{n+1} is tested, and if it is too large, $\dot{\varepsilon}^p_p$ is reduced by a factor of 0.9 and Step 7 is repeated. This reduction in $\dot{\varepsilon}^p_p$ continues until a positive Y^{n+1} calculation is achieved.

In Step 8, $\bar{h}$ is determined using the method described in Chap. 2. When $\dot{\varepsilon}^p_p$ is very small and equal to zero, a direct calculation of $\bar{h}$ is made by using the explicit form for h (Eqs. 2.15 and 2.16.)

The iterations between predicted and resulting plastic strain rates continue until the difference between them is 0.01 %. Each prediction of $\dot{\varepsilon}^p_p$ is made with an interpolation based on previous predictions $\dot{\varepsilon}^p_{p_1}$, $\dot{\varepsilon}^p_{p_2}$ and their resultants $\dot{\varepsilon}^p_{r_1}$ and $\dot{\varepsilon}^p_{r_2}$. In Step 10, the latest $\dot{\varepsilon}^p_p$ and $\dot{\varepsilon}^p_r$ are examined, and they replace the predicted and resultant pair which are furthest apart. Step 11 interpolates for a new $\dot{\varepsilon}^p_p$ and makes sure the prediction is greater than zero. When $\dot{\varepsilon}^p_p$ is less than zero, then $\dot{\varepsilon}^p_p$ is assumed to be equal to the resultant of the closest pair. The

procedure outlined here is by no means the optimum method, but it is typically capable of determining $\dot{\varepsilon}^p$ in 8 iterations.

STEP 1 : Define the input rate variables.

$$\dot{\epsilon}_{ij} = \frac{(\epsilon_{ij})^{n+1} - (\epsilon_{ij})^n}{\Delta t} \tag{C.1}$$

Determine ϵ_θ^{n+1}.

$$\dot{\epsilon}_\theta = \frac{\epsilon_\theta^{n+1} - \epsilon_\theta^n}{\Delta t} \tag{C.2}$$

Determine μ^{n+1} and λ^{n+1}

$$\dot{\mu} = \frac{\mu^{n+1} - \mu^n}{\Delta t} \tag{C.3}$$

$$\dot{\lambda} = \frac{\lambda^{n+1} - \lambda^n}{\Delta t} \tag{C.4}$$

STEP 2 : Calculate the trial stress.

$$\Delta\dot{\sigma}_{ij}^{Tr} = \Big[2\mu^n\dot{\epsilon}_{ij} + 2\dot{\mu}\left(\epsilon_{ij}^e\right)^n + \Big(\lambda^n\dot{\epsilon}_{kk} + \dot{\lambda}\left(\epsilon_{kk}\right)^n - (3\lambda + 2\mu)\left(\dot{\varepsilon}_t\right)^n\Big)\delta_{ij}\Big]\Delta t \tag{C.5}$$

$$\sigma_{ij}^{Tr} = \sigma_{ij}^n + \Delta\dot{\sigma}_{ij}^{Tr}\Delta t \tag{C.6}$$

STEP 3 : Calculate the approximate unit normal $\tilde{N}_{ij}$.

$$S_{ij}^{n+1} = \sigma_{ij}^{Tr} - \frac{1}{3}\sigma_{kk}^{Tr}\delta_{ij} \tag{C.7}$$

$$\sigma^* = \sqrt{3/2}\left|S_{ij}^{n+1} - \Omega_{ij}^n\right| \tag{C.8}$$

$$\tilde{N}_{ij} = \sqrt{3/2}\left(\frac{S_{ij}^{n+1} - \Omega_{ij}^n}{\sigma^*}\right) \tag{C.9}$$

STEP 4 : Test for plastic deformation.

Assume $\dot{\varepsilon}_p^p = 0$

Determine $Y^{n+1} = Y(\dot{\varepsilon}_p^p, \theta^{n+1})$

IF $\sigma^* < Y^{n+1}$ THEN

Elastic Process

$$\dot{\varepsilon}_{ij}^p = 0 \tag{C.10}$$

$$\varepsilon_c^p = 0 \tag{C.11}$$

GO TO STEP 12

Plastic Process

STEP 5 : Decide on monotonic versus cyclic hardening.

Assume Monotonic Hardening

$$\Omega_{max} = \frac{h_0 \varepsilon_0^p}{n_h} \left[1 - \left(1 + \frac{\varepsilon_m^p}{\varepsilon_0^p} \right)^{n_h} \right] \tag{C.12}$$

$$\Omega = \sqrt{3/2} \| \Omega_{ij}^n \| \tag{C.13}$$

IF $\Omega < \Omega_{max}$ and $\varepsilon_c^p \neq 0$ Assume Cyclic Hardening

IF $\| \sigma_{ij}^{Tr} - (\sigma_{ij})^n \| \leq \| (\sigma_{ij})^{n+1} - (\Omega_{ij})^n \|$ GOTO STEP 6

IF $\| \sigma_{ij}^{Tr} - (\sigma_{ij})^n \| < \| \sigma_{ij}^{Tr} - (\Omega_{ij})^n \|$ GOTO STEP 6

Assume Cyclic Hardening

$$\varepsilon_c^p = 0 \tag{C.14}$$

STEP 6 : Initialize plastic iteration variables.

$$K = 0 \tag{C.15}$$

$$\dot{\varepsilon}_p^p = 0 \tag{C.16}$$

For Monotonic Hardening

$$\varepsilon_c^p = 0 \tag{C.17}$$

$$(\varepsilon^p)^n = \varepsilon_m^p \tag{C.18}$$

For Cyclic Hardening

$$(\varepsilon^p)^n = \varepsilon_c^p \tag{C.19}$$

STEP 7 : Calculate $\bar{h}$.

IF $\dot{\varepsilon}_p^p < 10^{-9}$ THEN

For Monotonic Hardening

$$\bar{h} = h_0 \left(1 + \frac{(\varepsilon^p)^n}{\varepsilon_0^p}\right)^{-(n_h+1)} \tag{C.20}$$

For Cyclic Hardening

$$\bar{h} = h_0 \left(1 + \frac{(\varepsilon^p)^n}{2\varepsilon_0^p}\right)^{-(n_h+1)} \tag{C.21}$$

GO TO STEP 8

IF $\dot{\varepsilon}_p^p \geq 10^{-9}$ THEN

$$(\varepsilon^p)^{n+1} = (\varepsilon^p)^n + \dot{\varepsilon}_p^p \Delta t \tag{C.22}$$

For Monotonic Hardening

$$H^n = \frac{h_0 \varepsilon_0^p}{n_h} \left[1 - \left(1 + \frac{(\varepsilon^p)^n}{\varepsilon_0^p}\right)^{n_h}\right] \tag{C.23}$$

$$H^{n+1} = \frac{h_0 \varepsilon_0^p}{n_h} \left[1 - \left(1 + \frac{(\varepsilon^p)^{n+1}}{\varepsilon_0^p}\right)^{n_h}\right] \tag{C.24}$$

For Cyclic Hardening

$$H^n = \frac{2h_0 \varepsilon_0^p}{n_h} \left[1 - \left(1 + \frac{(\varepsilon^p)^n}{2\varepsilon_0^p}\right)^{n_h}\right] \tag{C.25}$$

$$H^{n+1} = \frac{2h_0 \varepsilon_0^p}{n_h} \left[1 - \left(1 + \frac{(\varepsilon^p)^{n+1}}{2\varepsilon_0^p}\right)^{n_h}\right] \tag{C.26}$$

$$\bar{h} = \frac{H^{n+1} - H^n}{\dot{\varepsilon}^p \Delta t} \tag{C.27}$$

STEP 8 : Calculate Y^{n+1} .

$$Y^{n+1} = \sigma^* - \left(3\mu^n + \bar{h}\right) \dot{\varepsilon}_p^p \Delta t \qquad (C.28)$$

IF $Y^{n+1} < 0$ GO TO STEP 9

$$\dot{\varepsilon}_p^p = 0.9 \ \dot{\varepsilon}_p^p \qquad (C.29)$$

REPEAT STEP 8

STEP 9 : Calculate $\dot{\varepsilon}_r^p$ with kinetic equation and test for convergence.

Determine $\dot{\varepsilon}_r^p = \dot{\varepsilon}_r^p(Y^{n+1}, \theta^{n+1})$.

IF $\left|\frac{\dot{\varepsilon}_p^p - \dot{\varepsilon}_r^p}{\dot{\varepsilon}_p^p}\right| > 10^{-4}$ GOTO STEP 10

$$\dot{\epsilon}_{ij}^p = \sqrt{3/2}\dot{\varepsilon}_p^p \tilde{N}_{ij} \qquad (C.30)$$

GO TO STEP 12

STEP 10 : Select plastic strain rate variables.

$$K = K + 1 \qquad (C.31)$$

IF $K > 50$ EXIT WITH ERROR

IF $K = 1$ THEN

$$\dot{\varepsilon}_{p_1}^p = \dot{\varepsilon}_p^p \qquad (C.32)$$

$$\dot{\varepsilon}_{r_1}^p = \dot{\varepsilon}_r^p \qquad (C.33)$$

$$\dot{\varepsilon}_p^p = \dot{\varepsilon}_r^p \qquad (C.34)$$

GOTO STEP 7

IF $K = 2$ THEN

$$\dot{\varepsilon}^p_{p_2} = \dot{\varepsilon}^p_p \tag{C.35}$$

$$\dot{\varepsilon}^p_{r_2} = \dot{\varepsilon}^p_r \tag{C.36}$$

GOTO STEP 11

IF $|\dot{\varepsilon}^p_{p_1} - \dot{\varepsilon}^p_{r_1}| > |\dot{\varepsilon}^p_{p_2} - \dot{\varepsilon}^p_{r_2}|$ THEN

$$\dot{\varepsilon}^p_{p_1} = \dot{\varepsilon}^p_p \tag{C.37}$$

$$\dot{\varepsilon}^p_{r_1} = \dot{\varepsilon}^p_r \tag{C.38}$$

GOTO STEP 11

$$\dot{\varepsilon}^p_{p_2} = \dot{\varepsilon}^p_p \tag{C.39}$$

$$\dot{\varepsilon}^p_{r_2} = \dot{\varepsilon}^p_r \tag{C.40}$$

STEP 11 : Interpolate for $\dot{\varepsilon}^p_p$ prediction.

$$x_p = \frac{log\left(\dot{\varepsilon}^p_{p_2}/\dot{\varepsilon}^p_{p_1}\right)}{\left(\dot{\varepsilon}^p_{p_2} - \dot{\varepsilon}^p_{p_1}\right)} \tag{C.41}$$

$$x_r = \frac{log\left(\dot{\varepsilon}^p_{r_2}/\dot{\varepsilon}^p_{r_1}\right)}{\left(\dot{\varepsilon}^p_{p_2} - \dot{\varepsilon}^p_{p_1}\right)} \tag{C.42}$$

$$\dot{\varepsilon}^p_p = \dot{\varepsilon}^p_{p_1} + \frac{log\left(\dot{\varepsilon}^p_{r_1}/\dot{\varepsilon}^p_{p_1}\right)}{\left(x_p - x_r\right)} \tag{C.43}$$

IF $\dot{\varepsilon}^p_p > 0$ GO TO STEP 7

$$\dot{\varepsilon}^p_p = \dot{\varepsilon}^p_{r_2} \tag{C.44}$$

IF $|\dot{\varepsilon}^p_{p_1} - \dot{\varepsilon}^p_{r_1}| < |\dot{\varepsilon}^p_{p_2} - \dot{\varepsilon}^p_{r_2}|$ GO TO STEP 7

$$\dot{\varepsilon}^p_p = \dot{\varepsilon}^p_{r_1} \tag{C.45}$$

GO TO STEP 7

STEP 12 : Determine σ_{ij}^{n+1}, $(\epsilon_{ij}^{p})^{n+1}$ and Ω_{ij}^{n+1}.

$$\sigma_{ij}^{n+1} = \sigma_{ij}^{Tr} - 2\mu\dot{\epsilon}_{ij}^{p}\Delta t \qquad (C.46)$$

$$\left(\epsilon_{ij}^{p}\right)^{n+1} = \left(\epsilon_{ij}^{p}\right)^{n} + \dot{\epsilon}_{ij}^{p}\Delta t \qquad (C.47)$$

$$\Omega_{ij}^{n+1} = \Omega_{ij}^{n} + \frac{2}{3}\bar{h}\dot{\epsilon}_{ij}^{p}\Delta t \qquad (C.48)$$

STEP 13 : Update plastic strain variables.

For Monotonic Hardening

$$\varepsilon_{m}^{p} = (\varepsilon^{p})^{n+1} \qquad (C.49)$$

For Cyclic Hardening

$$\varepsilon_{c}^{p} = (\varepsilon^{p})^{n+1} \qquad (C.50)$$

EXIT.

Appendix D

Finite Difference Heat Transfer

The thermal analysis of thermal cycling specimens has been carried out with a finite difference numerical method. This analysis is different from most other finite difference analyses in that the differential volume considered in the approximation varies. Thermal cycling test specimens are cylindrical in shape and variable in cross sectional area. In this analysis, the convective heat transfer between the specimen and the air is ignored. When convective heat transfer (assuming a free convective heat transfer coeffiecient of 25 W $m^{-2}K^{-1}$) is compared to the conductive heat transfer the resulting Nusselt No. is approximately 0.16. The significant heat transfer processes which must be considered are the heat generated by electrical resistance, and the heat conducted out of the specimen into the brass holding blocks.

The finite difference equations which are derived here are based upon the following set of assumptions and equations. Figure D.1a shows the finite difference model used in the analysis of the thermal cycling specimen. The model divides the specimen in half and then subdivides it into 27 segments of equal length. The boundary conditions used in this analysis are a constant temperature θ_0 at the end of the specimen and a zero temperature gradient at the center of the specimen. These boundary conditions are expressed in Eqs. D.1 and D.2 . z is the axial coordinate of the specimen in meters.

$$\theta_0 = 298 \quad K \tag{D.1}$$

$$\left.\frac{\partial \theta}{\partial z}\right|_{i=27} = 0 \tag{D.2}$$

The equation which governs this heat transfer problem is shown below. The finite difference solution for this equation requires additional focus into the heat transfer occurring in a single differential element volume.

$$\frac{\kappa}{dc_p}\frac{\partial^2 \theta}{\partial z^2} + \frac{\rho J^2}{dc_p} = \frac{\partial \theta}{\partial t} \tag{D.3}$$

Consider the single differential element shown in Fig D.1b. The element volume is a tapered cylinder with an area of A_i on the left and an area A_{i+1} on

the right. η is defined in Eq. D.4 as the ratio of these two areas. The volume of the differential element is given by Eq. D.5 .

$$\eta = A_{i+1}/A_i \tag{D.4}$$

$$V = \frac{\Delta z A_i}{3}\left(1 + \eta^{\frac{1}{2}} + \eta\right) \tag{D.5}$$

The heat transfer rate is q and its units are W. Heat flows across the element areas by conduction according to Eqs D.6 and D.7. A summation of the heat transfer rates and the ohmic heat generation is proportional to the rate of temperature change in the differential volume. This relationship is given by Eq. D.8. The superscripts t and $t + \Delta t$ refer to the finite difference times of the temperatures.

$$q_{i+1} = -\kappa \eta A_i \left(\frac{\theta_{i+1}^t - \theta_i^t}{\Delta z}\right) \tag{D.6}$$

$$q_i = -\kappa A_i \left(\frac{\theta_i^t - \theta_{i-1}^t}{\Delta z}\right) \tag{D.7}$$

$$dc_p V \left(\frac{\theta_i^{t+\Delta t} - \theta_i^t}{\Delta t}\right) = q_i - q_{i+1} + \rho J^2 V \tag{D.8}$$

Solving Eq. D.8 for $\theta_i^{t+\Delta t}$ and substituting Eqs. D.4-D.7 into the result gives the following iterative solution for the temperature at time $t + \Delta t$.

$$\theta_i^{t+\Delta t} = \theta_i^t + \left(\frac{3\kappa \Delta t}{dc_p \Delta z^2}\right)\left[\frac{\eta \theta_{i+1}^t - (1+\eta)\,\theta_i^t + \theta_{i-1}^t}{1 + \eta^{\frac{1}{2}} + \eta}\right] + \frac{\rho J^2 \Delta t}{dc_p} \tag{D.9}$$

This equation is used in a standard foreward finite difference method to determine the temperature distribution in the thermal cycling specimens as a function of both position and time. Normal considerations for an appropriately small time step and proper boundary conditions are made. The material constants κ, c_p and ρ are dependent on temperature, so the change in temperature with time must be smooth enough to also allow a smooth variation of these constants with time. Once again, the advantage of this particular finite difference formulation is the variable differential element volumes which allow easy analysis of various thermal cycling specimen geometries.

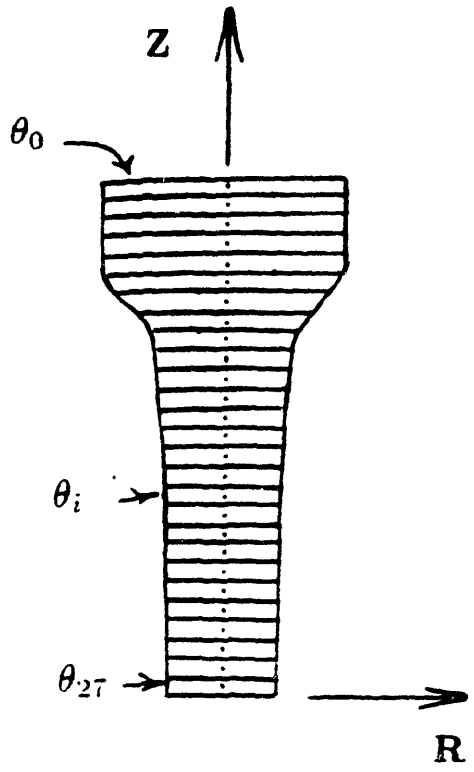

Fig. D.1 Finite difference model for the thermal analysis of the thermal cycling specimens.

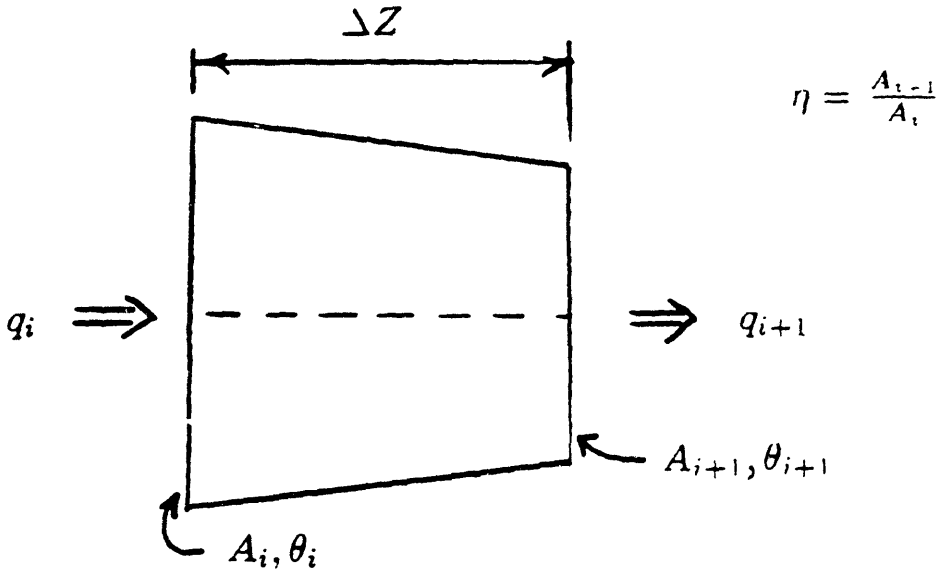

Fig. D.2 Discrete element of finite difference thermal model.

Appendix E

AFESA Documentation

This appendix contains a listing of the program AFESA, all the AFESA input commands and two example problems. Copies of this program can be obtained from the Francis Bitter National Magnet Laboratory. The program was developed on the VAX 11-780 computer, and it contains commands which can only execute on systems using the VAX VMS operating system (v4.0). AFESA does not have any preprocessing capabilities, so the finite element nodes and element geometry must be supplied by the user. Commands to generate a finite element model are stored in a file which is read by AFESA during execution. The input commands must match a defined input syntax, but numerical data is read with free format input statements. Two example sets of input commands are given in this appendix to show the AFESA input file syntax. The first example is the strain hardening problem discussed at the end of Chapter 3 (pg. 111), and the second example is the tapered test specimen analysis of Chapter 4 (pg. 127).

```
CCCCCCCCCCCCCCCCCCCCCCCCCCCCCCCCCCCCCCCCCCCCCCCCCCCCCCCCCCCCCCCCCCCCCCCCCCCCCCC
C
C       Axisymmetric Finite Element Solenoid Analysis
C
C       Written by Peter J. Raboin     9/85 - 2/89
C
CCCCCCCCCCCCCCCCCCCCCCCCCCCCCCCCCCCCCCCCCCCCCCCCCCCCCCCCCCCCCCCCCCCCCCCCCCCCCCC
C
C
C       This code is organized in three major sections that are called
C       by the main program AFESA.  Since finite element models vary in
C       size, a variable array size is used to minimize memory requirements.
C       First the model size is determined with the subroutine Intro.
C       Next, array sizes are set with the call statement
C       call lib$get_vm(# of bytes, memory location).  This allocates
C       virtual memory on the VAX 11-780 computer for the arrays.  The
C       subroutine ASSIGN then re-reads the input model and assigns the
C       data to arrays.  The next section is a frontal analysis which
C       assigns degree of freedom numbers to each node.  This minimizes
C       the required stiffness matrix size and decreases execution time.
C       The last section is the subroutine MAIN, and this subroutine
C       contains most of the finite element coding.  The subroutine
C       CONSIG is for graphic analysis and is not listed here.  This
C       code writes output files which contain nodal displacements and
C       element stresses and strains.
C
C
C       The program AFESA uses 8 node quadratic finite elements, and it
C       is applicable to small strain analyses only.  The axisymmetric
C       components of stress and strain are stored in the following order
C       with their arrays: radial, axial, shear and hoop components.
C
C       AFESA can perform eigther an entirely elastic analysis or an
C       elastic - plastic finite element analysis.  The implementation
C       of plasticity into AFESA is made with the subroutine TEPE (Thermal
C       Elastic Plastic Equations).  Various material laws have been
C       examined during the code development, but the version listed here
C       is the one described in Chapters 2 and 3.  The author suggests
C       that a good way to study this code is to begin where variables are
C       assigned (ASSIGN) to input parameters and then trace the variable
C       name through the code.  Variable names do not change in this code.
C       Each subroutine is preceeded by a short description of its purpose
C       and comment cards are included for additional information.  The
C       author does not believe he can adequately document this code
C       alone, because it requires a fresh, objective study by another
C       user to clarify confusing code sections  To help those who wish
C       to study and change this code, the following code ''map'' outlines
C       the path of program execution.  The items enclosed with parentheses
C       below are comments.
C
CCCCCCCCCCCCCCCCCCCCCCCCCCCCCCCCCCCCCCCCCCCCCCCCCCCCCCCCCCCCCCCCCCCCCCCCCCCCCCC
C
C
C       AFESA
C          |
C          |------- INTRO
C          |
C          |------- GAUSS
C          |
C          |----------------- ASSIGN
C          |                    |
C          |------- MATFIX      |------- MATL
```

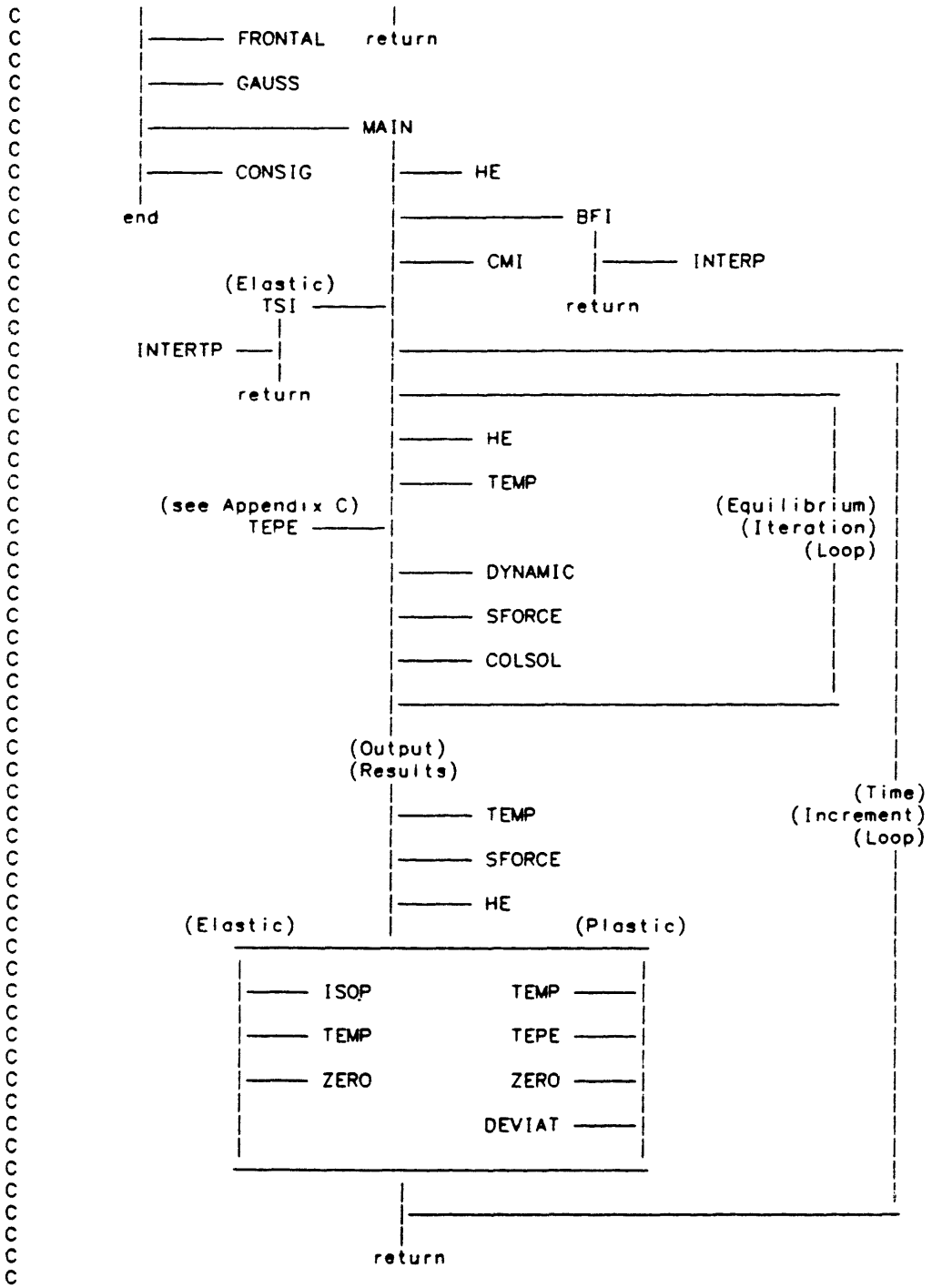

```
c         |                  |
c         |------ FRONTAL  return
c         |
c         |------ GAUSS
c         |
c         |--------------- MAIN
c         |                  |
c         |------ CONSIG     |------ HE
c         |                  |
c        end                 |------------- BFI
c                            |               |
c                            |------ CMI     |------ INTERP
c                (Elastic)   |               |
c                  TSI ------|             return
c                   |        |
c         INTERTP --|        |--------------------------------------
c                   |        |                                     |
c                 return     |---------------------------------    |
c                            |                                |    |
c                            |------ HE                       |    |
c                            |                                |    |
c                            |------ TEMP                     |    |
c      (see Appendix C)      |                   (Equilibrium)    |
c           TEPE ------------|                     (Iteration)    |
c                            |                          (Loop)    |
c                            |------ DYNAMIC                  |    |
c                            |                                |    |
c                            |------ SFORCE                   |    |
c                            |                                |    |
c                            |------ COLSOL                   |    |
c                            |                                |    |
c                            |---------------------------------    |
c                            |                                     |
c                         (Output)                                 |
c                         (Results)                                |
c                            |                                  (Time)
c                            |------ TEMP                   (Increment)
c                            |                                  (Loop)
c                            |------ SFORCE                        |
c                            |                                     |
c                            |------ HE                            |
c             (Elastic)      |              (Plastic)              |
c                 --------------------------------                 |
c                 |                              |                 |
c                 |------ ISOP         TEMP -----|                 |
c                 |                              |                 |
c                 |------ TEMP         TEPE -----|                 |
c                 |                              |                 |
c                 |------ ZERO         ZERO -----|                 |
c                 |                              |                 |
c                 |                  DEVIAT -----|                 |
c                 |                              |                 |
c                 --------------------------------                 |
c                             |                                    |
c                             |-------------------------------------
c                             |
c                           return
c
c
cccccccccccccccccccccccccccccccccccccccccccccccccccccccccccccccccccccccc
c
      implicit real*8(a-h,o-z)
      implicit integer(i-k,n,m)
```

```
      logical l

      dimension iplad(4),rplad(4),sp(7)
      character*30 fname,fnamein,fnamesave,t,fnameplt(16),
     &             fgeom,fnameout(16),title*78,ans*1

      n2=2
      n3=3
      n4=4
      n5=5
      n6=6
      n7=7
      n8=8
      n16=16

      write(6,6001)
      read(5,6002) fname

      write(6,6003)
      read(5,6004) ans
      ltout= false.
      if(ans .eq. 'y' .or  ans .eq. 'Y') ltout=.true.

      call INTRO(title,fname,fgeom,fnameplt,fnameout,fnamein,
     &           fnamesave,nmatt,nemat,nplm,nplfdv,n16,
     &           ix,iy,nn,ne,nlc,nkrd,nkad,nkrf,nkaf,
     &           nrbfrt,nrbfrdv,nrbfat,nrbfadv,
     &           nabfrt,nabfrdv,nabfat,nabfadv,nrtt,ntrdv,
     &           natt,ntadv,ildad,nlde,neas,lat,lstart,
     &           lsave,ldebug,lnodes,lelem,lmat,load,lerr,
     &           lplt,lrbf,lrbft,labf,labft,ltmp,ltmpt,
     &           lfout,leas,ltp,ldyn)


      if(lerr) then
         write(6,7005)
         goto 9999
      endif

      if(lnodes) then
         call lib$get_vm(8*nn*2,mx)
         call lib$get_vm(4*nn*2,mimap)
         call lib$get_vm(4*nn*2,mic)
         call lib$get_vm(4*nn*6,mnel)
      else
         write(6,7001)
         goto 9999
      endif

      if(ldyn) then
        ndn=nn
      else
        ndn=1
      endif
      call lib$get_vm(8*ndn*n2,mp1d)
      call lib$get_vm(8*ndn*n2,mp2d)
      call lib$get_vm(8*ndn*n2,mp3d)

      if(lelem) then
         call lib$get_vm(4*ne*8,mit)
         call lib$get_vm(4*ne,mimem)
         call lib$get_vm(4*ne,mies)
      else
```

```
   write(6,7002)
   goto 9999
endif

if(lmat) then
   call lib$get_vm(4*nmatt,mmca)
   call lib$get_vm(8*nmatt,mden)
   call lib$get_vm(8*nemat*n4*n4,mc)
   call lib$get_vm(8*nemat*n4,mct)
   call lib$get_vm(8*nemat*n3,mcmpa)
   call lib$get_vm(8*npltdv,mpmta)
   call lib$get_vm(8*nplm*npltdv*n5,mpmpa)
   call lib$get_vm(8*nplm*n7,mphas)
else
   write(6,7003)
   goto 9999
endif

call lib$get_vm(8*nlc,mtime)

if(.not. load) then
   write(6,7004)
   goto 9999
endif

call lib$get_vm(4*nkrd,miprd)
call lib$get_vm(8*nlc*nkrd,mprd)

call lib$get_vm(4*nkad,mipad)
call lib$get_vm(8*nlc*nkad,mpad)

call lib$get_vm(4*nkrf,miprf)
call lib$get_vm(8*nlc*nkrf,mprf)

call lib$get_vm(4*nkaf,mipaf)
call lib$get_vm(8*nlc*nkaf,mpaf)

call lib$get_vm(8*nlc*16,mbf)
if(lrbf) then
   call lib$get_vm(8*nlc*nrbfrt*nrbfat,mrbfd)
else
   call lib$get_vm(8,mrbfd)
endif
call lib$get_vm(8*nrbfrdv,mrbfrd)
call lib$get_vm(8*nrbfadv,mrbfad)

if(labf) then
   call lib$get_vm(8*nlc*nabfrt*nabfat,mabfd)
else
   call lib$get_vm(8,mabfd)
endif
call lib$get_vm(8*nabfrdv,mabfrd)
call lib$get_vm(8*nabfadv,mabfad)

call lib$get_vm(8*nlc,msol)
call lib$get_vm(8*nlc*16,mts)
if(ltmp) then
   call lib$get_vm(8*nlc*nrtt*natt,mtd)
else
   call lib$get_vm(8,mtd)
endif
call lib$get_vm(8*ntrdv,mtrd)
call lib$get_vm(8*ntadv,mtad)
```

```
      call lib$get_vm(4*ildad,mildа)

      call lib$get_vm(4*neas,mitasp)
      call lib$get_vm(8*neas,maspc)
      call lib$get_vm(8*neas,mpsd)
      call lib$get_vm(8*neas,maspd)
      call lib$get_vm(8*neas,maspod)

      call ASSIGN(%val(mx),nn,%val(mit),ne,%val(mimem),%val(mtime),
     &            nlc,%val(miprd),%val(mprd),nkrd,%val(mipad),
     &            %val(mpad),nkad,%val(miprf),%val(mprf),nkrf,
     &            %val(mipaf),%val(mpaf),nkaf,%val(mrbfd),nrbfrt,
     &            nrbfat,%val(mrbfrd),nrbfrdv,%val(mrbfad),nrbfadv,
     &            %val(mabfd),nabfrt,nabfat,%val(mabfrd),nabfrdv,
     &            %val(mabfad),nabfadv,%val(mtd),nrtt,natt,
     &            %val(mtrd),ntrdv,%val(mtad),ntadv,n2,n3,n4,n5,n8,
     &            %val(mc),%val(mct),%val(mcmpa),fname,%val(mmca),
     &            nmatt,nemat,nplm,nplfdv,%val(mpmta),%val(mpmpa),
     &            iplad,rplad,sp,%val(mildа),ildad,%val(mden),
     &            %val(mitasp),%val(maspod),eol,umax,%val(mpsd),
     &            %val(maspc),%val(maspd),neas,%val(mphas),n7)

      if( not. lat) call MATFIX(%val(mmca),%val(mimem),nmatt,ne)

      nkd=nkrd+nkad-2
      nud=2*nn-nkd
      nnm=nud+1
      nn2=nn*2

      call lib$get_vm(4*nnm,mmaxa)

      call FRONTAL(%val(mit),ne,%val(mimap),nn,%val(mmaxa),nnm,nud,
     &             %val(mic),nn2,%val(mies),%val(mnel),n2,n6,n8,
     &             %val(miprd),nkrd,%val(mipad),nkad,mt)

      call lib$get_vm(8*ix*iy,mwt)
      call lib$get_vm(8*ix*iy*8,mh)
      call lib$get_vm(8*ix*iy*8*2,mb)

      call lib$get_vm(8*ix*iy*4*4,mtsso)

      call GAUSS(%val(mwt),%val(mh),%val(mb),ix,iy,n2,n8)

      call lib$get_vm(8*mt,ma)

      call lib$get_vm(8*nud*nlc,msv)
      call lib$get_vm(8*nud,mosv)
      call lib$get_vm(8*nud,mdisp)
      call lib$get_vm(8*nud,mrv)
      call lib$get_vm(8*nud,mrvo)
      call lib$get_vm(8*nud,mdrvo)
      call lib$get_vm(8*nud,malpha)
      call lib$get_vm(8*nn*n2,mpid)
      call lib$get_vm(8*nn,mpit)
      call lib$get_vm(8*nn,mpft)

      call MAIN(fgeom,fnameplt,fnameout,title,%val(mit),ne,%val(mimap),
     &%val(mx),nn,n2,n8,n16,nlc,%val(mtime),%val(miprd),
     &%val(mprd),nkrd,%val(mipad),%val(mpad),nkad,%val(miprf),
     &%val(malpha),%val(mprf),nkrf,%val(mipaf),%val(mpaf),nkaf,
     &mrbfd,nrbfrt,nrbfat,%val(mrvo),%val(mdrvo),mrbfrd,
     &nrbfrdv,mrbfad,nrbfadv,mabfd,
```

```
     &  nabfrt,nabfat,mabfrd,nabfrdv,mabfad,nabfadv,mtd,nrtt,
     &  natt,mtrd,ntrdv,mtad,ntadv,%val(mc),%val(mct),
     &  %val(mcmpa),n5,n4,n3,nemat,%val(mwt),ix,iy,%val(ma),
     &  mt,%val(mmaxa),nnm,%val(msv),nud,%val(mimem),mb,mh,
     &  %val(msol),%val(mts),%val(mbf),%val(mdisp),%val(mrv),
     &  %val(mosv),%val(mpmta),%val(mpmpa),rplad,iplad,nplm,
     &  npltdv,%val(mmca),nmatt,%val(mpid),sp,%val(mtsso),
     &  %val(milda),ildad,nlde,%val(mitasp),%val(maspod),
     &  eol,umax,%val(mpsd),%val(maspc),%val(maspd),neas,
     &  ltp,%val(mphas),n7,%val(mden),%val(mp1d),%val(mp2d),
     &  %val(mp3d),ndn,fnamein,fnamesave,lstart,lsave,lat,
     &  lrbf,lrbft,labf,labft,ltmp,ltmpt,lplt,ltout,lfout,
     &  ldebug,leas,ldyn,%val(mpit),%val(mpft))

        if(lplt) call CONSIG(fnameplt,fnameout,ix,iy,nn,ne,nlc,n16,
     &                       ltout,lfout,mx,mit,mies,mnel,mwt,mh,mb)

6001    format(//'  Enter the name of the Finite Element input file : '$)
6002    format(a30)
6003    format(//'  Do you want terminal output (Y/N) : '$)
6004    format(a1)
7001    format(//,'  ---ERROR---',/,'  No nodes were specified !')
7002    format(//,'  ---ERROR---',/,'  No elements were specified !')
7003    format(//,'  ---ERROR---',/,'  No materals were specified !')
7004    format(//,'  ---ERROR---',/,'  No loads were specified !')
7005    format(//,'  ---ERROR---',/,'  Could not read input data
     &file !')
7099    format(//,'  ---EXECUTION STOPPED DUE TO INTERNAL ERROR
     & DETECTION---')

        stop
9999    write(6,7099)
        stop
        end



CCCCCCCCCCCCCCCCCCCCCCCCCCCCCCCCCCCCCCCCCCCCCCCCCCCCCCCCCCCCCCCCCCCCCCCCCCCCCCC
C
C       INTRO
C
C       This subroutine reads the finite element input model
C       to determine the array sizes needed for the analysis, and
C       to define logical variables.  If there are errors in the
C       model data format, they are detected here.
C
CCCCCCCCCCCCCCCCCCCCCCCCCCCCCCCCCCCCCCCCCCCCCCCCCCCCCCCCCCCCCCCCCCCCCCCCCCCCCCC

        subroutine INTRO(title,fname,fgeom,fnameplt,fnameout,fnamein,
     &                   fnamesave,nmatt,nemat,nplm,npltdv,n16,
     &                   ix,iy,nn,ne,nlc,nkrd,nkad,nkrf,nkaf,
     &                   nrbfrt,nrbfrdv,nrbfat,nrbfadv,
     &                   nabfrt,nabfrdv,nabfat,nabfadv,nrtt,ntrdv,
     &                   natt,ntadv,ildad,nlde,neas,lat,
     &                   lstart,lsave,ldebug,lnodes,lelem,lmat,
     &                   load,lerr,lplt,lrbf,lrbft,labf,labft,
     &                   ltmp,ltmpt,lfout,leas,ltp,ldyn)

        implicit real*8(a-h,o-z)
        implicit integer(i-k,n,m)
        logical l
```

```
      character*(*) title,fname,fnameplt(n16),fnameout(n16),
     &              fgeom,fnamein,fnamesave
      character*25 inp

      ix=3
      iy=3
      nmatt=1
      nemat=1
      nplm=1
      npltdv=1
      nlc=1
      nkrd=1
      nkad=1
      nkrf=1
      nkaf=1
      nrbfrt=1
      nrbfat=1
      nabfrt=1
      nabfat=1
      nrbfrdv=1
      nrbfadv=1
      nabfrdv=1
      nabfadv=1
      nrtt=1
      natt=1
      ntrdv=1
      ntadv=1
      ners=1
      neas=1
      ildad=1
      lnodes=.false.
      lelem=.false.
      lmat=.false.
      load=.false.
      lrbf=.false.
      labf=.false.
      ltmp=.false.
      lat=.true.
      lplt=.false.
      lfout=.false.
      lstart=.false.
      lsave=.false.
      ldebug=.false.
      lerr=.false.
      leas=.false.
      ltp=.false.
      ldyn=.false.
      title='NO TITLE'

      write(6,*)
      write(6,*) ' Echo output of input file :'
      write(6,*)
      open(unit=3,file=fname,readonly,status='old')
10    read(3,6001) inp
      call STR$UPCASE(inp,inp)

      write(6,6001) inp
      if(inp .eq. 'TITLE') goto 100
      if(inp .eq. 'NODES') goto 200
      if(inp .eq. 'ELEMENTS') goto 300
      if(inp .eq. 'ELASTIC MATERIALS') goto 400
      if(inp .eq. 'PLASTIC MATERIALS') goto 425
      if(inp .eq. 'TWO PHASE') goto 1400
```

```
      if(inp .eq. 'LOAD CASES') goto 450
      if(inp .eq. 'RADIAL DISPLACEMENTS') goto 500
      if(inp .eq. 'AXIAL DISPLACEMENTS') goto 550
      if(inp .eq. 'RADIAL NODE FORCES') goto 600
      if(inp .eq. 'AXIAL NODE FORCES') goto 650
      if(inp .eq. 'RADIAL BODY FORCES') goto 700
      if(inp .eq. 'AXIAL BODY FORCES') goto 750
      if(inp .eq. 'TEMPERATURES') goto 800
      if(inp .eq. 'GAUSS POINTS') goto 900
      if(inp .eq. 'AFESAPLT') goto 940
      if(inp .eq. 'AFESAOUT') goto 945
      if(inp .eq. 'ELASTIC') goto 950
      if(inp .eq. 'ELASTIC-PLASTIC') goto 960
      if(inp .eq. 'RESTART') goto 1100
      if(inp .eq. 'SAVE') goto 1125
      if(inp .eq. 'DEBUG') goto 1150
      if(inp .eq. 'SOLUTION PARAMETERS') goto 1200
      if(inp .eq. 'EXTERNAL AXIAL SPRINGS') goto 1350
      if(inp .eq. 'DYNAMIC') goto 1500
      if(inp .eq. 'EXIT') goto 9999
      write(6,6002)
      goto 9999

100   read(3,6009) title
      goto 10

200   read(3,*) nn
      do 210 i=1,nn
210   read(3,*) i1,d1,d2
      lnodes=.true.
      goto 10

300   read(3,*) ne
      do 310 i=1,ne
310   read(3,*) i1,i2,(i3,j=1,8)
      lelem=.true.
      goto 10

400   read(3,*) nemat
      if(nemat .ge. 1) then
         do 410 imat=1,nemat
410      read(3,*) i1,d1,d2,d3
         nmatt=nmatt+nemat
         if(.not. lmat) nmatt=nmatt-1
         lmat=.true.
         goto 10
      else
         write(6,6003)
         lerr=.true.
         goto 9999
      endif

425   read(3,*) nplm,npltdv
      if(nplm .ge. 1 .and. npltdv .ge. 1) then
         do 430 i=1,npltdv
430      read(3,*) d1
         do 440 i=1,nplm
         read(3,*) i1
         do 440 j=1,npltdv
440      read(3,*) d1,d2,d3,d4,d5
         nmatt=nmatt+nplm
         if(.not. lmat) nmatt=nmatt-1
         lmat=.true.
```

```
            goto 10
         else
            write(6,6003)
            lerr=.true.
            goto 9999
         endif

450      read(3,*) nlc
         read(3,*) (d1,i=1,nlc)
         goto 10

500      read(3,*) nkrd
         do 510 j=1,nkrd
510      read(3,*) i1,(d1,i=1,nlc)
         nkrd=nkrd+1
         goto 1000

550      read(3,*) nkad
         do 560 j=1,nkad
560      read(3,*) i1,(d1,i=1,nlc)
         nkad=nkad+1
         goto 1000

600      read(3,*) nkrf
         do 610 j=1,nkrf
610      read(3,*) i1,(d1,i=1,nlc)
         nkrf=nkrf+1
         goto 1000

650      read(3,*) nkaf
         do 660 j=1,nkaf
660      read(3,*) i1,(d1,i=1,nlc)
         nkaf=nkaf+1
         goto 1000

700      read(3,6001) inp
         call STR$UPCASE(inp,inp)
         lrbf=.true.
         if(inp .eq. 'POLYNOMIAL') then
            read(3,*) nrbfrt,nrbfat
            read(3,*) (d1,i=1,nlc)
            read(3,*) (d1,i=1,nlc)
            read(3,*) (d1,i=1,nlc)
            read(3,*) (d1,i=1,nlc)
            nrbfrdv=2*nlc
            nrbfadv=2*nlc
            do 710 i=1,nrbfat
            do 710 j=1,nrbfrt
710         read(3,*) (d1,k=1,nlc)
            lrbft=.true.
         elseif(inp .eq. 'INTERPOLATION') then
            read(3,*) nrbfrt,nrbfat
            nrbfrdv=nrbfrt
            nrbfadv=nrbfat
            do 720 i=1,nrbfrdv
720         read(3,*) d1
            do 730 i=1,nrbfadv
730         read(3,*) d1
            do 740 i=1,nrbfat
            do 740 j=1,nrbfrt
740         read(3,*) (d1,k=1,nlc)
            lrbft=.false.
```

```
      else
         write(6,6002)
         lerr=.true.
         goto 9999
      endif
      goto 1000

750   read(3,6001) inp
      call STR$UPCASE(inp,inp)
      labf=.true.
      if(inp .eq. 'POLYNOMIAL') then
         read(3,*) nabfrt,nabfat
         read(3,*) (d1,i=1,nlc)
         read(3,*) (d1,i=1,nlc)
         read(3,*) (d1,i=1,nlc)
         read(3,*) (d1,i=1,nlc)
         nabfrdv=2*nlc
         nabfadv=2*nlc
         do 760 i=1,nabfat
         do 760 j=1,nabfrt
760      read(3,*) (d1,k=1,nlc)
         labft=.true.
      elseif(inp .eq. 'INTERPOLATION') then
         read(3,*) nabfrt,nabfat
         nabfrdv=nabfrt
         nabfadv=nabfat
         do 770 i=1,nabfrdv
770      read(3,*) d1
         do 780 i=1,nabfadv
780      read(3,*) d1
         do 790 i=1,nabfat
         do 790 j=1,nabfrt
790      read(3,*) (d1,k=1,nlc)
         labft=.false.
      else
         write(6,6002)
         lerr=.true.
         goto 9999
      endif
      goto 1000

800   read(3,6001) inp
      call STR$UPCASE(inp,inp)
      ltmp=.true.
      if(inp .eq. 'POLYNOMIAL') then
         read(3,*) nrtt,natt
         read(3,*) (d1,i=1,nlc)
         read(3,*) (d1,i=1,nlc)
         read(3,*) (d1,i=1,nlc)
         read(3,*) (d1,i=1,nlc)
         ntrdv=2*nlc
         ntadv=2*nlc
         do 810 i=1,natt
         do 810 j=1,nrtt
810      read(3,*) (d1,k=1,nlc)
         ltmpt=.true.
      elseif(inp .eq. 'INTERPOLATION') then
         read(3,*) nrtt,natt
         ntrdv=nrtt
         ntadv=natt
         do 820 i=1,ntrdv
820      read(3,*) d1
         do 830 i=1,ntadv
```

```
830         read(3,*) d1
            do 840 i=1,natt
            do 840 j=1,nrtt
840         read(3,*) (d1,k=1,nlc)
            ltmpt=.false.
         else
            write(6,6002)
            lerr=.true.
            goto 9999
         endif
         goto 1000

900      read(3,*) ix,iy
         if(ix .lt. 1 .or. ix .gt. 5) goto 910
         if(iy .ge. 1 .and. iy .le. 5) goto 10
910      write(6,6004)
         goto 9999

940      lplt=.true.
         read(3,6001) fgeom
         do 941 i=1,nlc
941      read(3,6001) fnameplt(i)
         goto 10

945      lfout=.true.
         do 946 i=1,nlc
946      read(3,6001) fnameout(i)
         goto 10

950      lat=.true.
         goto 10

960      lat=.false.
         read(3,*) i1,i2,i3,i4,d1,d2
         goto 10

1000     load=.true.
         goto 10

1100     read(3,6001) fnamein
         lstart=.true.
         goto 10

1125     read(3,6001) fnamesave
         lsave=.true.
         goto 10

1150     ldebug=.true.
         read(3,*) nlde
         ildad=nlde
         read(3,*) (i1,i=1,nlde)
         goto 10

1200     read(3,*) d1,d2,d3,d4,d5,d6,d7
         goto 10

1350     read(3,*) neas,eol,umax
         do 1360 i=1,neas
1360     read(3,*) i1,d1,d2
         leas=.true.
         goto 10

1400     do 1410 i=1,nplm
```

```
1410    read(3,*) (d1,j=1,7)
        ltp=.true.
        goto 10

1500    do 1510 i=1,nmatt
1510    read(3,*) d1
        ldyn=.true.
        goto 10

6001    format(a30)
6002    format(//,'  ERROR !!:  Input command not recognized !')
6003    format(//,'  ERROR !!:  Incorrect number of materials specif
     &ied !')
6004    format(//,'  ERROR !!:  Incorrect number of Gauss points spe
     &cfied !')
6009    format(a78)
9999    close(unit=3)
        return
        end



CCCCCCCCCCCCCCCCCCCCCCCCCCCCCCCCCCCCCCCCCCCCCCCCCCCCCCCCCCCCCCCCCCCCCCCCCCCCCCC
C
C       ASSIGN
C
C       ASSIGN does just what its name implies and assigns the
C       finite element model data to variable arrays.
C
CCCCCCCCCCCCCCCCCCCCCCCCCCCCCCCCCCCCCCCCCCCCCCCCCCCCCCCCCCCCCCCCCCCCCCCCCCCCCCC

        subroutine ASSIGN(x,nn,it,ne,imem,time,nlc,iprd,prd,nkrd,
     &                    ipad,pad,nkad,iprf,prf,nkrf,
     &                    ipaf,paf,nkaf,rbfd,nrbfrt,nrbfat,
     &                    rbfrd,nrbfrdv,rbfad,nrbfadv,
     &                    abfd,nabfrt,nabfat,abfrd,nabfrdv,
     &                    abfad,nabfadv,td,nrtt,natt,
     &                    trd,ntrdv,tad,ntadv,n2,n3,n4,n5,n8,
     &                    c,ct,cmpa,fname,mca,nmatt,nemat,nplm,
     &                    npltdv,pmta,pmpa,iplad,rplad,sp,ilda,
     &                    ildad,den,itasp,aspod,eol,umax,psd,aspc,
     &                    aspd,neas,phas,n7)

        implicit real*8(a-h,o-z)
        implicit integer(i-k,n,m)
        logical l

        character*25 inp,dum*78,fname*(*)
        dimension x(nn,n2),it(ne,n8),imem(ne),time(nlc),den(nmatt),
     &            iprd(nkrd),prd(nlc,nkrd),ipad(nkad),pad(nlc,nkad),
     &            iprf(nkrf),prf(nlc,nkrf),ipaf(nkaf),paf(nlc,nkaf),
     &            rbfd(nlc,nrbfat,nrbfrt),rbfrd(nrbfrdv),rbfad(nrbfadv),
     &            abfd(nlc,nabfat,nabfrt),abfrd(nabfrdv),abfad(nabfadv),
     &            td(nlc,natt,nrtt),trd(ntrdv),tad(ntadv),mca(nmatt),
     &            c(nemat,n4,n4),ct(nemat,n4),cmpa(nemat,n3),sp(n7),
     &            pmta(npltdv),pmpa(nplm,npltdv,n5),iplad(n4),rplad(n4),
     &            ilda(ildad),psd(neas),aspod(neas),
     &            itasp(neas),aspc(neas),aspd(neas),phas(nplm,n7)

C       INITIALIZE SOLUTION PARAMETERS
        sp(1)=0.0
        sp(2)=1e-6
```

```
      sp(3)=1e-15
      sp(4)=1e-15
      sp(5)=30.0
      sp(6)=0.0
      sp(7)=0.0

      open(unit=3,file=fname,readonly,status='old')
10    read(3,6001) inp
      call STR$UPCASE(inp,inp)

      if(inp .eq. 'TITLE') goto 100
      if(inp .eq. 'NODES') goto 200
      if(inp .eq. 'ELEMENTS') GOTO 300
      if(inp .eq. 'ELASTIC MATERIALS') goto 400
      if(inp .eq. 'PLASTIC MATERIALS') goto 425
      if(inp .eq. 'TWO PHASE') goto 1400
      if(inp .eq. 'LOAD CASES') goto 450
      if(inp .eq. 'RADIAL DISPLACEMENTS') goto 500
      if(inp .eq. 'AXIAL DISPLACEMENTS') goto 550
      if(inp .eq. 'RADIAL NODE FORCES') goto 600
      if(inp .eq. 'AXIAL NODE FORCES') goto 650
      if(inp .eq. 'RADIAL BODY FORCES') goto 700
      if(inp .eq. 'AXIAL BODY FORCES') goto 750
      if(inp .eq. 'TEMPERATURES') goto 800
      if(inp .eq. 'GAUSS POINTS') goto 900
      if(inp .eq. 'AFESAPLT') goto 950
      if(inp .eq. 'AFESAOUT') goto 955
      if(inp .eq. 'ELASTIC') goto 10
      if(inp .eq. 'ELASTIC-PLASTIC') goto 960
      if(inp .eq. 'RESTART') goto 1100
      if(inp .eq. 'SAVE') goto 1100
      if(inp .eq. 'SOLUTION PARAMETERS') goto 1200
      if(inp .eq. 'DEBUG') goto 1150
      if(inp .eq. 'EXTERNAL AXIAL SPRINGS') goto 1350
      if(inp .eq. 'DYNAMIC') goto 1500
      if(inp .eq. 'EXIT') goto 9999

100   read(3,6001) dum
      goto 10
200   read(3,*) i1
      do 210 i=1,nn
210   read(3,*) i1,x(i,1),x(i,2)
      goto 10

300   read(3,*) i1
      do 310 i=1,ne
310   read(3,*) i1,imem(i),(it(i,j),j=1,8)
      goto 10

400   read(3,*) i1
      do 410 imat=1,nemat
      read(3,*) i1,ym,pr,al
      mca(i1)=imat
      cmpa(imat,1)=ym
      cmpa(imat,2)=pr
      cmpa(imat,3)=al
410   call MATL(c,ct,imat,ym,pr,al,nemat,n4)
      goto 10

425   read(3,*) i1,i2
      do 430 i=1,npltdv
430   read(3,*) pmta(i)
      do 440 i=1,nplm
```

```
        read(3,*) i1
        mca(i1)=-i
        do 440 j=1,npltdv
        read(3,*) ym,pr,vys,et,al
        pmpa(i,j,1)=ym
        pmpa(i,j,2)=pr
        pmpa(i,j,3)=vys
        pmpa(i,j,4)=et
440     pmpa(i,j,5)=al
        goto 10

450     read(3,*) i1
        read(3,*) (time(i),i=1,nlc)
        goto 10


500     read(3,*) i1
        do 510 j=1,nkrd-1
510     read(3,*) iprd(j),(prd(i,j),i=1,nlc)
        goto 10

550     read(3,*) i1
        do 560 j=1,nkad-1
560     read(3,*) ipad(j),(pad(i,j),i=1,nlc)
        goto 10

600     read(3,*) i1
        do 610 j=1,nkrf-1
610     read(3,*) iprf(j),(prf(i,j),i=1,nlc)
        goto 10

650     read(3,*) i1
        do 660 j=1,nkaf-1
660     read(3,*) ipaf(j),(paf(i,j),i=1,nlc)
        goto 10

700     read(3,6001) inp
        call STR$UPCASE(inp,inp)
        if(inp .eq. 'POLYNOMIAL') then
           read(3,*) d1,d2
           read(3,*) (rbfrd(i),i=1,nlc)
           read(3,*) (rbfrd(nlc+i),i=1,nlc)
           read(3,*) (rbfad(i),i=1,nlc)
           read(3,*) (rbfad(nlc+i),i=1,nlc)
           do 710 i=1,nrbfat
           do 710 j=1,nrbfrt
710        read(3,*) (rbfd(k,i,j),k=1,nlc)
        elseif(inp .eq. 'INTERPOLATION') then
           read(3,*) d1,d2
           do 720 i=1,nrbfrdv
720        read(3,*) rbfrd(i)
           do 730 i=1,nrbfadv
730        read(3,*) rbfad(i)
           do 740 i=1,nrbfat
           do 740 j=1,nrbfrt
740        read(3,*) (rbfd(k,i,j),k=1,nlc)
        endif
        goto 10

750     read(3,6001) inp
        call STR$UPCASE(inp,inp)
        if(inp .eq. 'POLYNOMIAL') then
           read(3,*) d1,d2
```

```
            read(3,*) (abfrd(i),i=1,nlc)
            read(3,*) (abfrd(nlc+i),i=1,nlc)
            read(3,*) (abfad(i),i=1,nlc)
            read(3,*) (abfad(nlc+i),i=1,nlc)
            do 760 i=1,nabfat
            do 760 j=1,nabfrt
760         read(3,*) (abfd(k,i,j),k=1,nlc)
         elseif(inp .eq. 'INTERPOLATION') then
            read(3,*) d1,d2
            do 770 i=1,nabfrdv
770         read(3,*) abfrd(i)
            do 780 i=1,nabfadv
780         read(3,*) abfad(i)
            do 790 i=1,nabfat
            do 790 j=1,nabfrt
790         read(3,*) (abfd(k,i,j),k=1,nlc)
         endif
         goto 10

800      read(3,6001) inp
         call STR$UPCASE(inp,inp)
         if(inp .eq. 'POLYNOMIAL') then
            read(3,*) d1,d2
            read(3,*) (trd(i),i=1,nlc)
            read(3,*) (trd(nlc+i),i=1,nlc)
            read(3,*) (tad(i),i=1,nlc)
            read(3,*) (tad(nlc+i),i=1,nlc)
            do 810 i=1,natt
            do 810 j=1,nrtt
810         read(3,*) (td(k,i,j),k=1,nlc)
         elseif(inp .eq. 'INTERPOLATION') then
            read(3,*) d1,d2
            do 820 i=1,ntrdv
820         read(3,*) trd(i)
            do 830 i=1,ntadv
830         read(3,*) tad(i)
            do 840 i=1,natt
            do 840 j=1,nrtt
840         read(3,*) (td(k,i,j),k=1,nlc)
         endif
         goto 10

900      read(3,*) d1,d2
         goto 10

950      read(3,6001) inp
         do 951 i=1,nlc
951      read(3,6001) inp
         goto 10

955      do 956 i=1,nlc
956      read(3,6001) inp
         goto 10

960      read(3,*) (iplad(i),i=1,4),(rplad(j),j=1,2)
         goto 10

1100     read(3,6001) inp
         goto 10

1150     read(3,*) nlde
         read(3,*) (ilda(i),i=1,nlde)
         goto 10
```

```
1200    read(3,*) (sp(i),i=1,7)
        goto 10

1350    read(3,*) neas,eol,umax
        do 1360 i=1,neas
        aspod(i)=0.
        psd(i)=0.
1360    read(3,*) itasp(i),aspc(i),aspd(i)
        goto 10

1400    do 1410 i=1,nplm
1410    read(3,*) (phas(i,j),j=1,7)
        goto 10

1500    do 1510 i=1,nmatt
1510    read(3,*) den(i)
        goto 10

9999    write(6,6002)
        close(unit=3)

6001    format(a30)
6002    format(//,'  Echo print of input file complete. ',//)

        return
        end



CCCCCCCCCCCCCCCCCCCCCCCCCCCCCCCCCCCCCCCCCCCCCCCCCCCCCCCCCCCCCCCCCCCCCCCCCCCCCCC
C
C       MATFIX
C
C       This subroutine assigns a negative element material number
C       to plastic materials.  imem is the element material number.
C
CCCCCCCCCCCCCCCCCCCCCCCCCCCCCCCCCCCCCCCCCCCCCCCCCCCCCCCCCCCCCCCCCCCCCCCCCCCCCCC

        subroutine matfix(mca,imem,nmatt,ne)
        implicit real*8(a-h,o-z)
        implicit integer(i-k,n,m)
        dimension mca(nmatt),imem(ne)

        do 20 i=1,ne
        if(mca(imem(i)) .lt. 0) imem(i)=-imem(i)
20      continue

        do 40 i=1,nmatt
        if(mca(i) .lt. 0) mca(i)=-mca(i)
40      continue

        return
        end



CCCCCCCCCCCCCCCCCCCCCCCCCCCCCCCCCCCCCCCCCCCCCCCCCCCCCCCCCCCCCCCCCCCCCCCCCCCCCCC
C
C       MATL
C
```

```
C       This subroutine calulates the elastic constitutive matrix.
C       for each elastic material type.
C
CCCCCCCCCCCCCCCCCCCCCCCCCCCCCCCCCCCCCCCCCCCCCCCCCCCCCCCCCCCCCCCCCCCCCCCCCCC

        subroutine MATL(c,ct,imat,ym,pr,al,nemat,n4)
        implicit real*8(a-h,o-z)
        implicit integer(i-k,n,m)
        dimension c(nemat,n4,n4),ct(nemat,n4)
        dimension db(4)

        f=ym/(1d0+pr)
        g=f*pr/(1d0-2d0*pr)
        h=f+g
        c(imat,1,1)=h
        c(imat,1,2)=g
        c(imat,1,3)=0d0
        c(imat,2,1)=g
        c(imat,2,2)=h
        c(imat,2,3)=0d0
        c(imat,3,1)=0d0
        c(imat,3,2)=0d0
        c(imat,3,3)=f/2d0
        c(imat,1,4)=g
        c(imat,2,4)=g
        c(imat,3,4)=0d0
        c(imat,4,1)=g
        c(imat,4,2)=g
        c(imat,4,3)=0d0
        c(imat,4,4)=h

        db(1)=al
        db(2)=al
        db(3)=0d0
        db(4)=al
        do 100 i=1,4
        ct(imat,i)=0d0
        do 100 j=1,4
100     ct(imat,i)=ct(imat,i)+c(imat,i,j)*db(j)

        return
        end



CCCCCCCCCCCCCCCCCCCCCCCCCCCCCCCCCCCCCCCCCCCCCCCCCCCCCCCCCCCCCCCCCCCCCCCCCCC
C
C       FRONTAL
C
C       FRONTAL is a subroutine which assigns degrees of freedom to
C       the finite element model.  Nodes which have defined displacements
C       are assigned negative degrees of freedom.  Besides the degrees
C       of freedom, this subroutine also calculates the skyline matrix
C       MAXA needed in COLSOL.
C
CCCCCCCCCCCCCCCCCCCCCCCCCCCCCCCCCCCCCCCCCCCCCCCCCCCCCCCCCCCCCCCCCCCCCCCCCCC

c       Finite Element Frontal Analysis of 8 node elements
        subroutine FRONTAL(it,ne,imap,nn,maxa,nnm,nud,
     &                     ic,nn2,ies,nel,n2,n6,n8,
     &                     iprd,nkrd,ipad,nkad,mt)
```

```
      implicit real*8(a-h,o-z)
      implicit integer(i-k,n,m)
      logical l

      dimension it(ne,n8),imap(nn,n2),maxa(nnm),
     &          ic(nn2),ies(ne),nel(nn,n6),
     &          iprd(nkrd),ipad(nkad)
      dimension ifl(4),itel(5,6)

c     Initialize and Load NEL (Nodal Element List)
      do 100 i=1,nn
      do 100 j=1,6
100   nel(i,j)=0
      ncn=0
C     NNE IS THE MAXIMUM NUMBER OF ELEMENTS CONNECTED TO A CORNER NODE
      nne=1
      do 120 i=1,ne
      do 120 j=1,8,2
      icn=it(i,j)
      do 110 k=1,6
      if(nel(icn,k) .ne. 0) goto 110
      if(k .gt. nne) nne=k
      nel(icn,k)=i
      goto 120
110   continue
120   continue

c     Find starting node for frontal analysis.
c     Look for corner node.
      do 130 i=1,nn
      if(nel(i,1) .eq. 0) goto 130
      if(nel(i,2) .ne. 0) goto 130
      its=1
      ies(1)=nel(i,1)
      goto 150
130   continue

c     Look for edge node
      do 140 i=1,nn
      if(nel(i,1) .eq. 0) goto 140
      if(nel(i,3) .ne. 0) goto 140
      its=2
      ies(1)=nel(i,1)
      ies(2)=nel(i,2)
      goto 150
140   continue
      ierr=.true.
      goto 460

c     Load ITEL (Temporary Element List)
150   isp=1
160   if(its .eq. ne) goto 330
      ice=ies(isp)
      isp=isp+1
      do 170 i=1,4
      k=0
      do 170 j=1,nne
      ite=nel(it(ice,2*i-1),j)
      if(ite .eq. ice) goto 170
      k=k+1
      itel(i,k)=ite
170   continue
      do 180 i=1,nne
```

```
180     itel(5,i)=itel(1,i)

c       Eleminate Elements in ITEL already in IES (Element Stack)
        do 220 i=1,4
190     do 210 j=1,nne
        if(itel(i,j) .eq. 0) goto 220
        do 210 k=1,its
        if(ies(k) .ne. itel(i,j)) goto 210
        do 200 n=j,nne
200     itel(i,n)=itel(i,n+1)
        itel(i,nne)=0
        goto 190
210     continue
220     continue

c       Determine IFL (Face elements List)
        do 300 i=1,4
        do 290 j=1,nne
        ite=itel(i,j)
        if(ite .eq. 0) goto 290
        do 280 k=1,nne
        if(ite .ne. itel(i+1,k)) goto 280
        ifl(i)=ite
        do 230 n=j,nne-1
230     itel(i,n)=itel(i,n+1)
        itel(i,nne)=0
        do 240 n=k,nne-1
240     itel(i+1,n)=itel(i+1,n+1)
        itel(i+1,nne)=0
        if(i .ne. 1) goto 260
        do 250 n=1,nne
250     itel(5,n)=itel(1,n)
        goto 300
260     if(i .ne. 4) goto 300
        do 270 n=1,nne
270     itel(1,n)=itel(5,n)
        goto 300
280     continue
290     continue
        ifl(i)=0
300     continue

c       Load ITEL into IES
        do 320 i=1,4
        if(ifl(i) .eq. 0) goto 310
        its=its+1
        ies(its)=ifl(i)
310     do 320 j=1,nne
        if(itel(i,j) .eq. 0) goto 320
        its=its+1
        ies(its)=itel(i,j)
        itel(i,j)=0
320     continue

        goto 160

c       Initialize and load the DOF IMAP (Degree Of Freedom)
330     do 350 i=1,nn
        imap(i,1)=0
350     imap(i,2)=0
        k1=0
        k2=0
        do 390 i=1,ne
```

```
      do 390 j=1,8
      icn=it(ies(i),j)
      if(imap(icn,1) .ne. 0) goto 390

      do 360 k=1,nkrd-1
      if(iprd(k) .ne. icn) goto 360
      k2=k2-1
      imap(icn,1)=k2
      goto 365
360   continue
      k1=k1+1
      imap(icn,1)=k1

365   do 370 k=1,nkad-1
      if(ipad(k) .ne. icn) goto 370
      k2=k2-1
      imap(icn,2)=k2
      goto 375
370   continue
      k1=k1+1
      imap(icn,2)=k1
375   continue

390   continue

c     load the Maxa matrix needed in COLSOL
      do 420 i=1,nn2
420   ic(i)=10000
      do 440 i=1,ne
      iln=10000
      do 430 j=1,8
      do 430 k=1,2
      nc=imap(it(i,j),k)
      if(nc .lt. 0) goto 430
      if(nc .lt. iln) iln=nc
430   continue
      do 440 j=1,8
      do 440 k=1,2
      nc=imap(it(i,j),k)
      if(nc .lt. 0) goto 440
      if(ic(nc) .gt. iln) ic(nc)=iln
440   continue
      maxa(1)=1
      mt=1
      do 450 i=2,nud
      mt=mt+1
      maxa(i)=mt
450   mt=mt+i-ic(i)
      maxa(nnm)=mt+1

460   return
      end



CCCCCCCCCCCCCCCCCCCCCCCCCCCCCCCCCCCCCCCCCCCCCCCCCCCCCCCCCCCCCCCCCCCCCCCCCCCCCCC
C
C     GAUSS
C
C     GAUSS calculates the interpolation matrix H and the strain-
C     displacement transformation matrix B for each interpolation
C     point.  The information for each interpolation point is stored
```

```
C       in the arrays wt, h and b.  The author believes this calculate
C       it (wt, h and b) once and store it method significantly reduces
C       repetitive calculations during execution.
C
cccccccccccccccccccccccccccccccccccccccccccccccccccccccccccccccccccccc

        subroutine GAUSS(wt,h,b,ix,iy,n2,n8)

        implicit real*8(a-h,o-z)
        implicit integer(i-k,n,m)
        logical l

        dimension wt(ix,iy),h(ix,iy,n8),b(ix,iy,n8,n2)

        dimension data(5),weight(5),rd(5),sd(5),xwd(5),ywd(5)

        ipass=1
        goto (10,20,30,40,50),ix
1       goto (10,20,30,40,50),iy

10      data(1)= .0
        weight(1)=2.0
        goto 60

20      data(1)=-.5773502691896257
        data(2)= .5773502691896257
        weight(1)=1.0
        weight(2)=1.0
        goto 60

30      data(1)=-.7745966692414834
        data(2)= .0
        data(3)= .7745966692414834
        weight(1)= .5555555555555556
        weight(2)= .8888888888888889
        weight(3)= .5555555555555556
        goto 60

40      data(1)=-.8611363115940526
        data(2)=-.3399810435848563
        data(3)= .3399810435848563
        data(4)= .8611363115940526
        weight(1)= .3478548451374539
        weight(2)= .6521451548625461
        weight(3)= .6521451548625461
        weight(4)= .3478548451374539
        goto 60

50      data(1)=-.9061798459386640
        data(2)=-.5384693101056831
        data(3)= .0
        data(4)= .5384693101056831
        data(5)= .9061798459386640
        weight(1)= .2369268850561891
        weight(2)= .4786286704993665
        weight(3)= .5688888888888889
        weight(4)= .4786286704993665
        weight(5)= .2369268850561891

60      if(ipass .eq. 1) then
           ipass=2
           do 70 i=1,ix
           rd(i)=data(i)
```

```
70          xwd(i)=weight(i)
            goto 1
         else
            do 80 i=1,iy
            sd(i)=data(i)
80          ywd(i)=weight(i)
         endif

         do 100 i=1,ix
         do 100 j=1,iy
         r=rd(i)
         s=sd(j)
         rm=1d0-r
         sm=1d0-s
         rp=1d0+r
         sp=1d0+s
         rs=1d0-r**2
         ss=1d0-s**2
         h(i,j,1)=rm*sm*(-r-s-1d0)/4d0
         h(i,j,2)=rs*sm/2d0
         h(i,j,3)=rp*sm*(r-s-1d0)/4d0
         h(i,j,4)=ss*rp/2d0
         h(i,j,5)=rp*sp*(r+s-1d0)/4d0
         h(i,j,6)=rs*sp/2d0
         h(i,j,7)=rm*sp*(-r+s-1d0)/4d0
         h(i,j,8)=ss*rm/2d0
         b(i,j,1,1)=sm*(2d0*r+s)/4d0
         b(i,j,1,2)=rm*(r+2d0*s)/4d0
         b(i,j,2,1)=-r*sm
         b(i,j,2,2)=-rs/2d0
         b(i,j,3,1)=sm*(2d0*r-s)/4d0
         b(i,j,3,2)=rp*(2d0*s-r)/4d0
         b(i,j,4,1)=ss/2d0
         b(i,j,4,2)=-rp*s
         b(i,j,5,1)=sp*(2d0*r+s)/4d0
         b(i,j,5,2)=rp*(r+2d0*s)/4d0
         b(i,j,6,1)=-sp*r
         b(i,j,6,2)=-b(i,j,2,2)
         b(i,j,7,1)=sp*(2d0*r-s)/4d0
         b(i,j,7,2)=rm*(2d0*s-r)/4d0
         b(i,j,8,1)=-b(i,j,4,1)
         b(i,j,8,2)=-rm*s
100      wt(i,j)=xwd(i)*ywd(j)

         return
         end


cccccccccccccccccccccccccccccccccccccccccccccccccccccccccccccccccccccccc
C
C        HE
C
C        This subroutine uses the H and B matrices to calculate the
C        element interpolation point position (rad,z) and the
C        interpolation point strain array E.
C
C
cccccccccccccccccccccccccccccccccccccccccccccccccccccccccccccccccccccccc

         subroutine HE(b,e,h,rad,w,xa,z,ir,is,ix,iy,n2,n4,n8,n16)
         implicit real*8(a-h,o-z)
```

```
      implicit integer(i-k,n,m)

      dimension b(ix,iy,n8,n2),e(n4,n16),h(ix,iy,n8),xa(n8,n2)
      dimension d(2,2),di(2,2)

      pi2=2.0*3.141592653589793
      rad=0d0
      z=0d0
      do 75 l=1,8
      rad=rad+h(ir,is,l)*xa(l,1)
75    z=z+h(ir,is,l)*xa(l,2)

c
c     EVALUATE JACOBIAN MATRIX
      do 100 i=1,2
      do 100 j=1,2
      d(i,j)=0d0
      do 100 k=1,8
100   d(i,j)=d(i,j)+b(ir,is,k,i)*xa(k,j)
      dt=d(1,1)*d(2,2)-d(2,1)*d(1,2)
      if(dt .gt. 0.) goto 101
      write(6,*) 'ERROR !!!  Jacobian Matrix Indefinite in HE.'

      write(6,*) d(1,1),d(1,2)
      write(6,*) d(2,1),d(2,2)
      goto 9000

101   dm=1./dt
      di(1,1)=d(2,2)*dm
      di(1,2)=-d(2,1)*dm
      di(2,1)=-d(1,2)*dm
      di(2,2)=d(1,1)*dm

C     EVALUATE STRAIN MATRIX FOR NON ZERO RADIUS
      if(rad .lt. 1e-9) goto 130
      k2=0
      do 120 k=1,8
      k2=k2+2
      e(1,k2-1)=0d0
      e(1,k2)=0d0
      e(2,k2-1)=0d0
      e(2,k2)=0d0
      do 110 i=1,2
      e(1,k2-1)=e(1,k2-1)+di(1,i)*b(ir,is,k,i)
110   e(2,k2)=e(2,k2)+di(2,i)*b(ir,is,k,i)
      e(3,k2)=e(1,k2-1)
      e(3,k2-1)=e(2,k2)
      e(4,k2)=0d0
120   e(4,k2-1)=h(ir,is,k)/rad
      goto 160

130   k2=0
      do 150 k=1,8
      k2=k2+2
      e(1,k2-1)=0d0
      e(1,k2)=0d0
      e(2,k2-1)=0d0
      e(2,k2)=0d0
      do 140 i=1,2
      e(1,k2-1)=e(1,k2-1)+di(1,i)*b(ir,is,k,i)
140   e(2,k2)=e(2,k2)+di(2,i)*b(ir,is,k,i)
      e(3,k2)=e(1,k2-1)
      e(3,k2-1)=e(2,k2)
```

```
      e(4,k2)=0d0
150   e(4,k2-1)=e(1,k2-1)

160   w=rad*dt*pi2
9000  return
      end



cccccccccccccccccccccccccccccccccccccccccccccccccccccccccccccccccccc
c
c     BFI
c
c     BFI (Body Force Integration) calculates the body force
c     loads for each element node for a given interpolation
c     point.  First the body force load corresponding to the
c     interpoation point location is calculated, and then the load
c     contribution to each element node is determined.
c
cccccccccccccccccccccccccccccccccccccccccccccccccccccccccccccccccccc

      subroutine BFI(bf,h,w,rad,z,i1,ir,is,ix,iy,nlc,n8,n16,lbft,
     &               sol,bfd,nbfat,nbfrt,bfrd,nbfrdv,bfad,nbfadv)

      implicit real*8(a-h,o-z)
      implicit integer(i-k,n,m)
      logical l

      dimension bf(nlc,n16),h(ix,iy,n8),bfd(nlc,nbfat,nbfrt),
     &          bfrd(nbfrdv),bfad(nbfadv),sol(nlc)


      if(lbft) then
         do 200 i=1,nlc
         rl=bfrd(i)
         rh=bfrd(nlc+i)
         al=bfad(i)
         ah=bfad(nlc+i)
         sol(i)=0d0

         if(rad .lt. rl .or. rad .gt. rh) goto 200
         if(z .lt. al .or. z .gt. ah) goto 200
         dumz=1d0
         do 190 j=1,nbfat
         dumr=1d0
         do 180 k=1,nbfrt
         sol(i)=sol(i)+bfd(i,j,k)*dumr*dumz
180      dumr=dumr*rad
190      dumz=dumz*z
200      continue
         goto 800
      else
         call INTERP(bfd,nbfat,nbfrt,bfrd,bfad,rad,z,nlc,sol)
      endif

800   do 880 j=1,nlc
      sol(j)=sol(j)*w
      do 880 i=1,8
880   bf(j,2*i-i1)=bf(j,2*i-i1)+h(ir,is,i)*sol(j)

      return
      end
```

```
CCCCCCCCCCCCCCCCCCCCCCCCCCCCCCCCCCCCCCCCCCCCCCCCCCCCCCCCCCCCCCCCCCCCCCCCCCCCCCCCCCC
C
C       TSI
C
C       TSI (Thermal Stress Integration) is used in elastic analyses
C       only.  This subroutine calculates the interpolation point
C       temperature, and then it determines the equivalent nodal forces
C       for the prescribed temperature change.
C
CCCCCCCCCCCCCCCCCCCCCCCCCCCCCCCCCCCCCCCCCCCCCCCCCCCCCCCCCCCCCCCCCCCCCCCCCCCCCCCCCCC

      subroutine TSI(tref,e,ct,iemt,rad,z,sol,ts,w,nemat,n4,n16,
     &                nlc,ltmpt,td,nrtt,natt,trd,ntrdv,tad,ntadv)

      implicit real*8(a-h,o-z)
      implicit integer(i-k,n,m)
      logical l

      dimension e(n4,n16),ct(nemat,n4),ts(nlc,n16),sol(nlc),
     &          td(nlc,natt,nrtt),trd(ntrdv),tad(ntadv)

      if(ltmpt) then
         do 200 i=1,nlc
         rl=trd(i)
         rh=trd(nlc+i)
         al=tad(i)
         ah=tad(nlc+i)
         sol(i)=tref
         if(rad .lt. rl .or. rad .gt. rh) goto 200
         if(z .lt. al .or. z .gt. ah) goto 200
         sol(i)=0.0
         dumz=1d0
         do 190 j=1,natt
         dumr=1d0
         do 180 k=1,nrtt
         sol(i)=sol(i)+td(i,j,k)*dumr*dumz
180      dumr=dumr*rad
190      dumz=dumz*z
200      continue
         goto 800
      else
         call INTERP(td,natt,nrtt,trd,tad,rad,z,nlc,sol)
      endif

800   do 900 i=1,nlc
      te=-(sol(i)-tref)*w
      do 850 j=1,16
      do 850 k=1,4
850   ts(i,j)=ts(i,j)+e(k,j)*ct(iemt,k)*te
900   continue

      return
      end



CCCCCCCCCCCCCCCCCCCCCCCCCCCCCCCCCCCCCCCCCCCCCCCCCCCCCCCCCCCCCCCCCCCCCCCCCCCCCCCCCCC
C
```

```
C       INTERP
C
C       This subroutine is used throughout AFESA to interpolate
C       data values from 2 dimensional data tables.  This interpolation
C       routine will extrapolate outside the input data ranges.
C
CCCCCCCCCCCCCCCCCCCCCCCCCCCCCCCCCCCCCCCCCCCCCCCCCCCCCCCCCCCCCCCCCCCCCCCCCCCCCCC

        subroutine INTERP(dv,nadv,nrdv,rda,ada,rad,z,nlc,sol)

        implicit real*8(a-h,o-z)
        implicit integer(i-k,n,m)
        logical l

        dimension ada(nadv),rda(nrdv),dv(nlc,nadv,nrdv),sol(nlc)
        iz=1
        if(nadv .eq. 1) goto 200
        iz=2
        if(z .le. ada(1)) goto 200
        if(z .le. ada(iz)) goto 200
        do 100 i=2,nadv
        if(z .gt. ada(i)) goto 100
        iz=i
        goto 200
100     continue
        iz=nadv
200     ir=1
        if(nrdv .eq. 1) goto 400
        ir=2
        if(rad .le. rda(1)) goto 400
        if(rad .le. rda(ir)) goto 400
        do 300 i=1,nrdv
        if(rad .gt. rda(i)) goto 300
        ir=i
        goto 400
300     continue
        ir=nrdv

400     do 1000 ii=1,nlc
        if(iz .eq. 1) goto 600
        dz=ada(iz)-ada(iz-1)
        if(ir .eq. 1) goto 500
        d1h=dv(ii,iz,ir-1)
        d1l=dv(ii,iz-1,ir-1)
        dv1=d1h+((d1h-d1l)*(z-ada(iz))/dz)
500     d2h=dv(ii,iz,ir)
        d2l=dv(ii,iz-1,ir)
        dv2=d2h+((d2h-d2l)*(z-ada(iz))/dz)
        if(ir .ne. 1) goto 800
        sol(ii)=dv2
        goto 1000
600     if(ir .ne. 1) goto 700
        sol(ii)=dv(ii,1,1)
        goto 1000
700     dv1=dv(ii,1,ir-1)
        dv2=dv(ii,1,ir)
800     dr=rda(ir)-rda(ir-1)
        sol(ii)=dv2+((dv2-dv1)*(rad-rda(ir))/dr)
1000    continue

        return
        end
```

```
CCCCCCCCCCCCCCCCCCCCCCCCCCCCCCCCCCCCCCCCCCCCCCCCCCCCCCCCCCCCCCCCCCCCCCCCCCCCCCC
C
C       ISOP
C
C       ISOP calculates the interpolation point temperature from the
C       element node temperatures.
C
CCCCCCCCCCCCCCCCCCCCCCCCCCCCCCCCCCCCCCCCCCCCCCCCCCCCCCCCCCCCCCCCCCCCCCCCCCCCCCC

        subroutine ISOP(temp,h,ta,ir,is,ix,iy,n8)
        implicit real*8(a-h,o-z)
        implicit integer(i-k,n,m)

        dimension h(ix,iy,n8),ta(n8)

        temp=0d0
        do 75 l=1,8
75      temp=temp+h(ir,is,l)*ta(l)

        return
        end



CCCCCCCCCCCCCCCCCCCCCCCCCCCCCCCCCCCCCCCCCCCCCCCCCCCCCCCCCCCCCCCCCCCCCCCCCCCCCCC
C
C       DYNAMIC
C
C       DYNAMIC is a subroutine which calculates equivalent nodal
C       forces based upon nodal accellerations.  AFESA uses the
C       Houbolt method (see ''Finite Element Procedures in Engineering
C       Analysis,'' K.J. Bathe, 1982).
C
CCCCCCCCCCCCCCCCCCCCCCCCCCCCCCCCCCCCCCCCCCCCCCCCCCCCCCCCCCCCCCCCCCCCCCCCCCCCCCC

        subroutine DYNAMIC(cmass,dyd,d1d,d2d,d3d,dyf,a0,a2,a4,a6,n16)

        implicit real*8(a-h,o-z)
        logical l
        dimension cmass(n16,n16),dyd(n16),d1d(n16),d2d(n16),dyf(n16)
        dimension d3d(n16)

        do 100 i=1,16
        dyf(i)=0.0
        do 100 j=1,16
        dyf(i)=dyf(i)+cmass(i,j)*(a0*dyd(j)-a2*d1d(j)-a4*d2d(j)-a6*d3d(j))
100     continue

        return
        end



CCCCCCCCCCCCCCCCCCCCCCCCCCCCCCCCCCCCCCCCCCCCCCCCCCCCCCCCCCCCCCCCCCCCCCCCCCCCCCC
C
C       CMI
C
C       This subroutine calculates the element mass matrix for the
```

```
C       dynamic analysis.
C
CCCCCCCCCCCCCCCCCCCCCCCCCCCCCCCCCCCCCCCCCCCCCCCCCCCCCCCCCCCCCCCCCCCCCCCCCCCCCCC

        subroutine CMI(cmass,h,w,rad,ir,is,ix,iy,n8,n16)

        implicit real*8(a-h,o-z)
        logical l
        dimension cmass(n16,n16),h(ix,iy,n8)

        do 100 i=1,8
        i1=2*i-1
        do 100 j=1,8
100     cmass(i1,2*j-1)=cmass(i1,2*j-1)+w*rad*h(ir,is,i)*h(ir,is,j)

        return
        end


CCCCCCCCCCCCCCCCCCCCCCCCCCCCCCCCCCCCCCCCCCCCCCCCCCCCCCCCCCCCCCCCCCCCCCCCCCCCCCC
C
C       MAIN
C
C       This subroutine contains the bulk of the finite element coding.
C       When the program reaches this point during execution, all
C       the virtual memory arrays have been assigned, all the input
C       data has been read and all the nodal degrees of freedom have
C       been determined.  The first thing MAIN does is initialize
C       displacements and open all the necessary files.  Secondly,
C       AFESA integrates the elements to determine body
C       force loads, the dynamic mass matrix and the thermal stress
C       loads.  The third stage in MAIN is the equilibrium iteratation
C       loop.  When the equilibrium displacemens have been determined,
C       MAIN enters the fourth and last stage where output information
C       is written to the screen, output files and plot files.  The
C       third and fourth stages are repeated for each sub-increment
C       load case.
C
CCCCCCCCCCCCCCCCCCCCCCCCCCCCCCCCCCCCCCCCCCCCCCCCCCCCCCCCCCCCCCCCCCCCCCCCCCCCCCC

        subroutine MAIN(fgeom,fnameplt,fnameout,title,it,ne,imap,x,nn,n2,n8,
     &        n16,nlc,time,iprd,prd,nkrd,ipad,pad,nkad,iprf,alpha,
     &        prf,nkrf,ipaf,paf,nkaf,mrbfd,nrbfrt,nrbfat,rvo,drvo,
     &                  mrbfrd,nrbfrdv,mrbfad,nrbfadv,mabfd,nabfrt,
     &                  nabfat,mabfrd,nabfrdv,mabfad,nabfadv,mtd,nrtt,
     &                  natt,mtrd,ntrdv,mtad,ntadv,c,ct,cmpa,n5,n4,n3,
     &                  nemat,wt,ix,iy,a,mwk,maxa,nnm,sv,nud,imem,mb,
     &                  mh,sol,ts,bf,disp,rv,osv,pmta,pmpa,rplad,
     &                  iplad,nplm,npltdv,mca,nmatt,pid,sp,tsso,
     &                  ilda,ildad,nlde,itasp,aspod,eol,umax,psd,
     &                  aspc,aspd,neas,ltp,phas,n7,den,p1d,p2d,p3d,
     &                  ndn,fnamein,fnamesave,lstart,
     &                  lsave,lat,lrbf,lrbft,labf,labft,ltmp,ltmpt,
     &                  iplt,ltout,lfout,ldebug,leas,ldyn,pit,pft)

        implicit real*8(a-h,o-z)
        implicit integer(i-k,n,m)
        logical l
        character*(*) title,fnamein,fnamesave,fnameplt(n16),
     &                fnameout(n16),fgeom
        character*30 fonm
```

```
      dimension it(ne,n8),imap(nn,n2),x(nn,n2),c(nemat,n4,n4),
     &    ct(nemat,n4),iprd(nkrd),prd(nlc,nkrd),ipad(nkad),
     &    pad(nlc,nkad),iprf(nkrf),prf(nlc,nkrf),ipaf(nkaf),
     &    paf(nlc,nkaf),time(nlc),wt(ix,iy),a(mwk),maxa(nnm),
     &    sv(nlc,nud),ts(nlc,n16),bf(nlc,n16),sol(nlc),
     &    imem(ne),cmpa(nemat,n3),disp(nud),rv(nud),rvo(nud),
     &     pmta(npltdv),pmpa(nplm,npltdv,n5),iplad(n4),
     &     rplad(n4),mca(nmatt),pid(nn,n2),sp(n7),Alpha(nud),
     &    tsso(ix,iy,n4,n4),ilda(ildad),itasp(neas),
     &    aspod(neas),aspc(neas),aspd(neas),psd(neas),
     &    phas(nplm,n7),osv(nud),den(nmatt),p1d(ndn,n2),
     &    pit(nn),pft(nn),p2d(ndn,n2),p3d(ndn,n2),drvo(nud)
      dimension db(4),e(4,16),ilis(16),sa(16,16),xa(8,2),
     &          u(16),strain(4),stress(4),f(16),eps(4),prop(5),
     &          epsp1(4),epsp2(4),sig(4),alfa1(4),alfa2(4),
     &          cep(4,4),up(16),ut(16),cmass(16,16),dyd(16),
     &          d1d(16),d2d(16),d3d(16),dyf(16),ta(8),ema(4),emb(4)
      dimension nelnu(16),iipt(8)

      common /PLASDAT/ epm,Sigmax,Tbar
      common /THERMDAT/ tref,temp1,temp2,tdot,ts1,ts2,xn,xo
      common /RATEDAT/ dt,epd1,epd2

c     Real Plastic Data
c     beta            Kinematic vs Isotropic Hardening constant
      beta=rplad(1)

c     Integer Plastic Data
c     luf             Logical user output flag
c     lym     Logical Non-Linear Young's Modulus
      luf=.false.
      if(iplad(1) .eq. 1) then
         luf=.true.
         write(6,8127)
         read(5,8128) fonm
         write(6,8130)
         read(5,*) nnels
         do 3 i=1,nnels
         write(6,8126)
3        read(5,*) nelnu(i),iipt(i)
         open(unit=11,file=fonm,status='new')
         write(11,*) (int(sp(6))+1)*nlc,nnels
      endif
      lym=.false.
      if(iplad(2) .eq. 1) lym=.true.

c     Solution Parameters
c     tref            Reference Temperature
c     tollv           Tolerance for tangental load iterations
c     zd              Zero value tolerance for displacements
c     tolz            Zero value tolerance for output
c     imax            Max. number of step iterations
c     nsi             Number of sub-increments
c     laap            Logical for Alpha Acceleration Procedure
      tref=sp(1)
      tollv=sp(2)
      zd=sp(3)
      tolz=sp(4)
      imax=int(sp(5))
      nsi=int(sp(6))
      laap=.false.
      if(int(sp(7)) .eq. 1) laap=.true.
```

```
c                File designation numbers
c       #2               Element Mass file
c       #3               AFESA Input file
c       #4               Plot Output file
c       #5               Screen Input
c       #6               Screen Output
c       #7               Restart file
c       #7               Save file
c       #8               AFESA Output file
c       #9               Elastic Element Stiffness file
c       #10              Plastic Integration file
c       #11              User Output File

        s12=dsqrt(1d0/2d0)
        s23=dsqrt(2d0/3d0)
        s32=dsqrt(3d0/2d0)
        iii=2
        nsv=1
        lerr=.false.
        ldout=.false.

        if(ldebug) write(6,8122)

C       INITIALIZE PRESCRIBED INITIAL DISPLACEMENTS
        if(lstart) then
           open(unit=7,file=fnamein,readonly,status='old')
           read(7,*) timeold
           do 5 i=1,nn
5          read(7,*) pid(i,1),pid(i,2),pit(i)
           if(leas) then
              do 7 i=1,neas
              aspod(i)=pid(itasp(i),2)
7             read(7,*) psd(i)
           endif
           do 8 i=1,nud
8          read(7,*) osv(i)
           if(ldyn) then
              do 9 i=1,ndn
9             read(7,*) p1d(i,1),p1d(i,2),p2d(i,1),p2d(i,2)
           endif
        else
           timeold=0d0
           do 12 i=1,nn
           pid(i,1)=0d0
           pid(i,2)=0d0
12         pit(i)=tref
           if(ldyn) then
              do 14 i=1,ndn
              p1d(i,1)=0d0
              p1d(i,2)=0d0
              p2d(i,1)=0d0
14            p2d(i,2)=0d0
           endif
        endif

C       INITIALIZE SOLUTION VECTOR AND DISPLACEMENTS
        do 16 j=1,nud
        disp(j)=0d0
        do 16 i=1,nlc
16      sv(i,j)=0d0

C       Open mass element matrix
        if(ldyn) open(unit=2,file='LIBD$:[scratch]jnk2.dat',
```

```
     &           access='DIRECT',status='SCRATCH',recl=1088)

C       OPEN ELASTIC ELEMENT STIFFNESS FILE
        open(unit=9,file='LIBD$:[scratch]jnk9.dat',
     &           access='DIRECT',status='SCRATCH',recl=1088)

C       OPEN PLASTIC INTEGRATION STIFFNESS FILE
        if(.not. lat) then
           open(unit=10,file='LIBD$:[scratch]jnk10.dat',
     &           access='DIRECT',status='SCRATCH',recl=160)
        endif

C       WRITE PLOT GEOMETRY FILE
        if(lplt .and. (.not. lstart)) then
           open(unit=4,file=fgeom,status='new')
           write(4,*) nn,ne,ix,iy
           do 20 i=1,nn
20         write(4,*) x(i,1),x(i,2)
           do 22 i=1,ne
22         write(4,*) abs(imem(i)),(it(i,j),j=1,8)
           close(unit=4)
        endif

C       CALCULATE ELASTIC STIFFNESSES
        knee=0
        knpe=0
        do 1000 ine=1,ne

C       INITIALIZE ELASTIC STIFFNESS MATRIX
        do 30 i=1,16
        do 30 j=i,16
30      sa(j,i)=0d0

C       INITIALIZE ELEMENT MASS MATRIX
        if(ldyn) then
           do 31 i=1,16
           do 31 j=1,16
31         cmass(j,i)=0d0
        endif

        if(ldebug) then
           ldout=.false.
           do 32 i=1,nlde
           if(ilda(i) .eq. ine) then
              ldout=.true.
              write(6,8119) ine
              goto 36
           endif
32         continue
        endif

C       DECIDE IF ELEMENT TYPE IS ELASTIC OR PLASTIC
36      iemt=imem(ine)
        if(iemt .gt. 0) then
           lplastic=.false.
           ielm=mca(iemt)
           knee=knee+1
           if(ldout) then
              write(6,*) '  Elastic material matrix : C '
              do 40 i=1,4
40            write(6,8110) (c(ielm,i,j),j=1,4)
           endif
        else
```

```
            iemt=-iemt
            lplastic=.true.
            iplm=mca(iemt)
         endif

C        READ IN ELEMENT NODE #'S AND NODE GEOMETRY
         do 50 i=1,8
         icn=it(ine,i)
         do 50 j=1,2
         ilis(2*(i-1)+j)=imap(icn,j)
50       xa(i,j)=x(icn,j)

C        INITIALIZE THERMAL AND LORENTZ LOADS
         do 110 i=1,nlc
         do 110 j=1,16
         ts(i,j)=0d0
110      bf(i,j)=0d0

C        INTEGRTE OVER ELEMENT INTEGRATION POINTS
         do 500 ir=1,ix
         do 500 is=1,iy

         call HE(%val(mb),e,%val(mh),rad,w,xa,z,ir,is,ix,iy,n2,n4,n8,n16)
         w=w*wt(ir,is)

         if(lrbf) call BFI(bf,%val(mh),w,rad,z,1,ir,is,ix,iy,nlc,
     &                     n8,n16,lrbft,sol,%val(mrbfd),
     &                     nrbfat,nrbfrt,%val(mrbfrd),nrbfrdv,
     &                     %val(mrbfad),nrbfadv)

         if(labf) call BFI(bf,%val(mh),w,rad,z,0,ir,is,ix,iy,nlc,
     &                     n8,n16,labft,sol,%val(mabfd),
     &                     nabfat,nabfrt,%val(mabfrd),nabfrdv,
     &                     %val(mabfad),nabfadv)

         if(ldyn) call CMI(cmass,%val(mh),w,rad,ir,is,ix,iy,n8,n16)

         if(.not. lplastic) then
C        INTEGRATE UPPER ELASTIC ELEMENT STIFFNESS MATRIX
            do 160 j=1,16
            do 131 k=1,4
            db(k)=0d0
            do 130 i1=1,4
130         db(k)=db(k)+c(ielm,k,i1)*e(i1,j)
131         continue
            do 150 i=j,16
            st=0d0
            do 140 i1=1,4
140         st=st+e(i1,i)*db(i1)
150         sa(i,j)=sa(i,j)+st*w
160         continue

            if(ltmp) call TSI(tref,e,ct,ielm,rad,
     &                     z,sol,ts,w,nemat,n4,n16,nlc,
     &                     ltmpt,%val(mtd),nrtt,natt,%val(mtrd),
     &                     ntrdv,%val(mtad),ntadv)

         else

C        INITIALIZE PLASTIC ELEMENT INTEGRATION POINT DATA
            knpe=knpe+1
            if(lstart) then
               read(7,*) temp1,epm,epd1,xo,
```

```
     &                    (eps(i),epsp1(i),sig(i),alfa1(i),i=1,4)
           else
              epm=0d0
              epd1=0d0
              temp1=tref
              xo=1d0
              do 300 i=1,4
              eps(i)=0d0
              epsp1(i)=0d0
              sig(i)=0d0
300           alfa1(i)=0d0
           endif
           write(10,rec=knpe)  temp1,epm,epd1,xo,
     &                    (eps(i),epsp1(i),sig(i),alfa1(i),i=1,4)

        endif

500     continue

        if(lplastic) goto 700

c       Fill out Stiffness Matrix
        do 510 j=1,16
        do 510 i=j,16
510     sa(j,i)=sa(i,j)

c       store elastic stiffness matrix
        write(9,rec=knee) ((sa(i,j),i=j,16),j=1,16)

c       Define the Load Vectors SV
c       Condense prescribed radial displacements
        do 550 i=1,16,2
        nc=ilis(i)
        if(nc .gt. 0) goto 550
        node=it(ine,(i+1)/2)
        do 540 k=1,nkrd-1
        if(node .ne. iprd(k)) goto 540
        do 530 ii=1,16
        nd=ilis(ii)
        if(nd .lt. 0) goto 530
        do 520 jj=1,nlc
520     sv(jj,nd)=sv(jj,nd)-sa(ii,i)*prd(jj,k)
530     continue
        goto 550
540     continue
550     continue

c       Condense prescribed axial displacements
        do 600 i=2,16,2
        nc=ilis(i)
        if(nc .gt. 0) goto 600
        node=it(ine,i/2)
        do 590 k=1,nkad-1
        if(node .ne. ipad(k)) goto 590
        do 580 ii=1,16
        nd=ilis(ii)
        if(nd .lt. 0) goto 580
        do 570 jj=1,nlc
570     sv(jj,nd)=sv(jj,nd)-sa(i,ii)*pad(jj,k)
580     continue
        goto 600
590     continue
600     continue
```

```
c       Add thermal and body forces
700     do 830 i=1,16
        nc=ilis(i)
        if(nc .lt. 0) goto 830
        do 820 j=1,nlc

820     sv(j,nc)=sv(j,nc)-ts(j,i)+bf(j,i)
830     continue

        if(ldout) then
           do 950 j=1,nlc
           write(6,8120) j
           do 950 i=1,8
           i1=2*i-1
           i2=2*i
950        write(6,8117) it(ine,i),ilis(i1),ilis(i2),xa(i,1),xa(i,2),
     &                   bf(j,i1),bf(j,i2),ts(j,i1),ts(j,i2)
        endif

C       Fill out mass matrix
        if(ldyn) then
           do 980 i=1,16,2
           do 980 j=i,16,2
           cmass(i,j)=den(iemt)*cmass(i,j)
980        cmass(j,i)=cmass(i,j)
           do 990 i=2,16,2
           do 990 j=2,16,2
990        cmass(i,j)=cmass(i-1,j-1)

c          store mass matrix
           write(2,rec=ine) ((cmass(i,j),i=j,16),j=1,16)
        endif

1000    continue
        close(unit=7)

c       Add prescribed radial forces
        do 1002 i=1,nkrf-1
        nc=imap(iprf(i),1)
        if(nc .lt. 0) goto 1002
        do 1001 j=1,nlc
1001    sv(j,nc)=sv(j,nc)+prf(j,i)
1002    continue

c       Add prescribed axial forces
        do 1004 i=1,nkaf-1
        nc=imap(ipaf(i),2)
        if(nc .lt. 0) goto 1004
        do 1003 j=1,nlc
1003    sv(j,nc)=sv(j,nc)+paf(j,i)
1004    continue

        if(ldebug) then
           ldout=.false.
           write(6,8121)
        endif



        llastime=.false.
        icon=0
c       Loop Through Time for the Solutions
```

```
      do 4000 isn=1,nlc
      if(ltout) write(6,8131) title
      dt=(time(isn)-timeold)/(nsi+1d0)

      if(ldyn) then
         do 1010 i=1,nn
         dar=p2d(i,1)
         daz=p2d(i,2)
         dvr=p1d(i,1)
         dvz=p1d(i,2)
         p1d(i,1)=pid(i,1)
         p1d(i,2)=pid(i,2)
         p2d(i,1)=pid(i,1)-dt*dvr+dt*dt*dar/2d0
         p2d(i,2)=pid(i,2)-dt*dvz+dt*dt*daz/2d0
         p3d(i,1)=pid(i,1)-2d0*dt*dvr+2d0*dt*dt*dar
         p3d(i,2)=pid(i,2)-2d0*dt*dvz+2d0*dt*dt*daz
1010     continue
         a0=2d0/(dt*dt)
         a1=11d0/(6d0*dt)
         a2=5d0/(dt*dt)
         a3=3d0/dt
         a4=-2d0*a0
         a5=-a3/2d0
         a6=a0/2d0
         a7=a3/9d0
      endif

c     Loop through subincrements
      llastinc=.false.
      do 3800 isin=1,nsi+1
      rtime=time(isn)-dt*(nsi+1-isin)
      if(isin .eq. nsi+1) llastinc=.true.
      if((isn .eq. nlc) .and. llastinc) llastime=.true.
      last=.false.

      write(6,8107) isn,isin,rtime
      if(.not. lat) icon=0
1020  if(lat .and. icon .gt. 0) goto 1450
      if(icon .gt. imax) then
         if(ltout) write(6,8114)
         goto 2000
      endif

C     INITIALIZE ITERATION ARRAYS
      if(icon .eq. 0) then
         iii=2
         do 1025 i=1,mwk
1025     a(i)=0.
         do 1026 i=1,nud
1026     alpha(i)=1d0
         if(laap) then
            do 1027 i=1,nud
1027        rvo(i)=disp(i)
         endif
      else
         iii=3
      endif
      do 1030 i=1,nud
1030  rv(i)=0d0


C     LOOP THROUGH ELEMENTS
      knee=0
```

```
      knpe=0
      do 1300 ine=1,ne

      if(ldebug .and. (icon .eq. 0)) then
         ldout=.false.
         do 1040 i=1,nlde
         if(ilda(i) .eq. ine) then
            ldout=.true.
            write(6,8119) ine
            goto 1050
         endif
1040     continue
      endif

C     LOAD ELEMENT NODE RESULTS
C     UT       TOTAL DISPLACEMENT VECTOR FOR STRAIN CALCULATIONS
C     UP       PRESCRIBED DISPLACEMENT INCREMENT VECTOR FOR LOAD CALCULATION
C     U        DISPLACEMENT VECTOR FOR CONDENSING ELASTIC STIFFNESS MATRIX
1050  do 1090 j=1,8
      icn=it(ine,j)
      icd=imap(icn,1)
      ilis(2*j-1)=icd
      xa(j,1)=x(icn,1)
      if(icd .lt. 0) then
         do 1060 ii=1,nkrd-1
         if(iprd(ii) .ne. icn) goto 1060
         if((icon .eq. 0) .and. (isn .eq. 1)) then
            if(lstart) then
               ut(2*j-1)=pid(icn,1)
               up(2*j-1)=(prd(isn,ii)-pid(icn,1))/(nsi+2d0-isin)
            else
               ut(2*j-1)=prd(isn,ii)*(isin-1d0)/(nsi+1d0)
               up(2*j-1)=prd(isn,ii)/(nsi +1d0)
            endif
         elseif(icon .eq. 0) then
            ut(2*j-1)=prd(isn,ii)-(prd(isn,ii)-prd(isn-1,ii))*
     &        (nsi+2d0-isin)/(nsi+1)
            up(2*j-1)=(prd(isn,ii)-prd(isn-1,ii))/(nsi+1d0)
         elseif(isn .eq. 1) then
            ut(2*j-1)=pid(icn,1)+(prd(isn,ii)-pid(icn,1))/
     &        (nsi+2d0-isin)
         else
            ut(2*j-1)=prd(isn,ii)-(prd(isn,ii)-prd(isn-1,ii))*
     &        (nsi+1d0-isin)/(nsi+1)
         endif
         u(2*j-1)=0d0
         goto 1070
1060     continue
      else
         if(isn .eq. 1 .and. icon .eq. 0 .and. lstart)
     &       disp(icd)=pid(icn,1)
         ut(2*j-1)=disp(icd)
         u(2*j-1)=disp(icd)
         up(2*j-1)=0d0
      endif
1070  icd=imap(icn,2)
      ilis(2*j)=icd
      xa(j,2)=x(icn,2)
      if(icd .lt. 0) then
         do 1080 ii=1,nkad-1
         if(ipad(ii) .ne. icn) goto 1080
         if(icon .eq. 0 .and. isn .eq. 1) then
            if(lstart) then
```

```
                  ut(2*j)=pid(icn,2)
                  up(2*j)=(pad(isn,ii)-pid(icn,2))/(nsi+2d0-isin)
               else
                  ut(2*j)=pad(isn,ii)*(isin-1d0)/(nsi+1d0)
                  up(2*j)=pad(isn,ii)/(nsi +1d0)
               endif
            elseif(icon .eq. 0) then
               ut(2*j)=pad(isn,ii)-(pad(isn,ii)-pad(isn-1,ii))*
     &           (nsi+2d0-isin)/(nsi+1)
               up(2*j)=(pad(isn,ii)-pad(isn-1,ii))/(nsi+1d0)
            elseif(isn .eq. 1) then
               ut(2*j)=pid(icn,2)+(pad(isn,ii)-pid(icn,2))/
     &           (nsi+2d0-isin)
            else
               ut(2*j)=pad(isn,ii)-(pad(isn,ii)-pad(isn-1,ii))*
     &           (nsi+1d0-isin)/(nsi+1)
            endif
            u(2*j)=0d0
            goto 1085
1080        continue
         else
            if(isn .eq. 1 .and. icon .eq. 0 .and. lstart)
     &          disp(icd)=pid(icn,2)
            ut(2*j)=disp(icd)
            u(2*j)=disp(icd)
            up(2*j)=0d0
         endif

C        Update Dynamic variables
1085     if(ldyn) then
            if(icon .eq. 0) then
               dar=(p1d(icn,1)-2d0*p2d(icn,1)+p3d(icn,1))/(dt*dt)
               daz=(p1d(icn,2)-2d0*p2d(icn,2)+p3d(icn,2))/(dt*dt)
               dvr=(p1d(icn,1)-p2d(icn,1))/dt
               dvz=(p1d(icn,2)-p2d(icn,2))/dt
               dyd(2*j-1)=p1d(icn,1)+dt*dvr+dt*dt*dar/2d0
               dyd(2*j)=p1d(icn,2)+dt*dvz+dt*dt*daz/2d0
            else
               dyd(2*j-1)=u(2*j-1)
               dyd(2*j)  =u(2*j)
            endif
            d1d(2*j-1)=p1d(icn,1)
            d1d(2*j)  =p1d(icn,2)
            d2d(2*j-1)=p2d(icn,1)
            d2d(2*j)  =p2d(icn,2)
            d3d(2*j-1)=p3d(icn,1)
            d3d(2*j)  =p3d(icn,2)
         endif

1090     continue

         iemt=imem(ine)
         if(iemt .gt. 0) then
            knee=knee+1

C        Read Elastic Stiffness Matrix and Calculate F Vector
            read(9,rec=knee) ((sa(i,j),i=j,16),j=1,16)
            do 1100 j=1,16
            do 1100 i=j,16
1100        sa(j,i)=sa(i,j)
            do 1110 i=1,16
            f(i)=0d0
            do 1110 j=1,16
```

```
1110        f(i)=f(i)+sa(i,j)*u(j)
         else



C        Calculate the Plastic Stiffness Matrix and F Vector
            iplm=mca(-iemt)
            do 1120 i=1,16
            f(i)=0d0
            do 1120 j=1,16
1120        sa(i,j)=0d0

C        Loop Through Integration Points
            do 1200 ir=1,ix
            do 1200 is=1,iy

C        Read The Element Integration Data
            knpe=knpe+1
            ipt=(ir-1)*iy + is
            read(10,rec=knpe)   temp1,epm,epd1,xo,
     &                    (eps(i),epsp1(i),sig(i),alfa1(i),i=1,4)

C        Calcuate Strains
            call HE(%val(mb),e,%val(mh),rad,w,xa,z,ir,is,ix,iy,
     &              n2,n4,n8,n16)
            w=w*wt(ir,is)

            do 1130 j=1,4
            strain(j)=0d0
            do 1130 k=1,16
1130        strain(j)=strain(j)+e(j,k)*ut(k)

            temp2=tref
            IF(LTMP) CALL TEMP(rad,z,temp2,nlc,ltmpt,%val(mtd),isn,
     &                nrtt,natt,%val(mtrd),ntrdv,%val(mtad),ntadv)

            temp2=temp1+(temp2-temp1)/(nsi+2-isin)
            tdot=(temp2-temp1)/dt

            call TEPE(strain,stress,sig,eps,epsp1,epsp2,alfa1,alfa2,
     &                pmta,pmpa,phas,cep,prop,last,ldebug,ltp,nplm,
     &                iplm,nplTdv,lym,n4,n5,n7)

         if(ldout) then
            write(6,*)
            write(6,*) '  Plastic material matrix : CEP '
            do 1135 i=1,4
1135        write(6,8110) (cep(i,j),j=1,4)
         endif

C        CALCULATE PLASTIC STIFFNESS
            if(icon .eq. 0) then
               do 1170 j=1,16
               do 1141 k=1,4
               db(k)=0d0
               do 1140 i1=1,4
1140           db(k)=db(k)+cep(k,i1)*e(i1,j)
1141           continue
               do 1160 i=j,16
               st=0d0
               do 1150 i1=1,4
1150           st=st+e(i1,i)*db(i1)
               sa(i,j)=sa(i,j)+st*w
```

```
1160          sa(j,i)=sa(i,j)
1170          continue
           endif

C       CALCULATE F MATRIX
           do 1190 i=1,16
           st=0d0
           do 1180 j=1,4
1180       st=st+e(j,i)*stress(j)
1190       f(i)=f(i)+st*w

1200       continue

C       CONDENSE PRESCRIBED DISPLACEMENT INCREMENTS
           if(icon .eq. 0) then
              do 1210 i=1,16
              do 1210 j=1,16
1210          f(i)=f(i)+sa(i,j)*up(j)
           endif

        endif

        if(ldout .and. (icon .eq. 0)) then
           write(6,*)
           write(6,*) 'Element Stiffness Matrix'
           write(6,8110) ((sa(i,j),i=j,16),j=1,16)
        endif

C       Determine Dynamic Loads and add to element load matrix
        if(ldyn) then
           read(2,rec=ine) ((cmass(i,j),i=j,16),j=1,16)
           do 1215 j=1,16
           do 1215 i=j,16
1215       cmass(j,i)=cmass(i,j)
           call DYNAMIC(cmass,dyd,d1d,d2d,d3d,dyf,a0,a2,a4,a6,n16)
           do 1220 i=1,16
1220       f(i)=f(i)+dyf(i)

C       Add appropriate Mass matrix for dynamic Analysis
           if(icon .eq. 0) then
              do 1230 i=1,16
              do 1230 j=1,16
1230          sa(i,j)=sa(i,j)+a0*cmass(i,j)
           endif
        endif

C       Load Element Load Matrix into Global Load Matrix
        do 1270 i=1,16
        nc=ilis(i)
        if(nc .lt. 0) goto 1270
        rv(nc)=rv(nc)+f(i)
1270    continue

C       Load Element Stiffness Matrix into Global Stiffness Matrix
        if(icon .eq. 0) then
           do 1290 i=1,16
           nc=ilis(i)
           if(nc .lt. 0) goto 1290
           do 1280 j=1,16
           nd=ilis(j)
           if(nd .lt. 0) goto 1280
           if(nc .lt. nd) goto 1280
           ml=maxa(nc)+nc-nd
```

```
            a(ml)=a(ml)+sa(i,j)
1280        continue
1290        continue
          endif
1300      continue
          if(ldebug) ldout=.false.

C         CALCULATE TANGENTAL LOAD VECTOR RV
          do 1390 i=1,nud
1390      rv(i)=-rv(i)+osv(i)+(sv(isn,i)-osv(i))/(nsi+2d0-isin)

C         ADD EXTERNAL SPRING FORCES
          if(leas) call SForce(aspc,aspd,psd,itasp,rv,disp,aspod,
     &    imap,umax,eol,last,ltout,lfout,neas,nn,nud,n2)

C         Examine the residual vector and test for convergence
          lrv=.true.
          if(icon .eq. 0) then
            osvn=svn
            osvt=svt
            lcut=.true.
            svn=0d0
            do 1430 i=1,nud
            rvs=rv(i)*rv(i)
            if(rvs .gt. svt*1e-6) lrv=.false.
1430        svn=svn+rvs
            svt=tollv * svn / nud
            rvn=svn
            prvn=svn
            if(lrv) then
              write(6,8116) icon,1.0
              svn=osvn
              svt=osvt
              goto 2000
            endif
          else
            prvn=rvn
            rvn=0d0
            do 1440 i=1,nud
            rvs=rv(i)*rv(i)
            if(rvs .gt. svt) lrv=.false.
1440        rvn=rvn+rvs
            if(rvn .gt. prvn) then
              lcut=.false.
              do 1445 i=1,nud
1445          alpha(i)=1d0
            if(rvn .eq. prvn) lrv=.true.
            endif
          endif
          write(6,8116) icon,rvn/svn
          if(lrv) goto 2000
          goto 1500

c         Load Elastic Forces
1450      do 1460 i=1,nud
          disp(i)=0d0
1460      rv(i)=osv(i)+(sv(isn,i)-osv(i))/(nsi+2d0-isin)

C         SOLVE FOR THE DELTA DISPLACEMENTS
1500      if(ldebug) then
            write(6,*)
            write(6,*) 'Load Vector'
            write(6,8110) (rv(i),i=1,nud)
```

```
      endif

      call COLSOL(a,rv,maxa,nud,mwk,nnm,iii,nsv,lerr)
      icon=icon+1
      if(lerr) goto 9999
      if(lat) iii=3

c     Increment displacement vector
      if(laap .and. (icon .lt. 7) .and. lcut) then
         if(mod(icon,2) .eq. 1) then
            do 1520 i=1,nud
            drvo(i)=rv(i)
            rvo(i) = disp(i)
1520        disp(i) = disp(i) + alpha(i) * rv(i)
         else
            do 1540 i=1,nud
            alpha(i) = alpha(i) + rv(i) / drvo(i)
1540        disp(i) = rvo(i) + alpha(i) * drvo(i)
         endif
      else
         do 1560 i=1,nud
1560     disp(i) = disp(i) + alpha(i) * rv(i)
      endif

      if(lat) goto 2000
      goto 1020

c     Finite Element Output
2000  if(ltout) write(6,8115) icon
      last=.true.
      if(lsave .and. llastime) then
         open(unit=7,file=fnamesave,status='new')
         write(7,*) rtime
      endif
      if(lfout .and. (isin .eq. 1)) open(unit=8,file=fnameout(isn),
     & status='new')
      if(lfout) write(8,8131) title
      if(lfout) write(8,8107) isn,isin,rtime
      if(luf) write(11,8132) rtime
      if(lplt .and. llastinc) open(unit=4,file=fnameplt(isn),
     & status='new')

c     Nodal Output
      if(ltout) write(6,8101)
      if(lfout) write(8,8101)
      do 2050 i=1,nn
      ir=imap(i,1)
      if(ir .lt. 0) then
         do 2010 j=1,nkrd-1
         if(iprd(j) .ne. i) goto 2010
         ur=pid(i,1)+(prd(isn,j)-pid(i,1))/(nsi+2d0-isin)
         goto 2020
2010     continue
         ur=d0
      else
         ur=disp(ir)
      endif
2020  iz=imap(i,2)
      if(iz .lt. 0) then
         do 2030 j=1,nkad-1
         if(ipad(j) .ne. i) goto 2030
         uz=pid(i,2)+(pad(isn,j)-pid(i,2))/(nsi+2d0-isin)
         goto 2040
```

```
2030        continue
            uz=d0
         else
            uz=disp(iz)
         endif
2040     utot=ur*ur+uz*uz
         if(utot .gt. 1d-20) utot=utot**.5
         if(dabs(ur) .lt. zd) ur=0d0
         if(dabs(uz) .lt. zd) uz=0d0
         if(dabs(utot) .lt. zd) utot=0d0
         if(mod(i,20) .eq. 0 .and. ltout) write(6,8101)
         if(mod(i,20) .eq. 0 .and. lfout) write(8,8101)

         temp2=tref
         temp1=pit(i)
         if(ltmp .or. (.not. lat)) then
            call TEMP(x(i,1),x(i,2),temp2,nlc,ltmpt,%val(mtd),isn,
     &                 nrtt,natt,%val(mtrd),ntrdv,%val(mtad),ntadv)
            temp2=temp1+(temp2-temp1)/(nsi+2-isin)
         endif

         pid(i,1)=ur
         pid(i,2)=uz
         pft(i)=temp2

         if(lsave .and. llastime) write(7,*) ur,uz,temp2
         if(lplt .and. llastinc) write(4,8108) ur,uz,temp2
         if(ltout) write(6,8125) i,x(i,1),x(i,2),ur,uz,utot,temp2
         if(lfout) write(8,8125) i,x(i,1),x(i,2),ur,uz,utot,temp2
2050     continue

C        External Axial Spring Output
         if(leas) call SForce(aspc,aspd,psd,itasp,rv,disp,aspod,
     &   imap,umax,eol,last,ltout,lfout,neas,nn,nud,n2)

C        Save External Axial Spring Data
         if(lsave .and. llastime .and. leas) then
            do 2052 i=1,neas
2052        write(7,*) psd(i)
         endif

C        Update old solution vector OSV
         do 2054 i=1,nud
2054     osv(i)=osv(i)+(sv(isn,i)-osv(i))/(nsi+2d0-isin)

C        Save Solution Vector Nodal Forces
         if(lsave .and. llastime) then
            do 2056 i=1,nud
2056        write(7,*) osv(i)
            if(ldyn) then
               do 2058 i=1,ndn
               dar=a0*pid(i,1)-a2*p1d(i,1)-a4*p2d(i,1)-a6*p3d(i,1)
               daz=a0*pid(i,2)-a2*p1d(i,2)-a4*p2d(i,2)-a6*p3d(i,2)
               dvr=a1*pid(i,1)-a3*p1d(i,1)-a5*p2d(i,1)-a7*p3d(i,1)
               dvz=a1*pid(i,2)-a3*p1d(i,2)-a5*p2d(i,2)-a7*p3d(i,2)
2058           write(7,*) dvr,dvz,dar,daz
            endif
         endif

C        ELEMENT OUTPUT ROUTINES
         if(ltout) write(6,8106)
         if(lfout) write(8,8106)
```

```
      knpe=0
      do 3000 ine=1,ne
      iemt=imem(ine)
      if(iemt .gt. 0) then
         lplastic=.false.
         ielm=mca(iemt)
      else
         iplm=mca(-iemt)
         lplastic=.true.
      endif

      if(ltout) write(6,8103) ine,(it(ine,j),j=1,8)
      if(lfout) write(8,8103) ine,(it(ine,j),j=1,8)

c     Load Element Node Results
      do 2090 j=1,8
      icn=it(ine,j)
      xa(j,1)=x(icn,1)
      xa(j,2)=x(icn,2)
      u(2*j-1)=pid(icn,1)
      u(2*j)=pid(icn,2)
      ta(j)=pit(icn)
2090  continue

      if(ltout .and. (lat .or. (.not. lplastic))) write(6,8104)
      if(lfout .and. (lat .or. (.not. lplastic))) write(8,8104)
      if(ltout .and. lplastic) write(6,8111)
      if(lfout .and. lplastic) write(8,8111)

      do 2600 ir=1,ix
      do 2600 is=1,iy

C     CALCUATE STRAINS
      call HE(%val(mb),e,%val(mh),rad,w,xa,z,ir,is,ix,iy,n2,n4,n8,n16)
      do 2100 j=1,4
      strain(j)=0d0
      do 2100 k=1,16
2100  strain(j)=strain(j)+e(j,k)*u(k)

C     DETERMINE INTEGRATION POINT STRESSES AND STRAINS
      if(dabs(rad) .lt. zd) rad=d0
      if(dabs(z) .lt. zd) z=d0
      if(lat .or. (.not. lplastic)) then

C     CALCULATE INTEGRATION POINT TEMPERATURE
         temp1=tref
         if(ltmp) call isop(temp1,%val(mh),ta,ir,is,ix,iy,n8)
         temp2=tref
         if(ltmp) call TEMP(rad,z,temp2,nlc,ltmpt,%val(mtd),isn,
     &              nrtt,natt,%val(mtrd),ntrdv,%val(mtad),ntadv)
         temp2=temp1+(temp2-temp1)/(nsi+2-isin)
         te=cmpa(ielm,3)*(temp2-tref)

         strain(1)=strain(1)-te
         strain(2)=strain(2)-te
         strain(4)=strain(4)-te

C     CALCULATE STRESSES
         do 2125 ii=1,4
         do 2125 j=1,4
2125     stress(j)=stress(j)+c(imem(ine),j,ii)*strain(ii)
         vm=(.5*((stress(1)-stress(2))**2+(stress(1)-stress(4))**2+
     &        (stress(2)-stress(4))**2)+3d0*stress(3)*stress(3))**.5
```

```
            call ZERO(strain,aver,n4,tolz)
            call ZERO(stress,aver,n4,tolz)
            if(dabs(vm/aver) .lt. tolz) vm=0d0

            if(ltout) write(6,8105) ir,is,rad,z,strain(1),strain(4),
     &strain(2),strain(3),stress(1),stress(4),stress(2),stress(3),vm
            if(lfout) write(8,8105) ir,is,rad,z,strain(1),strain(4),
     &strain(2),strain(3),stress(1),stress(4),stress(2),stress(3),vm
            if(lplt .and. llastinc) then

               write(4,*) (strain(i),i=1,4),(Stress(j),j=1,4)
            endif

         else

C        Read The Element Integration Data
            knpe=knpe+1
            ipt=(ir-1)*iy + is
            read(10,rec=knpe)  temp1,epm,epd1,xo,
     &                  (eps(i),epsp1(i),sig(i),alfa1(i),i=1,4)

C        CALCULATE INTEGRATION POINT TEMPERATURE
            temp2=tref
            call TEMP(rad,z,temp2,nlc,ltmpt,%val(mtd),isn,
     &           nrtt,natt,%val(mtrd),ntrdv,%val(mtad),ntadv)
            temp2=temp1+(temp2-temp1)/(nsi+2-isin)
            tdot=(temp2-temp1)/dt

            call TEPE(strain,stress,sig,eps,epsp1,epsp2,alfa1,alfa2,
     &              pmta,pmpa,phas,cep,prop,last,ldebug,itp,nplm,
     &              iplm,npltdv,lym,n4,n5,n7)

            write(10,rec=knpe) temp2,epm,epd2,xn,
     &                  (strain(i),epsp2(i),stress(i),alfa2(i),i=1,4)

            call ZERO(epsp2,aver,n4,tolz)
            call ZERO(strain,aver,n4,tolz)

            call ZERO(alfa2,aver,n4,tolz*tolz)
            call ZERO(stress,aver,n4,tolz)

C        STORE STRESSES AND STRAINS FOR OUTPUT
            ema(1)=strain(1)-ts2
            ema(2)=strain(2)-ts2
            ema(3)=strain(3)
            ema(4)=strain(4)-ts2
            do 2400 i=1,4
            tsso(ir,is,i,1)=alfa2(i)
            tsso(ir,is,i,2)=stress(i)
            tsso(ir,is,i,3)=epsp2(i)
2400        tsso(ir,is,i,4)=ema(i)

C        Calculate Effective mechanical and plastic strain
            call deviat(epsp2,emb,epp,n4)
            call deviat(ema,emb,ept,n4)
            call deviat(Stress,emb,Tbar,n4)
            epp=s23*epp
            ept=s12*ept
            Tbar=s32*Tbar

C        Call user output file
            if(luf) then
```

```
               do 2500 i=1,nnels
               if(nelnu(i) .eq. ine .and. iipt(i) .eq. ipt) then
                  write(11,8110) temp2,epm,epd2,xn,ts2,Tbar,Sigmax
                  write(11,8110) (strain(j),epsp2(j),j=1,4)
                  write(11,8110) (stress(j),alfa2(j),j=1,4)
               endif
2500           continue
            endif

C        PRINT PLASTIC RESULTS
            ixf1=int(50*(1+xn))
            ixf2=100-ixf1
            if(ltout) write(6,8112) ipt,ixf1,ixf2,temp2,ts2,epp,epd2,
     &                              ept,Tbar,Sigmax
            if(lfout) write(8,8112) ipt,ixf1,ixf2,temp2,ts2,epp,epd2,
     &                              ept,Tbar,Sigmax
         endif

2600     continue

C        OUTPUT PLASTIC STRESSES
         if(lplastic) then
            if(ltout) write(6,8118)
            if(lfout) write(8,8118)
            do 2620 ir=1,ix
            do 2620 is=1,iy
            if(ltout) write(6,8105) ir,is,(tsso(ir,is,i,1),i=1,4),
     &                                    (tsso(ir,is,j,2),j=1,4)
2620        if(lfout) write(8,8105) ir,is,(tsso(ir,is,i,1),i=1,4),
     &                                    (tsso(ir,is,j,2),j=1,4)
            if(ltout) write(6,8113)
            if(lfout) write(8,8113)

            do 2640 ir=1,ix
            do 2640 is=1,iy
            if(ltout) write(6,8105) ir,is,(tsso(ir,is,i,3),i=1,4),
     &                                    (tsso(ir,is,j,4),j=1,4)
            if(lfout) write(8,8105) ir,is,(tsso(ir,is,i,3),i=1,4),
     &                                    (tsso(ir,is,j,4),j=1,4)
            if(lplt .and. llastinc) then
               write(4,8109) (tsso(ir,is,i,4),i=1,4),
     &                       (tsso(ir,is,j,2),j=1,4)
            endif
2640        continue

         endif

3000     continue

         if(ltmp) then
            do 3010 i=1,nn
3010     pit(i)=pft(i)
         endif

         if(ldyn) then
            if(ltout) write(6,8123)
            if(lfout) write(8,8123)
            if(ltout) write(6,8124)
            if(lfout) write(8,8124)
            do 3100 i=1,nn
            if(mod(i,20) .eq. 0 .and. ltout) write(6,8124)
            if(mod(i,20) .eq. 0 .and. lfout) write(8,8124)
            dar=a0*pid(i,1)-a2*p1d(i,1)-a4*p2d(i,1)-a6*p3d(i,1)
```

```
            daz=a0*pid(i,2)-a2*p1d(i,2)-a4*p2d(i,2)-a6*p3d(i,2)
            dvr=a1*pid(i,1)-a3*p1d(i,1)-a5*p2d(i,1)-a7*p3d(i,1)
            dvz=a1*pid(i,2)-a3*p1d(i,2)-a5*p2d(i,2)-a7*p3d(i,2)
            if(ltout) write(6,8102) i,dvr,dvz,dar,daz
            if(lfout) write(8,8102) i,dvr,dvz,dar,daz
            if(isin .ne. (nsi+1)) then
               p3d(i,1)=p2d(i,1)
               p3d(i,2)=p2d(i,2)
               p2d(i,1)=p1d(i,1)
               p2d(i,2)=p1d(i,2)
               p1d(i,1)=pid(i,1)
               p1d(i,2)=pid(i,2)
            else
               p1d(i,1)=dvr
               p1d(i,2)=dvz
               p2d(i,1)=dar
               p2d(i,2)=daz
            endif
3100        continue
         endif

3800     continue

         if(lplt) close(unit=4)
         if(lfout) close(unit=8)
         timeold=time(isn)

4000     continue
         close(unit=9)
         if(luf) close(unit=11)

C        SAVE INTEGRATION POINT DATA AT END OF RUN
         if(lsave) then
            knpe=0
            do 5100 ine=1,ne
            iemt=imem(ine)
            if(iemt .gt. 0) goto 5100
            do 5000 ipt=1,ix*iy
            knpe=knpe+1
            read(10,rec=knpe)  temp1,epm,epd1,xo,
     &                  (eps(i),epsp1(i),sig(i),alfa1(i),i=1,4)
5000        write(7,*)  temp1,epm,epd1,xo,
     &                  (eps(i),epsp1(i),sig(i),alfa1(i),i=1,4)
5100        continue
            close(unit=7)
         endif
         if(.not. lat) close(unit=10)

8099     format(2x,16(1pe8.1))
8101     format(///,t33,'Nodal Output',//,3x,'Node',5x,'Radial',7x,'Axial
     &',5x,'Radial',6x,'Axial',7x,'Total',/,2x,'Number',5x,'Coor.',7x,'
     &Coor.',5x,'Disp.',7x,'disp.',7x,'Disp.',6x,'Temp.')
8102     format(2x,i5,6(2x,1pe10.3))
8103     format(//,30x,'Element Results',//,'  Element',35x,'Nodal'/'   N
     &umber',33x,'Topology'/,3x,i4,5x,8(3x,i5))
8104     format(//'                                  Element Strains & Stresses',
     &//,2x,'Guass',116x,'Von',/,2x,'Point',3x,'Radial',6x,'Axial',5x,'R
     &adial',7x,'Hoop',5x,'Axial',6x,'Shear',6x,'Radial',7x,'Hoop',6x,'A
     &xial',6x,'Shear',6x,'Mises',/,'   IR IZ',4x,'Coor.',6x,'Coor.',5x,'
     &Strain',5x,'Strain',5x,'Strain',5x,'Strain',5x,'Stress',5x,'Stres
     &s',5x,'Stress',5x,'Stress',5X,'Stress')
8105     format(2x,i2,1x,i2,11(1x,1pe10.3))
8106     format(///,t32,'Element Output')
```

```
8107    format(/,'  Load Case #',i3,'  Sub Increment #',i3,
     & '  Time =',1pe14.6)
8108    format(1x,2(1pe10.3,','),1pe10.3)
8109    format(1x,7(1pe10.3,','),1pe10.3)
8110    format(8(1x,1pe10.3))
8111    format(//,' Gauss   M / A              Thermal  ',
     &'  Plastic  Pl. Strain  Uniaxial   Uniaxial    Flow',/,
     &' Point   % / %     Temp.     Strain     Strain     ',
     &'  Rate        Strain       Stress       Stress')
8112    format(1x,i4,1x,i4,' /',i4,1x,F8.2,6(1x,1pe10.3))
8113    format(/'                                         Element Integration
     &Point Strains',/,' Guass       --------------Plastic--------------
     &        ---------------Total---------------',/,' Point   Radial
     & Axial       Shear       Hoop       Radial       Axial       Shear
     & Hoop',/,' IR IZ   Strain      Strain      Strain      Strain      St
     &rain      Strain      Strain      Strain')
8114    format(///,'  --  EXECUTION TERMINATED --',/,'  Maximum number of
     & time step iterations exceeded !')
8115    format(//,'  There were ',i3,' iteratations performed for this
     & solution.'//)
8116    format('  Iteration # : ',i3,'  R/S : ',1pe10.3)
8117    format(/,1x,i3,2x,i3,2x,i3,6(1x,1pe10.3))
8118    format(/'                                        Element Integration Po
     &int Stresses',/,' Guass      --------------Kinematic--------------
     &        ---------------Total---------------',/,' Point   Radial
     & Axial       Shear       Hoop       Radial       Axial       Shear
     & Hoop',/,' IR IZ  Stress      Stress      Stress      Stress      Str
     &ess      Stress      Stress      Stress')
8119    format(//,'  Element # : ',i5)
8120    format(' Load Case # : ',i3,/,' Node    Elem
     &                     Body                  Thermal',/,' No.     Dof.
     &               Coor.                 Forces                 Forces')
8121    format(///,'  Iterative solution phase.',//)
8122    format(///,'  Initialization and integration of elastic
     & components phase.',//)
8123    format(///,t23,'Dynamic Output')
8124    format(//,3x,'Node',4x,'Radial',7x,'Axial',6x,
     &'Radial',7x,'Axial',/,2x,'Number',4x,'Vel.',8x,'
     &Vel.',8x,'Acc.',8x,'Acc.')
8125    format(2x,i5,5(2x,1pe10.3),2x,g10.4)
8126    format(//,'  Enter the element # and Integration # : '$)
8127    format(//,'  Enter the user output file name : '$)
8128    format(a30)
8130    format(//,'  Enter the number of output points : '$)
8131    format(//,1x,a78)
8132    format(1x,1pe20.6)

9999    return
        end


cccccccccccccccccccccccccccccccccccccccccccccccccccccccccccccccccccccc
c
c       TEMP
c
c       This subroutine calculates the temperature from eigther a
c       polynomial or a data table using an input point given by (rad,z)
c
cccccccccccccccccccccccccccccccccccccccccccccccccccccccccccccccccccccc

        subroutine TEMP(rad,z,tmp,nlc,ltmpt,td,isn,nrtt,natt,
```

```
     &                    trd,ntrdv,tad,ntadv)

      implicit real*8(a-h,o-z)
      implicit integer(i-k,n,m)
      logical l

      dimension td(nlc,natt,nrtt),trd(ntrdv),tad(ntadv)

      if(ltmpt) then
         rl=trd(isn)
         rh=trd(nlc+isn)
         al=tad(isn)
         ah=tad(nlc+isn)
         if(rad .lt. rl .or. rad .gt. rh) goto 30
         if(z .lt. al .or. z .gt. ah) goto 30
         tmp=0d0
         dumz=1d0
         do 20 j=1,natt
         dumr=1d0
         do 10 k=1,nrtt
         tmp=tmp+td(isn,j,k)*dumr*dumz
10       dumr=dumr*rad
20       dumz=dumz*z
30       continue
      else
         iz=1
         if(natt .eq. 1) goto 200
         iz=2
         if(z .le. tad(1)) goto 200
         if(z .le. tad(iz)) goto 200
         do 100 i=2,natt
         if(z .gt. tad(i)) goto 100
         iz=i
         goto 200
100      continue
         iz=natt
200      ir=1
         if(nrtt .eq. 1) goto 400
         ir=2
         if(rad .le. trd(1)) goto 400
         if(rad .le. trd(ir)) goto 400
         do 300 i=1,nrtt
         if(rad .gt. trd(i)) goto 300
         ir=i
         goto 400
300      continue
         ir=nrtt
400      if(iz .eq. 1) goto 600
         dz=tad(iz)-tad(iz-1)
         if(ir .eq. 1) goto 500
         d1h=td(isn,iz,ir-1)
         d1l=td(isn,iz-1,ir-1)
         dv1=d1h+((d1h-d1l)*(z-tad(iz))/dz)
500      d2h=td(isn,iz,ir)
         d2l=td(isn,iz-1,ir)
         dv2=d2h+((d2h-d2l)*(z-tad(iz))/dz)
         if(ir .ne. 1) goto 800
         tmp=dv2
         goto 900
600      if(ir .ne. 1) goto 700
         tmp=td(isn,1,1)
         goto 900
700      dv1=td(isn,1,ir-1)
```

```
            dv2=td(isn,1,ir)
800         dr=trd(ir)-trd(ir-1)
            tmp=dv2+((dv2-dv1)*(rad-trd(ir))/dr)
900         continue
          endif

          return
          end



CCCCCCCCCCCCCCCCCCCCCCCCCCCCCCCCCCCCCCCCCCCCCCCCCCCCCCCCCCCCCCCCCCCCCCCCCCCCCCCCCCCCCCC
C
C         ZERO
C
C         This is a frivolous subroutine which sets array numbers
C         to zero if their relative magnitude (relative to other
C         array values) is less than tolz (tolz=1e-10).  The author
C         found it annoying to scan output results which were very
C         near zero.
C
CCCCCCCCCCCCCCCCCCCCCCCCCCCCCCCCCCCCCCCCCCCCCCCCCCCCCCCCCCCCCCCCCCCCCCCCCCCCCCCCCCCCCCC

          subroutine ZERO(array,aver,n,tolz)
          implicit real*8(a-h,o-z)
          implicit integer(i-k,n,m)
          logical l

          dimension array(n)
          aver=0d0
          do 100 i=1,n
100       aver=aver+dabs(array(i))
          aver=aver/n
          if(aver .eq. 0d0) aver=1e25
          do 200 i=1,n
          if(dabs(array(i)/aver) .lt. tolz) array(i)=0d0
200       continue

          return
          end



CCCCCCCCCCCCCCCCCCCCCCCCCCCCCCCCCCCCCCCCCCCCCCCCCCCCCCCCCCCCCCCCCCCCCCCCCCCCCCCCCCCCCCC
C
C         MTIP
C
C         This subroutine is used by the plastic analysis to determine
C         temperature dependent material properties.
C
CCCCCCCCCCCCCCCCCCCCCCCCCCCCCCCCCCCCCCCCCCCCCCCCCCCCCCCCCCCCCCCCCCCCCCCCCCCCCCCCCCCCCCC

          subroutine MTIP(tmp,pmta,pmpa,prop,nplm,iplm,npltdv,lym,n5)

          implicit real*8(a-h,o-z)
          dimension pmta(npltdv),pmpa(nplm,npltdv,n5),prop(n5)

C         PROP(1)= YOUNGS MODULUS
C         PROP(2)= POISSONS RATIO
C         PROP(3)= VIRGIN MATERIAL YIELD STRESS
C         PROP(4)= HARDENING MODULUS
```

```
C       PROP(5)= MEAN COEFFICIENT OF THERMAL EXPANSION

        il=1
        ih=npltdv
        do 20 i=2,npltdv
        if(tmp.le. pmta(i)) then
           ih=i
           goto 25
        endif
20      il=i
25      if(ih .eq. il) then
           xratio=0d0
        else
           xratio=(tmp-pmta(il))/(pmta(ih)-pmta(il))
        endif

        do 30 i=1,5
30      prop(i)=pmpa(iplm,il,i)+xratio*(pmpa(iplm,ih,i)-
     &          pmpa(iplm,il,i))

        if(lym) prop(1)=1.5374e11+4.41276e10*dexp(-(tmp/734.26)**3.81)

        return
        end



CCCCCCCCCCCCCCCCCCCCCCCCCCCCCCCCCCCCCCCCCCCCCCCCCCCCCCCCCCCCCCCCCCCCCCCCCCCCCCC
C
C       SFORCE
C
C       This is the spring force subroutine.  Based upon input
C       displacements, spring forces are calculated.  When a spring
C       displacement exceeds a prescribed maximum value (umax), then the
C       prescribed maximum displacement is used to calculate the
C       spring force.  These springs will only react in compression
C       and will not impart tensile forces.  Warning, this subroutine
C       causes convergence difficulties and should be used with caution
C       (this subroutine needs improvement).
C
CCCCCCCCCCCCCCCCCCCCCCCCCCCCCCCCCCCCCCCCCCCCCCCCCCCCCCCCCCCCCCCCCCCCCCCCCCCCCCC

        subroutine SForce(aspc,aspd,psd,itasp,rv,disp,aspod,imap,umax,
     &                    eol,last,ltout,lfout,neas,nn,nud,n2)

        implicit real*8(a-h,o-z)
        implicit integer(i-k,n,m)
        logical l

        dimension aspc(neas),aspd(neas),psd(neas),itasp(neas),
     &          rv(nud),disp(nud),imap(nn,n2),aspod(neas)

        if(last) then
           do 100 i=1,neas
           if(mod(i-1,40) .eq. 0) then
              if(ltout) write(6,6001)
              if(lfout) write(8,6001)
           endif
           nc=imap(itasp(i),2)
           if(nc .lt. 0) goto 100
           u=aspd(i)-disp(nc)-psd(i)
           if(u .gt. 0d0) then
```

```
            u=0d0
         else if(abs(u)  gt. umax) then
            u=-umax
            psd(i)=aspd(i)-disp(nc)-umax
         endif
         ut=u+psd(i)
         stress=eol*u
         f=aspc(i)*u
         if(ltout) write(6,6002) i,ut,psd(i),stress,f
         if(lfout) write(8,6002) i,ut,psd(i),stress,f
100      continue
      else
         do 300 i=1,neas
         nc=imap(itasp(i),2)
         if(nc .lt. 0) goto 300
         un=disp(nc)
         dun=aspd(i)-psd(i)-un
         if(dun .ge. 0d0) then
            f=0d0
         else
            f=aspc(i)*dun
            aspod(i)=un
         endif
         rv(nc)=rv(nc)+f
300      continue
      endif

6001  format(//,t2,'Elastic-Plastic Contact Springs',//,
     & t2,'Spring',3x,'Total Spring',3x,'Plastic Spring',6x,
     & 'Spring',10x,'Spring',/,t2,'  #',6x,'Displacement',3x,
     & ' Displacement',7x,'Stress',10x,'Force')
6002  format(t2,i6,3x,1pe12.4,4x,1pe12.4,4x,1pe12.4,4x,1pe12.4)

      return
      end



CCCCCCCCCCCCCCCCCCCCCCCCCCCCCCCCCCCCCCCCCCCCCCCCCCCCCCCCCCCCCCCCCCCCCCCCCCCC
C
C     TEPE
C
C     A description and flowchart for this subroutine are given in
C     Appendix C.  This subroutine implements the time-dependent
C     plasticity formulation discussed in Chapter 3.  Initially, TEPE
C     was developed for time-independent, bi-linear plasticity, and
C     the data input parameters for plastic materials is suited for
C     this older material model.  These input parameters are not used
C     by the version of TEPE listed here.  Another version of TEPE
C     exists for the older material model (see ''An Effective Solution
C     Algorithm for Finite Element Thermo - Elastic - Plastic and creep
C     Analysis,'' M.D. Synder, PhD Thesis, MIT 1982).
C
CCCCCCCCCCCCCCCCCCCCCCCCCCCCCCCCCCCCCCCCCCCCCCCCCCCCCCCCCCCCCCCCCCCCCCCCCCCC
      subroutine TEPE(strain,stress,sig,eps,epsp1,epsp2,
     &                alfa1,alfa2,pmta,pmpa,phas,cep,prop,last,
     &                ldebug,ltp,nplm,iplm,npltdv,lym,n4,n5,n7)

      implicit real*8(a-h,o-z)
      logical l
      dimension strain(n4),stress(n4),sig(n4),eps(n4),pmta(npltdv),
     &          epsp1(n4),epsp2(n4),alfa1(n4),alfa2(n4),
```

```
     &            pmpa(nplm,npltdv,n5),
     &            cep(n4,n4),phas(nplm,n7),prop(n5)
      dimension sig2(4),snor(4),TTh(4),a(4),b(4),c(4),eta(4)
      dimension cepdot(4,4)
      dimension epse(4),D(4),DP(4)
      common /PLASDAT/ epm,epc,Y2
      common /THERMDAT/ tref,temp1,temp2,tdot,ts1,ts2,xn,xo
      common /RATEDAT/ dt,epd1,epd2

      c23= 2d0 / 3d0
      s23= dsqrt(c23)
      s32= dsqrt(1d0/c23)



C     STEP 1.  Define the input rate variables.

C     Calculate elastic strain at time 1
      do 5 i=1,4
5     epse(i)=eps(i)-epsp1(i)

C     Determine Thermal States.
      call GBYP(temp1,pmta,pmpa,prop,G1,B1,E1,V1,nplm,iplm,npltdv,lym,n5)
      call GBYP(temp2,pmta,pmpa,prop,G2,B2,E2,V2,nplm,iplm,npltdv,lym,n5)
      Gdot=(G2-G1)/dt
      Bdot=(B2-B1)/dt
      Edot=(E2-E1)/dt
      Vdot=(V2-V1)/dt
      if(ltp) then
         call TPTS(ts1,ts2,xn,xo,tdot,temp1,temp2,tref,
     &        phas,iplm,nplm,n7)
      else
         ts2=prop(5)*(temp2-tref)
      endif
      tsdot=(ts2-ts1)/dt

      call EMAT(Edot,Vdot,cepdot,n4)
      call EMAT(E1,V1,cep,n4)

      cons=3d0 * (Bdot * ts1 + B1 * tsdot)
      TTh(1)=cons
      TTh(2)=cons
      TTh(3)=0d0
      TTh(4)=cons
      do 10 i=1,4
      do 10 j=1,4
10    TTh(i)=TTh(i)-cepdot(i,j)*epse(j)



C     STEP 2. CALCULATE TRIAL STRESS RATE AND STRESSES
C     Calculate total strain rate D.
      do 20 i=1,4
20    D(i) = (strain(i) - eps(i)) / dt

      do 30 i=1,4
      sig2(i) = sig(i) - TTh(i) * dt
      do 30 j=1,4
30    sig2(i) = sig2(i) + cep(i,j) * D(j) * dt

C     STEP 3. Calculate normal N
C     Account for kinematic effects
      do 40 i=1,4
```

```
40      a(i) = sig2(i) - alfa1(i)
        call DEVIAT(a,snor,tau,n4)
        T2 = tau * s32

C       Normalize snor with tau
        if(tau .gt. 1e-9) then
           do 50 i=1,4
50         snor(i) = snor(i) / tau
        else
           do 51 i=1,4
51         a(i)=sig(i)-alfa1(i)
           call DEVIAT(a,snor,tau,n4)
           if(tau .gt. 1e-9) then
              do 52 i=1,4
52            snor(i) = snor(i) / tau
           else
              do 53 i=1,4
53            snor(i) = 0d0
           endif
        endif


C       STEP 4.  Test for plastic deformation

C       Determine Y1 and Y2.
        epd2 = 0d0
        gpdp = 1d-15
        lmocy = .false.
        call YVALUE(temp1,epd1,Y1)
        call YVALUE(temp2,epd2,Y2)


C       Calculate Initial Deviatoric Yield Stress
        do 70 i=1,4
70      a(i)=sig(i)-alfa1(i)
        call DEVIAT(a,eta,etam,n4)
        T1 = etam * s32


        if(Y2 .gt. T2) then


C                       Elastic Process


C       Define Plastic Strain Rate
           do 80 i=1,4
80         Dp(i) = 0d0
           epc = 0d0
           epd2 = 0d0
           gpdp = 0d0


        else


C                       Plastic Process
```

```
C       STEP 5  Decide on monotonic versus cyclic hardening.

C       Initaliaze plastic variables ep1 and lmocy.
C       Determine previous state
           lmocy = .true.
           call HVALUE(epm,Hmax,lmocy)
           if(Hmax .eq. 0d0) then
              lsw   = .false.
              Omega = 0d0
              goto 88
           else
              call DEVIAT(alfa1,eta,tau,n4)
              Omega = tau * s32
              if(Omega .lt. Hmax .and. epc .ne. 0d0) lmocy=.false.
           endif

C       Determine Stress Distances
           do 84 i=1,4
           a(i) = sig(i) - alfa1(i)
           b(i) = sig2(i) - alfa1(i)
84         c(i) = sig2(i) - sig(i)
           call DEVIAT(a,eta,tau,n4)
           so1 = tau
           call DEVIAT(b,eta,tau,n4)
           so2 = tau
           call DEVIAT(c,eta,tau,n4)
           ss = tau
           call DEVIAT(sig,eta,tau,n4)
           s1 = tau * s32
           call DEVIAT(sig2,eta,tau,n4)
           s2 = tau * s32

C       Decide if Stress crosses elastic zone
           lsw=.false.
           if(ss .lt. 1d-6) goto 88
           Error=dabs((ss-so1)/ss)
C
C       The next two statements are not mentioned in Appendix C.
C       When the stress strain behavior is not uniaxial, the rules
C       created to decide on monotonic versus cyclic hardening break
C       down.  The first statement uses a switching variable lsw
C       which is true when the stress magnitude decreases to a value
C       less than Omega.  lsw is a variable designed to switch the
C       deformation mode to cyclic.  The second statement makes lsw true
C       when the stress magnitude approaches zero during a stress
C       reversal, but because of non uniaxial loading, the stress state
C       decreases and then increases without passing through a zero stress
C       state.
C
           if(s1 .gt. Omega .and. s2 .lt. Omega) lsw = .true.
           if(s1 .lt. 2*Omega .and. abs(s2-s1) .lt. .15*ss) lsw=.true.

           if(ss .le. so1 .or. Error .lt. 1d-3) goto 88
           if(ss .lt. so2) goto 88
           lsw=.true.

C       Determine what process takes place this time step.
88         if(lmocy) then
              if(lsw) then
                 lmocy=.false.
                 epc=0d0
                 ep1=0d0
              else
```

```
            call HEP(Omega,epm,Imocy,Irr,last)
            epc=0d0
            ep1=epm
         endif
      else
         if(lsw) then
            epc=0d0
            ep1=0d0
         else
            ep1=epc
         endif
      endif


C     Step 6.  Initialize plastic iteration variables.
      K=0
      gpdp1 = 1d-15
      gpdp2 = 1d-15
      gpdr1 = 1d-15
      gpdr2 = 1d-15
      gpda = 1d-15
      goto 95


C     Step 10.  Define gpd iteration parameters.

C     Although the steps seem out of order, notice
C     that step 6 has a goto which branches to step 7
C     and step 7 follows step 11.

91       if(k .eq. 1) then
            gpdp1 = gpdp
            gpdr1 = gpdr
            gpdp  = gpdr
            goto 95
         elseif(k .eq. 2) then
            gpdp2 = gpdp
            gpdr2 = gpdr
         elseif(abs(gpdp1-gpdr1) .gt. abs(gpdp2-gpdr2)) then
            if(abs(gpdp2-gpdp1) .lt. 1d-22) then
               gpdp2 = gpdp
               gpdr2 = gpdr
            else
               gpdp1 = gpdp
               gpdr1 = gpdr
            endif
         else
            if(abs(gpdp2-gpdp1) .lt. 1d-22) then
               gpdp1 = gpdp
               gpdr1 = gpdr
            else
               gpdp2 = gpdp
               gpdr2 = gpdr
            endif
         endif

c     Step 11. Interpolate for gpd prediction
         if(dabs(gpdp2-gpdp1) .lt. 1d-22) then
            gpdp = .8 * gpdp1
         else
            xp = log(gpdp2/gpdp1) / (gpdp2-gpdp1)
            xr = log(gpdr2/gpdr1) / (gpdp2-gpdp1)
```

```
            xx = 1d0 - xr/xp
            gpdp = (gpdp1*xx + log(gpdr1/gpdp1)/xp)/xx
         endif

c        Test for gpdp < 0
95          if(gpdp .le. 0d0) then
               gpdp=dabs(gpdr1)
               if(gpdr2 .gt. gpdr1) gpdp=dabs(gpdr2)
            endif


C        STEP 7. Calculate h using cyclic rules.
            gpda = (gpdp1 + gpdp2) / 2d0
            kk = 0

96          epd2 = s23 * gpdp
            call CYCLIC(hbar,epd2,ep1,dt,lmocy)
            hbar = c23 * hbar

C        Step 8. Calculate Y2
            Y2 = T2 - s32 * (2d0 * G1 + hbar) * gpdp * dt

c        Test gpdp for Y2 < 0 or gpdr < 0
            if(Y2 .lt. 0) then
               kk = kk + 1
               if(kk .gt. 100) gpda = .8d0 * gpda
               gpdp = (gpda + gpdp) / 2d0
               goto 96
            endif


C        STEP 9. Calculate gpdr.
            call EPDvalue(temp2,Y2,epdr)
            gpdr = s32 * epdr


C        Test convergence of plastic strain rate.
            k=k+1
            if(k .gt. 50) then
               if(dabs(gpdp1-gpdr1) .lt. dabs(gpdp-gpdr)) then
                  if(dabs(gpdp1-gpdr1) .lt. dabs(gpdp2-gpdr2)) then
                     gpdp = gpdp1
                  else
                     gpdp = gpdp2
                  endif
               elseif(dabs(gpdp-gpdr) .gt. dabs(gpdp2-gpdr2)) then
                  gpdp = gpdp2
               endif
               if(last .and. (gpdp*dt .gt. 1d-12)) then
                  write(6,*) 'Error in plastic strain rate convergence.'
                  write(6,*) gpdp1,gpdr1
                  write(6,*) gpdp2,gpdr2
                  write(6,*) gpdp
               endif
               goto 110
            endif
            if(gpdr .lt. 1d-15) then
               gpdr = 1d-15
               goto 91
            endif
```

```
            if(abs((gpdp-gpdr)/gpdr) .lt.  1d-4) goto 110
            if(abs(gpdp-gpdr)*dt .lt. 1d-12) goto 110
            goto 91

         endif


C        STEP 12.  Calculate final stress, plastic strain and back stress.

C        Calculate Plastic Strain Tensor DP and Hbar.
110      do 120 i=1,4
120      DP(i) = gpdp * snor(i)
         epd2 = s23 * gpdp
         call CYCLIC(hbar,epd2,ep1,dt,lmocy)
         hbar = c23 * hbar



C        Integrate elastic-plastic and thermal stress
         do 130 i=1,4
         stress(i) = sig(i) - TTh(i) * dt
         do 130 j=1,4
130      stress(i)=stress(i) + cep(i,j) * (D(j) - DP(j)) * dt



C        Integrate plastic strain, and back stress
         do 140 i=1,4
         epsp2(i) = epsp1(i) + DP(i) * dt
140      alfa2(i) = alfa1(i) + hbar * gpdp * snor(i) * dt



C        STEP 13  Update plastic strain variables
         if(last) then
         call DEVIAT(stress,a,etam,n4)
         Tbar = etam * s32
         if(epd2 .gt. 0) then
            if(lmocy) then
               call DEVIAT(alfa2,eta,tau,n4)
               Hmax = tau * s32
               call HEP(Hmax,ept,lmocy,lrr,last)
               if(ept .gt. epm) epm=ept
            else
               epc=ep1+epd2*dt
            endif
         endif
         endif

         return
         end




CCCCCCCCCCCCCCCCCCCCCCCCCCCCCCCCCCCCCCCCCCCCCCCCCCCCCCCCCCCCCCCCCCCCCCCC
C
C        EMAT
C
C        EMAT calculates the elastic constitutive matrix based
```

```
C       upon the input parameters ym and pr.
C
CCCCCCCCCCCCCCCCCCCCCCCCCCCCCCCCCCCCCCCCCCCCCCCCCCCCCCCCCCCCCCCCCCCCCCCCCCCCCCC

        subroutine EMAT(ym,pr,cp,n4)

        implicit real*8(a-h,o-z)
        dimension cp(n4,n4)

        a1=ym/(1d0+pr)
        c1=a1*.5
        a1=a1/(1d0-2d0*pr)
        b1=a1*pr
        a1=a1-b1

        do 10 i=1,4
        do 10 j=1,4
10      cp(i,j)=0d0
        cp(1,1)=a1
        cp(1,2)=b1
        cp(1,4)=b1
        cp(2,1)=b1
        cp(2,2)=a1
        cp(2,4)=b1
        cp(3,3)=c1
        cp(4,1)=b1
        cp(4,2)=b1
        cp(4,4)=a1

        return
        end



CCCCCCCCCCCCCCCCCCCCCCCCCCCCCCCCCCCCCCCCCCCCCCCCCCCCCCCCCCCCCCCCCCCCCCCCCCCCCCC
C
C       GBYP
C
C       This subroutine calculates the shear and bulk modulus
C       from the Young's modulus and the Poisson ratio.
C
CCCCCCCCCCCCCCCCCCCCCCCCCCCCCCCCCCCCCCCCCCCCCCCCCCCCCCCCCCCCCCCCCCCCCCCCCCCCCCC

        subroutine GBYP(tmp,pmta,pmpa,prop,G,B,Ym,Pr,
     &                  nplm,iplm,npltdv,lym,n5)

        implicit real*8(a-h,o-z)
        dimension pmta(npltdv),pmpa(nplm,npltdv,n5),prop(n5)

        call MTIP(tmp,pmta,pmpa,prop,nplm,iplm,npltdv,lym,n5)
        ym=prop(1)
        pr=prop(2)
        G=ym/(2d0*(1d0 + pr))
        B=ym/(3d0*(1d0 - 2d0 * pr))

        return
        end



CCCCCCCCCCCCCCCCCCCCCCCCCCCCCCCCCCCCCCCCCCCCCCCCCCCCCCCCCCCCCCCCCCCCCCCCCCCCCCC
```

```
C
C       Two Phase Thermal Strains
C
C       This subroutine calculates the thermal and phase transformation
C       strains (ts1,ts2) for times 1 and 2 based upon input temperatures
C       (tmp1,tmp2) and material phases (xo,xn).  This subroutine is
C       based upon the thermal and phase transformation model described
C       at the end of Chapter 2.
C
CCCCCCCCCCCCCCCCCCCCCCCCCCCCCCCCCCCCCCCCCCCCCCCCCCCCCCCCCCCCCCCCCCCCCCCCCCC

        subroutine TPTS(ts1,ts2,xn,xo,tdot,tmp1,tmp2,tref,
     &                  phas,iplm,nplm,n7)

        implicit real*8(a-h,o-z)
        implicit integer(i-k,n,m)
        logical l

        dimension phas(nplm,n7)

C       phas(iplm,1)    Martensite Thermal Coefficient of Expansion
C       phas(iplm,2)    Austenite Thermal Coefficient of Expansion
C       phas(iplm,3)    Austenite Start Temperature
C       phas(iplm,4)    Austenite Finish Temperature
C       phas(iplm,5)    Martensite Start Temperature
C       phas(iplm,6)    Martensite Finish Temperature
C       phas(iplm,7)    Phase Transformation Strain

C       Initial Condition
        if(tmp1 .lt. phas(iplm,6)) then
C       Fully Martensite response
           ts1=phas(iplm,1)*(tmp1-tref)
        else if(tmp1 .gt. phas(iplm,4)) then
C       Fully Austenite response
           ts1=phas(iplm,2)*(tmp1-tref)-phas(iplm,7)
        else
C       Martensite - Austenite Transition
           call TPI(tmp1,xo,ts1,tref,phas,nplm,iplm,n7)
        endif

C       Final Condition
        if(tmp2 .lt. phas(iplm,6)) then
C       Fully Martensite response
           xn=1d0
           ts2=phas(iplm,1)*(tmp2-tref)
        else if(tmp2 .gt. phas(iplm,4)) then
C       Fully Austenite response
           xn=-1d0
           ts2=phas(iplm,2)*(tmp2-tref)-phas(iplm,7)
        else if(tdot .gt. 0d0) then
           rtmp=phas(iplm,3)+(1-xo)*(phas(iplm,4)-phas(iplm,3))/2d0
           if(tmp2 .gt. rtmp) then
C       Martensite to Austenite transformation
             xn=1d0-2d0*(tmp2-phas(iplm,3))/(phas(iplm,4)-phas(iplm,3))
              call TPI(tmp2,xn,ts2,tref,phas,nplm,iplm,n7)
           else
C       Martensite - Austenite response
             xn=xo
             call TPI(tmp2,xn,ts2,tref,phas,nplm,iplm,n7)
           endif
        else
           rtmp=phas(iplm,6)+(1-xo)*(phas(iplm,5)-phas(iplm,6))/2d0
           if(tmp2 .lt. rtmp) then
```

```
C       Austenite to Martensite transformation
             xn=1d0-2d0*(tmp2-phas(iplm,6))/(phas(iplm,5)-phas(iplm,6))
              call TPI(tmp2,xn,ts2,tref,phas,nplm,iplm,n7)
           else
C       Austenite response
              xn=xo
              call TPI(tmp2,xn,ts2,tref,phas,nplm,iplm,n7)
           endif
        endif

300     return
        end


cccccccccccccccccccccccccccccccccccccccccccccccccccccccccccccccccccccc
C
C       TPI
C
C       TPI (Two Phase Interpolation) interpolates with the temperature
C       and material phase to determine the thermal and phase
C       transformation strain.
C
cccccccccccccccccccccccccccccccccccccccccccccccccccccccccccccccccccccc

        subroutine TPI(tmp,x,ets,tref,phas,nplm,iplm,n7)

        implicit real*8(a-h,o-z)
        implicit integer(i-k,n,m)
        logical l

        dimension phas(nplm,n7)

        t1=(x-1d0)*(phas(iplm,6)-phas(iplm,5))/2d0 + phas(iplm,6)
        t2=(x-1d0)*(phas(iplm,3)-phas(iplm,4))/2d0 + phas(iplm,3)
        r=2d0*(tmp-t1)/(t2-t1) - 1d0
        h1=(1d0-r)*(1d0+x)*(phas(iplm,1)*(phas(iplm,6)-tref))/4d0
        h2=(1d0+r)*(1d0+x)*(phas(iplm,1)*(phas(iplm,3)-tref))/4d0
        h3=(1d0+r)*(1d0-x)*(phas(iplm,2)*(phas(iplm,4)-tref)-
     &    phas(iplm,7))/4d0
        h4=(1d0-r)*(1d0-x)*(phas(iplm,2)*(phas(iplm,5)-tref)-
     &    phas(iplm,7))/4d0
        ets=h1+h2+h3+h4

        return
        end



cccccccccccccccccccccccccccccccccccccccccccccccccccccccccccccccccccccc
C
C       DEVIAT
C
C       DEVIAT calculates the mean of an input tensor, the deviatoric
C       tensor and the deviatoric radius.
C
cccccccccccccccccccccccccccccccccccccccccccccccccccccccccccccccccccccc

        subroutine DEVIAT(a,b,am,n4)

        implicit real*8(a-h,o-z)
        implicit integer(i-k,n,m)
```

```
      logical l

      dimension a(n4),b(n4)

C     Find mean component of sig
      sigm=(a(1)+a(2)+a(4))/3d0

C     Calculate deviatoric component of sig
      b(1)=a(1)-sigm
      b(2)=a(2)-sigm
      b(3)=a(3)
      b(4)=a(4)-sigm

C     Calculate Radius of b (dot) b

      am=dsqrt( b(1)*b(1) + b(2)*b(2) + 2d0*b(3)*b(3) +
     &  b(4)*b(4) )

      return
      end



CCCCCCCCCCCCCCCCCCCCCCCCCCCCCCCCCCCCCCCCCCCCCCCCCCCCCCCCCCCCCCCCCCCCCCCCCCCCCCCCCC
C
C     CYCLIC
C
C     This subroutine calculates the strain hardening coefficient.
C     The input parameters are the mode of cyclic deformation
C     (monotonic or cyclic, lmocy), the initial plastic strain
C     (ep1) and the strain increment (epd*dt).
C
CCCCCCCCCCCCCCCCCCCCCCCCCCCCCCCCCCCCCCCCCCCCCCCCCCCCCCCCCCCCCCCCCCCCCCCCCCCCCCCCCC

      subroutine CYCLIC(hbar,epd,ep1,dt,lmocy)

      implicit real*8(a-h,o-z)
      implicit integer(i-k,n,m)
      logical l

      dep = epd * dt
      ep2 = ep1 + dep
      h0 = 45483889739.6631
      ep0 = 6.53d-5
      en = -.198d0

      if(dep .lt. 1d-9) then
         if(lmocy) then
            hbar = h0 * (1d0 + (ep1/ep0))**(en-1d0)
         else
            hbar = h0 * (1d0 + (ep1/ep0/2d0))**(en-1d0)
         endif
      else
         call HValue(ep1,H1,lmocy)
         call HValue(ep2,H2,lmocy)
         hbar = (H2 - H1) / dep
      endif

      return
      end
```

```
CCCCCCCCCCCCCCCCCCCCCCCCCCCCCCCCCCCCCCCCCCCCCCCCCCCCCCCCCCCCCCCCCCCCCCCCCCCCCCC
C
C       HVALUE
C
C       HVALUE calculates the integrated strain hardening from
C       0 to ep for eigther monotonic or cyclic strain hardening.
C
CCCCCCCCCCCCCCCCCCCCCCCCCCCCCCCCCCCCCCCCCCCCCCCCCCCCCCCCCCCCCCCCCCCCCCCCCCCCCCC

        subroutine HValue(ep,H,Imocy)

        implicit real*8(a-h,o-z)
        logical I

        A = 150d6
        ep0 = 6.53d-5
        en = -.198d0

        if(ep .le. 0d0) then
           H = 0d0
           return
        endif

        if(Imocy) then
           H = A * (1d0 - (1d0 + (ep / ep0))**en)
        else
           H = 2d0 * A * (1d0 - (1d0 + (.5d0 * ep / ep0))**en)
        endif

        return
        end



CCCCCCCCCCCCCCCCCCCCCCCCCCCCCCCCCCCCCCCCCCCCCCCCCCCCCCCCCCCCCCCCCCCCCCCCCCCCCCC
C
C       HEP
C
C       This subroutine examines the integrated strain hardening
C       and calculates the total plastic strain increment associated
C       with this hardening.
C
CCCCCCCCCCCCCCCCCCCCCCCCCCCCCCCCCCCCCCCCCCCCCCCCCCCCCCCCCCCCCCCCCCCCCCCCCCCCCCC

        subroutine HEP(T,ep,Imocy,Irr,last)

        implicit real*8(a-h,o-z)
        logical I

        A = 150d6
        ep0 = 6.53d-5
        en = -1d0 / .198d0
        Irr=.false.

        if(T .le. 0d0) then
           ep = 0d0
           return
        endif

        if(Imocy) then
```

```
            if(T .ge. A) then
               if(last) then
            write(6,*) '  Error : Hardening too high for Monotonic T2'
            write(6,*) 'T,A',t,a
               endif
               lrr = .true.
               ep = 1e6
               return
            endif
            ep = ep0 * ((1d0 - (T / A))**en - 1d0)
         else
            if(.5d0 * T .ge. A) then
               if(last) then
            write(6,*) '  Error : Hardening too high for Cyclic T2'
            write(6,*) 'T,A',t,a
               endif
               lrr = .true.
               ep = 1e6
               return
            endif
            ep = 2d0 * ep0 * ((1d0 - (.5d0 * T/ A))**en - 1d0)
         endif

         return
         end



CCCCCCCCCCCCCCCCCCCCCCCCCCCCCCCCCCCCCCCCCCCCCCCCCCCCCCCCCCCCCCCCCCCCCCCCCCCCCCC
C
C        YVALUE
C
C        YVALUE determines the elastic limit strength for an input
C        temperature (t) and plastic strain rate (epd).  The subroutine
C        listed herre is for the Arrhenius rate equation.  A similar
C        subroutine exists for the Phenomelonological rate equation.
C
CCCCCCCCCCCCCCCCCCCCCCCCCCCCCCCCCCCCCCCCCCCCCCCCCCCCCCCCCCCCCCCCCCCCCCCCCCCCCCC

         subroutine Yvalue(t,epd,sig)

         implicit real*8(a-h,o-z)
         logical l

         dimension bg(11,2)

         en=6.725635
         eni=1d0/en
         ep0=1.215024e3
         ep0i=1d0/ep0
         delH0=222.868
         y0=2351.0
         rt=8.3145e-3 * t
         e1=7.0
         e2=6.0
         sl=-2.607838
         a=-((sl+e2)/(e2-e1))
         b=(sl+e1)/(e2-e1)

         G= (153.7 + 44.1 * exp( -(t/734)**3.81 ))/2.6
         test0 = log( ep0 * (y0/G)**en )
```

```
      ep=epd
      if(epd .lt. 1e-12) ep=1e-12

c     Set first limits for sig search
      Yl=1.0
      Yu=Y0

10    dY=(Yu-Yl)/10.0

c     Begin search for sig bounds
      do 50 i=1,11
      Yg = Yl + dY * (i - 1)

c     Calculate delH from Yg guess
      x=Yg/Y0
      v=1+a*(x**e1)+b*(x**e2)
      delH = delH0 * v

c     Calculate Yr
      test = log( ep ) + delH/rt
      if( test .ge. test0) then
         Yr = Y0
      else
         Yr = G * (ep*ep0i*exp(delH/rt))**eni
      endif

      bg(i,1) = Yg
      bg(i,2) = Yr

      if(Yr .lt. Yg) then
         Yl=bg(i-1,1)
         Yu=bg(i,1)
         k=i
         if((Yu-Yl)/Yl .lt. 1e-3) goto 100
         goto 10
      endif

50    continue
      Yl=Yl+(Yu-Yl)/2d0
      goto 10

c     Set up interpolation variables
100   Yp1 = bg(k-1,1)
      Yr1 = bg(k-1,2)
      Yp2 = bg(k,1)
      Yr2 = bg(k,2)
      di1 = abs(Yr1-Yp1)
      di2 = abs(Yr2-Yp2)

c     Make interpolation for new Yp
200   ysl = (Yr2 - Yr1) / (Yp2 - Yp1)
      yp = (Yr1 - ysl * Yp1) / (1d0 - ysl)

c     Calculate delH from Yp guess
210   x=yp/y0
      v=1+a*(x**e1)+b*(x**e2)
      delH = delH0 * v

c     Calculate Yr
      Yr = G * (ep*ep0i*exp(delH/rt))**eni
      di = abs( Yr - Yp )
```

```
c       Test for convergence
        if (di/yp .lt. 1e-6) goto 300

c       Replace largest difference
        if(di1 .gt. di2) then
           Yp1 = Yp
           Yr1 = Yr
           di1 = di
        else
           Yp2 = Yp
           Yr2 = Yr
           di2 = di
        endif
        goto 200

300     sig = 1e6 * Yp

        return
        end



CCCCCCCCCCCCCCCCCCCCCCCCCCCCCCCCCCCCCCCCCCCCCCCCCCCCCCCCCCCCCCCCCCCCCCCCCCCCCC
C
C       EPDVALUE
C
C       This subroutine calculates the plastic strain rate with
C       the Arrhenius rate equation.
C
CCCCCCCCCCCCCCCCCCCCCCCCCCCCCCCCCCCCCCCCCCCCCCCCCCCCCCCCCCCCCCCCCCCCCCCCCCCCCC

        subroutine EPDvalue(t,sig,epd)

        implicit real*8(a-h,o-z)
        logical l

        en=6.725635
        ep0=1.215024e3
        delH0=222.868
        y0=2351.0
        rt=8.3145e-3 * t
        e1=7.0
        e2=6.0
        sl=-2.607838
        a=-((sl+e2)/(e2-e1))
        b=(sl+e1)/(e2-e1)

c       Calculate Shear Modulus G
        G = (153.7 + 44.1 * exp( -(t/734)**3.81 )) / 2.6

c       Calculate delH from Yp guess
        y = sig * 1e-6
        x = y / y0
        v = 1 + a * (x**e1) + b * (x**e2)
        delH = delH0 * v

c       Calculate Epd
        Epd = ep0 * exp(-delH/rt) * (Y/G)**en

        return
        end
```

```
CCCCCCCCCCCCCCCCCCCCCCCCCCCCCCCCCCCCCCCCCCCCCCCCCCCCCCCCCCCCCCCCCCCCCCCCCCCCCCC
C
C       COLSOL
C
C       This subroutine was written by K.J. Bathe and is describe
C       in detail in his book '' Finite Element Procedures in
C       Engineering Analysis,'' 1982.  The subroutine stores just
C       the top half of the stiffness matrix using a skyline technique.
C       The subroutine is broken into two sections.  The first
C       triangularizes the stiffness matrix and the second section
C       reduces the load vector and back substitutes for the solution.
C
CCCCCCCCCCCCCCCCCCCCCCCCCCCCCCCCCCCCCCCCCCCCCCCCCCCCCCCCCCCCCCCCCCCCCCCCCCCCCCC
       subroutine COLSOL(a,sv,maxa,nn,nwk,nnm,kkk,nsv,ierr)
C-------------------------------------------------------------------------------
C   --- INPUT ---
C       A(NWK)          Stiffness matrix in compacted form
C       SV(NN,NSV)      Right hand side load vector
C       MAXA(NNM)       Diagnol address vector
C       NN              Number of Equations
C       NWK             Number of Elements below skyline
C       NNM             NN + 1
C       KKK             Input Flag
C                           .EQ. 1 Triangularize A
C                           .EQ. 3 Reduction and back substition of V
C                           .EQ. 2 Do kkk .eq. 1 & 3
C       NSV             Number of Solutions to be obtained
C   --- OUTPUT ---
C       A               D and L factors of A
C       SV(NN)          Displacement Vector
C-------------------------------------------------------------------------------
       implicit real*8(a-h,o-z)
       logical l

       dimension a(nwk),sv(nn,nsv),maxa(nnm)

       if(kkk .GT. 2) GOTO 150
40     do 140 n=1,nn
       kn=maxa(n)
       kl=kn+1
       ku=maxa(n+1)-1
       kh=ku-kl
       if(kh) 110,90,50
50     k=n-kh
       ic=0
       klt=ku
       do 80 j=1,kh
       ic=ic+1
       klt=klt-1
       ki=maxa(k)
       nd=maxa(k+1)-ki-1
       if(nd) 80,80,60
60     kk=min0(ic,nd)
       c=0d0
       do 70 nl=1,kk
70     c=c+a(ki+nl)*a(klt+nl)
       a(klt)=a(klt)-c
80     k=k+1
90     k=n
       b=0d0
```

```
      do 100 kk=kl,ku
      k=k-1
      ki=maxa(k)
      c=a(kk)/a(ki)
      b=b+c*a(kk)
100   a(kk)=c
      a(kn)=a(kn)-b
110   if(a(kn) .le. 0d0) then
         write(6,*) 'ERROR !! : Diagnol stiffness was negative !'
         ierr=.true.
         goto 9999
      endif
140   continue
      if(kkk .lt. 2) return

C     SOLVE LOAD VECTORS
150   do 300 isn=1,nsv
      do 180 n=1,nn
      kl=maxa(n)+1
      ku=maxa(n+1)-1
      if(ku-kl) 180,160,160
160   k=n
      c=0d0
      do 170 kk=kl,ku
      k=k-1
170   c=c+a(kk)*sv(k,isn)
      sv(n,isn)=sv(n,isn)-c
180   continue
      do 200 n=1,nn
      k=maxa(n)
200   sv(n,isn)=sv(n,isn)/a(k)
      if(nn .eq. 1) return
      n=nn
      do 230 nl=2,nn
      kl=maxa(n)+1
      ku=maxa(n+1)-1
      if(ku-kl) 230,210,210
210   k=n
      do 220 kk=kl,ku
      k=k-1
220   sv(k,isn)=sv(k,isn)-a(kk)*sv(n,isn)
230   n=n-1
300   continue

      return
9999  write(6,*) '*** Indefinite A Matrix ***'
      return
      end
```

AFESA Input Commands

The program AFESA begins by asking for an input file name. AFESA will open this file and read the AFESA input commands. The input commands are used to define the finite element model. There are 4 commands which must be specified to complete an analysis. These commands are NODES, ELEMENTS, ELASTIC or PLASTIC MATERIALS and some loading or displacement command(s). The input commands are read until the EXIT command is given, and then AFESA closes the input file.

In the listing of input commands which follows, capitalized words are input commands which must be entered just as they are typed here. Lower case letters and words represent numerical input. Groups of letters which begin with a capital letter and continue in the lower case are alphanumeric data (usually specifying a file name or title). The * character indicates a numeric input which must be repeated. When the * character is repeated on a single line, then all the data should be specified on one line and the repeat quantity is given in parenthesis. When the * character is repeated on successive lines, then the input statement is repeated. When the * character is indented and repeated on successive lines, then that group of lines is repeated. The repeat quantities are given with lower right subscripts. The description of repeat input statements here is confusing, but this will be made clearer when specific examples are shown. Each of the command definitions is followed by a description of its purpose and the input parameters.

```
TITLE
Title
```

The TITLE command will cause AFESA to read a Title which can be 78 characters long. This title is used for screen and file output.

```
NODES
nn
i_1,  r_1,  z_1
   *
   *
   *
i_nn,  r_nn,  z_nn
```

The NODES command tells AFESA to read the number of nodes nn. Then AFESA reads the node geometry with nn input statements. Each input line gives a node number i, and the node coordinates r and z.

```
ELEMENTS
ne
j_1,  m_1,  i_1,  i_2,  i_3,  i_4,  i_5,  i_6,  i_7,  i_8
   *
   *
   *
j_ne,  m_2,  i_9,  i_10,  i_11,  i_12,  i_13,  i_14,  i_15,  i_16
```

This command gives AFESA the number of elements ne, and the element geometry. Like the NODES command, the element geometry is read with ne input statements. Each input statement includes the element number j, the material number m for that element and the element topology which consists of a list of 8 node numbers (see Appendix A). In another command, material properties are assigned a material number. Here, each element is given a material number which assigns certain material properties to that element.

```
ELASTIC MATERIALS
nemat
m_1,  e_mn_1,  v_mn_1,  alpha_mn_1
   *
   *
   *
m_nemat,  e_nemat,  v_nemat,  alpha_nemat
```

The ELASTIC MATERIALS command specifies elastic stress-strain behavior and a linear thermal coefficient of expansion to all elements assigned that material number m. The parameter nemat gives the number of elastic materials nemat in the model nemat. The properties e,v and alpha are the Young's modulus, Poisson's Ratio and the thermal coefficient of expansion. The elastic material properties input statement is repeated for each of the elastic materials specified by nemat.

```
PLASTIC MATERIALS
nplm,npltdv
temp_1
   *
   *
   *
temp_npltdv
mn_1
e_1_1,  v_1_1,  y_1_1,  et_1_1,  al_1_1
      *
      *
e_1_npltdv,  v_1_npltdv,  y_1_npltdv,  et_1_npltdv,  al_1_npltdv
   *
   *
   *
mn_nplm
e_nplm_1,  v_nplm_1,  y_nplm_1,  et_nplm_1,  al_nplm_1
      *
      *
```

```
e_nplm_npltdv, v_nplm_npltdv, y_nplm_npltdv, et_nplm_npltdv, al_nplm_npltdv
```

This command specifies an elastic plastic stress-strain behavior to a material number m. This PLASTIC MATERIAL input command was designed to input the parameters necessary for a temperature dependent bi-linear stress strain approximation. The listing of AFESA given here does not use this material model, but a reference to a computer code which does (ADINA) is given in the AFESA listing. In any case, this command must be issued to make AFESA predict the stress strain behavior modeled in this thesis. So the values entered for this command will not affect the finite element results. The parameters nplm and npltdv are the number of plastic materials and the number of plastic temperature data values. The first set of input data is the plastic data temperatures. Next, the plastic data for each of the plastic materials is read. First the material number for the material data is read and then the Young's modulus e, the Poisson's ratio v, the initial flow stress y, the stress strain tangent modulus et, and the thermal coefficient of expansion al. This input statement is repeated for each of the plastic data temperatures, and then these statements are repeated for each of the plastic material numbers.

```
TWO PHASE
phas_1 , phas_2 , phas_3 , phas_4 , phas_5 , phas_6 , phas_7
```

The TWO PHASE command tells AFESA to implement the thermal and phase transformation strain model described at the end of Chapter 2. phas_1 and phas_2 are the thermal coefficients of expansion for the low (martensite) and high (austenite) temperature phase. For maraging steel, phas_3 and phas_4 are the austenite start and finish temperatures and phas_5 and phas_6 are the martensite start and finish temperatures. phas_7 is the phas transformation strain used in Eq. 2.23 of this thesis.

```
LOAD CASES
nlc
time_1
   *
   *
   *
time_nlc
```

The LOAD CASES command tells AFESA how many time steps there are in the analysis. After the number of load cases nlc is given, the time step times for each load case are read.

```
RADIAL DISPLACEMENTS
nkrd
i_1, d_1(time_1)  *  *  *  d_1(time_nlc)
```

```
    *
    *
    *
i_nkrd, d_nkrd(time_1)  *  *  *   d_nkrd(time_nlc)
```

This command is used to specify radial node displacements. The number of known radial displacements is nkrd. The node number is given with i, and the radial displacements must be specified for each load case time. This command can be used to constrain a node in the radial direction (zero displacement) and apply a displacement loading as well.

```
AXIAL DISPLACEMENTS
nkad
i_1, d_1(time_1)  *  *  *   d_1(time_nlc)
    *
    *
    *
i_nkad, d_nkad(time_1)  *  *  *   d_nkad(time_nlc)
```

This command is used to specify axial node displacements. The number of known axial displacements is nkad. The node number is given with i, and the axial displacements must be specified for each load case time. This command can be used to constrain a node in the axial direction (zero displacement) and apply a displacement loading as well.

```
RADIAL NODE FORCES
nkrf
i_1, f_1(time_1)  *  *  *   f_1(time_nlc)
    *
    *
    *
i_nkrf, f_nkrf(time_1)  *  *  *   f_nkrf(time_nlc)
```

This command can specify radial forces on specific nodes. The number of known radial forces is nkrf. The node number is given with i, and the radial forces must be specified for each load case time.

```
AXIAL NODE FORCES
nkaf
i_1, f_1(time_1)  *  *  *   f_1(time_nlc)
    *
    *
    *
```

```
i_nkaf, f_nkaf(time_1)  *  *  *   f_nkaf(time_nlc)
```

This command can specify axial forces on specific nodes. The number of known axial forces is nkaf. The node number is given with i, and the axial forces must be specified for each load case time.

```
RADIAL BODY FORCES
INTERPOLATION
nrbfrt,nrbfat
rbfrd_1
   *
   *
   *
rbfrd_nrbfrt
rbfad_1
   *
   *
   *
rbfad_nrbfat
rbfd_1_1(time_1)  *  *  *  rbfd_1_1(time_nlc)
     *
     *
rbfd_1_nrbfrt(time_1)  *  *  *  rbfd_1_nrbfrt(time_nlc)
   *
   *
   *
rbfd_nrbfat_1(time_1)  *  *  *  rbfd_nrbfat_1(time_nlc)
     *
     *
rbfd_nrbfat_nrbfrt(time_1)  *  *  *  rbfd_nrbfat_nrbfrt(time_nlc)
```

The RADIAL BODY FORCES command is used to enter a grid of radial body forces for each load case time. First, the number of radial body force radial and axial terms are specified, nrbfrt and nrbfat. Then, the radial and axial grid coordinates are entered with radial and axial data, rbfrd and rbfad. Finally, the three dimensional array of radial body force data rbfd is entered. Each radial body force input line contains data for all the time steps. When reading the radial and axial grid data, the axial grid position changes after all the radial grid positions at that axial position have been read.

```
AXIAL BODY FORCES
INTERPOLATION
nabfrt,nabfat
abfrd_1
   *
   *
   *
abfrd_nabfrt
abfad_1
```

```
   *
   *
   *
abfad_nabfat
abfd_1_1(time_1)  *  *  *  abfd_1_1(time_nlc)
     *
     *
abfd_1_nrbfrt(time_1)  *  *  *  abfd_1_nabfrt(time_nlc)
   *
   *
   *
abfd_nabfat_1(time_1)  *  *  *  abfd_nabfat_1(time_nlc)
     *
     *
abfd_nabfat_nrbfrt(time_1)  *  *  *  abfd_nabfat_nabfrt(time_nlc)
```

The AXIAL BODY FORCES command is used to enter a grid of axial body forces for each load case time. First, the number of axial body force radial and axial terms are specified, nabfrt and nabfat. Then, the radial and axial grid coordinates are entered with radial and axial data, abfrd and abfad. Finally, the three dimensional array of axial body force data abfd is entered. Each axial body force input line contains data for all the time steps. When reading the radial and axial grid data, the axial grid position changes after all the radial grid positions at that axial position have been read.

```
TEMPERATURES
INTERPOLATION
nrtt,natt
trd_1
   *
   *
   *
trd_nrtt
tad_1
   *
   *
   *
tad_natt
td_1_1  *  *  *  td_1_1(time_nlc)
     *
     *
td_1_nrtt(time_1)  *  *  *  td_1_nrtt(time_nlc)
   *
   *
   *
td_natt_1(time_1)  *  *  *  td_natt_1(time_nlc)
     *
     *
rbfd_natt_nrtt(time_1)  *  *  *  td_natt_nrtt(time_nlc)
```

The TEMPERATURES command is used to enter a grid of temperatures for each load case time. First, the number of radial and axial temperature terms are specified, nrtt and natt. Then, the radial and axial grid coordinates are entered with radial and axial data,

trd and tad. Finally, the three dimensional array of temperate data is entered, td. Each temperature input line contains data for all the time steps. When reading the radial and axial grid data, the axial grid position changes after all the radial grid positions at that axial position have been read.

EXTERNAL AXIAL SPRINGS
neas, eol, umax
itasp_1 , aspc_1 , aspd_1
    *
    *
    *
itasp_neas , aspc_neas , aspd_neas

The EXTERNAL AXIAL SPRINGS input command attaches spring elements to the finite element model. The parameters neas, eol and umax are the number of axial springs, the ratio of the Young's Modulus to spring length (used to calculate a spring stress) and the maximum spring displacement respectively. The last parameter can limit the force exerted by these springs. This spring model will only exert compressive forces on the finite element model. The individual springs are attached to a node number itasp, and each spring has its own spring constant aspc and a prescribed initial displacement aspd.

DYNAMIC
den_1
    *
    *
    *
den_nplm

The DYNAMIC command tells AFESA to include dynamic body forces in the finite element equilibrium equations. The densities den of all the input materials are read with this command.

GAUSS POINTS
ix,iy

This input command controls the number Gauss points used to integrate the finite elements. AFESA allows between 1 and 5 Gauss points for eigther the radial ix or axial iy integration data points.

```
AFESAPLT
Fgeom
Fplt_1
    *
    *
    *
Fplt_nlc
```

The AFESAPLT command causes AFESA to write output files which are used for post-processing. The file named Fgeom contains nodal and element geometry, and the plot files Fplt_1 through Fplt_nlc contain displacements, strains and stresses for each time step.

```
AFESAOUT
Fout_1
    *
    *
    *
Fout_nlc
```

This command writes the information printed to the screen to files specified by this command. The displacements, strains and stresses for each time step are written with descriptive format statements to these files.

```
ELASTIC
```

This single line input command tells AFESA the analysis is a linear elastic analysis only. This command shortens the execution time.

```
ELASTIC-PLASTIC
i1,i2,i3,i4,d1,d2
```

The ELASTIC-PLASTIC input command supplies input parameters for an elastic plastic finite element analysis. When i1 equals the integer 1, AFESA will interactively ask for an output file name and element integration point information so that displacements, strains and stresses can be saved for all the subincrement times during an analysis. When i2 equals the integer 1, the Young's modulus approximation (Eq. 1.1 of this thesis) for maraging steel is used. The parameters i3,i4,d1,d2 are not used at this time, but numbers should be entered to complete this input command.

SAVE
Fsave

This input tells AFESA to save all data necessary for continuing the finite element analysis after the last time step. Only a file name Fsave is required for this option. This option is needed when a lot of time steps (greater than 10) are used and/or the analysis is to be continued over several loading cycles.

RESTART
Frestart

This input command tells AFESA to initialize and restart the finite element analysis with the conditions specified in an Fsave file.

DEBUG
nlde
ilda_1 * * * ilda_nlde

The DEBUG command is for users wishing to make program changes and for those who want more program variable information during code execution. The element debug information is only written for elements specified with this command. The number of debug elements is given by nlde, and the element numbers ilda are read on the next line.

SOLUTION PARAMETERS
sp_1 , sp_2, sp_3, sp_4, sp_5, sp_6, sp_7

The SOLUTION PARAMETERS input command supplies solution parameters to the finite element analysis. sp_1 is the reference temperature used in the calculation of thermal strains. At the reference temperature, thermal strains are zero. sp_2 is the load vector convergence tolerance used to decide if equilibrium is satsified. sp_3 is the zero displacement tolerance which sets round-off error in the displacements to zero. sp_4 is the zero tolerance dimension which sets other round-off errors to zero. These last two parameters affect the printed results only. sp_5 is the maximum number of iteration steps allowed in equilibrium calculations. sp_6 is the number of sub-increments between time steps. When sp_7 equals 1, the alpha constant stiffness acceleration procedure (see Chapter 3) is used. For all other values of sp_7, the elastic stiffness matrix approximates the tangent stiffness matrix.

EXIT

The EXIT command terminates the reading of input commands from the input file.

Example 1

The input commands for this example generate a single element model. The element is subjected to a uniform axial strain which increases from 0 % at 0 s to 2 % at 1 s. Nodes which lie on the Z axis are restrained in the radial direction. Otherwise, there are no radial displacement restrictions. The element and reference termperature is 950 K, so the thermal strains are zero. There are 15 subincrement time steps (14 subincrements) in this example. The load vector convergence tolerance is 10^{-18} and up to 50 equilibrium iterations are allowed.

```
TITLE
1 ELEMENT; Test of hbar using subincrements
NODES
8
 1,  0.0   , 0.0
 2,  0.0015875 , 0.0
 3,  0.003175 , 0.0
 4,  0.0   , 0.005
 5,  0.003175 , 0.005
 6,  0.0   , 0.01
 7,  0.0015875 , 0.01
 8,  0.003175 , 0.01
ELEMENTS
1
1 1 1 2 3 5 8 7 6 4
LOAD CASES
1
1.0
PLASTIC MATERIALS
1,1
298.0
1
186.9e9,  0.3,  0.0,  0.0,  0.0
GAUSS POINTS
3 3
RADIAL DISPLACEMENTS
3
1, 0.0
4, 0.0
6, 0.0
AXIAL DISPLACEMENTS
6
1, 0.0
2, 0.0
3, 0.0
6, 2.0e-4
7, 2.0e-4
8, 2.0e-4
TEMPERATURES
INTERPOLATION
    1,      1
0.0
0.0
950.0
SOLUTION PARAMETERS
950.0, 1e-18, 1e-10, 1e-6, 50, 14, 1
ELASTIC-PLASTIC
1,1,0,0,0.0,0.0
EXIT
```

Example 2

This set of input commands generates the finite element model for the first thermal cycle of the tapered test specimen (see Chapter 4). The model has 271 nodes and 72 elements. Displacement boundary condition and temperature data are given for 8 time steps. There are 15 subincrement time steps (14 subincrements). The TWO PHASE input command is used here to model the phase transformation strain behavior of maraging steel. All the nodes which lie on the Z axis are radially constrained, and the nodes which lie on z = 0.0 and .012 m are axially constrained. The temperatures in this model are defined with 25 Z coordinate data points for each of the 8 time steps. The load vector convergence tolerance is 10^{-18} and up to 50 equilibrium iterations are allowed. After the last time step in the analysis, a restart file called Cyc.dat is written with the SAVE command. Another thermal cycling analysis can be performed with data saved in this file. Geometric output data are written to the file Geom.dat and output at each time step is written to the files Plt1.dat through Plt8.dat.

```
TITLE
 72 ELEMENT; Tapered test specimen analysis; 1st pulse
NODES
 271
 1              0               0
 2              .000205         0
 3              .00041          0
 4              .000615         0
 5              .00082          0
 6              .001025         0
 7              .00123          0
 8              0               2.50009E-04
 9              .00041          2.50009E-04
 10             .00082          2.50009E-04
 11             .00123          2.50009E-04
 12             0               5.00018E-04
 13             .000205         5.00018E-04
 14             .00041          5.00018E-04
 15             .000615         5.00018E-04
 16             .00082          5.00018E-04
 17             .001025         5.00018E-04
 18             .00123          5.00018E-04
 19             0               7.50027E-04
 20             4.100255E-04                    7.50027E-04
 21             8.20051E-04     7.50027E-04
 22             1.230076E-03                    7.50027E-04
 23             0               1.000036E-03
 24             2.050255E-04                    1.000036E-03
 25             4.10051E-04     1.000036E-03
 26             6.150765E-04                    1.000036E-03
 27             8.201021E-04                    1.000036E-03
 28             1.025128E-03                    1.000036E-03
 29             1.230153E-03                    1.000036E-03
 30             0               1.25004E-03
 31             4.105527E-04                    1.25004E-03
 32             8.211054E-04                    1.25004E-03
 33             1.231181E-03                    1.250043E-03
 34             0               1.500044E-03
 35             2.055272E-04                    1.500044E-03
 36             4.110543E-04                    1.500044E-03
 37             6.165815E-04                    1.500044E-03
 38             8.221086E-04                    1.500044E-03
 39             1.027636E-03                    1.500044E-03
 40             1.233163E-03                    1.500044E-03
 41             0               1.750029E-03
 42             4.121938E-04                    1.750029E-03
 43             8.243877E-04                    1.750029E-03
 44             1.236105E-03                    1.750036E-03
 45             0               2.000014E-03
 46             2.066667E-04                    2.000014E-03
 47             4.133333E-04                    2.000014E-03
 48             .00062          2.000014E-03
 49             8.266667E-04                    2.000014E-03
 50             1.033333E-03                    2.000014E-03
 51             .00124          2.000014E-03
 52             0               2.250029E-03
 53             4.143349E-04                    2.250029E-03
 54             8.286697E-04                    2.250029E-03
 55             1.243005E-03                    2.250029E-03
 56             0               2.500045E-03
 57             2.076682E-04                    2.500045E-03
```

58	4.153364E-04		2.500045E-03
59	6.230045E-04		2.500045E-03
60	8.306727E-04		2.500045E-03
61	1.038341E-03		2.500045E-03
62	1.246009E-03		2.500045E-03
63	0	2.750055E-03	
64	4.16632E-04	2.750055E-03	
65	8.33264E-04	2.750055E-03	
66	1.249896E-03		2.750055E-03
67	0	3.000065E-03	
68	2.089638E-04		3.000065E-03
69	4.179277E-04		3.000065E-03
70	6.268915E-04		3.000065E-03
71	8.358554E-04		3.000065E-03
72	1.044819E-03		3.000065E-03
73	1.253783E-03		3.000065E-03
74	0	3.250059E-03	
75	4.195383E-04		3.250059E-03
76	8.390766E-04		3.250059E-03
77	1.258615E-03		3.250059E-03
78	0	3.500053E-03	
79	2.105745E-04		3.500053E-03
80	4.21149E-04	3.500053E-03	
81	6.317235E-04		3.500053E-03
82	8.42298E-04	3.500053E-03	
83	1.052873E-03		3.500053E-03
84	1.263447E-03		3.500053E-03
85	0	3.750027E-03	
86	4.230745E-04		3.750027E-03
87	8.461489E-04		3.750027E-03
88	1.269223E-03		3.750027E-03
89	0	.004	
90	.0002125	.004	
91	.000425	.004	
92	.0006375	.004	
93	.00085	.004	
94	.0010625	.004	
95	.001275	.004	
96	0	4.250068E-03	
97	4.270838E-04		4.250068E-03
98	8.541676E-04		4.250068E-03
99	1.281251E-03		4.250068E-03
100	0	4.500136E-03	
101	2.145838E-04		4.500136E-03
102	4.291677E-04		4.500136E-03
103	6.437515E-04		4.500136E-03
104	8.583353E-04		4.500136E-03
105	1.072919E-03		4.500136E-03
106	1.287503E-03		4.500136E-03
107	0	4.750204E-03	
108	4.312516E-04		4.750204E-03
109	8.625032E-04		4.750204E-03
110	1.293755E-03		4.750204E-03
111	0	5.000272E-03	
112	2.166678E-04		5.000272E-03
113	4.333357E-04		5.000272E-03
114	6.500035E-04		5.000272E-03
115	8.666713E-04		5.000272E-03
116	1.083339E-03		5.000272E-03
117	1.300007E-03		5.000272E-03
118	0	5.250297E-03	
119	4.35899E-04	5.250297E-03	

120	8.71798E-04	5.250297E-03	
121	1.306631E-03		5.250329E-03
122	0	5.500321E-03	
123	2.192312E-04		5.500321E-03
124	4.384624E-04		5.500321E-03
125	6.576935E-04		5.500321E-03
126	8.769246E-04		5.500321E-03
127	1.096156E-03		5.500321E-03
128	1.315387E-03		5.500321E-03
129	0	5.750161E-03	
130	4.425645E-04		5.750161E-03
131	8.85129E-04	5.750161E-03	
132	1.326526E-03		5.750219E-03
133	0	.006	
134	2.233333E-04		.006
135	4.466667E-04		.006
136	.00067	.006	
137	8.933333E-04		.006
138	1.116667E-03		.006
139	.00134	.006	
140	0	6.250687E-03	
141	4.51576E-04	6.250687E-03	
142	9.031519E-04		6.250687E-03
143	1.354728E-03		6.250687E-03
144	0	6.501374E-03	
145	2.282427E-04		6.501374E-03
146	4.564853E-04		6.501374E-03
147	6.84728E-04	6.501374E-03	
148	9.129706E-04		6.501374E-03
149	1.141213E-03		6.501374E-03
150	1.369456E-03		6.501374E-03
151	0	6.75206E-03	
152	4.613945E-04		6.75206E-03
153	9.22789E-04	6.75206E-03	
154	1.384184E-03		6.75206E-03
155	0	7.002747E-03	
156	2.331518E-04		7.002747E-03
157	4.663037E-04		7.002747E-03
158	6.994555E-04		7.002747E-03
159	9.326073E-04		7.002747E-03
160	1.165759E-03		7.002747E-03
161	1.398911E-03		7.002747E-03
162	0	7.253214E-03	
163	4.722005E-04		7.253214E-03
164	9.44401E-04	7.253214E-03	
165	1.413624E-03		7.253424E-03
166	0	7.503681E-03	
167	2.390487E-04		7.503681E-03
168	4.780973E-04		7.503681E-03
169	7.17146E-04	7.503681E-03	
170	9.561946E-04		7.503681E-03
171	1.195243E-03		7.503681E-03
172	1.434292E-03		7.503681E-03
173	0	7.751841E-03	
174	4.907153E-04		7.751841E-03
175	9.814306E-04		7.751841E-03
176	1.466424E-03		7.752713E-03
177	0	.008	
178	2.516667E-04		.008
179	5.033334E-04		.008
180	.000755	.008	
181	1.006667E-03		.008

182	1.258333E-03		.008
183	.00151	.008	
184	0	8.271985E-03	
185	5.43089E-04	8.271985E-03	
186	1.086178E-03		8.271985E-03
187	1.599795E-03		8.284908E-03
188	0	8.543968E-03	
189	2.914223E-04		8.543968E-03
190	5.828447E-04		8.543968E-03
191	8.74267E-04	8.543968E-03	
192	1.165689E-03		8.543968E-03
193	1.457112E-03		8.543968E-03
194	1.748534E-03		8.543968E-03
195	0	8.771984E-03	
196	6.474432E-04		8.771984E-03
197	1.294886E-03		8.771984E-03
198	1.940483E-03		8.773553E-03
199	0	8.999999E-03	
200	3.560209E-04		8.999999E-03
201	7.120417E-04		8.999999E-03
202	1.068063E-03		8.999999E-03
203	1.424083E-03		8.999999E-03
204	1.780104E-03		8.999999E-03
205	2.136125E-03		8.999999E-03
206	0	9.228818E-03	
207	7.779322E-04		9.228818E-03
208	1.555864E-03		9.228818E-03
209	2.333797E-03		9.228818E-03
210	0	9.457639E-03	
211	4.219114E-04		9.457639E-03
212	8.438227E-04		9.457639E-03
213	1.265734E-03		9.457639E-03
214	1.687645E-03		9.457639E-03
215	2.109557E-03		9.457639E-03
216	2.531468E-03		9.457639E-03
217	0	9.728819E-03	
218	8.822863E-04		9.728819E-03
219	1.764573E-03		9.728819E-03
220	2.701176E-03		9.705706E-03
221	0	.01	
222	4.60375E-04	.01	
223	9.2075E-04	.01	
224	1.381125E-03		.01
225	.0018415	.01	
226	2.301875E-03		.01
227	2.76225E-03	.01	
228	0	.01025	
229	9.2075E-04	.01025	
230	.0018415	.01025	
231	2.76225E-03	.01025	
232	0	.0105	
233	4.60375E-04	.0105	
234	9.2075E-04	.0105	
235	1.381125E-03		.0105
236	.0018415	.0105	
237	2.301875E-03		.0105
238	2.76225E-03	.0105	
239	0	.01075	
240	9.2075E-04	.01075	
241	.0018415	.01075	
242	2.76225E-03	.01075	
243	0	.011	

```
 244             4.60375E-04    .011
 245             9.2075E-04     .011
 246             1.381125E-03                   .011
 247             .0018415       .011
 248             2.301875E-03                   .011
 249             2.76225E-03    .011
 250             0              .01125
 251             9.2075E-04     .01125
 252             .0018415       .01125
 253             2.76225E-03    .01125
 254             0              .0115
 255             4.60375E-04    .0115
 256             9.2075E-04     .0115
 257             1.381125E-03                   .0115
 258             .0018415       .0115
 259             2.301875E-03                   .0115
 260             2.76225E-03    .0115
 261             0              .01175
 262             9.2075E-04     .01175
 263             .0018415       .01175
 264             2.76225E-03    .01175
 265             0              .012
 266             4.60375E-04    .012
 267             9.2075E-04     .012
 268             1.381125E-03                   .012
 269             .0018415       .012
 270             2.301875E-03                   .012
 271             2.76225E-03    .012
ELEMENTS
 72
  1, 1,      1,      2,      3,      9,     14,     13,     12,      8
  2, 1,      3,      4,      5,     10,     16,     15,     14,      9
  3, 1,      5,      6,      7,     11,     18,     17,     16,     10
  4, 1,     12,     13,     14,     20,     25,     24,     23,     19
  5, 1,     14,     15,     16,     21,     27,     26,     25,     20
  6, 1,     16,     17,     18,     22,     29,     28,     27,     21
  7, 1,     23,     24,     25,     31,     36,     35,     34,     30
  8, 1,     25,     26,     27,     32,     38,     37,     36,     31
  9, 1,     27,     28,     29,     33,     40,     39,     38,     32
 10, 1,     34,     35,     36,     42,     47,     46,     45,     41
 11, 1,     36,     37,     38,     43,     49,     48,     47,     42
 12, 1,     38,     39,     40,     44,     51,     50,     49,     43
 13, 1,     45,     46,     47,     53,     58,     57,     56,     52
 14, 1,     47,     48,     49,     54,     60,     59,     58,     53
 15, 1,     49,     50,     51,     55,     62,     61,     60,     54
 16, 1,     56,     57,     58,     64,     69,     68,     67,     63
 17, 1,     58,     59,     60,     65,     71,     70,     69,     64
 18, 1,     60,     61,     62,     66,     73,     72,     71,     65
 19, 1,     67,     68,     69,     75,     80,     79,     78,     74
 20, 1,     69,     70,     71,     76,     82,     81,     80,     75
 21, 1,     71,     72,     73,     77,     84,     83,     82,     76
 22, 1,     78,     79,     80,     86,     91,     90,     89,     85
 23, 1,     80,     81,     82,     87,     93,     92,     91,     86
 24, 1,     82,     83,     84,     88,     95,     94,     93,     87
 25, 1,     89,     90,     91,     97,    102,    101,    100,     96
 26, 1,     91,     92,     93,     98,    104,    103,    102,     97
 27, 1,     93,     94,     95,     99,    106,    105,    104,     98
 28, 1,    100,    101,    102,    108,    113,    112,    111,    107
 29, 1,    102,    103,    104,    109,    115,    114,    113,    108
 30, 1,    104,    105,    106,    110,    117,    116,    115,    109
 31, 1,    111,    112,    113,    119,    124,    123,    122,    118
 32, 1,    113,    114,    115,    120,    126,    125,    124,    119
```

```
 33, 1,    115,    116,    117,    121,    128,    127,    126,    120
 34, 1,    122,    123,    124,    130,    135,    134,    133,    129
 35, 1,    124,    125,    126,    131,    137,    136,    135,    130
 36, 1,    126,    127,    128,    132,    139,    138,    137,    131
 37, 1,    133,    134,    135,    141,    146,    145,    144,    140
 38, 1,    135,    136,    137,    142,    148,    147,    146,    141
 39, 1,    137,    138,    139,    143,    150,    149,    148,    142
 40, 1,    144,    145,    146,    152,    157,    156,    155,    151
 41, 1,    146,    147,    148,    153,    159,    158,    157,    152
 42, 1,    148,    149,    150,    154,    161,    160,    159,    153
 43, 1,    155,    156,    157,    163,    168,    167,    166,    162
 44, 1,    157,    158,    159,    164,    170,    169,    168,    163
 45, 1,    159,    160,    161,    165,    172,    171,    170,    164
 46, 1,    166,    167,    168,    174,    179,    178,    177,    173
 47, 1,    168,    169,    170,    175,    181,    180,    179,    174
 48, 1,    170,    171,    172,    176,    183,    182,    181,    175
 49, 1,    177,    178,    179,    185,    190,    189,    188,    184
 50, 1,    179,    180,    181,    186,    192,    191,    190,    185
 51, 1,    181,    182,    183,    187,    194,    193,    192,    186
 52, 1,    188,    189,    190,    196,    201,    200,    199,    195
 53, 1,    190,    191,    192,    197,    203,    202,    201,    196
 54, 1,    192,    193,    194,    198,    205,    204,    203,    197
 55, 1,    199,    200,    201,    207,    212,    211,    210,    206
 56, 1,    201,    202,    203,    208,    214,    213,    212,    207
 57, 1,    203,    204,    205,    209,    216,    215,    214,    208
 58, 1,    210,    211,    212,    218,    223,    222,    221,    217
 59, 1,    212,    213,    214,    219,    225,    224,    223,    218
 60, 1,    214,    215,    216,    220,    227,    226,    225,    219
 61, 1,    221,    222,    223,    229,    234,    233,    232,    228
 62, 1,    223,    224,    225,    230,    236,    235,    234,    229
 63, 1,    225,    226,    227,    231,    238,    237,    236,    230
 64, 1,    232,    233,    234,    240,    245,    244,    243,    239
 65, 1,    234,    235,    236,    241,    247,    246,    245,    240
 66, 1,    236,    237,    238,    242,    249,    248,    247,    241
 67, 1,    243,    244,    245,    251,    256,    255,    254,    250
 68, 1,    245,    246,    247,    252,    258,    257,    256,    251
 69, 1,    247,    248,    249,    253,    260,    259,    258,    252
 70, 1,    254,    255,    256,    262,    267,    266,    265,    261
 71, 1,    256,    257,    258,    263,    269,    268,    267,    262
 72, 1,    258,    259,    260,    264,    271,    270,    269,    263
LOAD CASES
 8
 50e-6
 100e-6
 500e-6
 .005
 .05
 1.0
 4.0
 180.0
PLASTIC MATERIALS
 1,1
 298.0
 1
 186.9e9,  0.3,  0.0,  0.0,  0.0
TWO PHASE
 10.1E-6,17.7E-6,968.0,1008.0,473.0,373.0,7.523E-3
GAUSS POINTS
 3 3
RADIAL DISPLACEMENTS
 49
 1, 0.0, 0.0, 0.0, 0.0, 0.0, 0.0, 0.0, 0.0
```

```
 8, 0.0, 0.0, 0.0, 0.0, 0.0, 0.0, 0.0, 0.0
 12, 0.0, 0.0, 0.0, 0.0, 0.0, 0.0, 0.0, 0.0
 19, 0.0, 0.0, 0.0, 0.0, 0.0, 0.0, 0.0, 0.0
 23, 0.0, 0.0, 0.0, 0.0, 0.0, 0.0, 0.0, 0.0
 30, 0.0, 0.0, 0.0, 0.0, 0.0, 0.0, 0.0, 0.0
 34, 0.0, 0.0, 0.0, 0.0, 0.0, 0.0, 0.0, 0.0
 41, 0.0, 0.0, 0.0, 0.0, 0.0, 0.0, 0.0, 0.0
 45, 0.0, 0.0, 0.0, 0.0, 0.0, 0.0, 0.0, 0.0
 52, 0.0, 0.0, 0.0, 0.0, 0.0, 0.0, 0.0, 0.0
 56, 0.0, 0.0, 0.0, 0.0, 0.0, 0.0, 0.0, 0.0
 63, 0.0, 0.0, 0.0, 0.0, 0.0, 0.0, 0.0, 0.0
 67, 0.0, 0.0, 0.0, 0.0, 0.0, 0.0, 0.0, 0.0
 74, 0.0, 0.0, 0.0, 0.0, 0.0, 0.0, 0.0, 0.0
 78, 0.0, 0.0, 0.0, 0.0, 0.0, 0.0, 0.0, 0.0
 85, 0.0, 0.0, 0.0, 0.0, 0.0, 0.0, 0.0, 0.0
 89, 0.0, 0.0, 0.0, 0.0, 0.0, 0.0, 0.0, 0.0
 96, 0.0, 0.0, 0.0, 0.0, 0.0, 0.0, 0.0, 0.0
 100, 0.0, 0.0, 0.0, 0.0, 0.0, 0.0, 0.0, 0.0
 107, 0.0, 0.0, 0.0, 0.0, 0.0, 0.0, 0.0, 0.0
 111, 0.0, 0.0, 0.0, 0.0, 0.0, 0.0, 0.0, 0.0
 118, 0.0, 0.0, 0.0, 0.0, 0.0, 0.0, 0.0, 0.0
 122, 0.0, 0.0, 0.0, 0.0, 0.0, 0.0, 0.0, 0.0
 129, 0.0, 0.0, 0.0, 0.0, 0.0, 0.0, 0.0, 0.0
 133, 0.0, 0.0, 0.0, 0.0, 0.0, 0.0, 0.0, 0.0
 140, 0.0, 0.0, 0.0, 0.0, 0.0, 0.0, 0.0, 0.0
 144, 0.0, 0.0, 0.0, 0.0, 0.0, 0.0, 0.0, 0.0
 151, 0.0, 0.0, 0.0, 0.0, 0.0, 0.0, 0.0, 0.0
 155, 0.0, 0.0, 0.0, 0.0, 0.0, 0.0, 0.0, 0.0
 162, 0.0, 0.0, 0.0, 0.0, 0.0, 0.0, 0.0, 0.0
 166, 0.0, 0.0, 0.0, 0.0, 0.0, 0.0, 0.0, 0.0
 173, 0.0, 0.0, 0.0, 0.0, 0.0, 0.0, 0.0, 0.0
 177, 0.0, 0.0, 0.0, 0.0, 0.0, 0.0, 0.0, 0.0
 184, 0.0, 0.0, 0.0, 0.0, 0.0, 0.0, 0.0, 0.0
 188, 0.0, 0.0, 0.0, 0.0, 0.0, 0.0, 0.0, 0.0
 195, 0.0, 0.0, 0.0, 0.0, 0.0, 0.0, 0.0, 0.0
 199, 0.0, 0.0, 0.0, 0.0, 0.0, 0.0, 0.0, 0.0
 206, 0.0, 0.0, 0.0, 0.0, 0.0, 0.0, 0.0, 0.0
 210, 0.0, 0.0, 0.0, 0.0, 0.0, 0.0, 0.0, 0.0
 217, 0.0, 0.0, 0.0, 0.0, 0.0, 0.0, 0.0, 0.0
 221, 0.0, 0.0, 0.0, 0.0, 0.0, 0.0, 0.0, 0.0
 228, 0.0, 0.0, 0.0, 0.0, 0.0, 0.0, 0.0, 0.0
 232, 0.0, 0.0, 0.0, 0.0, 0.0, 0.0, 0.0, 0.0
 239, 0.0, 0.0, 0.0, 0.0, 0.0, 0.0, 0.0, 0.0
 243, 0.0, 0.0, 0.0, 0.0, 0.0, 0.0, 0.0, 0.0
 250, 0.0, 0.0, 0.0, 0.0, 0.0, 0 0, 0.0, 0.0
 254, 0.0, 0.0, 0.0, 0.0, 0.0, 0.0, 0.0, 0.0
 261, 0.0, 0.0, 0.0, 0.0, 0.0, 0.0, 0.0, 0.0
 265, 0.0, 0.0, 0.0, 0.0, 0.0, 0.0, 0.0, 0.0
AXIAL DISPLACEMENTS
 14
 1, 0.0, 0.0, 0.0, 0.0, 0.0, 0.0, 0.0, 0.0
 2, 0.0, 0.0, 0.0, 0.0, 0.0, 0.0, 0.0, 0.0
 3, 0.0, 0.0, 0.0, 0.0, 0.0, 0.0, 0.0, 0.0
 4, 0.0, 0.0, 0.0, 0.0, 0.0, 0.0, 0.0, 0.0
 5, 0.0, 0.0, 0.0, 0.0, 0.0, 0.0, 0.0, 0.0
 6, 0.0, 0.0, 0.0, 0.0, 0.0, 0.0, 0.0, 0.0
 7, 0.0, 0.0, 0.0, 0.0, 0.0, 0.0, 0.0, 0.0
 265, 0.0, 0.0, 0.0, 0.0, 0.0, 0.0, 0.0, 0.0
 266, 0.0, 0.0, 0.0, 0.0, 0.0, 0.0, 0.0, 0.0
 267, 0.0, 0.0, 0.0, 0.0, 0.0, 0.0, 0.0, 0.0
 268, 0.0, 0.0, 0.0, 0.0, 0.0, 0.0, 0.0, 0.0
 269, 0.0, 0.0, 0.0, 0.0, 0.0, 0.0, 0.0, 0.0
```

```
 270, 0.0, 0.0, 0.0, 0.0, 0.0, 0.0, 0.0, 0.0
 271, 0.0, 0.0, 0.0, 0.0, 0.0, 0.0, 0.0, 0.0
TEMPERATURES
INTERPOLATION
  1,  25
 .0
 .0
 .0005
 .001
 .0015
 .002
 .0025
 .003
 .0035
 .004
 .0045
 .005
 .0055
 .006
 .0065
 .007
 .0075
 .008
 .0085
 .009
 .0095
 .010
 .0105
 .011
 .0115
 .012
    614.1,   973.3,  1046.6,  1046.5,  1043.5,   945.9,   584.9,   298.0
    614.0,   973.1,  1046.4,  1046.0,  1041.8,   943.6,   583.7,   298.0
    612.5,   970.0,  1042.8,  1042.0,  1036.5,   936.5,   580.2,   298.0
    607.9,   960.5,  1031.8,  1031.4,  1027.4,   924.8,   574.4,   298.0
    602.1,   948.2,  1017.9,  1017.8,  1015.0,   908.5,   566.5,   298.0
    596.0,   935.5,  1003.5,  1003.1,  1000.0,   887.6,   556.5,   298.0
    588.5,   919.7,   986.0,   985.6,   982.5,   862.3,   544.5,   298.0
    579.6,   901.3,   965.5,   965.3,   962.9,   832.9,   530.9,   298.0
    570.0,   881.1,   943.3,   943.3,   941.4,   799.6,   515.7,   298.0
    560.4,   861.1,   921.2,   921.5,   917.7,   762.8,   499.2,   298.0
    553.0,   845.5,   903.8,   901.4,   890.1,   722.9,   481.5,   298.0
    536.4,   810.9,   865.8,   865.2,   856.4,   680.0,   462.6,   298.0
    519.2,   774.9,   826.0,   825.8,   816.2,   635.5,   443.4,   298.0
    502.2,   739.2,   786.6,   786.1,   766.8,   590.4,   423.9,   298.0
    485.2,   703.6,   747.0,   743.3,   702.7,   545.0,   404.4,   298.0
    460.0,   650.4,   687.6,   676.9,   620.2,   500.1,   385.1,   298.0
    407.9,   540.0,   565.9,   558.9,   527.2,   458.2,   367.2,   298.0
    353.6,   422.8,   437.2,   440.5,   450.0,   426.1,   353.5,   298.0
    325.1,   359.7,   367.3,   372.6,   399.5,   403.9,   344.0,   298.0
    314.5,   335.8,   340.6,   344.2,   369.4,   387.6,   336.9,   298.0
    312.0,   330.0,   333.9,   335.4,   351.5,   373.4,   330.8,   298.0
    312.0,   330.0,   333.7,   333.9,   339.8,   358.8,   324.5,   298.0
    312.0,   330.0,   333.7,   333.7,   331.0,   343.9,   318.0,   298.0
    312.0,   330.0,   333.7,   333.0,   322.1,   328.7,   311.4,   298.0
    311.9,   329.9,   333.0,   326.9,   311.0,   313.4,   304.7,   298.0
SOLUTION PARAMETERS
 298.0, 1e-18, 1e-10, 1e-6, 50, 14, 1
ELASTIC-PLASTIC
 1,1,0,0,0.0,0.0
SAVE
Cyc.dat
```

```
AFESAPLT
Geom.dat
Plot.dat
Plt2.dat
Plt3.dat
Plt4.dat
Plt5.dat
Plt6.dat
Plt7.dat
Plt8.dat
EXIT
```